Faculty of Science

Department of Physics and Astronomy

Development of Geopolymer Systems for High Temperature Applications

Les Vickers

This thesis is presented for the degree of

Doctor of Philosophy

of

Curtin University

October 2015

Declaration

To the best of my knowledge and belief this thesis contains no material previously published by any other person except where due acknowledgement has been made.

This thesis contains no material which has been accepted for the award of any other degree or diploma in any university.

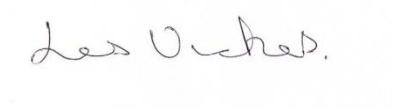

Signature

Date: 19 October 2015

Dedication

The Bomber Command of the Royal Air Force lost 55 573 members from a total of 120 000 who served during World War Two. Most who flew were very young, the great majority still in their late teens. Crews came from across the globe – from the UK, Canada, Australia, New Zealand and all corners of the Commonwealth, as well as from occupied countries including Poland, France and Czechoslovakia.

The young men of Bomber Command faced dangers that today we can barely imagine, all in defence of our freedom. Their sacrifice and extraordinary courage should never be forgotten.

This sacrifice was not recognised by successive governments until funds were raised by public subscription to erect a memorial to these men. The Bomber Command Memorial was opened in Green Park, London on 28th June 2012.

IN MEMORY

Able Seaman Arthur Leslie Holland, KIA 29 May 1940 on HMS Jaguar off Dunkirk.

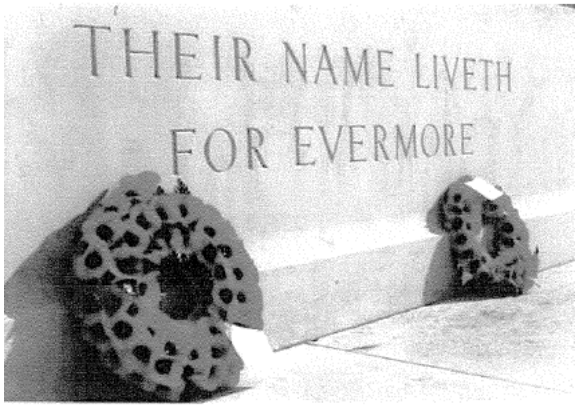

Abstract

Geopolymers are amorphous three dimensional inorganic structures based on silicon (SiO_4) and aluminium (AlO_4) tetrahedra. The bonding and composition of this inorganic structure suggests that it could be resistant to heat making it attractive for thermal and fire resistant applications. These applications can range from refractory foams through to binders for woven textiles, coatings and monolithic cast components such as fire resistant tunnel linings.

This thesis describes the research carried out to develop suitable geopolymer systems for thermal applications. The hypothesis that reducing the target Si:Al (molar) of a Collie fly ash based geopolymer to less than 2 to give improved thermal properties was tested with concomitant increase in compressive strength after firing to 1000^{o}C and the near elimination of expansive events at high temperature being achieved.

The overall chemical composition and phase analysis of the fly ash and their manipulation to give the values of available amorphous phases is critical to the manufacture of thermally resistant components. A targeted geopolymer Si: Al of 1.82 was selected based on a balance between compressive strength and fired thermal shrinkage.

The following properties were determined before and after firing to assist in the characterisation of specimens: compressive strength and density, thermal expansion, thermal conductivity, porosity, SEM imaging and EDS and XRD.

The addition of alumina and wollastonite thermally stable fillers at up to 10 vol. % to this base system showed further reduced thermal shrinkage and provided improvements in compressive strength and flexural strength in the case of wollastonite. Thermal shrinkage was reduced to less than 2% in these systems.

The addition of wollastonite increased retained flexural strength after firing at 1000^{o}C. Inclusion of wollastonite also showed a slower rate of macropore formation during firing, which can possibly be attributed to reductions in viscous flow and resulting lower shrinkage of the system.

Graded alumina was added at 41 and 51 vol. % together with a fibre tri-blend (polypropylene, wollastonite, and basalt fibres) to produce heat resistant composites which were also compression tested in-situ at elevated temperature. Thermal shrinkage of these composites was less than 1%. The in-situ testing showed a tenfold increase in strain to failure when tested at elevated temperature which was accompanied by a two fold increase in compressive strength. The addition of graded alumina extended the temperature for unrestricted flow from 320^{o}C for paste alone to 730^{o}C.

Polypropylene fibres were also added to mitigate spalling by sacrificial degradation to leave an extended pore network facilitating the escape of free water as the temperature increased.

Thermal post curing of paste, filled and composite samples up to 250^{o}C was undertaken to give controlled stabilisation (i.e. reducing shrinkage leading to crack control) of the system by controlled water loss prior to firing. Compressive strength properties improved after the post cure cycle. This may be attributed to the reactivation of the geopolymer reaction producing more reaction product, due to the alkaline pore solution, which is able to bind the system components better. Also the slow controlled temperature gradients during post curing should reduce crack initiation mechanisms due to dehydration processes.

Fire testing on 50 mm thick samples was undertaken in compliance with Australian Standard AS 1530.4. The composites filled with graded alumina retained their integrity after a 3 hour exposure time on the test furnace showing few fine cracks on both hot and cold faces. However, the presence of alumina and low water content contributed to reduced fire ratings by up to 60% compared to tested paste and lightly filled composites, which showed wider cracks on both hot and cold faces. The fire rating appears to be controlled by the thermal conductivity of the system and the water content. The thermal conductivity is also affected by water content. In the test methodology used the commencement and extent of the dehydration plateau on the test curve show the effect of water content. Beyond the plateau the thermal conductivity of a now dry specimen takes precedent. This is a convoluted mechanism which may be modified by the added water content and the amount and thermal conductivity of the aggregate.

The outcomes from this work suggest that fly ash geopolymer composites suitable for thermal applications can be produced. When compared to OPC based systems geopolymers showed extended thermal resistance (from 500^{o}C to 800^{o}C). This is attributed to stability of the geopolymer structure compared to the hydrated structure of OPC which loses water on heating. Replacing this OPC "lost" water results in expansive reactions which further weaken the structure. Most changes occurring above 500^{o}C in OPC are considered irreversible. The nature of the aggregates used also play a crucial role in thermal resistance.

The targeted areas of application for these types of products are not driven predominantly by price but by technical performance. In these areas geopolymer systems will compare favourably across the board.

Publications and Presentations

1. Performance of fibre reinforced, low density metakaolin geopolymers under simulated fire conditions. Rickard, W. D. A., Vickers, L. & van Riessen, A. *Applied Clay Science,* 73 (2013)**,** 71-77.

2. Strategies to control the high temperature shrinkage of fly ash based geopolymers. Les Vickers, William D.A. Rickard, Arie van Riessen. Thermochimica Acta, 580 (2014), 20–27.

3. A comparison between different foaming methods for the synthesis of light weight geopolymers. Masi, M., Rickard, W. D. A., Vickers, L. Bignozzi, M.C., van Riessen, A.. Ceramics International, 40 (2014), 13891-13902.

4. Fire Resistant Geopolymers, Role of Fibres and Fillers to Enhance Thermal Properties. Les Vickers, Arie van Riessen, William D.A. Rickard. Springer Briefs in Materials, 2015 ISBN 978-981-287-310-1; DOI 10.1007/978-981-287-311-8.

5. The Effect of Speciality Fibres and Fillers on the Thermal Properties of Fly Ash based Geopolymers. Les Vickers, William D.A. Rickard, Arie van Riessen. 10th Pacific Rim Conference on Ceramic and Glass Technology. June 2013, San Diego, USA

6. Thermal Properties of Geopolymers. Les Vickers, William D.A. Rickard, Arie van Riessen. CAMS 2014, Sydney, Australia.

7. Fire Resistant Fly Ash based Geopolymers. Les Vickers, Arie van Riessen, William D.A. Rickard. Geopolymers: The route to eliminate waste and emissions in ceramic and cement manufacturing. May 2015, Hernstein, Austria.

8. Controlling Thermal Properties for Enhanced Fire Resistance of Geopolymers. Les Vickers, Arie van Riessen, William D.A. Rickard. PACRIM 2015, September, Jeju, South Korea

Acknowledgements

I would like to acknowledge and offer thanks to the many people who have helped me during my journey to a PhD. This journey of discovery would not have been possible without their support and contributions.

First and foremost I wish to acknowledge the immeasurable contribution of my supervisor, Professor Arie van Riessen. Through his encouragement, guidance and friendship he opened my mind to many facets of the scientific process. His support has been critical to the completion of this thesis.

My wife, Dawne, who encouraged me to “do something different” for my thesis deserves a very special mention. For almost four years she has given me her unstinting support and love on my journey to a PhD. She will now be able to travel the world!

Coming back to university at a late age was something of a culture shock and I acknowledge the debt I owe to many people in the Physics department at Curtin University. Firstly, Dr. Will Rickard played an important role with many practical aspects of my research. He deserves my deepest thanks. I would also like to thank Dr. Cat Kealley, Dr. Xiaodong (Tony) Wang, Emily Xie, Elaine Miller, Glen Lawson, Ming Lim, Mark Winstanley, Ketesse Hansen and Melat Habtemariam as well as other staff and students for their assistance with technical equipment in the laboratories. One fellow HDR student who deserves a special mention is Marta Galindo Romero, physicist, talented artist and “computer wizard” who guided me through the maze of computer issues I encountered on my journey.

I would also like to thank Giulia Masi from the University of Bologna for testing samples using mercury intrusion porosimetry, Dr. Zhu Pan from the University of Western Sydney for high temperature in-situ compressive testing and Joris Bracke from IMCE, Belgium for Young’s modulus determination.

Lastly I would like to acknowledge the organisations and facilities that supported my research. Curtin University and the Centre for Sustainable Resource Processing provided me with financial support. Finally I would like to acknowledge the facilities of the Centre for Materials Research and the Curtin University Microscopy and Microanalysis facility.

“Those who dwell, as scientists or laymen, among the beauties and mysteries of the earth, are never alone or weary of life.”

Rachel Carson, American marine biologist, 1907-1964

Table of Contents

List of Figures

List of Tables

Abbreviations

AAC	Alkali Activated Cement
AIP	Aluminosilicate Inorganic Polymer
ARG	Alkali resistant glass
AS	Australian Standard
ASR	Alkali Silica Reaction
ASTM	American Society for Testing and Materials
BSE	Back scattered electron
CFRC	Carbon Fibre Reinforced Concrete
CH	Calcium Hydroxide
CMF	Carbon Micro fibre
CNF	Carbon Nano-fibre
CNT	Carbon Nano-tubes
C_2S	Dicalcium Silicate
C_3A	Tricalcium Aluminate
C_3S	Tricalcium Silicate
CSH	Calcium Silicate Hydrate
COTE/CTE	Coefficient of Thermal Expansion
DEF	Delayed Etteringite Formation
DSC	Differential Scanning Calorimetry
DTA	Differential Thermal Analysis
ECC	Engineered Cementitious Composite
EDS	Energy Dispersive X-ray Spectroscopy
FAA	Federal Aviation Administration
FTIR	Fourier Transformation Infra-Red Spectroscopy
FRC	Fibre reinforced Composite

FRP	Fibre reinforced plastics
FWHM	Full width half maximum
GBFS	ground blast furnace slag
GDM	Glass Diffraction Maximum
GRP	Glass Reinforced Plastic
HCM	Hydrocarbon Modified (curve)
HPC	High performance concrete
HSC	High strength concrete
ICP- MS	Inductively Coupled Plasma Mass Spectrometry
ITZ	Interfacial transition zone
LOI	Loss on ignition
M	Molar
M^+	Alkali metal group cation
MAS	Magic Spinning Angle
MWCNT	Multiwall Carbon Nanotubes
NMR	Nuclear Magnetic Resonance
OH&S	Occupational Health and Safety
OPC	Ordinary Portland cement
pbw	parts by weight
PCE	Polycarboxylate ether
PCM	Partial Charge Method
PVOH	Polyvinyl Alcohol
QXRD	Quantitative X-ray diffraction
R	Alkali metal group atom
RABT	Richtlinien fur die Ausstattung und den Betrieb von Strassenttunnein
SA	Sodium Aluminate

SAXS	Small Angle X-ray scattering
SCC	Self-Compacting Cement
SCM	Supplementary cementitious material
SEM	Scanning Electron Microscopy
SFRC	Steel fibre reinforced concrete
SHCC	Strain hardening cementitous composite
SMF	Sulphonated melamine formaldehyde
SNF	Sulphonated naphthalene formaldehyde
TAS	Total alkali silica (classification)
TGA	Thermogravimetric analysis
TMA	Thermo-Mechanical Analysis
tpa	tonnes per annum
UHMWPE	ultra high molecular weight polyethylene
uPVC	unplastised polyvinyl chloride
UV	Ultra-violet
VTOL	Vertical take-off and landing
w/c	water to cement ratio
XRD	X-ray diffraction
XRF	X-ray fluorescence
Z	Atomic number

CHAPTER 1

INTRODUCTION

1.1. Preamble

Geopolymers have been in service in the modern era since the 1960s when Glukhovsky in the Ukraine used alkali activated fly ash and slag to produce non-Portland cement concrete binders (Krivenko, 2005). Davidovits, beginning in the late 1970s carried out research to produce fire resistant binders suitable for the replacement of organic polymer binders. He introduced the term geopolymers for the range of products his team developed (1991). Geopolymers is used throughout this thesis to describe the reaction products of fly ash and alkaline activating solutions. These products contain alkali metals (sodium, potassium), aluminium and silicon in the binding entity. Terminology such as “Alkali Activated Materials”, “Aluminosilicate Inorganic Polymers” and “Alkali Activated Cement” is also used. Geopolymers are a subset of the alkali activated materials grouping

Geopolymers are inorganic condensation polymers based on aluminate and silicate entities. Typical sources of aluminosilicates are metakaolin and coal fly ash which are activated by alkaline media releasing the aluminate and silicate monomers which then condense to form the geopolymer. The resulting structures were initially elucidated by Davidovits (1989) as being sialates, sialate-siloxo, and sialate-disiloxo. They are based on silicon and aluminium centred tetrahedra with alkali metal ions providing charge balancing for the Al^{3+} centres (Barbosa et al., 2000a).

Geopolymers are a class of binding matrix with wide applicability from high strength concrete to low density foams (Hardjito and Rangan, 2005, Rickard et al., 2013). Their inorganic nature suggests utility in thermal applications including fire resistant products (Lyon, 1999, Rickard et al., 2013, Giancaspro et al., 2006).

The major impetus for geopolymer research has been environmental issues, particularly the potential replacement of Portland cement leading to reductions in carbon dioxide emissions from the Portland cement manufacturing process. The reduction in by-product stockpiles from energy generation (fly ash), metal smelting (slag and fume) and agriculture (rice hulls) by using these products as geopolymer precursers is an additional and important benefit. Fly ash and slags have a combined annual production of around 1300 million tonnes of which some already have captive markets including supplementary cementitious material in

OPC, which leaves a relatively small quantity (>50%) available for OPC replacement (Heidrich et al., 2013, Van Oss, 2014b).

The global output of Portland cement is estimated at 3800 million tonnes for 2013 (van Oss, 2014a). The replacement of Portland cement by geopolymer can therefore only account for a minor percentage of replacement (Scrivener, 2011).

In developing countries ready availability of fly ash and slag will be limited due to geographic and transportation issues. In these areas the use of more readily available aluminosilicate sources such as volcanic ashes and clays should be considered as geopolymer precursor alternatives to Portland cement in construction materials (Tchakoute Kouamoa et al., 2012, Xu and van Deventer, 2000).

Davidovits (2011) is a strong proponent of safer, less corrosive alkali activating systems for geopolymer manufacture. He believes that the use of “non-user friendly” systems has prevented the wider acceptance of geopolymer cement systems.

Geopolymers have been shown to exhibit improved durability compared to Portland cement products in areas of chemical resistance (Rostami and Brendley, 2003, Montes and Allouche, 2008, Bakharev, 2005b), thermal and fire resistance (Kong et al., 2007, Rickard et al., 2011, Provis, 2010). It is in these areas demanding better durability than that exhibited by existing products that geopolymers can find an effective market niche based on the fly ash quantities available.

Target applications can include coatings for existing structures based on reinforced concrete, steel and wood to upgrade fire resistance (Zhang et al., 2010, Temuujin et al., 2011, Temuujin et al., 2010). The manufacture of geopolymer based precast components for tunnels and other underground structures to enhance fire resistance is a viable market opportunity (Zhao and Sanjayan, 2012).

From a chemical durability perspective the use of geopolymers can enhance the service life of concrete components used in sewage, food processing and storage and chemical containment applications. Technical applications such as railroad sleepers require durability beyond that supplied by OPC in this application. In western Canada and northern USA freeze-thaw and chemical deterioration are major factors in OPC concrete sleeper failure.

There are an estimated 400 million concrete sleepers in the world rail system and between 2 and 5% require replacement every year. Geopolymer is one material being evaluated for this application (Ferdous, 2014). Figure 1.1 shows geopolymer replacement rail sleepers on the Sydney to Melbourne line.

Figure 1.1 Pre-stressed geopolymer rail sleepers installed as maintenance replacements (Gourley, 2014).

Rocla (figure 1.2) have developed a fibre reinforced spun cast geopolymer concrete pipe suitable for sewage handling.

Figure 1.2 Rocla geopolymer sewer pipes being installed (Gourley, 2014).

The application of geopolymers as binders for toxic, including radioactive, heavy metal based waste has attracted much research effort. These encapsulated systems are characterised by low leaching rates of the captured toxic metals(van Jaarsveld et al., 1997b, Nugteren et al., 2011).

The levels of a particular property required from geopolymers are formulation dependent and are tailored to specific applications. Optimum thermal resistant systems generally show much lower physical properties than binder systems developed for geopolymer concrete.

One major hurdle to the acceptance of geopolymer systems in the construction industry is the lack of national standards based on geopolymers. Existing standards are written to accommodate the usage of Portland cement which may not be totally relevant to geopolymer systems. The 28 day “standard “ cure time for OPC is a case in point;

geopolymers generally develop strength more rapidly and a seven day cure standard may be more appropriate.

A RILEM committee on alkali activated materials (TC 224-AAM) was established in 2007 with the goal of making recommendations to national standard organisations based on the current position and developing test methods for incorporation into the recommended standards. This committee reported in 2012 (van Deventer and Provis, 2014). A performance based approach to system formulation and testing was considered essential to these materials to enable scale up as a reliable method of concrete production.

1.2 Research Objectives.

The theme of this research is the development of geopolymer systems with utility at high temperatures for conditions that may be experienced in a fire protection or a refractory application. The systems must be processable (mixing, placing and curing) and show adequate physical and chemical properties for the chosen application. The influence of Si: Al (molar) in both the precursers and cured geopolymer has a significant effect on the resulting mechanical and thermal properties.

The range of thermal applications brings different thermal load demands to the geopolymer products. Refractory insulating products are exposed to long term elevated temperature conditions with gradual temperature changes, whilst fire resistant products are exposed to fast initial temperature increases with a few hours at maximum temperature. The cooling cycle after a fire may be rapid due to large quantities of water used to fight the fire or a slower decrease if the fire is allowed to die out due to fuel depletion. Rapid temperature changes can give rise to the formation of cracking due to a spread of thermal expansion/contraction events. These events are governed by the intrinsic thermal properties which also vary with temperature, the physical dimensions of components and the binder composition.

In order to optimise thermal properties, control of thermal expansion and retention/development of physical properties after elevated temperature exposure is desirable. The use of thermally stable (filler) materials to optimise thermal properties is

common place in other materials technology. The addition of inorganic fillers will modify the thermal expansion properties of polymers (Imerys Performance Minerals, 2010, Robinson, 2006).

The changes to the nature of the pore system with increasing temperature will have an effect on water transport through the geopolymer microstructure and hence influence the thermal properties.

Pore content and size distribution may be followed using Mercury Intrusion Porosimetry (MIP). A comparison of pore size obtained on cementitious material showed that results obtained from MIP were approximately three orders of magnitude smaller than the pore size observed in SEM images. (Kong et al. 2007).

The use of sacrificial polypropylene fibres at 0.25 to 0.5 vol% to act as pathway formers to allow moisture to readily escape in the event of a thermal excursion and reduce the incidence of explosive spalling occurring will be evaluated (Khoury, 2000).

Evaluations with inorganic particulate fillers at low volume additions have indicated a reduction in shrinkage after firing at temperatures up to 1000^{o}C. The reduction in shrinkage may have beneficial effects on the physical properties of fired systems with regards to crack formation and subsequent crack growth (Vickers et al., 2014).

The use of thermally stable aggregates (phase stable and exhibiting low coefficient of thermal expansion) in a suitable geopolymer matrix together with fibres to address both spalling and high temperature strength is the intended destination for this research (Barbosa and MacKenzie, 2003b).

Potential applications can be tunnel linings, panels for thermal insulation in wide ranging applications and thermally resistant concrete for nuclear power infrastructure and molten metal processing.

1.3 Research Significance.

Geopolymer formulated products for high temperature applications must be able to compete with existing products both technically and economically. For this to occur an in depth understanding of these geopolymer systems is required and the outcomes disseminated. The use of fly ash, an industrial by-product, in these systems is an ecological bonus.

Previous work was carried out on metakaolin based geopolymers where the lack of multiple phases, as is the case of fly ash, simplified the interpretation of experimental results. Work on fly ash systems used traditional quartz and granite aggregates(Kong and Sanjayan, 2010). The work in this thesis looks to extend this fly ash work by investigating the addition of thermally stable aggregates/fillers with high melting points, low thermal expansion properties and the absence of phase transitions in the temperature operating range.

1.4 Research Method

Previous work at Curtin University (Rickard, 2012) had used silicon to aluminium ratios in excess of 2 to produce fly ash based geopolymers and obtained large expansive events when using Collie fly ash. In this work this ratio is set at less than 2. This is expected to reduce these expansive events and improve thermal resistance. Figure 1.3 shows a schematic of the work flow involved.

This work cannot be an exhaustive investigation of all possible formulation permeations but is governed by readily available raw materials in Western Australia and test equipment availability.

1.5 Organisation of the Thesis.

Chapter 2 is a comprehensive literature review of geopolymers with major contributions on fibres, thermal properties and fire resistance of geopolymers. A background to geopolymers

compared to OPC, including chemistry, opens this chapter. Chapter 3 outlines the experimental methods and the raw materials used in research.

Chapter 4 presents the results of the raw material characterisation. Chapter 5 looks at the development of a thermally stable binder suitable for the incorporation of fillers and fibres. Chapter 6 investigates the influence of fillers and fibres on the geopolymerisation and thermal properties of the selected systems. Chapter 7 investigates the manufacture and properties of thermally resistant composites, whilst chapter 8 reports on the exposure of samples to a simulated fire exposure.

The outcomes of the above work are summarised in chapter 9 which also includes recommendations for future investigations.

Appendices are included to present supplementary information.

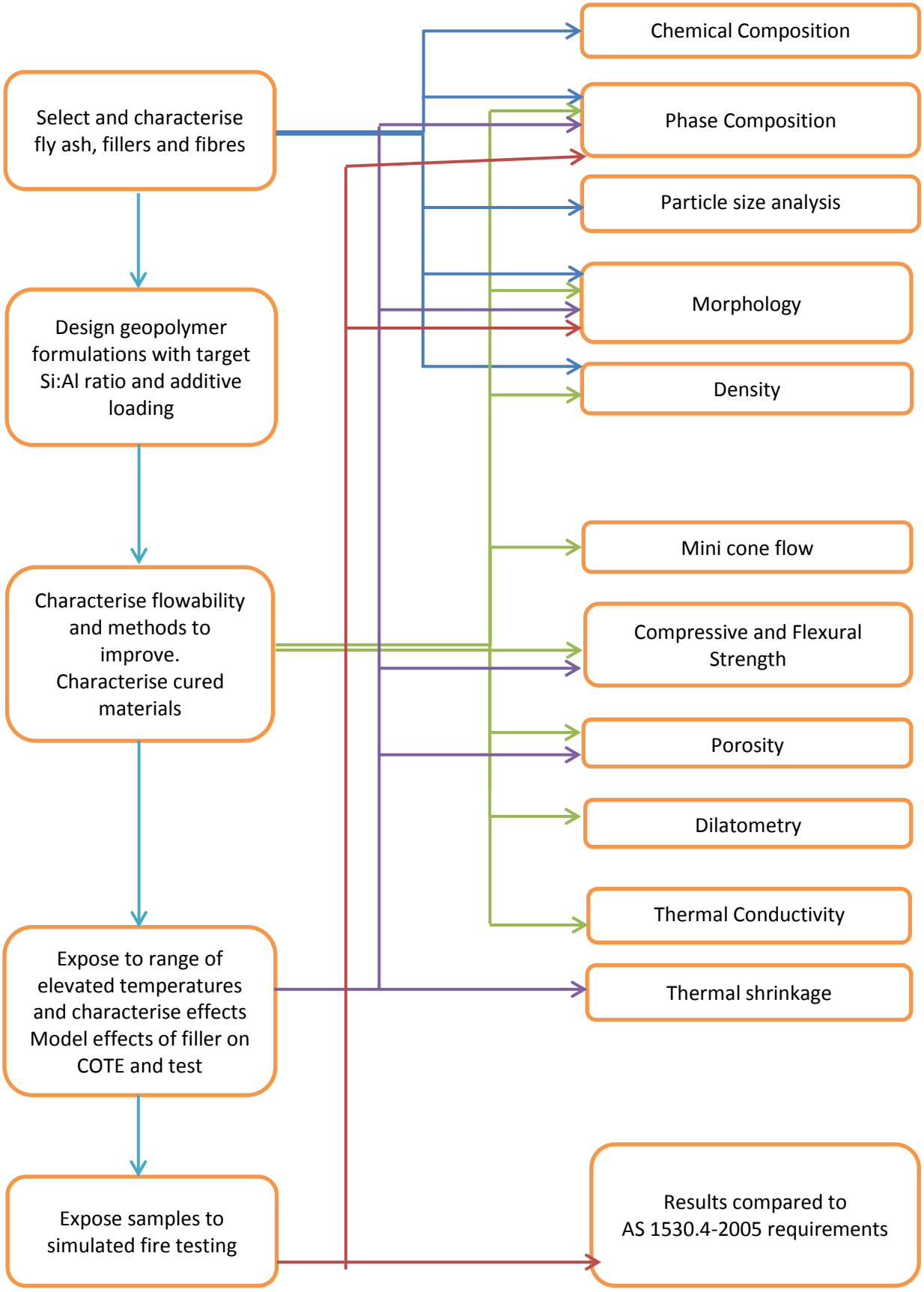

Figure 1.3 Work Flow

CHAPTER 2

Geopolymer Science and Technology Literature Review

This chapter is the basis for the following publication: Fire-Resistant geopolymers, Role of Fibres and Fillers to Enhance Thermal Properties. L. Vickers, A. van Riessen and W.D.A. Rickard Published by Springer Briefs in Materials, 2015. ISBN: 978-981-287-310-1.

2.1 Overview

Geopolymers, also referred to as Aluminosilicate Inorganic Polymers (AIP) and Alkali Activated Cement (AAC) are based on alkali soluble aluminium and silicon precursors (aluminosilicates). Structural differences and resulting properties of geopolymers can be explained by variation in the source silicon to aluminium amorphous molar ratio, alkali metal cation type and concentration, water content and curing regime amongst other variables in the geopolymer synthesis.

Figure 2.1 shows geopolymers to be part of the alkali activated family of cementitious materials, characterised by low calcium content. Early work by Purdon (1940) using sodium hydroxide solutions to activate ground blast furnace slags (GBFS) produced cementitous materials suitable for concrete production. Later workers showed that these materials were basically a calcium silicate hydrate based gel (Roy, 1999, Wang and Scrivener, 1995) with silicon present mainly in one dimensional chains and some substitution of aluminium for silicon and magnesium for calcium whereas the geopolymer gel is a three dimensional alkali aluminosilicate framework structure (Duxson et al., 2007). Calcium (~3 wt.%) in geopolymers acts as an accelerator for setting enabling ambient temperature curing of geopolymers to take place (Temuujin et al., 2009b). The defining characteristic of a geopolymer is that the binding phase consists of an alkali alumina silicate gel, with aluminium and silicon linked in a three dimensional tetrahedral gel framework of silicate and aluminate groups that is relatively resistant to dissolution in water. Charge balancing of the aluminate group is by alkali metal cations typically sodium and potassium.

Geopolymer may be considered a composite of partially reacted precursor, typically metakaolin or fly ash, solid reaction products, and pore space. Some of the pore space is filled with aqueous alkaline solution. The pore volume can be in the order of 1 to 40%, The solid reaction product is amorphous and is the inorganic polymer component (Maitland et al., 2011).

Geopolymers are inorganic materials based on the polymerisation of silicon and aluminium tetrahedra precursors in highly alkaline media with the alkali or alkaline earth metal cations providing charge balancing to the Al(IV) co-ordinated anion (Barbosa et al., 2000a). They are essentially amorphous in structure and can act as cementitous binders for mortars and concretes in the construction industry (Hardjito and Rangan, 2005), where they exhibit improved durability when compared to products based on Portland cement binders (Roy, 1999). This durability exhibits itself as superior chemical and heat, including fire, resistance. They have also been extensively researched as binders to immobilise toxic heavy metals e.g. from spent nuclear fuel and other toxic waste (Van Jaarsveld et al., 1997a) and as fabric laminating resins in the manufacture of high temperature composites (Lyon, 1999)

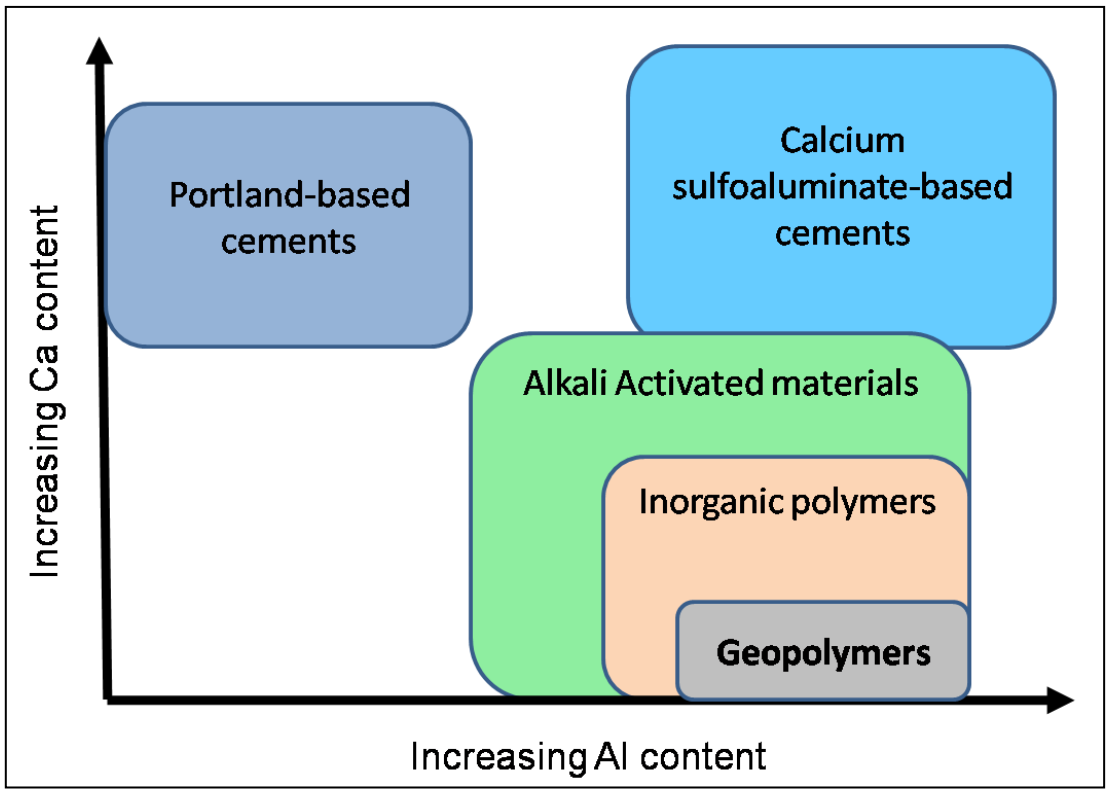

Figure 2.1 Schematic detailing of the grouping of geopolymers in terms of chemistry. Adapted from Provis (2014).

The impetus for the utilisation of geopolymers is their ability to consume readily available industrial by-products in their synthesis with the potential to reduce by-product stock piles, reduce dependency on shrinking natural resources and give a net reduction in carbon dioxide emissions from cement manufacture. World cement production in 2011 was

estimated at 3.4 billion tonnes (van Oss, 2012), which equates to carbon dioxide emissions attributed to clinker of 2.57 billion tonnes (Mehta and Meryman, 2009). Many of these industrial by-products are being stock piled in tailings dams which will contribute to environmental issues in the event of weather extremes such as high rain fall. These events can lead to overflowing and/or ruptured retaining walls with resultant flooding and water supply contamination. A case in point is the Kingston Fossil plant in Roane County, Tennessee in December 2008 when a period of twice average rainfall and freeze thaw cycles broke the retaining wall and deposited fly ash sludge over 12 hectares and up to 1.8 metres deep before spilling into the Emory river (Stephens, 2009).

The supply of suitable industrial by-products, particularly fly ash and blast furnace slag, is limited by location (place of production) and quantity. They are already being used as Supplementary Cementitious Materials (SCMs) to reduce the proportion of Portland cement used in concrete manufacture, which in turn reduces the available quantity for AAC binders. In the Third World production of fly ash and blast furnace slag is limited so alternative SCMs such as clays need to be developed for local cementitious binder production (Scrivener, 2011). The use of volcanic ashes is also a potentially useful raw material for AAC production (Lemougna et al., 2011).

Geopolymer precursors can be based on dehydroxylated clay i.e. metakaolin, and a wide range of industrial and agricultural by-products such as fly ash, aluminium and steel slags, spent metal treatment solutions (Nugteren et al., 2011), fume silicas from ceramic raw material preparation, rice husk ashes (Bernal et al., 2012b), and crushed glass (Naik, 2002). The precursors need to have significant amounts of aluminium and/or silicon entities in amorphous form to facilitate the alkali solubilisation and resulting geopolymer formation.

2.2 History of Geopolymers

Ancient mortars and concrete products have proven to be more durable and more resistant to acid attack and freeze-thaw cycles than products based on Ordinary Portland Cement (OPC) as shown by rapid failure of OPC repair materials on ancient concretes (Pacheco-Torgal et al., 2008b, Roy, 1999). The intrinsic properties of OPC based product leads to high permeability that enables water and other aggressive media to enter and take part in detrimental chemical reactions, particularly with the ever present calcium hydroxide (Pacheco-Torgal et al., 2008c). The Greeks and Romans used a concrete to construct buildings such as the Pantheon and the Coliseum. These concretes were based on cement derived from lime and pozzolans such as volcanic ash and clays. One theory for building the Cheops Pyramid at Gaza is the use of formed in-situ blocks based on alkali activated aluminosilicate materials (Demortier, 2004). Historically cementitious materials were being used in Sumeria (3600BC)(Bauer, 2007) Egypt (2500BC)(Davidovits, 2008c) , Rome (Davidovits and Davidovits, 1999, Davidovits, 2008b).

In 1940 Purdon carried out work on alkali activation of blast furnace slag. This work was based on 31 Belgian slags and used sodium hydroxide solutions of up to 10 wt. % concentration with maximum compressive strength (25 MPa for concrete) achieved in the range of 5 to 8 wt. % (pH values of 14.1 to 14.3). He also investigated the replacement of sodium hydroxide with blends of calcium hydroxide and sodium carbonate which react to produce sodium hydroxide in the presence of water. He showed that the sodium hydroxide liberated by the latter reaction brings about the setting of the slag. The addition of calcium hydroxide and sodium carbonate to the slag produced cement requiring only the addition of water to bring about setting. He also found that the alkali reactivity of the slag increased as the chilling temperature of the slag decreased with a corresponding increase in the amorphous content. Purdon proposed that the alkali acted as a catalyst for slag setting and hardening. This was confirmed by recovering all the added alkali from a set slag mortar. This explains the lower sodium hydroxide levels used here compared to geopolymer formation. He also identified one of the present drawbacks of geopolymer concrete manufacture – the use of corrosive alkaline solutions for the dissolution process (Purdon, 1940).

Glukhovsky and subsequently Krivenko in the USSR (Ukraine) from the 1950's onwards developed alkali activated binder systems due to the shortage of OPC raw materials in the then state controlled economy. Glukhovsky was the first to appreciate that the natural processes of the transformation of volcanic rocks into zeolites could be copied and carried out in cementitious systems to yield useful construction products. Glukhovsky analysed binders used by the Romans and Ancient Egyptians and based on this work developed binders called "soil cements". These were based on aluminosilicate containing slags mixed with alkali industrial waste. In the 1960's applications such as housing, railway sleepers, drainage and irrigation channels, flooring, and precast slabs and blocks were produced using these slag based systems (Krivenko, 2005).

Davidovits began investigating alkali activated cements following catastrophic fires in France in 1970 and 1973. The goal was to develop heat and fire resistant materials in the form of non-flammable "plastic like" materials. Davidovits gave the name geopolymers to these new materials which were predominantly based on metakaolin (Davidovits, 1989).

From the mid 1990s work by Palomo's group in Spain (1999), Rahier's (1997) work in Belgium and the group at the University of Melbourne (Xu and van Deventer, 2000, van Jaarsveld and van Deventer, 1999) began to de-mystify the geopolymer reaction kinetics and mechanisms. In the United States groups led by Balaguru (Lyon et al., 1997) and Kriven (2008) explored potential geopolymer applications in the fire resistant composite and refractory areas respectively. MacKenzie (Nicholson et al., 2005) in New Zealand has focussed on the synthesis and analysis, particularly NMR, of geopolymers. Sanjayan (Kong et al., 2005) at Monash University and van Riessen (2010) at Curtin University currently lead research teams carrying out geopolymer and precursor analysis and thermal property investigations with a strong emphasis on fire testing.

Geopolymer research is now wide spread both academically and industrially with greater emphasis being placed on application based research as commercialisation gathers momentum.

2.3 Portland cement (OPC) and concrete

The forerunner of Portland cement was developed in the late 18th century, when Smeaton calcined limestone and clay to form a cementitious material. Joseph Aspdin took out the patent for Portland cement in 1824. The Portland name was adopted because the colour of the hydrated cement was similar to that of limestone quarried at Portland in southern England. Over the next two hundred years it became the major construction material (Shi and Mo, 2008).

Portland cement initially gave variable properties due to the low calcination temperatures used to prepare the clinker which was finely ground and used as cement. In 1845 Isaac Johnson first burnt the raw materials at the required clinkering temperature to produce cement resembling the current era material (Gani, 1997).

The main application of OPC is to make concrete. Plain concrete made from OPC and aggregate is referred to as first generation concrete. Second generation concrete refers to steel bar reinforcement invented by Joseph Monier in 1849. Coignet patented a technique for reinforcing concrete using iron tirants. The first reinforced concrete bridge was built in 1889 in the Golden Gate Park in California (Li, 2011).

Prestressed concrete is referred to as third generation concrete. This was developed in the 1880's to overcome cracking in reinforced concrete. Prestressing is usually generated by the stretched reinforcing steel in a structural member. Prestressed concrete became accepted as a building material in Europe after WWII due to the shortage of steel. The Walnut Lane Memorial Bridge in Philadelphia, completed in 1951 was the first prestressed concrete structure in North America.

Compressive strength at an age of 28 days is the main design index for concrete due to concrete's use in structures mainly to resist compressive forces. The measurement of compressive strength is relatively easy and it is thought that other properties can be related to compressive strength. The pursuit of high compressive strength has been an important goal in concrete development.

Duff Adams in 1918 found that compressive strength of concrete is inversely proportional to the water-cement ratio (w/c). Hence a high compressive strength is obtained by reducing

the w/c ratio, but there is a minimum water requirement to maintain workability. For this reason progress in developing high compressive strength was slow prior to the 1960's. At that time 30 MPa compressive strength development was considered to be high strength concrete(Li, 2011).

Since the 1960's the development of high compressive strength has progressed due to two main factors, the invention of water reducing admixtures and the incorporation of mineral admixtures such as slag, fly ash and silica fume.

Water reducing admixtures help maintain good workability at low w/c ratios. The mineral admixtures have a small particle size and can react with calcium hydroxide, an hydration product in concrete, to give a denser microstructure. Silica fume also has a packing effect to further increase matrix density.

Concrete produced after the 1980's usually contains mineral and chemical admixtures so that the hydration mechanism and resulting hydration products and microstructure are very different to concrete produced without their addition. These new generation concretes are referred to as contemporary concrete (Li, 2011).

Two developments of note with contemporary concrete are self-compacting concrete (SCC) and high performance concrete (HPC). Concretes with compressive strengths of around 130 MPa are termed ultra-high performance concrete and are used in the latest generation of skyscrapers (Li, 2011).

SCC meets special requirements which cannot be achieved using conventional materials and techniques. The requirements may involve enhancement of installation techniques involving placement and compaction without segregation plus improved durability. SCC (with high flowability obtained with the addition of superplasticisers) is used to fill formwork, typically with closely spaced rebar, without the need for mechanical vibration. SCC was developed in Japan where highly reinforced concrete is required for earthquake resistance

It became clear that many concrete structures could not fulfil service demands due to a lack of durability. The development of HPC overcame some of these durability issues, but created specific issues when heat as in fire exposure became involved.

OPC is manufactured by milling raw materials such as limestone, clay and shale with an iron source. This blend is now fired in a rotary kiln at 1400 to 1500^{o}C. The resulting clinker is then cooled, ground again with gypsum, which acts as a set retarder, to give 90 to 95% of material finer than 325 mesh (10 to 15 µm median particle size). The alkali metal content is kept below 1% to minimise alkali silica reactions with added aggregates. Cement chemistry will vary from area to area because of variations in local raw materials. Typical ASTM C150 Portland cements are made up from 50 to 70% tricalcium silicate, (C_3S), 15 to 20% dicalcium silicate, (C_2S), 5 to 10% tricalcium aluminate, (C_3A), 5 to 15% ferrite phase and 3 to 5% gypsum (Vitro Minerals, 2010).

The presence of iron in conjunction with aluminium in the feedstock has a marked effect on liquid formation in the kiln, reducing the temperature from 2065^{o}C to the usual operating range of 1400 to 1500^{o}C (MacLaren and White, 2003).

Best quality cement requires the presence of tricalcium silicate (C_3S) and dicalcium silicate (C_2S) in the clinker (MacLaren and White, 2003). This paper also gives a comprehensive listing of the shorthand notations used to simplify descriptions of cement compositions. Both these materials react vigorously with water to produce the cement binder paste. Tricalcium silicate reacts and sets much faster than dicalcium silicate (hours verses days).

When cement hydrates the principle products formed are 50 to 70% calcium silicate hydrate (CSH), 10 to 15% ettringite (calcium sulfoaluminate) and 20 to 25% calcium hydroxide (CH). CSH is the strength building binder for concrete but the CH makes no contribution to strength and can lead to efflorescence and poor chemical resistance. Replacing cement with a pozzolan reduces the formation of CH (by dilution) whilst the pozzolan reacts with the remaining CH to form additional CSH binder with improvements in properties (Vitro Minerals, 2010).

All of the compounds capable of hardening do so at different rates and generate different quantities of heat per unit weight, but only silicates contribute to strength (Central Federal Lands Highway Division, 2008)

The typical heat generation stages due to cement hydration are shown in figure 2.2. During the initial hydration on mixing with water calcium and hydroxyl ions are released from the

C_3S surface causing the pH level to rise. When calcium and hydroxyl values reach a critical level, crystallisation of calcium hydroxide and CSH begins. These initial reactions are temperature dependent. This is followed by a dormant stage (no/little heat evolved) where the cement remains plastic. Calcium hydroxide crystallises from the solution and CSH develops on the surface of C_3S forming a coating. As the thickness of this coating increases the rate of water penetration decreases and the speed of the reaction becomes diffusion controlled. The C_2S is hydrating at a slower rate due to its lower reactivity. The end of this period is the initial set and acceleration of the hydration now occurs as the critical concentration of ions is reached and silicates hydrate rapidly. Maximum hydration rate occurs within this time span. The rate of reaction now slows and is completely diffusion dependent (Vitro Minerals, 2010).

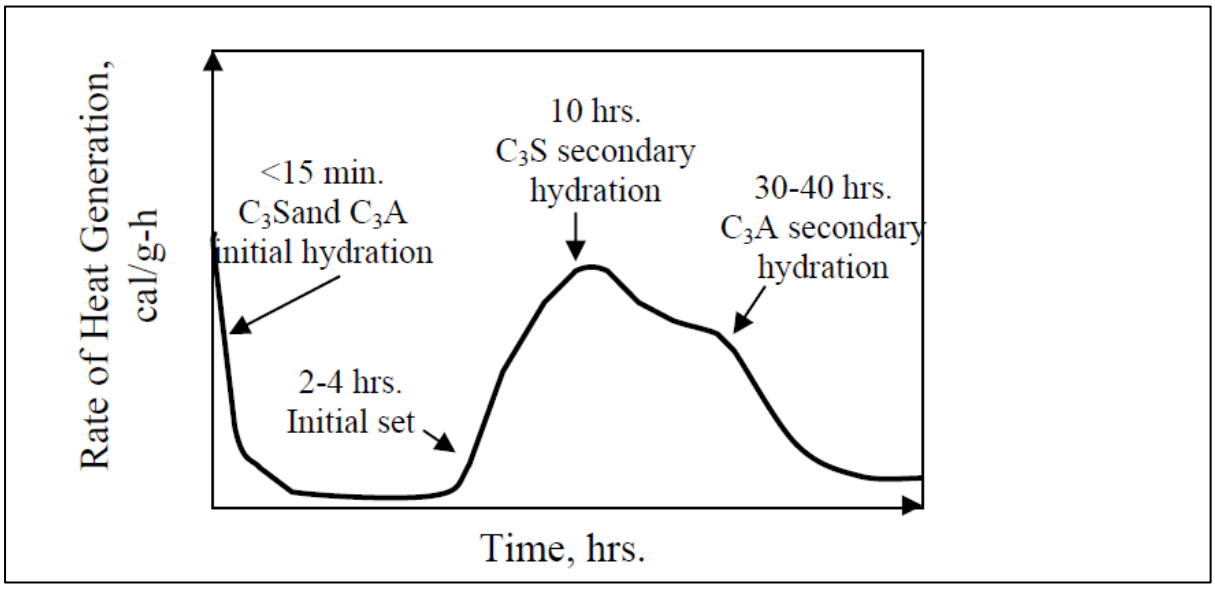

Figure 2.2 Typical rate of heat evolution during cement curing (Central Federal Lands Highway Division, 2008)

The rate and quantity of heat evolution is a function of cement chemical composition, cement fineness and particle size distribution, w/c ratio and reaction temperature. The reaction temperature is variable due to the heat of hydration and the size (surface area to volume ratio) of the cast part. Temperature increases of up to 40^{o}C are possible. The increase in temperature can affect the microstructure of the concrete reducing the molecular size of phases with resultant weakening and greater propensity to cracking.

Large structures such as dams, tunnel linings and drilled shafts can generate large quantities of heat leading to temperature differentials between the interior volume and exterior surface of the concrete. Temperature gradients can also arise in sections of varying thicknesses. Measures are required to manage these thermal effects such as internal cooling and exterior insulation. Maximum allowable temperature differentials are usually specified. In the United States this difference is commonly set to 20^{o}C.

Heat generated during concrete curing leads to thermal stresses and subsequent concrete cracking. Controls to combat thermal issues include using low heat generating cement and the use of aggregates with low coefficients of thermal expansion. These measures help to reduce the effects of heat build-up and can contribute to the performance and durability of the finished product. Reducing the placement temperature of the concrete helps reduce the rate of hydration with a corresponding reduction in peak temperature (Neville, 1995).

The quantity of cement present in a mix is the significant factor in heat generation. This is true whether the amount of cement is reduced, the water increased or pozzolans added. There are limits to these modifications as they also affect the intrinsic properties of the final concrete. All these measures reduce cracking and rigidity and the compressive and tensile strengths.

The action of water is a common factor in the processes of concrete degradation. Hardened cement is porous, containing a dual network of pores. The capillary pore system is characterised by pores of 50 to 1000 nm diameter and extends throughout the system acting as channels between the various components/phases. The cement gel contains a network of gel pores of 10 to 50 nm diameter. Physical properties of cement systems such as stiffness, fire resistance and durability are directly related to the amount of water present. Hardened cement generally contains 30 to 40% water occurring in 3 forms (MacLaren and White, 2003):

- Chemically bound water i.e. water of hydration which is chemically bound to cement precursors in the form of hydrates. This accounts for approximately 90% of the water.
- Physically bound water. This is water adsorbed onto the surface of the capillaries. Mainly found in the small gel pores of the system.

- Free water is found within the larger pores and is able to flow in and out of the system. The amount depends on the pore structure and volume, relative humidity and presence of water in direct contact with the hardened cement surface such as in water bearing pipes and marine structures.

The ability of water to dissolve cement components and its volume changes in freeze – thaw cycles can cause durability issues. Free water is particularly significant in durability issues as it is able move throughout the hardened cement.

As cement paste hydrates over several months the porosity decreases. Initially the drying process is by capillary flow of water through the larger pores. As the porosity decreases the water transport process becomes diffusive in nature. Higher w/c ratios result in larger pore sizes as the cement gel forms and these contain a larger volume of water. Larger pores give a faster drying rate which can create problems in low relative humidity curing conditions. If cement is exposed to long periods of low humidity and high temperatures, adsorbed water in the gel pores of the cement will evaporate. This process leads to drying shrinkage. Partially filled gel pores contain water menisci which exert tensile stresses on the walls of the pores leading to micro-cracking.

Freeze–thaw cycles occur when temperatures hover around $0^{o}C$ and can occur on a daily basis. Water shows a 9% volume increase on freezing. This expansion exerts stresses on the capillary walls causing micro-cracking. These micro-cracks fill up with water during the thaw cycle, freeze when the temperature drops causing more cracks to open (Neville, 1995).

Crystalline calcium hydroxide makes up about 10 wt. % of commonly used systems. Calcium hydroxide has an ambient temperature solubility in water of around 1.7 g/l and is readily dissolved in the free water in pores (MacLaren and White, 2003). Removal of calcium hydroxide by dissolution leaves voids in the system which can encourage deeper penetration of water. Carbon dioxide from the atmosphere can react with this calcium hydroxide in solution. The visible signs of this process, known as efflorescence, are the formation of white deposits of calcium carbonate on the exterior surfaces of the concrete. A similar reaction with calcium silicate hydrate is also possible (Neville, 1995).

Water can also carry aggressive chemicals into the cement paste where they attack the various components. Acidic attack reduces the pH of the pore water which will promote

corrosion of steel reinforcement members. The intrusion of chloride ions from sea water and de-icing compounds accelerates corrosive attack on steel reinforcement. Corrosive salts, particularly ammonium and magnesium sulphates, react with calcium hydroxide to form calcium sulphate which has approximately twice the volume of the removed calcium hydroxide. This increase in volume sets up internal stresses leading to cracking (MacLaren and White, 2003).

The alkali silica reaction (ASR) is caused by silica compounds in certain aggregates reacting with alkalis from within the concrete or from external sources e.g. de-icing salts, ground water and sea water. The result of the reaction is an expansive process leading to longitudinal, map or pattern cracking, spalls at joints and overall deterioration. The chemical reaction between soluble silica in the aggregate and soluble alkali produces an alkaline silica gel that swells when water is absorbed. The swelling of the gel may crack the concrete. Existing cracks can be filled with gel preventing them from closing and causing further cracking (Transportation Research Board, 2006). The type, size and amount of reactive aggregate play important roles in the reaction.

Early methods of prevention included limiting the total alkali content of cement below 0.6 wt. % of cement, but experience showed that <0.4 wt. % was required to prevent ASR occurring. When high amounts of alkali are present in cement, pozzolans (fly ash, silica fume and metakaolin), blast furnace slag, or lithium salts are used to inhibit the ASR reaction. Pozzolans and slag are effective because they tie up hydroxyl ions thereby preventing formation of expansive gel. They also reduce alkali concentrations by replacing portions of the OPC and reduce permeability which prevents penetration of alkalis from external sources. Lithium salts are thought to function by the formation of a non-swelling gel. Lowering internal relative humidity to less than 80% also stops ASR expansion (Ferraris, 1995).

The presence of ettringite, calcium sulphoaluminate, found in all OPC concrete can lead to long term crack formation. Gypsum and other sulphate compounds react with calcium aluminate in the cement to form ettringite within the first few hours after mixing with water. Essentially all the sulphur in the cement is consumed to form ettringite within 24 hours. The formation of ettringite results in a volume increase in fresh, plastic concrete.

However due to the plastic nature of the concrete this expansion is harmless (Portland Cement Association, 2012).

In the longer term ettringite will dissolve in water and reform in less confined areas e.g. white needle like crystals can be seen lining air voids. The phenomenon of delayed ettringite formation (DEF) is usually associated with heat cured concrete. The high temperature, typically 70^{o}C, decomposes any initially formed ettringite and the resulting sulphate and alumina entities are tightly bound in the CSH gel. In the presence of moisture the sulphate and alumina desorb from the CSH to form ettringite in confined locations in cooled, hardened concrete. Since the paste is rigid and there are insufficient voids to accommodate the ettringite volume increase expansion and resultant cracking occurs. In addition some of the initially formed ettringite may be converted to monosulphoaluminate at higher temperatures and on cooling revert back to ettringite. Ettringite takes up more space than the monosulphoaluminate from which it forms and the transition is therefore an expansive process (Collepardi, 2000).

In the case of fire and thermal resistance the transport of water through the cement body is essential to reduce spalling tendencies. The existing pore system can be supplemented by the addition of small diameter thermoplastic fibres which melt as the temperature increases forming channels for water transport. In the case of HPC, the addition of silica fume gives a dense microstructure with reduced pore interconnectivity. Thermoplastic fibres are essential in these systems to increase the interconnectivity of the pores, which facilitates water transport (Papworth, 2000, Kalifa et al., 2001).

The mechanical properties and volume stability characteristics of OPC are markedly reduced by exposure to elevated temperatures, which can lead to structural failures (Arioz, 2007). Release of chemically bound water from CSH becomes significant above 110^{o}C. This dehydration and expansion of aggregates increase internal stresses and beyond 300^{o}C micro-cracking occurs. Calcium hydroxide dissociates at 530^{o}C resulting in shrinkage. Water used to fight the fire results in the regeneration of calcium hydroxide resulting in cracking and crumbling of the concrete. Most changes occurring above 500^{o}C are considered irreversible. CSH gel undergoes further dehydration above 600^{0}C with the formation of cracks.

The interfacial transition zone (ITZ) between cement paste and aggregate is described as the most important interface in concrete (Scrivener et al., 2004). It has a major impact on strength and permeability. The ITZ arises from the “wall” effect of packing of cement grains against a relatively flat aggregate surface. The zone closest to the aggregate contains predominantly small grains and significantly higher porosity with coarser grains further out. In concrete this means that the size of the ITZ is comparable to cement particles (10 to 50 μm). The ITZ is generally weaker than either paste or aggregate due to high local w/c ratio and particle packing issues. In some cases large crystals of calcium hydroxide and ettringite are orientated perpendicular to the aggregate surface. Micro-cracking is common in the ITZ which can result in shear bond failure and interconnected macro-porosity, which influences permeability. The most effective way to modify the ITZ is to add a fine particle material such as fume silica. This is common practise in the production of HPC.

2.4 Geopolymer Applications

The hardened geopolymer has an amorphous glass-like structure which is capable of modification by aggregates, reinforcing agents and process aids during the mixing and shaping process. Potential applications include concretes and mortars (in competition with OPC) (Hardjito and Rangan, 2005, Skvara et al., 2006), specialised high temperature applications such as fire and heat resistant products (with superior durability to OPC), binders for encapsulation of toxic chemicals and nuclear waste and chemically resistant products (Rostami and Brendley, 2003, Nugteren et al., 2011, Palomo and Fernández-Jiménez, 2011).

The use of geopolymer systems for OPC replacement is likely to be limited to special high performance applications where their outstanding properties compared to traditional materials gives them a clear technical advantage. These limitations are based on a lack of long term performance data, a shortage of geopolymer feedstock compared to total OPC consumed and higher current costs together with adverse OH&S scenarios with Class 8 corrosive liquid alkaline activators (Scrivener, 2011).

Typical high performance applications are shown in Table 2. 1. They highlight the three key property areas, chemical, heat and fire resistance, where geopolymers have demonstrated a clear superiority over OPC based products.

The United States military have been a major driver of new technologies and the resultant higher service conditions placed on construction materials. The introduction of the AV8B (Harrier) VTOL aircraft led to spalling of concrete landing pads and degradation of asphalt based pads. The AV8B has an exhaust temperature of approximately 700^{o}C, which equates to a ground temperature of 450^{o}C. The new F35B has an exhaust temperature 205^{o}C higher and a ground temperature of at least twice that of the AV8B (Sweetman, 2011). US Navy specifications call for vertical landing pads to be made from high temperature concrete (Ceratech, 2011).

This ability to resist high temperatures coupled with inherent fire resistance will open up other military markets such as carrier launch deflector plates, armoured vehicle and marine turbine engine exhaust systems and fire walls for ammunition bunkers.

Efficient down hole cementing is essential for well recovery in low pressure and leaky strata in newer oil and gas production fields (Zhu et al., 2010). Compared to present cementing systems, the geopolymer cement investigated exhibited lower permeability, with all the pores smaller than 20 nm, and high early compressive strength (30 MPa after 24 hours at 80^{o}C). The flowability and setting times could be modified by the use of admixtures to enable pours to be completed to large depths.

US Patent 7794537 (Barlet-Gaudedard et al., 2010) is for a geopolymer composition with controllable thickening and setting times over a wide range of temperatures by the use of accelerators and retarders. The compositions have good mixability and pumpability (viscosity in the range 200 to 300 mPa s). Based on metakaolin, fly ash or slag with a typical silicon to aluminium ratio of 2, the compositions exhibit strength and permeability values suitable for well cementing applications. The binder compositions may be filled with light weight fillers such as cenospheres or high density fillers such as barytes to suit the end applications.

Nasvi (2012) compared a fly ash based geopolymer to conventional well cements and found a marked reduction in CO_2 permeability. Existing well cements degrade in the acidic CO_2 environment and allow release of the CO_2 to the atmosphere via the increased porosity in the well cement.

In a similar vein, geothermal energy functions by the use of a heat pump which transfers thermal energy from the ground through a closed buried pipe system sealed with a grouting material which ensures the stability and thermal transmission of the bore hole. The grout must bond well to the pipe work and have a thermal conductivity greater than 1.0 W/m.K. Cement and cement-bentonite blends have been used as binders and the fillers/aggregate thermally enhance the grout system. Whilst the use of geopolymer was not reported the use of slag as an SCM gave thermal conductivity values in the range of 1.8 to 2.0 W/m.K (Borinago-Trevino et al., 2012). This would be an application where the superior durability of geopolymers would be advantageous.

Thermal energy storage for solar power generation is a potential market for geopolymers. The use of concrete as a storage medium along with the use of a heat transfer fluid is being evaluated (Panneer Selvam and Hale, 2011). The original design involved a stainless steel tube embedded in high strength fibre reinforced concrete. The goal is to build “concrete” tubes which are durable to 600^{o}C with low porosity to retain the molten salt heat transfer fluid. This is an application with good potential for geopolymers.

TABLE 2.1 Potential high performance applications for geopolymers.

Military
Exhaust gas thermal insulation: VTOL landing pads, Carrier launch deflector plates, armoured vehicles. Naval turbine engine exhaust.
Marine: Fire resistant components.
Ammunition storage bunkers.
Fire resistant fuel storage bunds.
Civil
Chemical resistant bunding and flooring e.g. sewage treatment, dairy floors, electrowinning cells.
Solar power heat transfer components.
Oil & Gas downhole cementing.
Heat resistant coatings for steel, wood and existing OPC structures.
Tunnel linings.
Bench tops.
Extruded profiles for fire resistant door jambs and window frames. Elevator components.
Thermal Insulation systems including cellular products.
Railway sleepers, Sewage pipes.
Mining
Prefabricated components (chemical and fire resistant) for power generation and mineral processing) e.g. ducting.
Tunnel linings.
Geothermal grouting.
Back Fill.
Waste Management
Nuclear waste storage.
Toxic metal encapsulation.
Water purification.

OPC concrete is not well known for its inherent chemical resistance. This has led to the application of organic coatings based on, but not limited to, vinyl esters, epoxies and polyureas (Stavinoha, 1991, Guan, 2003) to reduce the ingress of corrosive liquids into OPC concrete. Polymer concrete, i.e. aggregate mixed into a polymeric binder, is also available to form monolithic chemical resistant structures. The use of organic based coatings leads to higher raw material and labour costs together with ongoing maintenance issues. There are wide ranging opportunities for chemically resistant geopolymer systems across several industry and infrastructure sectors.

Table2.2 shows the broad spectrum of acidic media sources. All these sources are threats to cementitious binder systems in several industry and infrastructure applications.

Table2.2 Sources of acidic media adapted from (Zivica and Bajza, 2001, Oualit et al., 2012).

Industrial Processes	Refineries, wood treatment and pharmaceutical production generate substituted phenols which are acidic. Detergents can be based on sulphonic acid derivatives. Power generation from coal emits acidic gases (SO_2, CO_2). Cement manufacture emits CO_2. Food production and storage.
Urban Activity	Oil based transportation systems emit CO, SO_2, NO_x gases. Wood and Oil based heating emits CO_2. Sewage treatment generates hydrogen sulphide.
Natural effects	Carbon Dioxide in water. SO_3^{-2} and SO_4^{-2} anions in peat bogs. Soil contains huminous acids. Sea water is a mix of inorganic and organic acids.
Bacteria	Bacteria break down proteins and hydrocarbons giving methane and hydrogen sulphide. Also reduce sulphate ions to sulphides (usually ferrous) which in turn gives hydrogen sulphide, a precursor for sulphuric acid.
Water	Solvent for aggressive media. Transport media for aggressive media and reaction products. Constituent of reaction products in OPC e.g. ettringite.

The degree of acidic aggression depends on the nature of the anions, which govern the strength of the acid, degree of dissociation and solubility of the salt formed. The

aggressiveness of organic acids towards OPC increases in order of their calcium salt solubility (Zivica and Bajza, 2001).

Bakharev (2005a) conducted testing of fly ash based geopolymers exposed to 5% acetic and 5% sulphuric acids. She found that the geopolymer performed better than OPC due to the lower calcium content of the geopolymer. The composition of the alkali activators used in the synthesis of the geopolymers had a large influence on the acid resistance. The best results were obtained from geopolymer prepared using sodium hydroxide as the sole activator and curing at elevated temperature. Two months immersion in both acids gave large weight changes for OPC (>10%) whilst the geopolymer showed less than 2% weight change.

In the food storage and processing industry several organic acids, lactic, acetic and formic are commonly used or formed by bacteria attack on sucrose and animal feed meal. Whilst they are classed as weak acids they readily attack the calcium hydroxide present in OPC to produce soluble calcium salts which are leached out of the concrete reducing the pH. This results in the binding agents being left in an unstable condition. This weakened material is now easily removed by animal scuffage and cleaning (DeBelie et al., 1997).

Milk processing causes severe OPC degradation due to lactic acid attack, and again the remedy can be the use of geopolymer based systems.

OPC is the main material of construction for sewage and waste water plant and the associated pipework. The concrete can be attacked from the inside by sulphuric acid generated by bacteria and externally by humic and carbonic acids formed naturally in the soils or from contaminated back fill (Oualit et al., 2012). This attack leads to a reduction in strength with increased risk of sewer pipe collapse. This could lead to flooding and rupture of other infrastructure services such as water and gas pipelines.

Montes and Allouche (2008) compared class C fly ash and metakaolin based geopolymers to OPC mortars for pipeline and sewage refurbishment using trenchless technology. The fly ash based geopolymer showed the best sulphuric acid resistance. Trenchless technology encompasses a wide range of techniques utilised for the installation and refurbishment of

underground services with minimal surface disruption from trench excavation. The technologies include in-situ pipe replacement and relining of existing structures. Geopolymer coatings for these applications are being investigated at the Louisiana Technical University Trenchless Technology Centre (2012).

Ammonium compounds tend to act as weak acids which will attack OPC. Ammonium nitrate is widely used in explosive and fertiliser manufacture where OPC attack is widely reported. The use of geopolymer based mortars can be used for remedial work or as part of the original installation.

MacKenzie (2011) recently reported on several new and potential geopolymer applications. The charge balancing Na^+ cations in conventional geopolymers can be exchanged for other cations (O'Connor et al., 2010). 100% exchange of Na^+ by K^+, NH_4^+, Ag^+ and Pb^{2+}, but less for other cations is achievable. The use of Ag^+ produces a material with strong antimicrobial properties which can be used as a bactericidal filter bed for water purification. A similar technique can be used for the removal of heavy metals from waste water streams e.g. 100% Pb^{2+} and 72% Cd^{2+} but this is unable to remove Hg^{2+}.

Porous cladding for passive cooling of buildings produced from metakaolin based geopolymer with the addition of fibres as pore formers have been evaluated. The fibres are removed after setting by controlled heating leaving continuous, aligned pores which can achieve up to 1 metre capillary lift for water. Cladding produced in this manner can effect cooling by latent heat of evaporation of the water (Okada et al., 2011). Engineering obstacles need to be overcome to give a practical system in terms of capillary lift heights.

The resistance of OPC to heat and fire is poor with rapid loss of strength above 450^{o}C and the manufacture of high performance concrete (HPC) exaggerates the situation due to lower (limited connectivity) porosity resulting in spalling. This spalling is a result of pressure build up caused by trapped water/steam which exceeds the tensile strength of the OPC and pieces of material are explosively ejected from the main body. The use of fibres to form pathways to allow water escape is well documented (Papworth, 2000, Heo et al., 2012).

Geopolymers generally do not show this spalling behaviour. Geopolymers based on fly ash have small, well interconnected pores, which allow easier permeation of water to the

surface. During heating pore volume initially increases as voids once filled with water are emptied. At higher temperatures melting of amorphous unreacted material from fly ash particles exposes additional pores from within these unreacted particles. This additional porosity increases the total interconnected porosity of the geopolymer (van Riessen et al., 2009).

Kong (2007) found that a fly ash based geopolymer had a large number of micropores (<1.25 nm) On heating up to 800^{o}C he believed that these micropores facilitated the escape of water from within the sample thus causing minimal damage to the specimen.

Bakharev (2006) found that in fly ash based geopolymers the cumulative pore volumes increased by 26% after heating to 800^{o}C and by 29% at 1000^{o}C compared to an unheated sample. Average pore size increased from 37.6 nm (unheated) to 121 nm (800^{o}C) and 1835 nm (1000^{o}C).

The increased pore volume connectivity of geopolymers compared to OPC during high temperature exposure will markedly increase transport of water through the binder with associated reduced spalling.

This, together with inherent heat resistance, very low smoke and toxic gas emissions indicates that fly ash based geopolymers will show improved fire resistance compared to OPC.

The use of geopolymers for fire resistant building products is illustrated by its use for window and door surrounds replacing organic materials (Reid, 2011) and fire resistant elevator doors (Krivenko, 2005). The use of geopolymers imparts greater structural integrity (as shown by enhanced glass retention), lower toxic gas emissions and reduced flammability.

Similarly the replacement of High Strength Concrete (HSC) by a geopolymer based concrete will give superior fire resistance due to higher mechanical properties at elevated temperatures and reduced spalling due to the geopolymer's interconnected pore system. This substitution will enhance the structural integrity of buildings and tunnel linings during and after fire events. Fire tests carried out on 75 MPa OPC and geopolymer concrete at

Monash University and reported by van Riessen et al. (2009) showed the superiority of the geopolymer concrete in resistance to spalling.

The use of geopolymers reinforced by woven textiles based on carbon fibres, basalt and glass were developed for aircraft applications to overcome the shortcomings of organic fibres (flammability and smoke evolution). Lyon (Lyon, 1996, Lyon et al., 1997) carried out work for the US Federal Aviation Authority and compared a range of organic polymers to a potassium geopolymer (silicon: aluminium = 32:1)in a carbon fibre composite using the following criteria: ignitability, heat release ,and smoke (ASTM E-1354), flame spread index (ASTM E-162-83) and residual flexural strength (ASTM D790). The geopolymer system was found to be superior in every category.

Research on foamed geopolymers has demonstrated their viability with applications in the construction, automotive and thermal insulation industries (Liefke, 1999). Applications listed by Liefke for these foams include thermal and sound insulation for plant and equipment, buildings and transportation, silencer and catalytic converter components and filtration supports.

Coatings based on geopolymers have been reported on by Temuujin (Temuujin et al., 2011, Temuujin et al., 2009a). Steel coupons coated with various formulations withstood thermal treatment from a gas torch without cracking. A suitable geopolymer based coating could have applications in treatment of steel, OPC and wood to enhance fire resistance and impart corrosion protection (Zhang et al., 2010). Medri (2011) used a geopolymer based on metakaolin activated with potassium silicate and potassium hydroxide to act as a binder for silicon carbide particles. These systems could be applied by brush and were cured at 80^{o}C. Good adhesion to substrate was observed together with low shrinkage after exposure to 1000^{o}C.

2.5 Precursors and Additives for Geopolymer Synthesis

The precursors and additives required for the synthesis of geopolymer systems are:

- Alkali soluble aluminosilicates
- Alkaline dissolution media
- Admixtures to develop specific properties
- Aggregates and fillers.

Alkali soluble aluminosilicate sources include granulated blast furnace slag (GBFS), fly ash, and volcanic ashes. Metakaolin, calcined clay, has an amorphous structure with silicon to aluminium ratio of 1. It is used to manufacture geopolymers and can increase the aluminium content of geopolymers when used with fly ash and GBFS. Materials such as silica fume from smelting operations and from rice husk ashes do not contain aluminium, but are alkali soluble and are used to adjust silicon content of geopolymers for property control. All the above materials have utility as Supplementary Cementitious Materials (SCM) in conjunction with Portland cement.

Sources of aluminium are limited to waste anodising solutions (Nugteren et al., 2011), sodium aluminates including Bayer liquor (Jamieson et al., 2012) and aluminium smelting slag although the latter is toxic and requires additional processing prior to use. These aluminium based materials may be used to adjust aluminium levels in geopolymer synthesis. A potential source of aluminium is waste water treatment sludge which has been evaluated in brick and cement manufacture (Babatunde, 2007).

Granulated Blast Furnace Slag

GBFS does not form geopolymers based on aluminium and silicon tetrahedra structures, but rather a calcium silicate hydrate which is also present in OPC. GBFS's calcium levels tend to be in excess of 40 wt. %. GBFS can be used in blends with fly ash to give hybrid structures (Buchwald, 2009, Sofi et al., 2007, Puertas et al., 2000). Alkali activated binders based on GBFS yield products with higher compressive strengths and durability compared to OPC (Fernández-Jiménez et al., 1999). The reactions of slags are dominated by small particles. Particles greater than 20 μm in size react only slowly, whilst particles less than 2 μm react

completely within 24 hours. To achieve these small particle sizes grinding of the granulated slag is required (Wan et al., 2004).

Coal Fly Ash

Fly ash is the by-product formed during power generation by the combustion of coal. It comprises fine particles which rise with the flue gases (ash that does not rise is termed bottom ash) and is collected by electrostatic precipitators or other filtration equipment prior to the flue gases reaching the exhaust chimneys.

The source and chemical composition of coal and the operating conditions of the combustion process have a major impact on the resulting fly ash chemical composition and physical properties. The main components of fly ash are silica, alumina, ferrous oxide and calcium oxide with variable amounts of carbon as shown by LOI (loss on ignition) results (Blissett and Rowson, 2012). They also observed that fly ashes derived from sub-bituminous and lignite coals are characterised by higher calcium oxide and lower silica and alumina contents compared to high grade bituminous and lignite coals (see table 2.3). Fly ash from coals containing less than 10% calcium oxide consists mainly of aluminosilicate glasses and do not usually contain crystalline calcium compounds. Fly ash with greater than 15% calcium oxide contained calcium aluminosilicate glasses and crystalline calcium compounds.

The Ash Development Association of Australia has published The Coal Combustion Products Handbook (Gurba et al., 2007). This handbook is a useful reference source for Australian fly ashes and their current and potential applications.

The morphology of fly ash particles is controlled in the main by combustion temperature and subsequent cooling rate. SEM imaging showed a mix of solid spheres, hollow spheres (cenospheres), irregular unburnt carbon, and mineral aggregates with quartz, corundum and magnetite. Mullite and quartz are the predominant crystalline constituents of Australian fly ashes (Rickard et al., 2011, French and Smitham, 2007).

Table 2.3 Bulk composition of fly ash by coal type modified from (Blissett and Rowson, 2012).

Component	**Bituminous**	**Sub-Bituminous**	**Lignite**
SiO_2 (wt.%)	20-60	40-60	15-45
Al_2O_3 (wt.%)	5-35	20-30	20-25
Fe_2O_3 (wt.%)	10-40	4-10	4-15
CaO (wt.%)	1-12	5-30	15-40
LOI (wt.%)	0-15	0-3	0-5

Kutchko (2006) studied 12 class F fly ashes from the United States using SEM-EDS. She found mainly amorphous aluminosilicate spheres with some iron rich spheres, the latter consisting of iron oxide and amorphous aluminosilicate. The morphology of the particles was used to determine the relative amorphous and crystalline compositions. Cross sections showed the iron oxide and aluminosilicate were mixed throughout the fly ash particles. The calcium was not associated with the aluminium or silicon. In addition to the particles reported above she also found agglomerated and amorphous material, the formation being attributed to inter-particle contacts.

The amount of alkali soluble (amorphous) fly ash material is the critical quantity for geopolymer synthesis calculations (Fernández-Jiménez and Palomo, 2003). Allowance must also be made for the fact that not all the amorphous material is accessible by the activating alkali solutions.

The total bulk elemental composition (as oxides) can be determined by X-ray fluorescence (XRF) and the phase abundance by quantitative x-ray diffraction (QXRD). If the composition of the crystalline component is subtracted from the total elemental composition what is left is the composition of the amorphous content some of which can react with alkaline activators to form geopolymer products. Chen-Tan et al. (2009) carried out this type of analysis on Collie fly ash. Rickard and Williams extended this work to several other

Australian fly ashes with a view to determining thermal properties of the synthesised geopolymers (Rickard et al., 2011, Rickard et al., 2012, Williams and van Riessen, 2010).

Font et al. designed a simplified XRD based method for determination of the glass content and mineralogy of coal based fly ashes. A glass standard based on a >99% aluminosilicate glass was added to fly ash in known proportions and the mixtures evaluated by XRD (Font et al., 2010).

Van Jaarsveld et al. (2003) carried out XRF to get the total elemental composition, but used FTIR to determine the aluminium co-ordination. Bands at 550 and 557 cm^{-1} had previously been assigned to aluminium in octahedral co-ordination. This latter co-ordination form will not form geopolymers. He attributed differences between two Port Augusta fly ash batches to slight differences in the silica amorphous phases. It was proposed that these differences could be due to variations in the coal feed stock composition or the variation in furnace temperatures.

Recent work using dilatometry by Provis et al. (2012) claims that mechanical properties of fly ash based geopolymers can be predicted from the temperature at which the high temperature expansion peak attributed to release of strongly chemically bound water is observed. High strength samples generally display this expansion at a higher temperature than low strength samples. Samples made either with poorly reactive fly ash or with an excessive amount of silica in the activating solution also expand by up to 10 to 15% below 200^{o}C. This was attributed to a combination of low extent of crosslinking by aluminium entities and vaporisation of added water to produce an expanded material. Additional water was added to the geopolymer synthesis mixture to give sufficient workability to fill the 4 mm diameter moulds for dilatometer test pieces. This will also reduce strength properties of these samples. This work was based on potassium silicate activating solutions for six different fly ashes. This method may have potential to screen the suitability of fly ash for geopolymer manufacture. The key outcome of this work is the influence of available (for geopolymerisation) aluminium from the fly ash on strength development.

There are national standards for fly ash for use in concrete and these also have relevance to geopolymer synthesis (ASTM Committee C09, 2012a). Table 2.4 outlines the basic

requirements of fly ash in ASTM C618-2 and EN450-1. EN 450-1 uses 3 LOI categories and 2 fineness categories for the initial classification of fly ash grades.

Class F fly ash is regarded as a pozzolanic material. A pozzolan has no intrinsic cementitious properties. It will react with calcium hydroxide at ambient temperatures and in the presence of water to form compounds exhibiting cementitious properties. The high calcium content of Class C fly ash will result in the formation of cementitious properties in the absence of calcium hydroxide and hence are not true pozzolans (Blissett and Rowson, 2012).

Table 2.4 ASTM and EN fly ash requirements adapted from (Blissett and Rowson, 2012).

ASTM C618-12	**SiO_2+Al_2O_3+Fe_2O_3**	**SO_3**	**Moisture**	**LOI**	**max retained on 45 µm sieve**
Class C	>50%	<5%	<3%	<6%	34%
Class F	>70%	<5%	<3%	<6%	34%
EN450-1	**SiO_2+Al_2O_3+Fe_2O_3**	**SO_3**	**Reactive silica**	**LOI**	**max retained on 45 µm sieve**
Category A	>70%	<3%	>25%	<5%	Category N <40%
Category B	>70%	<3%	>25%	2-7%	Category S <10%
Category C	>70%	<3%	>25%	4-9%	

All of the more reactive amorphous material (compared to crystalline phases) in fly ash does not react during alkaline dissolution. Amorphous material can be encased inside spheres and the deposit of alkali-fly ash reaction product on the spheres can act as a barrier to further dissolution. Mechanical activation of fly ash has been evaluated to increase the amount of fly ash material reacting with the alkaline solutions (Van Riessen and Chen Tan, 2013).

The simplest procedure is to screen the fly ash to remove particles retained on a 45 micron screen. This effectively increases the surface area of the material which has passed through the screen. Also larger sized non aluminosilicate materials such as quartz and carbon are

removed. The removal of the latter is important as it has a high water demand which can result in a drop in compressive strength (Silverstrim et al., 1997).

Nugteren (2009) separated raw fly ash into six different size fractions by air classification. Geopolymers were made from these fractions in combination with GBFS using potassium silicate solution as the alkaline activator. The window of workability varied with each fly ash fraction. He found that there was no clear trend for increases in compressive strength with finer fractions. However, mix proportions were varied for each fraction and this may have impacted on the results.

Several authors have investigated mechanical activation of fly ash (Chindaprasirt and Rattanasak, 2010, He et al., 2005, Kumar and Kumar, 2010, Temuujin et al., 2009c, Kumar et al., 2007).

Kumar (2007) compared raw fly ash (RFA) with mechanically activated material from vibratory milling (VMFA), attrition milled (AMFA) and jet milled classified (CFA). The median particle size of the RFA of 36 µm was reduced to 5 µm (VMFA), 4.3 µm (AMFA) and 2.8 µm (CFA). FTIR showed changes in peak intensity which was attributed to the structural rearrangements occurring during milling. Geopolymers made from mechanically activated fly ashes developed compressive strengths up to 120 MPa, with VMFA giving the highest rate of strength development.

Further work by Kumar (2010) investigated the effects of extended vibratory milling times. Particle size decreased and heat flow measured during the geopolymer synthesis increased with milling time. SEM and EDS results showed a more compact microstructure and no unreacted fly ash spheres for fly ash milled for 30 minutes compared to unmilled fly ash. EDS results for geopolymer based on raw fly ash gave silicon to aluminium ratios in the range 2.2 to 2.9 and silicon to sodium ratio in the range 0.9 to 1.2. Corresponding values for geopolymer based on fly ash milled for 30 minutes were silicon to aluminium of 2.9 to 3.2 and silicon to sodium of 3.5 to 4.2. Extended milling time also reduced setting time and increased compressive strength.

Temuujin (2009c) treated raw Collie fly ash in a vibratory mill for 60 minutes. SEM of the fly ash showed that the spherical morphology was substantially removed by milling. Particle

size was reduced from 14.4 µm to 6.8 µm by the milling procedure. Initially fast setting of the geopolymer based on milled fly ash was experienced. This was overcome by the addition of extra water which also gave suitable workability. Compressive strength, after an ambient temperature cure regime, was increased from 16 MPa to 45 MPa by virtue of using milled fly ash. This increase in compressive strength is claimed to be due to higher rates of geopolymerisation in samples based on milled fly ash. The ability of geopolymer systems, without added calcium compounds, to cure at ambient temperatures is imparted by the use of milled fly ash.

Temuujin (2009) investigated preliminary calcination of Collie fly ash at 500^{o}C and 800^{0}C as a potential activation method prior to synthesising geopolymer. This preliminary calcination caused crystallisation of mullite and hematite on the fly ash surface, lowering the reactivity of the fly ash as shown by the drop in compressive strength from 55.7 MPa (uncalcined) to 44.3 MPa (calcined at 800^{o}C).

Metakaolin

Metakaolin is produced by dehydroxylation of kaolin at between 650 and 800^{o}C. At temperatures beyond this metakaolin converts to spinel, which in turn converts to mullite (McCormick, 2007). Gastuche (1962) investigated the transformation of kaolin to metakaolin and concluded that (a) the reaction proceeded by stepwise removal of constitutional water from successive octahedral sheets, (b) water removal was accompanied by a gradual transformation of Al (VI) to Al (IV), (c)cohesion between individual layers is reduced and the internal surface becomes progressively more susceptible to acid attack, whereas the silica sheets still organised as a ”ring structure” remain and dissolve at a somewhat slower rate.

Metakaolin is used as an SCM with OPC where it functions by reacting with calcium hydroxide to forming hydrated calcium aluminates and silicoaluminates and thus improving the durability of the resultant binders. Metakaolin has a much greater surface area than cement (12,000 m^2/g compared to 333 m^2/g). This high surface area contributes to an increase in the water demand to maintain workability. The addition of superplasticisers can help to reduce this water demand (McCormick, 2007).

Metakaolin was the material used by Davidovits (2008a) for the early geopolymer development and commercialisation. Since then several research groups have used metakaolin to elucidate the kinetics, mechanisms and microstructure formation of geopolymer systems (Granizo et al., 2007, Barbosa et al., 2000a, Duxon et al., 2005, Duxson et al., 2006c, Duxson et al., 2006b, Duxson et al., 2006a, Fletcher et al., 2005, Rahier et al., 1997, Weng and Sagoe-Cretsil, 2007, Zuhua et al., 2009b, Duxon et al., 2006, Rahier et al., 2007, Zhang et al., 2010, Barbosa and MacKenzie, 2003a, Duxon et al., 2007a, Duxon et al., 2007b, Kamseu et al., 2010, Subaer and van Riessen, 2007).

The relative purity of metakaolin compared to fly ash and GBFS makes it eminently suitable for basic research into the many aspects of geopolymers. From a practical perspective metakaolin has a high water demand which can limit strength development and the relatively high aluminium content makes it suitable as a blending component with fly ash and GBFS to reduce the silicon:aluminium ratio of geopolymer systems where required (Phair et al., 2004).

Naturally occurring aluminosilicate sources

The investigation of volcanic ash for the production of geopolymers has become more common in recent years. Volcanic ash (44% SiO_2, 14% Al_2O_3, 10% CaO and 13% Fe_2O_3) from Cameroon was activated with caustic soda to synthesis geopolymer paste with a maximum compressive strength of 55 MPa after curing at 90^{o}C. Mortar with 40% sand gave a compressive strength of 30 MPa. This level of compressive strength exceeds the requirements of ASTM C216-12, Grade SW (severe weathering). ASTM C216 specifies the requirements for face brick (solid masonry units from clay or shale). The development of building products from readily accessible volcanic ash with suitable conversion techniques could have genuine economic benefits (Lemougna et al., 2011). The second piece of work (Tchakoute Kouamoa et al., 2012) uses volcanic ash activated by alkali fusion at 550^{o}C. Metakaolin is used to consume the excess alkali from the fusion process and to adjust aluminium levels in the geopolymer produced by activating with sodium silicate solutions. The Romans used volcanic ash (harena fossica) from the Naples area mixed with lime to produce concrete and mortar (Davidovits and Davidovits, 1999).

Other naturally occurring pozzolanic materials are suitable for geopolymer synthesis (Bondar et al., 2010). Xu and van Deventer (2000) investigated the geopolymerisation of 16 naturally occurring minerals using sodium and potassium hydroxides as activating materials and concluded that all 16 could be suitable geopolymer precursors.

Alkaline Activating materials

Alkaline dissolution media come from the family of alkali and alkali earth metal hydroxides, carbonates, aluminates and silicates. Sodium is the predominant metal (due to cost considerations) with the other members of the Group I family used for specific applications. Calcium (Group II), as the hydroxide, is the only alkali earth used.

In general alkali hydroxides and silicates at pH values of greater than 13 are required to activate aluminosilicates for geopolymer synthesis (Khale, 2007). Alkali metal carbonates as the sole activating agent are insufficiently alkaline for geopolymerisation reactions. However, sodium carbonate can react with calcium hydroxide to form sodium hydroxide in solution. Provis (2009) gives a good overview of alkali hydroxide solutions. There is a significant increase in solution viscosity of all alkali metal hydroxides at concentrations greater than 10 M. Efflorescence (formation of white crystalline sodium carbonates) is a known issue in geopolymers activated with an excess of sodium hydroxide. Atmospheric carbon dioxide reacts with the excess alkali to give white crystalline surface deposits which are mainly cosmetic in effect. Temuujin (2009b) found efflorescence containing phosphorus on ambient cured geopolymers. XRD showed this to be sodium phosphate hydrate and was assumed to derive from the 1.3 wt. % P_2O_5 in the Collie fly ash. Kani et al. (2012) believed that the tendency for geopolymers to show efflorescence was partly due to the open microstructure and partly to the high alkali content in the pore water. The addition of a source of soluble aluminium reduced efflorescence formation.

Potassium hydroxide activation imparts onset of densification at higher temperature than in sodium activated geopolymers (Barbosa and MacKenzie, 2003a, Duxon et al., 2007b). Blends of sodium and potassium hydroxides have been evaluated (Duxson et al., 2006b) with respect to thermal shrinkage of metakaolin based geopolymers with the blended cation geopolymer laying between the pure cation systems.

Alkali Metal Silicates

Alkali metal silicates, based on sodium and potassium are commercially available (PQ Europe, 2004). Production can be via the hydrothermal or furnace route. Generally silicates are identified by the SiO_2:M_2O ratio, known as the modulus. Commercially this ratio is normally specified in terms of weight. To convert to a molar ratio the following multiplier factors are used: sodium 1.033 and potassium 1.567. The viscosity of sodium silicate solutions is a function of concentration, modulus and temperature. Potassium silicate solutions show similar behaviour, but are more viscous than corresponding sodium silicate solutions at equal concentration. The pH of commercial silicate solutions is in the range of 10 to 13. Sodium silicate solutions will polymerise to form silica gel when the pH drops below 10. Solutions of sodium silicates react with dissolved polyvalent cations such as Ca^{2+} or Al^{3+} to form insoluble forms of silicates.

Potassium silicate resembles its sodium counterpart in physical properties but also shows several advantages: it does not develop efflorescence, displays higher solubility and compatibility with other additives and imparts higher refractoriness, flowing at higher temperatures than the sodium analogues.

Sodium and potassium silicate solutions consist of a range of silicate anions (PQ Corporation, 2005). The basic building block is the tetrahedral silicate anion, the monomer unit. These monomer units can link in a variety of ways to form linear, planar cyclic and three dimensional silicate anion structures. There are two main factors which influence the distribution of silicate anion types, the ratio of silica to alkali and the concentration. Figure 2.3 shows the distribution of silicate anion species as the modulus increases at constant concentration. Moving from left to right (reducing alkali content) shows a shift from high monomer (“monosilicate”) to more complex structures and polymers via a series of growing chains and rings.

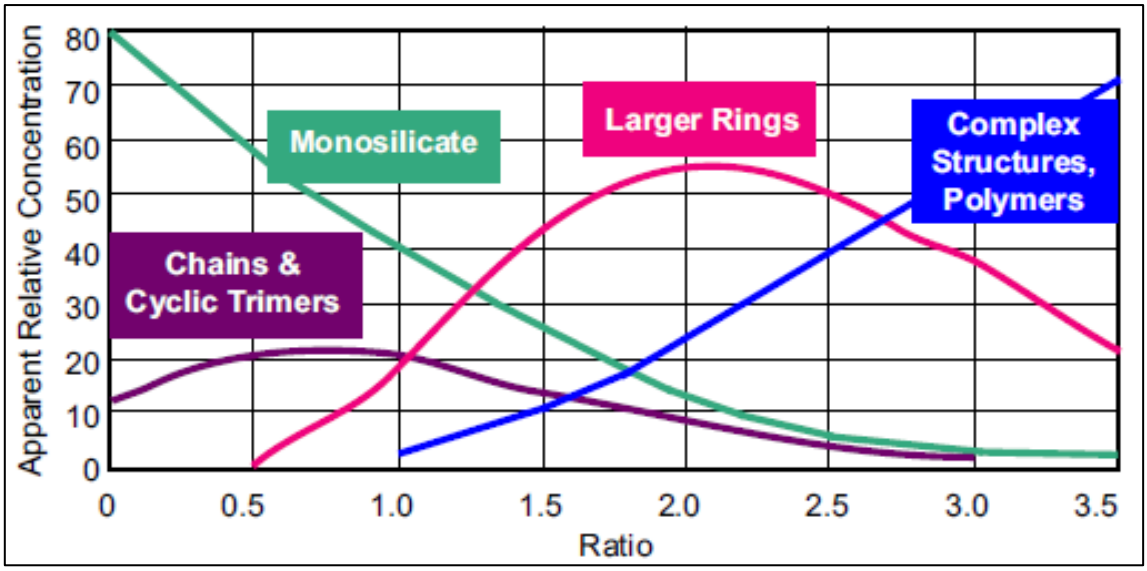

Figure 2.3 Silicate anion structure equilibria (1 M solution) (PQ Corporation, 2005).

The distribution of anionic species can be altered by the addition of alkali or dilution with water, known as respeciation. This causes the solution to change to the species distribution appropriate to the new modulus. A full strength solution can take up to 48 hours to respeciate at room temperature. In very dilute solutions it can occur in a matter of minutes.

The above confirms the work of Applin (1987) who thought that at pH values in excess of 13 the predominant species was $SiO_2(OH)_2^{2-}$.

Kinrade and Pole (1992) working on zeolites thought that three main structural directing roles could be attributed to M^+. Firstly it stabilises oligmeric "mineral precursor" species in aqueous alumina-silicate systems. Secondly hydrated M^+ have a templating effect whereby silicate and aluminate species replace water of hydration for a sufficient time to enable them to join together in a structural configuration. A third hypothesis was that the extent of condensation in alkali metal-silicate solutions increases slightly as the molecular weight of M^+ increases and M^+ forms ion-pairs with silicate anions. Higher silicate oligomers are favoured due to preferred ion-pairing with heavier cations.

They concluded that there are three means for alkali metal ions to influence aqueous silicate equilibria:

1. Electrostructive water structuring by small cations increases overall level of polymerisation. They thought that this was only relevant to lithium.

2. Ion pairing of silicate anions and M^+ increased polymerisation. Cations promote encounters between dissolved silicate anions by overcoming their electrostatic repulsion. Strongly paired cations will resist subsequent formation of a siloxane bond, thus the extent of polymerisation increases in the order $Li^+<Na^+<K^+<Rb^+<Cs^+$ (i.e. as the ion pair formation constants decrease).
3. Ion paired cations stabilise several specific oligomers by immobilising labile appendages and large ring structures.

Phair and van Deventer (2001) used ^{29}Si NMR to analyse the degree of polycondensation during geopolymerisation and confirmed that the basicity and hydration sphere of the alkali metal as well as it's concentration had a controlling effect on the degree of polycondensation and rate of dissolution from aluminosilicate minerals.

Sodium Aluminate

Sodium Aluminate (SA) is prepared by the action of sodium hydroxide solution on aluminium metal or by dissolving alumina in sodium hydroxide solution. Industrially aluminium hydroxide is dissolved in 20 to 25% sodium hydroxide. Higher concentrations of sodium hydroxide give a semi solid product. In the production of solid SA aluminium hydroxide is added to boiling 50% sodium hydroxide until a pulp forms. This pulp is cooled to give a 70% solids SA product which is crushed and dehydrated to give a solid product (Kirk-Othmer, 1991).

SA solutions tend to precipitate out alumina on standing unless stabilised with an excess of sodium hydroxide. Unstabilised SA solutions have a $Na_2O:Al_2O_3$ molar ratio of 1.51:1. Stabilised solutions have an excess of 11 to 13 % NaOH and a molar ratio in the range 1.75 to 1.95 (Orica Chemicals, 2011). Total solids should also be considered with 38 wt.% being usual (Southern Ionics, 2006). However the Coogee Chemicals (2012) stabilised product is a nominal 44.5 wt.% solids with alumina content of 19 wt.% and 25.5 wt.% NaOH.

SA may be obtained from the following waste product streams:

1. Aluminium industry as salt cake and spent potliner. Spent potliner is hazardous due to the presence of cyanides and fluorides and therefore requires pre-treatment to

obtain SA. Salt cake is a by-product of aluminium dross formation in the recycling of aluminium metal. Processes to obtain SA from the salt cake recycling process are available (Rayzman et al., 1998).

2. Anodising bath spent solutions (Nugteren et al., 2011).
3. Bayer liquor from alumina refineries (Sipos, 2009).

Aluminium does not appear to form products analogous to sodium and potassium water glass solutions even though it is present in the same tetrahedron configuration as silicon. This may be as a consequence of Lowenstein's rule. Catlow (1996) investigated the energies of formation and hydration of small clusters and rings containing silicon and aluminium. The results provided a rationalisation of Lowensteins rule in terms of the energetics of species containing Al-O-Al bridges. Whilst the formation of dimer is calculated to be energetically unfavourable in the unhydrated state, when the effects of solvation energies are added the reaction is now exothermic and possible. The formation of small rings involving Al-O-Al bridges is energetically unfavourable and hence further condensation of dimers is considered unlikely.

Moolenaar (1970) obtained vibrational spectra of sodium and potassium aluminates at a range of concentrations in sodium hydroxide solutions. Single crystal X-ray diffraction was used to determine the structure of potassium aluminate and demonstrated the presence of the dimer ion, $(OH)_3AlOAl(OH)_3^{-2}$, built up from two AlO_4 tetrahedra which share an oxygen. At less than 1.5 M (aluminium) $Al(OH)_4^-$ was the main component. At 6 M an equilibrium between $Al(OH)_4^-$ and $Na_2Al_2O_4^{-2}$ (dimer) co-existed. Also in this work stable solutions containing appreciable amounts of aluminium could not be prepared at pH values less than 13.

Chen (1992) prepared SA solutions of equal concentrations by two different methods.

Method 1 involved dissolving aluminium metal into highly concentrated NaOH solution. Method 2 involved dissolving aluminium metal in dilute NaOH solution, leaving it to stand for 15 days and solid NaOH added to bring the solution composition to that of Method 1.

Raman spectra of potassium and barium aluminate dimers show peaks at 540 cm^{-1} and 550cm^{-1} respectively. The spectra from material prepared by method 1 showed a higher peak in this region than did method 2 material. The authors believe that this is indicative of

higher sodium aluminate dimer content and this is supported by higher solution viscosity and lower electroconductivity in material from method 1 compared to material from method 2.

Nianyi and Honglin (1994) studied the aluminate ion using quantum chemical methods. The Al-O bonds (of the Al-O-Al bridge) in aluminate ions have significant covalent character so reactions involving the formation or cleavage of the Al-O bond may be a slow process. In UV spectra a broad absorption band near 2700 Å was assigned to the aluminate dimer ion. Excitation energy calculations gave a value of 2666 Å close to the experimental value. Excitation energy calculations for $Al(OH)_4^-$ and $Al(OH)_6^{3-}$ gave wavelengths of 2300 Å and 2645 Å respectively.

Concentrated sodium aluminate solutions with high Na_2O: Al_2O_3 ratio contain small amounts of Al(VI) as $Al(OH)_6^{3-}$. Ma et al. (2007) attributed a UV peak at 3700 Å to this Al(VI) co-ordinated species. They claim that this peak only appears when solutions are made by dissolving aluminium trihydroxide. This peak disappeared when the solution was heated to 135^oC.

Bands observed at 725 cm^{-1} (infrared) and 621 cm^{-1} (Raman) are attributed to asymmetric and symmetric Al-O stretching vibrations of the aluminate ion, $Al(OH)_4^-$ in solution. Other low intensity bands at 890 and 630 cm^{-1} (infrared) and 540 cm^{-1} (Raman) indicate the formation of a second aluminate ion species, the dimer.

Sipos (2009) reviewed the structure of aluminium in strongly alkaline aluminate solutions. Apart from $Al(OH)_4^-$ only one further Raman distinguishable aluminate species appears to exist in significant concentrations, the dimer.

One possible explanation of unusually high viscosity values of SA solutions is that aluminate ions in aqueous solutions form an extended network of ions (both same and opposite charge) which is held together by bridging counter ions and possibly hydrogen bonds. Such extended networks could explain the variations observed in transport properties of these solutions. This network cannot be described as a polymer, but as a diffuse network of hydrated closely packed ions.

Solutions of SA appear to contain monomer, dimer and some aluminium in VI co-ordinate form. Therefore care must be taken in identifying the composition of SA solutions prior to use in geopolymer synthesis.

Brew and MacKenzie (2007) produced a geopolymer by reacting sodium aluminate solution with a slurry of silica fume in sodium hydroxide. By keeping the H_2O: Na_2O ratio < 10 an X-Ray amorphous material was obtained. Higher ratios gave rise to crystalline zeolites.

^{27}Al MAS NMR of the sodium aluminate solution gave a sharp resonance at 78.3 ppm indicative of crystalline material containing aluminium in tetrahedral co-ordination. There is evidence of a very small aluminium resonance at 13 ppm indicative of octahedral aluminium. This latter peak remained in the geopolymer. Curing for 48 hours at 40^{o}C gave a compressive strength of 26 MPa.

Nugteren et al. (2011) investigated waste etching solutions as an alkaline source to activate fly ash and slag to manufacture geopolymers. Potassium silicate/potassium hydroxide/sodium aluminate blends were evaluated and compared to waste etch bath solution. Potassium silicate/potassium hydroxide activation gave a compressive strength of 94 MPa. Gradually replacing potassium hydroxide with sodium aluminate gave a dramatic drop in compressive strength to 3 MPa. This was attributed to preferential reaction of the potassium silicate and sodium aluminate with little waste activation occurring. Additional water was added to improve workability which would also have inhibited strength development. Using sodium aluminate as the sole activator saw compressive strength increase to 31 MPa, whilst the addition of the etch bath activator (polyalcohol/thiosulphate) at 0.4 wt. % saw a further increase to 38 MPa.

The use of the waste solution in combination with potassium hydroxide gave a range of compressive strengths between 43 and 59 MPa. Replacing potassium hydroxide with sodium hydroxide gave a drop in compressive strength from 59 to 49 MPa. Increasing the fly ash to slag ratio (reduced calcium) saw the compressive strength drop from 59 to 43 MPa.

The presence of calcium containing slags leads to the formation of calcium aluminate hydrates in which aluminium is present in VI co-ordinate state.

The authors commented that when excess silica (from potassium silicate) is available in solution, liberation of alumina may quickly result in the formation of sialate chains to form geopolymer precursors. These pastes will thicken and the setting point will be quickly reached. However when aluminate is present instead of silica, it will take time before sufficient silica is liberated from the fly ash to give a suitable silicon to aluminium ratio to form geopolymer gels. It will take longer to thicken and set.

Phair and van Deventer (2002) investigated alkali activation of various materials with several combinations of alkali activating solutions. In the case where ^{27}Al NMR and FTIR were performed on the sodium aluminate solution, they found that the sodium aluminate solution they used to be predominantly IV co-ordinate with a small amount of VI co-ordinate material. (Note: the SA specification was Al_2O_3: Na_2O = 0.89 and 26.5 wt. % Al_2O_3. This is an excess of around 12 wt. % alkali). FTIR of the geopolymer samples revealed a peak at 730 cm^{-1} indicating VI co-ordinate aluminium for 5.1 M aluminium. Peaks for IV co-ordinate aluminium were less prominent. Increasing the NaOH content has a minimal effect on reducing the VI co-ordinate aluminium or promoting the presence of IV co-ordinate material.

Bayer liquor is a by-product from alumina refineries. A typical composition is shown in table 2.5.(Marciano et al., 2006).

Table 2.5 Typical Bayer Liquor Composition based on Marciano et al. (2006).

Component	**Concentration**
Al_2O_3	96 g/l
Na_2O caustic	160 g/l
Na_2O carbonate	28 g/l
Organic carbon	10 g/l
Cl^-	3 g/l
SiO_2	1 g/l
SO_3^-	0.7 g/l
pH	~14
TDS	30 wt.%
Viscosity at 50^oC	3300 Pa.s

Bayer liquor (Jamieson et al., 2012) has been used to replace sodium silicate as an activator for fly ash based geopolymers. Compressive strengths in excess of 40 MPa were obtained for geopolymer pastes cured at ambient temperature.

Verdolotti (2008) compared NaOH and sodium aluminate slurry in NaOH to consolidate pozzolanic soils. They claim that the IV co-ordinate aluminium atoms present in the pozzolana and sodium aluminate change their co-ordination state splitting between IV and VI co-ordinate, modifying the traditional polysialate chemistry.

The pozzolana had silicon to aluminium compositional ratio of 3:1; this ratio in the geopolymer was 2.71:1 for 10 M NaOH and 2.28 for the sodium aluminate slurry in NaOH. This would indicate that the aluminium from the sodium aluminate is affecting the final composition.

The sample treated with 10 M NaOH showed the highest concentration of Q^4 (1Al). The presence of sodium aluminate promotes the co-ordination of four aluminium atoms to SiO_4 tetrahedra. SEM micrographs showed amorphous morphology from 10 M NaOH activated samples. The sample activated by sodium aluminate showed a less homogeneous structure plus needle like crystals spreading over the sample surface.

XRD patterns (Cu kα radiation) showed new crystalline peaks at 42^{o} (2ɵ) in both geopolymer samples and a peak at 27.5^{o} (2ɵ) in the sodium aluminate activated sample. Neither NaOH nor sodium aluminate have refractions at these positions. The peak at 42^{o} (2ɵ) can possibly be attributed to zeolite formation. The intensity of the peak at 27.5^{o} (2ɵ) reduced during the curing period. The authors, supported by FTIR and NMR data concluded that sodium aluminate activation was capable of generating VI co-ordinate aluminium at least during short term curing.

The presence of Al (VI) co-ordinated aluminium species, for short curing times, might affect the polysialate formation in terms of aluminium type and quantity available.

“This result represents further evidence that the polysialate chemistry based on IV co-ordinate aluminium is not capable of describing all the phases of geopolymers”.

The best compressive strengths, 20 MPa (10 M NaOH) and 45 MPa (10 M NaOH/sodium aluminate), were obtained after 300 days curing time.

Hajimohammadi (2008) described the development of a “ just add water” geopolymer cement based on sodium aluminate (solid) and geothermal silica. He observed that high early aluminium concentration inhibits geopolymerisation whilst high early silicon concentration enhances the reaction. To match these requirements the silica source must have a fast dissolution rate so that solutions will rapidly become rich in silicon entities similar to sodium silicate solutions. High early concentrations of aluminate are adsorbed onto the silica surface inhibiting dissolution and high early silicon forms silicate oligomers which can react with aluminate promoting geopolymerisation.

Admixtures

Additives to geopolymer systems are needed to enhance specific properties of the system. The term admixture (ASTM Committee C09, 2012b) is used to cover the wide range of materials added to OPC.

Improvements in workability and setting, reduction in final density, improvements in physical properties, particularly toughness and thermal performance can all be enhanced by the judicious choice of additive(s). The economics of geopolymer systems can be influenced

by the addition of a wide range of fillers (aggregates) of varying compositions and size. Materials such as fly ash, fume silica, metakaolin and slag are considered as admixtures in OPC (ASTM Committee C09, 2012a), but in geopolymers they are considered to be part of the binder system.

Test methods for workability have been reviewed (Koehler, 2009, Koehler and Fowler, 2003). Kantro (1980) developed the mini cone slump test which is suitable for evaluation of the addition of admixtures to cementitious pastes.

In OPC processing superplasticisers are used to improve workability (and reduce water demand) and there are several classes available commercially (table 2.6.).

Superplasticisers are polymeric molecules with several anionic segments. When anionic superplasticisers are added to cement the negative charged segments adsorb on to the surface of the cement particles increasing the overall negative charge. This causes mutual repulsion of the cement particles, breaking up the flocculation and releasing trapped water. This released water reduces the plastic viscosity, improving workability and hence the water-cement ratio can be reduced. In addition to electrostatic repulsion, superplasticisers containing non-polar polymer segments also function by steric hindrance. Segments of the polymer protrude out from the polymer surface into the aqueous phase preventing cement particles from agglomerating (BASF, 2008). Table 2.6 shows the chemical structure of the commonly available superplasticisers.

There are many references to the use of superplasticisers in OPC (Liu et al., 2012, Xiao et al., 2011, Bassioni, 2010, Wild et al., 1996a, Yilmaz et al., 1993, Jiang et al., 1999, Gołaszewski and Szwabowski, 2004, Fernàndez-Altable and Casanova, 2006b, Yllmaz et al., 1993, Wild et al., 1996b, Agullo et al., 1999, Fernàndez-Altable and Casanova, 2006a)

Table 2.6 Superplasticiser structures (after Rixon & Mailvaganam, 1999).

Class	Origin	Structure (typical repeat unit)	Relative cost
Lignosulphonates	Derived from neutralization, precipitation, and fermentation processes of the waste liquor obtained during production of paper-making pulp from wood	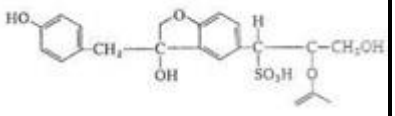	**1**
Sulphonated melamine formaldehyde (SMF)	Manufactured by normal resinification of melamine – formaldehyde	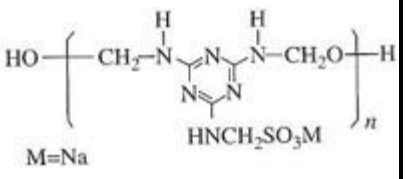	**4**
Sulphonated naphthalene formaldehyde (SNF)	Produced from naphthalene by oleum or SO_3 sulphonation; subsequent reaction with formaldehyde leads to polymerization and the sulphonic acid is neutralized with sodium hydroxide or lime	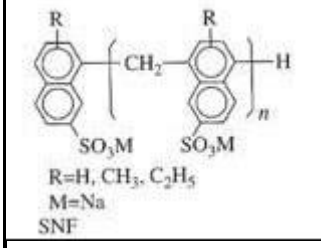	**2**
Polycarboxylic ether (PCE)	Free radical mechanism using peroxide initiators is used for polymerization process in these systems	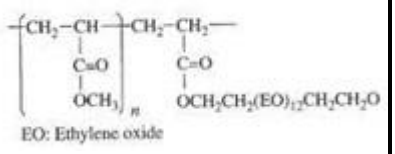	**4**

References to the use of superplasticisers in geopolymer are more limited and are generally based on slag based systems. Bakharev (2000) investigated a range of admixtures in alkali activated slag concrete and found that the air entraining agent improved workability. She suggested that admixtures with nonpolar molecules are better suited to work in a media of

strongly charged particles of alkali activated slag and activator. Palacios (2005) found that only a naphthalene based product retained paste fluidity in a sodium hydroxide activated paste. This was attributed to the good sodium hydroxide resistance of this admixture. The use of calcium hydroxide solution in the chemical resistance test did not affect any of the tested admixtures and confirmed their suitability for use in OPC.

Yilmaz et al. (1993) treated SMF and SNF superplasticisers in 1 M KOH solution. The SMF precipitated out of solution, whilst the SNF was substantially unaffected.

Work by Hardjito et al. (2005) on fly ash based geopolymer concrete used a naphthalene sulphonate type super plasticiser at up to 4 wt. % and achieved increased slump (Figure 2.4). Above 2 wt. % super plasticiser addition compressive strength began to decline.

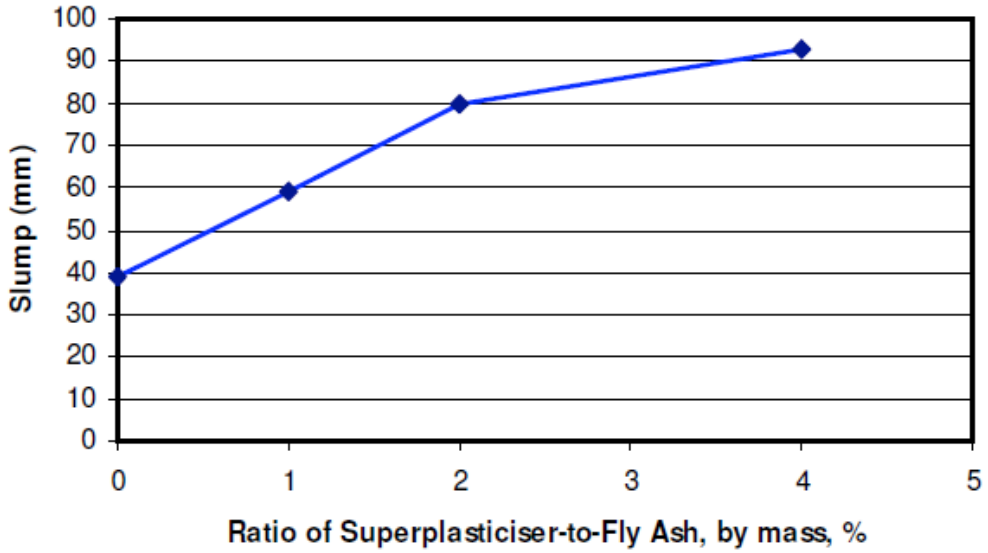

Figure 2.4 Geopolymer concrete slump verses superplasticiser content (Hardjito and Rangan, 2005).

Ghosh and Ghosh (2012) evaluated the workability of fly ash based geopolymer mortar using a mini slump cone. The effect of alkali content, silicon to aluminium ratio, water content and plasticiser dosage where evaluated. He considered that 150 mm flow diameter was the minimum value suitable for mortar that could be readily placed in a mould. Table 2.7 shows their suggested workability criteria for geopolymer mortars.

Table 2.7 Workability Criteria for Geopolymer Mortar (Ghosh and Ghosh, 2012).

Flow Diameter, mm	**Workability**
Above 250	Very High
180 to 250	High
150 to 180	Moderate
120 to 150	Stiff
Below 120	Very Stiff

Increasing alkali content and silica content reduced workability. Dosages of naphthalene super plasticiser above 1 wt. % gave marked improvements in workability.

Memon (2012) reported on the production of self-compacting geopolymer concrete. This type of concrete must be able to flow into position without the use of external vibration. They found that the addition of superplasticiser up to 7 wt. % not only improved flowability but increased compressive strength.

Moura (2011) investigated the formulation of metakaolin geopolymer repair mortars. He found that the use of 3 wt. % superplasticiser with 10 wt. % calcium hydroxide and using 10 M sodium hydroxide gave 80% increase in flow. Compressive strengths over 40 MPa were obtained.

Setting times can be adjusted by the use of accelerators and retarders. Calcium oxide and hydroxide have been reported to accelerate geopolymer setting (Jamieson et al., 2012, Temuujin et al., 2009b).

In US patent 7794537 (Barlet-Gaudedard et al., 2010) the use of lithium chloride, up to 7%, acts as an accelerator, whilst 0.65 wt. % sodium pentaborate extended setting time from 1.5 hours to 3 hours at 110^{o}C. Nicholson (2005) claimed the use of inorganic boron compounds for retarding the setting time of high calcium fly ash based geopolymers.

The introduction of gas cells into geopolymers gives rise to materials with good sound and thermal insulation properties. Air can be entrained in the system during the mixing process and the air bubbles are stabilised by the addition of air entraining admixtures, which reduce

the surface tension at the air-water interface. Alternatively gas bubbles can be generated in situ by chemical reaction. Blowing agents can be hydrogen peroxide, sodium perborates and the reaction of aluminium metal with the activating alkali solution (Liefke, 1999, Reid, 2011, Vaou et al., 2010). Bell and Kriven (2009) compared hydrogen peroxide and spherical aluminium powder as blowing agents in metakaolin based geopolymers. The hydrogen peroxide gave a non-percolating foam structure which cracked on firing. The aluminium powder gave irregular shaped pores with a wide pore size distribution which was crack free after firing.

Fibres

Cementitious materials, typically concrete, are the most widely used materials for infrastructure construction. They are typically characterised by low tensile strength and low strain capacity and are sensitive to micro cracking. Fibres and steel and FRP rebar may be incorporated into cementitious matrices to overcome these deficiencies giving materials with increased tensile strength, ductility, toughness and increased durability (Chanh, 2004, Hameed et al., 2009).

Steel bars are the materials of choice for structural applications, but the addition of “short fibres” now plays an important role in the processing and the development of early stage properties such as plastic and drying shrinkage. The addition of non-metallic structural fibres in geopolymers is opening up new applications. Table 2.8 compares the 3 main classifications of discontinuous fibres. Additionally microfibers can reduce spalling in fire situations. The cement and concrete Association of New Zealand has published a bulletin on fibre reinforced concrete (CCANZ, 2009).

Natural fibres are also finding utility in concrete (Buckeye Building Fibres, 2009, Hercules Fibres, 2011a). Both the natural cellulose fibres listed here are shorter than typical polypropylene fibres of the same diameter. This will lead to more fibre per unit volume of fibre and hence the possibility of better crack control. These shorter fibres should have less influence on workability.

For high temperature applications a range of fibres with increased thermal stability is available. These include, but are not limited to, alkali resistant glass fibre, basalt fibre,

carbon fibre, ceramic fibres (alumina and silicon carbide) and wollastonite (Thang et al., 2010, Fibres Unlimited, 2007, Morrison, 2008, Silva and Thaumaturgo, 2003, Chen and Chung, 1993).

Fibre blends have been introduced to overcome short comings in the use of single type/size fibres. A blend of long and short fibres, where the long fibre imparts structural improvements and the short fibre imparts shrinkage improvements is typical. These blends can be all steel fibres, all organic fibres or mixtures of the two (CCANZ, 2009).

Figure 2.5. and Table 2.8. show the types and properties of the two most commonly used fibre types i.e. steel and polypropylene.

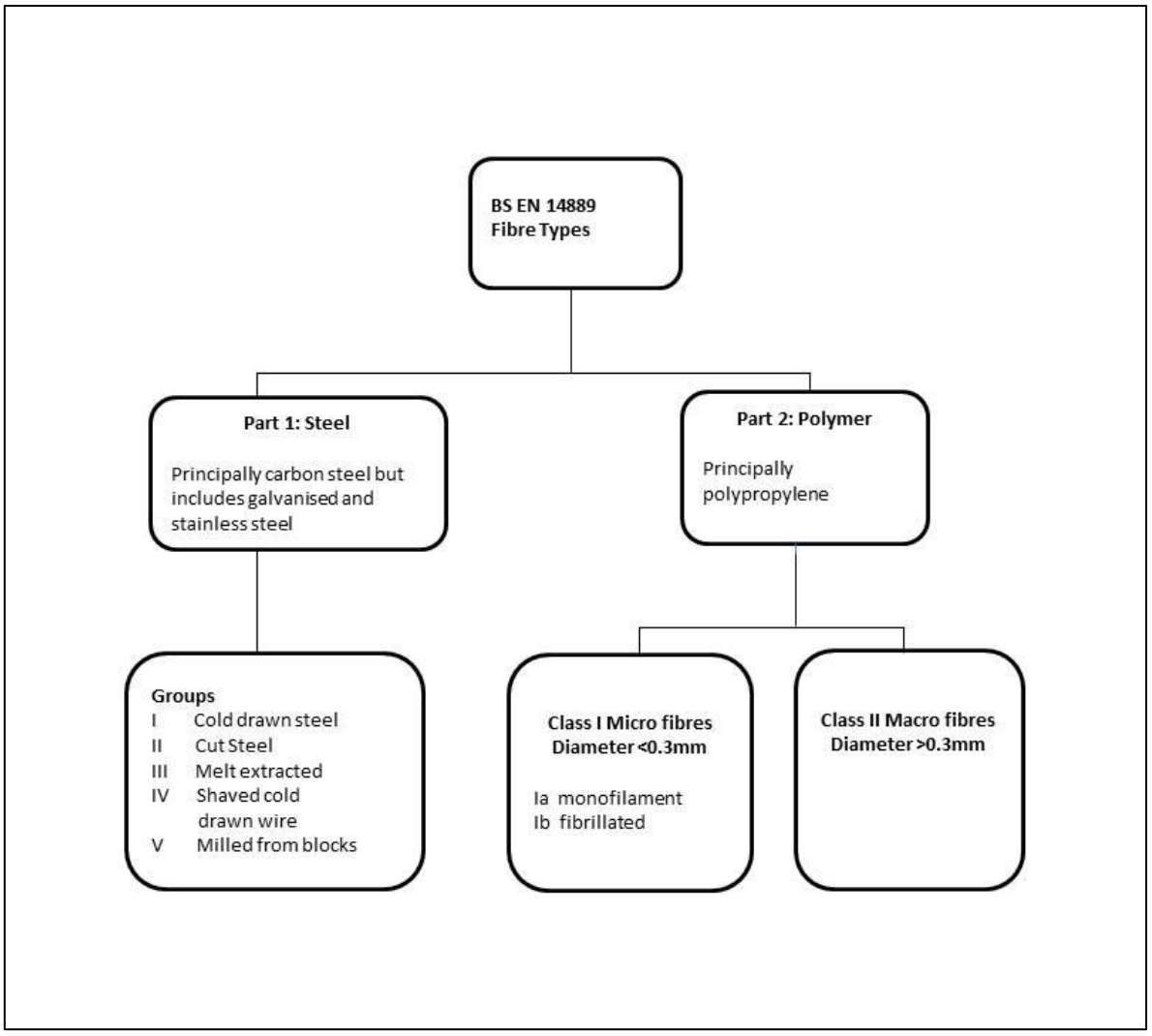

Figure 2.5 Fibre types to BS EN 14889 (Wimpenny et al., 2009).

Table 2.8 Comparison of steel and synthetic fibres (Wimpenny et al., 2009).

	Steel Fibres	**Synthetic micro-fibres**	**Synthetic macro-fibres**
PROPERTY	**Characteristic Property of Fibres**		
Shape/Texture	Cold drawn hooked ends	Straight smooth	Continuously embossed
Collation	Glued bundles	Fibrillated	Uncollated
Typical Length (mm)	60	12	48
Typical diameter (mm)	0.75	0.02 to 0.03	0.5 to 1
Tensile strength (MPa)	1050	30	550
Elastic modulus (GPa)	>200	2	10
Dosage (kg m^{-3})	25 to 35	1 to 2	6 to 10
Service temperature (^{o}C)	300	60	60
Melting point (^{o}C)	>800	150	150
Base material	Carbon steel	polypropylene	Polyolefin (polypropylene, polyethylene)
COMPARISON WITH CONVENTIONAL CONCRETE (UNREINFORCED except for *)			
Workability	Reduced	Slightly reduced	Slightly reduced
Plastic shrinkage cracking	Unaffected	Reduced	Slightly reduced
Early-age thermal cracking	Reduced	Unaffected	Reduced
Long-term shrinkage cracking	Reduced	Unaffected	No data

	Steel Fibres	**Synthetic micro-fibres**	**Synthetic macro-fibres**
Stray current corrosion	Reduced	Unaffected*	Eliminated
Durability in chloride exposure*	Increased	Unaffected*	Greatly increased
Fire spalling resistance	Slightly increased	Greatly increased	Increased
Compressive strength	Unaffected	Unaffected	Unaffected
Residual Flexural strength	Increased	Unaffected	Increased
Impact strength	Greatly increased	Unaffected	Increased
Flexural toughness	Increased	Unaffected	Increased
Abrasion Resistance	Increased	Slightly increased	Slightly increased
Freeze-thaw resistance	Slightly increased	Increased	Increased
Flexural energy absorption	Greatly increased	Unaffected	Greatly increased
Concrete permeability	Slightly increased	Slightly increased	Slightly increased
Pump wear	Increased	Reduced	Reduced
Safety*	Hazard from handling and protruding fibres	Increased	Increased
Finishing	Extra care during floating	Exposed fibres soon abrade	Fibres may float and protrude in poorly designed mixes

Concrete is a cement-water paste in which aggregate is embedded. Aggregate is granular material such as sand, gravel, crushed stone, and other speciality materials that occupy 60

to 75% of the concrete volume. Aggregate properties affect the plastic concrete (workability and drying shrinkage) and hardened properties such as durability, strength, thermal properties and density.

Aggregates are classified as natural, synthetic and recycled. Grading is by particle size and size distribution, particle shape and water content. Crushed aggregate obtained by quarrying and crushing of rock can contain substantial amounts of flat or elongated particles, whereas natural gravel has a rounded shape and smooth surface texture (Cement Concrete & Aggregates Australia, 2008). The ACI committee E-701 produced a bulletin on "Aggregates for Concrete" (2007).

Fine aggregates (<53 μm) can be used as fillers to improve specific properties. Wollastonite, chamotte, and α-alumina are all stable beyond 1000^{o}C and help to control shrinkage in high temperature applications (Kamseu et al., 2010, Buchwald et al., 2009).

2.6 CHEMISTRY

Essentially geopolymer formation is by alkali dissolution of an amorphous aluminosilicate material, followed by hydrolysis of dissolved Al^{3+} and Si^{4+} entities and condensation of the resulting silicates and aluminates to form a geopolymer (Weng and Sagoe-Cretsil, 2007).

The complexities of the geopolymerisation reaction demand that a model compound be used to elucidate the mechanisms involved. Metakaolin is the material of choice by many research groups (Weng and Sagoe-Cretsil, 2007, Rahier et al., 1996, Davidovits, 1991, Barbosa et al., 2000b, Alonso and Palomo, 2001, Rowles and O'Connor, 2003).

2.6.1 Metakaolin based geopolymers

Metakaolin reacts with alkaline sodium silicate solution at below $100^{o}C$ to produce an amorphous, glassy geopolymer (Rahier et al., 1996). Thermal analysis (DSC and TGA), XRD, NMR and mechanical testing were used to characterise the system. The exothermic reaction of metakaolin and sodium silicate solution was followed by DSC. This showed that realistic isothermal cures could be obtained at $60^{o}C$. The maximum heat flow is obtained at the beginning of the reaction and after 4 hours approximately 83% of the maximum reaction enthalpy had been realised. The maximum reaction enthalpy was determined to occur when the metakaolin to sodium silicate (silicon to aluminium) ratio was 1.0.

XRD scans show that metakaolin is predominantly amorphous apart from traces of titanium dioxide impurity from the source kaolin. The resulting geopolymer is also amorphous.

The ^{27}Al MAS NMR spectrum for the geopolymer formed shows a single peak at 58 ppm and a FWHM of 16ppm. This is indicative of tetrahedral aluminium surrounded by 4 silicon tetrahedra. Since only a signal for aluminium tetrahedra is observed in the geopolymer, the other aluminium sites present in metakaolin (Al (V) at 35 ppm and Al (VI) at 0 ppm) are transformed into Al (IV). The same transformation is observed when sodium and potassium hydroxides are used to react with metakaolin. Since the aluminium is four co-ordinated, a sodium ion is required for each aluminium ion for charge balancing and hence the 1:1 sodium to aluminium ratio seen in the DSC results (NOTE: If aluminium is already present in the raw material precursor as Al (IV), then it must already have a charge balancing cation associated with it and will not require M^{+} from the activating solution. Sodium to aluminium

ratios lower than unity can be used in these cases to prevent excess alkalinity which causes carbonation and efflorescence).

Compression testing also showed a maximum value of 60 MPa at a sodium to aluminium ratio = 1.

Rahier concluded that the silicate and aluminate monomers are combined in a random way but with the restriction that each aluminium centre must be linked to four SiO_4 groups so that no Al-O-Al are present. The silicon to aluminium ratio in the geopolymer cannot be influenced by the variability in the reaction mixture but must conform to a unique stoichiometry (NOTE: excess SiO_2 can form water soluble silicate polymers, which can be dissolved out, as shown by before and after leaching NMR spectra, but these polymers can also graft on to the 1:1 stoichiometric geopolymer). He also concluded that less than 5% of the total water in the reaction mixture was chemically bound as Si-OH.

Barbosa et al. (2000b) produced geopolymers from metakaolin (calcined for 6 hours at 700^{o}C) and sodium silicate (modulus=2.0) solutions. The silicon to aluminium ratio and sodium to silicon ratios were varied as was the water content of the reaction mixtures.

The viscosity of one sample (SiO_2: Al_2O_3 = 3.3, Na_2O: SiO_2 = 0.25, H_2O: Na_2O = 10), which gave the best compressive strength of 48 MPa after one hour cure at 65^{o}C was monitored over time. When the results were plotted on a log-log scale a marked change in slope after 40 minutes was observed. This is analogous to increases in melt viscosity as molecular weight increases in organic polymers. The authors proposed that at shorter times before the change point the growing oligmers behave as a dilute solution. As the concentration of oligomers grows they become closer together and are able to react increasing the molecular weight which shows as gel formation beyond the point of slope change.

Samples with H_2O:Na_2O ratios of 25 did not cure sufficiently at 65^{o}C and could not be tested. Samples with a H_2O:Na_2O ratio of 10 gave testable samples, which decreased in compressive strength as the SiO_2: Al_2O_3 and the Na_2O: SiO_2 ratios increased.

MAS NMR spectra were collected on well cured and under cured samples in the liquid phase. ^{29}Si spectra for the well cured sample showed an immediate broadening of the peak and a shift to less shielded values when metakaolin was added to the alkaline activating

solutions suggesting an immediate reaction between silicate solution and aluminate in metakaolin. As this mix was monitored the silicate peaks diminished in intensity over the first seven hours.

In the case of under cured samples peaks broadened on initial addition of metakaolin, suggesting an initial reaction , but the silicate peak intensities remain virtually unchanged up to fifteen hours after mixing, indicating that consumption of the silicate by polymerisation is not proceeding.

FTIR results showed the presence of sodium carbonate in the under cured samples, but not in the fully cured. The sodium carbonate is formed by reaction of sodium silicate and/or sodium hydroxide with atmospheric carbon dioxide. Attempts to detect the presence of a ^{27}Al NMR signal were unsuccessful indicating insignificant dissolution of aluminium from the metakaolin.

MAS NMR of ^{27}Al in the geopolymer showed a strong, narrow peak in the well cured geopolymer, but the under cured samples showed intensities of the same peak ranging from 3.4% to 11%. This indicates that the aluminate tetrahedra are more ordered in the well cured geopolymer.

The optimum conditions for geopolymer formation are when Na_2O: SiO_2 = 0.25, and H_2O: Na_2O = 10. This sodium level satisfies the charge balancing requirements without excess material for carbonation reactions which can disturb polymerisation reactions. Sufficient water is required for wetting and mixing and to provide a mechanism for ionic transport. The effect of extra water may be to dilute the reaction (reduce pH) and transport soluble species away from reaction zones.

Rahier (1996) had shown previously that the aluminium to silicon ratio in the geopolymer is the same as aluminium to silicon ratio in the precursors if M^+ : aluminium = 1. He then went on to investigate the reactions between sodium and potassium silicate solutions and metakaolin(Rahier et al., 1997). The influence of the molar ratios H_2O: R_2O (w) (between 6.6 and 21) and SiO_2: R_2O (s) (between 0 and 2.3) of the silicate solution were investigated.

Differential Scanning Calorimetry (DSC) could not be used for w = 6.6 (Na) and w = 8.1 (K) because of poor mixing. Poor wetting of the metakaolin particles at low w values could have

led to incomplete reaction with corresponding lower enthalpy values. The effect is more pronounced with sodium silicates due to a higher solution viscosity compared to potassium silicate solutions.

Rahier (1997) Showed that when the SiO_2: Na_2O ratio was greater than 0.8 amorphous geopolymer was formed. When the ratio was less than 0.8 the product was partially crystalline. This was attributed to depolymerisation of the larger silicate entities by the alkali cation.

The upper limit of the molar ratio, s, is also determined by the reaction rate which becomes slower with increasing s. For values above 2.3 for sodium silicate and 1.9 for potassium silicate the reaction does not go to completion within the time scale of days at ambient temperature. The reaction of metakaolin with potassium silicate is slower than for sodium silicate solutions with the same s and w values.

Zuhua (2009a) activated metakaolin with equal volumes of increasing molarity sodium hydroxide solution. He used calorimetry to measure the heat evolved as the molarity and time increased. There is an initial peak, the size of which increases with molarity. The author attributed this region to dissolution – hydrolysis. The heat evolution then decreases before increasing again. The rate of heat evolution and the maximum value of the second peak are higher for increasing molarity up to 9 M. Using 12 M NaOH led to a lower rate of heat evolution and second peak height. The high hydroxyl ion concentration is postulated to be having an adverse effect on the polycondensation reaction, possibly by hydrolysis of the formed condensed products. This region is attributed to hydrolysis-polycondensation. The 3 M NaOH solution showed very little heat evolution in either region and this was attributed to the high water content of this solution.

The next series of calorimetry work used 12 M NaOH at liquid to solid ratios of 1, 1.2 and 1.25. The higher liquid to solid ratio showed the highest reaction in the first region, but in the second region the mechanism changes from hydrolysis (using water) to polycondensation (releasing water) and the lower liquid to solid ratio showed the highest heat evolution.

Zuhua believes that water is a reactant in the initial region (hydrolysis) and the hydroxyl group is the catalyst (NOTE: Purdon stated that alkali was a catalyst in activation of slag). He gives a series of reaction equations to support this position. Similarly water is a product of the polycondensation reaction so lower water contents at this stage will help the reaction move from left to right (towards products) to establish equilibrium. This product water is now available to take part in further dissolution reactions which are taking place simultaneously with the polycondensation.

Weng (2007) reported that Henry (1992) demonstrated that the chemical reactivity of metal ions during the processes of hydrolysis and polycondensation can be predicted and explained by the partial charge distribution in molecular species. The values calculated are useful only for direct comparisons.

The initial step in the geopolymerisation mechanism is the dissolution of metakaolin which provides aluminate ions and, at least, part of the silicate ions. Based on the partial charge method (PCM) the calculated results indicate that $[Al(OH)_4]^-$ is the major Al species under alkaline conditions, while the major silicate structures are $[SiO(OH)_3]^-$ and $[SiO_2(OH)_2]^{2-}$. The concentration ratio of $[SiO_2(OH)_2]^{2-}$ to $[SiO(OH)_3]^-$ increases with alkalinity. This can be depicted as follows:

$$Al_2O_3 + 3H_2O + 2OH^- = 2\,[Al(OH)_4]^{-1} \qquad \text{Equation 2.1}$$

$$SiO_2 + H_2O + OH^- = [SiO(OH)_3]^{-1} \qquad \text{Equation 2.2}$$

$$SiO_2 + 2\,OH^- = [SiO_2(OH)_2]^{-2} \qquad \text{Equation 2.3}$$

This suggests that H_2O and OH^- are consumed during dissolution.

The setting and hardening of geopolymers occurs as a result of condensation between aluminate and silicate species and this reaction is more rapid than the reaction between silicate species.

Equation 2.4 below shows a molecule of water being released during the condensation reaction.

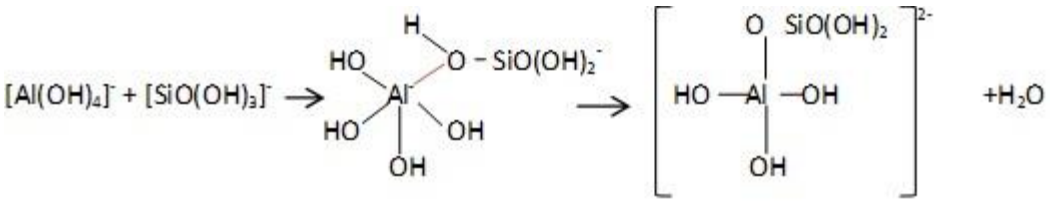

Equation2.4

The aluminate can react with either of the silicate species shown above and the authors show the range of stabilities of the various resultant products. To summarise the condensation between aluminate and silicate species is dependent on the speciation of the silicate entities. The condensation between $[Al(OH)_4]^{-1}$ and $[SiO_2(OH)_2]^{-2}$ tends to form small oligmers such as dimers and trimers , whilst the condensation with $[SiO(OH)_3]^{-1}$ results in larger oligmers and polymers. Therefore the formation of geopolymer depends on the concentration of $[SiO(OH)_3]^{-1}$ which favours lower alkalinity values.

They proceeded to evaluate the influence of increasing sodium hydroxide molarity on silicon and aluminium entity dissolution from metakaolin and also carried out calorimetry. The calorimetry showed an immediate large exotherm effect when metakaolin was mixed with sodium hydroxide solutions in the range 1 M to 15 M. A second exotherm evolved in the 5 M and 10 M solutions with that in the 10 M being faster and more pronounced. Dissolution of metakaolin in 2 M, 5 M and 8 M sodium hydroxide solutions showed that higher alkalinity resulted in higher amounts of dissolved aluminium and silicon entities. The digestion rates decreased at extended times and the aluminium component in the metakaolin dissolved more rapidly than the silicon component except in the 8 M solution at extended digestion times.

NMR results confirmed the presence of $[Al(OH)_4]^-$ but no monomeric silicate was observed. This was attributed to the fast reaction of aluminates and silicates and higher dissolved concentrations of aluminate compared to silicates. The formation of a shoulder in the ^{29}Si NMR spectra at -87 ppm is attributed to these aluminosilicate products with each silicon atom co-ordinated to 4 aluminium atoms. NMR also confirmed the decrease in free water.

The condensation reactions take place in an optimum band of alkalinity. At low molarity the dissolution rate is too slow to generate sufficient reactant products for condensation to

occur. If the alkalinity is too high then most of the silicate exists as $[SiO_2(OH)_2]^{2-}$ which is not favoured for the condensation process. The condensation reactions are only occurring in the range 5 M to 10 M as confirmed by the calorimetry results.

De Siva (2008) investigated the influence of aluminium and silicon concentrations on setting times and strength development of geopolymers based on metakaolin and sodium silicate. Setting times were controlled by aluminium concentration and were shown to increase with increasing SiO_2: Al_2O_3 ratios of the initial mixes. Increases in aluminium concentration led to low strength products which showed grain like structures in SEM images as opposed to amorphous geopolymer phases for higher silicon content geopolymers i.e. the strength characteristics depend more on the silicon content.

The authors suggested that the aluminium component of metakaolin is more readily soluble than the silicon component and in the lower silicon: aluminium systems it is possible that more monomeric aluminate ions are available for condensation. Polysialate structures are likely to be formed in this case. With increasing silicon content more silicate species are available for condensation, which can take place between silicate species resulting in oligmeric silicates. Further condensation between these oligmeric silicates and aluminates results in a three dimensional, rigid structure based on poly (sialate disiloxo) and poly (sialate-siloxo) derivatives. The rate of condensation between silicate entities is slower than that between aluminate and silicate resulting in slower setting with increasing silicon content.

Duxson (2007) presented a simplified model for the geopolymerisation process (figure 2.6). Dissolution of the aluminosilicate source by alkaline hydrolysis (consuming water) releases aluminate and silicate species. These then form an equilibrium mix with aluminosilicate material and any added silicate or aluminate species from the activating solutions. In concentrated solutions, as employed in geopolymer synthesis, this results in the formation of a gel as the oligmers in the aqueous phase form large networks by condensation releasing water which is consumed in the dissolution process. This water resides in the pores of the gel. Reorganisation of gel 1 to gel 2 occurs with the release of more water. Finally polymerisation via a condensation step occurs.

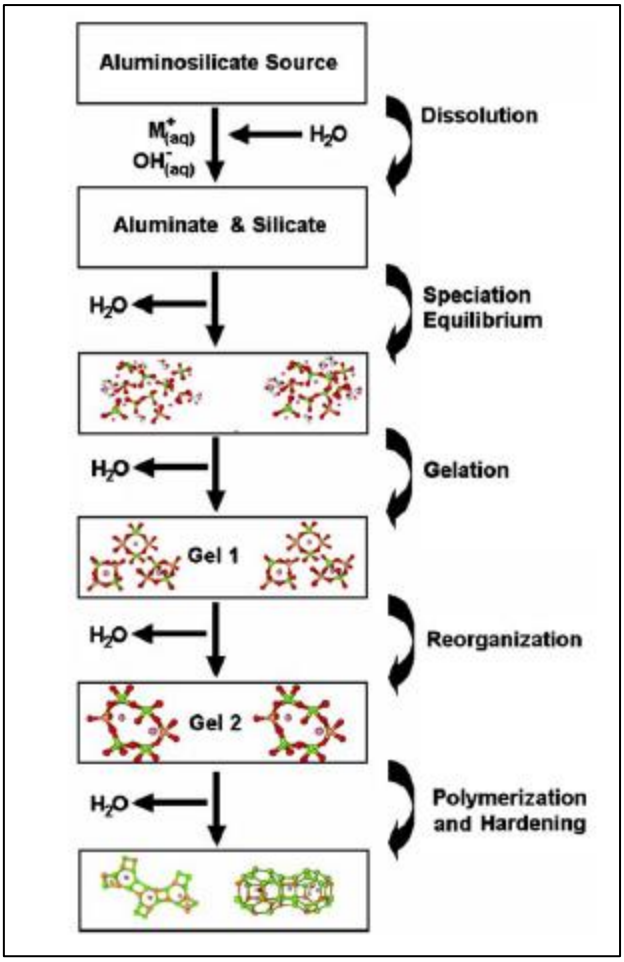

Figure 2.6 Simplified geopolymerisation process model Duxson et al. (2007).

Steins (2012) investigated the geopolymerisation step using rheology, small angle x-ray scattering (SAXS) and electron paramagnetic resonance (EPR). Metakaolin activated with sodium, potassium or caesium hydroxides with Al: M^+ adjusted to 1 was used in the investigations.

Dynamic rheological measurements were carried out using a controlled stress rheometer. Applied strain was 1 x 10^{-4} and frequency was 1 rad s^{-1}. The geopolymer paste was initially prepared outside the rheometer with 5 minutes mixing carried out in a bowl with a helical ribbon impellor and then introduced to the rheometer test cell. Transferring the paste to the measurement cell introduces stress which must be relieved prior to performing the test. This was achieved by applying a strain of 0.05 and a pulsation rate of 5 rad s^{-1}. Evolution of the viscoelastic parameters (G', the elastic modulus; G'', the loss modulus; tan δ, the ratio between G' and G'') was recorded during geopolymerisation at ambient temperature.

Regardless of the alkali activator used the geopolymerisation process is similar but dissolution and condensation rates are different. This was attributed to the different charge densities of the alkali cations. Small cations (Na^+) have a more compact hydration sphere than larger cations (K^+, Cs^+) which more readily bind with negatively charged silicates which are partly de-protonated at pH >> 10. The peak in the tan δ curve equates to gel time. See figure 2.7

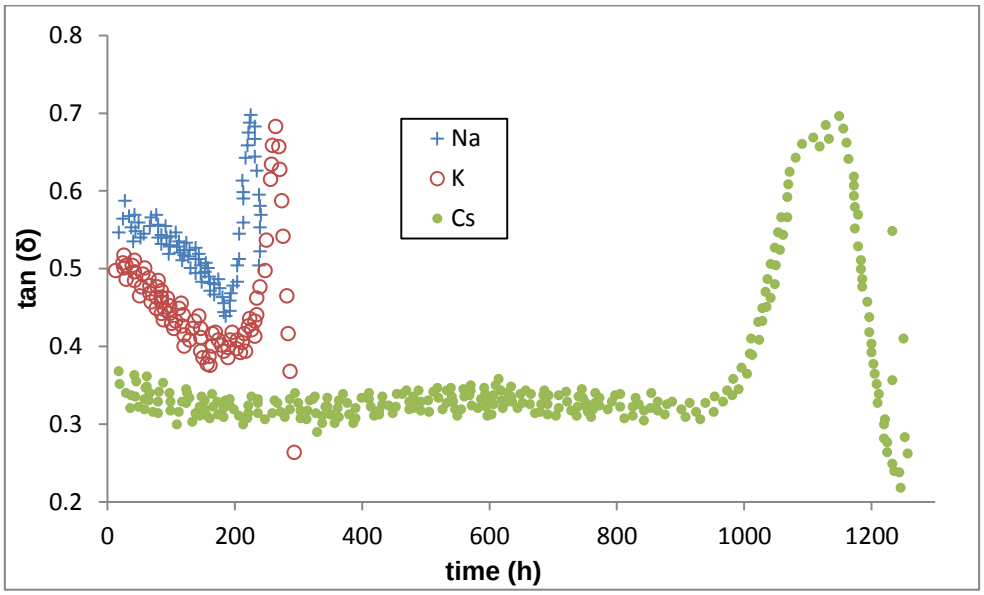

Figure 2.7 tan δ development at ambient temperature (Steins et al., 2012).

SAXS traces were run on the activating solutions and metakaolin dispersed in water to set up reference points. The geopolymer reaction mixtures were then run at intervals. A decrease in SAXS intensity is characteristic of the presence of sharp interfaces between two media of different electron density. This was attributed to metakaolin particles surrounded by activating solution. As the metakaolin dissolves there is a decrease in the signal at low q values and a simultaneous increase in the signal intensity for the formation of new monomers and then the formation of secondary structural units. Finally new aggregation is observed as shown by a scattering intensity decrease that reveals a new interface. The intermediate signal due to monomers has become small suggesting conversion to oligmers is complete. Several events occur simultaneously, the dissolution of the metakaolin leading to the appearance of monomers or oligmers in solution and the reaction of these with the activating solution leading to nano-metric structures which evolve into the geopolymer

network. At the end of geopolymerisation the intensity variation indicates a sharp, new interface of the solid geopolymer separated from pore solution.

The reaction dynamics of water during geopolymerisation was followed by EPR using a paramagnetic probe. Before the formation of a percolating network water is consumed during the hydrolysis/dissolution step and then regenerated during polycondensation reactions. In each case the energy of hydration and the alkali cation hydration sphere play an important role in local arrangement, gelation and consolidation of the geopolymer network.

The paramagnetic probe is gradually masked during geopolymerisation due to protonation of the nitroxide radical and reappears during polycondensation reactions (see equation 2.5).

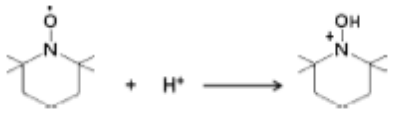

Equation 2.5

De Lacaillerie (2012) presented a similar body of work to Steins. He used NMR instead of EPR. In figure 2.8 he identified four regions for the geopolymer mechanism.

- Region 1. Initially aluminium goes into solution. Less than 1% aluminium is in solution at any one time. This is the rate determining step for geopolymerisation.
- Region 2. Aluminium rich gel forms around the grains resulting in an elastic modulus.
- Between regions 2 and 3 there is a transformation into a silicon rich gel.
- Region 3. Gel commences to harden and form geopolymer
- Region 4. Cured geopolymer.

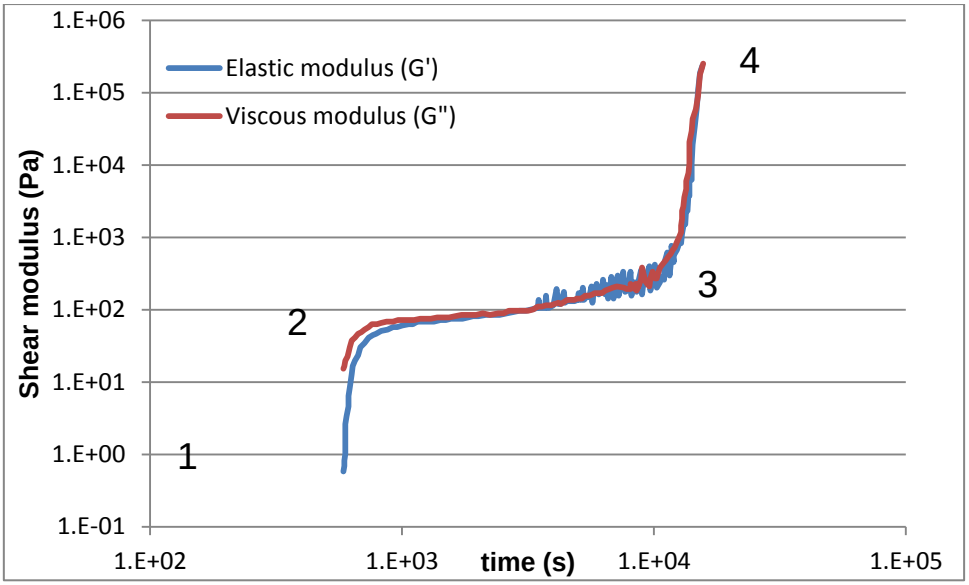

Test conditions: 0.5% strain at 1Hz. Pre-mix 5 minutes at 100Hz.

Figure 2.8 Development of shear modulus(De Lacaillarie et al., 2012).

The SAXS was used to investigate the effects of SiO_2: Na_2O ratio on the speciation of the silicate activating solution. NMR was used to follow changes in aluminium co-ordination in metakaolin through to hardened geopolymer.

The origin of the early elastic modulus cannot be ascribed to interactions between metakaolin particles or to the presence of sodium silicate as this is viscous. It is attributed to the formation of an aluminosilicate gel (Gel 1 in the Duxson model in figure 2.6).

2.6.2 Fly ash based geopolymers

The analysis of the geopolymerisation mechanisms and kinetics are made more difficult than those of metakaolin due to the presence of significant crystalline phases (typically mullite, quartz and haematite). The alkali reactive glassy aluminosilicates may not be readily accessible for alkali dissolution reactions, being shielded by non-reactive phases. Variations between fly ash types and between different batches of the same fly ash further complicate the issue. The presence of soluble calcium entities changes the kinetics of fly ash geopolymerisation.

Fernández-Jiménez et al. (2003) analysed five Spanish Class F fly ashes and used compressive strength to judge the suitability of the fly ashes for geopolymerisation. The

major factors in fly ash composition for geopolymerisation were determined to be the reactive silica content, vitreous phase content and particle size distribution.

Fernández-Jiménez et al. (2005) developed a model for the synthesis of geopolymers from fly ash using alkaline activation. In this model the glassy constituents of the fly ash are converted by highly alkaline activating solutions into cementitious geopolymers. Using SEM to observe changes to micro structure over the cure period at 85^{o}C the mechanism shown in figure 2.9 was developed.

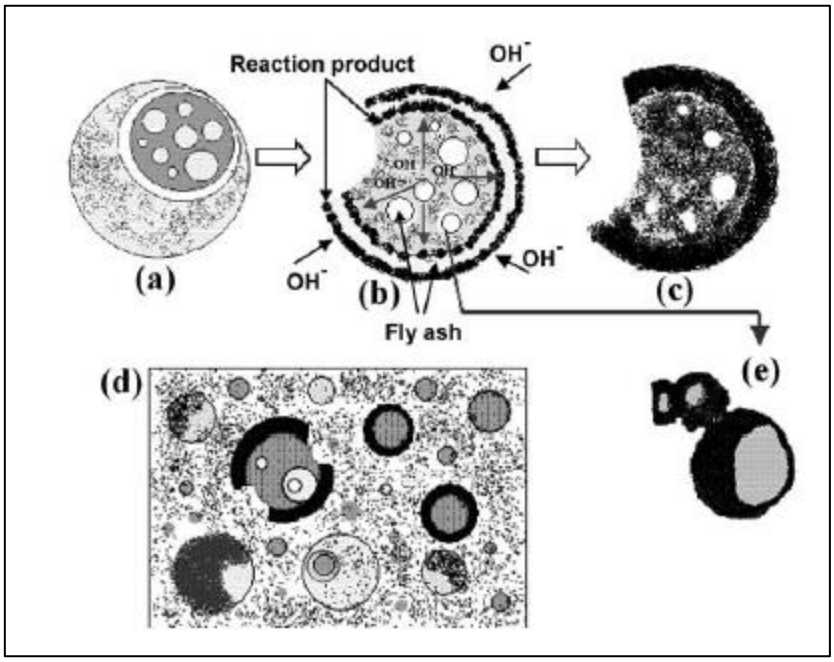

Figure 2.9 Alkali activation of fly ash model (Fernández-Jiménez et al., 2005).

Figure 2.9 shows the initial alkali attack at one point of the fly ash surface which then grows into a larger hole (figure 2.9b) exposing smaller spherical particles, which can be hollow or solid, to alkaline attack from the outside in and from the inside out. Reaction product is generated both inside and on the outside of the fly ash shell until the particle is almost or completely consumed (figure 2.9c). The mechanism involved at this stage is dissolution. One of the consequences of reaction product precipitation is that a layer of these products covers portions of the smaller fly ash spheres. This covering prevents access of the alkaline activating solution (figure 2.9e). As alkaline activation continues, the unreacted fly ash buried under the precipitates may not be affected by the high pH of the activating solution and a reduction in reaction rate may occur. Activation is now governed by a diffusion

mechanism. Several morphologies may co-exist in the paste, e.g. unreacted particles (both glassy and crystalline), particles attacked by alkali but retaining their spherical shape, reaction product etc. (figure 2.9d). This model was also applicable to activation by sodium silicate solutions.

Fernández-Jiménez et al. (2006) investigated three class F fly ashes with similar Si:Al ratios, but different reactivity, indicating that not all the silicon and aluminium entities are reactive towards alkaline activation. The degree of reaction was determined by using 5 wt. % hydrochloric acid, which dissolves the reaction products of alkali activation (aluminosilicates) but not the unreacted fly ash. The concentration of dissolved aluminium was determined by ICP-MS. Analysis of compressive strength, degree of reaction and microstructure characterisation showed that the preferred fly ash for alkaline activation should have high contents of reactive silica and alumina and $(Si:Al)_{Reactive}$ of less than 2. For short reaction times gels have an aluminium rich phase in which silicon tetrahedra are surrounded by four alumina tetrahedra ($Q_4(4Al)$). As the reaction progresses this phases evolves into a more stable silicon rich phase in which higher amounts of silicon occupy $Q_4(3Al)$ and ($Q_4(2Al)$. Improvements in mechanical properties are observed as the reaction progresses.

Van Jaarsveld and van Deventer (1999) concluded that the alkali metal cations control and affect all stages of the geopolymerisation reaction. During the dissolution process they arrange ions and soluble species and play a structure directing role during gel hardening and eventual crystallisation. Dissolution of fly ashes from different sources will dissolve with different silicon: aluminium ratios depending on the alkali cation present.

Criado (2007) investigated the effect of SiO_2: Na_2O on the alkali activation of fly ash. Four activating solutions with different soluble silica contents were used. The main reaction product was a sodium aluminosilicate gel with different zeolites appearing as minor phases. The amount and composition of the reaction products depended on the soluble silica content in the activating solutions and the thermal curing conditions. The amount of gel was related to the development of mechanical strength in the geopolymer.

XRF and QXRD were used to calculate the amorphous and crystalline components of the fly ash and reaction products. Curing was carried out at 85^{o}C for times ranging up to 180 days.

Determination of produced reaction products was carried out by dissolution in 1.76 % hydrochloric acid solution. The acid dissolves the reaction products (sodium aluminosilicate and zeolites) leaving insoluble fly ash residues behind.

At short cure times (8 hours) an increase in soluble silica concentration developed compressive strength > 30 MPa compared to ~15 MPa for the lower soluble silica content. After 20 hours all systems were showing > 40 MPa compressive strength. The long cure times (180 days) showed compressive strengths of > 70 MPa across all the systems investigated.

Crystalline zeolites, sodalite and chabazite-Na were found in the low soluble silica content systems even at the short cure times. Increasing the soluble silica level retarded the formation of zeolite species to longer cure times and promoted the formation of Zeolite Y and Zeolite P. The percentage of zeolites always grows at the expense of aluminosilicate gel which may confirm that the geopolymer gel is a zeolite precursor.

The amount of vitreous phase (from the fly ash) decreased with increasing cure time in all systems. The systems with high soluble silica contents showed a slower rate of vitreous phase consumption. This was attributed to the soluble silica being highly polymerised, which reduces the rate of ash dissolution. The delay in the initial dissolution of fly ash seen in systems with high soluble silica and reduction in the activation kinetics is offset by the formation of larger molecular species with a denser more compact gel.

The quartz and mullite phases from the fly ash were observed to decline slightly at the longer reaction times suggesting partial attack by the activating solutions.

Fernández-Jiménez (2005) first used the term N-A-S-H (sodium aluminosilicate hydrate) for the sodium aluminosilicate formed as the main reaction product of alkali activation of fly ash. Whenever an alkaline activating solution is used with fly ash an alkali metal aluminosilicate gel is formed as the main product. This gel is responsible for the mechanical properties. Alkaline activators based on sodium hydroxide, sodium hydroxide and sodium silicate and sodium hydroxide and sodium carbonate were evaluated with a class F fly ash.

The Na_2O content plays an important role in the development of physical properties. Increasing the Na_2O content in the sodium hydroxide activator system led to increases in

compressive strength up to 70.4 MPa. When soluble silica (sodium silicate) was added to the activating solution compressive strength showed further increases to 90 MPa after 20 hours curing at 85^{o}C. In addition to the SiO_2:Na_2O ratio, water to binder ratio needs to be considered. Higher water contents reduce the pH (lower HO^- concentration) and reduce the rate of dissolution. The presence of carbonate ions in the activating solution leads to low strength (35MPa) geopolymers even if Na_2O levels are high. Small amounts of zeolite crystals were detected and their presence probably indicates that these crystalline products are the thermodynamically stable phases towards which the system could evolve over time.

The mechanism controlling the chemical reaction giving rise to the aluminosilicate gel is initially associated to a dissolution process (the high concentration of OH^- ions in the system is responsible of the breakdown of the Si–O–Si, Si–O–Al and Al–O–Al bonds forming part of the vitreous phase of the ash and leading to the formation of Si–OH and Al–OH groups). Later on these chemical species condense giving place to the precipitation of precursor.

The addition of sodium silicate to the activating solution enhances the polymerisation process of the ionic species present in the system. Activating solutions made from sodium hydroxide and sodium silicate need to be optimised in terms of not only the SiO_2:Na_2O ratio but also the actual amounts. A threshold exists at Na_2O > 7% and SiO_2 > 1% above or below which mechanical strength development at 85^{o}C is less than 65 MPa. Equilibrium between NaOH and sodium silicate in the solution should be reached in order to maintain the system with a high pH and a high level of soluble silica.

When the activating solution is a mixture of sodium hydroxide and sodium carbonate, the main modification induced to the system is the incorporation of carbonate to the mixture, which promotes the formation of sodium bicarbonate (trona) among the reaction products. This involves a reduction in pH leading to lower amounts of aluminium and silicon dissolved from the fly ash. This could explain the porous microstructure and low strengths obtained with this activator solution.

The alkali metal cations play a charge balancing role where aluminium ions (Al^{3+}) have replaced silicon ions (Si^{4+}).

2.6.3 The role of calcium compounds

Van Deventer et al. (2007) found that the amount of Ca^{2+} and the form in which it is added both play a role in determining the properties of the final geopolymer. The level of dissolved silicate in the activating solution also plays a significant role in determining the effects of calcium on the final reaction product by influencing the pH of the reacting system and affecting the stability of the different calcium precipitates. The addition of highly alkaline activating solutions to a fly ash containing any calcium leads to rapid dissolution of the calcium from the ash followed by precipitation of calcium hydroxide. This has the effect of removing OH^- ions with consequent pH reduction which will influence the dissolution and condensation geopolymerisation processes. The addition of small amounts of calcium in the form of a soluble salt to a class F fly ash based geopolymer reaction system drastically increased the solidification rate and early yield stress.

Yip (2008) investigated the effect of different calcium silicate sources on geopolymerisation. Calcium dissolution from manufactured sources (Portland cement or blast furnace slag) at low alkalinity forms CSH phases in conjunction with the geopolymer gel. Less calcium dissolves from natural calcium silicate minerals with little formation of CSH phases. The undissolved mineral disrupts the geopolymer resulting in lower overall strength. The co-existence of CSH and geopolymer phases give rise to acceptable levels of mechanical properties of the binder systems synthesised at low alkalinities. At high alkalinity calcium plays a lesser role as it forms precipitates rather than hydrated gels.

Temuujin (2009b) studied the addition of calcium oxide and hydroxide at 1, 2, and 3 wt. % to a fly ash based geopolymer synthesis. Curing was carried out at 20 and 70^{o}C. Geopolymers made with calcium hydroxide showed higher compressive strengths than those produced with calcium oxide when cured at 20 and 70^{o}C. Higher levels of compressive strength were obtained at 70^{o}C in every case.

Dombrowski (2007) added up to 20 wt. % calcium hydroxide to a fly ash synthesis mix by replacing fly ash with an equivalent weight of calcium hydroxide. 8% substitution of fly ash gave the best compressive strength results after curing at 40^{o}C.

Diaz (2010) investigated factors involved in the suitability of fly ashes for the manufacture of geopolymers. He used five fly ashes with calcium oxide levels ranging from 1.97 wt.% to

22.45 wt.%. XRD scans (using a copper source) were performed on fly ashes and geopolymers. The glass diffraction maximum (GDM) is the highest point in the broad hump area. The location of the GDM in fly ash containing up to 20% CaO is typical of a siliceous glass structure with 2θ values of 22.7^{o} to 27.5^{o}. Above 20% CaO the GDM remains around 2θ values of 32.2^{o}, a value typical of calcium aluminate glass structure that is generally more reactive with water compared to the siliceous glass structure. This can lead to the formation of calcium silicate hydrate structures additional to the geopolymerisation products leading to improvements in mechanical properties.

Setting times as short as 1.5 minutes for the highest CaO content were recorded, whilst the lowest content gave 300 minutes setting time. Compressive strength increased with increasing CaO content of the fly ash (see figure 2. 10).

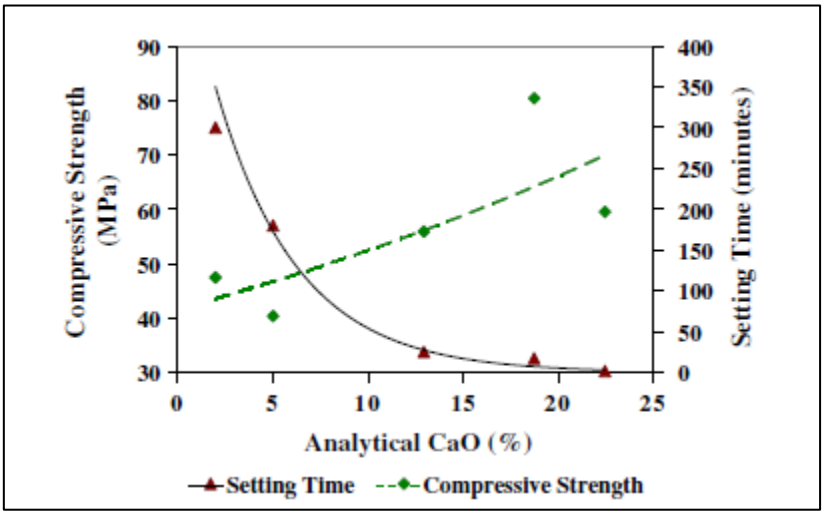

Figure 2.10 Changes in setting time and compressive strength with wt. % CaO (Diaz et al., 2010).

2.7 Fibres: Technical Benefits

Cementitious materials, typically concrete, are the most widely used materials for infrastructure construction. They are typically characterised by low tensile strength and strain capacity and are sensitive to micro cracking.

Fibres and steel and FRP rebar may be incorporated into cementitious matrices to overcome these weaknesses giving materials with increased tensile strength, ductility, toughness and increased durability (ACI E2-00, 2006).

The use of fibres to enhance the properties of construction materials dates back thousands of years to the use of straw and reeds in bricks and animal hair in plaster. Fibres can reduce plastic cracking in fresh concrete and improve the post crack ductility of hardened concrete. While the random orientation of the fibres means they are not as efficient as conventional reinforcement for dealing with predictable stresses, they are able to resist crack propagation under unforeseen stresses, particularly those arising close to the surface of elements during construction and service, particularly impact (Wimpenny et al., 2009).

In her PhD. thesis Jansson (2008) believed that the effect of fibres can be distinguished at two levels: the micro level and the macro level. The micro level covers a short stage after the linear elastic stage is surpassed, where small cracks arise from initial flaws in the matrix. As load increases the length of the micro-cracks increases and they coalesce and finally localise into macro-cracks. For a given fibre content, micro-fibres, due to their vast number are more likely to cross these micro-cracks. For microfibres to be effective they should have a high aspect ratio and stiffness to enable them to restrain the micro-cracks as they propagate into the cementitious binder. If an improvement in structural properties is desired e.g. in bending, then fibres must be selected with sufficient length to bridge macro-cracks and specific mechanical properties.

Jansson referred to Naaman (2003) who claimed that in order to be effective in concrete matrices, fibres must have the following properties:

- Tensile strength of approximately two to three orders of magnitude higher than that of concrete.
- Bond strength with the concrete matrix of the same order or higher than the tensile strength of the matrix.

- Elastic modulus in tension at least three times higher than that of the concrete matrix.

In order to overcome detrimental de-bonding the Poisson's ratio and the coefficient of thermal expansion should preferably be of the same order for both fibre and matrix. Introducing fibre surface deformation to create mechanical anchorage could help increase bonding performance.

As concrete is loaded, cracks form. Initially the cracks are short, discontinuous micro-cracks, which coalesce to form large macro-cracks. Fibres bridge cracks, transferring the load and delaying the coalescence of cracks. Crack formation and development is affected by the shape, size, type and volume of the fibre reinforcement. Steel bars are the materials of choice for structural applications, but the addition of "short fibres" now plays an important role in the processing and the development of early stage properties such as plastic and drying shrinkage (Banthia and Gupta, 2006). Additionally non-metallic structural fibres are finding application (Brugge, 2011, Forta Corporation, 1999).

The following attributes are required for a fibre to reinforce cement mortar (Karbhari, 1998):

- Strain to failure higher than that of cement mortar
- Small fibre diameter
- Hydrophilic surface that give good dispersing and bonding
- Long term durability in alkaline environments
- High strength and modulus
- Overall durability to harsh external environments

Drying and plastic shrinkage cracks are surface cracks that occur due to water evaporating too quickly from the surface of concrete during the curing process. This causes the surface of the concrete to dry quicker than the layers below and "shrink", leaving behind thousands of tiny cracks in the concrete (Cement Concrete and Aggregates, 2005).

The primary function of these microfibers is to modify the properties of fresh, plastic concrete. They can improve homogeneity, reduce bleeding and reduce plastic settlement and plastic shrink cracking. The influence of microfibers on the compressive properties of hardened concrete is relatively small but they can reduce permeability and increase resistance to impact, abrasion and shatter and can reduce spalling in the event of exposure to fire. They also provide some resistance to damage caused by frost (CCANZ, 2009).

Fibres may be classified by strength/stiffness i.e. high modulus such as steel and carbon fibres and low modulus such as polypropylene. The interface between the fibres and concrete is important to determining the properties of the composite (Naaman, 2008).

In OPC there is often nucleation and growth of calcium hydroxide on the surface of the fibres which results in the formation of a porous layer about 10 μm from the surface of the fibre (Bentur et al., 1985). This interface between fibre and matrix means an approaching crack can be diverted along the interface and run parallel to the fibre. The failure strain is only a fraction of the fibre yield strain and fibre pull out occurs rather than tensile failure of the fibre.

In High Performance Concrete (HPC) the presence of microsilica and low water/cement ratio used means that the porous layer is eliminated and fibre anchorage improved. This leads to improvements in strength, deformability, impact resistance and drying shrinkage of HPC by fibre additions (Gani, 1997). The addition of micrometre sized diameter thermoplastic fibres is critical to the survival of HPC in the event of high temperature excursions such as fire exposure (Papworth, 2000).

Fibres can be beneficial under extreme environments, such as chloride exposure and fire situations. Fire and wear resistance are enhanced and the discrete nature of fibres means that the risk of corrosion and spalling are reduced (Greenhalgh, 2003, Perry, 2006).

The mining and tunnelling industry make extensive use of fibres in sprayed concrete linings. Here fibres allow the lining to retain ductility under high deformation which is critical for safety. Precast tunnel segments have utilised both steel and organic fibres for component handling and fire resistance respectively. Marine installations use macro organic fibres to eliminate corrosion risk due to sea water exposure (Brugge, 2011, Wimpenny et al., 2009).

There are applications such as curtain walls and ducting where cement mortar could be used if tensile strength, flexural modulus and toughness could be improved. Asbestos fibres in the chopped form had been used for reinforcement in thin boards and panels to increase toughness and prevent cracking. Potential replacements for asbestos have ranged from steel fibres, polyolefin and nylon fibres through to aramid, glass and carbon fibres (Karbhari, 1998).

Kudar and Shah (2010) investigated the manufacture of cellulose fibre-cement boards with improvements in mechanical strength and freeze-thaw resistance to products made from the Hatschek process over those from extrusion processes.

Figure 2.11 demonstrates that unreinforced cementitious materials show strain softening (plain matrix curve) with low tensile strength and ductility. Conventional fibre reinforced composites (FRC) with typically 0.5 to 2 vol. % fibre also show strain softening with an increase in post peak ductility. High performance FRCC (30-35 vol. % fibre) show an increase in elastic limit, followed by a strain hardening response as multiple cracks form, but do not widen and finally strain softening as cracks widen.

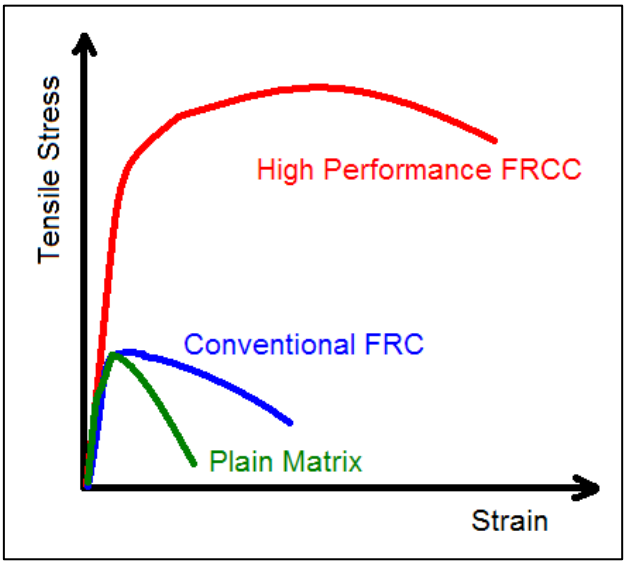

Figure 2.11 Effect of fibres on the tensile performance of cementitious composites (Kuder and Shah, 2010).

2.7.1. Reinforcement:

The use of fibres in OPC and Geopolymers is analogous to polymer (FRP, GRP) based composites which are in wide spread use.

The reinforcing fibres can be based on polymers, metals or ceramics and supplied in several forms such as:

- Rigid bars (Rebar)
- Woven mats
- Continuous cords and rovings
- Chopped fibres
- Nonwoven mats
- Milled fibres
- Nano material
- Whiskers.

Conventional FRP composites contain from 20 to 50 wt. % of glass or other reinforcement. In advanced composites based on epoxy resins and graphite this figure can increase to 70 wt. %. Figure 2.12 shows some commonly used reinforcement forms. Chopped fibres, flakes, particles and similar discontinuous reinforcement forms are usually not as effective as continuous reinforcements in increasing creep strength. However, discontinuous reinforcements enable less labour intensive application due to direct addition to the liquid matrix phase (Budinski and Budinski, 2005).

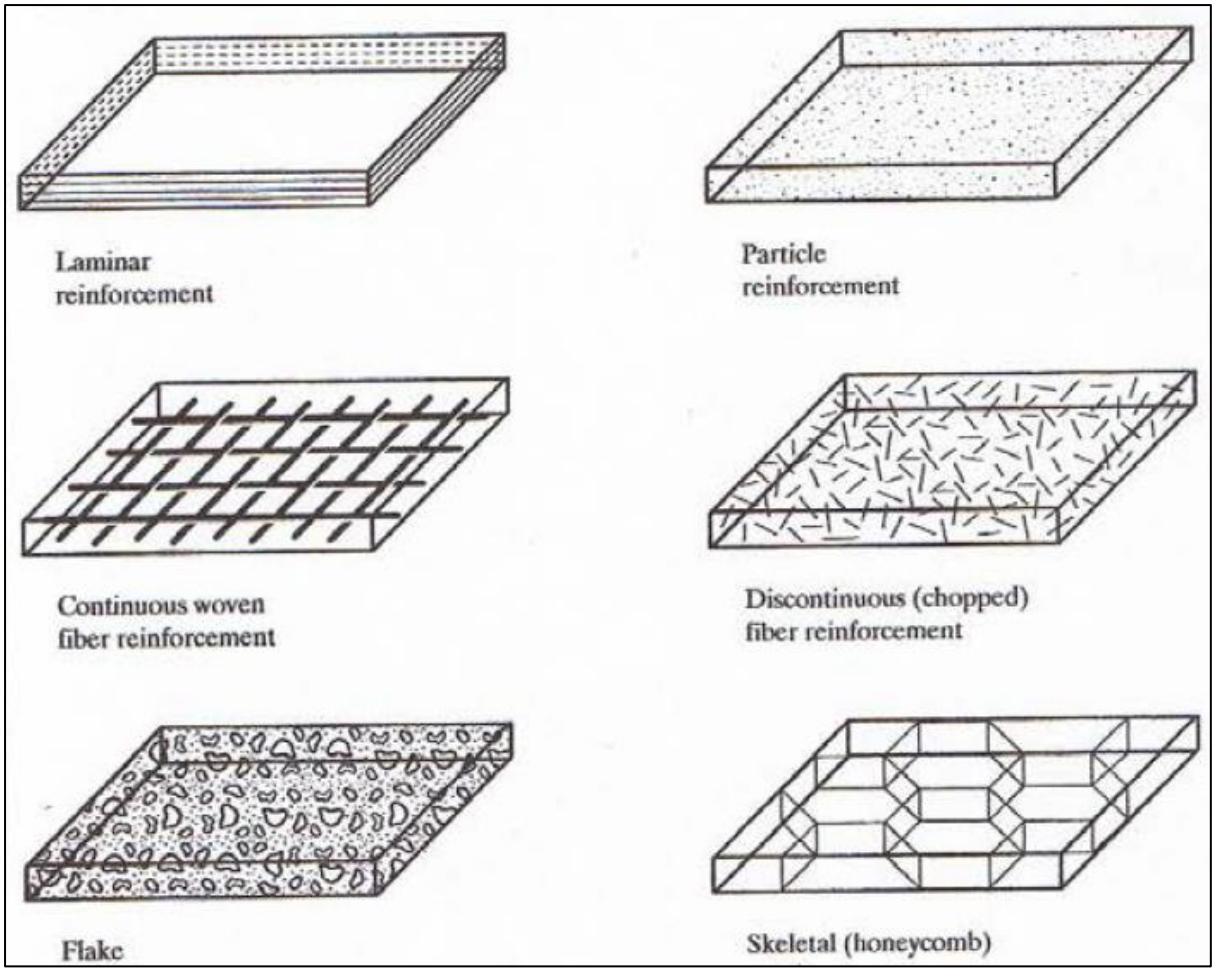

Figure 2.12 Common forms of glass fibre for composite reinforcement. (Budinski and Budinski, 2005).

2.7.2 Steel Fibre Reinforced Concrete (SFRC)

Katzer (2006) reviewed the history of steel fibre reinforced concrete. In 1874 Bernard, in California patented the idea of strengthening concrete with the addition of steel splinters. In 1910 Porter added short wire to concrete already reinforced with thick wire. In 1918, in France, Alfven patented a method of modifying concrete by long steel fibres in order to increase the tensile strength of concrete. He was the first to mention the effect of surface roughness on their adhesiveness to the matrix and the problems of anchorage of the fibres. Steel fibres patented by Constantinescu in 1943 were similar to existing fibres but gave information about the type and dispersion of cracks during loading of SFRC elements. It also referenced the large amount of energy absorbed by SFRC under impact.

Over 90% of produced steel fibres are shaped, the shapes adjusted to increase the anchorage of fibres in concrete. Length and cross section area can be varied for effect. Figure 2.13 shows the commonly available steel fibre types (CCANZ, 2009). 67% of fibres produced consist of a hook type.

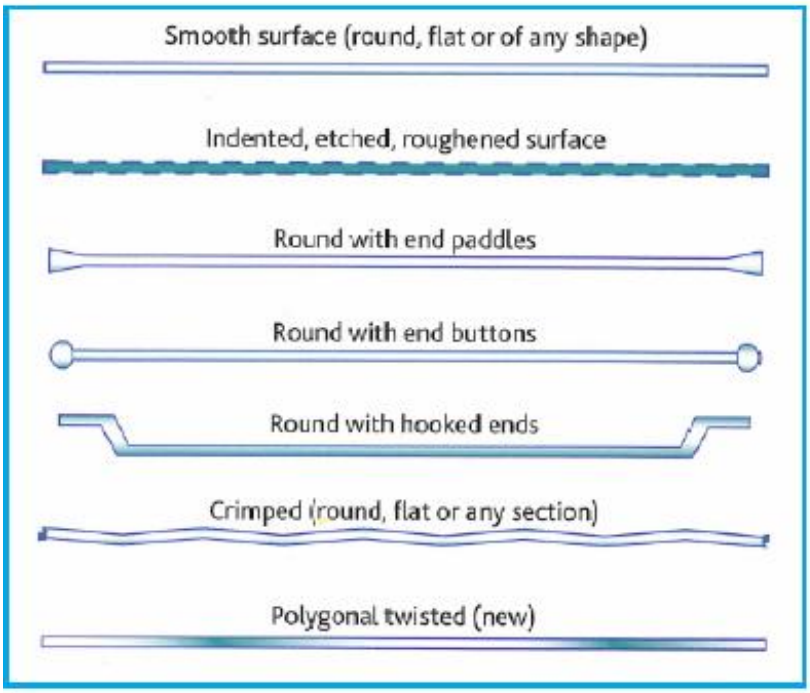

Figure 2.13 Steel fibre types for concrete reinforcement (CCANZ, 2009).

The efficiency of dispersing fibres in concrete depends mainly on the aspect ratio, which effects workability and spacing throughout the concrete. To maintain workability aspect ratio should be less than 150. 50% of all fibres produced worldwide lie in the aspect ratio range 45 to 63.5 (Katzer, 2006).

ASTM A820/A820M-11 (2011) has five types of steel fibre classified by the process or product used as a source for the steel fibres.

Romualdi et al. (Romualdi and Batson, 1963, Romualdi and Mandel, 1964, Swamy and Mangat, 1974) were amongst the first to clarify the science behind the functioning of steel fibres in concrete. Initial work in the early 1960s brought the use of steel fibres in concrete to the greater awareness of industry and pioneered the growth of SFRC applications.

The first major application of SFRC was to build airport runways in the USA. 28 installations were constructed between 1972 and 1980 using various steel fibre types at addition levels of 0.3 to 2.0 vol. %. Ongoing inspections showed only scarce cracks and local damage. Following on from this SFRC was used to build motorways, dams and canals. Shotcrete SFRC has been used to stabilise embankments and landslides in conjunction with previously installed steel mesh. Experience with this system built up confidence in shotcrete SFRC to the point where the labour intensive steel mesh installation could be eliminated (Katzer, 2006).

The addition of steel fibres to precast components significantly reduces the risk of cracks during transport and assembly. Tunnel linings have been installed in this fashion. Spun cast pipes up to 13 metres long are made in Sweden using SFRC which imparts improved durability to the end product. Prefabricated insulating panels with SFRC skins and a thermally insulating core are produced in Poland.

Chanh (2004) reported that SFRC composites showed superior resistance to cracking and crack propagation. These composites possessed increased extensibility and tensile strength, both at first crack and ultimate, particularly under flexural loading. The fibres were able to hold the composite together. Figure 2.14 shows that workability decreases as aggregate size increases above 5 mm, whilst below 5 mm sized aggregate there is little influence. Workability also decreases with increasing fibre length and it is difficult to obtain good workability above an aspect ratio of 100.

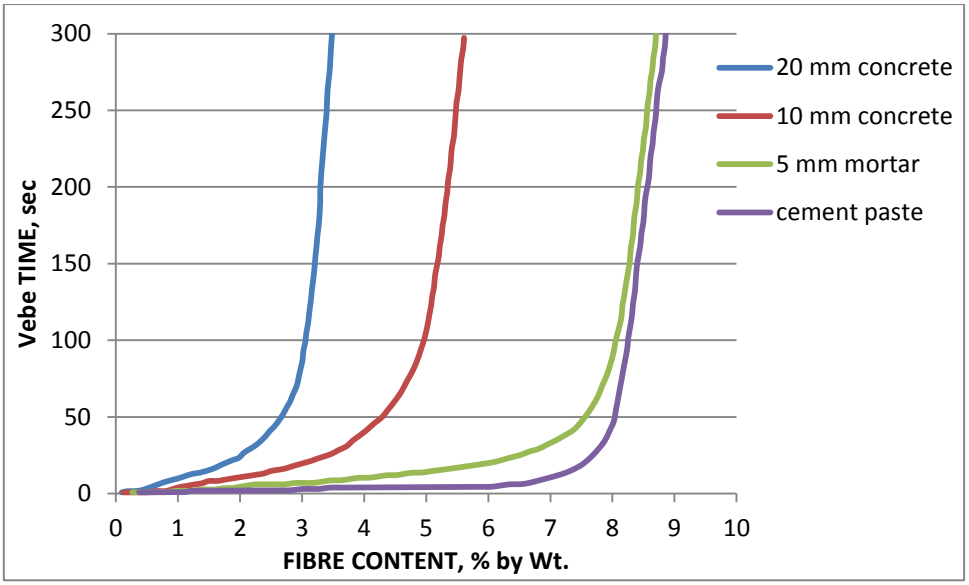

Figure 2.14 Workability verses fibre content for different aggregate sizes (Chanh, 2004).

One of the main difficulties in processing SFRC is the tendency for steel fibres to clump or ball together. Clumping may be caused by a number of factors:

- The fibres already clumped prior to adding to the mix. Normal mixing action will not break down these clumps.
- Fibres added too quickly to allow proper dispersion in the mix.
- Too high a volume of fibres may be added.
- The mixer is too worn or inefficient to achieve correct dispersion.
- Adding fibres before other ingredients may cause clumping.

The use of collated fibres held together with a water soluble size which dissolves in the mix water largely solves the clumping problem.

Ross (2009, 2012) states that combining SFRC with steel mesh enables the engineer to design for acceptable crack control that can reduce or eliminate joints. This would be beneficial in liquid tight concrete such as secondary bunds, water tight basements and dangerous goods stores. Using steel fibres can lead to a 50% reduction in conventional reinforcing with resulting material and labour savings.

Table 2.9 Comparison of fibres

Fibre Description	Supply Form	Fibre diameter µm	Aspect Ratio	Tensile Strength	Young's Modulus	Strain to failure, %	Density kg/m^3	Specific Strength*	Temp. Limit (^{o} C)	Alkali Resistance	Damage Resistance	Comments
Steel fibre	various	150 to 1000	100+	0.4 GPa	200 GPa	4 to 10	7.86	0.25	550	Good	NED	
Glass E glass	monofilament	15	900	3.5 GPa	76 GPa	4	2.6	1.33	600	Poor	Poor	
AR glass zirconia based	monofilament	13	900	2.5 GPa	70 GPa	1 to 3.5	2.7	0.96	600	Good	Poor	16% Zirconia minimum
Polyethylene (PE)	Fibrillated/ monofilament	25 to 1000	50	0.2 GPa	5 GPa	8 to 10	0.95	0.22	110	Excellent	NED	low melting point
Polypropylene (PP)	Fibrillated/ monofilament	20 to 1000	50	0.5 GPa	4 GPa	5 to 25	0.91	0.6	150	Excellent	NED	
Polyamide (Nylon)	Fibrillated/ monofilament	20 to 400	50	1.0 GPa	5.6 GPa	16 to 20	1.14	0.87	200	Good	NED	Nylon 6.6
Polyvinyl Alcohol (PVOH)	Fibrillated/ monofilament	27 to 660	50	1.3 GPa	30 GPa	8 to 11	1.3	1	175??	Excellent	NED	
ARAMID (Kevlar)	Pulp	10		2.8 GPa	58 GPa	4	1.44	1.92	480	Poor	NED	Kevlar 29
Wood Cellulose	Pulp	25 to 75		0.7 GPa	4.8 GPa	8	1.5	0.47	200	Poor	NED	
Carbon Fibre PAN based	monofilament	7 to 10	10 to 1000	4.3 GPa	225 GPa	1.90	1.82	2.36	400	Excellent		Tenax
Carbon Fibre Pitch based		18		1.3 GPa	31 GPa	2 to 2.5	1.65	0.76	400	Excellent		Isotropic Pitch based
Carbon Nanofibres (CNF)		0.06 to 0.2	500 to 1500	7 GPa	600 GPa		1.8	3.89	400			Pyrograf III (PR-24-PS)

Fibre Description	**Supply Form**	**Fibre diameter µm**	**Aspect Ratio**	**Tensile Strength**	**Young's Modulus**	**Strain to failure, %**	**Density kg/m^3**	**Specific Strength***	**Temp. Limit (^{o} C)**	**Alkali Resistance**	**Damage Resistance**	**Comments**
Silicon Carbide		10		2.7 GPa	310 GPa		2.95	0.92	1200	Good		Sylramic,COI Ceramic
Alumina		10 to 12		2 GPa	245GPa		3.9	0.51	1000	Good		Nexel 720 ex 3M
Basalt	monofilament	7 to 15		4.3 GPa	110 GPa	3.30	2.65	1.62	700	Good		BCF, Fibres
Asbestos		0.02 to 0.05		1 GPa	110 GPa	1 to 2	3.2	0.31	900	Excellent		Comparison
Concrete, OPC				5 MPa	30 Gpa	0.0 2	2.7	0.002	350			Comparison
Cement Matrix				3.7 MPa	1to5 GPa	0.02	2.5	0.0015	350			Comparison

* Tensile strength/density

NED=Not easily damaged

Hameed et al. (2009) compared two stainless steel fibres with differing aspect ratios (125 verses 105) in OPC. Flexural toughness with 2 vol.% added fibre increased approximately 3 fold for the fibre with the 105 aspect ratio and approximately 5 fold for the 125 aspect ratio compared to a control with no fibre. He also reported a Post Crack Strength (PCS) method for converting load deflection curves in to equivalent flexural strength curves (see figure 2.15).

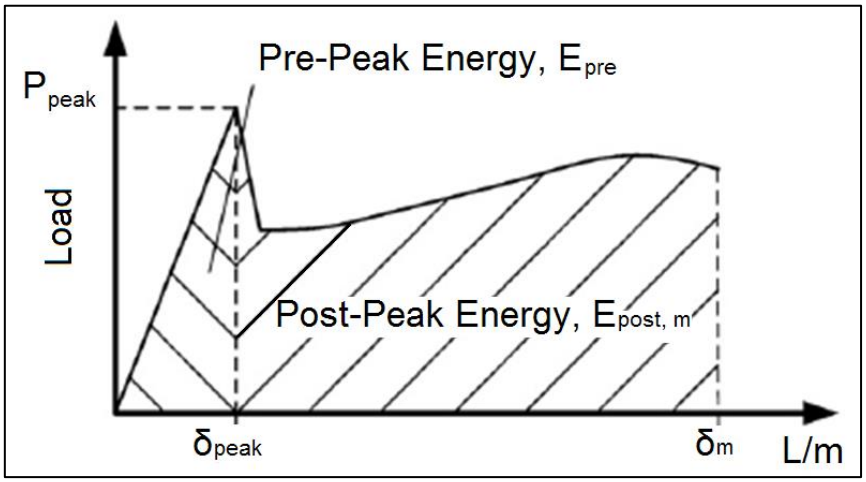

Figure 2.15 PCS analysis on an FRC beam (Hameed et al., 2009).

Stainless steel fibres are available for refractory applications beyond 1200^{o}C where conventional steel fibres are unsuitable (Fibretech, 2001).

Wang et al. (2010) found that the three point bending strength and toughness of the steel reinforced mortar are related to the interfacial characteristics and microstructure morphology near the fibre surface.

Bernal et al. (2006) found that alkali activated slag concretes reinforced with steel fibres exhibited higher mechanical properties than an OPC control with respect to toughness in both un-notched and notched samples.

Eswari (2008) reported on the use of blends of different fibres in concrete. The use of two or more fibres can produce a composite with better engineering properties than the individual

fibres. These synergistic blends of fibres are commonly referred to as hybrid fibre blends. Typical blends are steel and polypropylene fibres, where the steel fibre improves the first crack and ultimate strengths and the polypropylene fibres imparts improved toughness and strain capacity in the post cracking region. The fibres used in this work were a macro polypropylene fibre (length = 48 mm; aspect ratio = 40) and hooked steel fires (length = 30 mm; aspect ratio = 60).They found that a 2 vol. % hybrid fibre blend of 70/30 steel/polypropylene enhanced ductility and improved flexural strength.

Peng (2006) investigated hybrid blends of steel and polypropylene fibres to improve spalling resistance at temperatures up to 800^{o}C. He found that the hybrid blend showed better overall performance in improving spalling resistance than tests involving both fibres separately.

2.7.3 Organic fibres

Several different polymer fibres are in common use (see Table 2.9). They can be classified by performance and size into macro and micro fibres.

Macrofibres were introduced in the 1990s. They are used to control cracking due to shrinkage and thermal movements and to increase post cracking energy absorption (toughness) (CCANZ, 2009).

Most macro fibres have dimensions similar to steel fibres, but are made from polymers with a density in the range of 0.9 to 1.2 g/cm^{3}. Typical diameters are in the range of 0.5 to 1.0 mm, with tensile strengths of 350 to 700 MPa and typical modulus of elasticity values of 3 to 10 G Pa. The shape of the fibres can range from cylindrical to rectangular with a crimped or ribbed surface, whilst others are thin and flat. They are generally from 40 to 60 mm long with aspect ratios from 70 to 90 (CCANZ, 2009).

Macrofibres rely on an adequate level of bonding to the cement paste. Flat shaped fibres are designed to increase surface area to volume ratio. Macrofibres are beneficial when crack widths greater than 0.5 mm can be tolerated. This is typically in applications such as shotcrete for ground support applications and concrete slab on grade (CCANZ, 2009).

Microfibres (CCANZ, 2009) are specially designed for concrete and their primary function is to modify the plastic properties of concrete. They increase the homogeneity, and reduce bleeding, plastic settlement and plastic shrinkage cracking.

The effect of microfibres on hardened concrete properties is limited, but they can reduce permeability, increase resistance to impact, abrasion and scatter. Freeze-thaw and spalling resistance may also be improved (CCANZ, 2009)

Characteristic dimensions of microfibers are 5 to 30 mm in length and diameters of a few tens of micrometres. Most commonly available in polypropylene they are also available in polyamide, polyester, acrylic and polyvinyl alcohol. (Note: ceramic fibre based on glass and basalt is available in this format). They are also classified as monofilament or fibrillated.

Microfibres function by evenly distributing tens of millions of fibres throughout the volume of concrete in every direction to control cracking of the concrete in the plastic state. The fibres intersect micro-cracking that occurs as the concrete shrinks. The fibres provide enough strength to prevent the micro-cracks from widening during the first few hours after the concrete is placed. Fibrillated fibres offer longer term crack resistance than monofilament types due to their structure and greater physical dimensions (CCANZ, 2009)

Monofilament microfibres improve spalling resistance in fire situations by vaporising and hence forming channels to allow water escape (Adfil, 2010).

Microfibres do not provide any appreciable amounts of residual strength in concrete after cracking.

The levels of fibrillated fibres used are slightly higher than that used for monofilament types, as they are thicker, to enable an equal number of fibres to be added. Typically 0.25% by volume is added.

2.7.3.1 Polypropylene and other polyolefin fibres

The drive to replace asbestos fibres for health and safety reasons in the 1960s led to the introduction of polypropylene, amongst other materials, for concrete reinforcement.

ASTM D7508M-10 (2010) gives a good terminology of polyolefin fibres. ASTM C1116-10a classifies polyolefin fibres as Type 111 (2010).

Polypropylene fibres may be used in different ways to reinforce cementitious binders. In thin sheet like components it supplies primary reinforcement but must be present at high (>5 vol. %) fractions. A second application is as a secondary reinforcement where low modulus polypropylene fibres at around 0.1 vol. % are added to reduce plastic shrinkage with no influence on cured composite crack control (Banthia and Gupta, 2006).

These low modulus polypropylene fibres are also used for fire protection. In the event of fire the fibres melt/vaporise leaving channels to facilitate the movement of water and reduce the tendency for spalling (Adfil, 2010, Kalifa et al., 2001, Peng et al., 2006).

Wang and Niu (2012)found that 0.1 vol. % of polypropylene micro-fibre improved freeze thaw resistance of OPC when de-icing salt was used.

Mazeheripour et al. (2011) evaluated the effect of polypropylene microfibres on the production of self-compacting concrete. High levels (0.35 vol. %) of fibre impacted adversely on the rheology of the mixes even when additional superplasticiser was added. At 0.15 vol. % addition of fibre adequate flow was achieved and improvements in splitting tensile strength and flexural strength were recorded. This paper gave a detailed account of mix design to conform to the requirements for self-compacting concrete outlined by JCSE (Japanese Society of Civil Engineering).

Toutanji et al. (1998) compared permeability and impact resistance in OPC using two lengths (12.5 and 19 mm) of polypropylene fibre at a range of loadings up to 0.5 vol. %. Silica fume (5 and 10 wt. %) was included in the investigation. Longer fibres showed increased permeability, but silica fume at both loadings showed marked reductions in permeability. The longer fibres showed marginally higher impact strength, but again silica fume showed much higher results. The effect of the silica fume is to improve dispersion of the fibres in the matrix. Nili and Afroughsabet (2010) carried out a similar evaluation and confirmed Toutanji's findings.

Puertas et al. (2003) compared polypropylene micro-fibre in alkali activated slag, fly ash based geopolymer, a blend of these two and OPC. The fibres improved impact strength, but other results did not show any advantage for the fibres.

Zhang et al. (2009) investigated the effect of 3 mm long x 10 µm diameter fibres with a density of 1.38 to 1.40 g/cm^3 and an elastic modulus of 13.5 GPa in a metakaolin-fly ash geopolymer. Increasing the fibre content from 0 to 0.75 wt. % reduced the fluidity but had little effect on setting time. Flexural strength and impact strength were improved by fibre additions. He states that geopolymer shrinks during curing leading to the formation of micro-cracks and even some visible cracks and reported reductions in shrinkage of up to 44.6% at 0.75 wt. % fibre addition. SEM showed fibres bridging over pores.

Akers et al. (2009) described a bi-component polyolefin macro-fibre. This had a high modulus core (10 GPa) with a sheath material which included an embossed surface optimised for adhesion to the cementitious matrix. He detailed a test method for determination of critical fibre length and reported test results compared to steel fibres. This type of product is available commercially for use in concrete and shotcrete (Brugge, 2011).

Forta Corporation (1999) employed a different approach to macro-fibre construction. They took a twisted bundle of non-fibrillating monofilament and combined it with a fibrillating fibre system. This synergistic combination is 54 mm long and can perform the functions of a micro and macro fibre. Tensile strength of the fibre is reported as 620 to 758 MPa, but no elastic modulus value was given. The addition of 2 vol. % of these fibres enhanced residual strength after first crack.

Hu et al. (2010) produced light weight concrete containing a 38 mm long x 0.5 mm diameter polypropylene fibre. The modulus of the fibre was reported as 4.2 GPa and the density as 0.91 to 0.93 g/cm^3. The slump of all the mixes was controlled at 210 to 230 mm. Flexural strength, splitting tensile strength and toughness were all improved by addition of the polypropylene macro-fibres.

Ikai et al. (2006) developed a polypropylene fibre suitable for the manufacture of fibre-cement board using the Hatschek process. The aim was to replace expensive polyvinyl alcohol which had in its turn replaced asbestos fibres. A major part of the development was

activation of the fibre surface to increase adhesion to the cementitious matrix. Interfacial friction bonding increased from 0.22 MPa for the initial untreated fibre to 0.7 MPa for the latest generation treated fibre. An average fibre modulus of 9.1 GPa and an elongation of 20.9% were achieved over a 12 month production period.

With asbestos and polyvinyl alcohol fibres the adhesion levels are very high causing fibres to break rather than “pull out” limiting the amount of energy absorbed. With the polypropylene fibres additional energy is required to debond the fibres and then pull them out of the matrix. This leads to superior impact resistance with products containing the polypropylene fibres.

A polypropylene fibre (Hansen, 1994) called Krenit produced by splitting extruded tapes, which were pre-stretched and heat treated has been produced. The following properties are claimed: Tensile strength = 600 MPa, Young’s modulus = 8.5 to 12.5 GPa, Ultimate Elongation = 5 to 8%. The surface of the fibres is electrically treated to improve adhesion. The fibres are available in two cross sections, 100 µm x 20 µm and 300 µm x 30 µm and lengths from 3 to 20 mm.

Fibres based on ultra high molecular weight polyethylene (UHMWPE) are available (Honeywell, 2010). They are characterised by high Young’s modulus values (70 to 80 GPa). Wang et al. (1991) compared UHMWPE fibres, aramid fibres and conventional polypropylene fibres in OPC mortar. In samples containing well dispersed fibres (UHMWPE and PP) fibre pullout and stretching were the dominant mechanism. In the case of the aramid samples fibres were mainly present as bundles. These bundles cause the propagating cracks to deflect out of plane thereby increasing the splitting tensile strength. However energy absorption was relatively low with the aramid due to lack of fibre pullout.

Low melting point grades of polyethylene are available (Minifibers, 2010). Their primary function is to melt and provide release of gases with resultant reduction in pressure build up.

The unique properties of asbestos fibre made it impossible to replace with a single fibre (Minifibers, 2006). In the Hatschek process a blend of reinforcing and process fibres are required to replace asbestos. The process fibre is required to trap cement particles and

control drainage. Fibrillated polyethylene is able to function as a process fibre in cement fibre production. Figure 2.16 shows the extensive fibrillation (centre image).

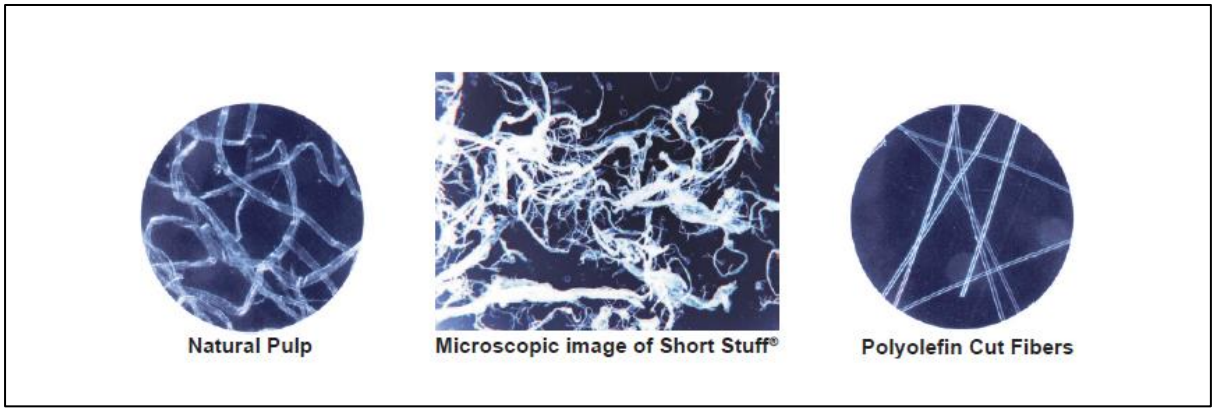

Figure 2.16 Polyolefin supply forms (Minifibers, 2006).

2.7.3.2 Polyvinyl Alcohol Fibres

Polyvinyl alcohol fibres (PVOH) were one of the initial fibres considered as an asbestos replacement (Minifibers, 2006, Ikai et al., 2006). PVOH fibres are characterised by high tensile strength and Young's modulus (900 to 1600 MPa and 20 to 40 GPa, respectively). Typical elongation at break is 7 to 8%. Specific gravity is 1.3. They also exhibit outstanding acid and alkali resistance (Kuraray, 2007).

The chemical structure of PVOH with a pendant hydroxyl group enables very high bond strengths to be evolved with cementitious matrices. This may be a disadvantage in some applications e.g. strain hardening cementitious composites (SHCC), where fibre treatment strategies are required to give controlled fibre pull out. Oiling of the fibres is used to control fibre bonding (Kendall et al., 2008, Rotstein, 2011). Van Zijl and Wittmann (2010) reviewed typical SHCC formulations based on PVOH fibres and one high modulus polyethylene fibre. Increasing the oiling agent and PVOH fibre volume increased ultimate tensile strength and strain, increased first crack stress and reduced crack width and spacing. Polyethylene fibre did not require oiling.

This SHCC concept was developed by Li and Maalej (1996) and named engineered cementitious composites (ECC)(Li, 1998). ECC generally exceeds 1% strain capacity with the most ductile composite in the 6 to 8% range. Coarse aggregates are not used in ECC as they affect the ductile behaviour of the composite. In general less than 2% of discontinuous fibre

is used with PVOH fibre being the most common. Fibres used in ECC must have tensile strengths of 1000 MPa, an inelastic failure strain greater than 5% and a fibre diameter between 30 and 50 μm (Lepech et al., 2008).

Unoiled PVOH fibres, available in micro and macro-fibre styles, can be used to produce conventional fibre reinforced concretes (Nycon, 2012, Nycon, 2011b).

Yunsheng et al. (2006) produced extruded geopolymer boards based on metakaolin and fly ash and reinforced with PVOH fibres (6 mm long x 14 μm diameter). In the metakaolin geopolymers toughness of the boards increased as the fibre volume content increased. As the fly ash content of the geopolymer increased and with fibre kept at 2 vol. %, the toughness peaked at 10 wt. % fly ash addition. The fly ash greatly improved the extrusion performance of the mixes. The same authors (Yunsheng et al., 2008) reported more fully on the extrusion process. The addition of fly ash reduced the bulk yield stress and total extrusion pressure. Durability testing of the extruded boards was included with good resistance to freeze thaw and sulphuric acid (pH = 1) recorded.

2.7.3.3 Other organic fibres.

Many other polymers can form fibres, polyamides, polyesters, acrylics, aramids (Zhang et al., 2011) and a host of naturally occurring cellulose based products (cotton, hemp, sisal, jute) and fibres derived from sugar, coconut and banana processing are available (Cement & Concrete Institute, 2010).

Recycled fibres from carpets have also been investigated for concrete reinforcement (Nycon, 2009). Nycon have commercialised a shaped (trilobal) monofilament produced from recycled nylon, which exhibits higher mechanical properties than polypropylene fibres.

The use of naturally occurring fibres for concrete reinforcement is of interest for economic and environmental reasons. Sisal fibre has been used to make roof tiles, corrugated sheets, pipes, silos and tanks. Elephant grass reinforced mortar has been used in low budget housing projects. Wood derived cellulose fibres have commercial applications in the manufacture of flat and corrugated sheeting and non-pressure pipes (Cement & Concrete Institute, 2010).

Natural fibres may be used in the chemically unprocessed state or as is the case with wood cellulose processed via the Kraft process which involves digestion in alkali to reduce the lignin content. Lignin can retard or completely inhibit cement set due to its sugar content.

Davis (2007) presented an overview of natural fibre reinforced concrete. Clumping of fibres during mixing and durability were noted as two areas requiring redress.

ASTM D7537 (2012), cellulose fibres for concrete references ASTM D6942, stability of cellulose fibres in alkaline environments. The alkali resistance of natural fibres needs to be addressed for cementitious applications (Hercules Fibres, 2011b, Buckeye Building Fibres, 2009, Tonoli et al., 2009).

Alzeer and MacKenzie (2012) added 5% of wool (washed and recycled) to a metakaolin based geopolymer and achieved up to 40% increase in flexural strength. Only partial degradation of the wool was observed under geopolymerisation alkaline conditions. The surface of the wool was treated with formaldehyde to improve the alkali resistance.

The use of nano and micro cellulose fibres in cement mortar was investigated by Peters et al. (2010). The work showed that the addition of a hybrid blend at 3 vol. % fraction increased the fracture energy by 50%. Changes to the superplasticiser addition levels were required to maintain consistent workability, and water levels increased with fibre addition.

Okada et al. (2011) used the poor alkali resistance of polylactic acid (PLA) fibres to manufacture a porous metakaolin geopolymer to enhance capillary rise for passive cooling applications. Large amounts (13 to 28 vol. %) of PLA fibre increasing as the fibre diameter increased from 12 to 29 µm diameter were used. All the fibres were 0.5 mm long. Combinations of alkali and temperature based on the melting point and thermal decomposition temperatures of the fibres were evaluated to “remove” the fibres and leave a porous structure behind. A combination of NaOH solution (pH = 12) and heating at 330^{o}C gave the best results with 28% of the 29 µm diameter fibre giving the best capillary rise result.

2.7.4 Carbon based reinforcing fibres:

Reinforcement of cementitious materials is typically provided at the millimetre and/or micro scale using micro and macro fibres respectively. Cementitious materials also exhibit flaws at the nano level where traditional reinforcement is ineffective (Metaxa et al., 2010). The use of nanofibres such as carbon nanotubes (CNT) and carbon nanofibres (CNF) are expected to show several advantages as a reinforcement material for cement compared to traditional fibres.

- Greater strength and stiffness compared to traditional fibres
- Higher aspect ratio is expected to arrest nano cracks and require greater energy for crack propagation
- Nanofibres are expected to be closely spaced in the cement matrix (if correctly dispersed)

Besides the benefits of reinforcement, autogenous shrinkage results indicate that CNTs can have beneficial effects on transport properties of cementitious materials leading to improved durability.

Carbon fibres are available in three basic types:

Macro fibres, longer than 1 mm with diameters around 7 µm.

Microfibers, with lengths in the 100 µm range and diameters up to 20 µm.

Nanotubes and nanofibres with lengths in the 2 to 4 µm micron range and diameters of around 100 nanometres.

Carbon macro and mini fibres are produced by graphitisation of fibres (polyacrylonitrile or rayon) or of aromatic pitches based on coal tar. The latter material yields lower production costs, but gives fibres with lower stiffness properties.

Carbon nanotubes (CNT) and carbon nanofibres (CNF) are attracting a lot of research interest in OPC and geopolymers. Industrial production is limited to probably a few hundred tonnes per annum, but Bayer commissioned a 200 tpa pilot plant in Leverkusen in 2010.

Bayer believes that the carbon nano material market will grow at 25% per annum with a potential market of several thousand tonnes per annum. This will be mainly in the engineered plastics market segment (Bayer Materials Science, 2007).

Dispersion of carbon nano materials into the matrix material is an ongoing issue. The de-aggregation of nano particles must be carried out in a manner that does not damage the primary reinforcing particles and interfere with the cement hydration process (Yazdanbakhsh et al., 2010). They used ultrasonication and a superplasticiser to achieve a water dispersion of CNFs in water. This dispersion was added to cement to achieve a 0.4 wt. % ratio (based on cement). The dispersion of the CNFs was not uniform and this was attributed to cement particles absorbing superplasticiser and causing CNFs to re-agglomerate. One suggested solution is to functionalise the surface of the CNFs to improve wettability.

Bayer Material Science (2008) claim that carbon nanotubes can be dispersed in low viscosity media such as water using a jet disperser or ultrasonic treatment. Stabilisers need to be added to aqueous dispersions to ensure that re-agglomeration of nanotubes does not occur.

Eden Energy has undertaken research involving concrete reinforced with carbon nano-fibres (CNF) and carbon nano-tubes (CNT). The nano-carbon is produced by Hythane, a US subsidiary of Eden Energy. Hythane used a surfactant to disperse the carbon nano materials which showed increases in 7 day flexural strength (ASTM C348) ranging from 15 to 30% (Eden Energy, 2011).

Applied Sciences Inc. (2001) manufacture the Pyrograf range of carbon fibres, carbon nanofibres and microfibers. These materials are claimed to mitigate crack formation in concrete. The coefficient of thermal expansion (CTE) of these materials is listed as -1.0 ppm. This will lead to a reduction in the COTE of composites containing these materials coupled with lower thermal strain.

ASI also claim that CNF reinforced concrete is highly resistant to micro cracking, which can reduce failure of cement and concrete products due to “freeze-thaw” cycles (Ohio Coal Development Office, 2004).

Cwirzen et al. (2009) used functionalised (with –COOH) multiwalled carbon nanotubes (MWCNT) and carbon micro fibres (CMF) to investigate crack formation and propagation of cement based matrices. Internal tension forces were introduced by repeated freeze-thaw cycles. The sample containing CMFs exhibited no micro-cracking and showed significant increase in flexural strength compared to the reference (no fibres) and that containing MWCNTs. The fibres were dispersed in water using a polycarboxylate superplasticiser and ultrasonic energy. A mini cone flow test was carried out, with levels of MWCNT of 0.5 wt.% inhibiting flow. Up to 2.9 wt. % of CMF had 90% of the reference flow. The level of sonication affected the morphology of the nanofibres, causing length reduction which prevented efficient transfer of stress.

The Transportation Research Board of the USA recently completed a project entitled “Crack Free Concrete made with Nanofiber Reinforcement”. Metaxa (2010)reported on this work. Cementitious matrices exhibit flaws at the nano-scale where traditional reinforcement is ineffective. Evidence from SEM imaging showed that CNFs were able to control cracking by bridging nano-cracks and pores in the cementitious matrix. Additionally SEM showed good bonding between the CNFs and cement hydration products indicating that the nanofibres can be sufficiently secured in the matrix to ensure the full capacity of the fibres is utilised to transfer the load (figure 2.17.).

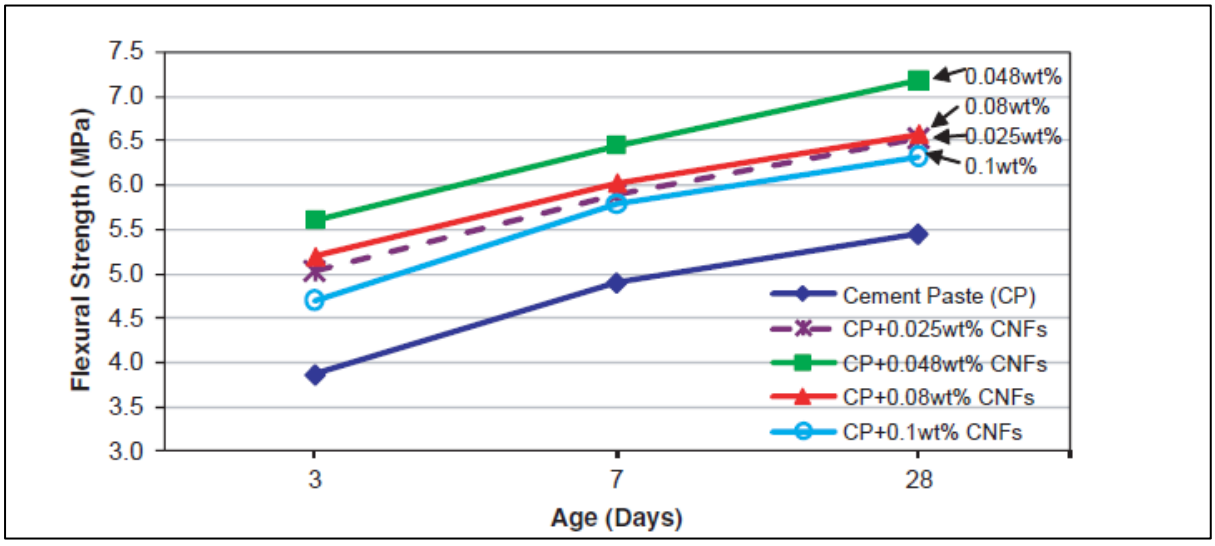

Figure2.17 Effect of CNF concentration on Flexural Strength of cement paste (water-cement ratio = 0.5) (Metaxa et al., 2010).

Chung (1992) added short pitch based carbon fibres (0.05 wt. % of cement) to concrete and obtained a flexural strength increase of 85% and a flexural toughness increase of 205%. The air content was 6%, so freeze-thaw durability was improved, even in the absence of an air entrainer. The fibre length decreased from 12 mm to 7 mm during mixing. The drying shrinkage was decreased by up to 90%. She found that pre-dispersing the carbon fibres in water using a dispersing agent and a defoamer was the most practical approach.

Lin (2009a) reinforced a metakaolin based geopolymer (silicon to aluminium = 4) with short (7 mm) carbon fibres which had been dispersed by sonication, filtered out by a wire sieve to form a preform of carbon fibres 0.15 to 2mm thick. These preforms were impregnated with the geopolymer and between 20 and 50 layers laminated together using a vacuum bag, then cured at 80^{o}C for 24 hours. Maximum toughening was obtained at 3.5 to 4.5% volume fraction.

Kumar (2012) found that 0.5 wt. % (of cement) of carbon nanotubes was the optimum addition level for compressive strength and splitting tensile strength. He thought that higher levels were not sufficiently dispersed even with extended sonication.

Chung (2005) investigated dispersion of short fibres in cement by measuring electrical resistivity of the composite. She found that the effectiveness of a fibre for improving functional properties was greatly affected by degree of fibre dispersion. This was particularly important when fibre volume fractions are low. Fibre dispersion is enhanced by increasing the hydrophilicity of the fibre. She investigated the effect of various admixtures (silica fume, water based polymer dispersions and solutions and silanes). Silica fume (15 wt. % on cement) increased tensile strength and reduced electrical conductivity when used with 0.35 vol. % carbon fibre (15 μm diameter x 5 mm long). The use of water soluble methyl cellulose (0.4 wt. % on cement) had a similar effect. The use of latex and polymer dispersions also improved fibre dispersion in the region of 10 to 20 wt. % addition on cement. The use of silica fume and methyl cellulose together had a synergistic effect on fibre dispersion.

Several other authors have investigated dispersion of discrete carbon based reinforcement in cement pastes (Manzur and Yazdani, 2010, Gay and Sanchez, 2010, Konsta-Gdoutos et al.,

2010). They all used sonication in conjunction with a surfactant to obtain optimum dispersion of the carbon reinforcement.

Chen et al. (2011b) reviewed the current position of carbon nanotube-cement composites with respect to the fabrication, hydration, mechanical properties, electrical resistivity and transport properties of CNT-OPC composites. The authors thought that more work was required in all the fore mentioned areas to generate composites suitable for stronger and more ductile applications.

Rodriquez et al. (2010) compared the properties of two rebar reinforced concrete beams, one of which contained 1% CNF by volume. The CNF had a diameter of 149 nm and a length of 19 µm giving an aspect ratio of 128. A polycarboxylate superplasticiser was used in both mixes and the workability was adequate to pour the two beams. The CNF increased both the strength and ductility of the beam and in addition the hardened CNF containing mix was suitable for use as a reversible strain sensor.

Work with carbon fibre to reinforce OPC began in the 1970's. Research in Japan and the USA with chopped and milled fibres based on pitch based low modulus carbon fibres has been reported on by Banthia (1994). Fibre lengths were in excess of 3 mm and had diameters of 14.5 µm and silica fume was used as a dispersing agent. Additions of carbon fibre up to 5 vol. % were evaluated with increases in tensile, flexural and impact strengths reported. Improvements in water and acid resistance were obtained as the carbon fibre loading increased. These composites also showed good resistance to freeze-thaw cycling.

Banthia (1994) also reviewed applications for carbon fibre reinforced composites. One of the major uses is for thin precast products such as roofing sheets, panels, tiles, curtain walls, wave absorbers and I and L beams. CFRC curtain walls have been in use in Japan for some time. CFRC has potential for use in structures in seismic regions, for thin repairs and machinery bases. The good conductivity of these composites may be utilised in secondary anode systems in cathodic protection of reinforced concrete bridge decks.

Lyon et al. (Lyon, 1996, Lyon et al., 1997, Lyon, 1999) produced a woven carbon fibre-geopolymer composite with outstanding fire resistance. Tran et al. (2009) used a geopolymer based on thermal silica, kaolin and potassium waterglass to laminate a woven

carbon fibre textile. The laminates contained between 37 and 40 wt. % carbon fibre and were cured at a range of temperatures between 55^{o} and 115^{o}C. Optimum flexural strength was obtained between 75^{o} and 100^{o}C. He also claimed that the geopolymer used gave better results than one based on metakaolin. SEM showed the formation of cavities in the laminate cured above 100^{o}C. This was attributed to trapped water volatilising above 100^{o}C.

C-GRID (Chomarat, 2009) is a carbon fibre-epoxy based reinforcement suitable for a range of building products from precast sections, shotcrete, and double tees. Concretes using C-GRID are characterised by light weight and high strength to weight ratio compared to steel mesh, excellent crack control and no corrosion staining.

Vera-Agullo et al. (2009) compared CNFs and MWNTs with a nanosilica (particle size 3 to 15 nm and a BET surface area between 20 and 1000 m^2/g) in OPC. The nanosilica showed the best early strength development, which was attributed to the pozzolanic effect of the nanosilica. The CNF and MWCNT both increased the flexural strength at 28 days.

2.7.5. Inorganic fibres

The predominant inorganic fibre used in cementitous systems is alkali resistant glass (ARG), which has a minimum zirconia content of 16 wt. % zirconia (ASTM Committee C27-40, 2008). Nippon Electric Glass (2007) manufacture a 19 wt.% zirconia glass with outstanding alkali resistance.

The Fibreglass Reinforced Concrete Association have published a specification for the various manufacturing formats of glass reinforced concrete (Concrete Society, 2010). In addition to the conventional mortar and concrete techniques, the spray up application similar to polymer based FRP is covered.

ARG will reduce plastic shrinkage in concrete (NipponElectricGlass., 2000) and at the levels used will not affect slump resistance.

Nycon AR-DM (Nycon) is designed for dry mix applications where the fibres are exposed to highly abrasive conditions. This is achieved by a fibre coating which breaks down on water addition.

Vijai et al. (2012) added alkali resistant glass (6 mm long x 14 µm diameter) to a fly ash based geopolymer concrete at 0.1 to 0.03 vol. % based on the concrete. In order to achieve room temperature cure 10 wt. % of the fly ash was replaced by Portland cement. The 0.03 vol. % fibre addition gave small increases in compressive and splitting tensile strength and a 16% increase in flexural strength.

Fibres based on basalt are being promoted for composite reinforcement in a range of binders. Basalt is naturally occurring and less energy demanding compared to glass fibre production.

Relative to most common igneous rocks, basalt compositions are rich in MgO and CaO and low in SiO_2 and the alkali oxides, i.e., $Na_2O + K_2O$, consistent with the TAS (total alkali silica) classification. The TAS classification is used to classify volcanic rocks (Australian Museum, 2007).

Basalt generally has a composition of 45-55 wt. % SiO_2, 2-6 wt. % total alkalis, 0.5-2.0 wt. % TiO_2, 5-14 wt. % FeO and 14 wt. % or more Al_2O_3. Contents of CaO are commonly near 10 wt. %, those of MgO commonly in the range 5 to 12 wt. %.

De Fazio (2011) suggested that only basalt with silica contents greater than 46% were suitable for fibre formation. Also the presence of iron improved acid resistance. This work rated basalt fibres behind ARG (with added zirconia) with regards to alkali resistance.

Lipatov et al. (2012) investigated the effects of adding zirconia to basalt fibres at the manufacturing stage. They concluded from XRF results that the maximum solubility in basalt was 7.1 wt. %. XRD showed that the zirconia was present in the tetragonal and monoclinic forms. Optimum alkali resistance (2 M NaOH for 3 hours at 98^{o}C) was obtained at 4 wt. % added zirconia (3.1 wt. % in the fibre). At 4 wt. % added zirconia, tensile strength of the fibres decreased by more than 50%.

Jung and Subramanian (1994) coated basalt fibres with zirconium-n-propoxide stabilised by chelation with ethyl acetoacetate or without stabilisation. Alkali attack on the uncoated fibres results in dissolution of SiO_2, Al_2O_3, and CaO with the formation of insoluble hydroxides of iron, magnesium and titanium from the constituents of the basalt. These

reactions are supressed by the unstabilised zirconia coating on the basalt fibre. The tensile strength of uncoated fibres is drastically reduced by alkali attack, whilst the coated fibres maintained their strength after 90 days immersion.

Scheffler et al. (2009) investigated the alkali resistance of basalt and alkali resistant glass fibres in 5% NaOH (pH > 14) and filtered cement solutions (pH = 12.8 to 12.9). The attack on the fibres by NaOH leads to a strong dissolution of the outer layers of both fibres with the formation of an extensive shell like layer and a reduction in fibre diameter. In cement solution the attack is more localised shown by the formation of holes of varying size and no reduction in fibre diameter. An insoluble calcium rich surface layer appears to inhibit further attack on the fibre surface. When sizes based on epoxy film formers and silanes are applied to the fibres less shell like layer was formed suggesting improved NaOH resistance.

Dias and Thaumaturgo (2005) investigated the addition of basalt fibres (45 mm x 9 µm) to metakaolin based geopolymer and OPC at 0.5 and 1 vol. % fraction. The basalt fibres were more efficient at reinforcing the geopolymer system. This could probably be related to the bond between fibre and matrix.

Kriven et al. (2008) used a metakaolin geopolymer with a nominal SiO_2:Al_2O_3 = 4:1 as a binder for woven basalt fabric and chopped basalt fibre (4 mm long x 10 µm diameter). Beyond 1% chopped fibre addition the paste became un-pourable. Using 6 layers of woven basalt fibre, three point bend strength and work of fracture increased from 2.75 MPa to 10.25 MPa and from 0.05 kJ/m^2 to 21.82 kJ/m^2 respectively. Also in this work stainless steel powder was added to the geopolymer with increases in compressive strength and flexural strength up to 15 wt. % addition (note: this is about 1% by volume of stainless steel). It was suggested that the stainless steel particles were blunting propagating cracks.

Rill et al. (2010) added chopped basalt fibres (6 mm long x 13 µm diameter) at up to 10 wt. % to a metakaolin based geopolymer (activated with potassium and SiO_2:Al_2O_3 = 4:1). A 10 wt. % addition was the limit due to workability issues. Adding the fibres in an IKA shear mixer or a Thinky centrifugal mixer caused the fibres to break down to about 100µm long. The fibres were therefore blended in by hand. The flexural strength increased from 1.75 MPa to 19.5 MPa (10 wt. % fibres). The basalt fibres had been supplied with a silane size. In

a separate evaluation the size was removed by calcination at 600^{o}C for 1 hour. When this material was added to the geopolymer at 1 wt. % the flexural strength was 2.4 MPa compared to 3.6 MPa for sized fibres. The presence of the sizing helped the workability by reducing clumping during mixing. Samples containing 7 wt. % fibres were heated to 500 and 1000^{o}C. The 500^{o}C sample exhibited micro-cracking but showed a flexural strength of 4.7 MPa (16.5 MPa for unfired). The 1000^{o}C sample showed high shrinkage and was too weak to test. These observations were attributed to dehydration and crystallisation of the geopolymer at the higher temperature. No SEM was undertaken to investigate changes in the basalt fibres at elevated temperatures.

Fibres Unlimited (2007) compared basalt fibres with polypropylene and polyacrylonitrile fibres with respect to workability and final properties in OPC.

Fellicetti et al. (2001) investigated two basalt fibre grades for down hole cementing slurries. One grade proved superior in alkali resistance and was used for the balance of the work. In down hole cementing flowability is critical and evaluation with a mini cone was carried out with 10 µm diameter fibres. A 1 to 2 vol. % addition of 1 mm long fibre gave optimum flow results. Longer fibres (up to 5.5 mm long) gave pronounced improvements in composite toughness.

Many new supply forms and applications based on basalt are currently available (Kamenny Vek, 2012, ReoforceTech, 2012a, ReoforceTech, 2012b). The main areas of usage are reinforcement in composites, high temperature insulation and fire protection.

The 3M company manufacture a range of alumina fibres under the brand name Nexel (3M., 2003) They have increasing crystalline Al_2O_3 contents with corresponding lower amorphous silica contents. The top end grades (Nexel 610 and 720) are completely crystalline with melting points of 2000^{o} and 1800^{o}C, respectively. Individual fibre diameters are in the 10 to 12 µm range. Nexel 610 and 720 are used for load bearing composite applications over a wide temperature range.

Foerster et al. (1994) added alumina particles, fibres and woven fabric to geopolymer (Geopolymite). Short fibres (150 µm long x 3 µm diameter) gave a rapid increase in viscosity above 5 vol. %, with increases in toughness and compressive strength. The addition of

particles (fillers) gave much slower increases in viscosity and strength up to 25 vol. %. A 2 ply woven alumina fabric laminate (35 vol. % alumina) only provided 50% of the stiffness of a carbon fibre rovings laminate (75 vol. % carbon). However this was double the stiffness obtained with 6 vol. % of short alumina fibre in the binder. The authors also reported that Nexel 312 alumina weaves (a product of 3M) were badly degraded with loss of strength.

Defazio et al. (2006) evaluated three alumina ceramic supply forms alumina tissue/paper, milled alumina fibres, and short, 3 mm, fibres (chopped). Three manufacturing techniques were utilised, hand layup combined with vacuum bagging, pour/vibrate, and vacuum bagging followed by curing under pressure in a heated press at 80^{o}C. The geopolymer was varied from SiO_2:Al_2O_3 ratios of 1:1 to 5:1, but no other compositional information was given. The primary objective was to develop a composite with an operating temperature of 1350^{o}C and a flexural strength of 75 MPa. Maximum flexural strength (97 MPa) was obtained using the heated press and 11.3% loading of short ceramic fibres.

Nguyen Thang et al. (2010) added alumina nanofibres to a geopolymer matrix (Q17 from the Geopolymere Institute). This blend was now used as a laminating binder system for carbon fibre, basalt fibre and glass fibre unidirectional rovings. Additions of nanofibres in 0.5 wt. % steps from 0.5 to 2 wt. % were made. Flexural strength values peaked at 1 wt. % with each of the unidirectional fibres. The authors believe that a dispersing and/or bonding agent for the nanofibres could be of great interest.

Nazari et al. (2010) added alumina nanoparticles (average diameter = 15 nm) to OPC concrete in 0.5 wt. % steps up to 2 wt. %. Initial setting time was reduced by 50% and final setting time by 33%. Only small increases in splitting tensile strength and flexural strength were seen and the authors thought that “needle like particles would be more beneficial. However these nano particles were having a beneficial influence on cement hydration.

Bernal et al. (2012a) investigated the effects of milled recycled refractory brick and an alumina/silica/zirconia fibre at elevated temperatures in a metakaolin geopolymer. Unfilled geopolymer showed high shrinkage and cracks due to severe dehydration above 200^{o}C. Filled samples were pre-dried at 65^{o}C prior to further heating. The recycled aluminosilicate brick was used to even out the differences in thermal expansion and reduce formation of cracks. The addition of the fibres led to workability issues which the authors believe lead to

high variability of the strength test results. However the presence of fibres controlled the formation of visible cracks.

Silicon carbide based fibres and woven fabrics are available commercially (COI Ceramics, 2006).

Davidovits (1991) reported on the use of woven silicon carbide fabrics in geopolymer with superior high temperature thermal strength compared to E-glass and carbon fibre composites.

Silva et al. (1999) used naturally occurring wollastonite fibres (aspect ratio = 10 to 20:1) to reinforce a metakaolin based a geopolymer. Toughness of the system increased as fibre volume increased to 5 vol. %. The wollastonite is compatible with the pH levels in geopolymer synthesis and a dense interfacial transition zone, matrix-fibre, was developed.

Figure 2.18 shows an SEM image of commercially available wollastonite, Nyad MG ex Nyco Minerals. The acicular nature and wide size distribution is clearly visible.

Fine aggregates (<53 μm) can be used as fillers to improve specific properties. Wollastonite, mullite, and α-alumina are all stable beyond 1000^{o}C and help to control shrinkage in high temperature applications (Kamseu et al., 2010, Buchwald et al., 2009).

Davidovits (2008b) compared cordierite (magnesium aluminosilicate) and mica in K-polysialate geopolymer and in a (Na, K) polysialate and measured thermal behaviour after an initial post cure of two hours at 650^{o}C. In the second heating cycle the cordierite filled (Na, K) polysialate showed an expansion of 0.1% up to 600^{o}C before undergoing strong shrinkage above this. The mica filled system showed 0.5% expansion up to 600^{o}C before shrinking. Davidovits attributed this shrinkage to the collapse of the sodalite cage. A Na polysialate filled with cordierite and post cured for 3 hours at 500^{o}c gave an average COTE between 20 and 700^{o}C of 1.9 x 10^{-6} K^{-1}.

Barbosa and MacKenzie (2003b) added various inorganic fillers to a metakaolin based geopolymer activated with sodium silicate and measured physical properties and thermal shrinkage of the composites. The fillers included crushed building brick, powdered granite, kaolinite, iron sand (black titanomagnetite with 7% TiO_2), α-alumina and β-Sialon. All the

filled geopolymer composites showed reductions in strength which was attributed to the lack of reaction between the fillers and the geopolymer binder.

Lin et al (2009b) investigated the use of alumina as a filler in a metakaolin based geopolymer and found marked reductions in shrinkage after elevated temperature exposure.

Siva and Thaumaturgo (2003) used wollastonite to improve fracture toughness of a metakaolin based geopolymers. The addition of 2 vol. % of wollastonite gave the optimum toughening effect.

Temuujin et al. (2012) added ground vermiculite to a fly ash based geopolymer to improve the thermal properties of a sprayed coating. Vermiculite expands when heated above 300^{o}C showing low thermal conductivity. The ground sizes used were -63 µm and -250 µm. The presence of vermiculite modified the water release mechanism on heating. The early water loss shown by unfilled geopolymers up to 400^{o}C is replaced by a more continuous loss up to 1000^{o}C. This latter effect has a more beneficial influence on fire resistance.

Mullite is usually present in coal fly ash and remains reasonable stable through the geopolymerisation process and any elevated temperature exposures up to 1000^{o}C (Williams and van Riessen, 2010, Rickard et al., 2012). This probably contributes to the thermal stability of fly ash based geopolymers. Mullite is available commercially (Washington Mills, 2008) and is used commercially in the manufacture of refractory products where resistance to spalling and low thermal conductivity are important. Mullite also possesses a low (5.62 x 10^{-6} K^{-1}) COTE between 25 and 1500 ^{o}C without any phase changes occurring in this range.

Medri et al. (2011) used a potassium activated metakaolin as a binder for recrystallised silicon carbide to produce refractory coatings for silicon nitride-titanium nitride substrates. After curing at 80^{o}C and subsequent water removal, a coating with 90 wt. % silicon carbide was obtained. Long term oxidative testing of the silicon carbide grains and the filled geopolymer coating was carried out for 100 hours at 1200^{o}C. The weight gain of the silicon carbide coating in this test was 7% and is around 50% lower than for the grains. Shrinkage of these coatings after one hour at 1300^{o}C in argon was 0.1%. Adhesion of the coating is good as shown by the absence of exfoliation detachment when cutting or polishing the cross sections prior to and after high temperature exposure.

Wang et al. (2011) added hollow cenospheres sourced from coal fly ash to geopolymers to reduce density and reduce thermal conductivity in the composites. The geopolymer was a potassium activated metakaolin and the cenospheres were claimed to have good alkali resistance. The addition of 40 vol. % of cenospheres reduced compressive strength from 105 to 40 MPa, the thermal conductivity from 0.361 to 0.173 W m^{-1} K^{-1} and density from 1.37 to 0.82 g cm^{-3}.

Chen et al. (2011a) developed a sodium activated metakaolin geopolymer suitable for coating concrete where good thermal insulation properties were required. The addition of mica (15%) and wollastonite (10%) together with 5% of a silane gave a product with good compressive strength (27.4 MPa) and adhesion (5.14 MPa). To reduce the thermal conductivity hollow glass spheres (20 to 50 µm diameter) were added to the filled geopolymer. A 4:1 by volume of glass spheres to geopolymer mix gave the optimum results with respect to compressive strength (18.9 MPa), adhesion (4.78 MPa) and thermal conductivity (0.21 W m^{-1} K^{-1}).

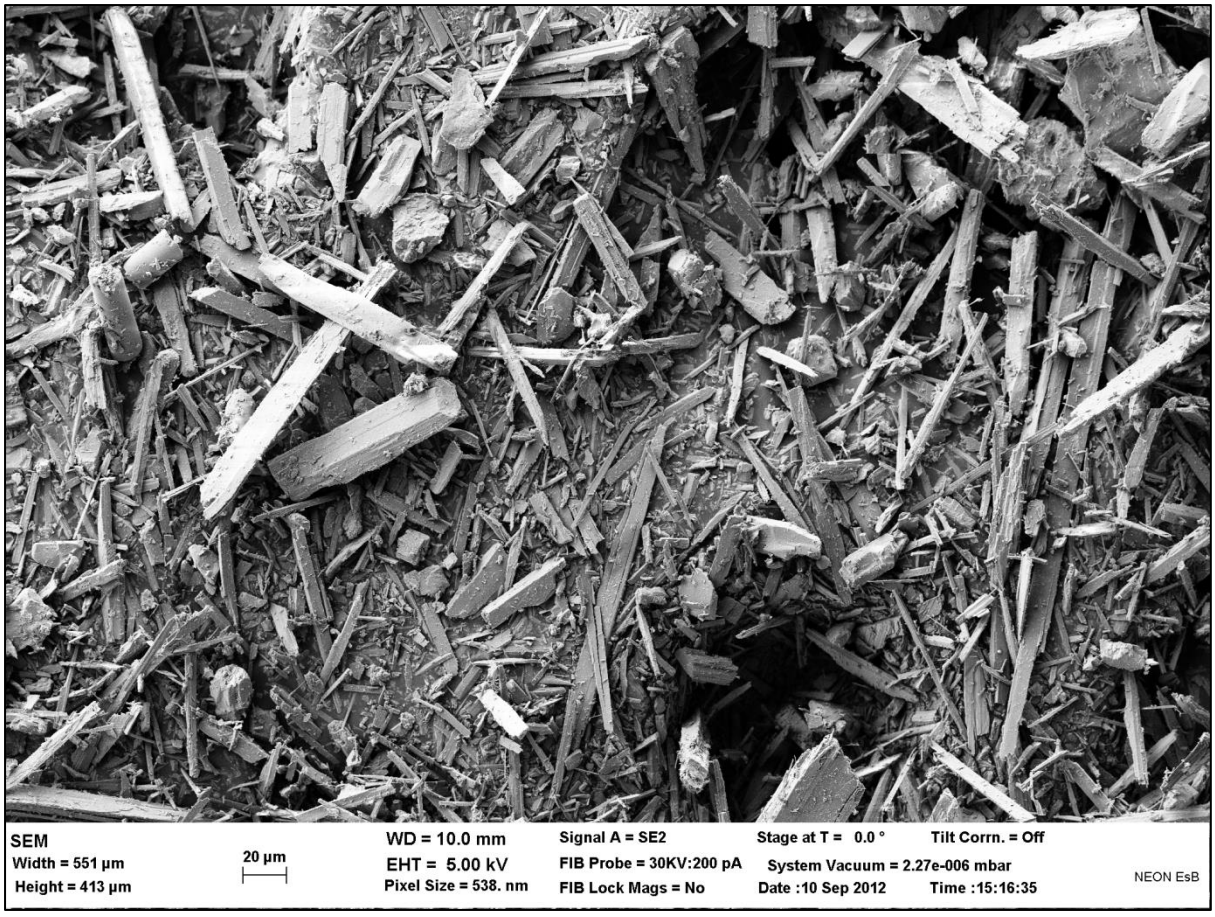

Figure 2.18 Wollastonite fibres (Nyad MG).

2.8 Thermal Properties of Geopolymers

Geopolymers based on metakaolin and fly ash are considered in this section. The amorphous inorganic structure of the geopolymers lends itself to good thermal resistance which leads to potential applications as thermal insulation in industrial, military and domestic sectors. Fire resistance is a large subset of thermal properties and will be considered in a dedicated section.

Thermal properties of interest are:

- Thermal expansion and shrinkage
- Thermal conductivity
- Strength retention
- Explosive spalling
- Microstructure including phase stability and resultant changes, pore size and distribution, weight changes including dehydration and rehydration.

Thermal analysis techniques such as, thermogravimetric analysis (TGA), differential scanning calorimetry (DSC), and differential thermal analysis (DTA), can be used to gather information on phase stability and thermodynamic properties of materials.

The composition of the geopolymer will have an influence on performance at elevated temperatures. The ratio of silicon to aluminium (Si: Al) plays a large part in the development of geopolymer properties and the influence of heat on these properties. This ratio should refer to the material contained in the polymer (binder ratio) and not the precursors (overall ratio) as complete conversion to geopolymers rarely occurs. Some authors use the SiO_2:Al_2O_3 ratio which will give a higher numerical value than the Si: Al ratio for the same material. These nomenclature issues are in need of resolution to bring more clarity to geopolymer research.

2.8.1 Measurement of thermal transport properties

The analysis of heat transfer through structures is of great importance in civil engineering problems such as heat flow into buildings in energy efficient designs, thermal loadings of buildings due to daily temperature variations, design of buildings for thermal comfort,

radiation shield design in nuclear power stations, analysis of bridge decks and other surfaces exposed to solar thermal loading (Khan, 2002).

The word heat should only be used to describe energy transfer from one place to another. Heat flow is an energy transfer that takes place as a consequence of temperature differences only (Serway, 1992).

The heat capacity, c, of a specific specimen of a substance is defined as the amount of heat energy needed to raise the temperature of that specimen by one degree Celsius (Serway, 1992).

If Q units of heat cause a temperature change of ΔT then:

$$Q = c.\Delta T \qquad \text{Equation 2. 6}$$

The heat capacity of a specimen is proportional to its mass. It is convenient to define the heat capacity per unit mass of substance, as the specific heat, C:

$$C = \frac{c}{m} \qquad \text{Equation 2.7}$$

Latent heat is the energy required to change the phase of a substance e.g. solid to liquid or liquid to gas or changes to crystalline structures. The temperature does not rise during a phase change.

Specific Heat and latent heat may be determined by differential scanning calorimetry (DSC). DSC measures the difference between heat flows from the reference and sample sides of a sensor as a function of time or temperature. Differences in heat flow occur when a sample absorbs or releases heat due to thermal events such as melting, crystallisation, and chemical reactions.

Heat transfer processes include conduction, convection and radiation. The conduction of heat only occurs if there is a temperature difference between two parts of the conducting medium. If we have a slab of cross sectional area, A and thickness, Δx, with opposite faces at temperatures T_1 and T_2, the heat flow, H, is found to be proportional to the temperature difference, and the cross sectional area and inversely proportional to the thickness. We can write:

$$H = -kA\frac{dT}{dx} \qquad \text{Equation 2.8}$$

k is the thermal conductivity of the material with units of W m^{-1} K^{-1}.

Table 2.10 lists thermal conductivity values for metals, non-metals and gases. Metals typically have high thermal conductivities due to the high number of electrons that are relatively free to move and transport energy over large distances. Non-metals have covalent or ionic bonds which conduct heat predominantly by phonon vibrations, whilst gases show no order with high separation distances between molecules at ambient temperatures giving rise to few collisions able to transfer energy.

Table 2.10 Thermal Conductivity, k, values (Serway, 1992).

Metals at 25°C	k	Gases at 20°C	k	Non-metals	Approximate Values of k
Aluminium	238	Air	0.0234	Asbestos	0.08
Copper	397	Helium	0.138	Concrete	0.8
Gold	314	Hydrogen	0.172	Glass	0.8
Iron	79.5	Nitrogen	0.0234	Ice	2
Lead	34.7	Oxygen	0.0238	Rubber	0.2
Silver	427			Water	0.6
				Wood	0.08

The two approaches to measuring thermal conductivity: steady state and transient (non-steady state) techniques are outlined below.

In steady state techniques a measurement is performed when the temperature of the measured specimen does not change with time. A solid sample of known dimensions is placed between two temperature monitored plates. One plate is heated whilst the other plate is cooled and their temperatures monitored until they are constant. The thermal conductivity is calculated from the steady state temperatures, specimen dimensions and heat input.

Sample preparation can be extensive and testing time will be in the range of hours. Analysis of outputs is relatively straight forward. The guarded hot plate is a commonly used steady state test procedure as outlined in ASTM C518-10 and ASTM C177-10 (ASTM Committee C16.30, 2010b, ASTM Committee C16.30, 2010a).

In transient techniques (hot wire method) as per ASTM D5930-09 (ASTM Committee D20.30, 2009) a measurement is made during the heating process of the specimen and measurements can be recorded relatively quickly. The measurements are plotted as a function of time. Whilst the testing period is short, mathematical analysis of the data is generally more complex.

The hot wire method involves inserting a wire into the sample either during the moulding process or by a post cure machining technique. A current passed through the wire generates heat which flows out radially from the wire and the temperature (T) of a fixed point close to the wire is recorded by a thermocouple inserted into the sample (Glatzmaier and Ramirez, 1988).

$$T\ (t,r) = \frac{Q}{4\pi k}\left\{-\gamma - \ln\left(\frac{rx^2}{4at}\right) + \ln(t)\right\} \qquad \text{Equation 2.9}$$

Where:

T = Temperature; t = time of heating; r = radial distance to line source;

Q = power per unit length; k = thermal conductivity of sample;

ϒ = Euler constant (0.577); α = thermal diffusivity;

By plotting the temperature of this fixed point verses the natural logarithm of time, thermal conductivity can be measured from the slope given knowledge of the input power, Q (refer to equation 2.9).

A variation of the hot wire method is the transient plane source method that employs two sample halves, in between which the sensor is sandwiched. The sensor consists of a double spiral of electrically conducting nickel metal which is encapsulated in thin polyimide film, which provides electrical insulation and mechanical protection. During testing a constant

electrical signal is passed through the conducting spiral, increasing the sensor temperature. The heat dissipates into the specimen on either side of the sensor at a rate dependent on the thermal transport properties of the specimen. Typically temperature increases are less than 2^{o}C. Recording of time and temperature in the sensor allows the thermal properties to be calculated. The rate of increase of the sensor voltage is used to determine thermal conductivity, thermal diffusivity and specific heat capacity of the specimen.

The modified transient plane source method uses a heating element that is supported on the back side by an insulating material thus allowing one directional heat flow. The equipment uses a one sided, interfacial heat reflectance sensor that applies a momentary constant heat source to the sample. This modification provides one sided facial measurements of liquids, powders, pastes and solids. Little if any sample preparation is required and testing time is seconds (C-Therm, 2010).

The laser flash method is based on the measurement of the temperature rise at the rear face of a thin disc specimen. The temperature rise is produced by a short energy pulse on the front face. An infra-red detector is used to measure temperature. Sample preparation is extensive and operator dependent but measuring times are short. This method can be used for evaluations up to 2000^{o}C (Kamseu et al., 2012a).

Samples with low emissivity or absorptivity are coated with a graphite film to increase energy absorbed on the laser side and increase temperature signal on the back side. Infrared radiation transparent materials must be coated with a metal film (typically 0.1µm gold) on both sides to prevent penetration of the laser beam at the front and to prevent infrared detectors viewing into the sample at the back.

$$k = \rho \,.\, Cp.\, \alpha \qquad \text{Equation 2.10}$$

Where: k = Thermal conductivity, ρ = density,

Cp = heat capacity (from DSC), α = thermal diffusivity.

Substances with high thermal diffusivity rapidly adjust their temperature to that of their surroundings because they conduct heat quickly in comparison to their volumetric heat capacity. Thermal diffusivity can be measured by the laser flash method.

Thermal conductivity is the property that determines how much heat will flow in a material, while thermal diffusivity determines how rapidly heat will flow within the material.

A sample's thermal resistance (R value) is equal to its thickness, x, divided by its thermal conductivity, k. Thermal resistance measures the ability of materials to resist heat transfer (Kamseu et al., 2012a).

2.8.2 Thermal Expansion

The coefficient of linear expansion (CTE or COTE or α) is a material property that is indicative of the extent by which a material expands or contracts on heating. The value varies over the wide range of available materials and over small temperature ranges is proportional to temperature change. Thermal expansion can generate destructive internal stresses when structural parts are heated and restrained from moving.

$$\propto = (\Delta L/L_i)/\Delta T \quad \text{Equation 2.11}$$

Where: L_i = initial length; ΔL = change in length; ΔT = change in temperature.

Equation 2.11 (Serway, 1992) assumes α is constant over the temperature range. However this is only true over limited temperature ranges. For a solid the coefficient of volume expansion, β, is three times α. This assumes that the material is isotropic (same in every direction).

To determine CTE the displacement and temperature must be measured on a specimen that is exposed to a thermal cycle. The main techniques are dilatometry (ASTM Committee E37, 2011), interferometry (ASTM Committee E37, 2010) and thermomechanical analysis (TMA) (ASTM Committee E37, 2012).

In the case of dilatometry a uniform section specimen is heated in a furnace and displacement of the ends of the specimen are transmitted to a sensor by means of push rods. Push rods can be made from vitreous silica, high purity alumina (service temperature up to 1600^{o}C) and isotropic graphite (up to 2500^{o}C). Compensation for the expansion of the push rod material during the test heating cycle has to be allowed for (ASTM Committee E37, 2011) The setup of dilatometer experiments is kept as force free as possible. Dilatometer measurements are generally applicable to materials with linear CTE of 0.5 µm m^{-1} K^{-1}.

With optical interference methods a sample of known geometry can be given polished reflective ends or placed between flat reflective surfaces (mirrors). The mirrors are flat uniform thickness pieces of silica or sapphire with surfaces partially coated with gold or other reflective metal. Light either from a laser or monochromatic source illuminates each (end) surface simultaneously to produce a fringe pattern. As the sample is heated (or cooled) expansion (or contraction) causes a change in the fringe pattern due to the optical path length differences between the end reflecting surfaces. This change is detected and converted into a length change from which CTE may be determined. Interferometry is normally used in the range of -150 to 700^{o}C. Precision at +/- 40 nm m^{-1} K^{-1} is significantly better then dilatometry or thermomechanical analysis techniques. This technique is suitable for materials having low (< 5 µm m^{-1} K^{-1}) or negative CTE (ASTM Committee E37, 2010).

Unlike traditional methods such as the dilatometer, in thermomechanical analysis measurements a constant small load (0.1 to 5 g) is applied to the specimen via a vertically adjustable quartz glass probe. This probe is integrated into an inductive position sensor. As the sample expands (or contracts) under heating it moves the probe and the recorded signal manipulated to give CTE. A range of probes are available for TMA to allow measurements of CTE, penetration for T_g determination, a tension jig for films and fibre evaluations. Testing of non-uniform samples and powders is possible by immersing the sample in a known volume of liquid, typically silicone oil, in a suitable retaining vessel which is attached to a suitable probe. Figure 2.19 shows several probes used in TMA (Anasys Thermal Methods Consultancy, 2012).

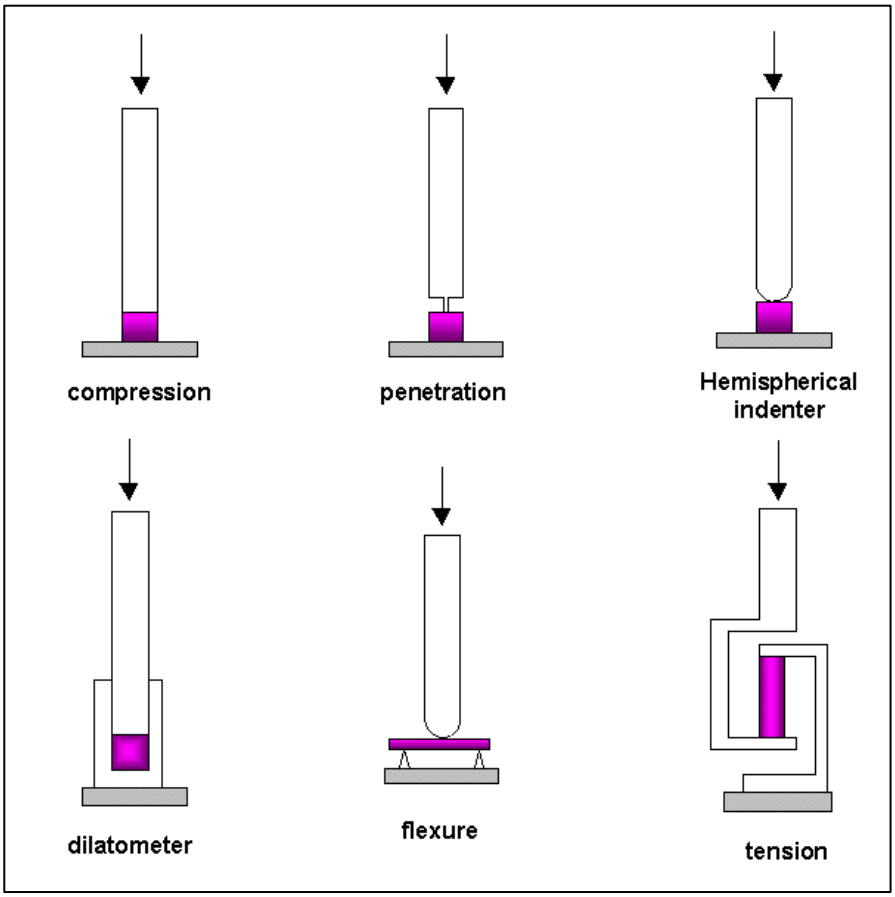

Figure 2.19 Different probes used in TMA (Anasys Thermal Methods Consultancy, 2012).

Barbosa and MacKenzie (2003a, 2003b) made geopolymers from metakaolin and either sodium hydroxide or potassium hydroxide and measured the thermal resistance of the resulting materials. They also investigated the addition of 10 vol. % of various inorganic fillers on strength and thermal properties and the influence of water content of the geopolymer formulation. Water contents (H_2O:Na_2O) of 10, 17.5 and 25 were evaluated, but only the lower water content cured sufficiently for dilatometer and strength testing. The results are shown in figure 2.20.

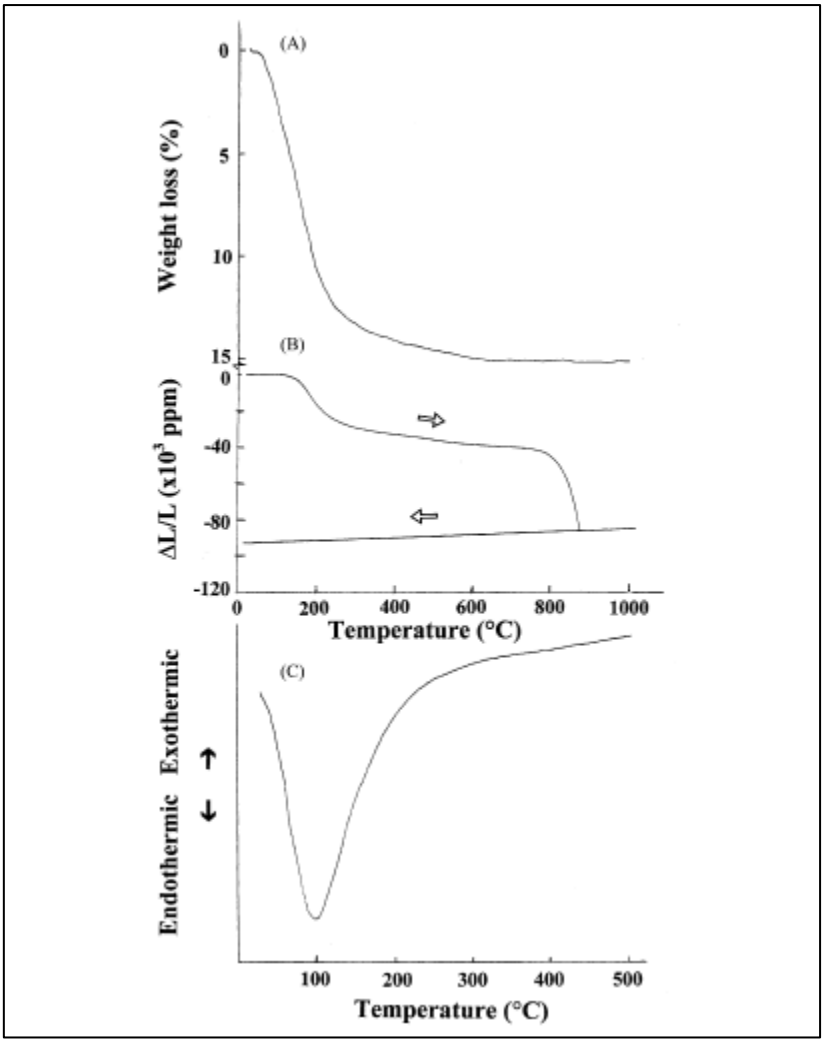

Figure 2.20 TG (curve A) at 20^{o}Cmin^{-1}, dilatometer (curve B) at 1^{o}C min^{-1} and DSC (curve C) at 10^{o}C min^{-1} (Barbosa and MacKenzie, 2003b).

The TG curve (A) showed that the well cured samples retain 15% water of which 12% is lost below 230^{o}C, the balance is either chemically bound or unable to migrate out of the sample readily. However, it continues to evolve gradually up to 500^{o}C. The DSC curve shows that the energy associated with the endothermic water loss is -0.24 kJ g^{-1}.

The dilatometer curve (B) shows that the water loss is associated with a small shrinkage value, and the material is essentially stable between 250 and 800^{o}C. Above 800^{o}C further shrinkage takes place due to densification and/or volume changes as a result of crystallisation and subsequent melting. The shrinkage stops at 880^{o}C and becomes dimensionally stable up to 1000^{o}C, the limit of the experiment. The sample retains this stability on cooling and during further thermal cycling.

The addition of 10 vol. % of inorganic filler to the geopolymer binder resulted in a drop in compressive strength with the samples containing alumina and β-sialon showing the most marked decrease in strength. This was attributed to both of these fillers being unreactive at ambient temperatures and unable to bond with the binder. They dilute the geopolymer without contributing to the strength of the composite. Dilatometer testing of these filled composites showed a flat portion in the curves up to 800^{o}C indicating an upper service temperature similar to pure geopolymer.

The authors also commented that microcracking after demoulding could be reduced by the addition of up to 5% glycerol, which plasticised the mix.

Rahier et al. (1997) used thermomechanical analysis to study metakaolin geopolymers produced from sodium or potassium silicates of varying moduli. All samples showed shrinkage due to dehydration up to around 230^{o}C. A second shrinkage event was dependent on the silicate modulus and alkali metal cation type. In the case of sodium silicate an increase in modulus from 1.4 to 1.9 resulted in the onset temperature increasing from about 650^{o}C to about 800^{o}C whilst changing the cation from sodium to potassium, at a modulus of 1.4 resulted in an onset temperature of about 900^{o}C.

Duxson et al. (2006a) used metakaolin geopolymers and investigated the influence of initial curing conditions on thermal shrinkage. He compared samples cured at 80^{o}C and those matured at 20^{o}C for 24 hours prior to curing at 40^{o}C. The specimen cured at the higher temperature began to shrink at a lower temperature but is ultimately more stable and densifies at a higher temperature. The sample matured prior to curing at 40^{o}C showed the same properties as that only cured at 20^{o}C. He believed that this indicated that thermal shrinkage outcomes were determined by curing temperature and not pre-maturation.

Duxson et al. (2006b, 2007a) carried out detailed work on metakaolin based geopolymers for a range of silicon: aluminium ratios using sodium and potassium silicates and their blends, measuring the thermal shrinkage of these materials and introducing the concept of four temperature regions to characterise the changes taking place:

Region I involves the loss of freely evaporable water with only minimal shrinkage.

Region II shows the start of initial shrinkage and continued significant weight loss.

Region III is characterised by gradual weight loss and thermal shrinkage.

Region IV involves densification and sintering and is characterised by rapid shrinkage and small weight loss.

The mechanism of shrinkage in region II is thought to be capillary shrinkage from evaporation of free water with the extent of shrinkage increasing with water content. The rate of shrinkage in region III was similar in all specimens regardless of silicon: aluminium ratio. However the temperature span of region III was related to the silicon: aluminium ratio by dehydroxylation. The high temperature required for condensation of aluminol groups is thought to increase the temperature required for complete dehydroxylation in specimens with low silicon: aluminium ratios. The onset temperature of region IV decreased with increasing silicon: aluminium ratio due to incomplete incorporation of aluminium from the metakaolin providing free sodium cations.

Rickard et al. (2010) expanded the above as shown in figure 2.21 and Table 2.11 to include characteristics specific to fly ash based geopolymers. The temperature range for each region is variable and dependent on sample composition and heating rates.

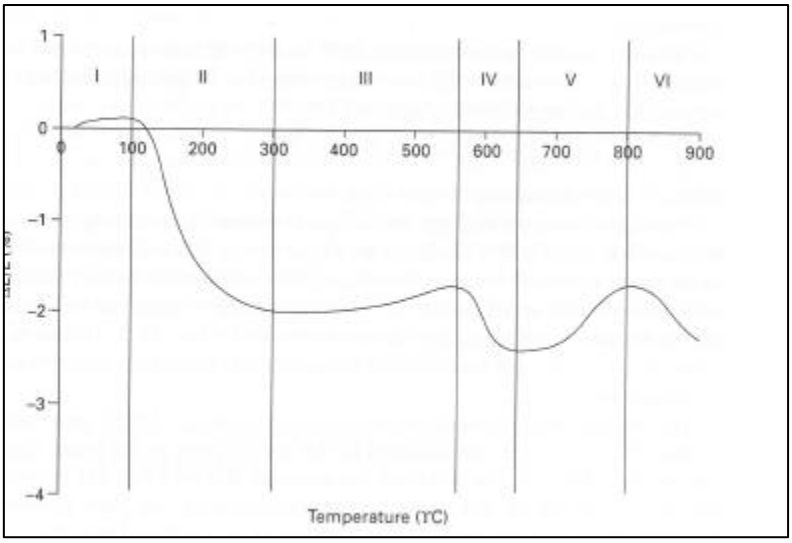

Figure 2.21 Thermal expansion of a fly ash geopolymer

(Si:Al (molar) = 2.3, w/c = 0.2)(Rickard et al., 2010).

Table 2.11 Thermal shrinkage/expansion characteristics of geopolymers (Rickard et al., 2010).

Region	Temperature Range, (^{o}C)	Description	Effect	Factors
I	0-150	Resistive dehydration	Slight expansion	Young's modulus of sample. Heat rate
II	100-300	Dehydration of free water	Significant shrinkage	Water content. Heat Rate
III	250-600	Dehydroxylation	Minimal shrinkage	Abundance of hydroxyl groups and chemically bound water.
IV	550-900	Densification by vitreous sintering	Significant shrinkage	Residual water content Si:Al molar ratio
V	Above densification temperature	Crystallisation in the geopolymer paste. Expansion due to cracking	Moderate expansion	Compositional ratio Concentration and type of impurities
VI	Above densification temperature	Further densification	Large shrinkage	Compositional ratio

Geopolymers expand on heating (region I), however they contain varying amounts of water that exist either adsorbed in the pores or chemically bound in the structure. On heating the water dehydrates at various stages depending on the energy requirements. Dehydration leads to a shrinkage event and the overall thermal expansion is a convolution of the solids expansion and the shrinkage of the pores (region II).

The slight thermal shrinkage occurring in region III between 300^{o}C and 600^{o}C is due to physical contraction as the hydroxyl groups are released creating shorter T-O-T links. The

small amount of shrinkage can be masked by the expansion of secondary phases particularly the high concentration of impurities found in fly ash.

$$T - OH + HO - T \equiv \rightarrow \equiv T - O - T + H_2\,\text{O} \quad \text{Equation 2.12}$$

Where T is an aluminium or silicon atom.

The second major shrinkage event occurs between 550^{0}C and 900^{o}C (region IV) due to densification of the geopolymer as the paste sinters and viscous flow fills any voids present in the material. Duxson (2007a) found that the presence of residual water in the material after dehydration reduces the activation energy for viscous flow.

Beyond the densification region (region V) no consistent trends are observable. The differences in thermal expansion in this region are believed to be due to compositional differences and the presence of impurities in precursor material. Rickard et al. (2010) and Rahier et al. (1997) reported expansive behaviour, whilst Duxson et al. (2007a) and Dombrowski et al. (2007) saw thermal shrinkage events. Barbosa and MacKenzie (2003a) stated that samples were thermally stable. The formation of cracks and changes to the nature of the pore structure also influence thermal expansion in region V.

In region VI the thermal expansion is characterised by large and rapid shrinkage events. The causes of this shrinkage may be attributed to continued densification, destruction of crystalline phases formed in region V, collapse of the pore system or sample melting.

Dombrowski et al. (2007) evaluated the effect of added calcium to fly ash geopolymers and found there was an optimum level at 8% calcium hydroxide for both mechanical strength and heat resistance. He set 2% for the acceptable maximum for thermal linear shrinkage. The 8% calcium content mix reached this value at 1050^{o}C compared to 810^{o}C and 960^{o}C for 0% and 20% respectively. He also carried out a creep test at 960^{o}C for 25 hours under compression where the 8% mix did not shrink below 2%. The 20% mix dropped just below 2% whilst the 0% mix dropped to 6%. He claimed that the 8% calcium lead to the formation of more crystalline compounds whilst at 20% the calcium depressed the melting point. The 8% calcium sample showed the highest concentration of nepheline at 800^{o}C and feldspar at 1000^{o}C, which contributed to highest strength and lowest shrinkage.

Subaer et al. (2007) investigated the addition of aggregates to metakaolin based geopolymers and their influence on thermal properties. The water loss of about 15 wt. % from ambient to 250^{o}C gave rise to approximately 2% shrinkage. Between 250 and 800^{o}C the sample was thermally stable, indicating the maximum service temperature. Beyond 800^{o}C further shrinkage occurred due to densification. The foregoing data is for a geopolymer with silicon: aluminium = 1.5 and sodium: aluminium = 0.6. Adding 20% wt. % aggregate to the geopolymer reduced the shrinkage to around 1% in the range of 23 to 500^{0}C. A further reduction in shrinkage was obtained by increasing the aggregate to 40 wt. %.

Geopolymers containing quartz aggregate show an abrupt expansion between 500 and 540^{o}C followed by further shrinkage as the temperature increases. There is a low-high quartz transition at 574^{o}C (The quartz page, 2012). The discrepancy arises from the geopolymer being hotter in the interior due to its exothermic nature as indicated by DSC. This transition is the reason fire resistant OPC is never produced from quartz aggregate(Neville, 1995). Granite filled geopolymer is stable up to 800^{o}C.

Lin et al. (2009b) added up to 30 wt. % of 0.75 µm α- alumina to a metakaolin geopolymer which had been synthesised by reaction with potassium silicate. Using TG-DTA they demonstrated that α-alumina had little effect on the thermal evolution of geopolymers at high temperatures. The endotherm up to 300^{o}C is attributed to water loss. The endothermic peaks at 958^{o}C (no added alumina) and 985^{o}C (~20% alumina) were attributed to crystallisation of the geopolymer.

XRD scans of these two systems showed a characteristic amorphous hump at ~28^{o} (2θ using copper Kα radiation) in samples exposed up to 600^{o}C. The sharp diffraction lines of leucite ($KAlSi_2O_6$) are seen in the alumina free geopolymer at 800^{o}C and remained until 1400^{o}C. However, in the case of the 20% alumina containing geopolymer leucite only appeared at 1000^{o}C. From this Lin concluded that the presence of alumina increases the crystallisation onset temperature and also the rate of crystallisation.

Lin also measured the thermal volume shrinkage of specimens after exposure to elevated temperature and saw significant reductions in shrinkage values above 20 wt. % alumina additions. This was particularly marked above 800^{o}C. Density and porosity showed marked

changes above 600^{o}C. The higher alumina contents showed increased porosity. Flexural strength was independent of alumina content, but increased markedly in all samples above 600^{o}C. The fracture surface of geopolymer samples heat treated at 1000^{o}C became rougher with increasing numbers of pores. Lin believed that this showed alumina has a negative influence on densification of geopolymers at high temperatures, but that it is beneficial for reducing thermal shrinkage.

Kamesu et al. (2010) made potassium activated metakaolin geopolymers which were extended with fine particle size quartz or α-alumina to evaluate the thermal properties of the blends. The total shrinkage in the range 25^{o}C to 900^{o}C was less than 3%. The maximum shrinkage of the unfilled geopolymer was 17% recorded at 1000^{o}C which was reduced to 12% by addition of alumina. The temperature where maximum densification occurred in the unfilled geopolymer was 1000^{o}C which shifted to 1150^{o}C and 1200^{o}C for 75 wt. % silica and alumina filled blends, respectively. Addition of water to obtain processable blends was between 34 and 44%. No physical property data was reported for the investigated blends.

Rickard et al. (2010) produced geopolymers from fly ash containing 20 wt.% α-quartz and 15 wt.% iron oxide impurities. Expansions on either side of the quartz high-low transition at 574^{o}C were minor in nature due to only 15 wt. % of the geopolymer being quartz. The quartz did not react with the geopolymer as the temperature increased and therefore did not influence post heating morphology or phase composition.

On the other hand the iron oxide content directly influenced the thermal expansion by altering the phase composition and morphology after heating. After heating in air at 900^{o}C a portion of the amorphous iron oxide from the fly ash converted to hematite. This was confirmed by weight increases in TGA and the appearance of hematite in XRD traces. A thermal expansion event observed in region 5 (fig. 2.21) was attributed to the formation and subsequent growth of cracks in the specimens. This thermal expansion event had not been observed in either fly ash or metakaolin geopolymers previously and was attributed to the high iron oxide content.

Bakharev (2006) activated two Australian fly ashes with sodium and potassium based activating solutions. One of the fly ashes contained 13 wt. % iron oxides. The author thought that the large shrinkage and loss of compressive strength on firing to 1000^{o}C could be

attributed to the presence of these iron oxides. Shrinkage increased with increased water to binder ratio, increased alkali content and increasing the firing temperature from 800 to 1000^{o}C. Melting occurred at a lower temperature when the alkali content increased. The second fly ash, with high silica content, showed thermal expansion which resulted in the formation of foam at 1200^{o}C. Sodium activated fly ash gave geopolymers which exhibited a rapid deterioration in strength at 800^{o}C. This was connected to a rapid increase in pore size. However, geopolymers produced from potassium activated fly ash remained predominantly amorphous up to 1200^{o}C.

Pan et al. (2009) exposed fly ash based geopolymer mortars to 800^{o}C and found that strength after exposure sometimes decreased and at other times increased. Specimens produced from two fly ashes showed strengths in the range of 5 to 60 MPa. The strength loss decreases were reduced with increasing ductility, with strength gains evident at the highest levels of ductility. This was attributed to mortars with high ductility having a high capacity to accommodate thermal incompatibility. Two opposing mechanisms are thought to occur in mortars:

- Further geopolymerisation and/or sintering at high temperatures leading to strength gains.
- Damage to the mortar because of thermal incompatibility arising from non-uniform temperature distribution.

The strength gain or loss occurs depending on the dominant process.

Thermal incompatibility occurs due to heat flow in solids taking time to reach a steady state. The thermal incompatibility in non-homogeneous, multi-phase materials e.g. concrete or mortar occurs because of different expansive responses to the applied heat.

Ductility of specimens was calculated from the compressive stress-strain curves. The mortars with lower initial strength exhibited greater ductility as evidenced by a rounder shaped curve. Mortars with the higher initial strength show a narrower curve with a different response in the descending part and exhibited lower ductility.

Ductility was defined by two methods as shown in Figure 2.22. One method is to divide strain ε_2 by strain ε_1. Strain ε_1 represents a strain at the limit of elastic behaviour. Strain ε_2

corresponds to 0.85 of the peak stress in the descending part of the curve. Another method to define the ductility index is by dividing the total energy at failure by the elastic energy stored at peak load (Pan et al., 2009).

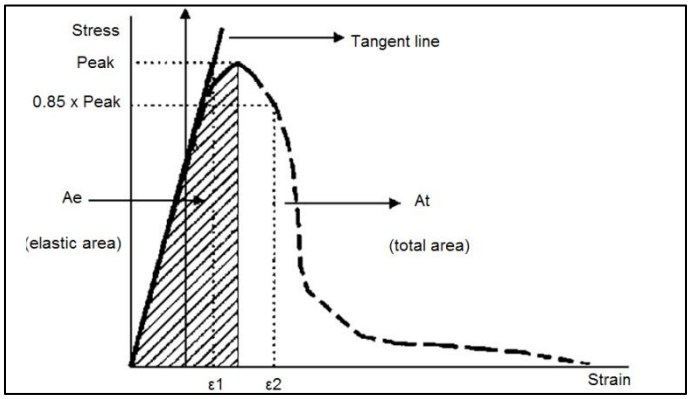

Figure 2.22 Derivation of ductility index (Pan et al., 2009).

Pan and Sanjayan (2012) was able to measure stress-strain properties in-situ at elevated temperatures. Geopolymers based on class F fly ash were prepared by activation with sodium, potassium and sodium/potassium blend solutions at various addition levels. The softening point of the sodium based geopolymer remained the same (610 +/- 20^{o}C) regardless of silicate concentration, fly ash composition and test load. Potassium based geopolymers softened at 800^{o}C and the sodium potassium blend at 570^{o}C. Increases in strength for sodium based geopolymers were seen at 530^{o}C and at 730^{o}C for potassium based geopolymers. This increase in strength was seen in conjunction with heat release indicating that an exothermic event was occurring. The author suggested that further geopolymerisation reactions were occurring at between 300 to 500^{o}C accounting for the increase in strength.

Two types of test were carried out:

1. Study of the deformation of heated geopolymers under constant load. Tests were carried out at stress levels of 0.05 σ_r and 0.55 σ_r (σ_r is the reference strength at ambient temperature). Deformation was measured until 83% of the initial height was reached.

2. Compressive strength at elevated temperature where specimens were preheated without load to target temperature (50^{o}C below softening point) and then soaked for one hour before testing at 20 MPa min^{-1} to failure.

Specimens with an embedded thermocouple in the centre and one on the outside were heated at 5^{o}C min^{-1} to 800^{o}C. There was an initial expected lag between outer and inner temperatures which peaked at around 200^{o}C. The difference then started to decrease even becoming negative (centre hotter than outside) in 2 cases i.e. heat was evolved in the centre of the sample. This continued to around 300^{O}C. The highest degree of strength increase is associated with a high degree of heat evolution. The geopolymer with the lowest initial strength was hypothesised to have higher unreacted precursor levels which can convert to geopolymer at high temperature and therefore increase the strength.

Guierri and Sanjayan (2010) showed that higher initial geopolymer strengths were associated with lower ductility. These high strength samples have less capacity to accommodate thermal incompatibility due to temperature differences between the exterior and interior of specimens during heating. This was the reason for low strength retention values in these initially strong samples.

Kong et al. (2007) compared geopolymers based on metakaolin and fly ash at elevated temperatures. The strength of the fly ash geopolymer increased after firing at 800^{o}C whilst the metakaolin showed a decrease in strength. The metakaolin mix had a solid to liquid ratio of 0.8 whilst the fly ash was 3.0. The metakaolin geopolymer pores were predominantly mesopores (1.25 to 25 nm) whilst the fly ash geopolymer pores had a significant proportion of micropores which facilitate water escape at elevated temperatures thus causing minimal damage to the geopolymer structure. The strength increase in the fly ash based geopolymer is also attributed to sintering of unreacted fly ash remnants.

Kong and Sanjayan (2008) investigated the effect of commonly used coarse aggregates in geopolymers. Aggregates are usually added to geopolymer pastes at 70 to 80 vol. % and therefore contribute markedly to the overall thermal expansion of the resulting composite. The presence of aggregate resulted in a reduction in compressive strength of the composite after exposure to elevated temperatures. This is attributed to the mismatch in thermal

expansion between geopolymer paste and aggregate. Figure 2.23 shows the thermal expansion of some coarse aggregates.

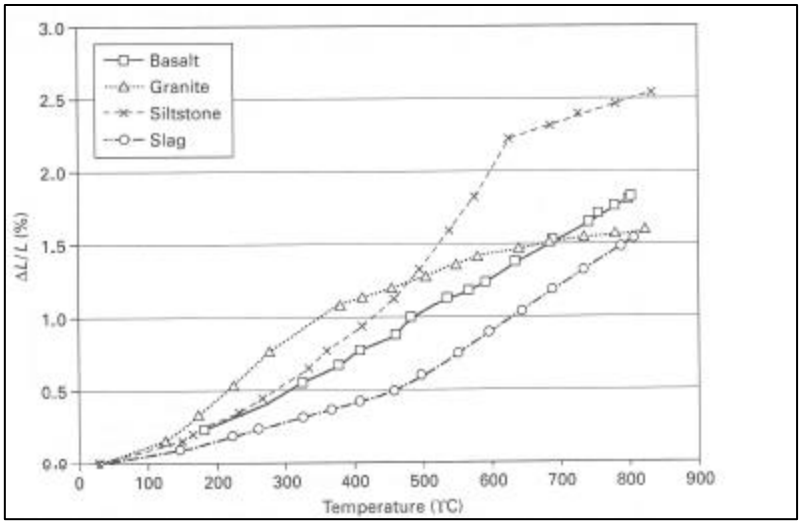

Figure 2.23 Thermal expansion of coarse aggregates (Kong and Sanjayan, 2008).

Kong and Sanjayan (2010) produced fly ash based geopolymer binders using sodium silicate and potassium hydroxide. Coarse aggregates based on crushed basalt and steel mill slag were used to produce concretes. The fine aggregate was river sand with 3 mm maximum size. This work compared geopolymer paste (no added aggregate), mortar (added sand only) and concrete (using sand plus aggregates ranging from 2.37 mm to 20 mm).

The 3 day compressive strengths of paste, mortar and concrete were similar, but after heating the paste had a 73.4% strength loss, the mortar showed 100% strength loss and the concrete 58.4% strength loss.

Three sizes of compression strength sample based on paste were produced, cubes 25 x 25 x 25 mm^3, and cylinders 70 mm high x 35 mm diameter and 200 mm high x 100 mm diameter.

Exposure to elevated temperature affected strength changes to larger specimens more adversely than smaller specimens. The cube specimens showed a small gain of 6.4% whilst the cylinders showed strength losses of 52.3% and 73.4% with increasing cylinder dimensions. The variation in strength loss was attributed to larger thermal gradients in larger specimens which led to thermally induced cracking.

The addition of coarse aggregate to form geopolymer concrete showed that aggregate size is important to thermal stability. Concretes made with aggregate size grading of 2.36 to 5 mm and 5 to 10 mm exhibited spalling at 420^{o}C and 505^{o}C, respectively. A consistent 61.8% strength loss was recorded for the 10 to 14 mm and the 20 mm sized aggregates.

The aggregate which has a higher stiffness than geopolymer paste, restrains the matrix shrinkage. This restraining effect sets up radial and tangential stresses around the aggregate particles. The shrinkage arising from water loss enhances these stresses, leading to the development of extensive cracking. This behaviour is more evident in concretes made with smaller sized aggregate.

Fernández-Jiménez et al. (2010) compared OPC paste with fly ash based geopolymer and a blend of 70% fly ash and 30% OPC activated with sodium carbonate and sodium silicate both in solid form. Physical tests were carried out in-situ at elevated temperature up to 600^{o}C and post firing after exposure in steps from 200^{o}C to 1000^{o}C followed by cooling to ambient temperature.

At temperatures from 400 to 600^{o}C Portland cement strength declined drastically due to water loss and degradation of the CSH phase. This occurred in both test regimes. Once the material cooled it failed to regain any of the initial strength. The fly ash based geopolymer performed better than Portland cement with residual strength being maintained or showing some gains. The presence of alkali in the geopolymer favoured the formation of a molten phase at 600 to 700^{o}C. The solidification of this molten phase on cooling may explain the increased strength on cooling. The presence of this liquid phase could also account for the drop in strength at 600^{o}C in the in-situ test regime.

The fly ash - OPC blend showed intermediate behaviour, with lower initial strength than the both pure systems, but performed better at high temperature than the OPC.

Research by Chen-Tan et al. (2009) had shown that only amorphous aluminosilicates in the fly ash will react to form geopolymers.

Rickard et al. (2011) characterised three Australian fly ashes in order to gain an understanding of the properties relevant to producing geopolymers with good elevated temperature resistance. Variation arises in fly ash due to coal composition and power

station furnace operating conditions. The total composition was obtained by X-Ray fluorescence (XRF) and crystalline phase components by X-Ray diffraction (XRD). Loss on ignition (LOI) was determined up to 1000^{o}C.

The amount of potentially reactive amorphous material is obtained by manipulation of XRF and quantitative XRD (QXRD) results. Geopolymers from the three fly ashes were produced at a range of silicon: aluminium ratios and then fired at 1000^{o}C. Changes in strength after firing were recorded. In two of the samples sintering of unreacted fly ash material occurred at elevated temperature leading to strength increases of 200 to 400%. The other fly ash geopolymer exhibited high strength prior to firing, but showed a marked decrease in strength (>70%) after firing. This was attributed to oxidation of iron compounds which led to a thermal expansion with resulting crack formation. XRF showed that this latter fly ash had 13.2 wt. % iron oxides. This particular fly ash would be unsuitable for the manufacture of geopolymers for high temperature applications

SEM showed that the initial low strength geopolymers contained partially reacted fly ash particles bonded by the geopolymer gel. For all samples the higher the silicon to aluminium ratio the higher the retention of strength after firing.

The following additional points were made:

- Finer fly ash particles are preferable for higher initial strength properties.
- A spherical morphology is more suitable for low water mixes without loss of workability. Lower water content is also beneficial for reduced shrinkage at elevated temperatures.
- The presence of quartz particles in the fly ash can reduce workability and may also lead to expansion cracking at elevated temperatures.

Rickard et al. (2012) continued the above work with a more extensive investigation of fly ashes from five Australian power stations. Geopolymers were synthesised from each fly ash at a range of silicon to aluminium ratios. Only the amorphous (glassy) components were considered as reactive in geopolymerisation.

The silicon to aluminium ratio in the glassy component of the fly ash influenced the thermal properties of the geopolymers. High silicon to aluminium ratios (>5) showed compressive

strength gains and better dimensional stability after exposure to 1000^{o}C, whilst low silicon to aluminium ratios (<2) exhibited loss of strength and decreased dimensional stability.

In this work dilatometry was performed across the range of geopolymer samples with silicon to aluminium ratios of 2.0, 2.5 and 3.0. Marked differences between individual fly ashes were observed and in some cases with changing silicon to aluminium ratio of the geopolymer made from the same fly ash.

Geopolymers made with added alkali silicate solutions to achieve the required silicon to aluminium ratios showed higher shrinkage levels and even major expansion events in two cases. This expansion was attributed to swelling of unreacted silicate phases present from the activating solution.

Using SEM a higher proportion of binding phase was observed in geopolymers produced by silicate activation which led to greater initial strength than sodium aluminate activated geopolymers. After firing geopolymer strengths were affected by variations in phase changes in the non geopolymer phases as well as damage due to dehydration. Sintering was the main factor leading to compressive strength increases as it released more aluminosilicate material from the unreacted fly ash and activating solution remnants into the binding phase and improved inter-particle connectivity. This effect was consistently evident across all the samples and as such the cause for variable post fired strength must lie elsewhere. It is thought that activating solutions with high silicate levels showed incomplete incorporation of the silica leaving residual silicate phases which lead to lower post fired compressive strength.

Whilst all the geopolymer samples exhibited strength improving microstructural changes such as improved particle-particle bonding after firing, the instability of the non geopolymer phases after firing led to strength reductions. Typically oxidation of iron oxide phases leading to thermal expansion and associated cracking and the expansion of added unreacted silicate phases can be the cause of strength losses after firing.

2.8.3 Thermal Conductivity

Thermal conductivity, k, determination is required to assess geopolymers' suitability for potential applications in thermal barriers and construction structural members. Insulators

require a low k value to reduce heat flow by conduction. Structural concrete requires higher k values to allow for a reduction in thermal gradients and resulting reduced expansive stresses (Subaer and van Riessen, 2007). Subaer obtained a 40% increase in thermal conductivity (0.65 to 0.91W m^{-1} K^{-1}) by adding 40 wt. % quartz aggregate to a metakaolin based geopolymer.

Liefke (1999) produced geopolymer foams with densities in the range 100 to 800 kg m^{-3} with a k value of 0.037 W m^{-1} K^{-1}. He also reported on open cell foams with densities in the range 350 to 400 kg m^{-3} and a k value of 0.16 W m^{-1} K^{-1}. This latter foam is suitable for automotive exhaust silencer components.

Rickard et al. (2013) produced metakaolin foams of various densities and measured k values. Foam with a density of 800 kg m^{-1} gave a k value of 0.3 W m^{-1} K^{-1}. The fire rating of this sample tested to AS1530.4 was 64 minutes for a 50 mm thick specimen.

Jonker et al. (2009) developed a geopolymer foam system suitable for refractory service. The material was based on a blend of fly ash and metakaolin (5:1 by weight) and activated with sodium silicate and sodium hydroxide. Powdered aluminium metal was the foaming agent. The density was 750 kg m^{-3} after drying at 110^{o}C and 600 kg m^{-3} after firing at 1100^{0}C. Compressive strength was 4 MPa and increased to 14 MPa after firing at 1100^{o}C. Fired shrinkage was less than 2%. Thermal properties are shown in table 2.12.

Porosity was the main influence on lowering thermal conductivity. The pores should be as small as possible and cracks and coarse pores of more than 5mm should be avoided. The higher content of small pores is beneficial to decreasing thermal conductivity and increasing strength of the material.

Table 2.12 Thermo-physical properties of geopolymer insulating material (Jonker et al., 2009).

Temperature, ^{o}C	Thermal Diffusivity, $mm^2\ s^{-1}$	Specific Heat, $J\ g^{-1}\ K^{-1}$	Thermal Conductivity, $W\ m^{-1}\ K^{-1}$
23	0.378	0.740	0.227
199	0.348	0.935	0.264
401	0.350	1.037	0.293
601	0.366	1.098	0.326
800	0.387	1.171	0.368
998	0.416	1.230	0.415
1098	0.447	1.273	0.462

The value of k is driven by different mechanisms in different materials. Metals have high electrical and thermal conductivity. Metals with a face centred cubic structure e.g. silver (k = 430 W m^{-1} K^{-1}) have the highest electrical and thermal conductivity; whilst body centred cubic metals are an order of magnitude lower. Ceramics show low conductivity due to the large band gap between valence and conduction bands (Rollett, 2007).

In solids the carrier of heat is the phonon, a quantum of lattice vibrational energy. Whilst the theoretical model for the mechanism of phonons in heat transfer is based on crystalline solids some of the basic ideas may be used to gain some understanding of thermal conductivity in other materials. The mean free path is the distance between phonon scattering centres. Heat is mostly carried by phonons in the acoustic range i.e. with frequencies less than 20 kHz. Equations 2.13 and 2.14 show the relationship between thermal conductivity and phonon velocity. The phonon velocity is related to the material density and Young's modulus.

$$k = \frac{1}{3} C\ v\ l \qquad \text{Equation 2.13}$$

$$v = \sqrt{(E/\rho)} \qquad \text{Equation 2.14}$$

Where:

k = thermal conductivity of medium, C = specific heat of medium,

v = velocity of the carrier of heat (phonons), l = mean free path,

E = Young's modulus of medium, ρ = density of medium

Klemens and Gell (1998) reviewed the thermal conductivity of thermal barrier coatings based on ceramic materials. Heat is conducted by lattice waves and by a radiative component which becomes significant at elevated temperatures. Point defects such as added cations and lattice vacancies reduce the lattice thermal conductivity by scattering high frequency lattice waves (phonons). Grain boundaries scatter lattice waves in the low frequency part of the spectrum. Both effects can be enhanced by adding cations and decreasing average grain size. To reduce the radiative component larger imperfections around 1 μm in size are required. These imperfections could take the form of heat stable solids or preferably pores.

Clarke (2002) reviewed the theories of thermal conductivity with reference to temperatures beyond the Debye temperature. He discussed the influence of pores on decreasing the conductivity of materials. The volume fraction of pores, their aspect ratio and spatial distribution all need to be considered. An illustration of this is the formation of flat "pancake" like pores perpendicular to the temperature gradient during plasma spray application of ceramic coatings which led to the greatest decrease in thermal conductivity. He concluded that a material will have low thermal conductivity at high temperatures if it satisfies:

- High molecular weight
- Complex crystal structure
- Non-directional bonding
- Large number of different atoms per molecule

The data shown in table 2.13 and figure 2.24 was used to select additives for alumina and zirconia based thermal coatings to reduce thermal conductivity levels.

Table 2.13 Calculated minimum thermal conductivities (W m^{-1} K^{-1}) (Clarke, 2002).

Compound	K_{min}	Compound	K_{min}	Compound	K_{min}
BeO	3.78	$MgAl_2O_4$	2.34	NiO	1.48
SiC	3.00	TiO_2	2.07	$LaMgAl_{11}O_{19}$	1.48
Al_2O_3	2.89	Mg_2SiO_4	2.00	$Gd_2Zr_2O_7$	1.14
MgO	2.56	Mullite	1.68	Monazite	1.13
AlN	2.45	ZrO_2 (YSZ)	1.49	ThO_2	0.98

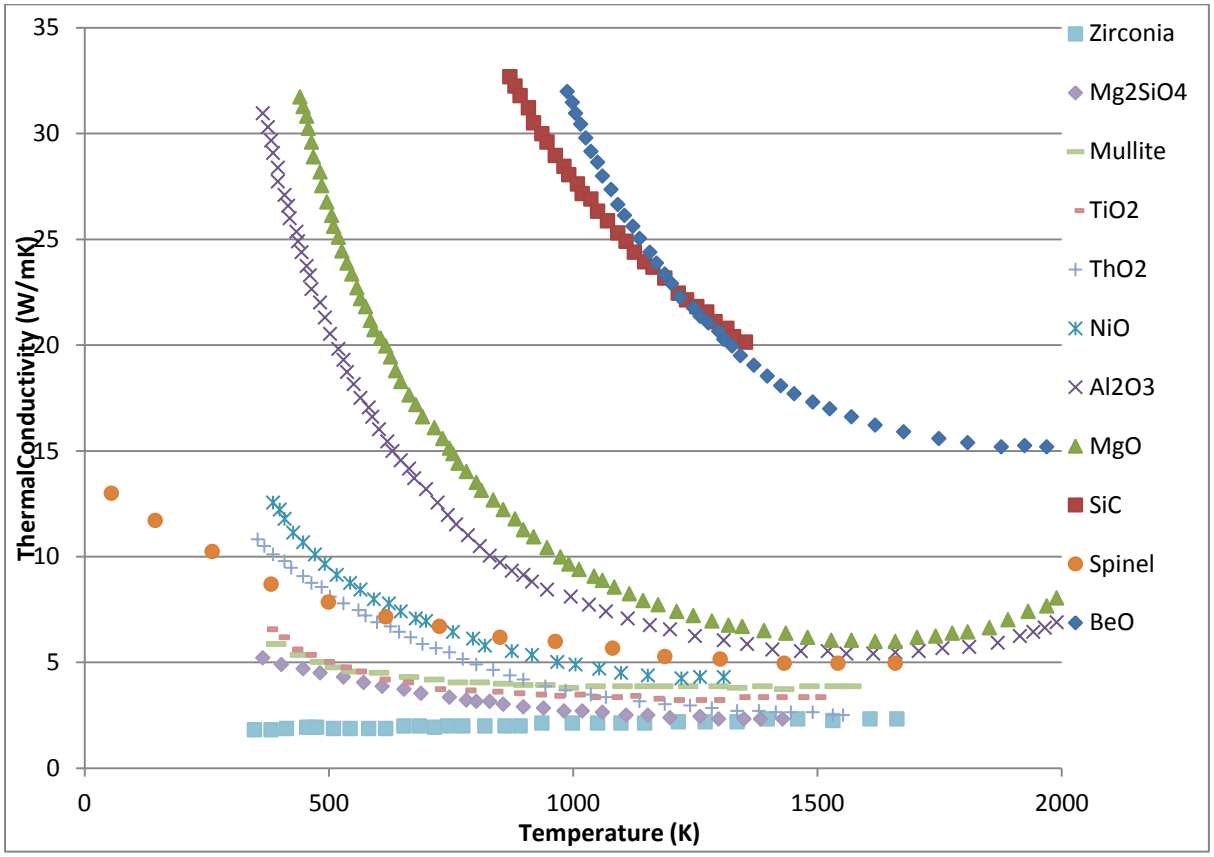

Figure 2.24 Temperature dependence of thermal conductivity (Clarke, 2002).

Duxson et al. (2006) used thermal conductivity measurements to investigate the microstructure of metakaolin based geopolymers up to 100^{o}C. Water will still be present up to 100^{o}C and this can have a masking effect on measurements. Increasing silicon to aluminium ratios between 1.15 and 2.15 gave increased k values with sodium activated geopolymers giving slightly higher values than potassium activated geopolymers. Over the temperature range investigated k values showed minor changes.

Kamesu et al. (2012a) produced geopolymers using metakaolin from two sources, one of which had high quartz content, and measured the following thermal properties, thermal diffusivity, thermal resistance and thermal conductivity. Thermal diffusivity was determined by the laser flash method and the thermal conductivity determined from equation 2.10.

Porosity determination and water contents were measured and related to thermal properties. As the silicon to aluminium ratio of the geopolymers increased, thermal diffusivity increased. At Si: Al = 1.23, the thermal diffusivity was 2.24 x 10^{-7} m^2 s^{-1} and increased to 3.83 x 10^{-7} m^2 s^{-1} at Si: Al = 2.42. These results equate to thermal conductivity values of 0.3 to 0.59 W m^{-1} K^{-1}.

Increasing the silicon to aluminium ratio leads to a decrease in cumulative pore volume with a corresponding reduction in average pore size. The thermal properties are related to porosity and pore interconnectivity of the geopolymer. The following mechanisms were suggested for the change in humidity of geopolymer specimens:

1. Chemical fixing of atmospheric water which is more predominant in the case of higher Si: Al ratio specimens. This is via reaction of water with silicon sites to form $Si(OH)_4$. For samples with low Si: Al molar ratio it takes longer for the humidity to be fixed due to a lower concentration of active silica sites.
2. Physical absorption of atmospheric water in the pores.

The authors concluded that thermal conductivity for insulation applications can be influenced by Si: Al molar ratio, alkali content, and crystalline phase content.

Kamesu et al. (2012b) produced geopolymer foams from calcined silica rich kaolin and presented two theoretical models for the variation of effective thermal conductivity with total porosity. The variation in Si: Al ratio in these formulations also includes the residual

quartz which is not transformed in the kaolin calcination step. Residual quartz will increase the effective thermal conductivity of the geopolymer since crystalline quartz has k values in the range of 6 to 11 W m^{-1} K^{-1} whilst amorphous silica is three to five times lower.

With the increase in total porosity, the effective thermal conductivity decreases. This is illustrated in figure 2.25. The addition of blowing agent (aluminium powder) changes the pore size, volume fraction and spatial arrangement of the pores.

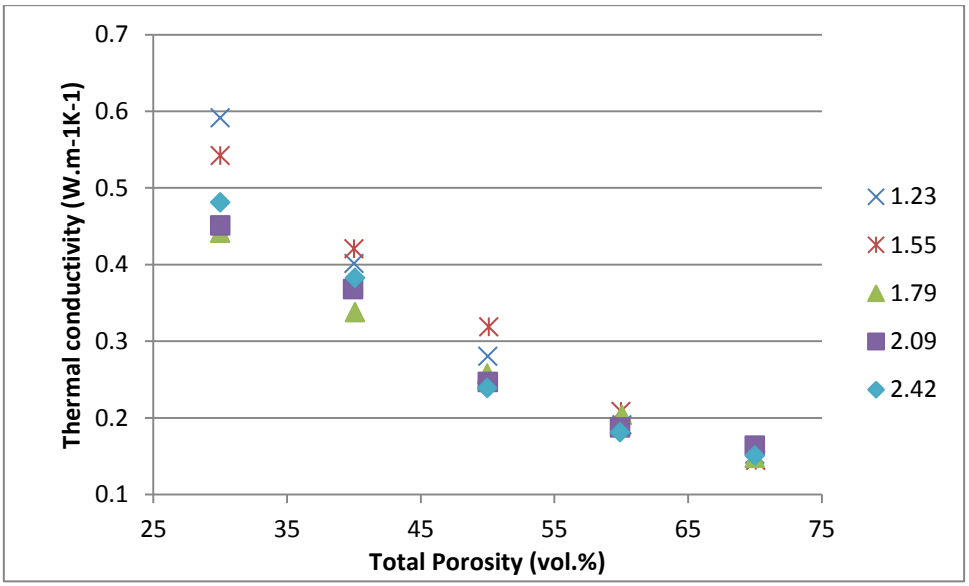

Figure 2.25 The influence of total porosity on thermal conductivity (Kamseu et al., 2012b).

Khan (2002) measured thermal conductivity on a range of aggregates alone and in OPC concrete. Moisture played an important role on the measured thermal conductivity value.

Tables 2.14 and 2.15 show the variation of aggregate and concrete thermal conductivity values due to water content. Sand I is quarried sand whilst sand II is river sand containing mica. The higher thermal conductivity values for sand I were attributed to the higher quartz content.

Table 2.14 Thermal conductivity of aggregates (Khan, 2002).

Type of aggregate	Thermal Conductivity, W m^{-1} K^{-1}		Specific Gravity
	Dry state	Wet state	
Basalt	4.03	4.30	2.70
Limestone	3.15	3.49	2.69
Siltstone	3.52	5.22	2.66
Quartzite	8.58	8.63	2.67

Table 2.15 Thermal conductivity of mortar and concrete in dry and fully saturated state (Khan, 2002).

Type of concrete	Thermal Conductivity, W m^{-1} K^{-1}			
	SAND I		SAND II	
	Dry	Fully saturated	Dry	Fully Saturated
Mortar	1.90	2.65	1.37	1.95
Basalt concrete	2.26	3.52	1.97	3.24
Limestone concrete	2.03	2.92	1.60	2.71
Siltstone concrete	2.21	3.61	1.91	2.90
Quartzite concrete	2.77	4.18	2.29	3.49

2.9 FIRE RESISTANCE

The influence of fire on materials is governed mainly by the composition of the material exposed with the following properties being the key to determining the level of fire resistance:

- Inorganic/organic component ratio;
- Phase changes e.g. formation of chars, thermal expansion/shrinkage events, melting points and other transitions;
- Presence of pores which affects thermal insulation and vapour transportation;
- Presence of volatiles e.g. water;

Geopolymer based systems have inherently superior fire resistance compared to Portland cement based and organic polymer systems. The fire resistance of cementitious systems is controlled by a range of factors. Geopolymer systems are substantially inorganic based and are considered incombustible, emitting no toxic fumes when exposed to fire. Compared to Portland cement based systems geopolymers retain a significant level of structural stability after exposure to fire events and show little if any explosive spalling. This lack of explosive spalling in geopolymers is attributed to an interconnected pore system which allows easy passage of volatiles, predominantly water, through the geopolymer structure when a thermal gradient is applied. The majority of the water in geopolymers is not bound in hydrates as is the case with Portland cement based systems. In the latter case the loss of water from the hydrates present results in the reduction of strength and consequent load bearing ability (van Riessen et al., 2009, Kong et al., 2007).

Resistance of geopolymers to fire exposure is managed by the techniques used to control thermal expansion/shrinkage events and loss of volatiles, predominantly water, to leave a post fire material in a serviceable condition.

The fire supplies the thermal energy which drives the changes to the exposed material. A fire requires a fuel source, an oxidising agent and an ignition source. The reaction is exothermic in nature and proceeds via a free radical mechanism (Higgins, 2008).

One of the earliest attempts to investigate the combustion reaction was by Michael Faraday (1861) who presented his findings in a series of lectures for juveniles at the Royal Society in 1860/61. These six lectures were published as “The Chemical History of a Candle” and are still in print to this day.

2.9.1 Portland cement

Denoël (2007) reviewed fire safety and concrete structures for the Federation of the Belgian Cement Industry. This covered the choice of concrete, regulations, fire resistance, fire risk, fire safety engineering and repair of concrete after fire.

Hertz (2003) investigated spalling in traditional and high strength concrete back to the mid 1980s and gives a comprehensive list of possible causes of spalling. Several other authors (Papworth, 2000, Kalifa et al., 2001, Peng et al., 2006) have carried out fire testing of high strength concrete.

Papworth (2000) tested steel reinforced slabs 4.5 m x 1.1 m x 0.250 m thick containing silica fume and nylon fibres which he considered gave advantages over polypropylene. The fire curve used was based on AS 1530.4. (Standards Australia, 2005). The slab containing the nylon fibre and silica fume showed some fine cracks on the fire side, but no spalling. Three other samples, two with silica fume only and a control (no silica fume) showed significant spalling. The slabs were cured for 28 days prior to testing to ensure moisture was still present in the slabs. This was an attempt to replicate a tunnel lining where the buried inner concrete surface has access to ground moisture.

Kalifa et al. (2001) added polypropylene fibres to high strength concrete to reduce spalling. Pore pressure measurements performed on heated concrete showed the presence of fibres lead to a large decrease in the extent of pressure zones which built up in the porous network. Fibres were found to have only a small effect on the thermal properties of concrete. In the fire test using the ISO 834 fire curve, the temperature rise shows a plateau effect that starts above 100^{o}C and ends between 160 and 220^{o}C, which is in the melting range of the fibres. In plain concrete the plateau ends at around 250^{o}C. This phenomenon is associated with the consumption of energy due to water vaporisation in the porous network. The end point of this phenomenon correlated with the measured pressure peak. The melted fibres enable vaporised water to be expelled from the concrete at lower temperatures. Pressure versus time curves have a similar shape at all fibre dosages, but the pressure peak height is drastically reduced with increasing fibre dosage.

Peng et al. (2006) added hybrid fibre blends, based on polypropylene and steel, to high strength concrete and obtained improvements in fracture energy which could be correlated to improved spalling resistance. Exposure to 400^{o}C showed a drop in residual strength, but fracture energy was higher than at ambient temperature only in the samples containing steel fibres. An increase in fibre pull out values was observed in samples heated to 400^{o}C. Above 400^{o}C strength reduced rapidly in all specimens. Peng concluded that a hybrid fibre

blend using polypropylene fibres to form a pathway for water vapour escape after melting and a steel fibre to inhibit crack propagation during heating would be beneficial to heat resistance. Spalling was observed in some of the samples containing polypropylene fibre and this was attributed to the low loading (0.25 kg m^{-3}) and the dense structure of the concrete made at a w/c of 0.26. He suggested increasing polypropylene dosage to 2 kg m^{-3} to improve spalling resistance.

Both (2003) considered there were three options to improve spalling resistance of concrete:

1. Increase permeability preferably during the duration of the fire to avoid durability issues;
2. Increase fracture energy of the concrete;
3. Reduce difference in coefficient of thermal expansion between matrix and aggregates.

He considered low melting point fibres to address option 1. Two types of polypropylene fibres were compared at 2 kg m^{-3} in a standard tunnel lining concrete mix. The first was a monofilament, 12 mm long x 18 µm diameter and the second was a fibrillated fibre also 12 mm long, but 60 µm diameter. Fibrillated fibres have been processed to give a branched structure with increased surface area compared to the parent monofilament fibre. 0.35 m thick concrete slabs with 4% water were exposed to the RWS fire curve. Test results showed that the samples containing monofilament were only superficially damaged whilst the fibrillated samples showed spalling to a depth of 35 mm.

Based on the above work three levels (1, 2, and 3 kg m^{-3}) of polypropylene monofilament were compared to a fibre free control in the standard tunnel mix. The fire curve applied in this test was the RABT ZTV curve, but with the 1200^{o}C plateau extended out to 120 minutes. Spalling depths decreased from an average of 95 mm (265 mm maximum) for the fibre free control to 7mm average (25 mm maximum) for the 3 kg m^{-3} mix.

To address option 2 the use of a hybrid blend of steel fibres (50 kg m^{-3}) and fibrillated polypropylene (0.9 kg m^{-3}) in a 50 MPa compressive strength concrete mix was evaluated using the RABT ZTV curve with the heating plateau extended to 120 minutes. A complex set of stresses is set up during heating when expansion is restricted. The face exposed to the heat source is in compression, but with tensile forces further into the body of the concrete.

The steel fibres can control these tensile stresses and reduce the spalling tendencies. An average spalling depth of 30 mm was obtained with a standard deviation of 20 mm.

Bilodeau et al (2004) investigated the resistance of high strength concrete, filled with expanded slate as part of the aggregate, to exposure to a hydrocarbon fire curve. Two w/c ratios, 0.33 and 0.42 were evaluated together with the addition of two types of polypropylene fibre at a range of dosages. The fibres were described as fibrillated with a length of 20 mm and as a multifilament, 12.5 mm long and significantly thinner than the fibrillated fibre. He concluded that there were more fibres per unit volume of the thinner fibre and that this contributed to the improved spalling resistance.

The thinner 12.5 mm long fibre was more efficient than the 20 mm fibre in preventing spalling. 1.5 kg m^{-3} of the thinner fibre was required compared to 3.5 kg m^{-3} of fibrillated fibres. This is in line with the work of Both.

2.9.2. Geopolymer

Davidovits' original impetus with geopolymer research was driven by the development of fire resistant systems after several tragic fires in Europe in the 1970s (Davidovits, 1989). Davidovits (2008d) used a 10 mm thick geopolymer panel which was exposed to a 1000^{o}C flame and measured the cold side temperature. After 30 minutes the values shown in table 2.16. were obtained.

Table 2.16 Temperature and heat evolution during fire test (Davidovits, 2008d).

Geopolymer type	30 min temp.	Si:Al	ΔH Kcal/mole water	ΔH Cal/mole GP
Na-poly(sialate)	180^{o}C	1	30	300-500
K-poly(sialate-siloxo)	270^{o}C	2	22	100-200
K-poly(sialate-disiloxo)	300^{o}C	3	20	50-100

The dehydroxylation heat (endothermic) of chemically bound water and hydroxyl groups varies with geopolymer type (and Si: Al ratio) and the higher ΔH values can explain the lower

cold side temperatures. More heat is required for the water release mechanism to occur therefore less is available to raise the sample temperature. In figure 2.26 a plateau exists between 4 and 12 minutes for the Na-poly (sialate) sample which is related to the higher enthalpy demand for this sample.

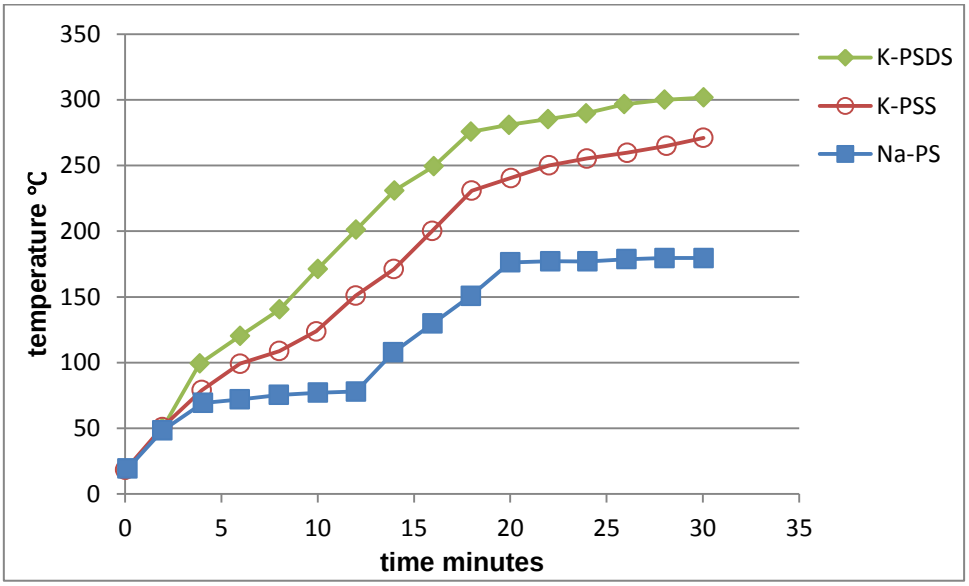

Figure 2.26 Fire test from Davidovits (2008d).

Lyon working in conjunction with Davidovits used geopolymers as binders for cross woven fabric laminates for aircraft applications (Lyon et al., 1997, Lyon, 1996, Lyon, 1999). Organic binders based on epoxy, vinyl ester, phenolic, advanced thermosets and high temperature engineering plastics were reinforced with either woven glass or carbon fibre fabrics and compared to carbon fibre reinforced geopolymer. The geopolymer outperformed every other system in fire testing in terms of weight loss, time to ignition, smoke, total heat release and flashover.

Fire resistant coatings based on geopolymers have been reported in the literature (Temuujin et al., 2011, Temuujin et al., 2010, Temuujin et al., 2012, Chen et al., 2011a). Giancaspro et al.(2006) applied a thin coating of geopolymer containing glass microspheres to balsa wood sandwich panels to act as a fire resistant barrier. A 1.8 mm thick coating satisfied the requirements of the Federal Aviation Administration (FAA) for both heat release and smoke generation.

Palomo and Fernández-Jiménez (2011) investigated the use of fly ash based geopolymers for coatings to improve the fire resistance of fibre reinforced panels. Cement powder was used as a calcium source to obtain ambient cure. Coatings were 3 to 5 mm thick and the addition of 10% filler increased fire resistance from 4 to 40 minutes. UNE-EN-ISO 11925-2 (International Organisation for Standardisation, 2010) was the relevant standard used to obtain the fire resistance.

Won et al. (2012) investigated OPC/alkali activated blast furnace slag blends filled with ground porcelain for fire resistant systems suitable for lining of tunnels. The temperature curve used was the German RABT ZTV (van Alken, 2012) curve which is suitable for the testing of linings for tunnels (figure 2.27).

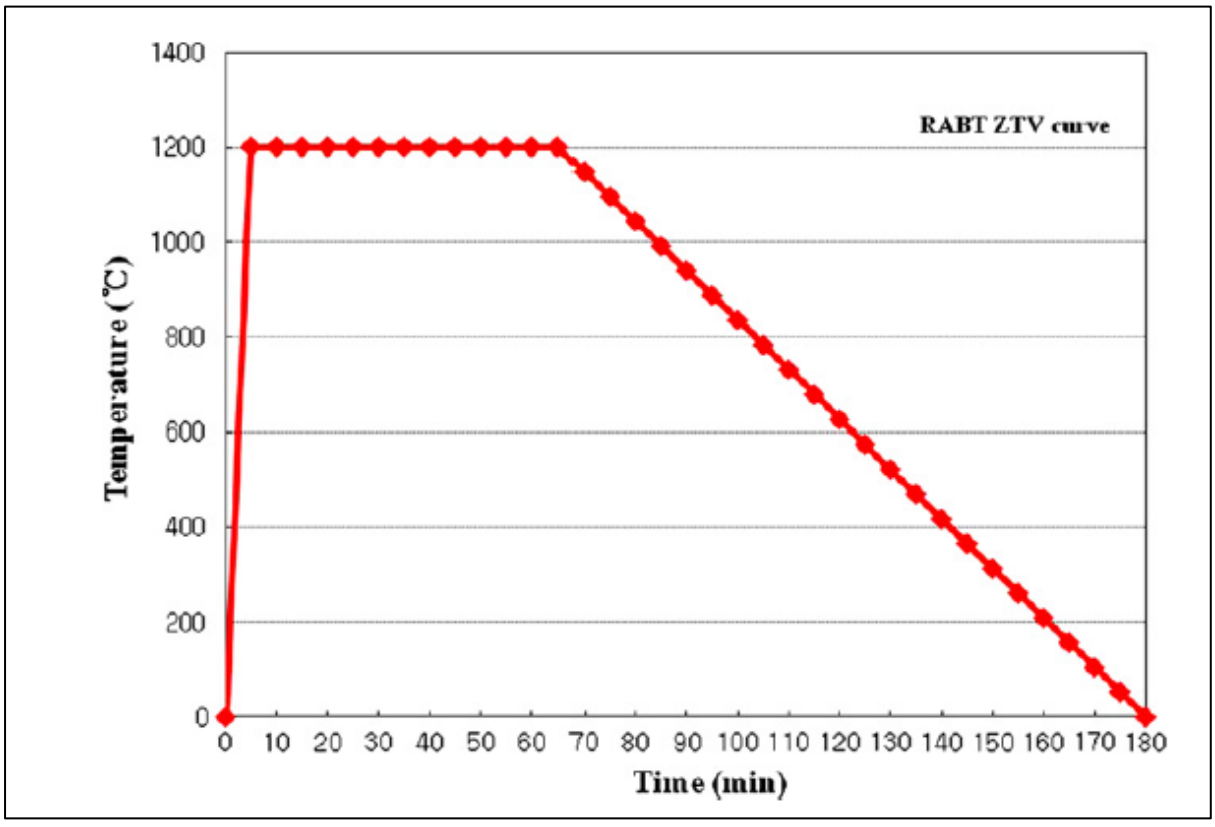

Figure 2.27 RABT ZTV Curve (Won et al., 2012).

Won measured residual compressive strength after fire testing. In the case of formulations with added porcelain (particle size = 4 to 6 µm) residual compressive strength increased as the amount of porcelain increased to a maximum of 30% porcelain content. The effect of the porcelain was attributed to the formation of a vitreous phase by reaction of porcelain with silicate and alkali metal ions and resultant densification. Spalling occurred in some

samples but this was alleviated by the addition of fibrillated polypropylene fibres (36 µm diameter and 6mm long).

Zhao and Sanjayan (2012) compared OPC and fly ash based geopolymers at the same strength levels (40 to 100 MPa compressive strength) with regards to spalling resistance. He elucidated three possible mechanisms for spalling resistance:

1. Moisture clog spalling caused by steam pressure build up in the pores of the concrete in fire situations. When heated the water will begin to vaporise and pore pressure will increase. The vapour will migrate along the temperature gradient and either escape or condense if it reaches a sufficiently cool area in the concrete. This process continues forming a fully saturated layer. This saturated layer inhibits further migration of pore water. If vaporised water cannot escape quickly enough the internal pore pressure will continue to rise until it exceeds the tensile strength of the concrete and spalling occurs;
2. Spalling results from restrained thermal dilation close to the heated surface which, leads to compressive stresses parallel to the heated surface leading to brittle fracture of the concrete;
3. Thermal expansion incompatibility between concrete paste and aggregates, particularly siliceous types, can cause spalling.

Zhao and Sanjayan (2012) states that the probable cause of spalling is a combination of the presence of water and rapid heating rates. He also developed a test method to investigate spalling which applied a fire curve similar to a hydrocarbon fire to concrete cylinders. No spalling occurred in any of the geopolymer samples, but the high strength OPC samples containing silica fume showed severe spalling. Normal strength OPC showed minor spalling. Sorptivity, the ability to absorb and transmit water through the matrix by capillary suction was determined using ASTM C 1585. Sorptivity is a measure of the openness of the concrete pore structure. Lower sorptivity results indicated poorer spalling resistance.

Cheng (Cheng and Chiu, 2003, Cheng, 2003) investigated the production of fire resistant materials from blast furnace slag and waste serpentine mineral. Varying levels of potassium hydroxide and sodium silicate additions to slag/metakaolin blends were evaluated. Fire testing was carried out on 10 mm thick panels which were exposed to an 1100^{o}C flame and

the cold side temperature tracked against time. Increasing potassium hydroxide concentration reduced the cold side temperature of the sample (figure 2.28).

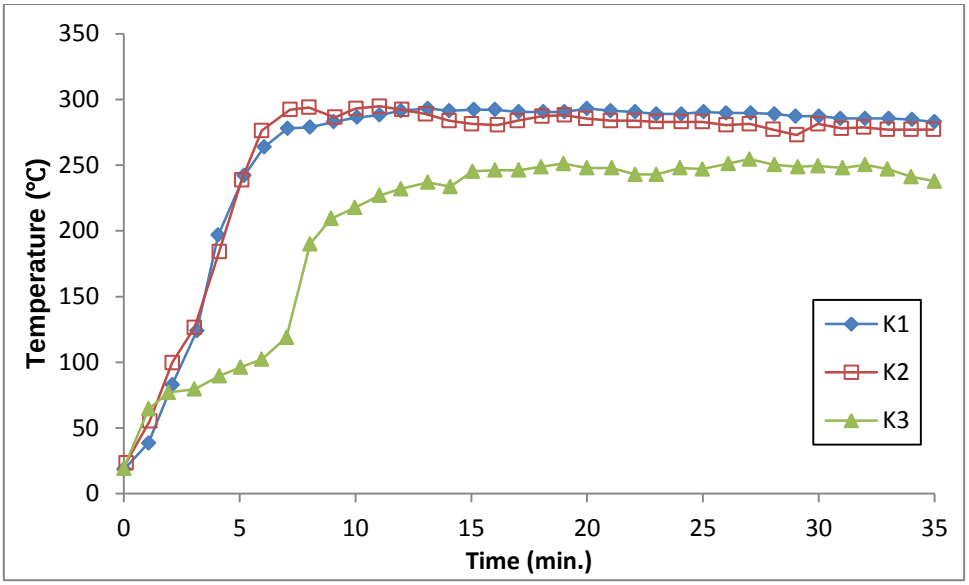

Figure 2.28 Effect of KOH concentration on cold side temperature (Cheng and Chiu, 2003).

K1 = 5 M; K2 = 10 M; K3 = 15 M

Increasing metakaolin levels had a similar but smaller effect on cold side temperature, whilst increasing sodium silicate addition showed little effect.

Cheng (2003) blended waste serpentine with metakaolin which was then activated with potassium hydroxide and sodium silicate. 10 mm thick panels were tested as above and compared to commercially available calcium silicate board. Both samples reached around 400^{o}C, but the geopolymer ramped up slower with a 4 to 6 minute plateau at 100^{o}C.

The most important application for fire resistant concrete is tunnel linings. These can be in the form of precast segments, sprayed shotcrete and other coatings. Kim et al. (2010) reviewed the current scenario with tunnel linings and introduced a proposed coating for new and remedial concrete works. When tunnels are exposed to fire they can undergo severe damage and partial collapse. The high relative humidity in tunnels (75% +) can lead to explosive spalling due to water in the porous tunnel lining material. Tunnel linings are tested using the more stringent hydrocarbon fire curve. Loss of strength of tunnel linings can bring about long term loss of accessibility to the tunnel infrastructure with large economic losses.

Kim et al. (2010) lists four types of tunnel fire protection:

1. Start with a fire resistant shotcrete material as the main lining;
2. Use a coating material that is able to prolong heat transfer;
3. Spray a secondary lining onto the tunnel surface;
4. Install precast segments or panels.

A major focus has been on developing coatings using light weight or porous aggregates. However, properties of these systems tend to be low with compressive strengths typically less than 10 MPa. Pressures on tunnel linings due to typical road and rail traffic are in the range of 25 to 600 Pa. High speed train services produce higher pressures and induce vibrations in the lining. These high pressures and vibrations can cause negative pressures on the tunnel lining and result in spalling and fatigue failure. The use of fibres has improved the spalling resistance but can lead to lower strength linings.

The lining developed by Kim is based on OPC with bottom fly ash as the filler and 0.25 vol. % polypropylene fibre. This material is a pre-mix type suitable for casting and shotcreting. The properties obtained are more than double those of currently used linings. Fire testing was carried out using the RABT curve designed to replicate tunnel fire conditions typical of hydrocarbon fires. 20, 30, and 40 mm thick coatings of the new system were applied over a sample slab of typical tunnel structure containing steel reinforcement and allowed to cure unsealed for 28 days at ambient. Whilst the 20 mm thick coating showed spalling, the other two thicknesses did not.

Tarada and King (2009) concluded that polypropylene fibres could contain explosive spalling during cellulosic and hydrocarbon fires but were inadequate for the RWS fire curve. In the latter case the polypropylene could be augmented by panels and/or coatings. In the aftermath of a fire concrete assessment should be carried out in areas where the fibres have melted. This assessment should include as a minimum, concrete strength reduction and load bearing capability, permeability of the remaining concrete and influence on ongoing durability and risk of further spalling.

The panel and/or coating scenario must be designed so that their interface with the structural concrete does not exceed 350^{o}C in the event of a fire which will prevent spalling and significant changes in the structural concrete mechanical properties. Spray-on coatings

have a one off use in a fire event and require replacement after such events. Typical panel thicknesses are 20 to 30 mm and coating applications are up to 50 mm.

Geopolymer based cellular materials (Rickard et al., 2013) have been evaluated for fire resistance. These metakaolin based geopolymers used aluminium metal to generate hydrogen gas as the blowing agent during processing. Fire ratings in excess of 60 minutes were obtained for 50 mm thick panels using the AS 1530.4 fire curve. Polypropylene fibres were used to control the extent of foam growth during the expansion process.

CSENG Ventures (Reid, 2011) have a patent for fire resistant door and window frames where a hollow plastic, typically uPVC, section is filled with metakaolin based geopolymer foam. The geopolymer foam has sufficient structural stability in the event of a fire to seal off the fire compartment and prevent the ingress of air. Traditional wood and plastic frames burn and/or melt allowing air ingress to the fire.

2.9.3 Fire Testing

The development of standard fire testing regimes needs to account for the wide range of conditions which may occur. In addition to the actual exposure temperatures occurring the rate of temperature increase needs accommodating in the test plan. Opinion of what should constitute a “standard fire” has led to considerable discussion. Van Riessen et al. (2009) showed a temperature versus time curve for a typical room fire (figure 2.29) which consisted of three stages:

1. The growth or pre-flashover stage where the average temperature is low and the fire is localised in the vicinity of its origin;
2. The fully developed or post-flashover fire. All the combustible materials in the room are involved and flames appear to fill the entire room volume;
3. Decay or cooling period.

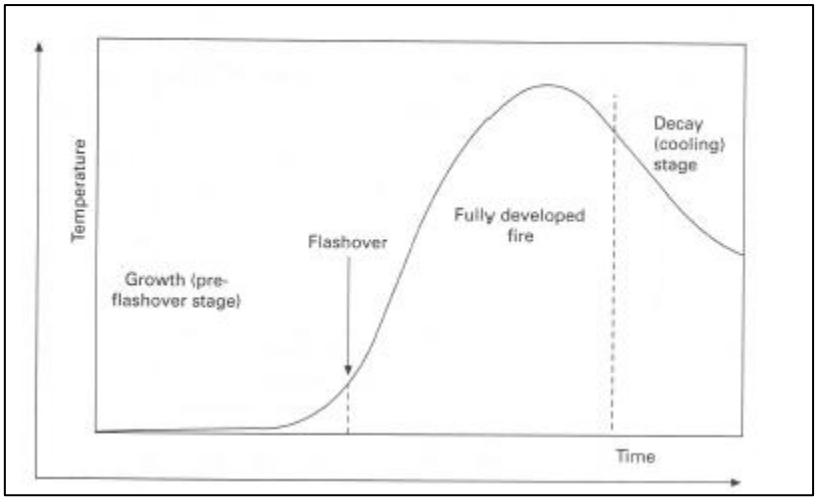

Figure 2.29 Typical room fire curve (Institution of Engineers Australia, 1989).

Flashover is a phenomenon unique to compartment fires, where products of incomplete combustion collect at the ceiling and then ignite leading to total involvement of the compartment materials and signalling the end of human survivability. The time to flashover is the available escape time. The Federal Aviation Administration (FAA) has used time to flashover of materials in aircraft cabin tests as the basis for acceptance criteria for commercial aircraft cabin materials (Lyon et al., 1997).

In the case of geopolymers no incomplete combustion products are formed during a fire so flashover times are theoretically infinite. Organic polymers used as binders for fibre reinforcement in composites generate smoke (incomplete combustion products), which lead to flash over times of 10 to 25 minutes. Fibre content of conventional composites is in the range 20 to 50 wt.%, whilst advanced composites can have fibre contents as high as 70 wt.% (Budinski and Budinski, 2005).

Lawson (2009) reviewed the history of fire testing. The statement of the first law of thermodynamics in the nineteenth century led to the development of tools for calorimetry. In the early twentieth century the global recognition that scientific based fire standards were needed to protect lives and assets was realised. In the latter part of the twentieth century the development of data recording and analysis has led to more detailed studies of fire behaviour.

Ongoing developments based on the above have led to improvements in the testing of structural components, assemblies and systems under realistic fire and loading conditions.

This should lead to enhanced structural performance to ensure building fires do not lead to partial or complete collapse scenarios. In addition improvements in ignition resistance, surface flammability, fire growth and smoke and toxic gas evolution of materials has led to the use of safer materials of construction.

The use of standard fire curves (temperature verses time) to measure the fire resistance of and compare a range of materials is mandatory before materials may be used in construction. The scale of the testing (laboratory to full scale) also needs to be considered when evaluating the results of fire tests. The fire curves shown in figure 2.30 are for cellulosic fuel supply (AS1530.4/ISO 834 and ASTM E119) and hydrocarbon fuel source (Eurocode 1991-1-2). The cellulosic curve is derived from the fire curve in figure 2.29 and is used to replicate residential and commercial building fire scenarios. The hydrocarbon curve shows a greater rate of temperature increase and is used to replicate fires occurring in tunnels, chemical plant and oil and gas production and refining.

The Cement, Concrete and Aggregates Association of Australia issued report TC 61 (2010).

It listed three relevant concrete failure criteria:

1. Structural adequacy (ability to resist load);
2. Integrity (ability to resist the passage of flames);
3. Insulation (the ability to prevent fire spread due to unacceptable temperature rise of the unheated face).

In the same reference the importance of real fires (as opposed to standard fire curves) is emphasised. The rate of temperature rise is dictated by the rate at which fuel is pyrolised i.e. converted from solid to combustible gases, and then burnt when these gases come into contact with air. Once burning occurs there is an increase in pyrolisation due to heating. Given more air additional heat is generated. A test conducted in a compartment with a toughened glass façade found that glass breakage occurred after 18 minutes and gave rise to temperatures in the order of 1000^{o}C. The final increase of air temperature from 300 to 1000^{o}C took 5 minutes. AS 1530.4 requires a temperature of 841^{o}C after 30 minutes and to reach 1006^{o}C after 90 minutes. Real fires can achieve conditions outside of those specified and these extreme events need to be factored into fire safety calculations.

Several fire curves have been developed for specific applications. The RWS curve was developed by Rijkswaterstaat, Ministry of Transport in the Netherlands. This curve is based on a worst case scenario that a 50 m^3 fuel, oil or petrol tanker fire with a fire load of 300 MW could occur, lasting up to 120 minutes. The RWS curve was based on results of testing carried out by TNO in 1979. This is the basis for the Hydrocarbon curve (HC).

The RABT curve was developed in Germany in 1994 as a result of a series of test programmes. In the RABT curve the temperature rise is very rapid up to 1200^oC within five minutes. The duration of the 1200^oC exposure is shorter than other curves with the temperature drop off beginning at 30 minutes for car fires and 60 minutes for train fires. The 110 minutes cooling period is the same for both cases.

The HCM (hydrocarbon modified) curve is a French regulation with a maximum exposure temperature of 1300^oC compared to the 1100^oC of the standard HC curve.

The initial temperature gradient of all these curves is severe possibly causing thermal shock to the exposed concrete with resultant spalling.

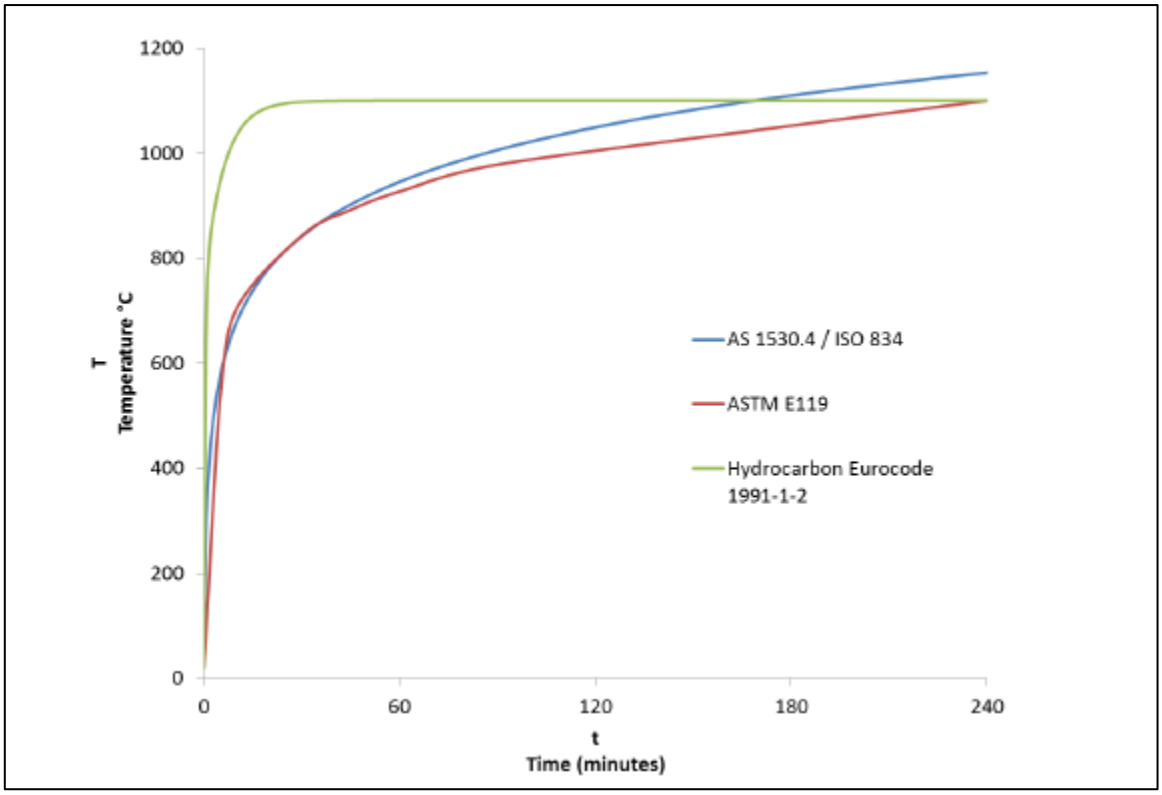

Figure 2.30 Temperature verses time curves for standard fires (van Riessen et al., 2009).

Provis (2010) carried out fire testing on geopolymers based on blast furnace slag and fly ash using the ASTM E119 fire curve. The test was run for 4 hours using 150 mm thick samples and the maximum cold side temperature recorded was 105.3^{o}C. An apparent flattening of the rate of temperature increase in the temperature-time curve occurred between 100 and 160^{o}C. This was associated with the passage of the boiling front through the slab. The author attempted to estimate the pore pressures from the boiling point of water, figure 2.31. The boiling point of water increases with pressure. Steam tables show the relevant pressures for individual temperatures. The plateau temperature value of the temperature-time curve corresponds to the boiling of water. By measuring the plateau temperature at different depths through the concrete specimen we can estimate the pressure at each depth .This is indicative of the passage of the boiling front. The curve flattening close to the hot face is not always distinct due to the fast passage of the boiling front at these positions.

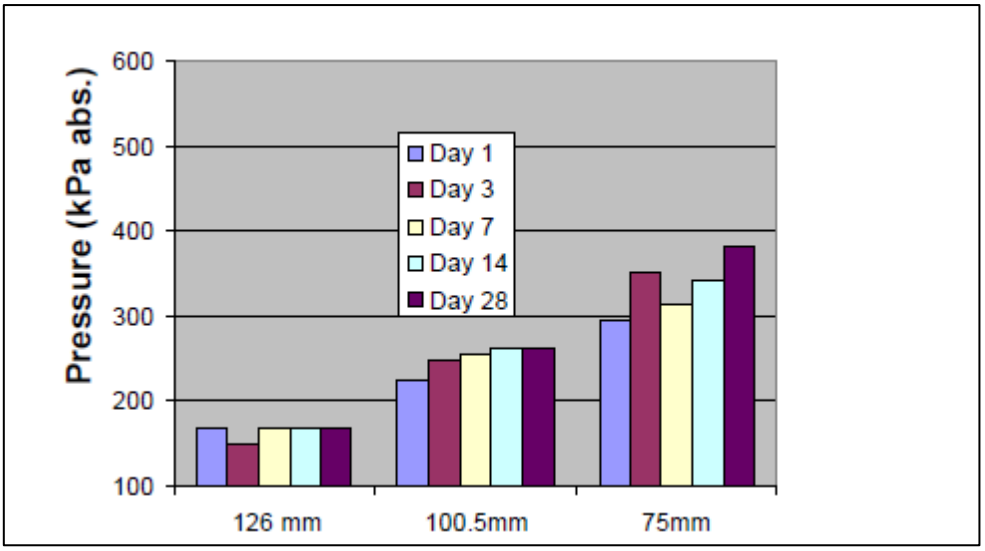

Figure2.31 Pore pressures estimated from the boiling points of water at different depths from hot face in concrete slab (Provis, 2010).

The columns in figure 2.31 are indicative of sealed curing times at ambient temperature. The samples were then unwrapped and left to age at ambient temperature for 56 days when fire testing occurred. The shorter the sealed curing time the lower amounts of water at the start of fire test. No spalling was observed in any of these tests.

Alarcon-Ruiz et al. (2005) used thermal analysis to follow the irreversible decomposition reactions taking place as cured cement paste was fired in 100^{o}C steps up to 800^{o}C. The thermal composition of the cement paste was studied by thermogravimetric analysis (TGA) and the derivative thermogravimetric (DTG) curves. Such techniques should be able to determine fire conditions and the resultant deterioration of the cement paste. These techniques can be used to assess the state of concrete after fire exposure. The TGA work showed that the dehydration and decarbonation reactions are irreversible in the cement paste and can be used as tracers in determining temperature history after fire exposure. The dehydroxylation reaction of portlandite is reversible with the reaction occurring rapidly after heat treatment

2.10 Conclusion

The current extent of geopolymer commercialisation in dollar terms is extremely difficult to estimate. This can be attributed to the confidential technical and commercial aspects governing the competitive world of business. Many companies claim to have commercially available products based on geopolymers, but no output volumes are available. Certainly the green environmental aspects of geopolymers compared to OPC based products are widely used to promote geopolymer based products (Concrete Institute of Queensland, 2010, Achille, 2010, Banh UK Ltd, 2010)

The short term future for geopolymer based products is factory manufactured precast components, where heat curing and an acceptable level of technical control are readily available. This will enable speciality products such as sewage and chemical contacting components and thermally resistant parts such as tunnel linings to gain a market presence based on technical superiority. The move to ambient curing of geopolymer systems generally involves the introduction of calcium based products which can adversely impact on the excellent durability profile of geopolymers.

The large variations in fly ash composition and its influence on the geopolymerisation process and end product properties is still a major hurdle for larger scale acceptance of geopolymer based products. The current national standards for fly ash do not consider its application as a geopolymer feedstock. Specific test methods to classify fly ashes for the geopolymerisation process should be a priority for the relevant fly ash producers and marketing bodies. This will ensure that the majority of fly ash can be safely utilised in commercial products instead of creating environmental hazards.

CHAPTER 3

EXPERIMENTAL METHODS

3.1. Introduction

Raw materials were selected that were readily and commercially available to ensure that any follow up work or larger scale pilot plant tests could be accomplished. All the test procedures with the exception of four, XRF, particle size distribution (PSD) surface area (BET), and mercury intrusion porosimetry (MIP) were available within the Department of Imaging and Applied Physics. Three tests were outsourced to commercial organisations, Bureau Veritas (XRF) and CSIRO, Waterford (PSD and BET), while MIP was carried out at the University of Bologna, Italy.

3.2 Raw Materials

3.2.1. Aluminosilicate sources

Fly ash from Collie power station in Western Australia was used in this work. The chemical composition of fly ash varies between power stations and over time at the same power station due to variations in coal feed stock composition, furnace operating conditions and cooling conditions (Blissett and Rowson, 2012). The fly ash used in this work was sourced from one bulk bag containing approximately 800 kg. Analysis of chemical composition by XRF, crystalline phase identification by QXRD and determination of amorphous (glassy) content by manipulation of the two preceding tests was carried out. Determination of particle size distribution (PSD) together with specific surface area was also undertaken.

3.2.2 Alkaline Activating Materials

Two alkaline activating materials were used, sodium hydroxide and sodium silicate. Where solutions were produced in the laboratory deionised water was used.

Sodium hydroxide (NaOH) pellets were sourced from Rowe Scientific, Australia, with a minimum assay of 97%. Preparation of sodium hydroxide solutions was carried out in screw cap polyolefin containers to minimise evaporative losses due to the dissolution exothermic heat. Pressure build up was controlled by carefully loosening the screw cap at regular intervals during the heat evolution cycle. Gentle agitation was applied to ensure complete dissolution of the NaOH pellets. Solutions were prepared at least 24 hours prior to use.

Sodium silicate was sourced from PQ Corporation. The grade used was PQ-D A53 which had a supply specification of 29.4 wt.% SiO_2, 14.7 wt.% Na_2O, and 55.9 wt.% water (PQ Corporation, 2013). This is equivalent to a silicate solution modulus of two.

3.2.3 Fillers and fibres

Four thermally stable fillers were chosen for evaluation; wollastonite (calcium silicate), α-alumina, mullite and chamotte.

Wollastonite, Nyad MG (NYCO Minerals, 2013), was sourced from Nyco, USA. Wollastonite is a naturally occurring mineral which is mined in an open pit and then processed using crushing, milling and screening techniques to produce a range of sizes for commercial applications

α-alumina was sourced from Doral Minerals of Western Australia (Doral, 2011). Fused alumina is produced by heating high purity alumina to 2100^{o}C in an electric arc furnace. After cooling the product is crushed and milled to produce a range of graded sizes. Grade 325F, a ball milled grade was selected for this initial work. It is >99 wt.% alumina with a specific gravity of 4.0 and a particle size of less than 10% retained on a 45 μm screen. Coarser grades are also available and these were evaluated for the production of mortars and concretes.

Mullite was sourced from Washington Mills (USA) (2008) and is a high purity grade produced by the electric furnace fusion of Bayer process alumina and high purity silica. There is a slight excess of alumina, above the normal mullite ratio ($3Al_2O_3 : 2SiO_2$) to ensure that all of the silica is entrained within the mullite and is not present as a glassy phase. Magnetic iron is substantially removed by an intensive magnetic separation. The grade supplied is Duramul 325/F indicating a particle size of minus 45 μm.

Chamotte, sometimes referred to as grog, is produced by firing clay in the temperature range 1200 to 1450^{o}C (Abu-Hamatteh and Al-Taie, 2003, Yatsenko and Rat'kova, 2003). The chamotte reduces drying and firing shrinkage when used to manufacture refractory bricks. The post fired clay (chamotte) is ground and screened to give a range of particle size fractions. These sizes are typically described as coarse (2.5 to 6 mm), medium (1 to 2.5 mm)

and fine (0 to 1 mm). The chamotte used in this evaluation was sourced from Sila Australia, a Western Australian company, producing refractory materials.

The fibres utilised in this research are detailed in Table 3.1.

Polypropylene fibres used to prevent spalling of concrete in fire situations were sourced from Adfil in the UK via the Australian distributor (Reoco Performance Fibres, 2011).

The following fibres which exhibit greater degrees of thermal stability were also sourced: alkali resistant glass fibre, and chopped basalt fibre.

The alkali resistant glass from Nycon(2011a) of the USA contains 16 wt.% zirconia to give improved alkali resistance. This material meets the requirements of ASTM C1666 (ASTM Committee C27-40, 2008).

Chopped basalt was sourced from Technobasalt, Ukraine (2012). The grade was RBR- 16 – T5/5 1%. The fibre diameter is 16 µm and the length is 5 mm. A size (T5) is applied to the surface of the fibres to enhance adhesion to matrix materials fibres. The moisture content is specified to be 1 wt. % maximum.

Table 3.1 Specifications of Fibres utilised in this project.

	Adfil Ignis	**RBR-16-T5/5 1%**	**NYCON AR-HD**
Composition	Polypropylene	Basalt	Alkali resistant glass
Specific Gravity	0.91	2.68	2.7
Fibre diameter	18 µm	16 µm	10 µm
Fibre length	6 mm	5 mm	13 mm
Tensile Strength	600 MPa	2.9 GPa	1.7 GPa
Tensile Modulus	N/A	110 GPa	N/A
Melting point	165^{o}C	~1350^{o}C	1121^{o}C

N/A “–“indicates no supplier data was available.

3.2.4. Superplasticisers

Workability of cementitous systems can be improved by admixtures such as super plasticisers. Two such materials were evaluated in the geopolymer systems investigated in this thesis. The two materials, Sikament NN (ex Sika) and Tamol NH 3703 (ex BASF), are based on the sodium salts of sulphonated naphthalene formaldehyde polymers. Table 3.2 shows the specified values.

Table 3.2 Superplasticiser specifications.

	Tamol NH3703	**Sikament NN**
Colour	Dark brown solution	Brown solution
Specific Gravity	1.2	1.2
pH	8.0-9.0	6.5-7.5
Solids content,%	40.5-42.0	40.0

3.3 Experimental Methods

3.3.1. Characterisation of Aluminosilicate sources

To assess the reactivity of aluminosilicate sources the amorphous glassy component, which is soluble in strong alkaline activating solutions, must be determined. The first step is to determine the individual element composition using X-ray fluorescence spectroscopy (XRF)(Sampling Technologies, 2012). The XRF results in this work were determined by Bureau Veritas, Canning Vale, Western Australia. The powdered samples are ground to a particle size of less than 75 μm and fused in a silicate glass disc with a 12:22 flux of lithium tetraborate and lithium metaborate (Ultratrace method XRF 202). Analysis was performed on a PANalytical Magix Fast x-ray spectrometer with a 4 kW rhodium tube using Super Q software. Loss on ignition (LOI) is determined by drying a sample in air at 105^{o}C and subsequently measuring the mass loss after heating to 1000^{o}C for 2 hours. The results of the testing are reported as a percentage of the relevant oxide. This is the total elemental content and does not differentiate between crystalline and amorphous phases of the fly ash

samples. The report also included details of a number of standards measured during the analysis. Uncertainties were determined by calculating the mean percentage variation from the standards for each oxide.

The next step is to determine the crystalline and amorphous phase contents and composition. This is accomplished using Quantitative X-Ray Diffraction (QXRD). A nominal dry weight of 3 g of fly ash was mixed with 0.3333 g of Fluorite (calcium fluoride, 325 mesh with purity of 99.5%+ ex Sigma Aldrich) as an internal standard. The use of an internal standard allows the concentration of the crystalline phases to be determined on an absolute basis allowing the amorphous fraction to be also determined. This blended powder together with 7 ml of AR grade ethanol was now added to a McCrone micronizer mill utilising sintered alumina grinding media and run for 5 minutes to obtain a particle size around 5 μm. The milled sample was now poured into a polypropylene tray and dried at 70^{o}C for 24 hours. The dried powder was collected in a polypropylene vial for storage prior to analysis. The milling was to ensure adequate particle statistics were present in the x-ray beam during data collection. The micronizing also generated a uniform dispersion of the components, enabling accurate quantitative analysis of the crystalline phase to be carried out. The sample packing is important to ensure a random orientation (as opposed to a preferred (more regular) orientation) is obtained. QXRD analysis depends on measurements of peak intensity ratios which are greatly distorted by the preferred orientation. The dried micronised mixture was hand packed into a Perspex sample holder and consolidated by tapping on the bench top. The filled specimen holder was then loaded into the automatic feeder of a Bruker D8 Advance diffractometer. This instrument was operated at 40 kV and 40 mA using Cu Kα radiation. The data for the patterns was collected with a Lynx Eye detector using a nominal 2θ step size of 0.01^{o}, a count time of 0.5 seconds and a 2θ range of 10 to 120^{o}. A knife edge collimator and tight detector discriminator settings were applied to reduce air scatter and iron fluorescence signals, respectively.

Crystalline phases were identified using DIFFRAC.EVA version 3.1 (Bruker-AXS, Germany), a search-match programme. The individual diffraction pattern files were loaded into EVA 11.0 and the background stripped. The search-match of phases present was then conducted using the Powder Diffraction File (PDF4+ 2012 edition). Rietveld modelling with the XRD

data was carried out using Bruker AXS TOPAS (Total Pattern Analysis Solution) version 4.2. TOPAS is based on a general non-linear least squares fitting system written specifically to integrate various types of powder diffraction and single crystal analyses. Most materials cannot easily be grown as single crystals for XRD evaluation, hence the use of powder diffraction techniques based on small crystallites. The results obtained in powder XRD compared to single crystal techniques differ in that the diffraction peaks grossly overlap in the former preventing proper determination of the material structure. The Rietveld method creates a virtual separation of the overlapping peaks allowing a more accurate determination of structure.

The elemental composition of the amorphous phase is determined by subtracting the contribution of the crystalline phases from the XRF data.

Particle size distribution of the fly ashes was determined at CSIRO, Waterford using a Malvern Laser diffraction instrument (Malvern Instruments Ltd, 2005). Sodium hexametaphosphate was added as a dispersant to water, the fly ash (0.0078 vol. %) added and the mixture sonicated for 20 minutes in an ultrasonic bath to prepare the fly ash for testing.

The volume weighted mean, D [4,3] determined by static light scattering measures the contribution of each particle relative to the volume of that particle. The volume weighted mean reflects the bulk of the particles which make up the sample and is most sensitive to the presence of large particles. This relative contribution is proportional to $(size)^3$.

The surface weighted mean, D [3,2] is most important where specific surface area is important e.g. reactivity or dissolution and is most sensitive to the presence of fine particles in the particle size distribution (Malvern Instruments, 2012).

d (0.5) is the median particle size by volume and is the maximum particle diameter below which 50% of the particles exist. Similarly d (0.1) and d (0.9) are the maximum particle diameters below which 10% and 90% respectively exist. 44.5 vol. % of particles are below 10 μm.

Density measurements of dry powders were determined using a Quantachrome (USA) Upyc 1200e V5.03 pycnometer (2013) in the School of Mines, Curtin. This equipment has a software package which calculates the standard deviation of five individual runs to four decimal places. The pycnometer measures the true volume of a known weight of a solid sample utilising Archimedes' principle of fluid displacement and Boyle's law (gas expansion).

A gas typically helium is used as the displacing fluid since it can penetrate the fine pores assuring maximum accuracy. Helium's small atomic size and ideal gas behaviour gives the optimum results. Nitrogen may also be used, as in these determinations, with no measurable differences.

3.3.2. Synthesis of geopolymers

Mixing of the geopolymer formulations was carried out using two different mixers that are described below.

The Thinky ARE-250 mixer (Thinky Corporation, Japan) is a centrifugal mixer suitable for small batches up to 200 g. All the ingredients, liquids first, are loaded into the mixing vessel which is sealed and then placed in the mixer. Five minutes at 1300 rpm was selected followed by a degassing cycle at 800 rpm. The Thinky mixer generates mechanical heat in addition to the exothermic chemical heat and this can lead to concerns over the flowability results. Flow maybe curtailed due to fast setting of the system or extended due to viscosity/thixotropy decreases from the temperature rise.

For larger batches, up to 2 kg, a Hobart 0.12kW planetary mixer model N50 (2011) was used. Table 3.3 shows the range of speeds available. There is a central boss (the agitator) which rotates anti-clockwise. An attachment, in this case a flat beater, is located on the boss and rotates clockwise.

Table 3.3 Hobart mixer speed settings.

Speed	Agitator (rpm)	Attachment (rpm)
Low	136	60
Intermediate	281	124
High	580	255

The aluminosilicate source (fly ash or metakaolin) was added to the mixing bowl first followed by the activating solution(s). The mixer was run at low speed for one minute to wet out the powders. During this period the sides of the mixing bowl were scraped with a plastic spatula to push residual powders into the mixing space. After this initial period the speed was increased to high speed for a further four minutes. Any filler or fibre additions were now made and the mixer was run at low speed for an additional one minute. The speed was now increased to high speed for a period of four minutes giving a total cycle time of ten minutes.

Mini-cone Flow Testing

Material was now withdrawn from the mix for flow testing (using a mini cone) and determination of Vicat setting time if required.

The mini cone was developed by Kantro (1980) to evaluate the effect of water reducing admixtures on the rheological properties of OPC paste. The mini-cone shown in figure 3.1 has a top diameter of 19 mm, a bottom diameter of 38 mm and a height of 57 mm. These dimensions are in the same proportions as the slump cone in ASTM C143-12 (ASTM Committee C09.60, 2012).

The machined steel cone was lightly coated with machine oil and placed large diameter down on a steel plate. Mixed geopolymer was now poured into the cone and any entrained air removed by a spatula moved in lateral and vertical directions. Excess geopolymer was removed from the top of the cone with a flat blade. The cone was now moved upwards at a steady rate and the geopolymer mix allowed to flow out of the cone thus forming a disc of

the slurry (figure 3.2.) on a steel plate. After 60 seconds the diameter of this disc was measured in two places at right angles to each other using a divider.

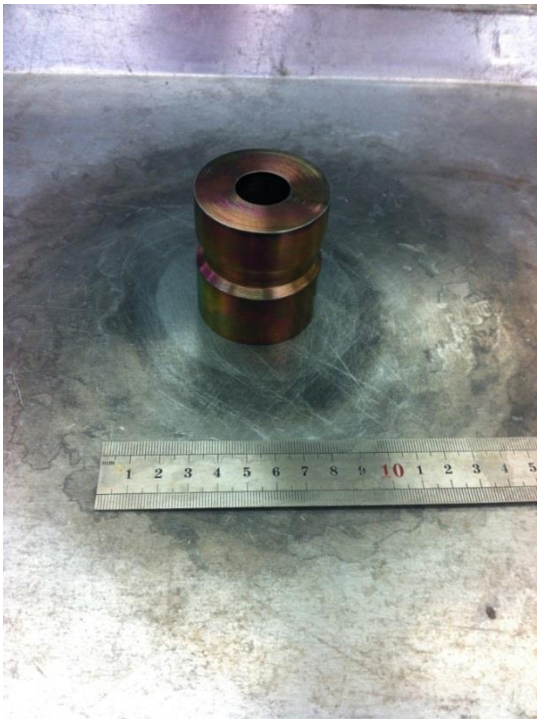

Figure 3.1 Mini cone for flow testing

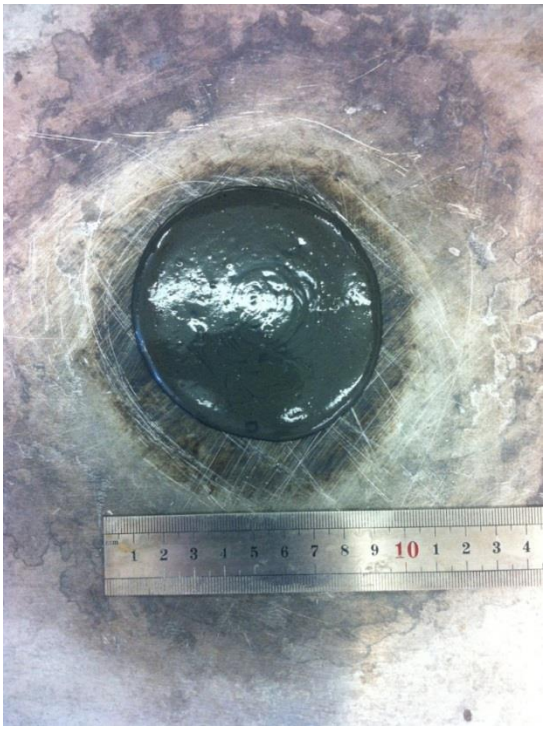

Figure 3.2 Example of a geopolymer paste flow disc.

Vicat setting time determination was loosely based on ASTM C191 (ASTM Committee C01, 2008). The mixed geopolymer was allowed to commence setting at ambient temperature or at 70^{o}C in the oven. Periodic penetration tests were performed on this paste by allowing a 10 mm diameter rod to settle into this paste. Vicat initial time of setting was the time elapsed between the initial contact of the aluminosilicate source and alkaline activating solution and the time when the penetration was measured or calculated to be 25 mm. The Vicat final time of setting was the time elapsed between initial contact of the aluminosilicate source and alkaline activating solution and the time when the rod does not leave a complete circular impression in the paste surface.

Moulds of various materials of construction and geometry were used to manufacture test specimens. Mould materials were typically polypropylene, uPVC, UHMWPE, Perspex and concrete formwork board. The latter material is a laminated bonded board with a radiate core and hardwood veneer faces with a high density resin overlay. Carnuba wax was initially used as the release agent, which also had the advantage of protecting the board moulds from alkali attack. A water based release agent recommended for use with geopolymers, URA 295, (ex UGP, Australia) was now applied to the mould internal surface and allowed to stand at ambient temperature until dry. To ensure the moulds do not leak a smoothed bead of silicone sealant was applied over the outer joints of the moulds.

The liquid geopolymer mix was run down the side of the tilted mould to minimise air entrapment. The mould was filled in three stages with vibration applied by a pneumatic vibrating table between additions. Any visible air bubbles were removed at this point using a wood skewer.

Filled moulds were now sealed with screw caps in the case of polypropylene vials or with 1 mm polyethylene builder's film held in place my screwing down the lid or with self-adhesive duct tape.

3.3.3. Curing of geopolymers

Filled, sealed moulds were placed in an hot air oven set to the required temperature, but typically 70^{o}C, for the prescribed time, but typically 24 hours. After removal from the oven the sealed moulds were left at ambient temperature for a further two days before demoulding took place. Used moulds were cleaned and had release agent applied prior to reassembly for further use.

The de-moulded specimens were placed in plastic bags which were sealed and stored in a room at ambient temperature and a relative humidity of approximately 50% prior to required sample preparation. Relative humidity inside the storage bag would be much higher due to release of water from the geopolymer.

3.3.4 Cured sample preparation

For compression strength testing this involved cutting and sanding cylinders to give parallel faces. Cutting was undertaken on a Struers Minitom diamond blade variable speed cut off saw using water coolant. Larger samples were cut on a diamond blade brick saw (figure 3.3). Sanding was by hand using 80 grit then 220 grit silicon carbide abrasive papers. Samples for flexural testing (20 x 20 x 90 mm) were cut from 20 mm thick cured slabs using a tile saw fitted with a diamond blade.

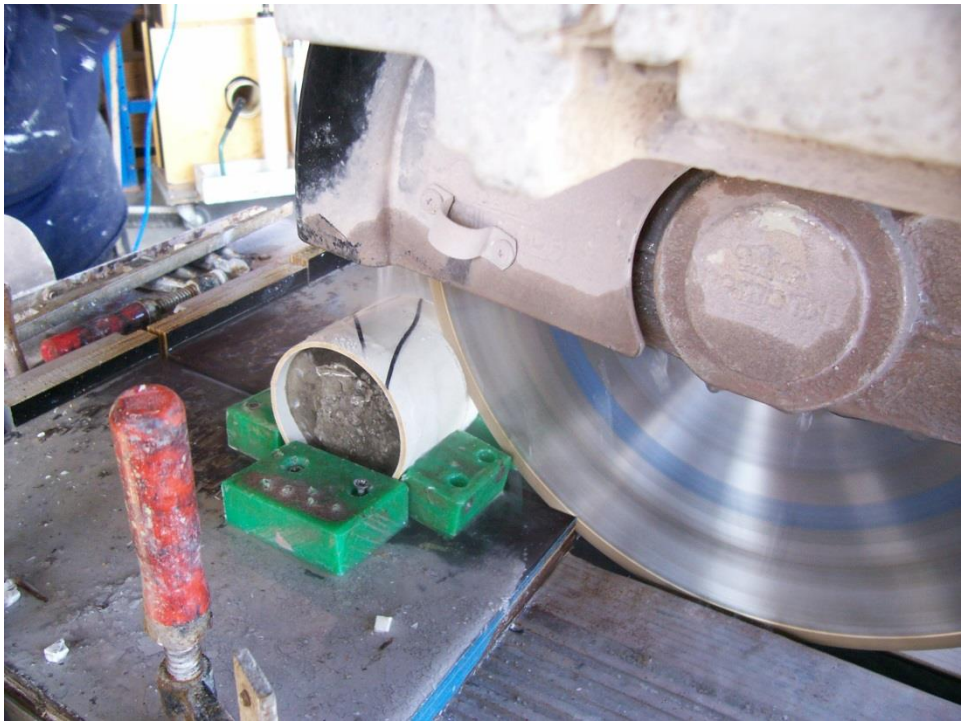

Figure 3.3 Diamond blade brick saw cutting thermal conductivity specimens.

3.3.5 Sample conditioning

Post treatment of samples prior to testing was undertaken when required by a stepwise thermal cycle up to 250^{o}C (figure 3.4). This was to facilitate controlled removal of water from the geopolymer prior to firing at still higher elevated temperatures. This post treatment cycle was developed using events identified from dilatometer curves and the increase in the vapour pressure of water as temperature increases. Above 65^{o}C the vapour pressure of water increases exponentially as shown in figure 3.5. This is due to a decrease in hydrogen bonding and increased molecular mobility. Therefore any initial heating to remove water should be undertaken at this temperature to reduce the possibility of crack formation. Figure 3.6 shows that above 100^{o}C the rate of steam pressure increase is very rapid. The pressure of steam can exceed the tensile strength of cementitious materials, typically less than 5 MPa (Hardjito and Rangan, 2005).

The rate of temperature increase also needs calculating to avoid large temperature gradients which can induce thermal cracking particularly in thicker test specimens. The size

(thickness), thermal conductivity and coefficient of thermal expansion (COTE) together with their variation with temperature all need taking into account when calculating post treatment cycles for components.

Some post treatment schedules are shown in figure 3.4. The evolution of these schedules was based on the thickness of the specimens, water vapour and steam pressures development with temperature and shrinkage values obtained from dilatometer testing at elevated temperatures. When the temperature reaches values above 65^{o}C a slower rate of temperature increase is applied for thicker samples. There is also a long hold time for thicker samples at this temperature to facilitate water release prior to a rapid increase in vapour pressure (see figure 3.5). The next temperature plateau is at 100^{o}C to enable water to escape prior to the exponential steam pressure increase. The temperature is then increased in steps of 50^{o}C to a maximum of 250^{o}C, the region where the maximum dehydration shrinkage was measured. Rates of temperature increase were limited to 1^{o}C maximum per minute to minimise thermal gradients which may initiate crack formation. Cooling was allowed to occur naturally but samples can be removed from the oven once the temperature falls below 100^{o}C.

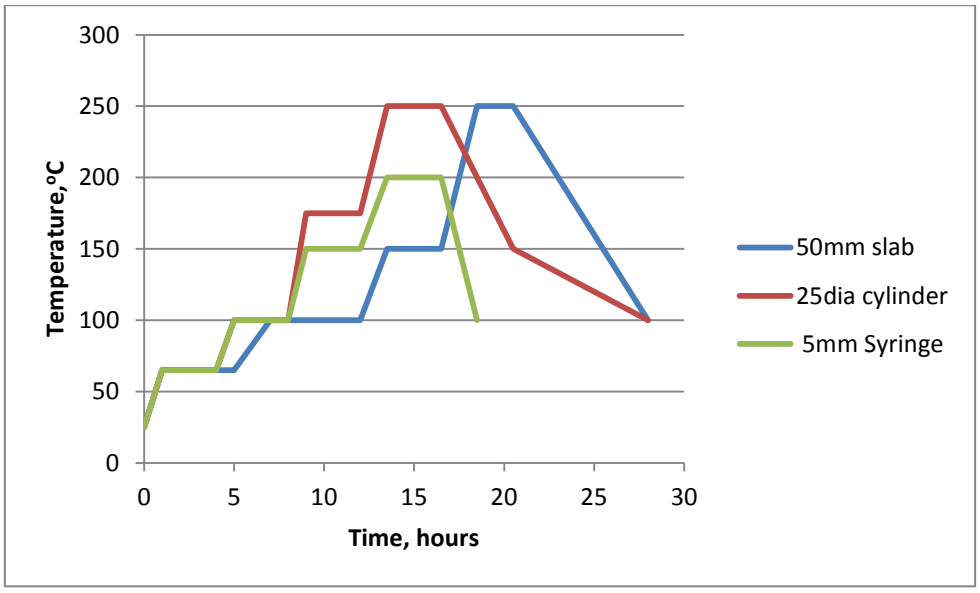

Figure 3.4 Geopolymer post cure schedules adopted in this project.

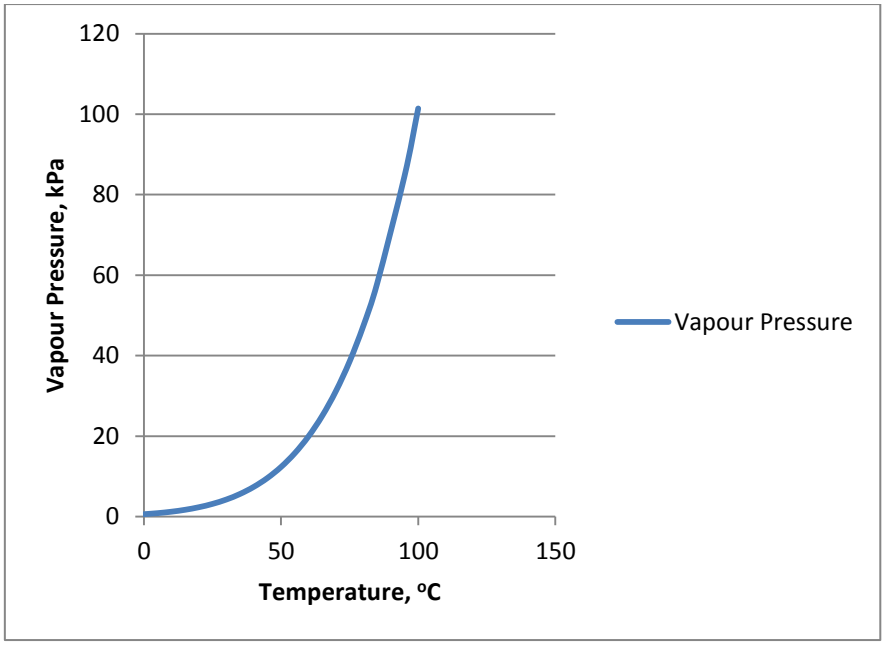

Figure 3.5 Vapour pressure of water (Green and Perry, 2007).

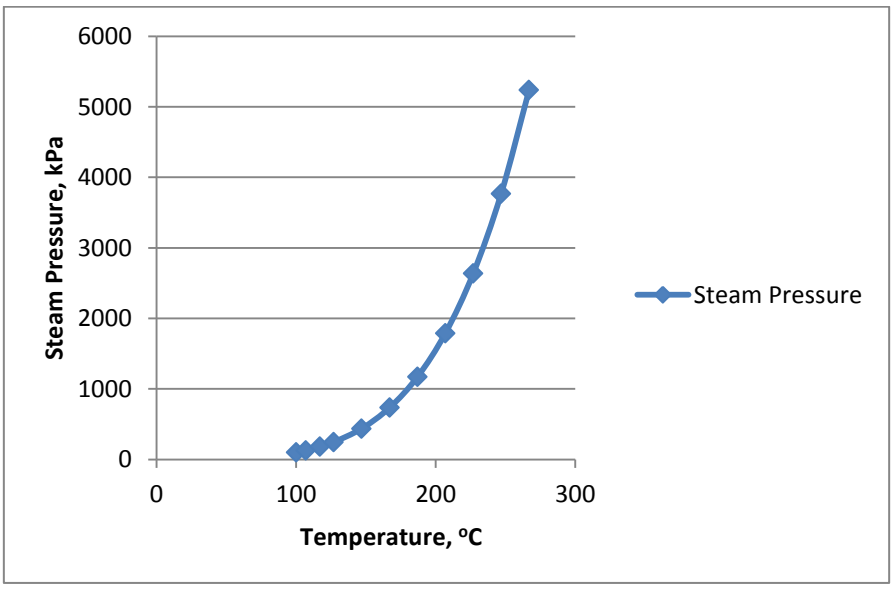

Figure 3.6 Steam pressure verses temperature (Green and Perry, 2007).

3.3.6 Mechanical testing

As there are no national standards dedicated to the testing of geopolymer based cementitious materials, the use of standards for organic polymers and OPC based materials is widely used with modifications as required. Typically the use of samples with smaller dimensions than specified in OPC related standards is used in this research to facilitate the utilisation of existing equipment.

Mechanical properties, compressive strength and flexural strength, were determined on a Lloyds Universal Tester EZ50 (UK) fitted with a 50 kN load cell, suitable platens and sample testing jigs.

Compressive strength evaluation was carried out on samples with a height of approximately 40 mm x 25 mm diameter. The loading rate was set at 0.25 MPa s^{-1} to comply with ASTM C39/C39M (2012). An initial rate of loading of 5 mm min^{-1} up to 2000 N was applied to smooth out the initial stage of the stress-strain curve. After attaining 2000 N, the rate of loading of 0.25 MPa s^{-1} was applied until sample failure. Figure 3.7 shows the set up for compressive testing with the safety guards removed for clarity.

Compressive strength is generally specified in design and quality control because it is relatively easy to measure and is thought to be related to other properties which can be deduced from compressive strength data.

The lower the rate of loading the lower is the measured compressive strength. This is attributed to the slower rate allowing more critical crack growth to occur leading to the formation of larger flaws and hence smaller apparent loads. Also slower rates may allow creep to occur which will increase the amount of strain at a given load.

The compression test assumes a state of pure uniaxial compression. However the presence of friction between the ends of the test specimen and the platens of the test machine gives rise to forces due to differences in the Young's modulus and Poisson's ratio for steel and cementitious materials. The platens act to restrain the lateral expansion of the ends of the specimen and thus introduce a shear stress that is greatest at the specimen ends and gradually dies out at a distance of (√3/2) d, where d is the specimen diameter or width. This

is the source of the cone (or pyramidal) failure mode. Columnar vertical cracking through both ends with no well-formed cones is indicative of pure compression (Li, 2011).

Compressive strength was evaluated using equation 3.1.

$$\sigma_{c} = \frac{F}{A} \qquad \text{Equation 3.1}$$

Where

σ_c = compressive strength (MPa)

F = load at failure (N)

A = Area of load bearing surface (m^2)

Young's modulus was determined from the compressive strength test data. Young's modulus is a measure of the stiffness of an elastic material. The slope of the stress-strain curve in the elastic region is used to determine Young's modulus (equation 3.2).

$$E = \frac{\sigma}{\epsilon} \qquad \text{Equation 3.2}$$

Where

E = Young's modulus, MPa

σ = stress, MPa

ε = strain, change in length/original length

Figure 3.7 Compressive strength testing equipment.

Three point flexural strength testing was carried out based on ASTM D790-10 (2010). The available jig (figure 3.8) to suit the Lloyds universal tester was designed around this standard. A specimen of square cross section rests on two supports and is loaded by a cylindrical loading nose of radius 5 mm midway between the supports. The sample is deflected until rupture occurs in the outer surface of the test specimen. The maximum axial stress occurs on a line under the loading nose in the three point test.

ASTM C1609M-10 (2010) is the standard for three point flexural strength testing of fibre reinforced cementitious products. Variation in the specimen test piece size is allowable within the stated guide lines. This standard also gives definitions of the material physical properties to be determined.

The sample size for three point flexural testing was 20 mm x 20 mm x 90 mm. The span was set to 60 mm to ensure a span to depth ratio of at least 3. An applied deflection rate of 1 mm min^{-1} was used for testing. For a 20 mm thick specimen this is equivalent to a loading rate of 0.05 mm/mm/min. This was determined by measuring the time to cracking at a range of speeds and ensuring that the failure time was within 60 seconds from initial load application.

The flexural strength and modulus of elasticity in bending were determined using equations 3.3 and 3.4.

$$\sigma_f = \frac{3PL}{2bd^3} \qquad \text{Equation 3.3}$$

$$E_B = \frac{L^3 m}{4\mathrm{b}d^3} \qquad \text{Equation 3.4}$$

Where

σ_f = flexural strength

P = load

E_B = Modulus of Elasticity in bending

L = support span

b = width of specimen

d = depth of specimen

m = the slope of the tangent to the initial straight portion of the curve

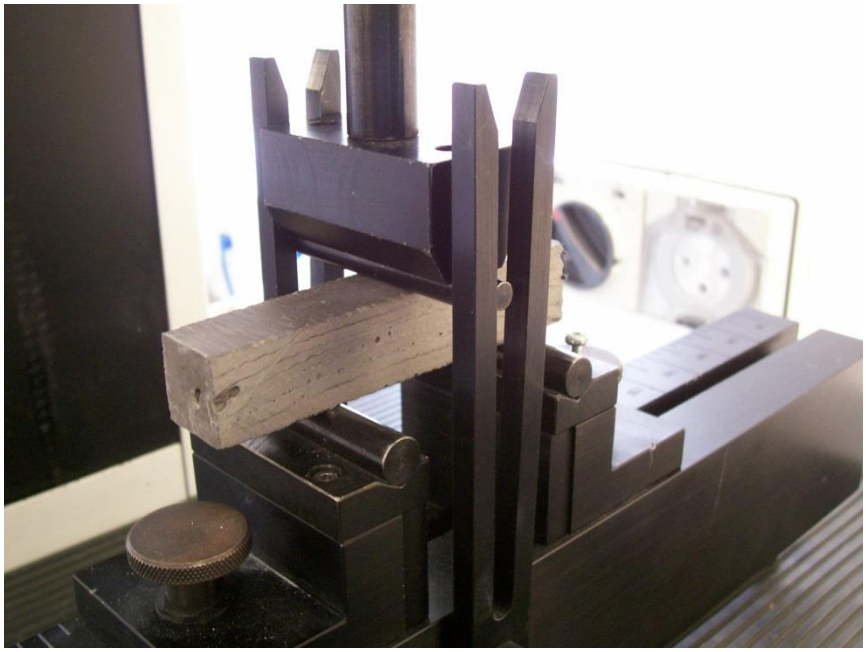

Figure 3.8 Flexural strength testing jig.

Density of the geopolymer mortars was determined by weighing and measuring uniform specimens and using equation 3.5.

$$\rho = \frac{M}{V} \qquad \text{Equation 3.5}$$

Where

ρ = density (g cm^{-3}) M = mass (g) V = volume (cm^3)

For a cylinder, $V = \pi r^2 h$ where r = radius (cm) and h = height (cm).

3.3.7 Heat treatment and dilatometry

Cylindrical compression test samples were heated in a muffle furnace (figure 3.9) at 200, 400, 600, 800 and 1000^{o}C. Bar samples for flexural testing were heated at 600 and 1000^{o}C. The Muffle furnace was fitted with a microprocessor to allow a wide range of thermal cycles to be applied to specimens. The heating rate was 5^{o}C min^{-1} to target temperature, which was held for one hour. Samples were then allowed to cool naturally in the furnace. Dimensional and mass changes of all samples were determined for each test. Compressive and flexural strengths were determined on fired samples after cooling to ambient temperature.

Figure 3.9 Muffle furnace.

Thermal expansion of a material is the manner in which its volume changes as the temperature increases. Equation 3.6 shows the relationship between linear expansion and temperature change (Serway, 1992).

$$\frac{\Delta L}{L_o} = \alpha \Delta T \qquad \text{Equation 3.6}$$

Where

ΔL = fractional change in length L_o = original length

α = average coefficient of linear (thermal) expansion (K^{-1})

ΔT = temperature difference (K).

A DI-24 Adamdel Limohargy (alumina push rod dilatometer)(figure 3.10) was used to determine the thermal expansion and shrinkage on 4.7 mm diameter x 15 mm long geopolymer cylinders, except in the case of formulations which would not flow sufficiently to fill the 4.7 mm diameter mould. In these cases a 10 mm x 12 mm rectangular block was cut from moulded cylinders. Figure 3.10 shows a cut sample in position after testing. The alumina push rod is clearly visible. The measurements were made over the range 25 to 1000^{o}C at a heating rate of 5^{o}C min^{-1}. A pre-load of 100 mN was applied to the sample prior to heating to allow data from shrinking samples to be collected in order to comply with ASTM E228-11 (2011). The intersection of tangents to the curve in sections of large change was used to determine the inflexion points in the data.

The dilatometer software compensates for the expansion/shrinkage of the alumina push rod to give the values related to the test sample only.

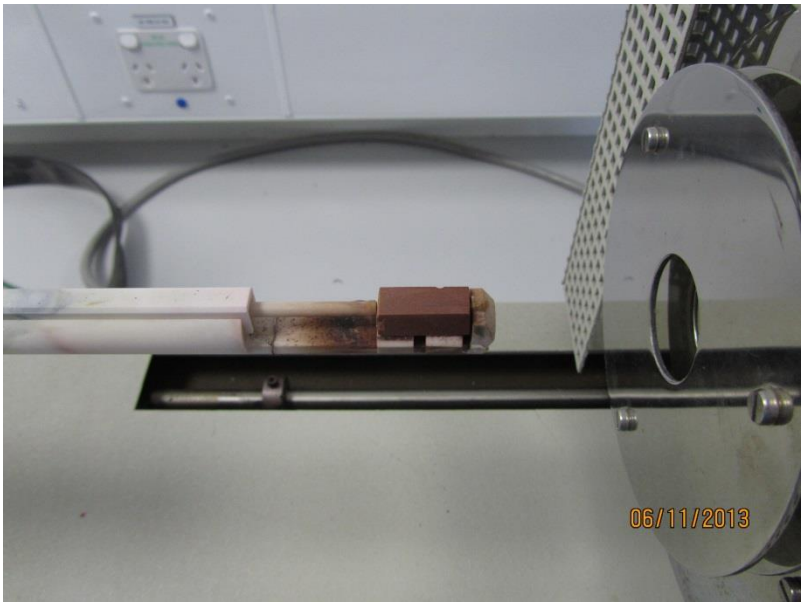

Figure 3.10 DI-24 dilatometer.

3.3.8. Thermal Conductivity

The method used was based on a steady state technique using an Hukseflux HFP 01 heat flux transducer, which generates an electrical signal proportional to the heat flow across it (2012). The actual sensor is a thermopile (Weekmann, 1997) and the output voltage is measured in the millivolt (mV) range. This voltage is converted to a heat flux by dividing by the sensitivity. The sensitivity is a constant supplied with each instrument.

This particular methodology was developed to simplify sample preparation compared to the transient hot wire method used previously (Subaer and van Riessen, 2007, Rickard et al., 2013).

In this new methodology, discs of 50 to 75 mm diameter or blocks up to 50 mm square and 10 to 20 mm thick are used as test samples. In the case of geopolymers, cylinders 125 mm high and 76 mm diameter were cast and cured for 24 hours at 70^{o}C. A PVC pipe bonded to a form plywood base using silicone sealant was used for the mould. The open end was covered with plastic film held in position with tape during the cure cycle.

After three days the cylinder (still in the PVC pipe) was cut into discs of the required thickness using a diamond blade saw. Discs were wet polished using ethanol and 180 and 240 grit silicon carbide abrasive papers to remove cutting marks. These discs were stored in sealed plastic bags until the next stage of conditioning/testing.

The newness of this methodology required several evaluation tests using a material of known thermal conductivity. Polytetrafluoroethylene (PTFE) (density = 2.16, thermal conductivity = 0.23 to 0.25 $Wm^{-1}K^{-1}$) was used for these evaluations.

Figure 3.11 shows the apparatus set up. The lower aluminium cylinder with inlet and outlet ports is fed from a circulating water chiller (flow rate 10.5 l min^{-1}) set to 17^{o}C. The upper surface of this cylinder has a K-type thermocouple embedded at the centre approximately 1 mm below the surface. The heat flux transducer sits above this. The test sample sits on the heat flux transducer with a 4 mm thick aluminium plate complete with K-type thermocouple sitting on the upper surface of the sample. This aluminium plate is to disperse the heat output from the 50 mm diameter DC heater which is placed on the aluminium plate.

Figure 3.12 shows the draught protector placed over the test apparatus together with a multimeter to measure the output of the heat flux transducer, a DC current output transformer and a Fluke thermometer to measure hot and cold side temperatures.

Initial evaluations of the PTFE sample lead to the use of thermal paste between all mating surfaces, the addition of foam installation around the circumference of the sample and around the circumference and top of the heater block to direct the heat flow into the test assembly.

DC current settings were set between 0.8 and 1.0 A; equivalent to a voltage of 3.0 to 3.5 V. A steady state was assumed when the hot side temperature did not change by more than 0.1^{o}C over 4 readings at 5 minute intervals and the difference between hot and cold side temperatures did not change by more than 0.1^{o}C in the same interval. A running time of approximately two hours elapsed before a steady state was achieved.

The thermal conductivity was determined from equation 3.7.

$$k = Q.\frac{\Delta x}{A.\Delta T} \qquad \text{Equation 3.7}$$

Where:

k = thermal conductivity, $Wm^{-1}K^{-1}$

Q* = heat flow rate, Js^{-1}

Δx = thickness of sample, m

ΔT = temperature difference across the sample thickness, K

A = exposed surface area of sample, m^2

* Q is derived from the output, in mV, of the heat flux transducer and the calibrated sensitivity of the transducer (63.41 μV/Wm^{-2})

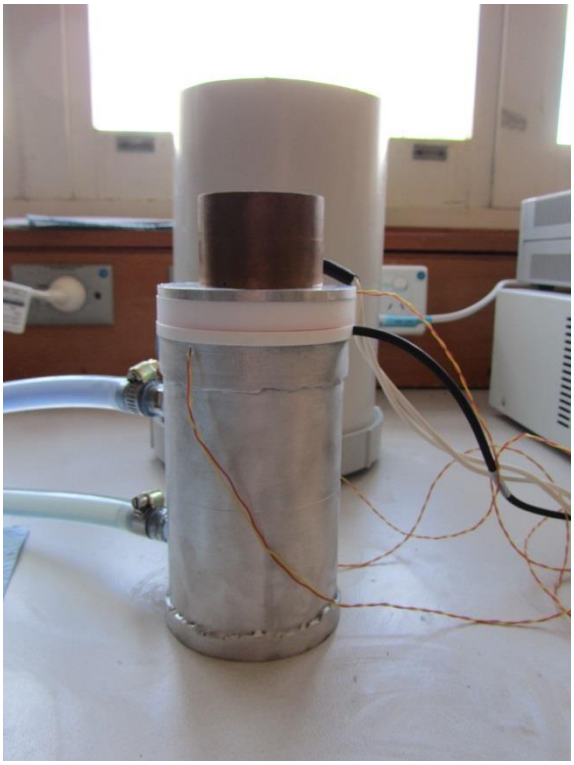

Figure 3.11 Thermal conductivity test apparatus.

Figure 3.12 Thermal conductivity ancillary test equipment.

3.3.9 Scanning electron microscopy (SEM)

Scanning electron microscopy (SEM) is a versatile tool used to observe material surfaces. When a specimen is irradiated with an electron beam secondary electrons are emitted from the top few nanometres of the sample. The topography of the surface can be observed by two dimensional scanning of the electron beam over the specimen surface and acquisition of an image from the detected secondary electrons.

In addition to secondary electrons, back scattered electrons (BSE) are also emitted from the body of the sample. BSEs have higher energy than secondary electrons thus information from deeper in the specimen may be obtained. BSEs are sensitive to sample composition. As the atomic number (Z) of the constituent elements increases, the BSE yield increases. Higher Z value elements show up as brighter areas in the BSE images.

The SEM may also be used for energy dispersive X-ray spectroscopy (EDS). Incident electrons interact with the sample and electrons of various energies and electromagnetic waves are emitted. X-rays are amongst these waves and show characteristic energies associated with the various constituent elements in the specimen. These characteristic X-rays are collected and “counted” over a designated period to produce an X-ray spectrum. The use of standards, of known composition, enables this technique to be used for quantitative elemental determination.

SEM provides information (related to geopolymers) about surface morphology, phase distribution, the size and distribution of pores and presence of cracks.

Samples for use in SEM must be electrically conductive and vacuum stable. Samples were mounted on double sided conductive carbon tape fixed to an aluminium stub. Powder samples such as fly ash and fillers were lightly sprinkled on the tape and any excess removed using a light air flow. To prepare fracture surfaces a small section, between 2 and 10 mm, was removed from the bulk with a scalpel. This section was now mounted on the tape and dried in a vacuum desiccator for 48 hours prior to coating.

Samples were also encapsulated in epoxy resin and allowed to cure for several days prior to polishing with silicone carbide paper initially followed by diamond paste of decreasing particle size down to a minimum of 1 µm on a Struers polishing machine. Water was used as

the polishing lubricant. This enables high quality images to be obtained and in conjunction with carbon coating allows EDS to be carried out.

A conductive coating of metal (gold or platinum) or carbon was now applied using an ion sputter coater. Coating thicknesses are typically 2 to 5 nm. Carbon coatings (up to 10 nm) are used for EDS work due to carbon's low Z value showing minimal X-ray interference.

Scanning electron microscopy (SEM) was performed on a NEON 40EsB field emission SEM (Zeiss, Germany). Additional imaging was also carried out using a TESCAN MIRA3 SEM with an Oxford Instruments X-Max^N 150 EDS detector.

Samples containing fracture surfaces or powder samples were mounted on aluminium stubs using carbon tape. These samples were stored under vacuum prior to coating with 5 nm of platinum. The coated samples were then imaged in the SEM with an accelerating voltage of 5 kV using secondary electron imaging.

INCA-Analyser software (Oxford Instruments, UK) was used to analyse the collected EDS X-ray spectra. Collection conditions were in spot mode at 10 kV accelerating voltage, a working distance of 7.7 mm, an aperture of 60 μm and high current on. Calibration of the Inca software was carried out with an albite ($NaAlSi_3O_8$) standard.

3.3.10 Porosity determination:

Pore size and structure plays an important role in the transport of water (and other chemicals) through the geopolymer structure. This is particularly marked on heating to elevated temperatures where ready escape of water is essential to prevent cracking and explosive spalling.

The classification of pore sizes (Sing, 1985) is shown in table 3.4.

Table 3.4 IUPAC pore Classification (Sing, 1985).

Pore Description	Size Range
Macropores	> 50 nm
Mesopores	2 to 50 nm
Micropores	< 2 nm

Two techniques for pore determination are described below.

Mercury Intrusion Porosimetry (MIP).

MIP is a widely used method for the determination of mesopores and macropores. This method is based on the fact that a non-wetting liquid requires a positive excess hydrostatic pressure be applied to enable it to enter pores. The excess pressure required varies inversely with pore radius. Mercury is the only known liquid really suitable for porosity determination. Mercury does not wet most substances and will not penetrate by capillary action due to its high surface tension. As a consequence of this property entry of mercury into pores requires the application of pressure in inverse proportion to the opening size (Klobes et al., 2006).

MIP is only applicable to comparisons of similar material. The absolute accuracy of the test data is dependent on several assumptions. In similar materials these assumptions can cancel out allowing comparisons to be made. Results are still limited in three ways. MIP determines the largest entrance to a pore and not the actual pore size. Pore size measured by MIP will always be smaller than that measured from SEM images The smallest pore size that can be filled with mercury is limited to the maximum applicable pressure (3.5 nm for 400 MPa assuming a 140^{o} wetting angle). The largest pore measurable is determined by the height of the sample which determines the minimum head pressure. A 10 mm high sample is roughly equivalent to a 1 mm pore diameter (Giesche, 2006).

This work was carried out in the Department of Civil, Environmental and Materials Engineering at the University of Bologna.

Samples for porosimetry were cut using a wet diamond saw to give samples of approximately 1 cm^3. These were then dried under vacuum to remove free water and stored in a vacuum desiccator over P_2O_5 prior to testing. Free water will remain in the pores making them inaccessible to mercury intrusion and must be removed prior to testing. The equipment used was a Carlo Erba, model 2000 fitted with a Fisons Instruments model 120 macropore unit. The equipment used was only capable of resolving pore radii down to 4 nm i.e. 8 nm wide.

A dried weighed sample is placed in a robust penetrometer and a vacuum applied to evacuate the air. Mercury is then admitted to fill the cell and surround the sample. Hydrostatic pressure is progressively increased and at each pressure the corresponding intruded volume of mercury is recorded.

To calculate the pore size distribution it is assumed that mercury enters pores in decreasing order of size as the pressure is increased. If ΔV is the volume intruded between pressures P and P+ΔP it will equal the volume of pores with radii between r and Δr. This gives rise to the Washburn equation (equation 3.8):

$$r = 2\sigma \cos\theta / P \qquad \text{Equation 3.8}$$

Where:

P = pressure

σ = surface tension of mercury (480 mNm^{-1})

Θ = wetting contact angle (~141.3^o for mercury)

r = pore radius

In real systems the prescence of network effects may invalidate the decreasing size order of filling. The sequence of filling may be primarily governed by the pore system interconnectivity. The radius, r, is not a literal pore dimension but rather the size of an equivalent cylindrical pore that would be filled at a given pressure.

Hysteresis between mercury intrusion (increasing pressure) and extrusion (decreasing pressure) is always evident. Giesche (2006) discussed three possible causes; contact angle hysteresis, the ink bottle theory and the percolation-connectivity model. Contact angle hysteresis cannot explain several of the observed effects. In the ink bottle theory the entrance to the pore is smaller than the diameter and mercury will enter at a pressure determined by the entry size and not the actual pore size. When the mercury extrusion process takes place a break in the mercury network at a (lower) pressure equivalent to the entry size occurs leaving residual mercury in the pore.

The connectivity model looks at a system of pores together with the connections between the pores. For a pore to fill with mercury it must be exposed to the relevant pressure for its size and have a continuous path of mercury leading to that pore. During extrusion this connectivity may be broken (due to pore size – pressure dependency) and mercury is left trapped in the pore.

In figure 3.13 Ma et al (2013) showed that the differences for alkali activated fly ash between the mercury intrusion and extrusion curves gave a measure of ink-bottle porosity and effective porosity. The ink bottle porosity is a measure of the volume of mercury remaining in the pores after extrusion. The pore diameter corresponding to the highest rate of mercury intrusion per change in volume (dV/dD) is known as the critical or threshold diameter (figure 3.13).

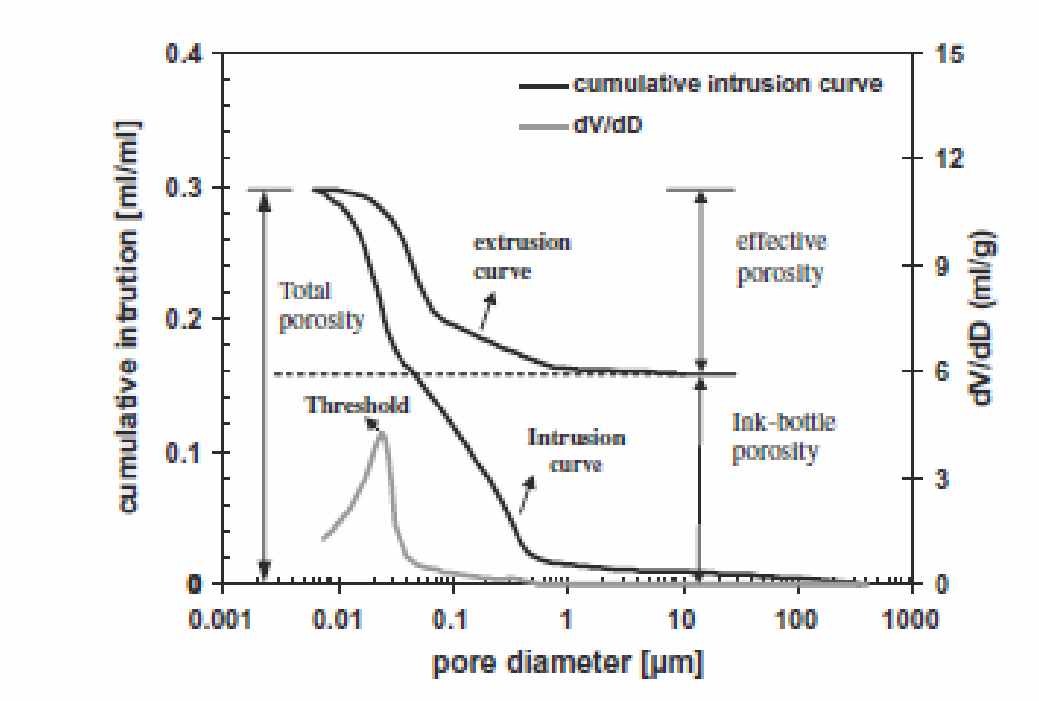

Figure 3.13 Schematic illustration of porosity using MIP (Ma et al., 2013).

Boiling water air displacement method.

ASTM C20-00 (2000) gives test methods for the determination of apparent porosity, water absorption, apparent specific gravity and bulk density. This methodology is based on displacing air in a dried sample by boiling water. The standard is for testing burned refractory bricks and is considered to be appropriate for geopolymers which may be fired. This method is not suitable for materials which react with water. Sample sizes used in these evaluations were in the range 1 to 2 cm^3.

Samples are dried to constant weight in a drying oven at 105^{o}C for 24 hours (weight D). These dried samples are then submerged in boiling water for 2 hours and left to cool suspended in water for at least 12 hours, to ensure full saturation of the sample. A measurement of saturated weight suspended in water was taken (weight S) and a saturated weight in air was taken (weight W). Equation 3.9 and equation 3.10 were used to find density (ρ) and apparent porosity (P) respectively.

$$\rho = \frac{D}{W-S}$$ Equation 3.9

$$P = \left[\frac{W-D}{V}\right] \times 100$$ Equation 3.10

The volumes of open pores and impervious portions of the sample are determined from the following:

Volume of open pores = W-D

Volume of impervious portion = D-S

3.3.11 Fire testing

Fire testing of cementitious products is covered by several national standards. The test furnace at Curtin University is designed to comply with the heating regime of AS1530.4-2005 which is shown in figure 3.15 (Standards Australia, 2005). A schematic view of the furnace is shown in figure 3.14.

The temperature of the furnace is controlled to vary with time in accordance with equation 3.11.

$$T = 345 \log_{10} (8t+1) + 20$$ Equation 3.11

Where

T = furnace temperature at time, t (^{o}C)

t = time into test, measured from the ignition of the furnace, in minutes.

The test panel is 290 mm x290 mm x 50 mm thick, which gave a hot side exposed surface area of 210 x 210 mm. Three k type thermocouples were placed on the cold side, one in the centre of the exposed area and the other two either side along the diagonal half way to the edge of the exposed area. The three cold side thermocouples were held in place with 20 g

alumina ceramic tube weights. The outputs from these three thermocouples plus the furnace thermocouple were recorded every 10 seconds using a Vernier LabQuest (USA). Panels were weighed before and after testing. Observations such as the formation of cracks or evolution of vapour during the test period are recorded.

Two failure conditions are specified in AS1530.4-2005:

Failure condition 1: where the average temperature of the cold side of the test sample exceeds the initial sample temperature by more than 140^{o}C.

Failure condition 2: where the temperature of any location on the cold side of the test sample exceeds the initial sample temperature by more than 180^{o}C.

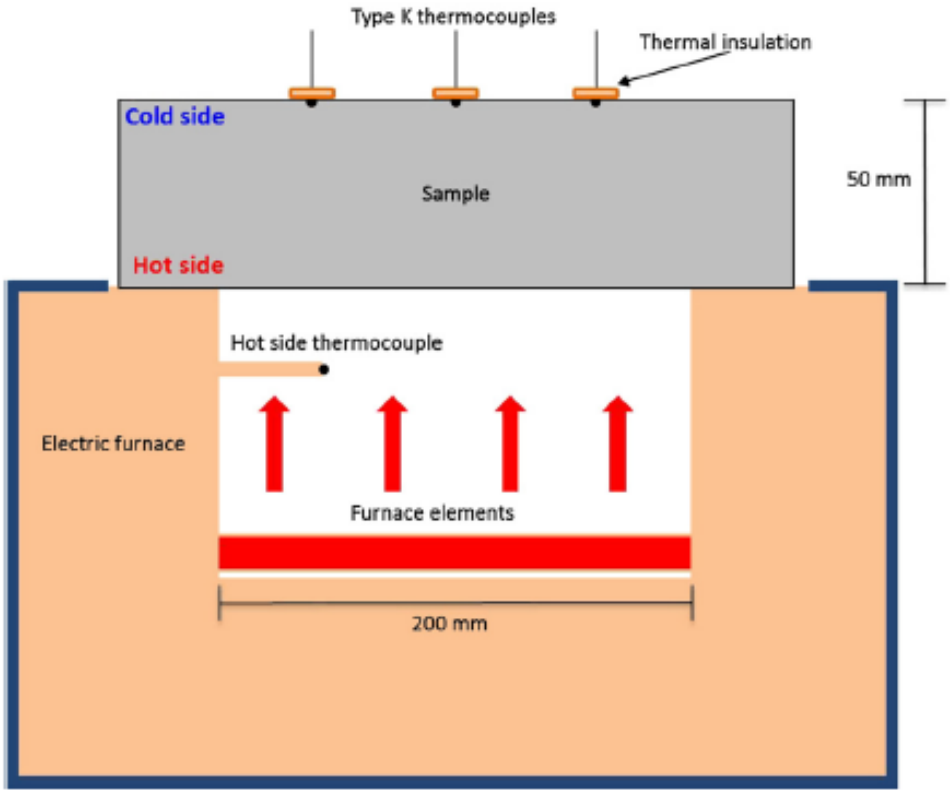

Figure 3.14 Schematic of fire test furnace (Rickard et al., 2013).

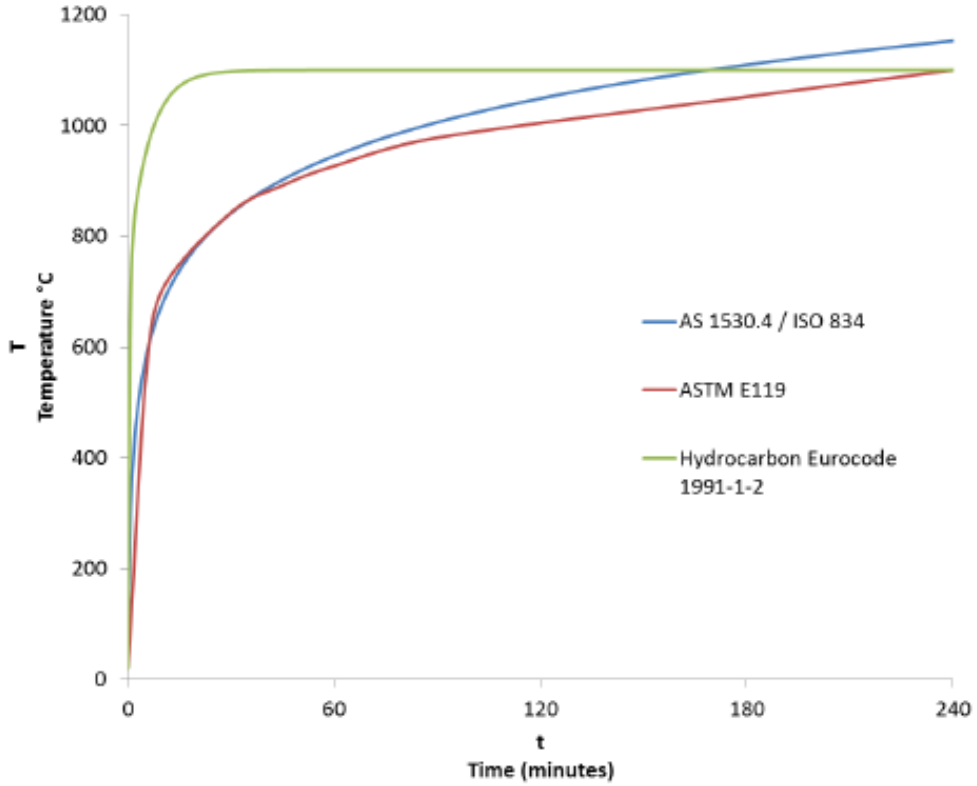

Figure 3.15 Standard fire curves(van Riessen et al., 2009).

The main difference between thermal testing in a muffle furnace and a fire test is the rate of temperature increase. Figure 3.15 clearly shows the rapid temperature increases used in fire testing, typically a target temperature in the furnace of 576^{o}C after only 5 minutes.

CHAPTER 4.

Characterisation of Raw Materials

4.1 Introduction

The characterisation of aluminosilicate precursors such as the fly ash used in this work is essential to give a meaningful starting point for the design of geopolymer synthesis formulations. The physical characteristics of the fly ash (particle size distribution, morphology) and chemical composition (elemental ratios, loss on ignition component) influence the formation rates and physical properties of the cured geopolymer (Bakharev, 2006, Fernández-Jiménez et al., 2006, Shi et al., 2006, Williams and van Riessen, 2010).

Initial characterisation of additives such as fillers and fibres is required to give a base line for following any changes occurring during the synthesis and subsequent testing of the geopolymers. Commercially sourced materials are often accompanied by insufficient data leading to the need for additional specific testing.

The theme of this thesis is heat resistant geopolymers with an emphasis on fire resistance. The raw materials selected to meet these criteria must impart thermal resistance as shown by strength retention after high temperature exposure, minimise thermal shrinkage to reduce cracking tendencies and minimise spalling during rapid rates of temperature increase.

The formulations evaluated must also be capable of being converted into cured samples which have the required properties. The water content of geopolymer systems plays a crucial role in workability and final property development. Unfortunately the water content has a competing influence on both these critical properties so a careful trade off needs to be achieved for successful outcomes.

4.2 Characterisation of Raw Materials

4.2.1. Fly ash

Elemental composition and phase abundance

Fly ash from Collie power station in Western Australia was evaluated. A sufficiently large quantity of the Collie fly ash was available to minimise the possibility of inter batch variations. Table 4.1 shows the chemical composition of the batch of fly ash used in this work. Crystalline oxides are determined by QXRD (figure 4.1). Calcium fluoride was used as an internal standard for the quantitative evaluation of the crystalline phases present as well as the amorphous component. The amorphous composition is the difference between the XRF results and the crystalline component from the QXRD results. Table 4.2 shows the abundance of the crystalline phases as determined by Rietveld modelling using TOPAS software (Bruker V 4.2).

The fly ash composition (Table 4.1) yields an amorphous Si: Al of 1.62 which is suitable for producing geopolymers with a Si: Al of less than 2. The determined level of amorphous material is used to design geopolymer formulations, bearing in mind that not all the amorphous material may be accessible by or reactive with the alkaline activating solutions.

Apart from an amorphous iron oxide content of 8.54 wt. % the other components are at low levels and not expected to greatly influence the formation of geopolymers or their resulting properties. The iron oxide may influence thermal properties due to their oxidation to hematite which results in an expansion event (Rickard et al., 2010).

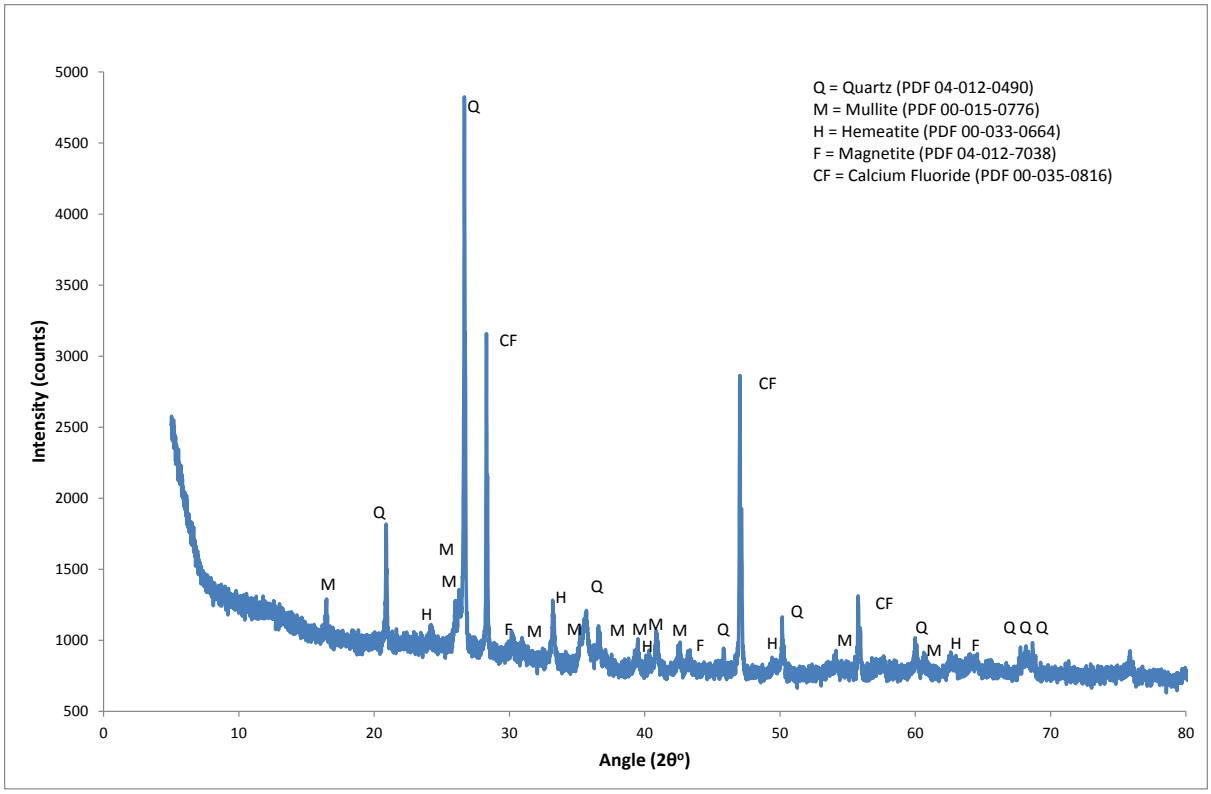

Figure 4.1 Diffraction pattern Collie fly ash with calcium fluoride internal standard. Pattern collected using Cu Kα radiation.

Characterisation of the fly ash phases is important for thermal applications due to the presence of crystalline phases which can undergo phase changes as the temperature increases. The crystalline phases are shown in table 4.2. Mullite is expected to enhance thermal properties due to its low coefficient of thermal expansion (COTE). Quartz undergoes a high-low transformation at 573^{o}C which leads to an increase in volume. Quartz was evident as distinct free particles and also as small particles dispersed within the fly ash particles.

Table 4.1 Collie fly ash composition.

Oxide	**XRF Results, wt.%**	**Calculated Amorphous, wt.%**
SiO_2	50.03 (16)	24.84 (81)
Al_2O_3	24.93 (20)	13.03 (36)
Fe_2O_3	16.40 (4)	8.54 (45)
CaO	1.77(10)	1.77 (10)
K_2O	0.61 (8)	0.61 (8)
MgO	1.29 (6)	1.29 (6)
Na_2O	0.33 (10)	0.33 (10)
P_2O_5	1.50 (4)	1.50 (4)
SO_3	0.34 (1)	0.34 (1)
TiO_2	1.37 (2)	1.37 (2)
BaO	0.41 (1)	0.41 (1)
Other	0.47 (12)	0.47 (12)
LOI	0.55	0.55
SUM	100.00	55.05
SiO_2 / Al_2O_3	2.01	1.91
Si / Al (molar)	1.70	1.62

The quoted uncertainties (in brackets) represent the estimate of the 95% confidence level based on the variation in repeated analysis.

Table 4.2 Collie fly ash crystalline phase composition.

Phase	Structure	Composition, wt.%
Amorphous content	N/A	55.06
Mullite ICSD 66447	$Al_{4.64}\ Si_{1.36}\ O_{9.68}$	16.01
Quartz low ICSD 83849	SiO_2	21.08
Maghemite C ICSD 87119	Fe_2O_3	4.90
Hematite ICSD 88417	Fe_2O_3	2.96

Particle size, density, surface area

Table 4.3 and figure 4.2 show the relevant data for the Collie fly ash. The Collie fly ash meets the fineness requirements of ASTM C618-12 (2012a) for coal fly ash for use in concrete. The requirement is for a maximum of 34 wt. % to be retained on a 45 µm aperture (325 mesh) screen. Several screens of descending relevant aperture sizes are stacked on top off each other, filled with a known amount of material and clamped together in a mechanical vibrator. The screen allows passage of particles smaller than the aperture size and retains those of larger size. After a fixed period of vibration the residue on each screen is collected, weighed and converted to a percentage of the initial weight.

Table 4.3 Collie fly ash particle size data, surface area and density.

Fly ash property	Data
Volume weighted mean, D[4,3]	27.048 µm
Surface weighted mean, D[3,2]	4.184 µm
d(0.1)	1.491 µm
d(0.5)	12.526 µm
P80	43.591 µm
d(0.9)	74.2 µm
Specific surface area	1.43 m^2 cm^{-3}
Density	2.6277 (0.0033) g cm^{-3}

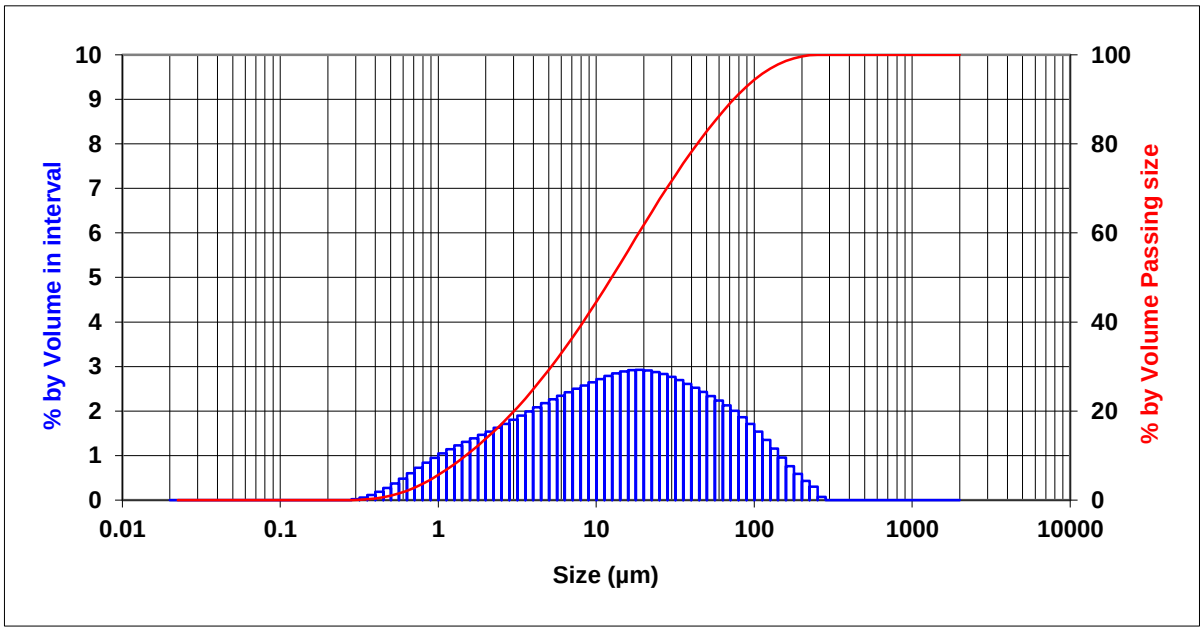

Figure 4.2 Particle size distribution of Collie fly ash.

pH of Collie fly ash in water: This work was carried out to gain some insights into the interaction of Collie fly ash with aqueous systems.

20 g of Collie fly ash were mixed with 100 g of de-ionised water in a plastic beaker and stirred with a magnetic stirrer at ambient temperature. The pH of the system was measured at the time intervals shown in table 4.4. A Thermo Scientific Orion 4 Star meter was used

fitted with an electrode type 9156BNWP. The meter was calibrated using reference standards of pH 4 and 7.

Table 4.4 Water leaching of Collie fly ash.

Time	pH
0	7.01 (0.02)
5 min	4.20 (0.02)
10 min	4.16 (0.02)
15 min	4.16 (0.02)
20 min	5.18 (0.02)
25 min	5.28 (0.02)
30 min	5.28 (0.02)
18 hours	5.27 (0.02)
34 days	6.70 (0.02)

The pH dropped from 7.01 at time zero to 4.2 at 5 minutes where it remained until 20 minutes when it increased to 5.18. Extended water leaching (34 days without stirring) gave a pH of 6.7. The fly ash particles in the slurry would be expected to be well wet out during the stirred stage of the test. On standing the heavy components, probably iron based as they adhered to the magnetic stirrer, settled out to form a black layer. The lighter components settled above the iron layer. The dispersed particles possibly had an hydration sphere formed at the surface. The 34 day extended storage was probably sufficiently long for an equilibrium condition to be established due to the small fly ash particle size.

The Collie fly ash has high amorphous aluminium content and this could contribute to a nett positive surface charge. Silicon is more electronegative than aluminium hence will be negatively charged compared to the aluminium atom. This will direct water molecules to hydrogen bond with aluminium centres on the fly ash surface via the negatively charged oxygen atom. This hydrogen bonded structure can now rearrange producing a proton and an hydroxyl group which bonds to an aluminium atom. [This hydrated proton is the possible source of the acidic pH of the Collie fly ash.]

Over time the pH increases due to removal of hydrated protons. This may be attributed to the aluminium centres being completely reacted and the hydrated protons linking up with the partially negatively charged silicon centres to form silanol groups. The extent of this reaction is limited by total conversion of aluminium centres.

Surfaces tend to be more energetic than the material bulk. The environment at the surface is very different to that in the bulk of the material. In the bulk each atom is surrounded by similar atoms. However at the surface an asymmetric state exists and atoms here have a different energy distribution compared to those in the interior. These differences between bulk atoms and surface atoms are manifest as surface free energy (surface tension in liquids). This may be attributed in part to “unassociated” (unused) valence orbitals on the surface. These orbitals may be empty, partially filled or fully filled.

SEM imaging of Collie ash

Collection of fly ash SEM imaging was a collation of previous work (as referenced) and my images. This was to obtain the best presentation from all the available data together with efficient and economic usage of equipment.

Figure 4.3 was obtained using back scattered electrons and highlights the presence of spheres containing crystalline iron compounds (bright particles). The spherical nature of the fly ash is evident.

Figure 4.4 shows the SEM image of Collie fly ash which has been encapsulated in epoxy resin and polished down to 1 µm surface roughness. The spherical morphology is clearly evident with most of these particles being less than 10 µm in diameter. The smooth surface finish is indicative that the spheres are predominantly glassy as opposed to an angular crystalline finish. Additionally there are irregular and/or porous particles which appear to be much larger than the spherical particles. The arrow in figure 4.4 shows one such particle. Plerospheres, from the Greek plërës (filled), hollow particles containing other particles, are also present.

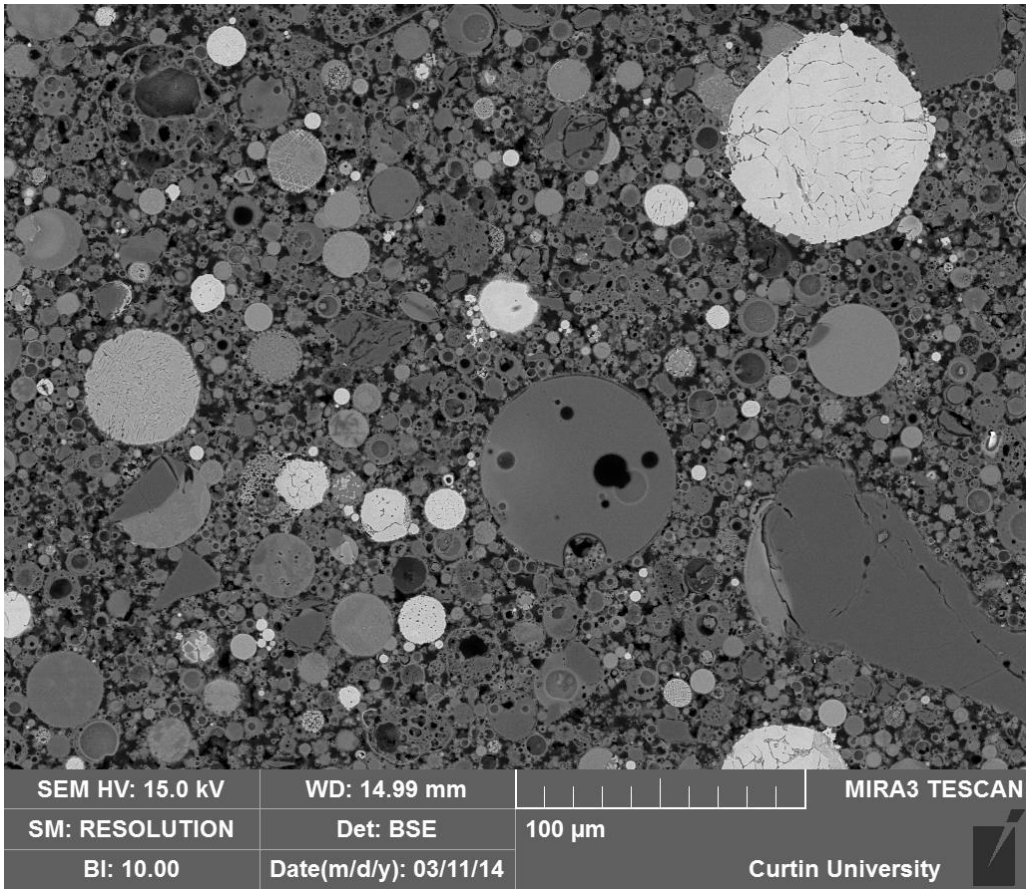

Figure 4.3 Collie fly ash polished sample morphology using back scattered electrons.

Figure 4.5a shows a solid fly ash particle containing blocky crystalline material which may be quartz. Figure 4.5b shows a coarse (220 x 96 µm) free quartz particle. Figure 4.5c is a plerosphere containing a range of fly ash spheres, irregular particles and porosity. Figure 4.5d is a crystalline iron compound contained in a fly ash particle. The images were collected using an accelerating voltage of 5 kV and the collected signal was secondary electrons.

The Collie fly ash shows a wide range of morphological states. This may be attributed to the equally wide range of local conditions through coal composition, burning and cooling conditions and fly ash collection and any post-collection classification (Blissett and Rowson, 2012). The spherical morphology will facilitate workability by reducing water demand with a resulting reduction in dehydration shrinkage (Kong et al., 2007). The small spherical spheres are likely to be mainly glassy due to rapid cooling of the melt. The larger porous particles are formed by entrapment of combustion gases.

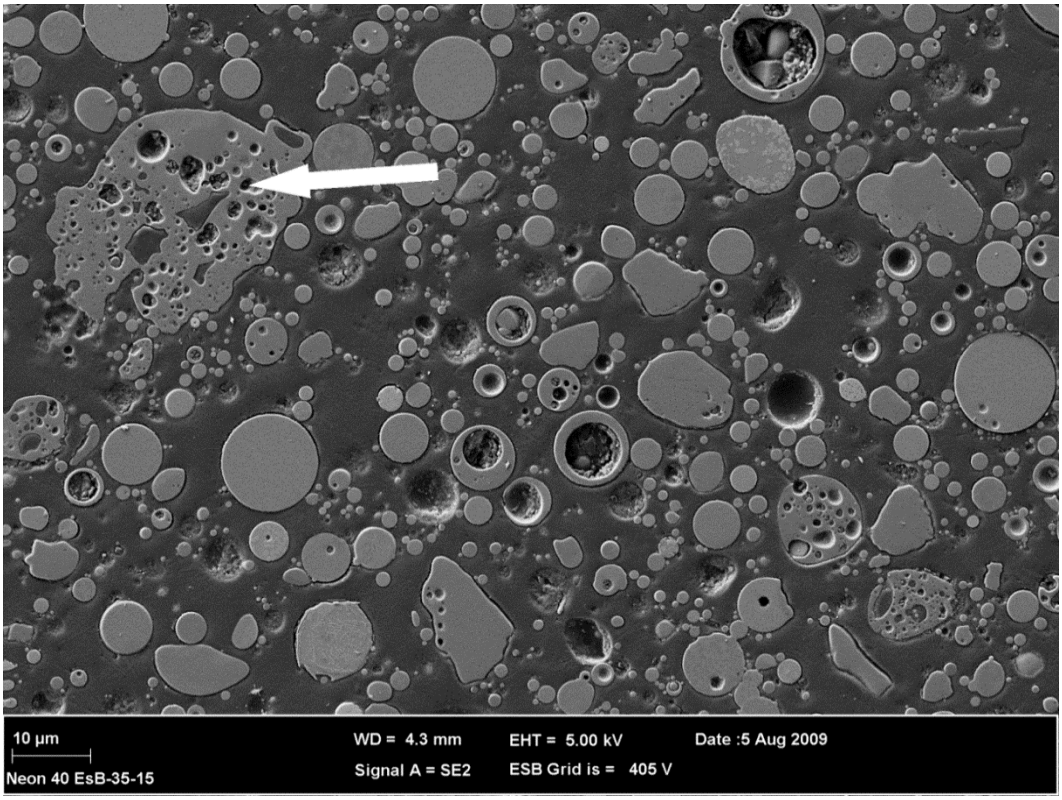

Figure 4.4 Collie fly ash polished sample morphology (Rickard, 2012).

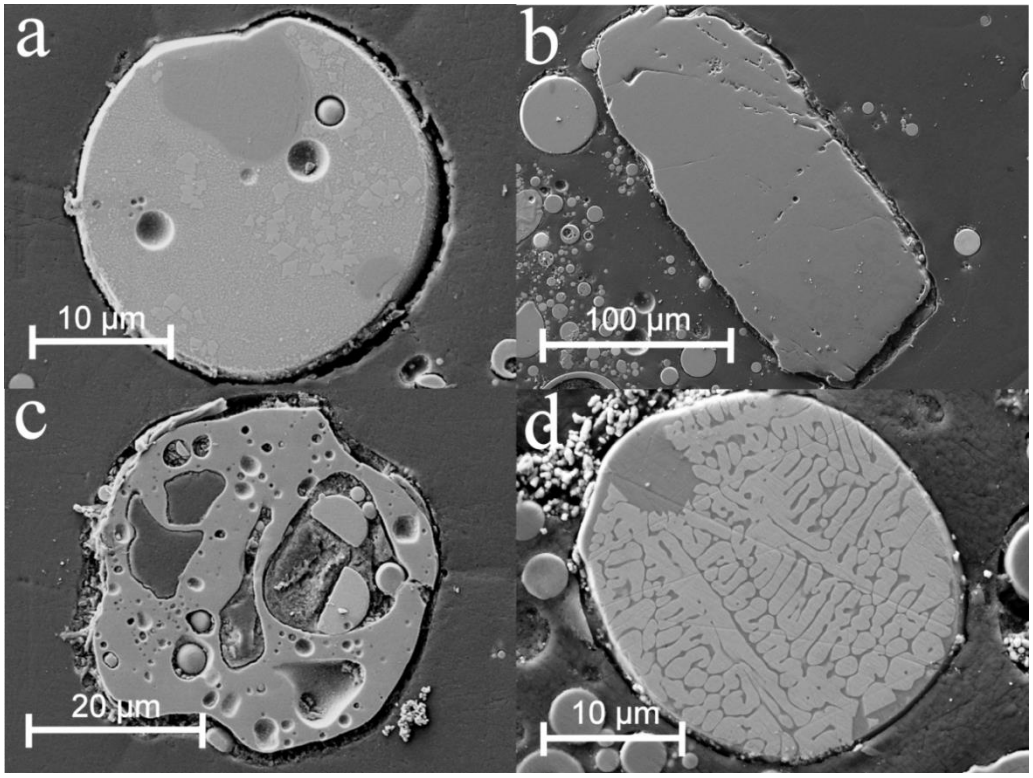

Figure 4.5 Collie fly ash individual particle morphology (Rickard, 2012) obtained by backscattered electron imaging.

4.2.2. Fillers

The properties of fillers selected for evaluation in thermally resistant geopolymers are outlined below. Fillers to enhance thermal resistance would be expected to show the following characteristics:

- Low COTE
- High melting point
- Phase stability with low degree of morphological change
- Low thermal conductivity (although higher thermal conductivity could be advantageous in certain applications to reduce thermal gradients)

4.2.2.1 α-alumina: This material, Doral 325F, was sourced from Doral Fused Minerals (2011) and the chemical composition as determined by XRF is shown in Table 4.5. The specific gravity is 4.02 and bulk density is 1.36 g cm^{-3}. The Doral 325F showed 8.6 wt. % retained on a 45 µm aperture screen.

Table 4.5 Chemical Composition of supplied Doral 325F.

Oxide	**Weight %**
Al_2O_3	99.6
SiO_2	0.04
Fe_2O_3	0.01
TiO_2	0.00
Na_2O	0.23
CaO	0.07

Reported values (Munro, 1997) for COTE (α) of alumina are 8.1 x 10^{-6} K^{-1} (0 – 1000^{o}C) and thermal conductivities are 33 (20^{o}C) and 7.22 (1000^{o}C) W m^{-1} K^{-1}. COTE values (x 10^{-6} W m^{-1} K^{-1}) at 20^{o}C (4.6), 500^{o}C (7.1) and 1000^{o}C (8.1) are also reported by Munro. This indicates that thermal expansion of α-alumina is relatively small in the range 500 to 1000^{o}C and suggests that this material will be useful as a filler to control expansion over this

temperature range. Alumina is anisotropic, existing in the hexagonal crystal lattice form. The COTE values reported above are an average based on $(2\alpha_a + \alpha_c)/3$, where α_a and α_c refer to the COTE of the individual lattice parameters. A melting point of 2050^{o}C has been reported (NIST, 2001). Figure 4.6 shows the morphology of Doral 325F. The irregular shaped particles with surface score marks are typical of milled materials.

Ball milled alumina is available in a series of size ranges from 20-10 mm through to 1-0.5 mm. This will enable a range of geopolymer concretes to be produced for thermally resistant applications.

Figure 4.7 shows the surface of a 1 mm alumina aggregate produced by crushing. The steplike cleavage planes will enhance mechanical keying of these particles into the geopolymer matrix.

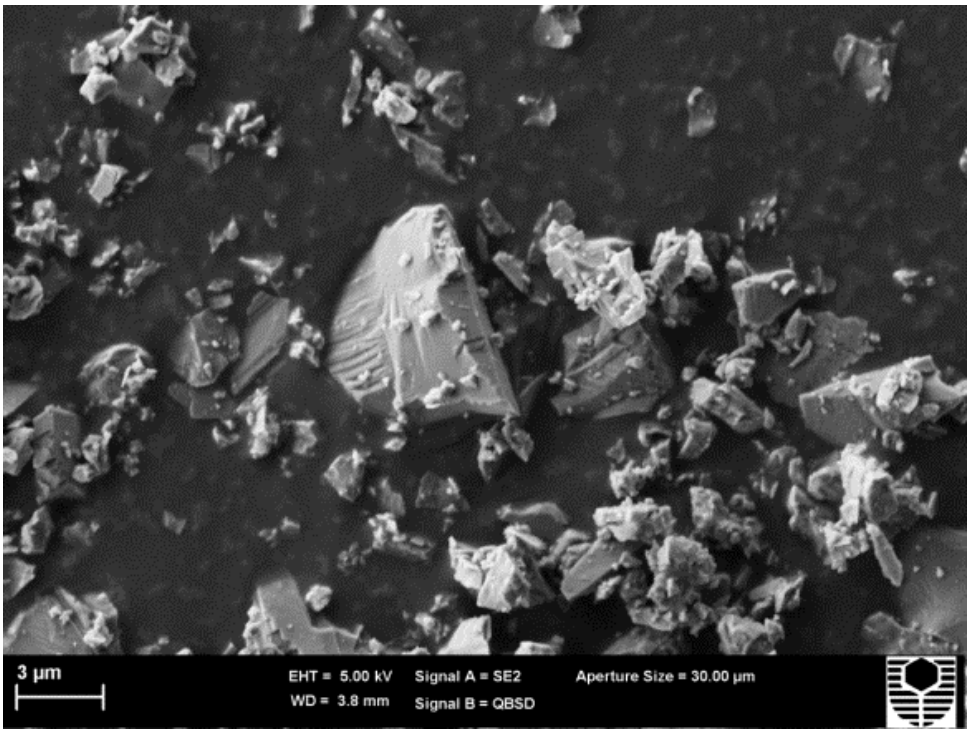

Figure 4.6 SEM image of α-alumina filler (Doral 325F).

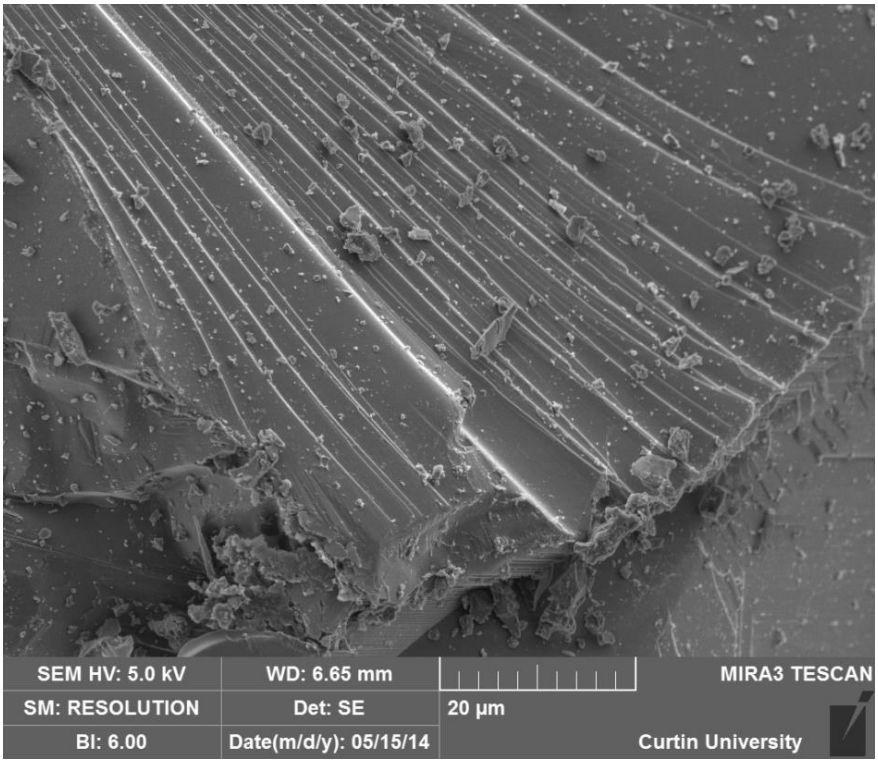

Figure 4.7 surface morphology detail of 1 mm alumina particle.

4.2.2.2 Wollastonite: This material (NYAD MG) is sourced from NYCO Minerals of the USA. The M prefix indicates the source as its Mexican deposit. Tables 4.6 and 4.7 are extracted from the NYAD MG technical data sheet. Table 4.6 indicates that the composition is substantially calcium silicate.

The thermal conductivity is reported as 2.70 ±0.07 W m^{-1} K^{-1} by Nyco Minerals and this is close to the value of 2.6 W m^{-1} K^{-1} at 30^{o}C reported by Lee et al. (2006). A search for higher temperature values of thermal conductivity was unsuccessful.

Figure 4.8 shows the cumulative particle size distribution for Nyad MG and figure 4.9 shows the acicular shape of the particles. Measurements of the particles shown in figure 4.9 indicate an aspect ratio (length to diameter ratio) in the range 4.3 to 7.6 with an average of 7.1. In figure 4.10 the irregular surface of the particles is evident. This irregularity can enhance mechanical keying of filler particles into the geopolymer matrix. The step like fracture mode forms sharp corners which can be areas of high surface energy. It may be possible for alkali attack to occur in these areas leading to the formation of chemical bonds between the filler and matrix. The acicular nature of the wollastonite may allow it to behave as a microfibre which could enhance the toughness of the filler-geopolymer composite.

Table 4.6 Nyad MG properties (NYCO Minerals, 2013).

Typical Property	**Value**
Morphology	Acicular
Specific gravity	2.9
pH (10% slurry)	9.9
Water solubility, g/100 cm^3	0.0095
MOHS hardness	4.5
Coefficient of expansion (mm/mm/^oC); 25 to 800^oC	6.5 x 10^{-6}
Melting point, ^oC	1540
Microtrac median particle size, µm	28
Surface area (BET), $m^2 g^{-1}$	0.5
Bulk density loose, g cm^{-3}	0.55
Moisture, %	0.05

Table 4.7 Nyad MG chemical composition (NYCO Minerals, 2013).

Oxide	**Weight %**
CaO	45.72
SiO_2	46.52
Fe_2O_3	0.25
Al_2O_3	0.25
MnO	0.02
MgO	0.71
TiO_2	0.05
K_2O	0.2
LOI 1000^oC	6.3

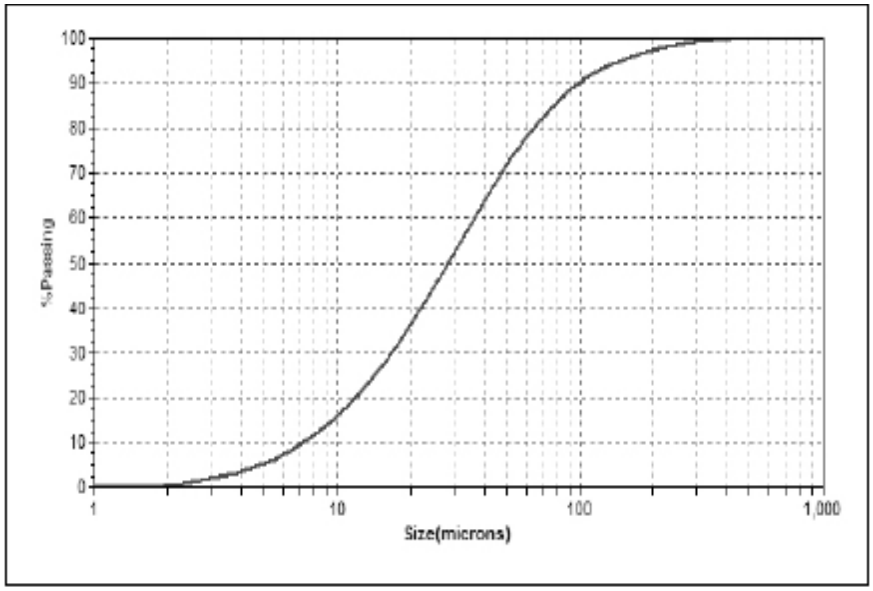

Figure 4.8 Particle size distribution of Nyad MG (NYCO Minerals, 2013).

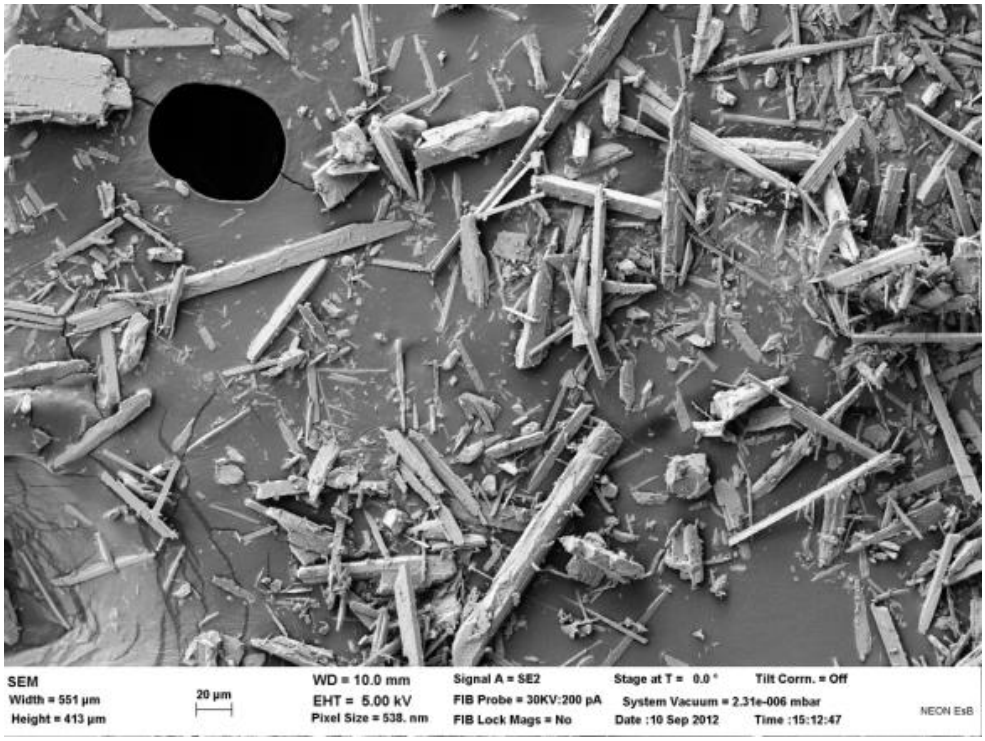

Figure 4.9 SEM image of Nyad MG using secondary electrons.

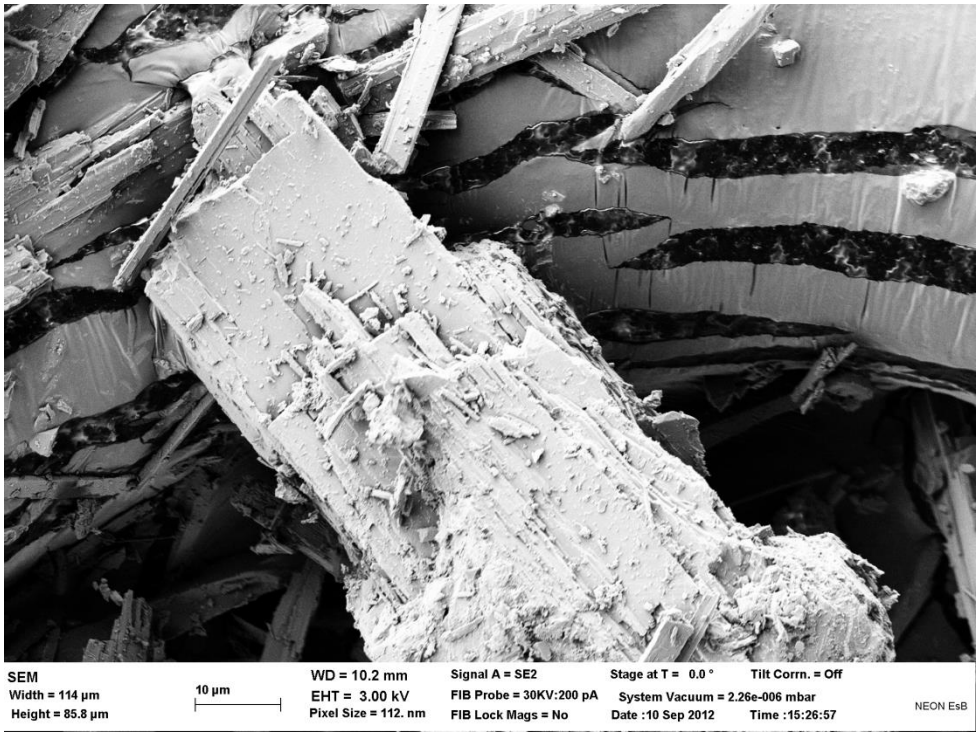

Figure 4.10 SEM image of Nyad MG showing irregular surface

4.2.2.3 Mullite: The mullite used in this study is from Washington Mills of the USA (2008). It is produced in an electric arc furnace using a slight excess of alumina to ensure all the silica is combined in the mullite phase. Table 4.8 is extracted from the Duramul data sheet. Conversion of thermal conductivity units from cal s^{-1} cm^{-1} $^{o}C^{-1}$ to W m^{-1} K^{-1} was accomplished by multiplying by 418.6.

The small difference in COTE (0.5 x 10^{-6} K^{-1}) between 500 and 1000^{o}C will be beneficial in controlling thermal expansion in this temperature range. The thermal conductivity is lower than that of alumina.

Table 4.8 Properties of Mullite (Washington Mills, 2008).

Chemical Composition	**weight %**
Al_2O_3	75.0
SiO_2	24.7
Na_2O	0.3
Property	
Colour	White
Specific Gravity	3.15
Melting point, ^oC	1830
Thermal Conductivity at 100^{o}C, W $m^{-1}K^{-1}$	6.07
Thermal Conductivity at 1000^{o}C, W $m^{-1}K^{-1}$	3.77
COTE 25 to 500^{o}C, K^{-1}	4.63 x 10^{-6}
COTE 25 to 1000^{o}C, K^{-1}	5.13 x 10^{-6}

The sample of supplied (Duramul 325F) is specified to pass a 45 µm opening screen. This size is confirmed in figure 4.11, which also shows the irregular, non-spherical particle shape and size. Figure 4.12 shows the wide range of particle shapes produced by crushing; a few long particles have passed longitudinally through the screen. This back scattered electron micrograph shows a predominantly uniform elemental composition of the larger particles. The small bright particles are possibly traces of haemite not removed during magnetic separation during manufacture and found in the XRD evaluation. An alternative explanation is that we are seeing low level charging of particles less than 5 µm which are on the main particle surface.

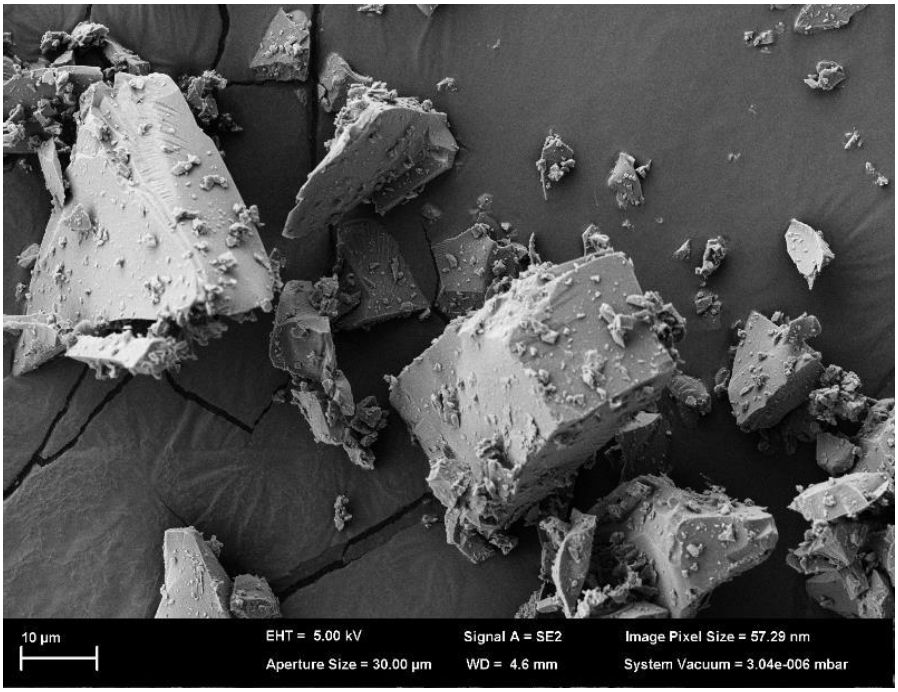

Figure 4.11 SEM image of Duramul 325F (Mullite) particles.

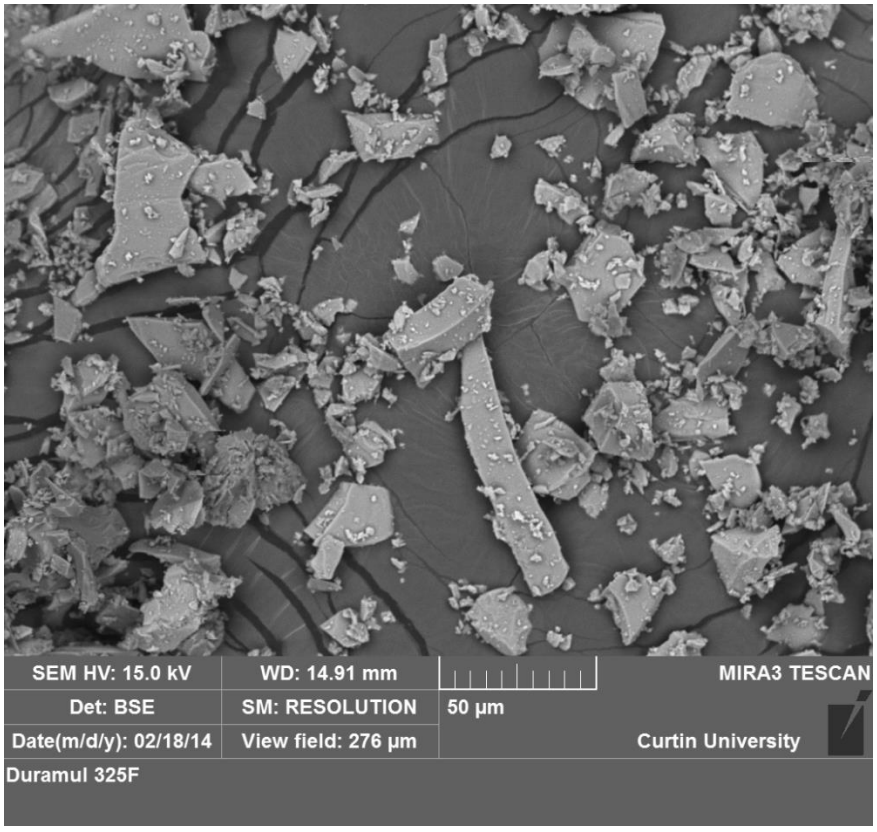

Figure 4.12 SEM back scatter electron image of Duramul 325F.

4.2.2.4 Chamotte: The material supplied had a specified particle size range of up to 1 mm. The supplied chemical composition is shown in table 4.9.

The original sample was screened through a 150 µm opening sieve with 9.47% of the feed passing this size. This finer material was needed to enable a comparison with the other materials all of which passed a 45 µm opening sieve. Only 1.06% of the original sample passed a 53 µm sieve opening and this quantity would not have been adequate for geopolymer synthesis. The passing 150 µm fraction was used for comparison purposes. The measured density of the passing 150 µm chamotte fraction was 2.7310 (0.0032) g cm^{-3} using a gas pycnometer as above.

Table 4.9 Chemical composition of up to 1 mm chamotte.

Oxide	**Weight %**
K_2O	0.14
Al_2O_3	47.24
TiO_2	0.84
Fe_2O_3	1.03
SiO_2	49.11
CaO	0.28
MgO	0.09
Other	2.27

Figure 4.13 shows the diffraction pattern for the original chamotte sample plus the calcium fluoride internal standard for QXRD evaluation. The results of QXRD are shown in table 4.10. The presence of an amorphous phase (16.4 wt. %) suggests that some reaction with alkaline activating solutions is possible.

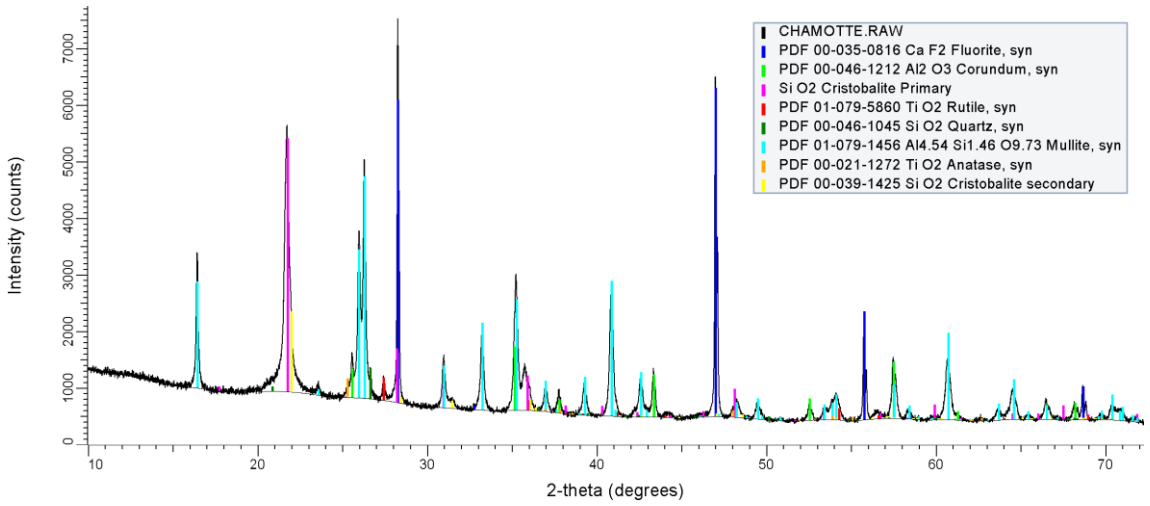

Figure 4.13 Diffraction pattern for Chamotte.

Table 4.10 Chamotte phase composition from QXRD.

Phase	**Weight %**
Mullite (PDF 01-079-1456)	52.95 (0.14)
Corundum (PDF 00-046-1212)	9.08 (0.11)
Rutile (PDF 01-079-5860)	1.35 (0.07)
Cristobalite (PDF 00-039-1425)	20.19 (0.09)
Amorphous	16.43 (0.41)

Figure 4.14 shows the irregular angular shaped particles of the screened component smaller than 150 mesh (106 µm). In figure 4.15 the extremely rough surface of the chamotte particles is clearly shown. Plate like particles are evident, which may be clay derived residues from the production firing process.

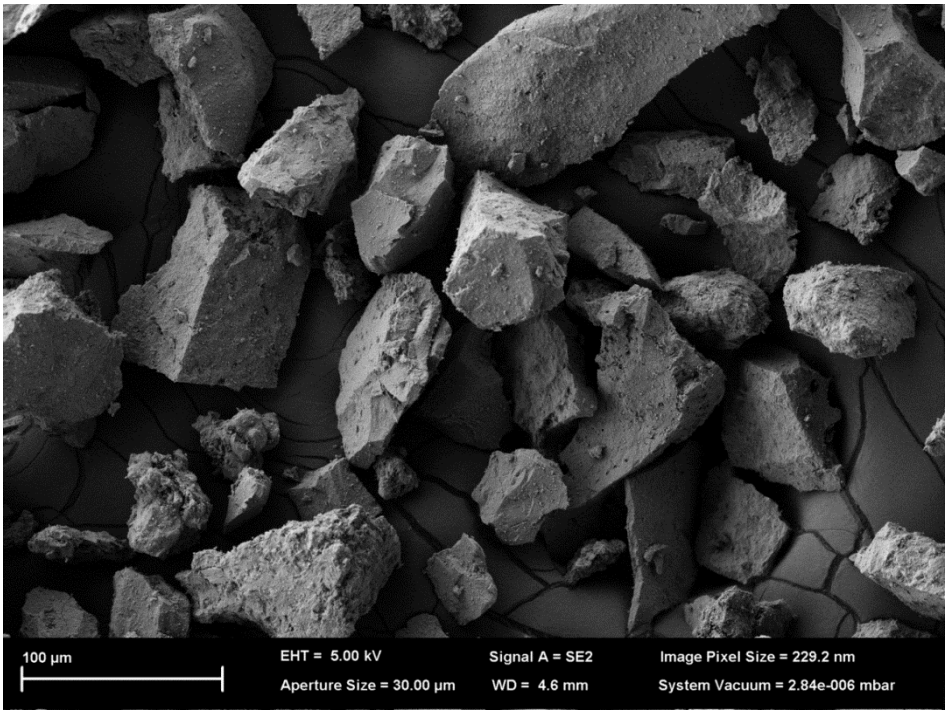

Figure 4.14 SEM image of chamotte particles (minus 150 mesh).

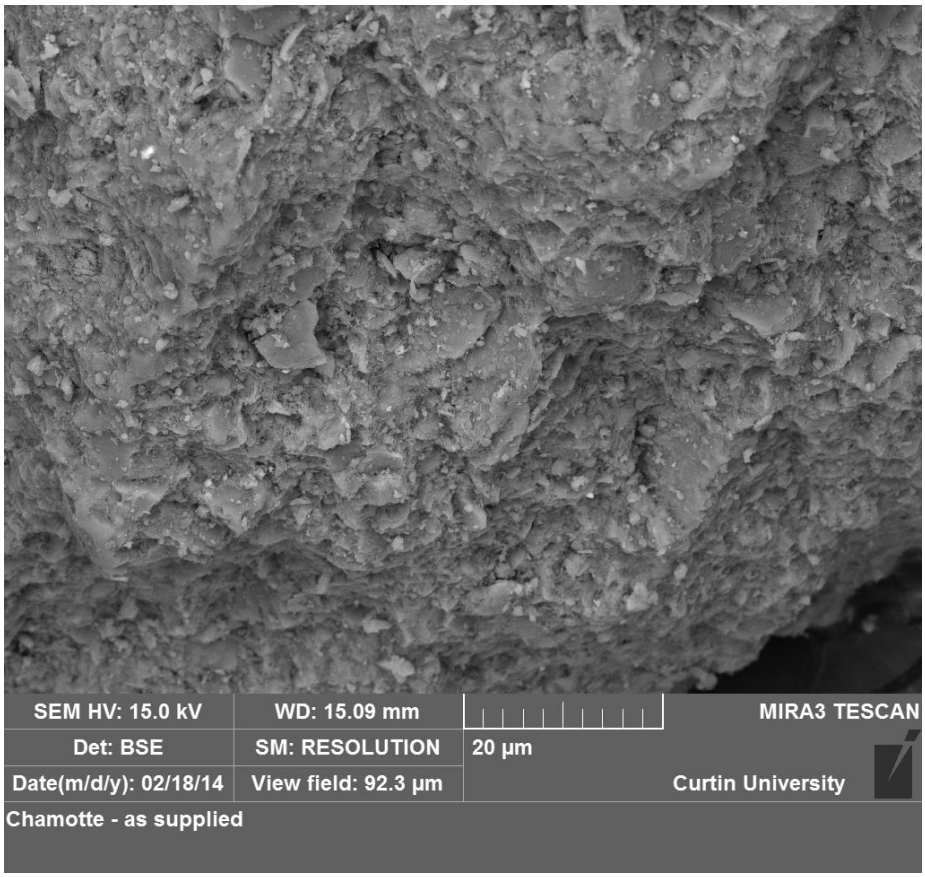

Figure 4.15 SEM back scatter electron image of Chamotte particle surface, plate-like material.

4.2.3 Fibres

The use of fibres in OPC and ceramics serves two purposes. The major area is to improve the mechanical properties of these materials particularly with respect to flexural strength and toughness. A wide range of metallic, organic polymers and inorganic fibres are typically used.

The second area of application is based on thermoplastic fibres which are added to form pathways for volatiles during high temperature excursions. These temperature excursions may be in the manufacturing process typically during firing and post curing of components or in service where passive fire resistance is the most widely used application for thermoplastic fibres. The use of thermoplastic fibres is a sacrificial methodology. However, the pathway system formed is present for subsequent temperature excursions.

Table 4.11 shows the fibres selected for this evaluation. The data is from supplier's data sheets (Nycon, 2011a, Reoco Performance Fibres, 2011, Technobasalt, 2012).

Table 4.11 Properties of fibres.

	Adfil Ignis	**RBR-16-T5/5 1%**	**NYCON AR-HD**
Composition	Polypropylene	Basalt	Alkali resistant glass
Specific Gravity	0.91	2.68	2.7
Fibre diameter	18 µm	16 µm	10 µm
Fibre length	6 mm	5 mm	13 mm
Tensile Strength	600 MPa	2.9 GPa	1.7 GPa
Melting point	165^{o}C	~1350^{O}C	1121^{o}C

The chemical compositions of the inorganic fibres shown in figure 4.12 were obtained by XRF. The presence of zirconia in the Nycon AR HD enhances resistance to alkaline solutions used in the processing of cementitious systems. The LOI values can be attributed to organic sizes applied to the fibres during manufacture to prevent clumping during storage and mixing.

Table 4.12 Chemical composition of glass and basalt fibres.

Oxide	**Nycon AR HD**	**Basalt Fibre**
SiO_2	61.6	54.9
Al_2O_3	0.35	15.2
CaO	5.94	6.92
Fe_2O_3	0.07	8.96
K_2O	0.11	2.29
MgO	0.07	4.97
Na_2O	14.6	3.88
P_2O_5	0.035	0.38
SO_3	0.07	0.04
TiO_2	0.09	0.84
MnO_2	<0.01	0.14
ZrO_2	16.2	0.02
LOI	0.75	1.18

Figure 4.16 shows the smooth surface finish of the polypropylene fibres which suggests no mechanical keying into the matrix will take place. Polypropylene is inert to alkalis, therefore no chemical bonding should take place between the matrix and fibre surface.

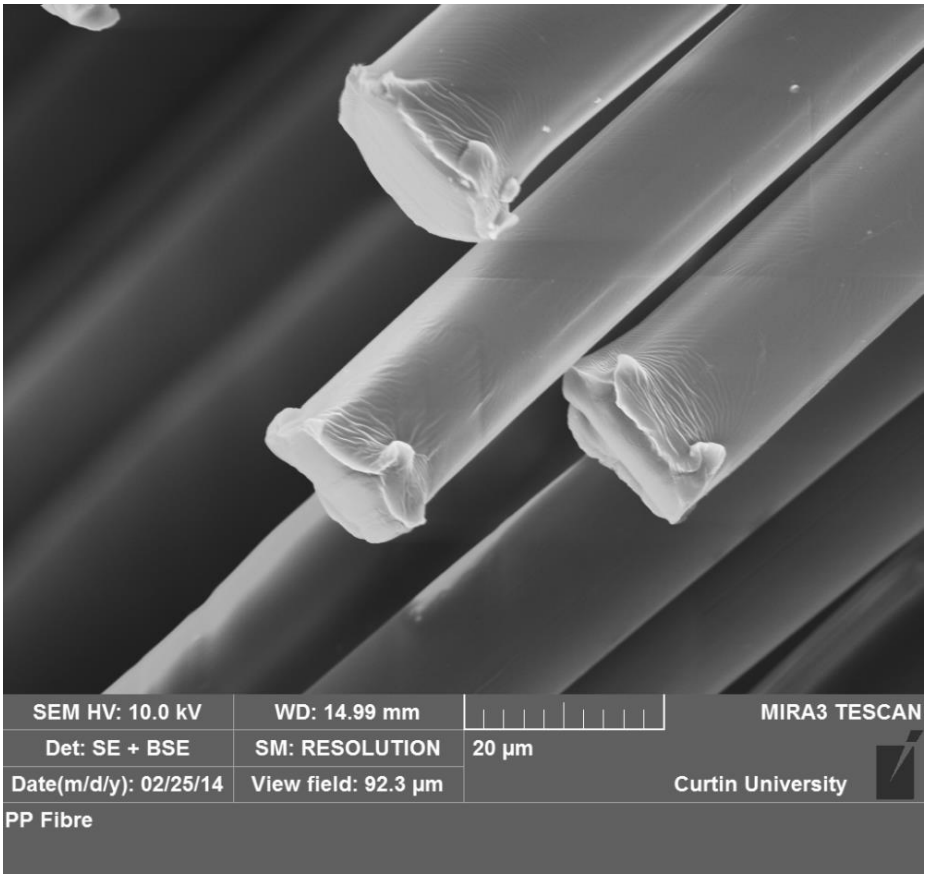

Figure 4.16 SEM image of polypropylene fibres.

In figure 4.17 the basalt fibre shows a smooth surface which would again show a limited ability to mechanically key into the matrix. However, the basalt is based on an aluminosilicate with calcium, iron, magnesium and sodium present as the major charge balancing cations (table 4.12). This may lead to the possibility of chemical attack at the basalt fibre surface by the alkaline activating solution.

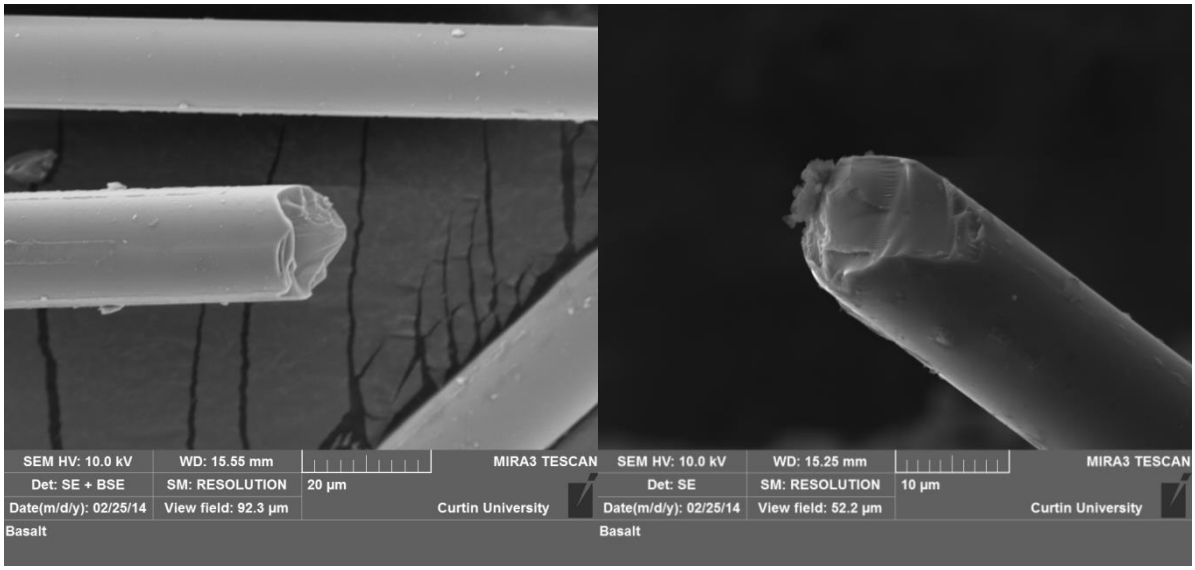

Figure 4.17 SEM images of basalt fibres.

Alkali resistant glass shown in figure 4.18 exhibit surface protrusions formed during the glass fibre drawing process. The right hand figure (BSE) could indicate the presence of a size over the inorganic fibre (lighter areas). These sizes are generally organic polymer film formers with a silane coupling agent. This size may be chemically compatible with the geopolymer matrix.

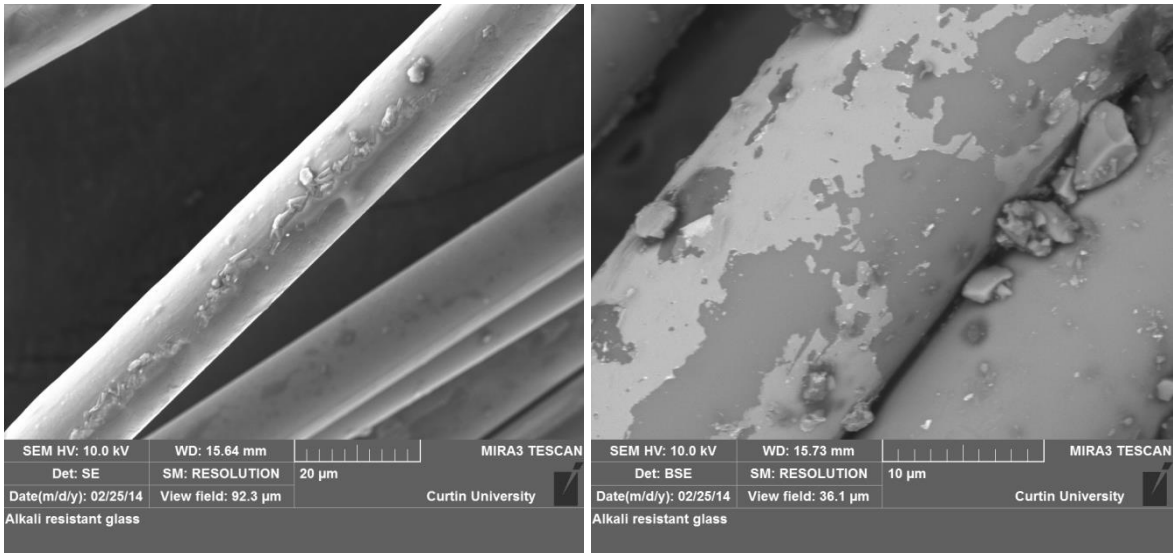

Figure 4.18 SEM images of alkali resistant glass fibres.

4.3 Alkaline activating materials

Sodium hydroxide pellets with a minimum assay of 97% were used. Deionised water was used to produce activating solutions.

PQ-D A53, sodium silicate solution was used as received from PQ Australia. The grade used was PQ-D A53 which had a supply specification of 29.4 wt. % SiO_2, 14.7 wt. % Na_2O, and 55.9 wt. % water.

4.4 Summary

A base line for comparison with geopolymer data derived from synthesis using the above materials is now available. The acicular nature of the wollastonite suggests that it could impart flexural strength properties to the geopolymer systems similar to the effect of conventional fibre addition.

CHAPTER 5

Evaluation of Geopolymer Binder for Enhanced Thermal Resistance

5.1 Introduction

In this chapter the hypothesis that reducing the targeted silicon to aluminium molar ratio (Si: Al) to less than two in a Collie fly ash based geopolymer will result in enhanced thermal resistance is tested. The evaluations to optimise the thermal resistance were based on geopolymer pastes. The physical properties achieved are also reported to confirm that systems with suitable properties are available for further thermal testing after addition of fibres and fillers.

The effect of varying sodium hydroxide and water contents on physical properties were evaluated to establish resulting physical properties. Suitable sample formulations will then be selected to determine thermal properties by dilatometer tests supported by firing samples stepwise to 1000^{o}C.

The majority of fly ash based geopolymer research has concentrated on binders with Si: Al greater than 2. The actual ratio used by workers in this field is somewhat uncertain due to limited characterisation of the precursors and the resulting paste. Development of geopolymers has focused on optimising the physical properties of the binders to compete technically with the widely used OPC concrete systems (Hardjito and Rangan, 2005). Increasing the Si: Al led to the availability of larger quantities of soluble silica from the activating solution may lead to the presence of polysilicate phases which have an adverse effect on thermal resistance (Rickard et al., 2011, Provis et al., 2012).

The choice of Si: Al (molar) was guided by the requirement for good thermal properties. Rickard et al. (2012) in previous work at Curtin showed that Collie fly ash based geopolymers with Si:Al >2 exhibited large expansive events in dilatometer evaluations and large loss of strength after firing to 1000^{o}C.

Figure 5.1 shows that these expansive events occur at a lower temperature and are of a greater magnitude as the Si: Al ratio is increased.

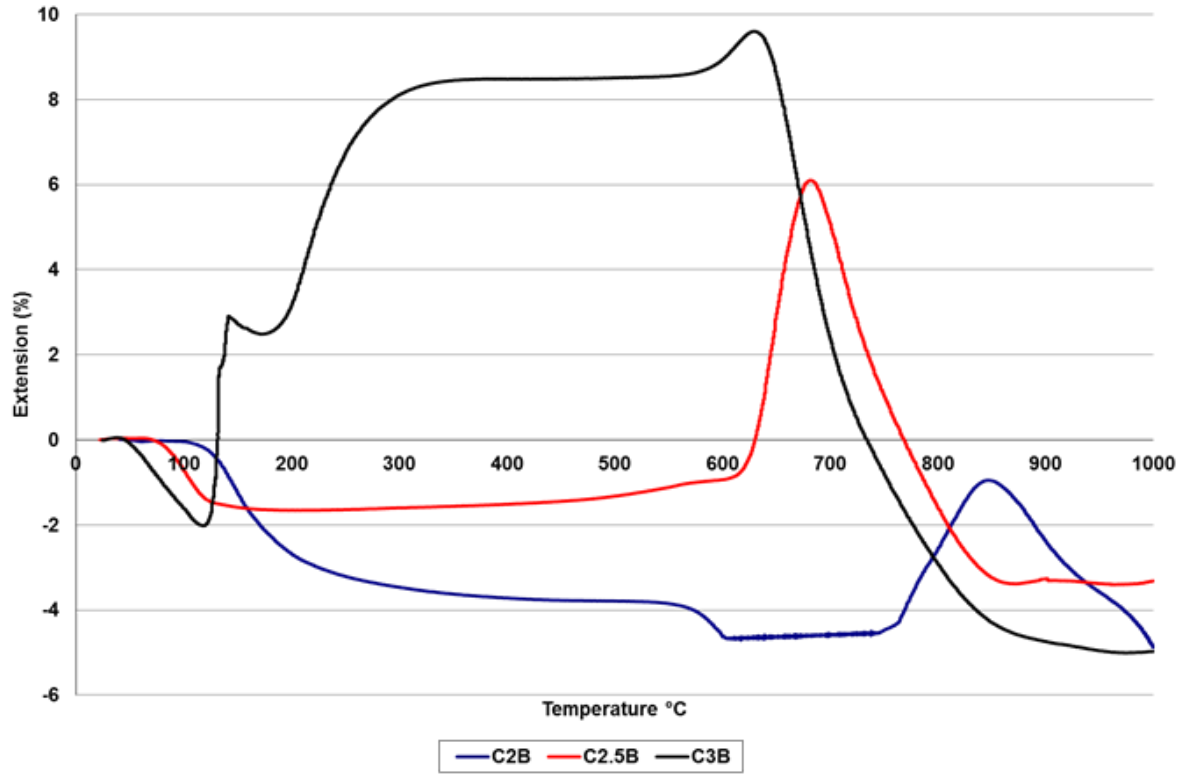

Figure 5.1 Dilatometer results from Collie fly ash geopolymers with Si: Al of 2, 2.5 and 3 (Rickard et al., 2012).

Rickard et al. (2011) also investigated the effect of firing to 1000^{o}C on the compressive strength of the geopolymers based on the paste formulations evaluated in figure 5.1. Table 5.1 shows the results of this evaluation.

Table 5.1 Influence of Si: Al on fired strength of Collie fly ash geopolymers (Rickard et al., 2011).

Si: Al molar	**(Water: Si)**	**28 day compressive strength, MPa**	**Compressive Strength after firing to 1000^{o}C, MPa**
2.0	5.0	128(9)	24(9)
2.5	4.5	53(10)	15(4)
3.0	6.0	29(3)	Too weak to test

The results in table 5.1 and figure 5.1 show that as the Si: Al is reduced from 3 to 2 the as cured compressive strength increases dramatically. Unfortunately in every case the strength

after firing to 1000^{o}C reduced significantly. The obvious question is what impact will a reduction in Si: Al, to less than 2, have on strength before and after firing?

The properties of geopolymers are dependent on many formulation variables (Williams and van Riessen, 2010, van Jaarsveld and van Deventer, 1999, Zuhua et al., 2009a, Pacheco-Torgal et al., 2008a). The chemical composition and physical characteristics of the aluminosilicate precursors and alkaline activating solutions together with processing conditions contribute to the microstructure of the final product. The microstructure will control the level of properties achieved and will continue to evolve with time and/or thermal exposure.

The amorphous aluminosilicate content of the precursors is the alkaline reactive component and its concentration and accessibility by the activating solutions will play an important role in property development. The accessibility of the amorphous aluminosilicate by the alkali solution will govern the resulting Si: Al which will normally be lower than the calculated or targeted value.

The level of alkalinity indicated by the alkali metal content and the water content play roles in both geopolymer formation and the response of the geopolymer to thermal exposure.

5.2 Calculation of Compositional ratios

The three most important ratios used in this work are:

- Silicon to aluminium molar ratio (Si: Al);
- Sodium to aluminium molar ratio (Na: Al);
- Water content, normally given as a percentage of the total weight of the formulation.

The choice of elemental molar ratios was selected over the use of oxide ratios to avoid confusion with the supplied analytical data. Both the XRF results and sodium silicate suppliers give compositional data in weight percentage of oxides. It is the preferred scientific notation to work in molarities, oxide or elemental, rather than weight percentages. Some researchers prefer to work in oxide molar ratios (Davidovits, 2008a).

In order to manage the geopolymer compositional data a simple Excel spread sheet was developed. Figure 5.2 shows an extract (in Word format) for formulation C1.82C. The weight inputs for the amorphous content of the aluminosilicate precursor, Collie fly ash, batch BB09, were obtained from the XRF and QXRD results (section 4.2.1). To simplify the calculations 100 parts by weight of the precursor were taken as the starting point in each case. By manipulating the quantities of sodium hydroxide and sodium silicate additions the compositional ratios can be determined to meet targeted or theoretical requirements. The total water content is made up of the contributions from the sodium hydroxide, the water of dissolution of the sodium silicate and added demineralised water.

The weight of relevant oxide is converted to moles of oxide by dividing by the oxide molecular weight as shown in figure 5.2. From the moles of oxide result the moles of relevant element are determined by multiplying the molar oxide result by the number of atoms of relevant element contained in one molecule of oxide as shown in figure 5.2.

The compositional ratios (figure 5.2) are then determined by division of the relevant value in the totals row.

Geopolymer formulation sheet (see text for additional explanation)

Material	Weight (g)		Al_2O_3 Wt. (g)	Al_2O_3 (moles)	Al (moles)	SiO_2 Wt. (g)	SiO_2 (moles)	Si (moles)	Na_2O Wt (g)	Na_2O (moles)	Na (moles)	Water Wt. (g)	Water (moles)
CFA BB09	100.0		13.03	0.13	0.26	24.84	0.41	0.41					
NaOH	9.0								6.98	0.11	0.22	2.03	0.11
PQ-D	10.5					3.09	0.05	0.05	1.54	0.02	0.05	5.87	0.33
Water	20.0											20.00	1.11
Totals	139.5		13.03	0.13	0.26	27.93	0.46	0.46	8.52	0.13	0.27	27.89	1.55

Collie fly ash (CFA). C1.82C

Material	Molecular Wt./Composition (wt. %)	Elemental moles/molecule
Al_2O_3	102	Al = 2
SiO_2	60	Si = 1
$Ca(OH)_2$	74	Ca = 1
Water	18	
NaOH	40 (Na_2O = 77.5%; water = 22.5%)	Na = 2
KOH	56 (K_2O = 83.9%; water = 16.1%)	K = 2
$NaAlO_2$	82	Na = 1; Al = 1
CaO	56	Ca = 1
PQ-D	Na_2O=14.7%; SiO_2=29.4%; water = 55.9%	

Theoretical Compositional Ratios

Ratio		Value
Si: Al	molar	1.82
Na: Al	molar	1.08
Water: Na	molar	5.64
SiO_2: Al_2O_3	molar	3.64
% water	Wt %	20.00

Figure 5.2 Geopolymer compositional ratio spread sheet.

The Na: Al is generally set to near 1.0 as this allows charge balancing of Al^{3+} centres by the addition of Na^{+}. The presence of alkali metal and alkali earth metal cations in the fly ash is ignored in this calculation. There is no certainty of the availability of these cations to take part in the charge balancing process.

A deficiency of Na^{+} can lead to reduced dissolution and lower geopolymer formation as demonstrated by lower strength values. An excess of Na^{+} has a detrimental effect on thermal properties where it acts as a fluxing agent promoting viscous flow with resultant shrinkage (Bakharev, 2006, Fernández-Jiménez et al., 2010).

5.3 Evaluation of compositional ratios

Trial mixes with Si: Al of <2 (Table 5.2) were made to evaluate the effect of sodium hydroxide level on thermal response in order to check the validity of the above assumptions. It should be noted that the target Si: Al of 1.82 is unlikely to be achieved as not all the fly ash will be dissolved. Thus the actual Si: Al is expected to be lower than that targeted and the measured values are shown below.

The Na: Al levels selected are a compromise between fly ash dissolution with resulting higher physical properties from the higher value and thermal properties with reduced fluxing and shrinkage at the lower value. In the case of Si: Al a value below 2 is required for improved thermal resistance in the case of Collie fly ash. The use of Si: Al of 1.82 was driven primarily by the fly ash composition together with the use of a low concentration of soluble silicon in the activating solution.

Table 5.2 Initial formulations adopted with the same Si: Al but different sodium hydroxide level.

	C1.82 A	**C1.82 B**
Collie fly ash	100.0	100.0
NaOH	5.6	9.0
PQ-D	10.5	10.5
Water	15.0	15.0
Total	131.5	134.5
Targeted Si: Al	1.82	1.82
Targeted Na: Al	0.74	1.08
% water	16.9	17.0

Quantities are in parts by weight (pbw)

Tables 5.3 and 5.4 together with figures 5.3 and 5.4 show the results obtained from the above initial evaluation.

Table 5.3 Evaluation of C1.82A after heating to various temperatures.

Heat treatment	**Compressive Strength, MPa**	**Young's Modulus, GPa**	**Weight loss, wt.%**	**Volume Shrinkage, %**
As cured	14.4 (2.4)	1.50 (0.06)	-	-
24 hrs/105^{o}C	21.8 (5.0)	1.80 (0.20)	13.37 (0.04)	1.8 (0.1)
3 hrs/300^{o}C	21.7 (1.0)	1.76 (0.15)	16.14 (0.05)	3.4 (0.2)
3 hrs/500^{o}C	20.9 (2.3)	1.90 (0.13)	16.57 (0.06)	4.1(0.1)
3 hrs/800^{o}C	19.0 (2.2)	1.83 (0.13)	16.61 (0.03)	7.5 (0.1)
3 hrs/1000^{o}C	12.5 (2.1)	1.42 (0.11)	16.76 (0.08)	18.4 (0.9)

Table 5.4 Evaluation of C1.82B after heating to various temperatures.

Heat Treatment	Compressive Strength, MPa	Young's Modulus, GPa	Weight loss, %	Volume Shrinkage, %
As cured	38.7 (4.9)	2.10 (0.2)	-	-
24hrs/105^{o}C	30.3 (5.9)	2.15 (0.05)	13.96 (0.04)	2.8 (0.5)
3hrs/300^{o}C	30.8 (6.8)	2.12 (0.07)	16.30 (0.02)	4.8 (0.2)
3hrs/500^{o}C	31.1 (10.3)	2.09 (0.29)	16.36 (0.58)	5.1 (0.2)
3hrs/800^{o}C	31.0 (3.8)	2.22 (0.16)	16.97 (0.13)	9.4 (0.3)
3hrs/1000^{o}C	19.9 (0.4)	1.63 (0.13)	16.81 (0.20)	12.6 (0.1)

Note: Residual properties were determined after a 4^{o}C min^{-1} temperature rise followed by a 3 hour hold at target. Samples were allowed to cool naturally in the furnace before determination of weight loss and linear shrinkage. The 105^{o}C test was carried out in a hot air drying oven.

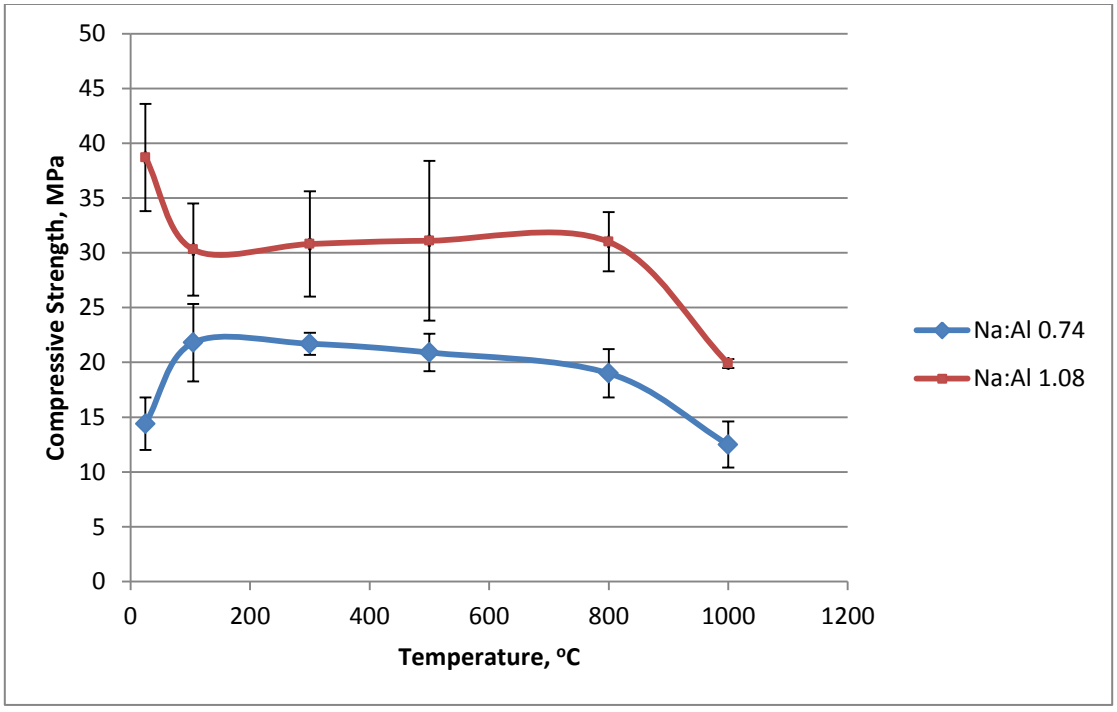

Figure 5.3 Change in compressive strength with thermal treatment for Si: Al = 1.82.

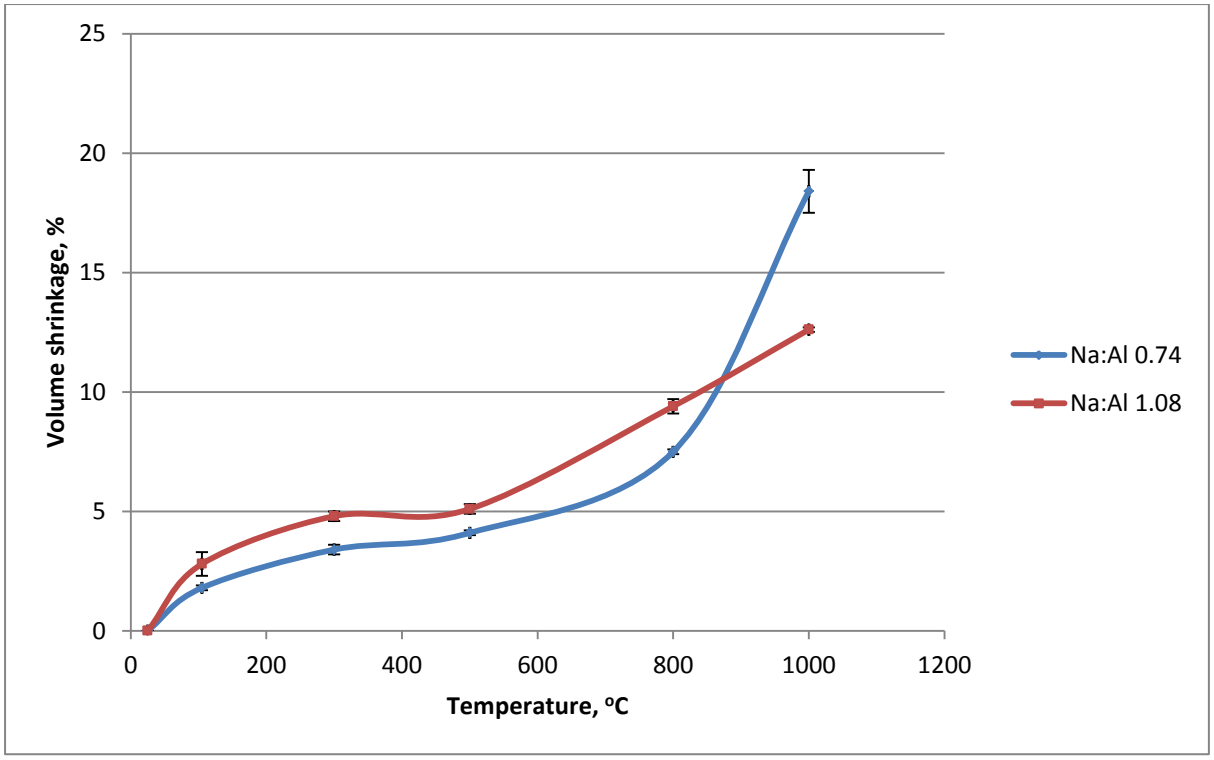

Figure 5.4 Change in volume shrinkage with thermal treatment for Si: Al = 1.82.

The lower Na: Al in C1.82A shows consistently reduced compressive strength and Young's modulus compared to C1.82B. C1.82A showed a compressive strength increase at200^{o}C, but then a gradual decrease to 12.5 MPa after exposure at 1000^{o}C. C1.82B had a compressive strength of 38.7 MPa (as cured), remained reasonably steady around 30 MPa up to 800^{o}C and then decreased to 19.9 MPa after exposure at 1000^{o}C. Figures 5.5 and 5.6 compare the microstructure of C1.82A and B, respectively. The lower sodium hydroxide content in C1.82A produced little geopolymer gel as demonstrated by the unconsolidated microstructure including fly ash spheres coated with reaction product. Conversely C1.82B demonstrated a continuous phase with embedded fly ash spheres. Weight loss, attributed to loss of water, is approximately the same for both formulations as expected from the similar water contents. C1.82A shows lower shrinkage values up to and including 800^{o}C. It is in the temperature range of 500 to 600^{o}C that the fluxing effect of sodium will be most active and hence the slightly higher shrinkage values for 1.82B are achieved. At 1000^{o}C formation of new phases will be more prevalent. The reversal in position of the shrinkage at 1000^{o}C may be attributed to the contribution of unreacted amorphous material from the fly ash converting to crystalline phase(s). C1.82A would have a higher amount of unreacted

amorphous material due to the lower amount of added alkali activator and hence a higher shrinkage value at 1000^{o}C. Figures 5.7 and 5.8 confirm this with C1.82A showing unconsolidated material around a dense phase. C1.82B has a predominantly consolidated porous structure.

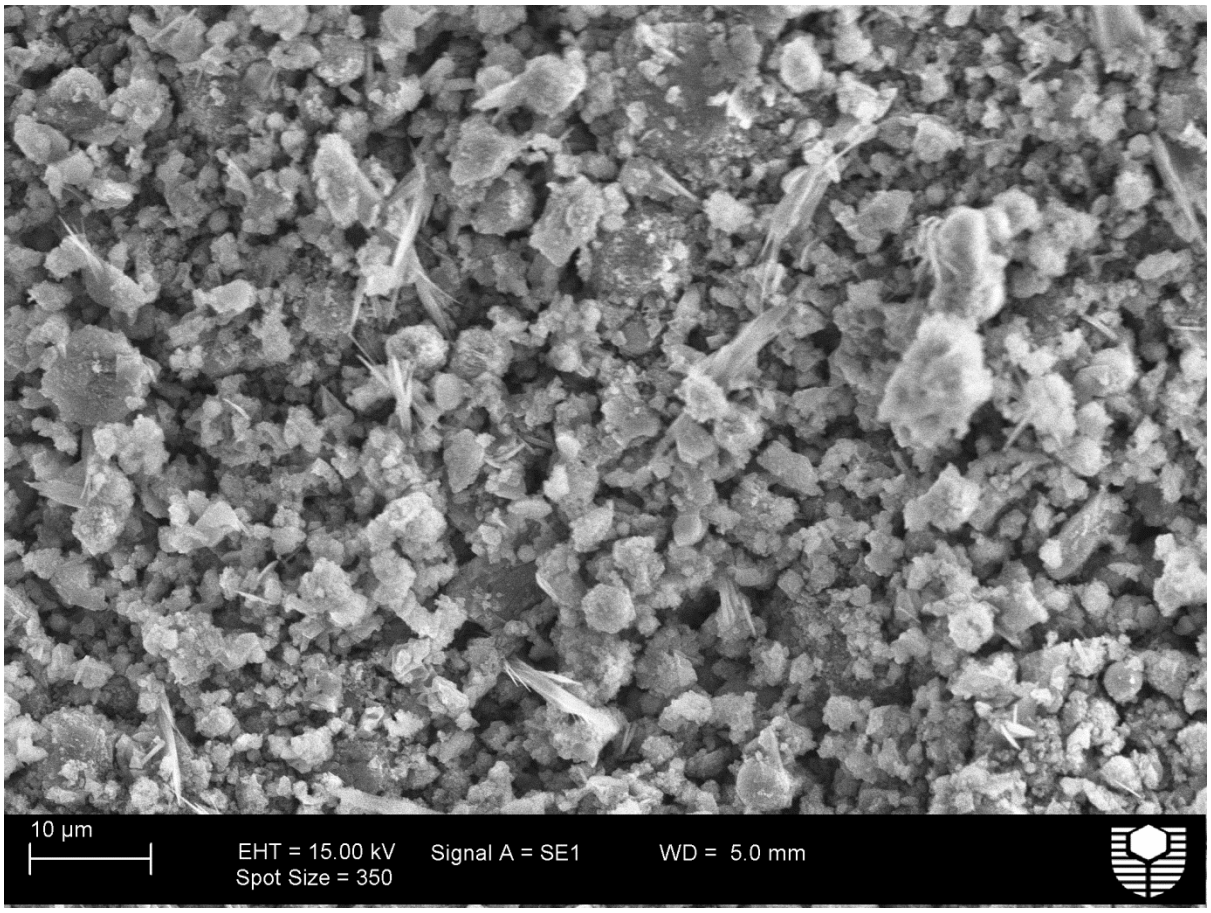

Figure 5.5 SEM fracture surface image of C1.82A (as cured).

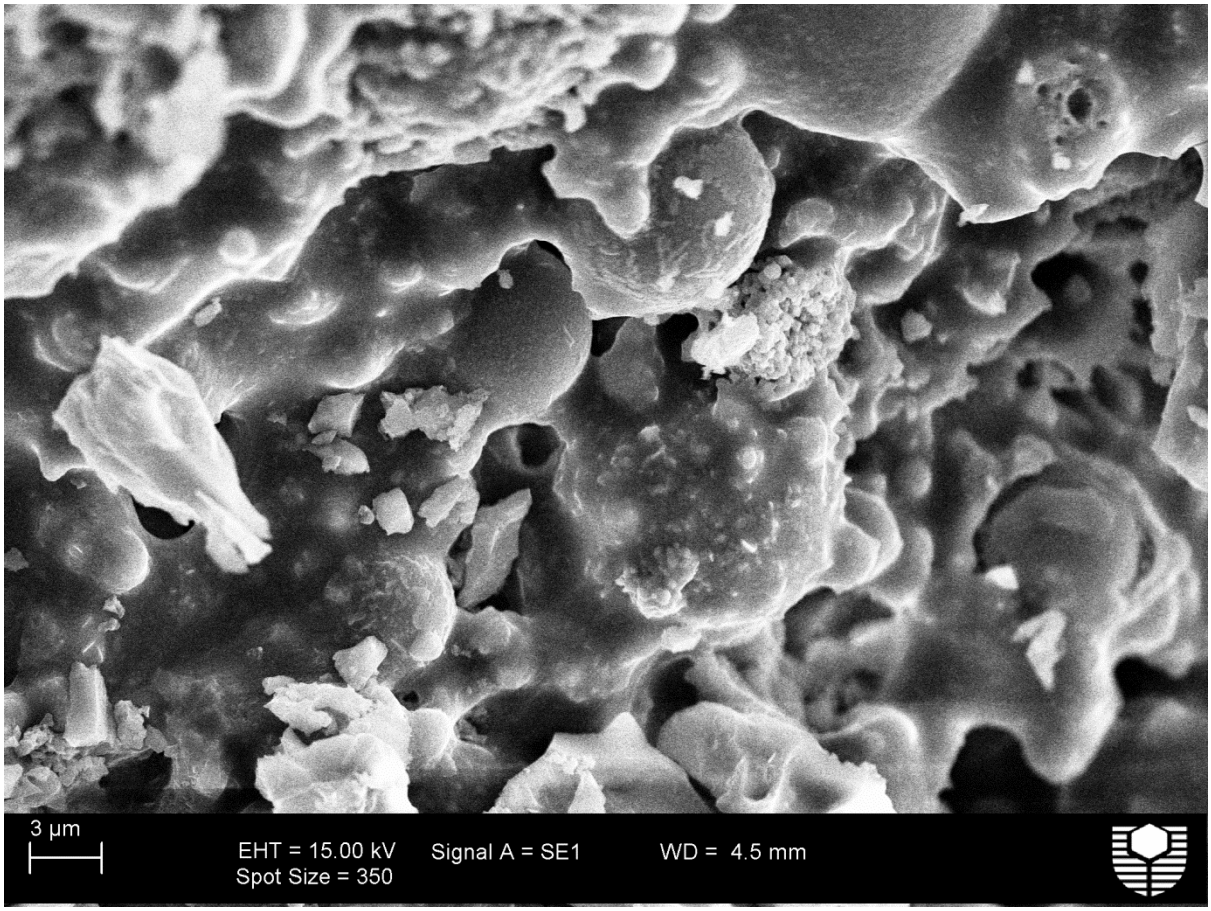

Figure 5.6 SEM fracture surface image of C1.82B (as cured).

The fluxing effect of Na^+ has largely diminished by 800^{o}C due to its capture by aluminosilicate phases and resulting formation of crystalline compounds as shown in the XRD results (table 5.9). Above 800^{o}C shrinkage is driven by thermal effects which may result in lower melt viscosity and melting of solid phases which enhance viscous flow and sintering with resultant densification.

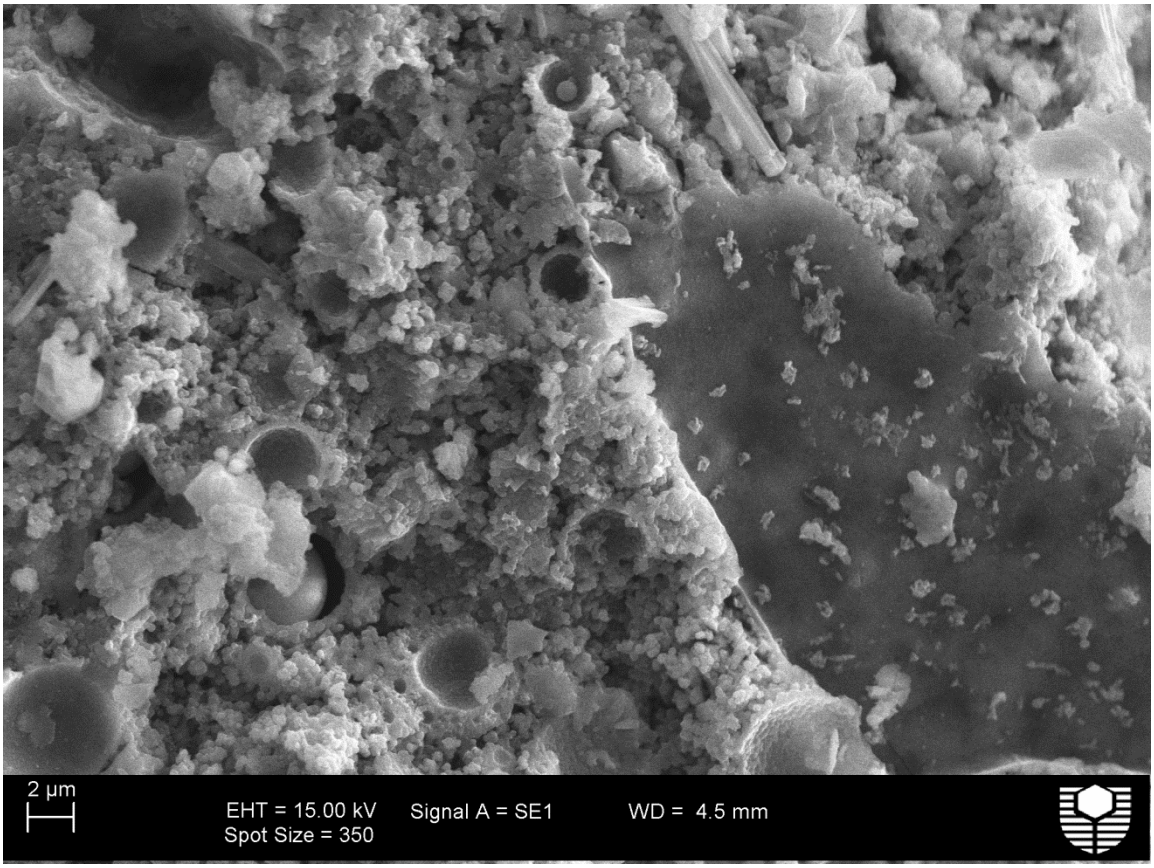

Figure 5.7 SEM fracture surface image of C1.82A microstructure after firing at 1000^{o}C.

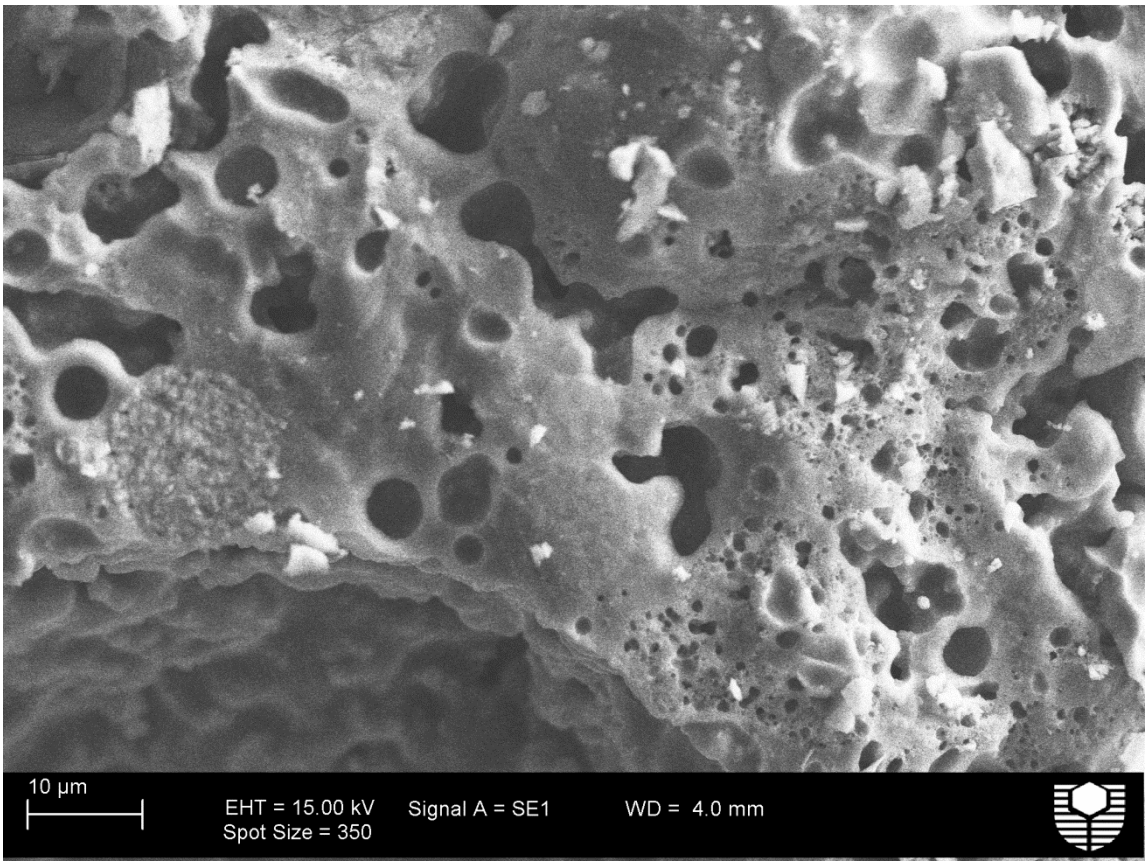

Figure 5.8 SEM fracture surface image of C1.82B microstructure after firing at 1000^{o}C.

Geopolymer with a targeted Si: Al =1.82 resulted in good retention of compressive strength after firing at 1000^{o}C. This is in contrast to Rickard's work where a large decrease in compressive strength (-81.3%), albeit from a high level, was obtained after firing at 1000^{o}C with Si: Al = 2 based on Collie fly ash. The comparison is shown in table 5.5.

As C1.82B (Na: Al = 1.08) exhibited superior as cured properties compared to C1.82A it was selected for further investigation.

Table 5.5 Comparison of Si: Al and sodium hydroxide content on residual compressive strength after firing at 1000^{o}C.

Si:Al	**Sample code**	**28 day compressive strength, MPa**	**Compressive Strength after firing to 1000^{o}C, MPa**	**% Change in Compressive strength**
2.0	C2B	128(9)	24(9)	-81.3
1.82	C1.82A	14.4(2.4)	12.5(2.1)	-1.9
1.82	C1.82B	38.7(4.9)	19.9(0.4)	-48.6
1.82	C1.82C	27.8 (3.3)	64.7(7.9)	+132

Sample C2B from (Rickard et al., 2011).

The low Si: Al selected for the geopolymer (C1.82C) has exhibited lower shrinkage (table 5.7) and an increase in strength (figure 5.9) after firing.

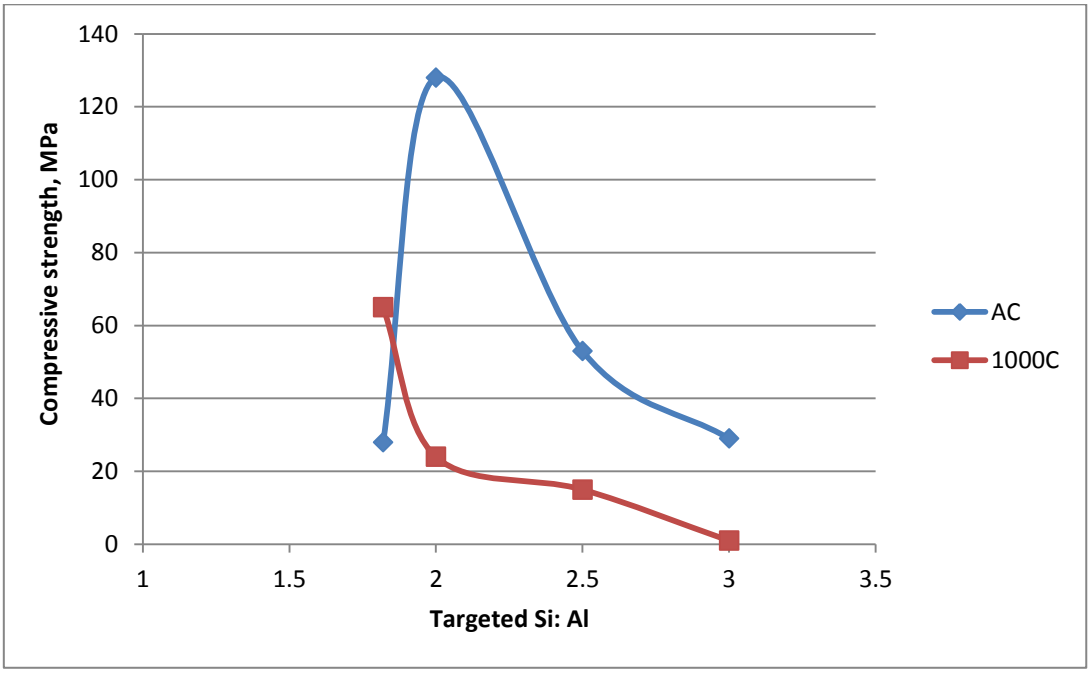

Figure 5.9 Influence of targeted Si: Al on as cured and fired compressive strength. Note that for Si: Al of 2 and above results represent the work of Rickard et al.

5.4 Effect of Water Content.

Having determined SI: Al and Na: Al for the test formulation it was necessary to ascertain the appropriate water content. The 17 wt. % water content selected for C1.82B provided adequate workability for a paste only mix but allowance had to be made for planned addition of fillers and fibres. Thus a range of different water levels were trialled to establish the extent of property changes.

Based on the results shown in Table 5.6 a value of 20 wt. % total water was chosen for the ongoing work to allow for adequate workability in filled systems while retaining an acceptable level of physical properties. This formulation was named C1.82C. Table 5.7 shows the residual properties of this system over a range of temperatures.

Table 5.6 Effect of total water content on the as cured physical properties of the C1.82 system.

Total water, Wt.%	**Compressive strength, MPa**	**Young's Modulus, GPa**	**Density g cm^{-3}**	**Porosity, % ASTM C20**
17.0	38.7 (4.9)	2.10 (0.20)	2.08 (0.01)	31.7 (0.1)
20.0	23.7 (0.9)	1.50 (0.01)	1.88 (0.02)	41.3 (0.1)
22.5	13.9 (1.3)	1.07 (0.13)	1.79 (0.02)	47.0 (0.1)
25.0	11.2 (2.9)	1.04 (0.19)	1.71 (0.01)	44.6 (0.2)

Table 5.7 Evaluation of C1.82C after heating to various temperatures.

Heat Treatment	**Compressive strength, MPa**	**Young's Modulus, GPa**	**Weight loss, %**	**Volume Shrinkage, %**
As cured	27.8 (3.3)	1.7 (0.1)	-	-
1hrs/200^{o}C	36.7 (1.7)	1.8 (0.1)	8.6 (0.9)	3.4 (0.3)
1hrs/400^{o}C	44.5 (1.7)	1.8 (0.1)	10.1 (0.4)	4.7 (0.3)
1hrs/600^{o}C	20.3 (2.4)	0.9 (0.1)	10.7 (0.2)	5.3 (0.5)
1hrs/800^{o}C	46.9 (6.2)	2.0 (0.1)	11.4 (0.1)	11.1 (0.4)
1hrs/1000^{o}C	64.7 (7.9)	2.2 (0.1)	11.3 (0.5)	15.3 (0.4)

The thermal treatment conditions for this series were changed to a 5^{o}C min^{-1} rise to target temperature followed by a one hour hold at target temperature. This was to follow the guidelines in RILEM TC129MHT (1995).

5.5 Quantitative Energy Dispersive X-ray Spectroscopy (QEDS)

Determination of the two key ratios (Si: Al and Na: Al) of polished geopolymer samples was undertaken on the EVO 40XVP SEM using 15 kV accelerating voltage. Williams et al. (2011) calculated that the 99% information depth of x-rays for a silicon, aluminium and sodium composition at this voltage was approximately 2.2 µm based on a metakaolin based geopolymer. The Inca–Analyser EDS software was used to analyse the collected X-ray

spectra. Back scattered electron images were used to select suitable areas for evaluation. A geopolymer phase is considered to be one containing silicon, aluminium, sodium and oxygen. The sodium content of Collie fly ash is only 0.33 wt. % (as Na_2O) and therefore the majority of sodium found in the EDS evaluation must have originated from the activating solution. Several other non-geopolymer components in the samples were also evaluated.

From 23 spectra containing silicon, aluminium and sodium Si: Al was found to range from 0.43 to 12.95 and Na: Al from 0.07 to 2.48. These wide ranging elemental ratios are due to either a non- uniform dissolution and condensation process or experimental difficulties related to interaction volumes of the beam and sample. As analysis regions were carefully selected it is believed that the large variations are likely due to non-uniform dissolution and condensation of the precursor and the reaction products respectively (refer figure 5.10). Further investigation of the data reveals that three classifications can be identified

- Aluminium rich species with Si: Al <1
- Geopolymer phases with 2< Si: Al >1
- Silicate rich species with Si: Al >2

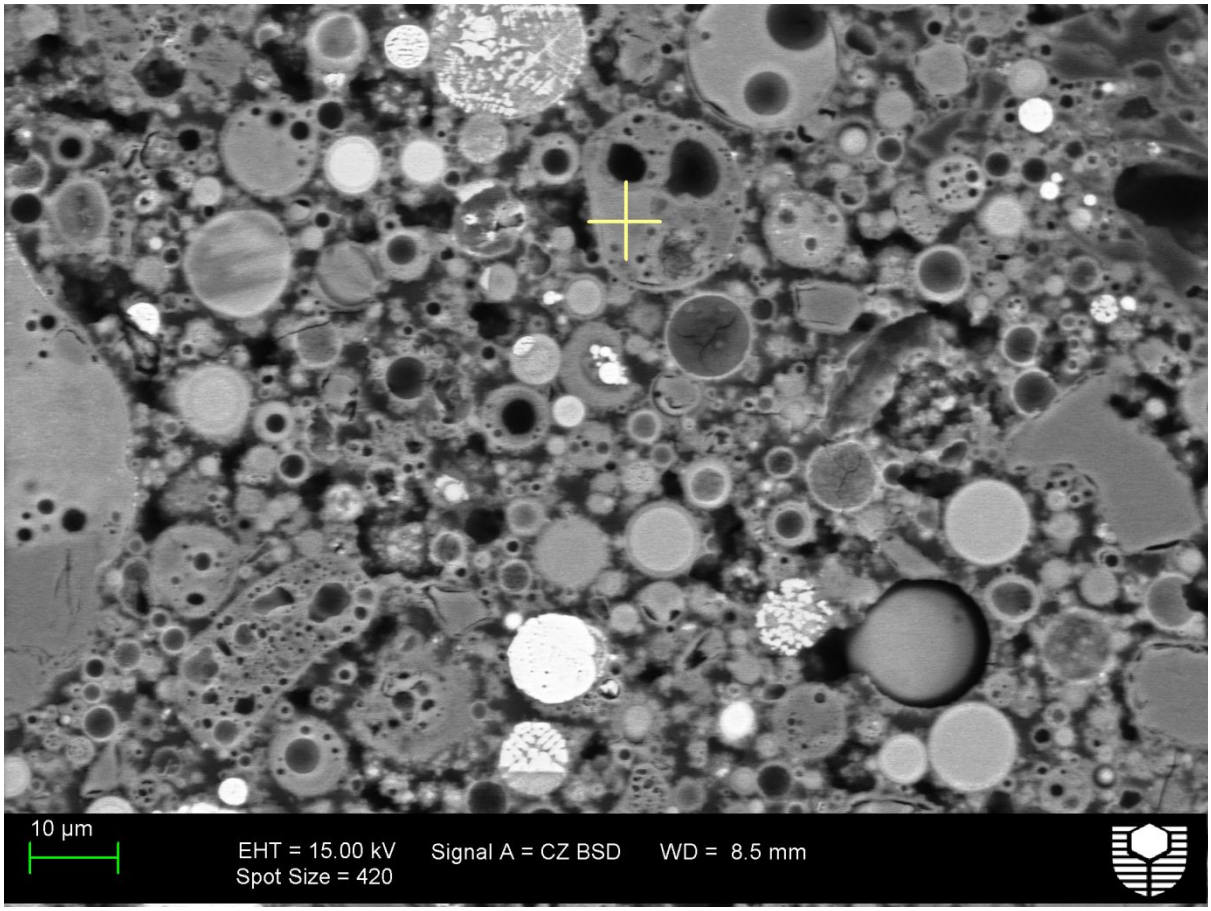

Figure 5.10 SEM image of polished as cured geopolymer sample showing the heterogeneous microstructure encountered in EDS evaluations. The yellow cross indicates position of one particular EDS measurement

The results for the geopolymer phases gave an average Si: Al = 1.25 (12) and a Na: Al = 0.50 (27) for as cured samples. The range of results was 1.15 to 4.34 and 0.41 to 0.77, respectively. The molar ratio of oxygen to (silicon + aluminium) was 2.06. This is within experimental error of the theoretical value of 2.

NOTE: The theoretical value is based on the silicate and aluminate entities being present as tetrahedron as would be expected if geopolymer (and silicate from the activating solution) is present. Each silicon or aluminium centre is surrounded by four oxygen atoms; two between the centres and four towards other centres (which also share these oxygen atoms). This gives half of the four plus two in the centre equals four, divided by two centres is two. Higher values than two may be attributed to T-OH content of the system, where T is aluminium or silicon.

The average measured Si: Al is lower than targeted value of 1.82 as not all the aluminosilicate (from the fly ash which had an amorphous Si: Al of 1.62) has dissolved. This is evident from the SEM images showing residual spherical and partly reacted particles. The results within a sample were wide spread which is indicative of limited transport of precursor components through the system and the heterogeneity of the precursor particles. The individual results reflect the composition of the precursor in that region and not the overall average. The increase in system viscosity as dissolution and condensation occurs will further limit transport of reactive entities. For such an inhomogeneous system it is obvious that 23 spectra are not sufficient to obtain the Si: Al for the system. However, the data collected reveals a great deal about the variability of the microstructure composition.

EDS spectra collected on 5 areas of a sample fired at 1000^{o}C gave Si: Al = 2.76 (1.56) and Na: Al = 0.61 (0.14). Ranges were 1.15 to 4.34 and 0.41 to 0.77 respectively. The microstructure is more consolidated, with iron containing fly ash particles still visible (refer figure 5.11).

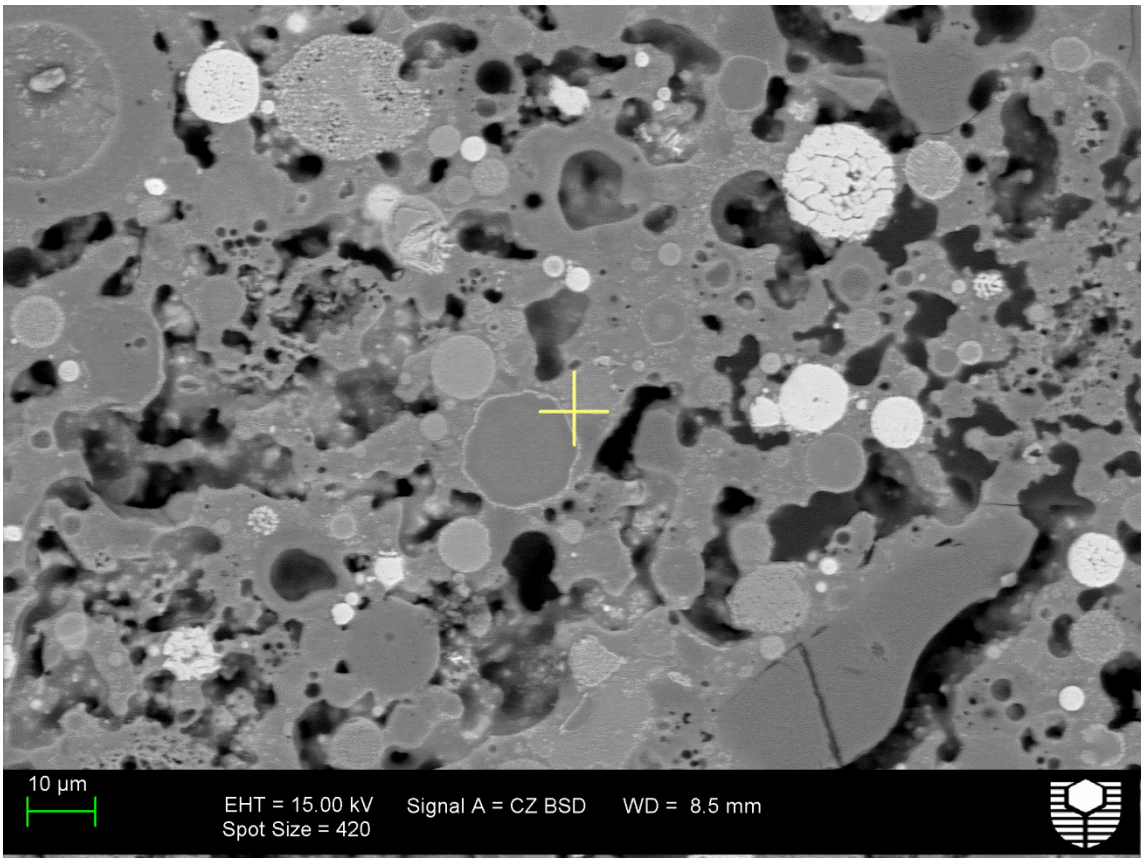

Figure 5.11 SEM image of polished fired geopolymer sample showing a more consolidated microstructure with coarser porosity.

The measurement of sodium using EDS is complicated by the high diffusion coefficient for sodium ions. Figure 5.12 (Atkins et al., 2006) illustrates the high mobility of sodium ions. The gradient of the line is proportional to the activation energy for diffusion. Application of the electron beam to the sample can impart sufficient energy to the sodium ions in the sample that enable them to readily diffuse away from the interaction volume of the electron beam with the sample.

Sodium not required for charge balancing will reside in the pore water. On vacuum drying the sample this water is evaporated leaving the sodium to be deposited on the pore walls and not measurable as part of the aluminosilicate gel unless captured in the interaction volume of the electron beam.

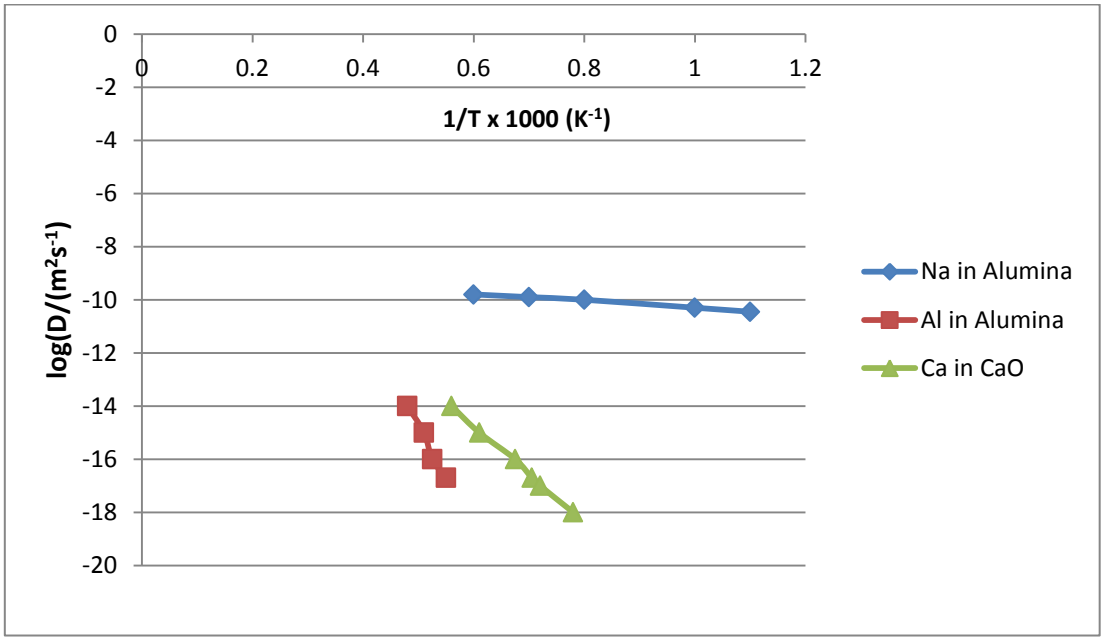

Figure 5.12 Diffusion coefficient as a function of inverse temperature for mobile ions in selected solids adapted from Atkins et al. (2006).

Aluminium rich spectra: measurement of 12 spectra revealed a Si: Al of less than 1 (a range of 0.4 to 0.9 with a mean of 0.67 (0.16). These had associated Na: Al between 0.05 and 0.39 with a mean value of 0.22 (0.09). These spectra, with one exception, also showed the presence of calcium, titanium and iron.

It is hypothesised that these spectra represent early dissolved aluminium atoms, from the fly ash, attached to monomeric and dimer silicate entities from the activating solution. In this work the quantity of added silicate is relatively low. If Lowensteins rule (Catlow et al., 1996) is to be obeyed only silicate entities may add to aluminium growth centres. If no silicate entity is available in the vicinity of the aluminium growth centre further polymerisation reaction is not possible.

Silicate rich spectra: Two spectra showed high silicon to aluminium ratios of 23.05 and 12.91. This is indicative of long segments of silicate tetrahedra with few (one) aluminium tetrahedra either inserted in the silicate chain and acting as a potential branch point along the chain, or at the end of a chain. The Na: Al ratios associated with these two spectra are 1.58 and 2.48, respectively. These high values can be explained by charge balancing of the aluminium centre and sodium anions associated with the silicate structure from the activating solution. Table 5.8 shows the results for spectra with Si: Al greater than 2. The Na: Al are all greater than 1 which is required for aluminium charge balancing. The additional sodium is associated with the charged silicate species which are derived from the activating solution. The Si: Na has been reported by weight to allow comparison with the sodium silicate solution modulus which was 2 for the product used.

The spectra reported on in this section represent aluminosilicate amorphous oligmers which can evolve into three dimensional geopolymer phases by reaction with aluminium growth centres if transport and kinetic barriers can be overcome e.g. during firing.

Table 5.8 EDS spectra analysis for silicon rich regions.

Spectrum number	**Si: Na wt.**	**Si: Al molar**	**Na: Al molar**
54	1.80 (11)	2.15 (12)	1.46 (11)
55	2.07 (11)	2.48 (12)	1.47 (10)
56	2.73 (16)	3.6 (20)	1.61 (13)
57	2.11 (13)	2.61 (14)	1.52 (11)
66	2.26 (13)	2.83 (15)	1.53 (11)

Four spectra were obtained on residual fly ash particles, which may have had some geopolymer reaction product present. Table 5.9 shows these results. The wide range of both reported elemental ratios confirms the heterogeneity of the fly ash particles. The amorphous Si: Al for the fly ash (from XRF and QXRD) was 1.62 (0.18) and the target Si: Al for the geopolymer was 1.82.

Table 5.9 Quantitative EDS results for remnant fly ash particles in C1.82 (as cured).

Spectrum number	Si:Al molar	Na:Al molar	NOTES
35	1.4 (7)	0.96 (7)	$Na_2Al_2Si_3O_{10}$
36	1.79 (10)	0.0	Also present: Ca = 9.54 wt.%; Fe = 11.6 wt.%
37	0.89 (3)	0.19 (2)	Metal cation: Al = 0.32 molar
59	1.11 (6)	0.08 (2)	Also present: Ti = 3.0 wt.%; Fe = 4.5 wt.%

Analysis of spectrum 35 results indicates the following formula: $Na_2Al_2Si_3O_{10}$. We are possibly seeing a coating of geopolymer reaction product on the fly ash surface. The sodium content of the raw fly ash is 0.33 wt. % and cannot account for the much higher level of sodium which must have been derived from the activating solution.

NOTE: Results of the analysis can be used to derive empirical formula of a compound. The analysis results give the elemental proportions by mass. The number of moles of each atom present can be determined from the element molar mass. The simplest whole number ratio by moles is used to write the empirical formula.

Spectrum 36 contained no sodium, but contained both calcium and iron. The particle appeared very bright in the BSE image and is thought to be a calcium-iron aluminosilicate which will show low response to alkali activation. Chen Tan et al. (2009) analysed Collie fly ash to determine the alkali reactive content and found that "quantitative evaluation of minerals by scanning electron microscopy (QEMSEM) results showed an increase of iron oxide concentration in the undissolved component with increase in dissolution time leading to the conclusion that the amorphous iron does not participate in the geopolymerisation process". If the Fe is present as Fe–Al spinels or Fe-rich glass, the presence of Fe may inhibit dissolution, lessening the amount of Si and Al available for geopolymerisation.

Spectrum 37 is aluminium rich with a marked deficiency of sodium cations for charge balancing. Other metal cations (K, Ca, Fe) can also perform the charge balancing role. If these are taken into account we arrive at a metal cation: Al molar ratio of 0.32. There is a possibility that some of the aluminium is present as six co-ordinated and does not require charge balancing cations as does four co-ordinate aluminium. This material may exhibit a spinel structure, XY_2O_4, where X is a cation with a charge of +2 and Y is a cation with a charge of +3. In spinel, $MgAl_2O_4$, aluminium is present in octahedral sites.

Spectrum 59 appears to be an aluminosilicate with titanium and iron charge balancing cations which is insoluble in the activating solution.

Part of the amorphous aluminosilicate content is locked in alkali insoluble species and cannot take part in the geopolymerisation reactions.

The disparity in Na: Al measured on geopolymer phases and silicate rich phases could indicate differences in the bound state of the sodium cations. The sodium in the silicate rich phases appears to be less mobile than in the geopolymer phases. The sodium in the

geopolymer phases may undergo repulsion by aluminium cations thereby reducing the activation energy for the diffusion of the sodium ion during EDS measurements. However, the sodium cations associated with silicate centres are expected to be tightly bound due to electronic attraction resulting in higher activation energies being required to initiate diffusion in this case.

It appears that the utilisation of low quantities of soluble silicate in the activating solution is required to synthesise fly ash geopolymers with low targeted Si: Al giving rise to low volumes of geopolymer together with aluminium and silicate rich phases. These latter phases may also contribute to the matrix strength at room temperature. It is postulated that these latter two phases are more active during firing at elevated temperatures where they are able to sinter and (inter)react to form densified phases which give rise to the increased compressive strength seen above.

The wide range of results obtained in this evaluation can be attributed to measuring across regions within the sample which are not comparable in precursor or reaction product composition. The initial fly ash microstructure is also widely heterogeneous which adds further to the structural complexity of these alkali activated systems.

5.6 Phase Analysis

Table 5.10 summarises the results of XRD data from as cured and fired samples C1.82A, B and C. Mullite, quartz, hematite and magnetite are remnants from the fly ash and appear throughout the results. The appearance of hydroxysodalite in the as cured samples seems to be dependent on the sodium level. Its presence in the 1000^{o}C fired samples is surprising as its thermal stability in the range of 600 to 800^{o}C is reported before converting to nepheline (Fernández-Jiménez et al., 2010, Bakharev, 2006).

Several workers (Criado et al., 2007, Fernández-Jiménez and Palomo, 2005) have shown that reduced amounts of silica in the activating solution increases the formation of crystalline/zeolite type materials such as hydroxysodalite and herschelite. These crystalline materials are produced at the expense of geopolymer gel and contribute to lower physical properties than those found in higher silica content systems.

Table 5.10 Crystalline phases identified using XRD in as cured and fired samples.

Geopolymer system	As Cured	Fired 1000^{o}C
C1.82A Na: Al = 0.74 Water = 16.9 wt.%	Mullite Quartz Hematite Magnetite	Mullite Quartz Hematite Albite Nepheline Hydroxysodalite Sodium silicate
C1.82B Na: Al = 1.08 Water = 17 wt.%	Mullite Quartz Hematite Magnetite Hydroxysodalite	Mullite Quartz Hematite Nepheline Anorthite Hydroxysodalite
C1.82C Na: Al = 1.08 Water = 20 wt.%	Mullite Quartz Hematite Magnetite Hydroxysodalite Hatrurite	Mullite Quartz Hematite Magnetite Nepheline Hydroxysodalite

PDF numbers:

Mullite	04-016-1587	Quartz	00-033-1161
Hematite	01-076-4579	Magnetite	04-015-9120
Nepheline	00-035-0424	Sodalite	04-009-5213
Hatrurite	04-009-8695	Albite	01-080-1094
Sodium silicate	00-038-0019	Anorthite	01-076-0948

NOTE: The PDFs were used in the search match process for phase identification. Peak positions and relative intensity are used to confirm the search result. The presence of

sodalite is unlikely and is more probably hydroxysodalite (as reported above) for which there is currently no PDF. Hydroxysodalite has therefore been used in table 5.10. The structure differences revolve around sodalite having two chlorine atoms whilst hydroxysodalite has two hydroxyl groups which is the more likely structure.

5.7 Dilatometer Evaluations

The thermal expansion/shrinkage of samples was measured in the dilatometer to allow comparison with Rickard's results (figure 5.1) and assess the impact of using a lower Si: Al to formulate geopolymer.

Figures 5.13 and 5.14 show the smaller shrinkage events for the lower Si: Al system. These smaller shrinkages may be attributed to reduced active (silica) species in the C1.82 activating solutions compared to Rickard's work. Figure 5.13 shows C1.82C which contains 20 wt. % water (water: Si = 3.3), a lower level than that utilised in figure 5.1 tests.

The increase in water content has little effect on shrinkage up to around 550^{o}C. The onset of high temperature shrinkage occurred at a lower temperature (579^{o}C verses 623^{o}C) for the higher water content samples. A glass transition temperature of 762^{o}C was measured for C1.82B (17 wt. % water) compared to 693^{o}C for C1.82C (20 wt. % water). Jewell et al. (1993) reported that small amounts of water can cause the glass transition temperature (Tg) of a sodium aluminosilicate glass to decrease by up to 60^{o}C. The ΔTg passes through a maximum for a glass composition near to Al^{3+}: Na^{+} = 1. Viscosity and viscous flow activation energy was also significantly decreased by an increase in water content.

The intersection of tangents to the dilatometer curves may be used to estimate the glass transition temperature. Pan and Sanjayan (2012) used this technique to determine the softening points of fly ash based geopolymers. Additional information is given in chapter 6.

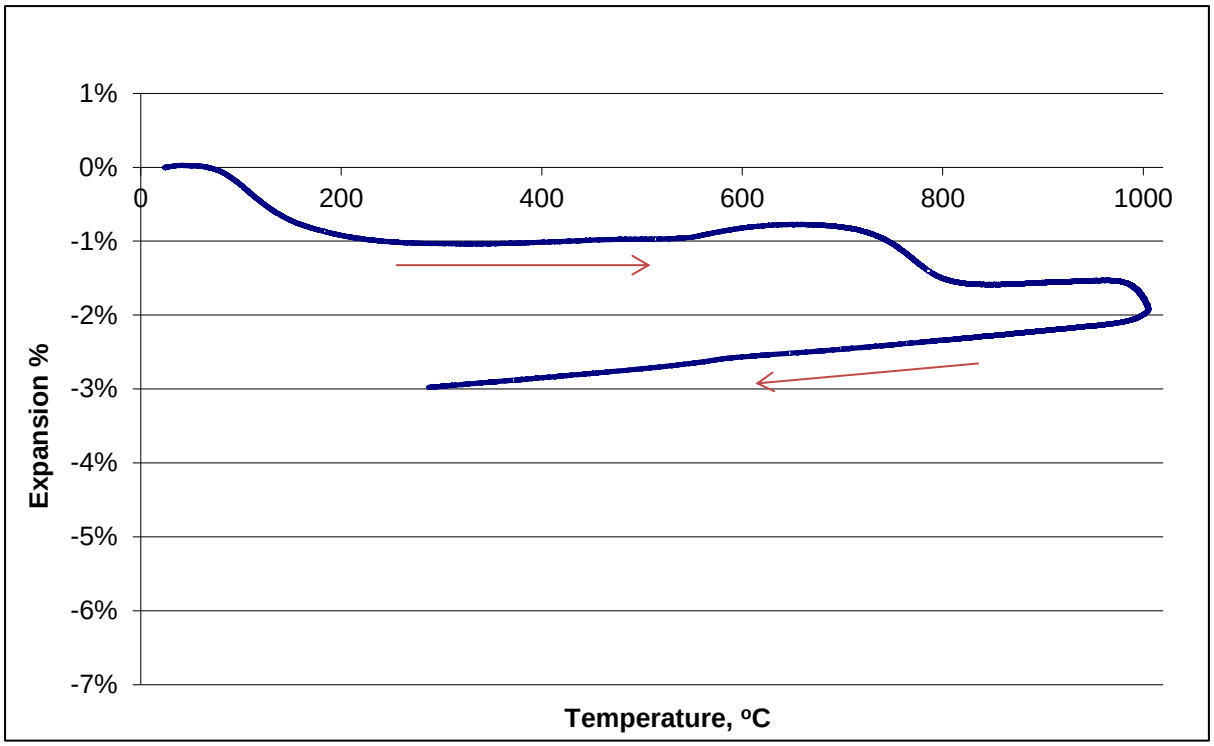

Figure 5.13 Thermal shrinkage for C1.82B (17 wt. % water).The lower section of the curve is recorded in cooling mode.

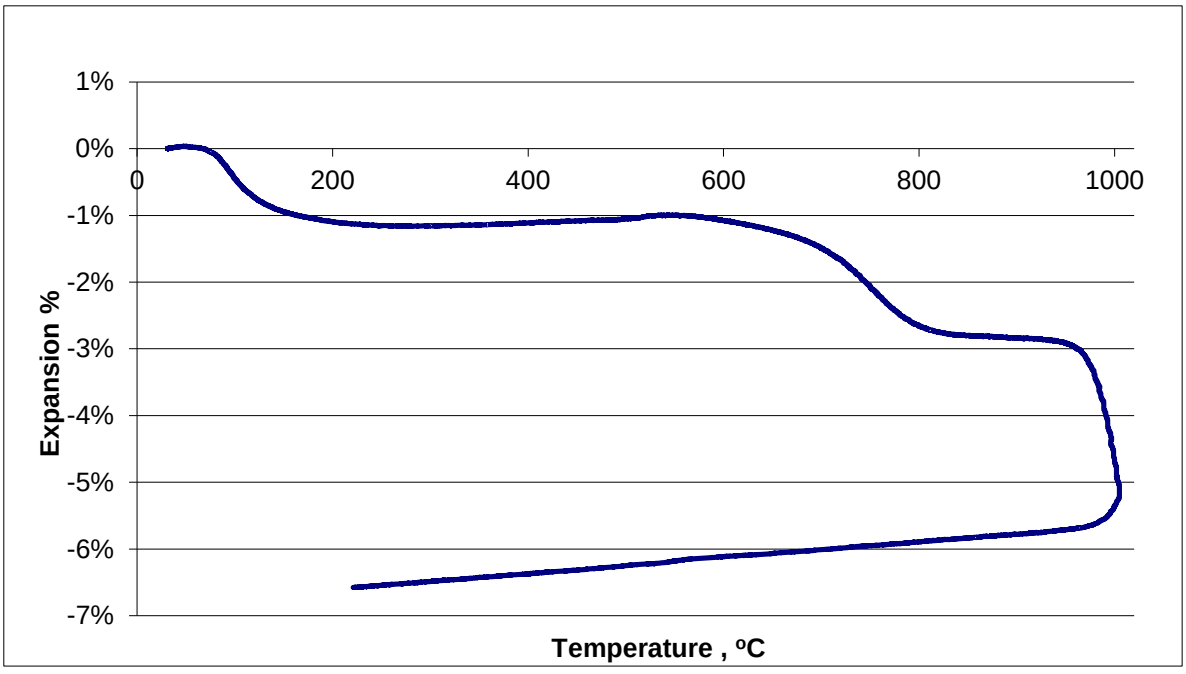

Figure 5.14 Thermal shrinkage for C1.82C (20 wt. % water).

5.8 Summary

The low Si: Al selected for the geopolymer has exhibited low shrinkage and an increase in strength after firing (figure 5.9). The influence of water content and sodium concentration in this chosen system has been demonstrated and values of 20 wt.% water content and a Na: Al = 1.08 selected for further work.

The utilisation of the chosen Si: Al has shown a poorly developed as cured geopolymer network with the presence of zeolite phases in the 17 and 20 wt. % water containing systems. The sparse nature of the geopolymer binder made interpretation of the QEDS data difficult. The QEDS indicates regions of aluminium rich material. This can possibly be attributed to early release of aluminium monomers from the fly ash which reacts with added silicate forming precipitates on the fly ash surface which hinder further dissolution of precursors. These modified precursors show activity as the temperature is increased forming a more consolidated microstructure consistent with increases in compressive strength. Increasing temperature will increase diffusion of activating solution remnants through the deposited reaction products.

The attainment of a specific targeted Si: Al is difficult due to the following reasons; alkali insoluble glass, encapsulated soluble glass, precipitation of reaction product on previously exposed soluble glass and activating solution transport properties. Reducing the Si: Al further (by reduction of added silicate solution) would probably yield low strength geopolymers due to low dissolution of precursors and higher zeolite contents. The latter is detrimental to physical properties and thermal resistance.

CHAPTER 6

THERMAL PROPERTIES OF GEOPOLYMER COMPOSITES

6.1 Introduction

It is possible to routinely produce materials with impressive thermal properties by careful selection of starting material and complex processing. However, in this work we are endeavouring to utilise industry by-products which can impose constraints on what we can achieve regarding workability or end properties.

This chapter presents the results of the thermal characterisation of Collie fly ash geopolymer paste with targeted silicon to aluminium ratio of 1.82, which has been modified with a range of thermally stable fillers and fibres. The paste system used in these evaluations was the outcome of the work reported in chapter 5. Change in sample dimensions with increasing temperature was evaluated by a dilatometer and additionally by evaluation of a range of properties measured before and after firing samples in a furnace.

The various systems are characterised by measuring the following properties: compressive strength, Young's modulus, flexural strength, porosity, density, mass changes, thermal expansion/COTE and thermal conductivity.

Samples described as "as cured" (AC) denotes that no firing or post cure cycle (PC) has been applied to the samples after the standard curing regime and prior to testing, or "fired" indicating exposure in a furnace at the temperature specified. The furnace temperature increase was $5^{o}C\ min^{-1}$ with a one hour hold at target temperature followed by natural cooling back to ambient temperature in the furnace.

Publications and presentations

This chapter is the basis in part on the following publications and presentations:

1. Strategies to control the high temperature shrinkage of fly ash based geopolymers. Les Vickers, William D.A. Rickard, Arie van Riessen. Thermochimica Acta, 580 (2014) 20–27.

2. The Effect of Speciality Fibres and Fillers on the Thermal Properties of Fly Ash based Geopolymers.

Les Vickers, William D.A. Rickard, Arie van Riessen. 10th Pacific Rim Conference on Ceramic and Glass Technology. June 2013, San Diego, USA

3. Thermal Properties of Geopolymers. Les Vickers, William D.A. Rickard, Arie van Riessen. CAMS 2014, Sydney, Australia

6.2 Thermal expansion

Linear thermal expansion measurements in the following work were determined using an alumina push rod dilatometer over the range 25 to 1005^{o}C at a heating rate of 5^{o}C min^{-1}. The intersection of tangents to the curve (figure 6.1) in regions of large change was used to determine the temperature of any major shrinkage events in the data.

Shrinkage of moulded samples was determined by firing in a furnace in 200^{o}C steps up to 1000^{o}C.

The following sample descriptions apply throughout this chapter:

C1.82C	Geopolymer paste control containing no filler
ALOX 5 and ALOX 10	5 and 10 vol. % alumina filler in C1.82C
WOL 5 and WOL 10	5 and 10 vol. % wollastonite filler in C1.82C
MUL 10	10 vol. % synthetic mullite filler in C1.82C
CH 10	10 vol. % chamotte filler in C1.82C
ARG 1.5	1.5 vol. % alkali resistant glass fibre in C1.82C
BAS 1.5	1.5 vol. % basalt fibre in C1.82C

Figure 6.1 shows the temperature regions for the various stages of the evolution of the geopolymer structure as the temperature increases. The descriptions of the six regions (I to VI) are listed below in figure 6.1. The red lines shown in figure 6.1 are tangents to the dilatometer curves. Moving vertically to the temperature axis gives the temperature of this shrinkage occurrence. Pan and Sanjayan (2012) used this technique to determine the softening points of fly ash based geopolymers.

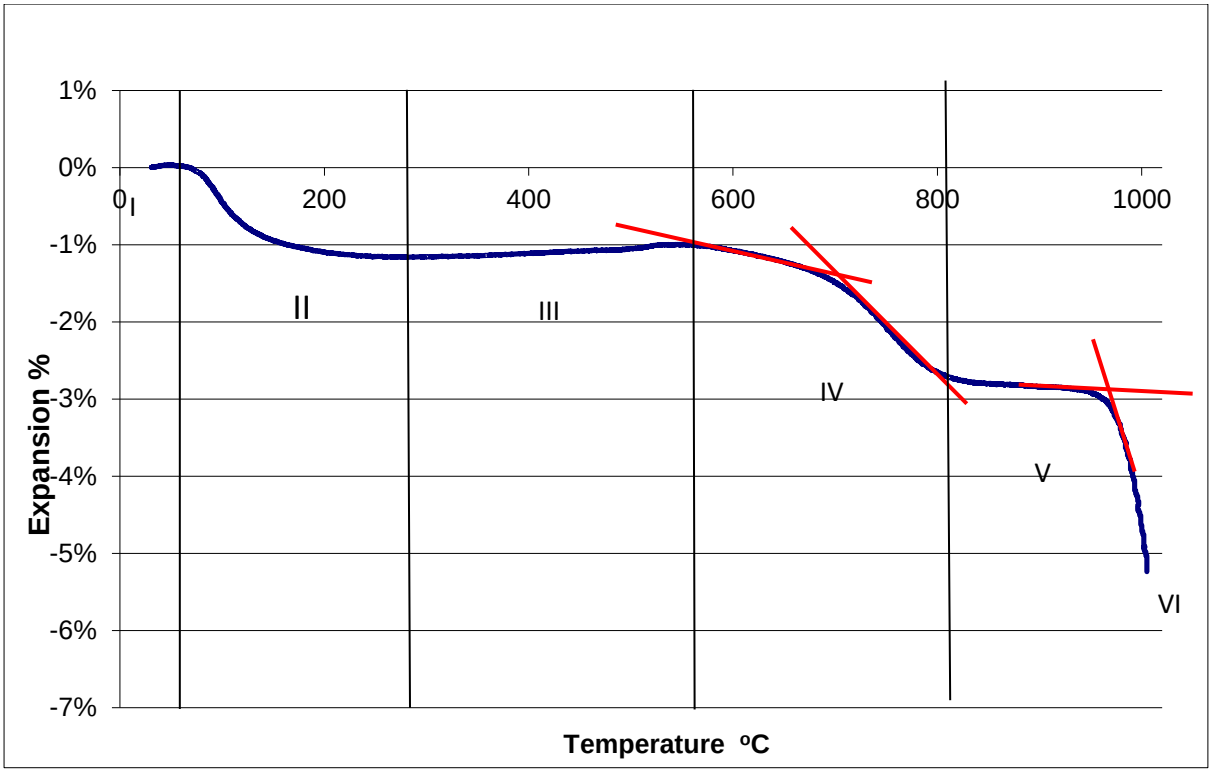

Figure 6.1 Temperature regions showing typical linear shrinkage of geopolymer paste investigated in this work.

Region I: Slight expansion with some free water loss

Region II: Dehydration (of free water) shrinkage occurring

Region III: Limited thermal expansion occurring with dehydroxylation

Region IV: 1st densification zone via viscous sintering.

Region V: Thermally stable region, exhibiting a low level rate of expansion or shrinkage depending on the formulation.

Region VI: 2nd densification zone via crystallisation.

This type of regional description of thermal expansion was first proposed by Duxson et al. (2007a) who described four temperature regions for sodium based metakaolin geopolymers. He used regions I to III above, but had a region IV from 700 to 1000°C. Rickard et al. (2009) extended this regional classification to six zones for fly ash geopolymers and the work reported in this thesis follows this classification.

The temperature range of each zone and the associated shrinkage will be dependent on the formulation composition (Si: Al, water content, filler type and addition level).

6.2.1 The effect of fillers

The effect of fillers on thermal shrinkage is shown in figures 6.2 and 6.3. Figure 6.2 illustrates the initial work using alumina and wollastonite at two levels of addition compared to the control paste (C1.82). Two additional candidate fillers, mullite and chamotte were acquired in small quantities and are compared to the previous two fillers at 10 vol. % in figure 6.3.

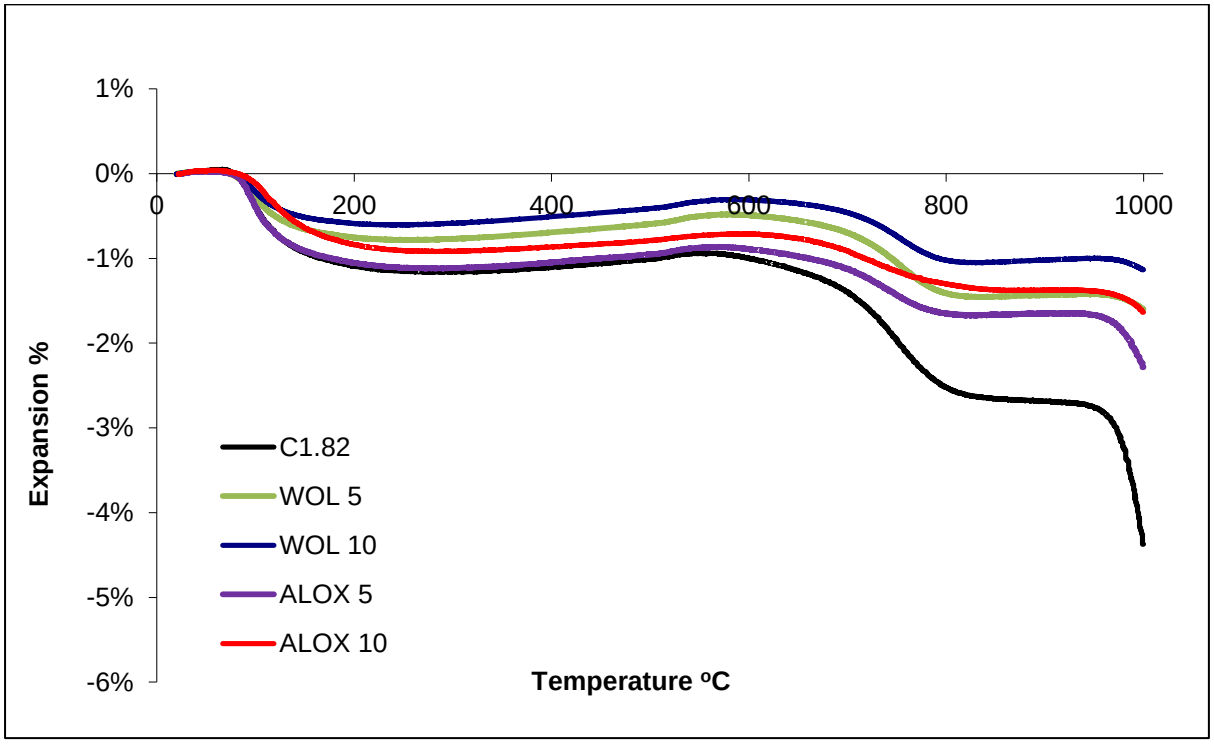

Figure 6.2 Thermal expansion for geopolymer composites with 5 and 10 vol. % alumina and wollastonite.

The initial shrinkage event (region II) between approximately 60^{o}C and 300^{o}C is attributed to loss of free (physically bound) water. The addition of fillers with a positive COTE results in lower shrinkage values in this region. Minor expansion (Region III) now occurs up to the range of 550^{o}C to 600^{o}C before the commencement of further shrinkage (Region IV) up to 800^{O}C. The shrinkage here is attributed to viscous flow of the amorphous glasses aided by the fluxing ability of sodium entities. A plateau of relatively small change (Region V) now occurs for the filler containing specimens up to the next inflexion point which is followed by

further shrinkage (Region VI). The value of the shrinkage reported at 1005°C is the temperature limit of the equipment. The critical data points are presented in Table 6.1.

The addition of filler controls the level of shrinkage over the entire temperature range and also favourably influences the rate of shrinkage as shown by the smaller gradients of the curves for filled samples compared to the control (C1.82) in shrinkage region IV.

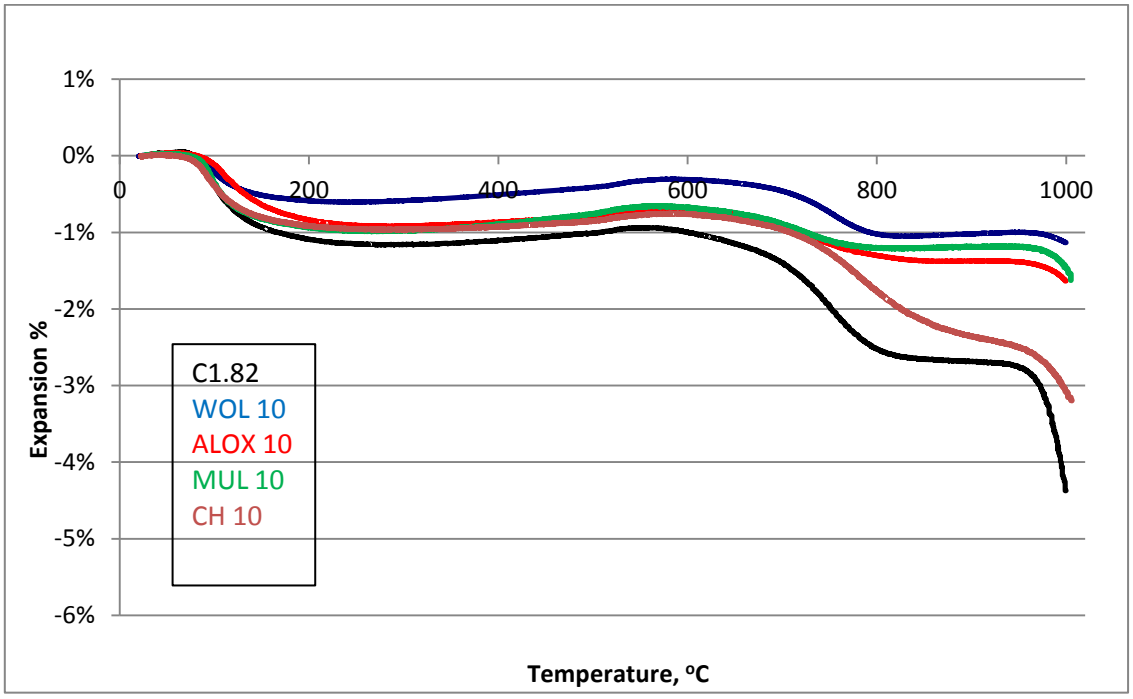

Figure 6.3 Thermal expansion for geopolymer composite with 10 vol. % selected fillers.

Table 6.1 Critical data points extracted from dilatometry curves.

	Region II Maximum linear shrinkage, %	**Region IV Inflexion point, °C**	**Region V Linear shrinkage,% Curve gradient**	**Region V Width of region °C**	**Region V-VI Boundary temperature, °C**	**Region VI Linear shrinkage at 1000 °C, %**
C1.82	1.14(3)	698	2.75 (8)/-ve	176	975	5.23
WOL 5	0.78 (2)	708	1.45 (4)/+ve	187	996	1.64
WOL 10	0.61 (2)	703	1.0 (3)/+ve	198	982	1.55
ALOX 5	0.83 (2)	687	1.53 (4)/+ve	187	974	2.24
ALOX 10	0.98 (3)	678	1.49 (4)/+ve	183	980	1.67
CH 10	0.96 (3)	720.5	2.36 (7)/-ve	129	974	3.19
MUL 10	0.96 (3)	721	1.19 (3)/+ve	211	985	1.60

Uncertainties in temperature values are +/- 5°C. The number in parenthesis is the uncertainty in the last figure of the adjacent value.

The maximum linear shrinkage in region I is controlled by the amount of freely evaporable water and the material stiffness, (Young's modulus) of the material. The inflexion point in region IV is an indication of the system's softening point. Beyond this point viscous flow is prevalent. Region V shows relatively stable behaviour in terms of thermal expansion with small gradient changes. The width of this region gives some indication of the stability. The temperature of region V to VI boundary is commencement of a second shrinkage event.

In the region of thermal stability (Region V), WOL, ALOX and MUL showed a slight expansion with increasing temperature. C1.82 (no filler) showed slight shrinkage and CH showed marked shrinkage. Chamotte is produced by firing clay, and contains 16 wt. % amorphous material and it is this material which is melting with the resulting shrinkage. The amorphous material in the chamotte is stable to approximately 730^{o}C after which it starts to melt resulting in shrinkage. This temperature value may well be influenced by the presence of sodium entities from the activating solution which exhibit strong fluxing capabilities. Figure 6.4 shows the transformation of unconsolidated CH10 containing coated fly ash particles and small amounts of geopolymer at 600^{o}C through 800^{o}C to 1000^{o}C with increasing consolidation from viscous flow together with coarsening of the porosity.

SEM images over the temperature range to 1000^{o}C, in 200^{o}C steps, are shown in Appendix B for all the systems shown in table 6.1.

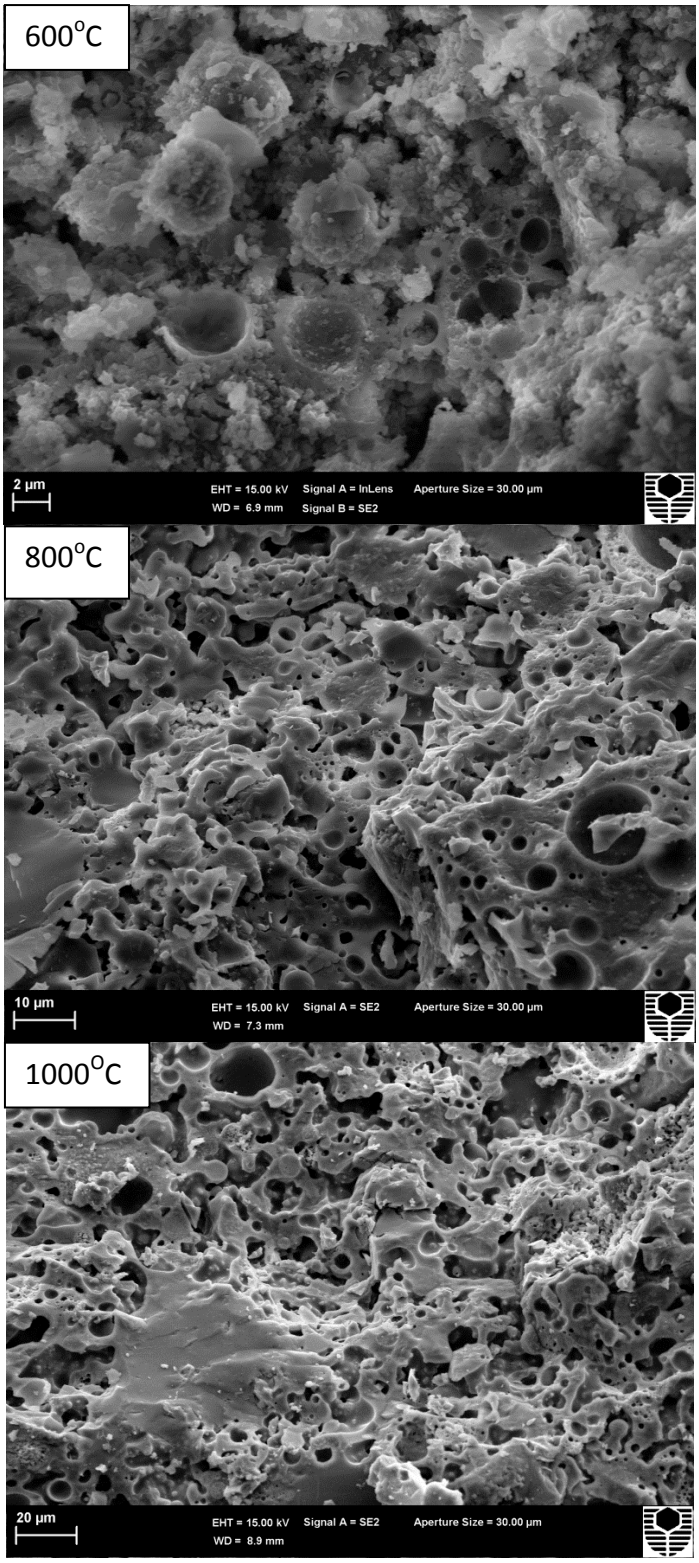

Figure 6.4 CH10 SEM images after heating at 600, 800 and 1000°C showing increased consolidation and coarsening of pores.

In table 6.2 all systems show an increase in compressive strength and Young's modulus after firing at 1000^{o}C. Both WOL 5 and 10 show very good fired (1000^{o}C) compressive strengths of 53 and 101 MPa respectively. This is attributed to viscous flow and sintering giving a compact microstructure. Reaction of the wollastonite with the geopolymer matrix to form a consolidated transition zone is also proposed as a contributing factor. Figures 6.12 and 6.13 plus additional information in Appendix C describes this effect.

Table 6.2 Summary of results for thermally stable fillers.

	Density, AC g cm^{-3}	**Compressive Strength, AC MPa**	**E_o, AC GPa**	**CS after heating to 1000^{o}C, MPa**	**E_o, after heating 1000^{o}C, GPa**	**Volume shrinkage % after heating 1000^{o}C**
C1.82	1.91 (0.01)	27.9 (3.3)	1.67 (0.07)	64.7(12)	2.24 (0.07)	15.3 (0.4)
WOL 5	1.92 (0.02)	29.7 (1.6)	1.63 (0.10)	52.8 (5.8)	2.28 (0.02)	9.50 (0.3)
WOL 10	1.98 (0.01)	41.6 (3.3)	1.80 (0.11)	101.4 (3.2)	2.13 (0.08)	8.19 (0.2)
ALOX 5	2.04 (0.03)	24.0 (1.8)	1.60 (0.06)	51.0 (6.53)	2.17 (0.06)	10.6 (0.4)
ALOX 10	2.04 (0.04)	29.9 (3.1)	1.81 (0.07)	106.3 (2.9)	2.51 (0.02)	10.1 (0.5)
CH 10	2.03 (0.04)	29.9 (4.1)	2.09 (0.11)	50.8 (6.1)	2.71 (0.09)	12.9 (0.1)
MUL 10	2.06 (0.03)	22.7 (1.2)	2.01 (0.06)	52.6 (12.9)	2.66 (0.22)	7.6 (0.6)

The ALOX 5 and 10 also show good fired (1000^{o}C) compressive strength of 51 and 106 MPa. It has been difficult to identify these small alumina particles in SEM images, attributed to coating of particles with geopolymer reaction product. The surface chemistry and morphology of the alumina particles could have played a role during firing to give a similar consolidated transition zone to that seen with the wollastonite systems. The ALOX 5 AC image shows loosely adhered GP reaction product on the alumina surfaces. Fired images (figures 6.5 and 6.6) are showing a more compact microstructure around the few potentially identified alumina particles.

The as cured density values for ALOX 10 and WOL 10 are lower than that calculated using the law of mixtures. The mini-cone flow of these two composites was much reduced compared to the paste control, to the extent that ALOX 10 showed no flow. These viscous

mixes showed air entrainment, even after vibration, with a corresponding reduction in density.

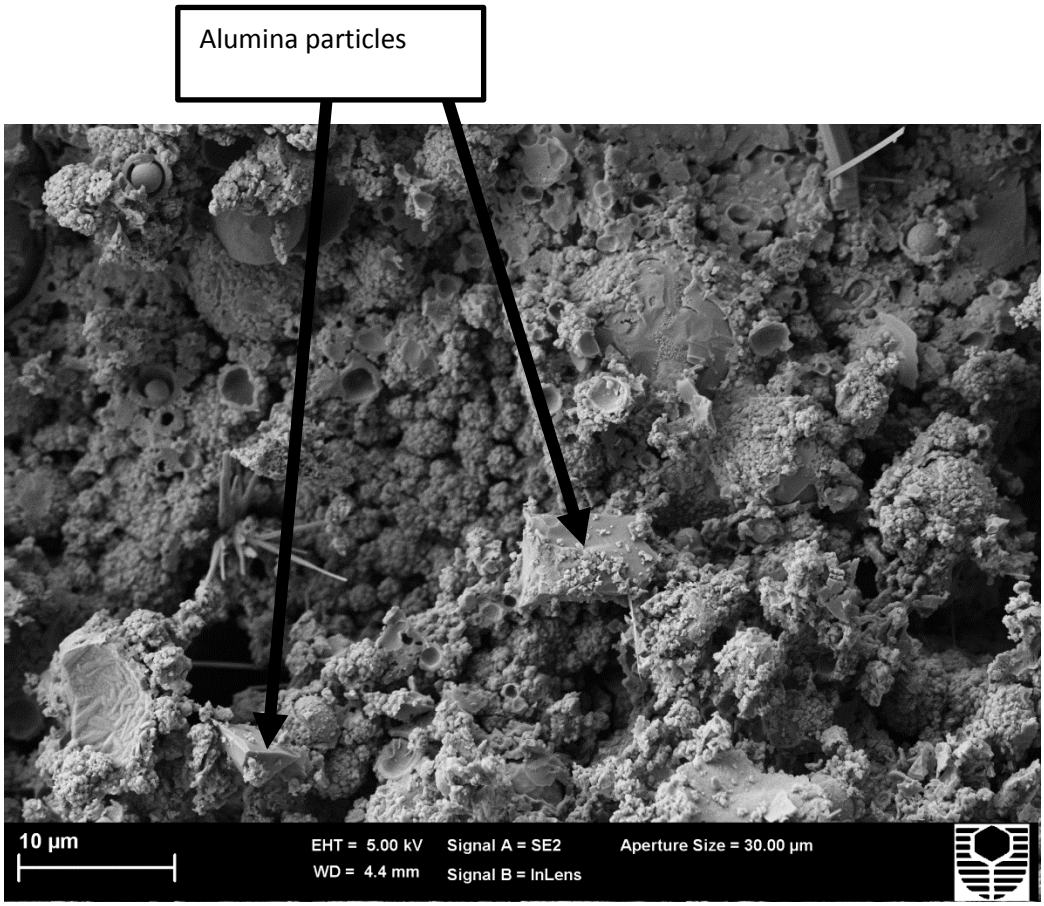

Figure 6.5 SEM image of ALOX 5 AC showing small alumina particles (< 10 microns).

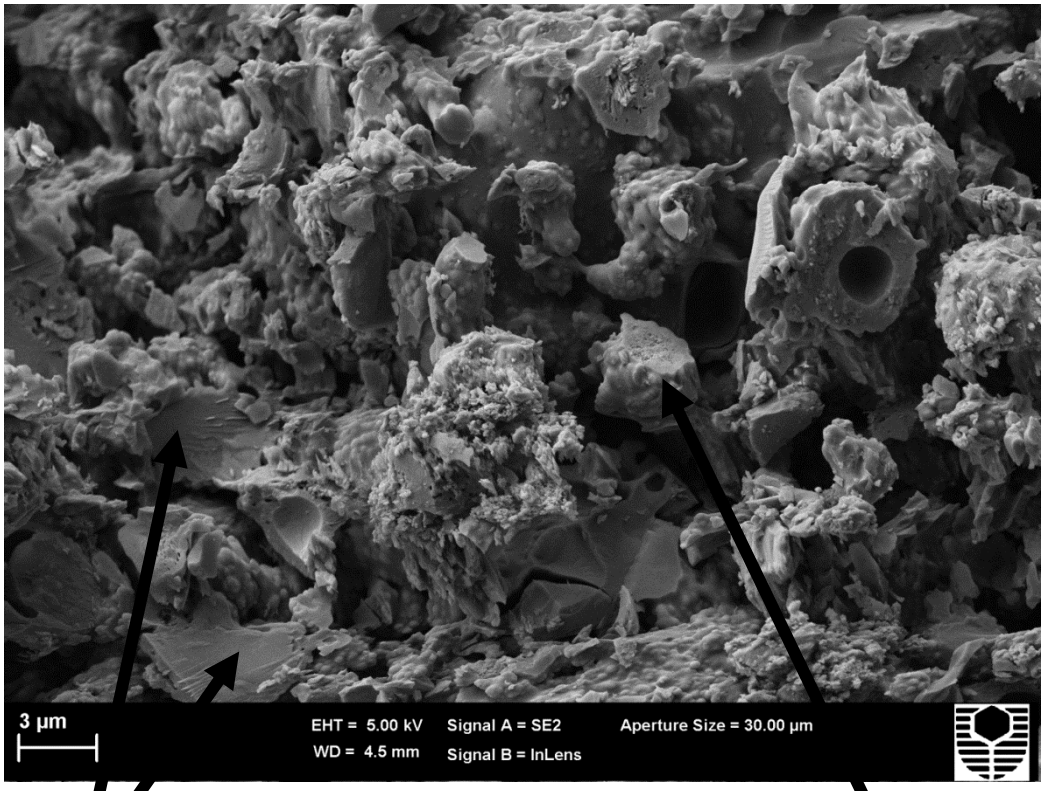

Figure 6.6 SEM image of ALOX 10 fired at 800^{o}C.

The evolution of density shown in figure 6.7 helps to confirm the descriptions of the temperature regions. The rapid decrease in density at 200^{o}C is associated with free water loss and limited volume shrinkage. The gradual decrease in density between 200 and 600^{o}C results from a convolution of the dehydroxylation of chemically bound water and the expansion of the system. Above 600^{o}C melting and associated viscous flow begins to occur with resultant densification associated with a reduction in porosity and the formation of crystalline phases. Further increases in temperature continue this process albeit at a lower rate as shown by the gradual increase in expansion or shrinkage in Region V. A point is reached at the boundary between regions V and VI where shrinkage becomes significant as further melting occurs.

Figure 6.8 supports this explanation with greater rates of volume shrinkage occurring above 600^{o}C. The chamotte curve shows a large shrinkage value at 800^{o}C followed by a significant reduction at 1000^{o}C. This shrinkage is attributed to the amorphous content (~16%) of the chamotte which is exhibiting flow at 800^{o}C as shown in figures 6.3 and 6.4.

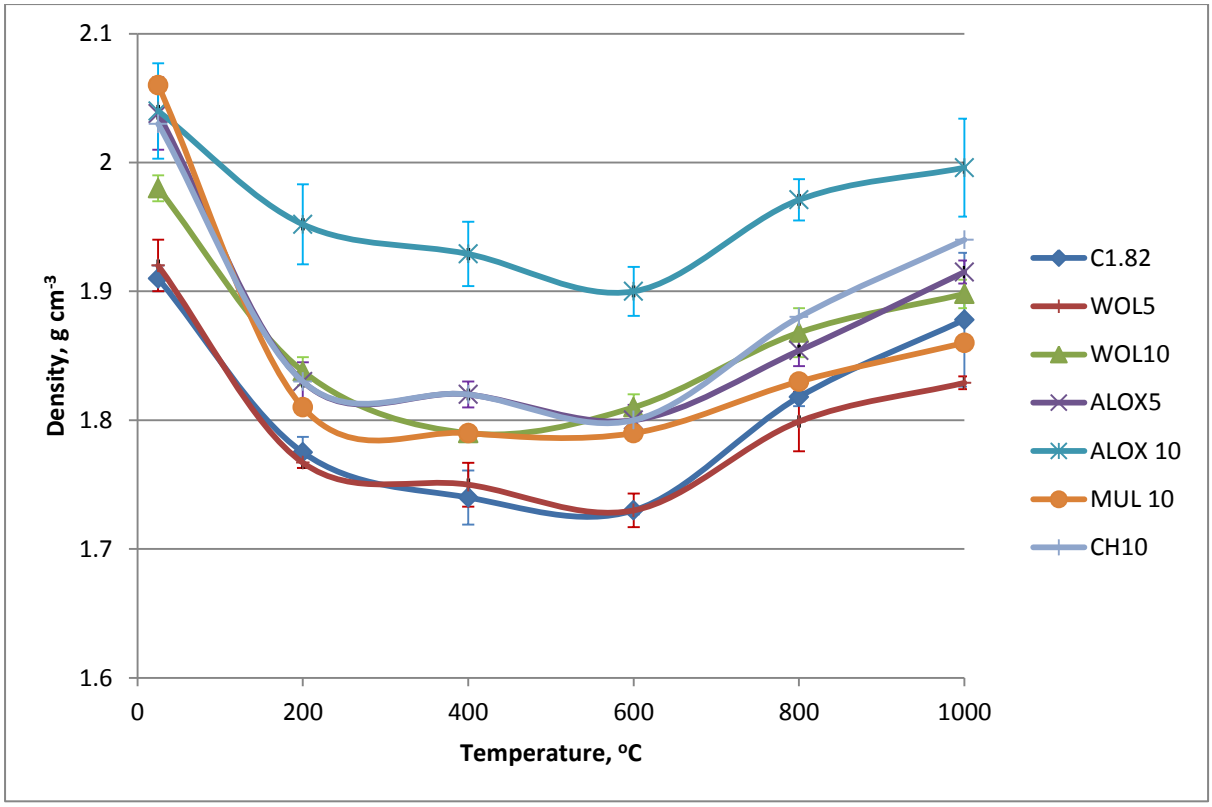

Figure 6.7 Variation in density of filled systems based on C1.82 after thermal treatment.

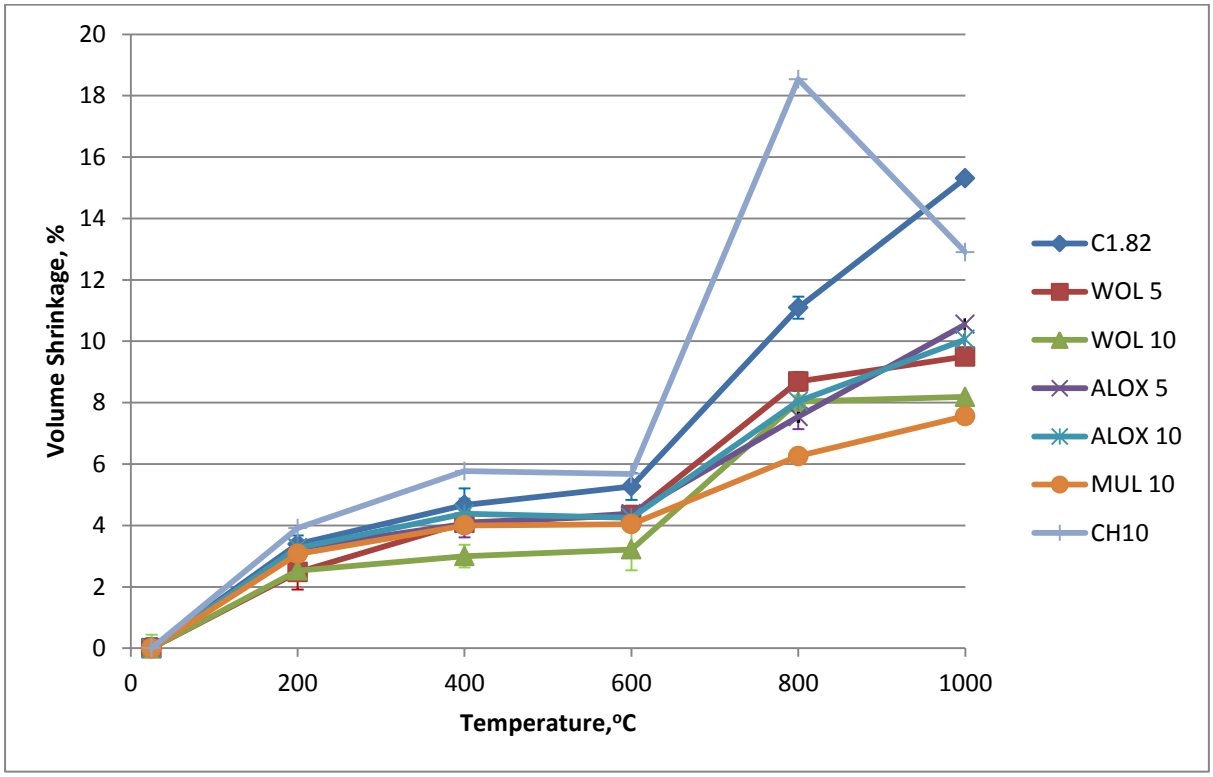

Figure 6.8 Volume shrinkage of filled systems based on C1.82 after thermal treatment of specimens.

A selection of SEM images is presented below in figure 6.9 to demonstrate the thermal evolution of the as cured specimens from a microstructure based on fly ash particles bonded together with geopolymer reaction product to a consolidated system at temperatures beyond 800^{o}C. It is clear that unreacted fly ash spheres do not survive at temperatures beyond 800^{o}C and are incorporated into the structure with a resultant change in Si: Al, as shown by QEDS (see section 5.5). At the same time the high temperature treatment creates a strong material with larger pores. The microstructure of these fired samples is certainly a convolution of new crystalline phases formed by viscous flow and sintering and fly ash residues such as mullite and iron containing spheres (see chapter 5). The targeted Si: Al used in this evaluation had low levels of added soluble silicate and this has led to low levels of geopolymer formation, with the presence of crystalline zeolites and nepheline (see chapter 5).

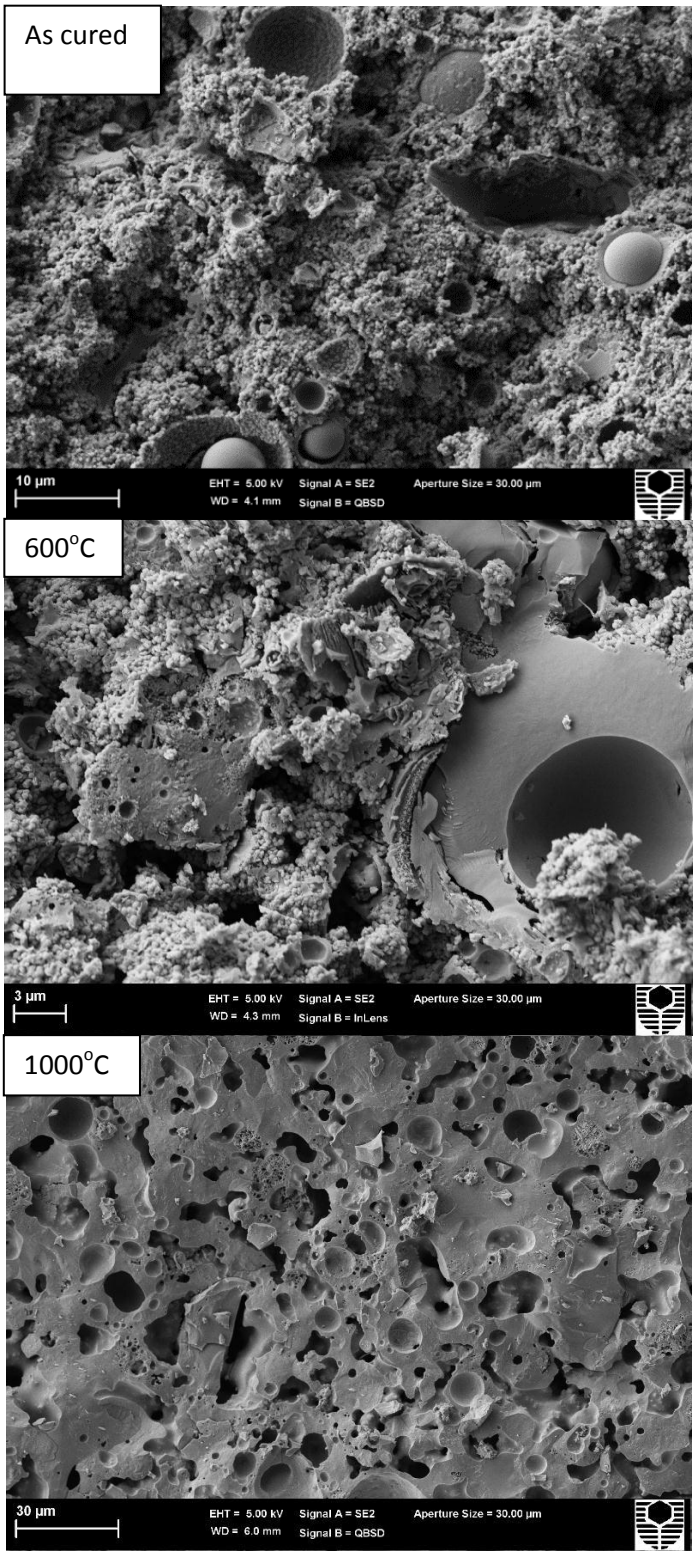

Figure 6.9 SEM images of C1.82 as cured and after heating to 600°C and 1000°C.

The presence of filler does not appear to change the basic evolution mechanism only the temperatures at which changes occur. Further examples of the specimen microstructures up to 1000°C are presented in Appendix B.

6.2.2 The effect of inorganic fibres

The addition of inorganic fibres was predominantly to improve flexural strength and crack resistance. Any influence on thermal properties was also investigated. The low level of fibres added had little effect on the composite shrinkage as shown in figure 6.10. The length of fibre, 5 mm for basalt and 13 mm for alkali resistant glass, were difficult to disperse and reduced flowability on the processing scale utilised in this research. Fibre additions of 1.5 vol. % produced specimens suitable for testing while greater volume additions proved impracticable from a processing perspective.

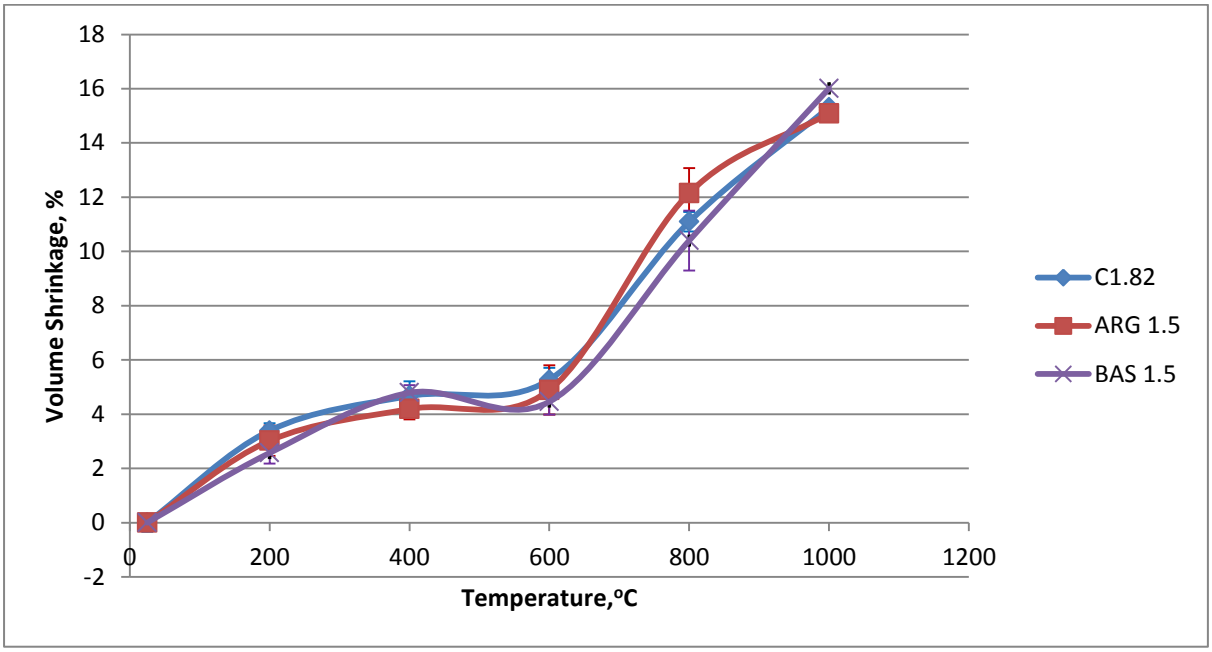

Figure 6.10 Influence of fibre addition on volume shrinkage. Fibres added: Alkali resistant glass (ARG 1.5 vol. %) and basalt (BAS 1.5 vol. %).

Flexural strength testing was used to evaluate suitability of fibres for elevated temperature service. Figure 6.11 shows these results. The length of the ARG and basalt fibres categorises them as macro fibres, which are considered suitable for the restraint of macro-crack growth. Wollastonite, a micro fibre, is also included for comparison. The relatively high addition levels of wollastonite means that a larger number of individual fibres will be present across a given area compared to the macro fibres and this goes some way to explaining the higher levels of flexural strength with wollastonite containing composites. The crossover of the

WOL 5 and WOL 10 flexural strength values after firing at 1000°C can most probably be attributed to sample quality as shown by the big difference in the range of the error bars.

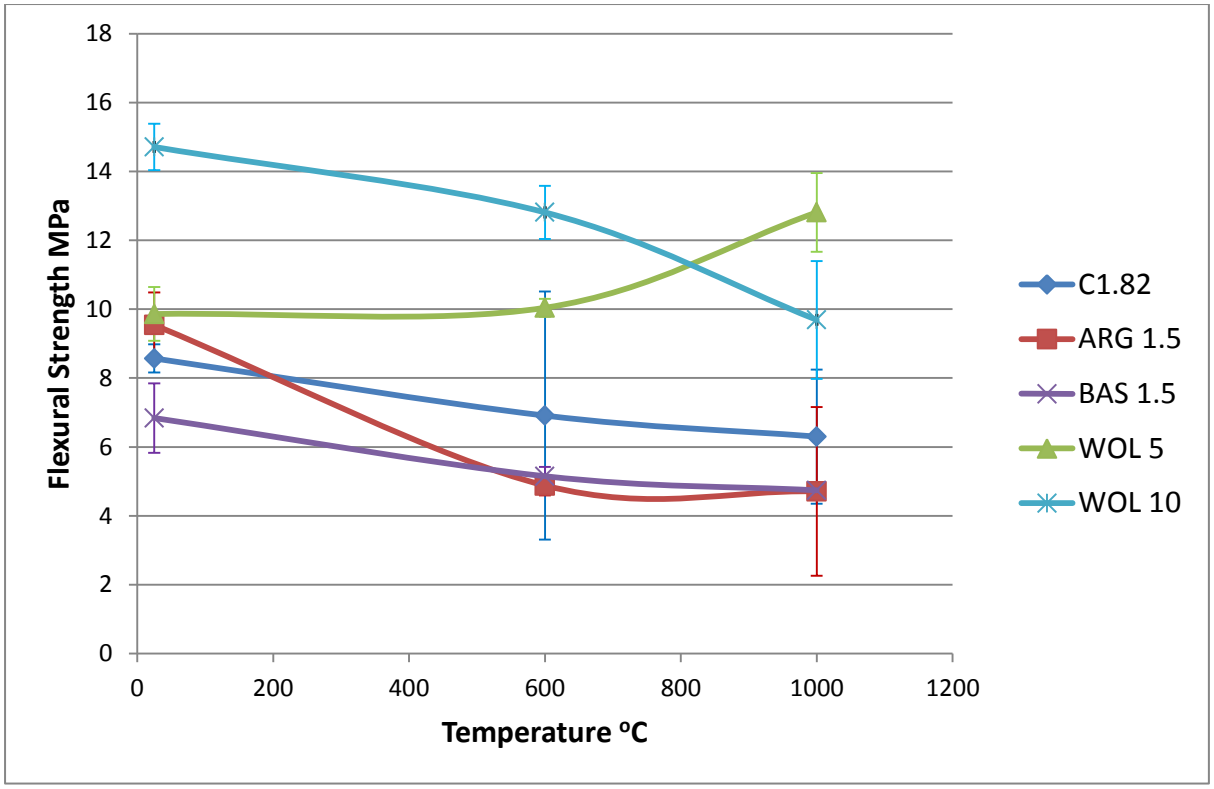

Figure 6.11 Flexural strength evaluations of geopolymer with fibre addition after thermal treatment.

Figure 6.12 shows a wollastonite particle exhibiting fracture perpendicular to its length. It has not shown the pull-out mechanism generally associated with macro fibres. The geopolymer reaction product appears loosely bonded to the wollastonite particles.

Appendix C gives more information on the as cured wollastonite – geopolymer matrix interactions.

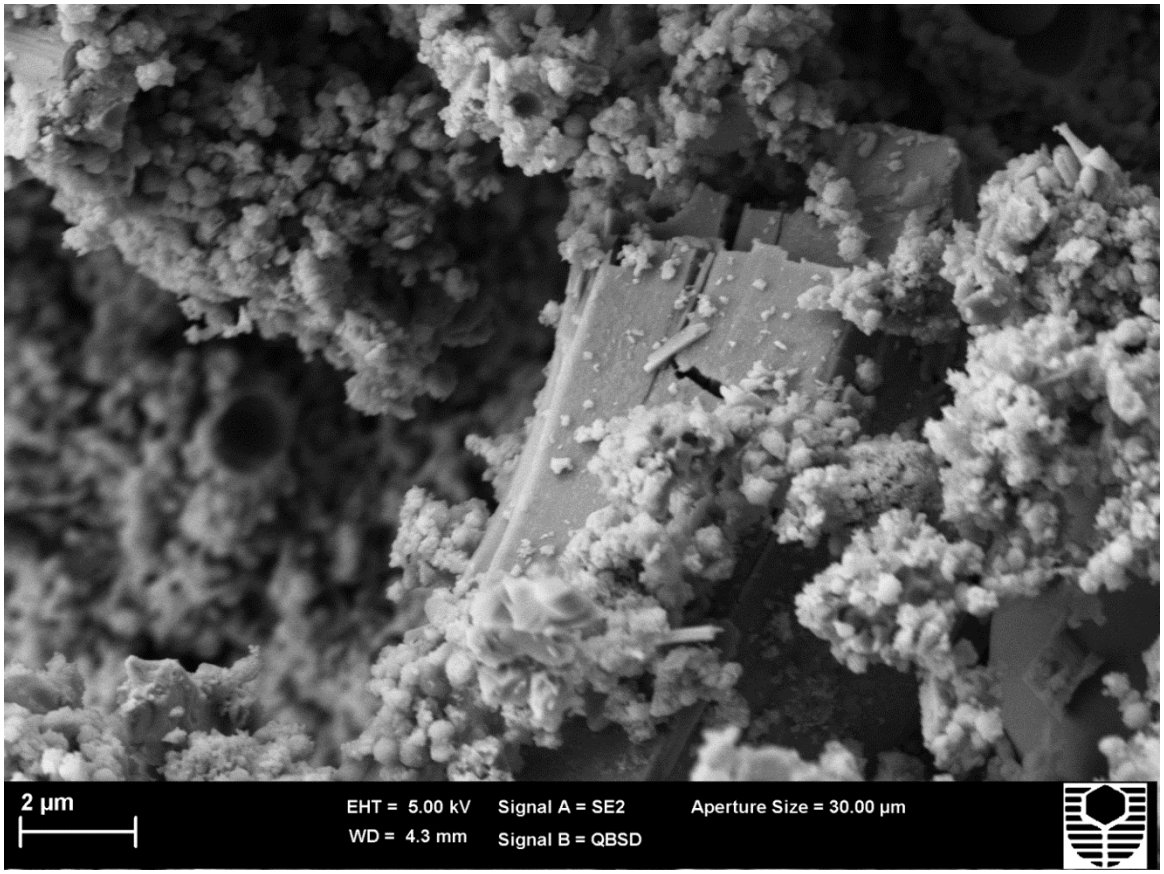

Figure 6.12 SEM image of WOL 5 as cured showing fractured wollastonite particle.

In figure 6.13 a wollastonite particle embedded in the fired matrix shows failure by longitudinal shearing. The wollastonite appears bonded with the matrix which will enhance applied stress distribution. Figure 6.14, WOL 5 fired at 800^{o}C, reinforces this mechanism showing several well bonded and longitudinally sheared wollastonite particles. The effect of firing these composites is the evolution of a more compact microstructure. This may possibly be the result of a sintering mechanism between the wollastonite surface and the geopolymer reaction product.

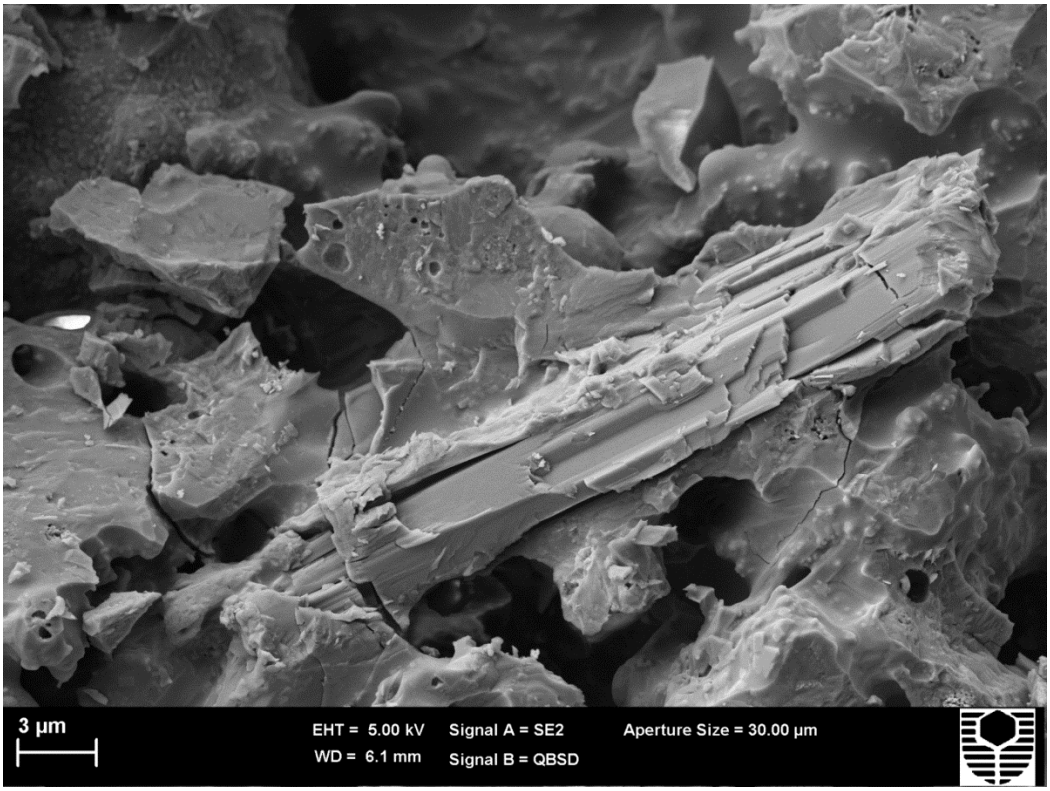

Figure 6.13 SEM image of WOL 5 fired at 1000^{o}C showing longitudinal shear fracture.

Figure 6.14 SEM image of WOL 5 fired at 800^{o}C showing several wollastonite particles bonded into the matrix and exhibiting longitudinal shear fracture.

Figure 6.15 shows evidence of the fibre pull out in basalt fibre composites. In the SEM image little geopolymer reaction product is adhered to the basalt fibre surfaces. Surprisingly, no evidence of basalt fibres was seen in SEM images of fired composites even though the melting point of basalt is 1050^{o}C. The absence of fibres in fired composites can tentatively be attributed to either complete coating of the fibre by consolidated reaction product or alkali attack on the fibre followed by melting and recrystallization into new compounds.

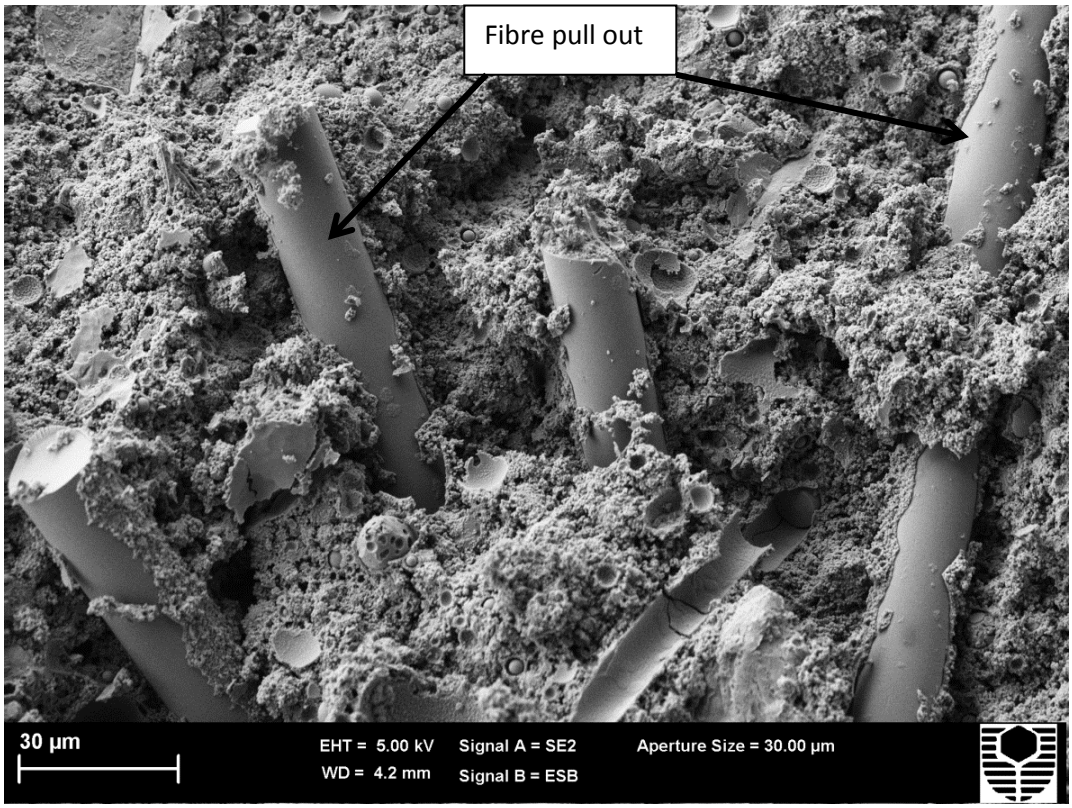

Figure 6.15 SEM image of BAS 1.5 as cured showing fibre pull out.

6.3 Thermal post curing of geopolymer composites.

Several segments of the polymer industry apply a controlled heating-cooling cycle to products prior to entering service. This is referred to as post curing. In the case of large components or in-situ installations a controlled temperature ramp up to service levels may also be utilised. The use of a post curing cycle helps to remove unwanted volatiles in a controlled manner, can increase glass transition temperatures using a stepwise post cure, pre-shrink components prior to entering service and enhance physical and durability properties. In the case of organic polymers the final post cure temperature is generally 10^{o}C

higher than the intended service temperature. This is to ensure any changes that could occur through application of elevated temperature have occurred prior to the component reaching service temperature.

Some initial work on the dilatometer where samples were repeatedly run showed that these additional thermal cycles lead to a levelling off of the thermal expansion/shrinkage curves, reductions in shrinkage and reductions in COTE. This led to the development of a post cure regime to improve the performance of the composites at elevated temperatures.

In the case of geopolymers various regions of shrinkage occur as the temperature increases (figure 6.1). In region II, up to 300^{o}C, around 1% of shrinkage is typical and associated with dehydration of free water in the system pores. If we can remove this shrinkage from the system prior to service, stress development and associated crack formation may possibly be alleviated at higher temperatures. To assist the escape of water polypropylene fibres are added and evaluated in a separate experiment. These begin to melt at approximately 165^{o}C forming channels for water vapour transport thus preventing pressure build up, which can lead to explosive spalling.

Initially a post cure cycle, PC1, limited to 100^{o}C was evaluated. The PC1 post cure cycle involves a one hour rise to 65^{O}C followed by a one hour hold at 65^{o}C then a one hour rise to 100^{o}C with a 3 hour hold at 100^{o}C followed by natural cooling in the oven. The PC1 cycle is the first four steps of PC2. The maximum temperature in PC1 is inadequate to remove polypropylene fibres. However, some results of the PC1 evaluations are included later to confirm some of the outcomes of dilatometer experiments

The following post cure cycle (PC2) shown in figure 6.16 was investigated. An initial slow increase to 65^{o}C was applied to allow uniform heating below the temperature where the water vapour pressure curve gradient steepens. This gradient increase may be attributed to a decrease in the level of hydrogen bonding in water. Next a step up to 100^{o}C with a 3 hour hold point followed by a rapid rise to 175^{o}C, to initiate the melting of the polypropylene fibres, then a 3 hour hold point. Finally a ramp up to 250^{o}C with a 3 hour hold point was applied before allowing natural cooling of the specimens to below 50^{o}C.

The PC2 cycle will only influence changes occurring in region II temperature range. The effect of firing these post cured samples on physical properties was investigated.

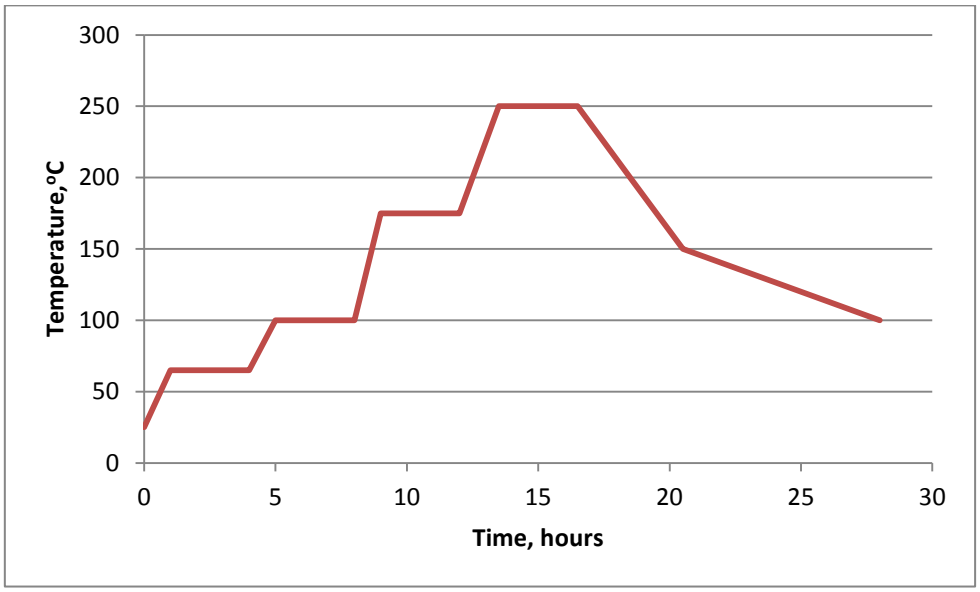

Figure 6.16 Post cure cycle (PC2) for geopolymer specimens.

Figure 6.17 shows an actual cycle using a 25 mm diameter x 45 mm high cylinder with a k-type thermocouple embedded at the centre point.

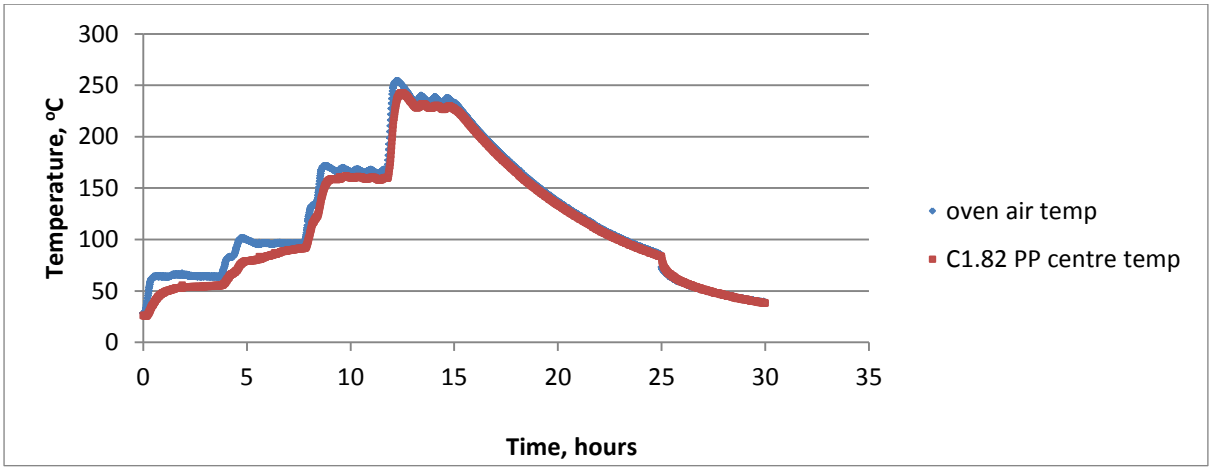

Figure 6.17 Confirmation of PC2 cycle using a thermocouple embedded in a cured cylinder.

Table 6.3 collates the results from thermal treatment of C1.82 AC using the PC2 post cure cycle, followed up by firing at 600, 800 and 1000^{o}C. The drop in compressive strength for the PC2 + 800^{o}C samples may be attributed to cracking of the specimens which was evident after firing. There were a few visible cracks on the surface of PC2 + 1000^{o}C sample which

have not detrimentally influenced the compressive strength. Viscous flow from 800 to 1000^{o}C may have healed cracks formed at 800^{o}C.

The increase in compressive strength after thermal treatment, particularly after the PC2 cycle can possibly be attributed to further geopolymerisation taking place during the relatively long cycle. The pore water contains alkaline species (possibly aluminate and silicate precursors amongst others) which can be transported by the movement of water during drying. These species can be precipitated at unreacted precursors initiating the additional geopolymerisation. In dried specimens that are now fired at 600^{o}C and beyond these species may promote viscous flow and consolidation of the binder. The presence of sodium ions will be particularly beneficial to viscous flow.

Table 6.3 Post cure and thermal treatment of C1.82 AC.

	Density g cm^{-3}	**Volume shrinkage,%**	**Weight loss, %**	**Compressive strength, MPa**	**Young's modulus, GPa**
C1.82 AC	2.00 (0.03)	-	-	18.4 (3.8)	1.8 (0.2)
*C1.82 PC2	1.74 (0.01)	5.86 (0.4)	17.78 (0.71)	51.3 (4.7)	2.65 (0.06)
$^{\#}$PC2 + 600^{o}C	1.72 (0.01)	0.57 (0.15)	1.86 (0.01)	43.3 (5.0)	2.4 (0.2)
$^{\#}$PC2 + 800^{o}C	1.82 (0.01)	6.21 (0.33)	2.27 (0.05)	24.2 (6.0)	2.1 (0.3)
$^{\#}$PC2 + 1000^{o}C	1.89 (0.01)	10.38 (0.12)	2.41 (0.03)	73.9 (4.7)	2.89 (0.01)

*Weight loss and volume shrinkage relative to C1.82 AC

$^{\#}$ Weight loss and volume shrinkage relative to C1.82 PC2

The removal of the bulk of the water (17.78 wt.% from a theoretical total of 20 wt.%) occurred during the post curing cycle with 5.86 % volume shrinkage taking place.

The applied post cure cycle has removed the polypropylene fibres as shown by the optical microscopy in figure 6.18. Table 6.4 shows the effect of 0.15 vol. % of polyethylene and polypropylene fibres after application of PC2. Polyethylene has a lower melting point (120^{o}C) compared to polypropylene (165^{o}C). Both fibres increased the weight loss, relative

to composites with no fibre, by 12 and 13.6 wt. % respectively, whilst both fibres reduced volume shrinkage compared to the fibre free paste.

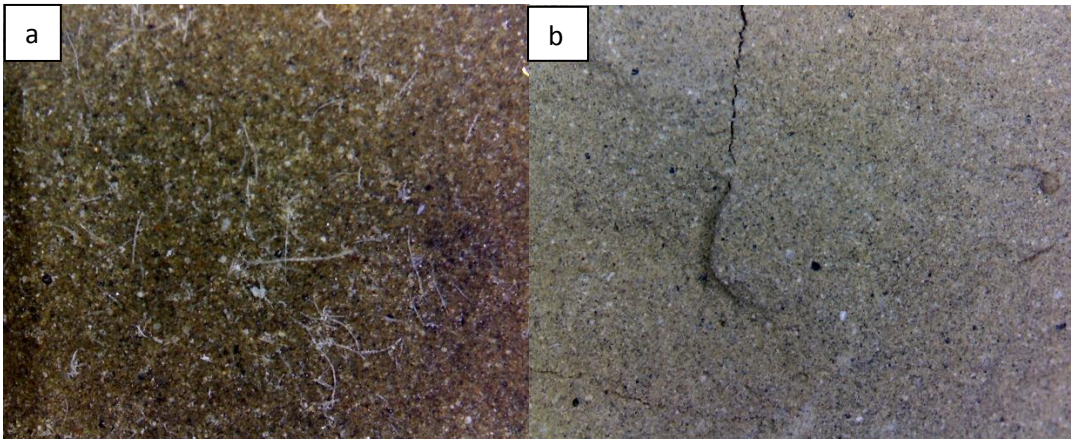

Figure 6.18 Optical microscope images of C1.82-PP as cured (a) and after PC2 (b). Magnification x25

One drawback of the use of fibres (in paste) is the marked reduction in compressive strength (55%) and Young's modulus (36%). This can be attributed to poor dispersion of the fibre in the paste where clumps of fibres act as flaws. It might be concluded that if even dispersion of fibres is not possible then further investigation into their use in geopolymer should be curtailed. However, as will be demonstrated later, the addition of filler and/or aggregate aids in fibre dispersion justifying their use. Both fibre containing composites showed higher weight losses than the control after the application of PC2 indicating their efficiency in the controlled release of volatiles. This indicates that approximately 10 % of the theoretical water content is retained in non-connected pores in the control (no fibre).

The polyethylene and polypropylene fibres showed equivalent effects with regards to water release and levels of mechanical properties. Ongoing work was based on polypropylene fibre due to ready availability and applicability in cementitious systems.

Table 6.4 The effect of polyethylene and polypropylene fibres before and after application of PC2 cycle.

	Density g cm^{-3}	**Volume shrinkage,%**	**Weight loss, %**	**Compressive strength, MPa**	**Young's modulus, GPa**
C1.82PE AC	1.96 (0.01)	-	-	8.17 (1.2)	1.2 (0.2)
C1.82PP AC	1.98 (0.01)	-	-	8.18 (0.7)	1.04 (0.12)
C1.82PE PC2	1.65 (0.01)	3.14 (0.2)	19.9(0.1)	12.7 (0.8)	1.43 (0.05)
C1.82PP PC2	1.64 (0.01)	4.1 (0.1)	20.2(0.2)	11.65 (2.5)	1.29 (0.26)

Effect of post cure on filled composites

Weight loss and shrinkage of post-cured and filled samples was assessed by heating samples in the dilatometer and collecting the data to generate the curves shown below. The dilatometer samples used in this work (table 6.5) were 28 weeks old and had more opportunity to equilibrate with the atmosphere resulting in 9.33 wt. % loss due to heating (C1.82 AC). This is to be compared with C1.82 AC samples tested just 28 days after processing which resulted in approximately 17 wt. % loss. The difference in sample age prior to testing is due to the concept of post curing being developed at a later date after second cycle dilatometer runs showed improved thermal stability. The concept of a post-cure (at less severe heating conditions) was to reduce thermal shrinkage.

Table 6.5 Weight loss and shrinkage determined on dilatometer specimens.

	Weight loss, wt.%, after heating to 1000 ^{o}C	**Weight loss, wt.%, after post cure and heating to 1000^{o}C**	**Linear shrinkage, %, after heating to 1000^{o}C**	**Linear shrinkage, %, after post cure and 1000^{o}C**
C1.82 AC	9.33 (0.12)	-	5.85 (0.16)	-
C1.82 PC1	6.0 (0.08)	3.4 (0.04)	5.56 (0.16)	0.36 (0.01)
C1.82 PC2	3.42 (0.04)	6.56 (0.08)	4.87 (0.14)	1.34 (0.04)
ALOX 5 AC	8.63 (0.11)	-	3.75 (0.11)	-
ALOX 5 PC1	5.96 (0.07)	2.88 (0.04)	2.9 (0.08)	0.52 (0.01)
ALOX 5 PC2	2.14 (0.03)	6.2 (0.08)	2.42 (0.07)	1.51 (0.04)
WOL 5 AC	8.92 (0.11)	-	2.07 (0.06)	-
WOL 5 PC1	6.73 (0.08)	3.05 (0.04)	3.0 (0.08)	0.31 (0.01)
WOL 5 PC2	5.41 (0.07)	6.06 (0.08)	1.42 (0.04)	1.45 (0.04)

Dilatometer results for C1.82, WOL 5 and ALOX 5, before and after post cure (PC 2) are shown in figures 6.19, 6.20 and 6.21. Table 6.6 summarises the key results from the dilatometer curves. In general, application of the PC2 cycle resulted in a reduction in the shrinkage range (minimum value to maximum value at 1000^{o}C) in each case evaluated. Application of PC2 to a specimen tended to level out the curve up to around 500^{o}C before the usual shrinkage events occurred, albeit in a smaller shrinkage range in specimens exposed to the post cure cycle.

The addition of 5 vol. % wollastonite imparted the lowest shrinkage and shrinkage range values. It is suggested that the wollastonite plays a function in the viscous flow and resultant densification mechanism which commence around 700^{o}C. Whilst the temperatures utilised in this work are significantly below the melting point of wollastonite it is possible that the surface morphology of wollastonite particles can exhibit areas of relatively high surface energy which can lead to interactions with the geopolymer reaction products. The presence of calcium in wollastonite may also take part in these proposed surface reactions.

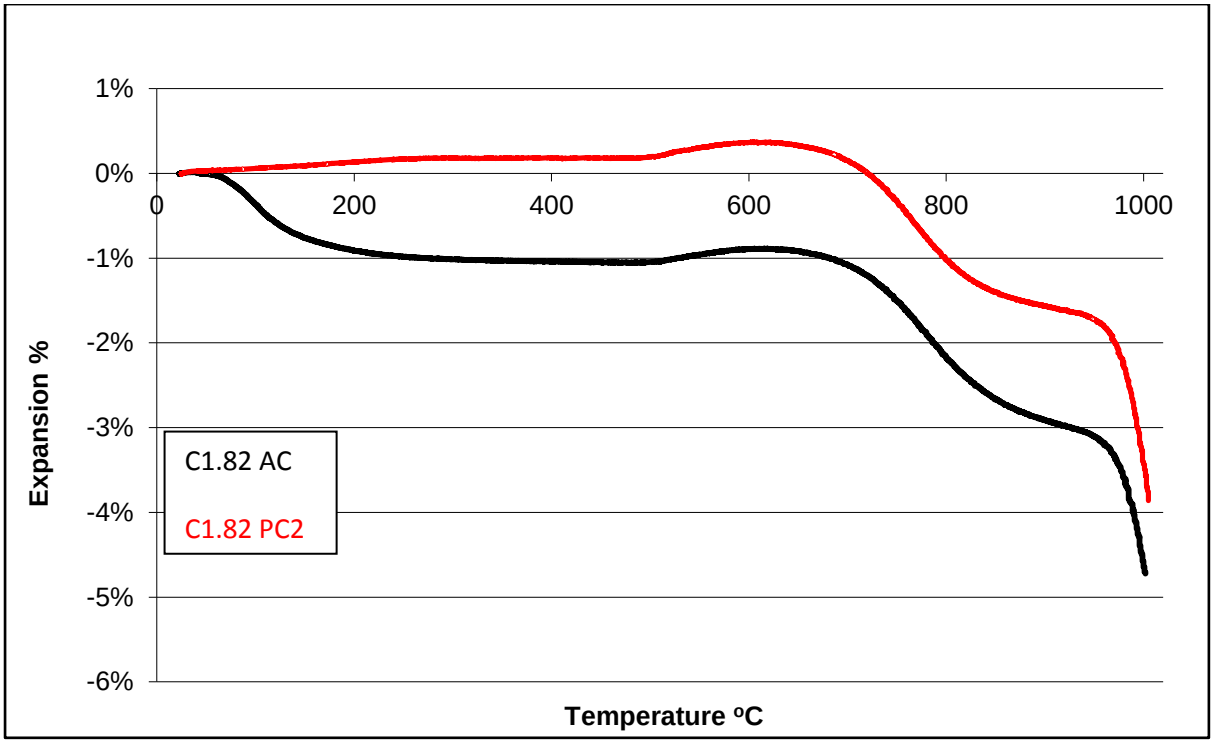

Figure 6.19 Thermal expansion of C1.82 before and after PC2.

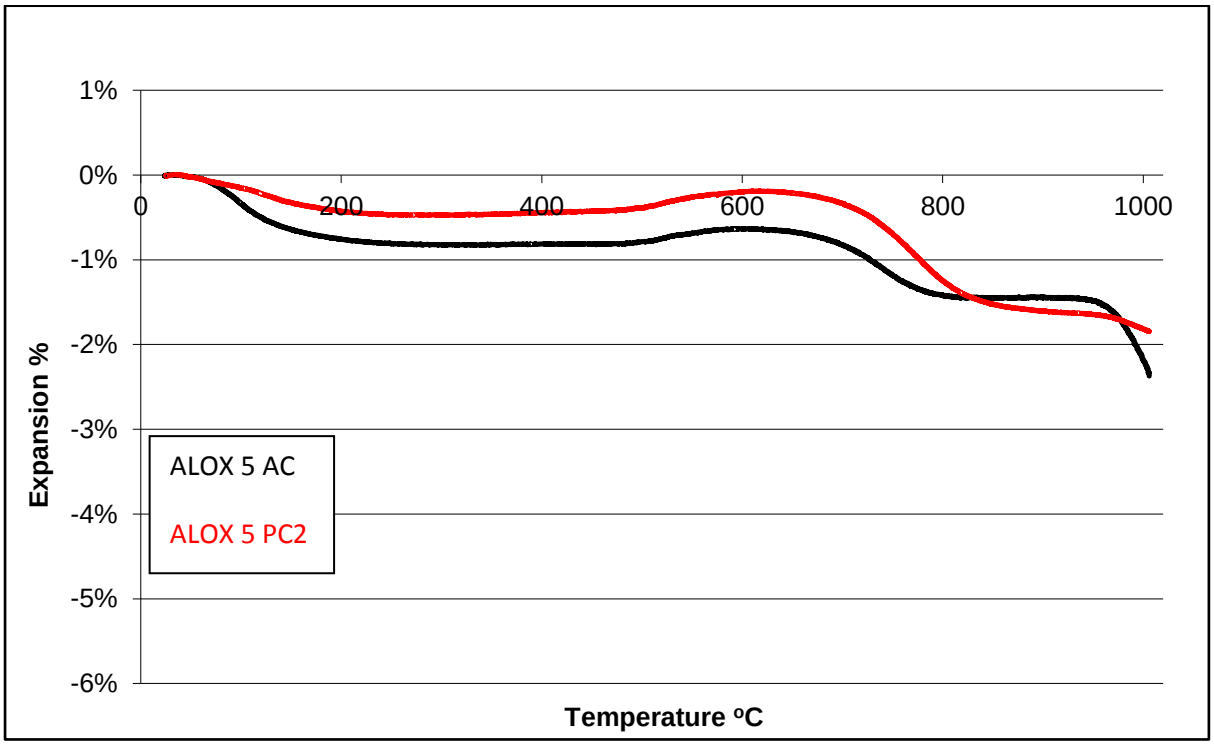

Figure 6.20 Thermal expansion of ALOX 5 before and after PC2.

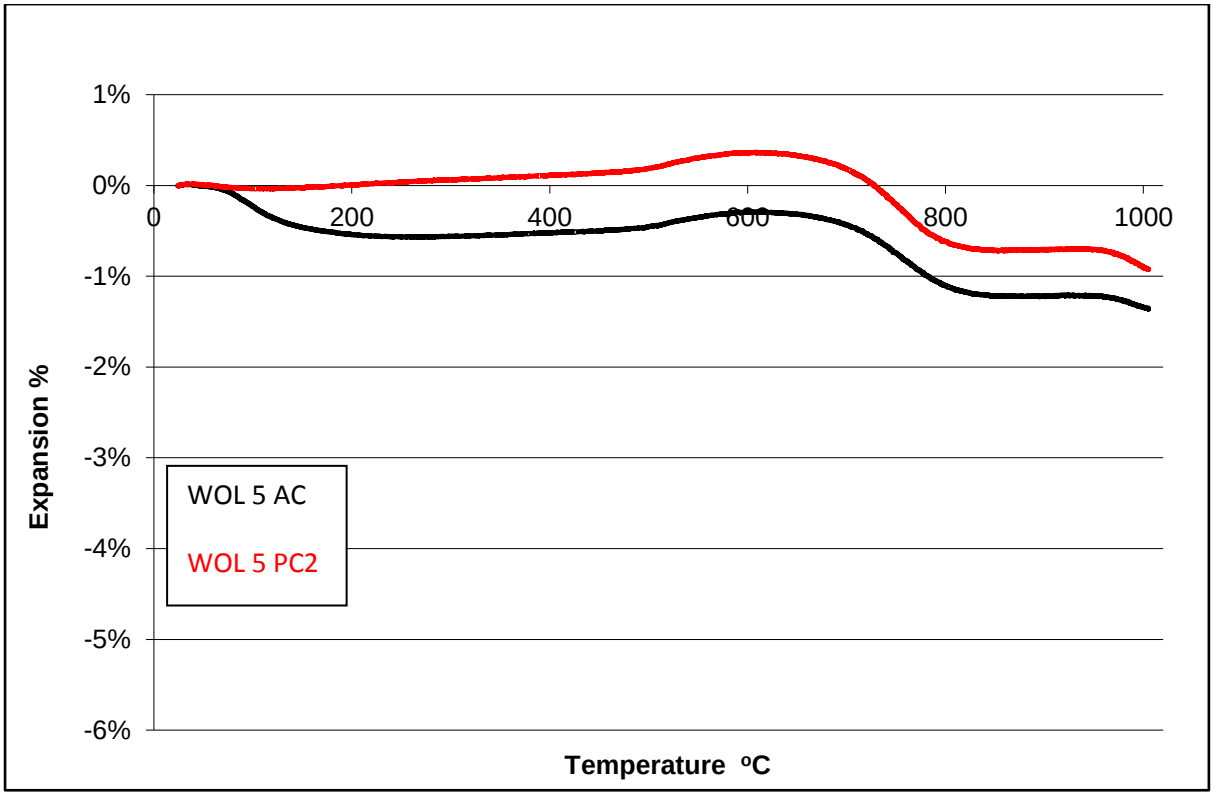

Figure 6.21 Thermal expansion of WOL 5 before and after PC2.

Table 6.6 Summary of dilatometer data for post cured filled composites.

	Region II Maximum linear shrinkage, %	Region IV Inflexion point, °C	Shrinkage range,%	Region V Width of region °C	Region V-VI Boundary temperature, °C	Region VI Linear shrinkage at 1000 °C, %
C1.82 AC	1.06(0.03)	721	4.72	136	973	4.72 (0.13)
C1.82 PC2	0.0 (0.03)	714	4.21	143	976	4.21 (0.12)
WOL 5 AC	0.56 (0.02	692	1.39	182	982	1.39 (0.04)
WOL 5 PC2	0.0 (0.03)	706	0.94	178	980	1.33 (0.04)
ALOX 5 AC	0.83(0.02)	692	2.39	182	971	2.39 (0.07)
ALOX 5 PC2	0.47(0.01)	719	2.14	149	980	2.14 (0.06)

Uncertainties in temperature values are ±5°C.

The application of PC2 to specimens reduced the shrinkage range and shrinkage value. The removal of water up to 250°C in the post-cure has smoothed out the dilatometer curve below 300°C without major changes to the key points in the dilatometer curve above this temperature

6.4 Coefficient of Thermal Expansion of Geopolymer Composites

The dilatometer provided the recording of COTE changes with temperature in addition to shrinkage measurements. COTE values are normally quoted over a temperature range. In the case of the dilatometer the COTE value quoted is calculated using a ΔT value determined by subtracting the initial temperature, typically 25^{o}C, from the furnace temperature where the specimen length is measured. ΔL is calculated by subtracting the initial length from the measured length at the furnace temperature. Therefore the COTE values quoted on the graphs are the value for the particular temperature range (furnace temperature to ambient temperature) using the initial sample length as $L_{o.}$ This methodology is only suitable for comparative purposes. Comparison in gradient changes, both size and direction, together with the position of turning points may be compared to estimate the extent of thermal expansion and explain the effect on mechanical properties.

Figure 6.22 shows the influence of increasing water content of the control paste system. Increasing water content markedly increases COTE in the drying region of the curve. Beyond this region the curves have similar shapes with the 25% water composite showing greatest COTE values. This higher water content system may have produced less geopolymer and possibly contains zeolitic structures such as hydroxysodalite, as shown in table 5.15. Comparison of the thermal expansion/shrinkage curves with COTE curves shows that COTE is more sensitive to changes in structure and composition in the range 200-600 C. The loss of free water results in a negative gradient on the COTE – temperature graphs, which becomes positive (expansion now occurring) after loss of the free water from the system. Further expansion due to the physical process of thermal expansion takes place up to the softening point where shrinkage again becomes the dominant process driven by viscous flow.

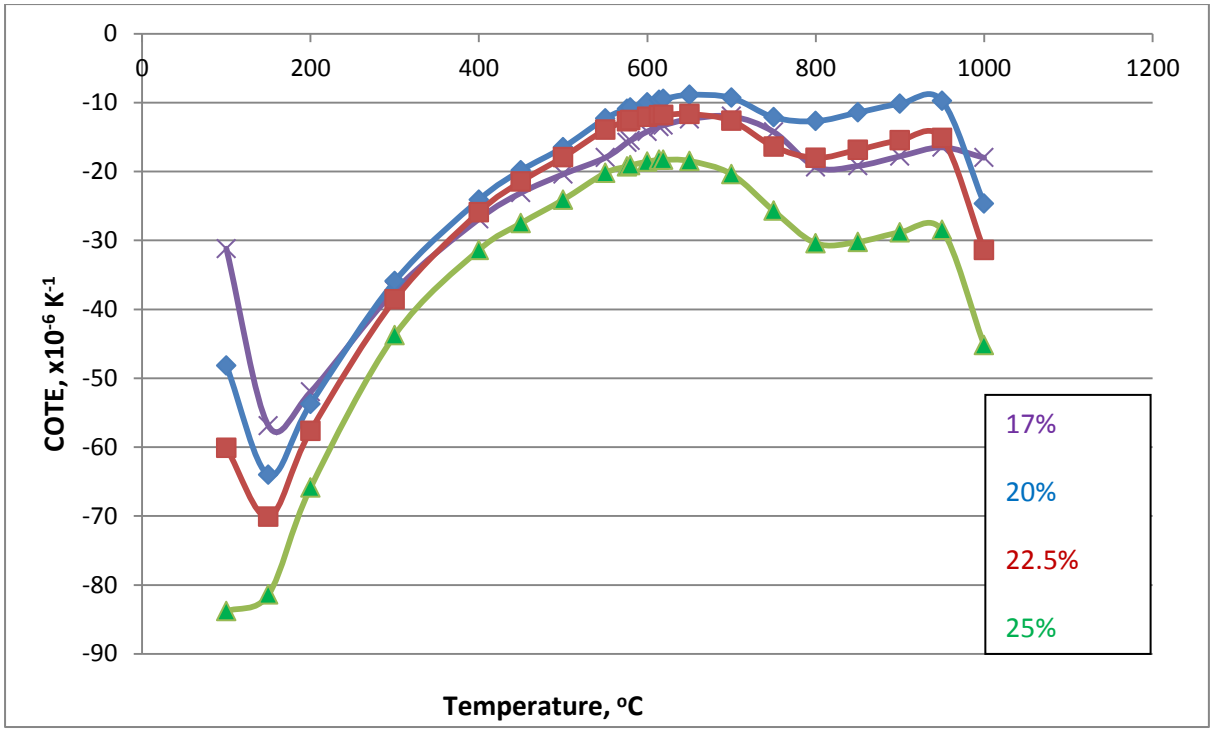

Figure 6.22 Influence of water content (17 to 25%) on COTE of control paste (C1.82).

In figure 6.23 increasing the post cure temperature from 100 to 250°C showed significant changes in COTE values up to 600°C. Above this temperature all three curves have similar shapes and inflexion points albeit at different levels. The post cure cycles employed here have no effect on the sintering and viscous flow mechanisms occurring above 600°C, but in the case of PC2 give smoother more uniform COTE changes up to this temperature. This is important as sharp changes in thermal gradient can induce cracking in the system with resultant strength losses. The controlled, slow rate of application of post curing conditions takes the system through these gradient changes in a manner which minimises thermal stress and stresses associated with free water loss. The PC1 cycle shows intermediate levels with a pronounced dip between 100 and 150°C, attributed to the balance of physically bound water.

The as cured specimens undergo a wide change in COTE, from +10 x 10^{-6} at ambient temperature, down to -51 x 10^{-6} at 200°C and increasing to -36 x 10^{-6} at 300°C. These changes over 300°C will lead to the imposition of severe if not catastrophic stresses in the specimen. The application of the post cure cycle, particularly PC2, has markedly reduced the

extent of the COTE excursion. This will lead to lower thermal stresses with an improved ability to survive high temperature exposure.

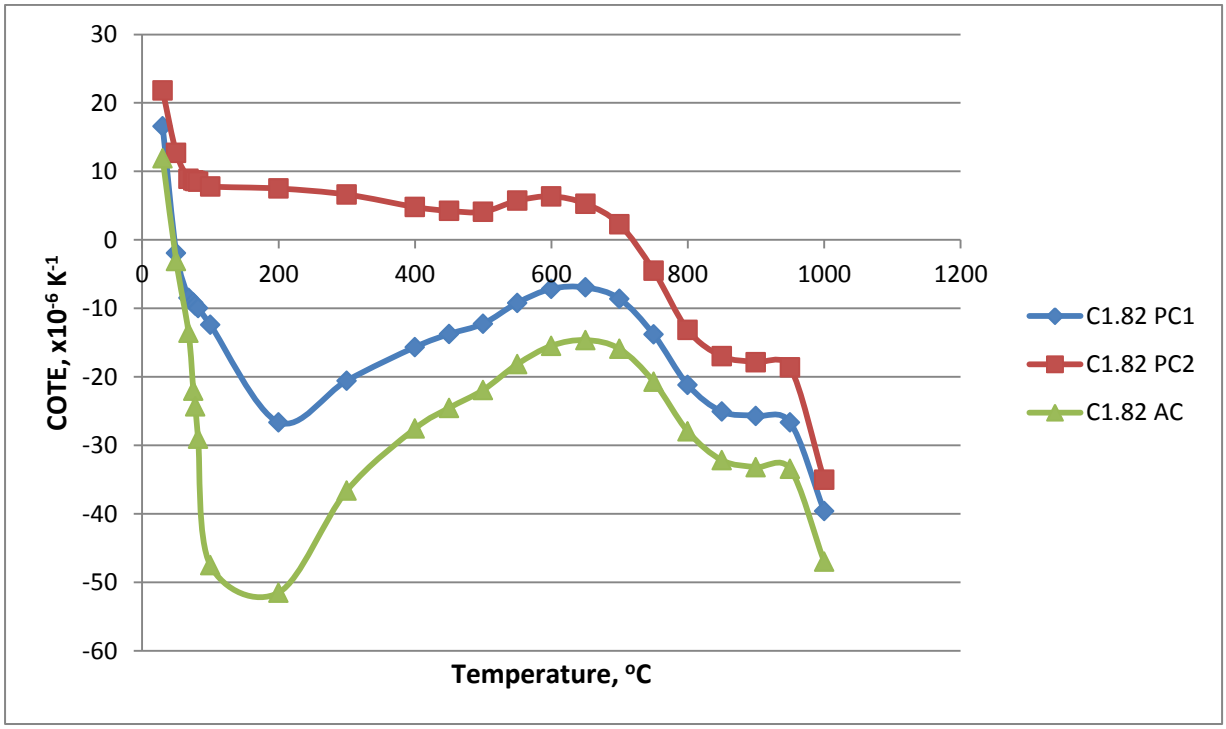

Figure 6.23 Effect of post cure temperature on COTE for paste samples.

The results from the two preceding figures illustrate the critical role of water content on evolution of the geopolymer structure up to 600°C. The introduction of a post cure cycle using low temperature gradients to enable smooth dehydration resulted in a marked reduction in curve gradients with the PC2 cycle (250°C) exhibiting a narrow band of results up to 300°C.

In figures 6.24 and 6.25 the influence of adding wollastonite and alumina to the matrix clearly show the reduction in COTE compared to the control (graph 20W in figure 6.21). The WOL 5 specimen showed lowest COTE even in the as cured state and exhibited a positive COTE after exposure to the PC2 cycle

The effect of the post cure cycles on the alumina containing composite was not as significant as that on the wollastonite containing composites. This may be attributed to

wollastonite being more susceptible to the formation of filler-matrix transition zones with the geopolymer than is alumina and possibly the differences in pore sizes (see figure 6.27).

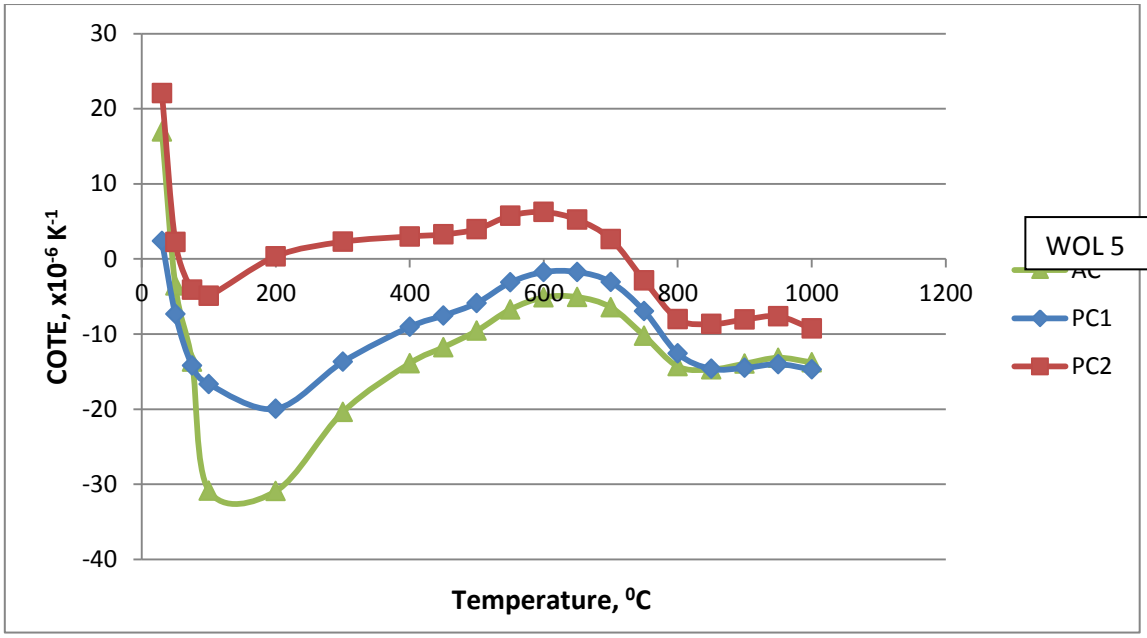

Figure 6.24 COTE of WOL 5 before and after post cure.

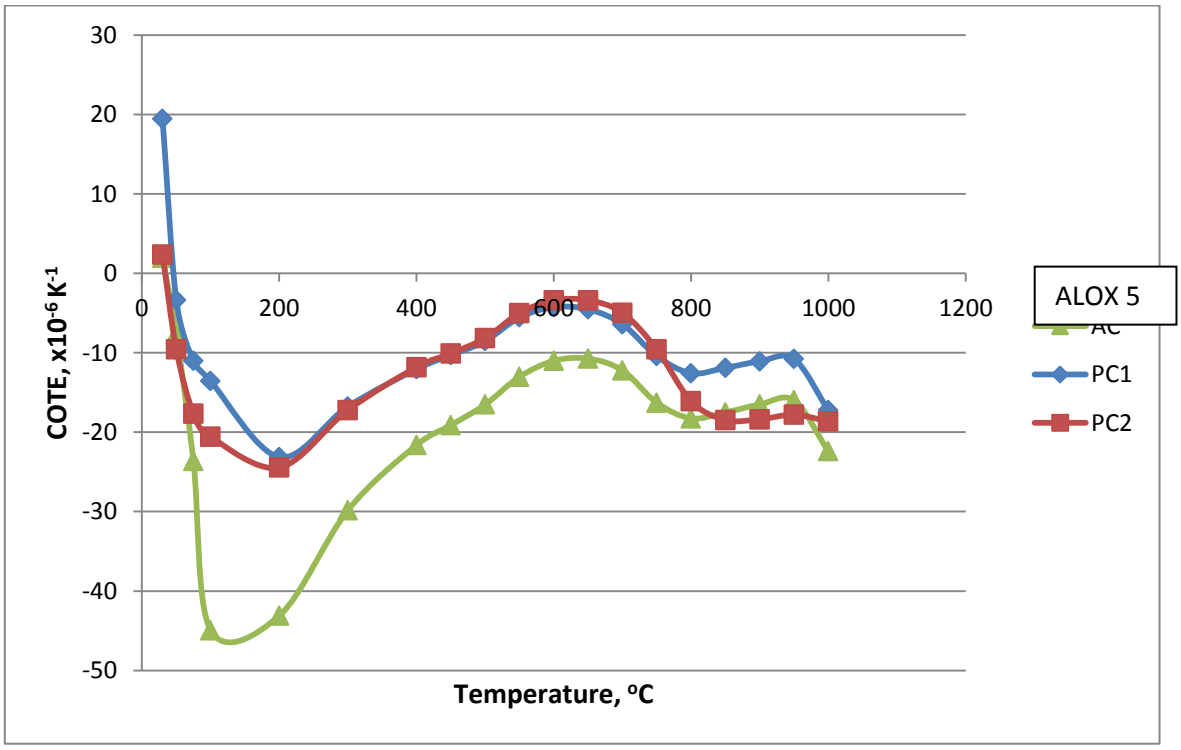

Figure 6.25 COTE of ALOX 5, before and after post cure.

6.5 Porosity of thermally treated geopolymer composites

Porosity plays a significant role in the transport of water through geopolymers (and OPC). The effect of the addition of fillers and the application of thermal treatments on porosity is investigated in the following reported evaluation. Two test methods, mercury intrusion porosimetry (MIP) and air displacement with subsequent replacement in the pores by boiling water using a modified ASTM C20-00 method (2000) were utilised. The MIP testing was undertaken by the University of Bologna.

The IUPAC nomenclature for pore size was adopted (Sing, 1985). Table 6.7 shows the range of pore sizes.

Table 6.7 IUPAC Pore size classification (Sing, 1985).

Pore width	**Pore description**
<2 nm	Micropores
2 to 50 nm	Mesopores
50+ nm	Macropores

The MIP method is limited to a minimum pore width of approximately 4 nm and therefore the measurement of micropores is not possible. The water displacement method does not discriminate between pore sizes, but gives an indication of the interconnected pore volume.

MIP results:

Estimates of the uncertainties in the MIP results are taken from the literature. Giesche (2006) stated that pore size and pore volume determination is repeatable to better than 1% standard deviation, but the results are limited in three ways:

- MIP determines the largest entrance to a pore and not an “actual” pore size.
- The smallest pore size that can be filled is limited by the maximum pressure applied e.g. 3.5 nm diameter at 400 MPa assuming a contact angle of 140^{o}.
- The largest measurable pore size is limited by the height of the sample which determines a minimum head pressure. A 10 mm high sample is equivalent to a pore size of 1 mm diameter.

Cook et al. (1999) working with cement pastes found that the reproducibility between duplicates for total porosity measurements was less than 4%.

Results, shown in figure 6.26, are from one test run per sample only.

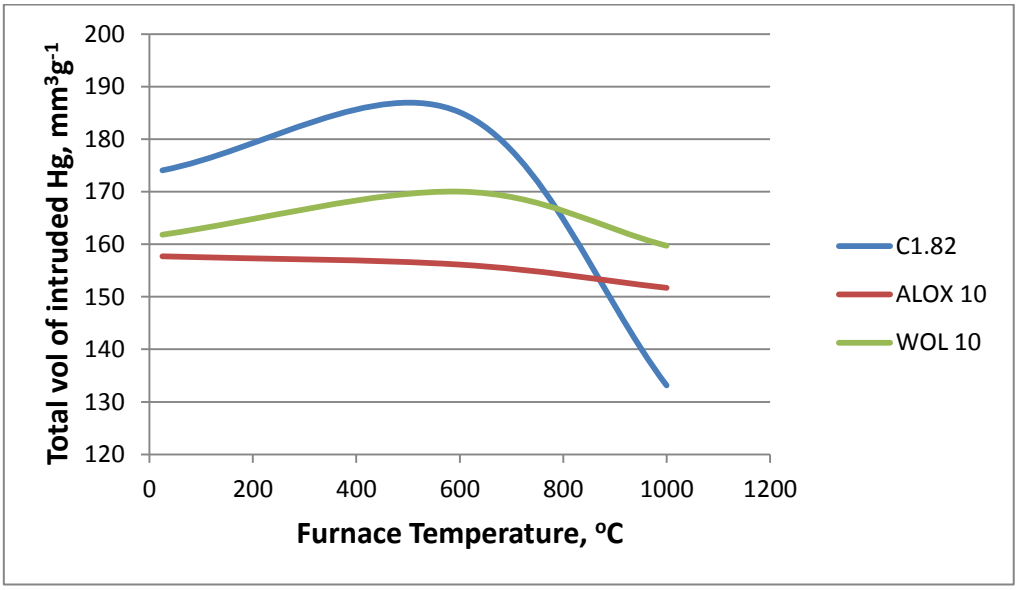

Figure 6.26 Intruded porosity as a function of firing temperature.

Table 6.8 Total intruded porosity as a function of firing temperature.

	C1.82	ALOX 10	WOL 10
Temperature, °C	Intruded Hg mm^3 g^{-1}	Intruded Hg mm^3 g^{-1}	Intruded Hg mm^3 g^{-1}
25	174.06	157.7	161.82
600	185.11	156.12	170.01
1000	133.13	151.7	159.71

Table 6.9 Pore size distribution.

	C1.82	C1.82	ALOX 10	ALOX 10	WOL 10	WOL 10
Temperature, °C	Mesopores Vol. %	Macropores Vol. %	Mesopores Vol. %	Macropores Vol. %	Mesopores Vol. %	Macropores Vol. %
25	11.2	88.8	7.7	92.3	25.7	74.3
600	8.8	91.2	7.9	92.1	20	80
1000	5.6	94.4	3.4	96.6	1.8	98.2

The addition of alumina and wollastonite fillers showed only small decreases in the intruded volume as the firing temperature has increased whereas the control showed a 23.5% decrease in volume (figure 6.26 and table 6.8). In table 6.9 the increase in macropores with increasing firing temperature is evident in each case. The control and ALOX 10 specimens showed high levels of macropores at all temperatures (table 6.9). However, in the case of the WOL 10 specimens the percentage of mesopores is above 20% up to 600^{o}C before increasing to 98.2% after firing at 1000^{o}C. The addition of filler, particularly wollastonite, may be modifying the viscous flow mechanism hence the lower macropore content of the WOL specimens. At 1000^{o}C there is sufficient energy available to overcome activation energy barriers and a different composition (to that at 600^{0}C) is now melting. The pore system converts to predominantly macropores, which are expected to have a lower surface area with corresponding energy. The SEM images For WOL5 and WOL 10 before and after firing are shown in Appendix B. This is evidence for pore coarsening between firing at 600^{o}C and 1000^{o}C.

The commencement of viscous flow effects is around 600^{o}C. Generally porosity content reduces, but becomes coarser as the firing temperature increases (Budinski and Budinski, 2005). Figure 6.27 illustrates this point with the systems investigated in this work.

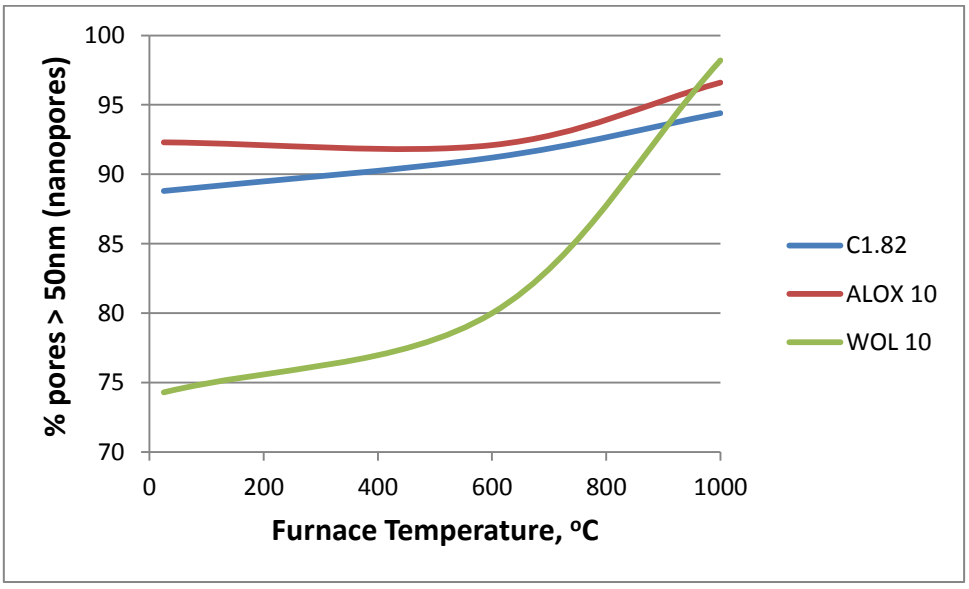

Figure 6.27 Macropore content as a function of firing temperature.

The effect of post cure and firing on MIP results

The outcome of the application of the PC2 post cure cycle and subsequent firing to 1000°C on porosity measured by MIP is illustrated in figure 6.28 and detailed in table 6.10. There is very little change after exposure to PC2 only. After firing at 600°C an increase in total porosity is shown. This increase in porosity does not affect the coarser pore size content. The application of firing at 800 and 1000°C shows a move to lower porosity levels compared to 600°C, accompanied by a move to a coarser pore size distribution.

The formation of coarser pores is energetically preferred due to the associated lower surface area energy. This reduction in surface energy is a driving force for the sintering process.

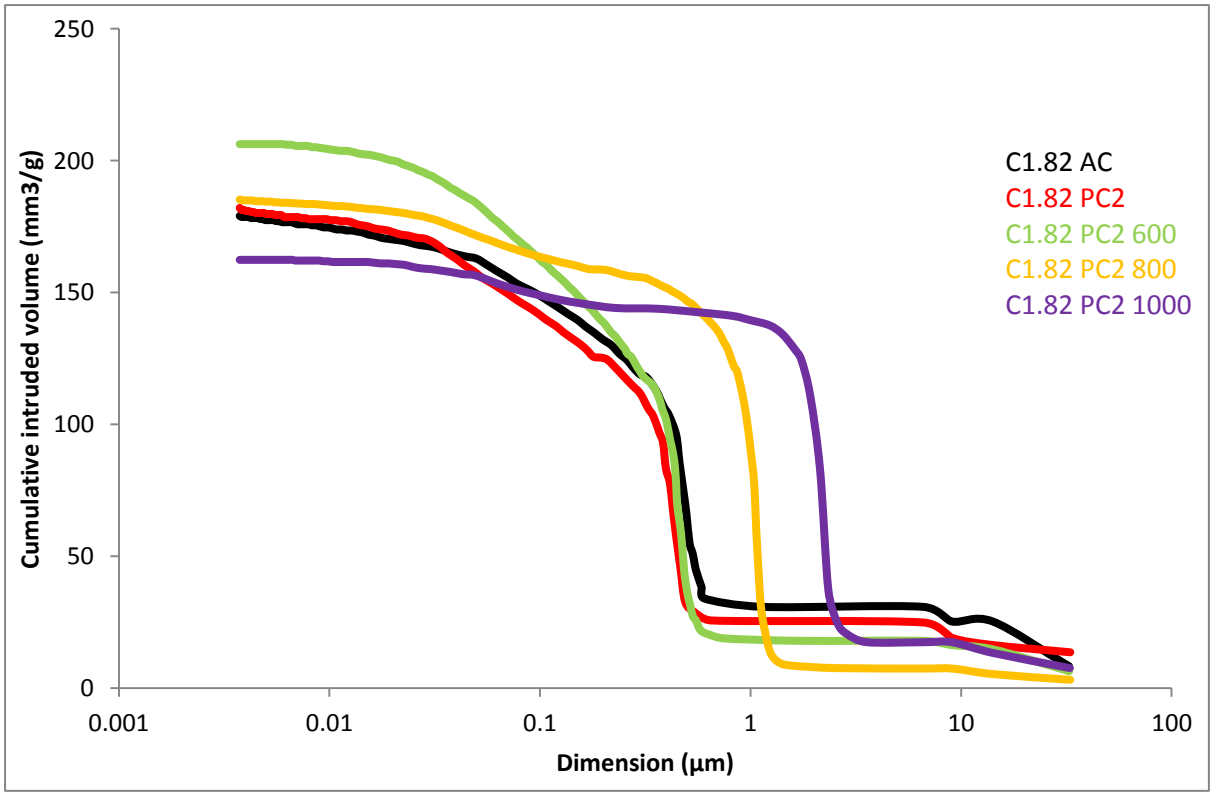

Results are from one test run per sample only.

Figure 6.28 Effect of thermal treatment on porosity from MIP.

Table 6.10 Pore size distribution due to thermal treatment.

	Total porosity, $mm^3 g^1$	**mesopores Vol. %**	**macropores Vol. %**
C1.82 AC	179.1	16.8	83.2
C1.82 PC2	182.1	21.9	78.1
C1.82 PC2 and fired at 600°C	206.3	20.9	79.1
C1.82 PC2 and fired at 800°C	185.2	11.8	88.2
C1.82 PC2 and fired at 1000°C	162.4	14.1	85.9

Water absorption results

Table 6.11 details the porosity values obtained by the water saturation method for the PC2 evaluations. Results were converted to $mm^3 g^{-1}$ for comparison with the MIP data. The data follows the trend in MIP porosity for fired specimens but at a lower porosity value and the values diverge more as the firing temperature increases.

Differences in the test fluids, viscosity and surface tension and testing parameters, pressure and temperature, will make a direct comparison of results from the two methods difficult. MIP is regarded as a technique suitable for comparison only. This is outlined in section 3.10.

Table 6.11 Porosity values by the water saturation method for the PC2 evaluations.

	% Porosity	**Porosity, $mm^3 g^{-1}$**
C1.82 AC	29.8 (1.6)	183.7
C1.82 PC2	40.0 (2.2)	206.3
C1.82 PC2 and fired at 600°C	31.0 (1.7)	179.4
C1.82 PC2 and fired at 800°C	29.2 (1.6)	158.0
C1.82 PC2 and fired at 1000°C	25.4 (1.4)	130.8

6.6 Thermal Conductivity of Geopolymer Composites

All thermal conductivity testing was carried out at ambient temperature following various thermal treatment regimes listed below. Results are the average of two tests.

Figure 6.29 shows the influence of thermal treatment temperature on the thermal conductivity of the control paste. A rapid drop in thermal conductivity is seen after application of the PC2 post cure cycle. This is attributed to loss of water. The measured weight loss was 16.45%. A further small decrease in thermal conductivity was seen when a 600^{o}C firing cycle was applied and a weight loss of 19.5% was measured (theoretical water content = 20%). After 800 and 1000^{o}C firing cycles, thermal conductivity increased with weight losses of 17.75% and 17.28%, respectively. This lower weight loss is attributed to oxidation of iron based compounds to crystalline iron oxides which would show a weight increase offsetting the loss of water. During the high temperature firing cycles other crystalline compounds are formed (e.g. nepheline). Crystalline compounds generally exhibit higher thermal conductivity than amorphous glasses (Khan, 2002, Kamseu et al., 2012a).

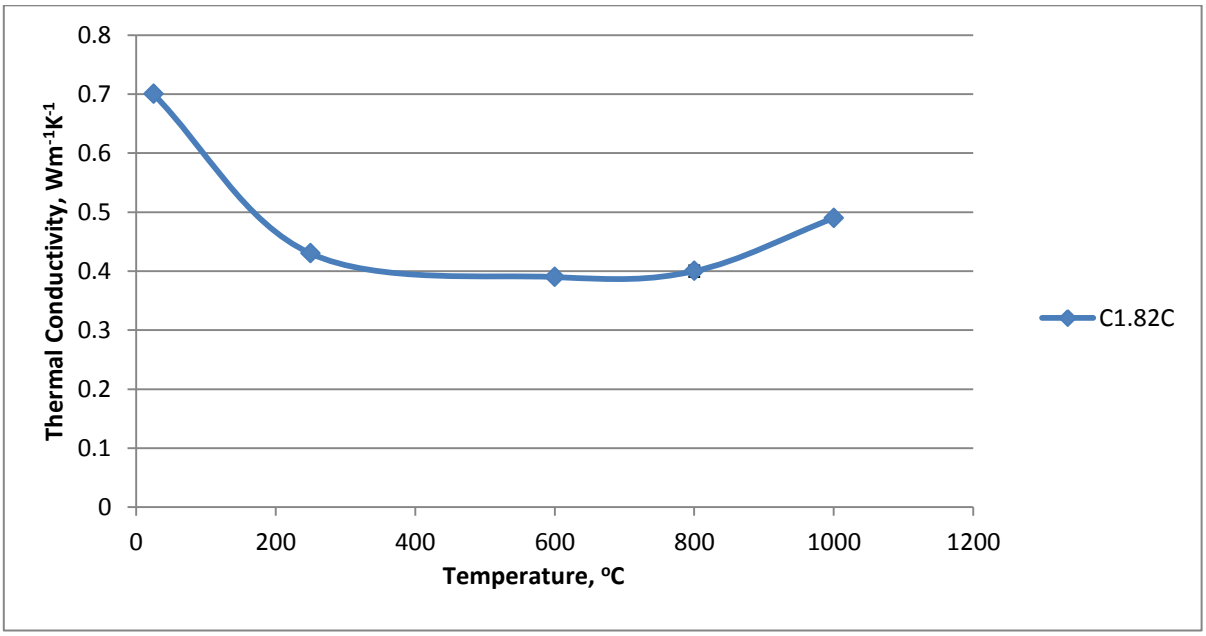

Figure 6.29 Influence of thermal treatment on the thermal conductivity of C1.82C control. Uncertainties in k are +/- 1.6% for AC samples and +/- 0.8% for thermally treated samples. The height of the error bars is smaller than the size of the datum points. Measurements are ex situ at ambient temperature

Table 6.12 tabulates the data from the effect of thermal treatment on the thermal conductivity. The larger uncertainties for the as cured tests are attributed to loss of some water during temperature stabilisation (overnight) between repeat tests. The loss of water has a major influence on the decrease in thermal conductivity below 600^{o}C, whilst the formation of crystalline compounds, together with densification, above 600^{o}C leads to increases in thermal conductivity. The movement of water through the as cured pore system will readily transport heat leading to higher thermal conductivity values than in dried samples.

Table 6.12 Summary of data for C1.82.

	Thermal Conductivity W m^{-1} K^{-1}	**Density g cm^{3}**	**Weight loss, %**
C1.82 AC	0.70 (0.01)	1.95 (0.03)	-
C1.82 PC2	0.43 (0.01)	1.69 (0.01)	16.5 (0.2)
C1.82 600^{o}C	0.39 (0.01)	1.67 (0.01)	19.5 (0.2)
C1.82 800^{o}C	0.40 (0.01)	1.74 (0.01)	17.8 (0.2)
C1.82 1000^{o}C	0.49 (0.01)	1.81 (0.01)	17.3 (0.2)

Figure 6.30 shows the dominant effect of water on the thermal conductivity of filled composites up to 250^{o}C. Above this temperature the densification of the matrix by viscous flow with the formation of crystalline compounds is prevalent. The lower value for WOL 10 above 600^{o}C can possibly be associated with the lower shrinkage and higher macropore content associated with lower viscous flow in the wollastonite containing composites.

The thermal conductivity of wollastonite is 2.7 W m^{-1} K^{-1} at 30^{o}C and that of alumina is 33 W m^{-1} K^{-1} at 20^{o}C. This difference could explain the higher values of ALOX 10 thermal conductivity after firing at beyond 600^{0}C. The WOL 10 specimen showed a greater porosity than that of ALOX 10 (see figure 6.26). The SEM images for these two specimens (appendix B) confirm that the WOL 10 sample to be more porous after firing at 800 and 1000^{o}C. The higher porosity of the WOL 10 sample could explain the lower thermal conductivity values in fired samples.

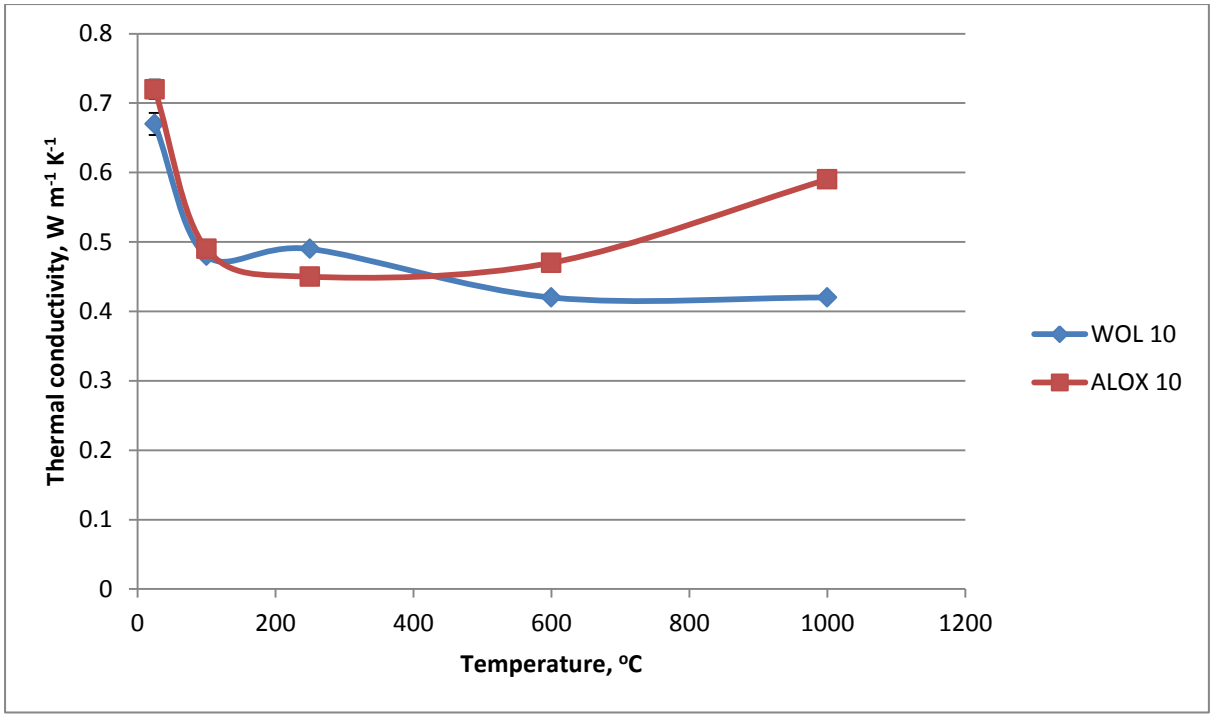

Figure 6.30 Effect of thermal treatment on the thermal conductivity of composites with 10 vol. % filler.

Uncertainties in k are +/- 1.6% for AC samples and +/- 0.8% for thermally treated samples.

The height of the error bars is smaller than the size of the datum points.

Measurements are ex situ at ambient temperature

6.7 Summary

The work reported on in this chapter demonstrates the complexity of the thermal properties of the Collie fly ash and the targeted silicon to aluminium ratio (1.82) used. This targeted ratio did not exhibit large expansive events seen in previous work and attributed to Si-O vaporisation particularly in the presence of water vapour (Clarke, 2002, Provis et al., 2012). This absence of large expansive events was beneficial for thermal stability.

Several mechanisms come into play over the temperature range studied. The addition of thermally stable fillers to the matrix reduces the range of thermal shrinkage of the composites. Applying a post cure cycle to the composites further enhanced this reduction up to the point of commencement of viscous flow. Beyond this point the addition of fillers also reduced the shrinkage at 1000^{o}C (limit of test equipment). The rate of change of shrinkage (with temperature) was also reduced by filler addition.

The addition of wollastonite to the composite gave significant improvements in thermal properties and was particularly effective in delaying the formation of macro pore porosity on firing. Wollastonite appears to be reacting with the geopolymer precursors at the synthesis stage and this reaction product could be a factor in the wollastonite containing composite thermal property suite.

CHAPTER 7

High Temperature Geopolymer Composites

7.1 Introduction

The outcomes of the work reported in chapter six, based on lightly filled (10 vol. % maximum) composites, prompted further research to produce materials with still lower levels of thermal shrinkage. The addition of more thermally stable filler to the C1.82 matrix is investigated. To enable production of composites with acceptable workability, blends of larger particle size (lower surface area) fillers were evaluated. This blend of particle sizes is to optimise packing and keep water content to a practical minimum is common practice in the concrete and refractory industries.

If the sustainability benefits of geopolymers are to be fully optimised then the geographic availability of all the raw material together with a loading based on raw material production input, i.e. manufacturing input and transport input of each material used to arrive at a CO_2 equivalent per unit measure must be taken into consideration. All the raw material should optimally be available (and produced) in say a 100 km radius of the geopolymer manufacturing plant. However speciality additives, generally produced offshore, such as fibres and super plasticisers with low levels of addition (3 vol. % maximum) will generally not meet this criteria, but the low levels of addition of these speciality additives will not markedly increase the already low CO_2 contribution factor of these composites.

Fused alumina is the only readily available suitable material in a range of sizes (5-3 mm, 2-1 mm, and 0.5-0.2 mm) in Western Australia. Other thermally stable fillers, e.g. synthetic mullite, are available in similar size ranges in other parts of the world

Three different fibres are utilised in the manufacture of composites:

- Wollastonite, (Nyad MG, ex NYCO, USA). Wollastonite, a micro fibre, gave low thermal shrinkage and good retention of properties after firing.
- Basalt fibre, (ex Technobasalt, Ukraine). This material was 5 mm long and is used to control macro cracking.
- Polypropylene fibre, (Adfil Ignis, ex Adfil Construction Fibres, UK). Polypropylene fibres undergo sacrificial melting at approximately 165^{o}C to form channels which allows escape of water vapour and thus limits the possibility of explosive spalling on high temperature exposure.

This blend of fibres is expected to handle crack propagation in the micrometre to millimetre range. Blends with other fillers could lead to thermal property synergistic effects. This is an area needing further investigation.

7.2 Conceptual evaluation of high temperature composite (HTC) formulation

Several small mixes were tested to give a basis for the manufacture of larger batches (~9 litres). The grades of alumina available for the initial evaluation were 2-1 mm and 0.5-0.2 mm. The initial trial formulation is shown in table 7.1.

Table 7.1 Initial HTC trial formulation, HTC1.

Material	pbw
Collie fly ash	100
Na- silicate (PQ-D)	10.5
NaOH pellets	9
Water	24
Wollastonite ,Nyad MG	10
Polypropylene, Adfil Ignis	0.15
Alumina 2-1 mm	150
Alumina 0.5-0.2 mm	75
Total	398.65

pbw = parts by weight

The above formulation contains 36 vol. % of alumina, 13 vol. % water (on total weight) and 37.2 vol. % (on geopolymer binder content). The slump in the mini-cone was 14 mm (cone height = 59 mm) and is shown in figure 7.1. Specimens from this batch were cured for 24 hours at 70^{o}C and stored for 7 days prior to firing at 1000^{o}C.

The results are shown in table 7.2. The majority of the weight loss, free water, is occurring up to 250^{o}C (limit of the PC2 cycle) with small amounts above this temperature attributable to dehydroxylation and material from the loss on ignition fraction of the fly ash and other additives. Firing at 1000 to 1100^{o}C gave a 100% increase in compressive strength accompanied by an average shrinkage of 1.5%. Firing at 1200^{o}C lead to a 196% increase in compressive strength with a small expansion. This is attributed to sintering and formation of crystalline compounds. Figure 7.2 a and b show SEM images for as cured and fired at 1200^{o}C specimens. The major change from the unconsolidated as cured morphology to the compact

uniform morphology after firing at 1200^{o}C explains the increases in compressive strength outlined in table 7.2.

Figure 7.1 Mini cone and HTC1 slump sample.

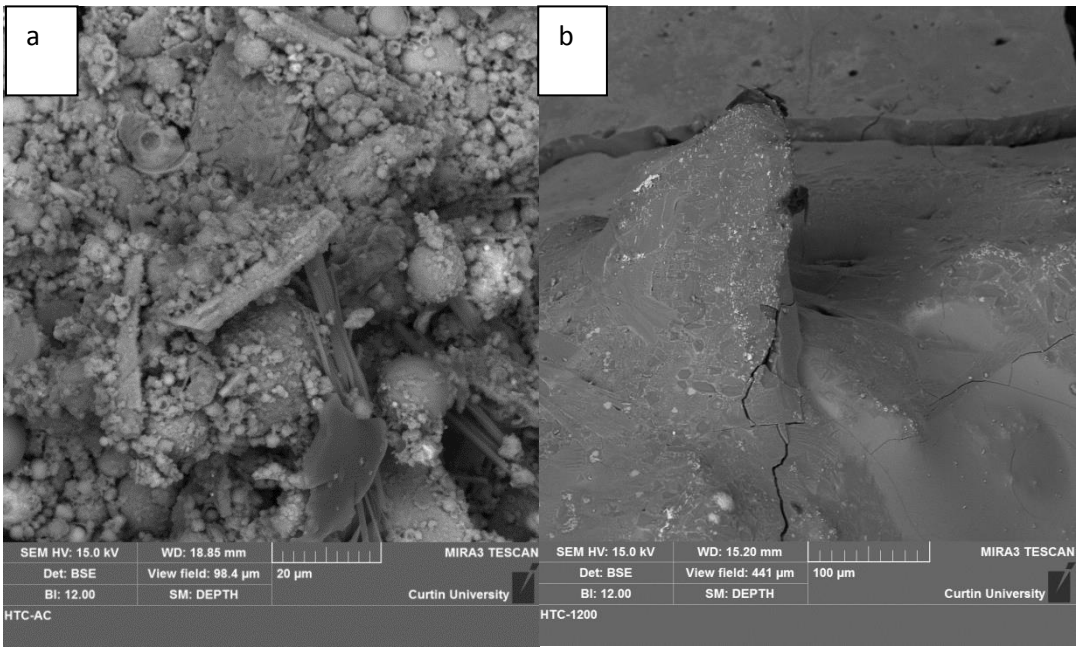

Figure 7.2 SEM images of HTC1, (a) as cured and (b) fired at 1200^{o}C.

Between 5 and 6% of water content is unaccounted for in the weight change results (table 7.2). Compressive strength samples were cut from 20 mm thick slab to give a cube. These 20 mm slabs were 28 days old prior to firing and subsequent testing. The unaccounted water was probably lost due to equilibrium drying.

Table 7.2 Properties of thermally treated HTC1 samples.

	% weight change	**% volume change**	**Compressive Strength, MPa**	**Young's Modulus GPa**
As cured	-	-	17.7 (1.0)	0.9 (0.1)
Post cure cycle PC2	-7.1 (0.2)	-2.7 (0.2)	21.5 (1.3)	0.6 (0.1)
1000^{o}C	-7.7 (0.2)	-2.0 (0.1)	35.4 (0.4)	1.2 (0.1)
1050^{o}C	-7.9 (0.2)	-1.0 (0.1)	38.9 (1.5)	1.1 (0.1)
1100^{o}C	-7.7 (0.2)	-1.5 (0.1)	35.3 (2.04)	1.1 (0.1)
1200^{o}C	-7.5 (0.2)	+0.08 (0.01)	52.4 (4.95)	1.3 (0.1)

The relatively high water content (37.2 wt. % based on geopolymer binder) has limited the development of compressive strength and Young's modulus in the as cured and post cured specimens. However the levels obtained are suitable of elevated temperature exposure applications.

This formulation gave an as cured density of 2.57 g cm^{-3} with a thermal conductivity of 0.74 W m^{-1} K^{-1} and 1000^{o}C fired results of 2.55 g cm^{-3} and 0.72 W m^{-1} K^{-1}, respectively. The lower than expected as cured thermal conductivity may be attributed to the high water content in this system. The thermal conductivity of the fired sample would be expected to show lower values due to loss of water but higher values due to the formation of crystalline phases which generally exhibit higher thermal conductivity values than amorphous phases (Shackleton, 2005). A convolution of these properties has led to only a small variation after firing. Density would also have been expected to have been higher after firing due to the formation of a more compact microstructure and loss of low density water. Some air entrainment will also have occurred during casting contributing to lower density and thermal conductivity. The thermal properties of the large vol. % of graded alumina is masking any changes which are occurring in the binder phase.

The presence of a large proportion of alumina in HTC1 gave rise to different phases (compared to unfilled or lightly filled systems) after firing. Table 7.3 lists the phases

identified by XRD in as cured and specimens fired at 1200^{o}C. The phases listed for the 1200^{o}C sample were also present in specimens fired at 1000, 1050 and 1100^{o}C.

Table 7.3 HTC1 XRD phases before and after firing.

Phases present in as cured samples	**Phases present in samples after firing at 1200^{o}C**
Corundum (04-004-5434) Al_2O_3	Corundum (04-004-5434) Al_2O_3
Hematite (01-076-4579) Fe_2O_3	Hematite (01-076-4579) Fe_2O_3
Quartz (01-087-2096) SiO_2	Quartz (01-087-2096) SiO_2
Siderite (00-002-0837) $FeCO_3$	Siderite (00-002-0837) $FeCO_3$
Sodium Aluminium oxide (04-010—5172) $Na_{0.5}Al_{11.5}O_{17.5}$	Sodium Aluminium oxide (04-010—5172) $Na_{0.5}Al_{11.5}O_{17.5}$
Mullite (04-016-1587) $Al_{2.26}Si_{0.74}O_{4.87}$	Nepheline (04-016-1738) $Na_{3.6}Al_{3.6}Si_{4.4}O_{16}$
Wollastonite (00-043—1460) $CaSiO_3$	Albite, calcian (01-079-1148) $Na_{0.499}Ca_{0.491}Al_{1.488}Si_{2.506}O_8$
Aluminium silicon phosphate (00-047-0616) $Al_{0.47}Si_{0.15}P_{0.38}O_{4.87}$	Anorthite, sodian (01-073-6461) $Na_{0.34}Ca_{0.68}Al_{1.66}Si_{2.34}O_8$

Corundum (alumina) was added at 36 vol. % and is expected to be present after firing. Hematite and quartz are fly ash remnants and also expected to be present after firing. In previous work (see Table 5.9) mullite has remained after firing at 1000^{o}C but this is not the case here. It is postulated that the large amount of alumina present is having a nucleating effect on mullite and wollastonite (both of which were absent after firing) to form new compounds such as albite and anorthite and other amorphous phases. Figure 7.3 shows the irregular surface of an alumina particle in HTC1 AC. These surface corners will be areas of high surface energy with the stoichiometry of the surface probably balanced with hydroxyl groups or Na^{+}-O^{-}T groups (T= Al). The nucleating effect of nano-alumina for geopolymer formation was reported on by Rees (2007). Similar effects may be possible for the formation of crystalline phases at the alumina particle high surface energy locations.

The presence of sodium aluminium oxide may also be attributed to the surface effects of alumina. In alumina the Al: O molar ratio is 0.67, in the sodium aluminium oxide this ratio is 0.66. The decrease in ratio means that another atom, in this case sodium, is required to balance the stoichiometry. This may be indicative of sodium ions combining with surface hydroxyl groups on the alumina and initiating the formation a new crystalline phase whilst the bulk of the alumina remains unchanged. This phase is present in the as cured and fired specimens suggesting that a reaction between the alumina and sodium hydroxide is taking

place to form this phase during the initial geopolymer synthesis. The initial step in this reaction is possibly reaction of surface hydroxyl groups with sodium cations forming Na-O-T entities as above.

A significant impact of the firing is the appearance of albite calcian and anorthite sodian (end members of the plagioclase feldspar group) together with the disappearance of wollastonite. As wollastonite has always been present after firing when used as the sole filler in other geopolymer samples it suggests that the presence of alumina may have had a catalytic effect on the phase transformations.

Nepheline ($NaAlSiO_4$) crystallises from sodium based geopolymers fired up to 1000^{o}C. Further heating of nepheline leads to the formation of albite. In the presence of calcium compounds anorthite would also be formed. This gives a second route to the formation of anorthite.

The siderite, (ferrous carbonate), is derived either from the basalt fibres (Fe_2O_3 = 8.965 wt. % and Na_2O content = 3.88 wt. % from XRF) by reaction with the alkaline activating solution and carbon dioxide from the atmosphere or more probably from amorphous ferrous compounds in the fly ash During the firing procedure there has been insufficient oxygen due to low diffusion and/or time for oxidation to Fe^{3+} to occur.

Aluminium silicon phosphate is attributed to efflorescence. Phosphate based efflorescence has previously been seen in geopolymers based on Collie fly ash (Temuujin et al., 2009b). 100 g of Collie fly ash has 1.5g P2O5 which is equivalent to 0.64 g of phosphorus. If all this phosphorus is converted to the phosphorus containing phase (10.7 wt. % of phosphorus) we can produce 5.98g of phase from 100 g of fly ash or 398.65 g of HTC1. A 1g sample for XRD will have 0.015 g of phase which has been detected. On firing phosphorus compounds are either oxidised to volatile phosphorus oxides or may be incorporated into the silicon and aluminium tetrahedra structures in an amorphous form hence the absence from the XRD data. The presence of phosphorus after firing should be confirmed by XRF analysis. Phosphorus exists in a tetrahedral structure and geopolymers based on phosphorus with silicon and aluminium have been reported (Davidovits, 2008e).

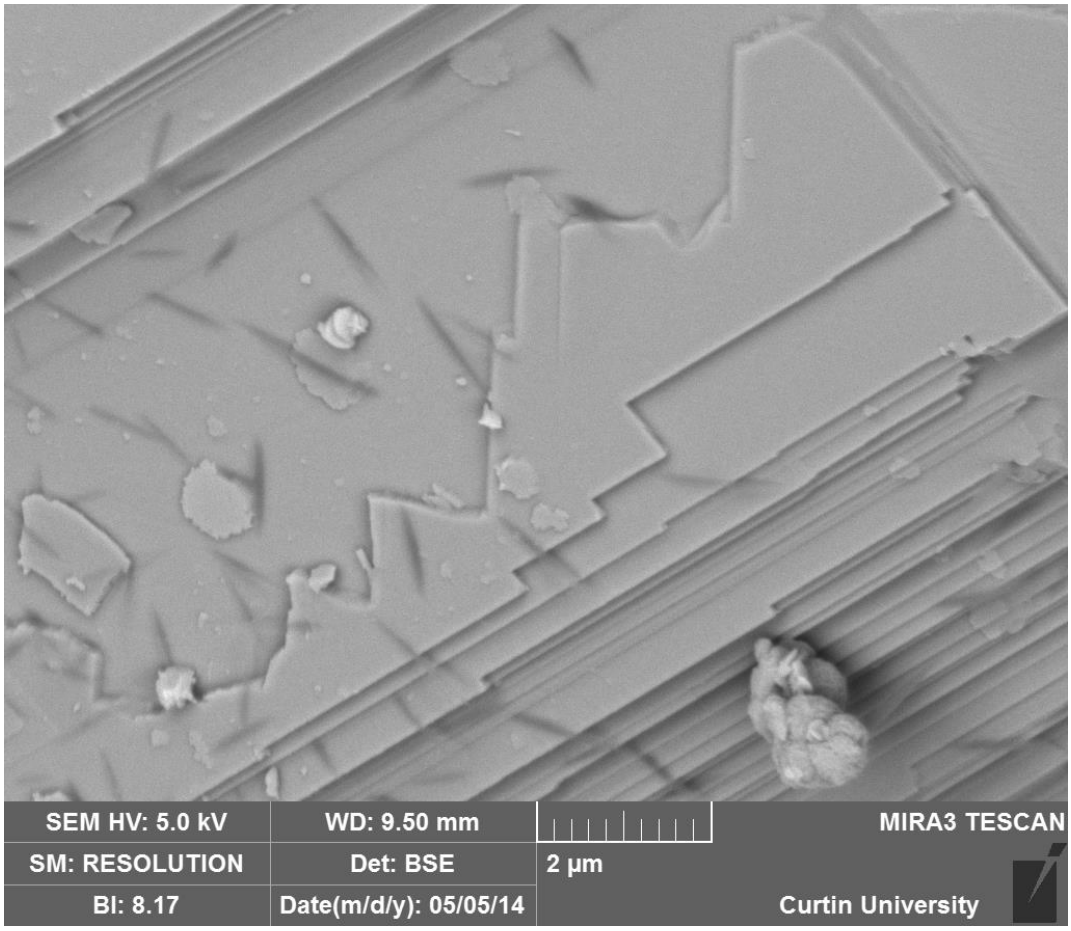

Figure 7.3 SEM image showing surface morphology of alumina filler particle in HTC 1 AC

The thermal expansion curve shown in figure 7.4 shows the heating/cooling cycle results for the as cured sample (first cycle) and a second cycle carried out on the same specimen. The first cycle heating curve exhibits the water loss and shrinkage phenomenon of Region II, albeit at very low levels of thermal expansion. Expansion occurring from around 200 to 660^{o}C is linear before levelling off at 0.25 to 0.3%. Cooling down from 1000 ^{o}C to 200^{o}C was linear, with a final shrinkage of 0.5%. This is a thermal expansion range of 0.8% inclusive for both the heating and cooling stage. The thermal expansion of the alumina is masking the geopolymer paste shrinkage. Inflection points at approximately 636^{o}C and 820^{o}C correspond to the region IV commencement and completion points albeit at 15^{o}C higher than the control paste and at lower thermal expansion values.

The second applied cycle over the same temperature range gave linear heating and cooling shrinkages with a range of 0.9%. The weight loss after the first cycle was 7.5% and 0.01% after the second cycle. Measured shrinkage on specimens post dilatometry for cycle one

and cycle two were 0.40% and 0.18%, respectively. The first thermal cycle initiated the majority of the physical phase changes leaving a material which was thermally stable in any subsequent thermal cycles not exceeding the maximum temperature of the preceding cycle(s). The second thermal cycle produced further shrinkage which suggests that a small quantity of thermally unstable phase was still present. It is proposed that the fired material will become thermally stable (up to the firing temperature) after 2 to 3 firing cycles when no further phase changes can occur. Further changes in thermal stability of the system will occur if the maximum service temperature is increased and oxidation reactions occur over the long term. In table 7.2 firing at 1200^{o}C showed a reduction in thermal shrinkage compared to 1000 to 1100^{o}C.

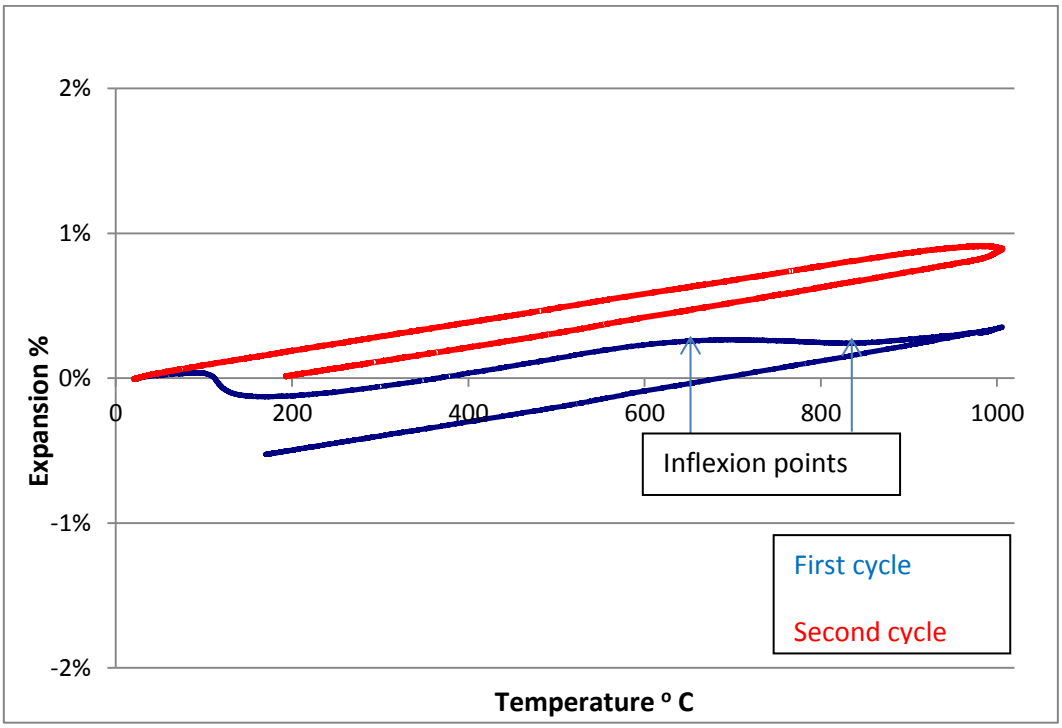

Figure 7.4 HTC1 thermal expansion curves.

A reduction in water content is required to improve the levels of physical properties of the composite. Two naphthalene formaldehyde sulphonate superplasticisers (details in Table 7.4) were evaluated at lower water contents. Table 7.4 outlines two mortar formulations with lower water contents and with 2.5 pbw (1 pbw active) of two different superplasticisers.

Table 7.4 Trial mortar mixes.

	HTM 2; pbw	**HTM 3; pbw**
Collie Fly ash	100.0	100.0
Activating solution	39.5	39.5
Wollastonite	10	10
Alumina 0.5-0.2 mm	207.6	225
5 mm Basalt fibre	1.0	1.0
Adfil Ignis polypropylene fibre	0.15	0.15
Mixing water	2.0	6.0
Superplasticiser 1 (Tamol NH3703)	-	2.5
Superplastiser 2 (Sikament NN)	2.5	-
Total	362.75	384.15
Wt.% water on geopolymer binder	22.5	25.4
Wt.% water on total	8.7	9.2
Vol.% alumina	39	40
Calculated density, g cm^{-3}	2.7	2.69
Measured density, g cm^{-3}	-	2.08

Both mixes gave non-flowing pastes and testing of the Tamol mix (HTM 2) gave poor compressive strength (3.88(0.18) MPa) and Young's modulus (0.39(0.02) GPa). The cured density of the Tamol mix was 2.08 g cm^{-3} compared to a calculated value of 2.69 indicating the presence of voids and poor compaction. The as cured thermal conductivity of this mix was 0.29 W m^{-1} K^{-1}. The superplastiser is behaving as an air entraining agent leading to reduced densities and thixotropy. A formulation for HTC concrete based on aggregate sizes up to 5 mm and containing Tamol also foamed giving a density of 1.84 g cm^{-3} and a thermal conductivity of 0.18 W m^{-1} K^{-1}. These results suggest that superplasticisers could be utilised for the manufacture of foamed high temperature composites for thermal insulation applications but not in their intended role as superplasticisers. The use of these superplasticisers was not pursued in ongoing work due to their foaming tendencies.

7.3 Formulation design

Using the data acquired in section 7.2 further formulations using less water and graded alumina aggregate were designed. The level of water addition was determined during mixing, the criteria being a mix that could be placed in the moulds easily and respond to vibration for compaction. The choice of alumina aggregate size and blending ratio was based

on practical experience from filled epoxy systems to enable compacted specimens to be produced. Small scale mixing trials were undertaken prior to larger scale mixing. Table 7.5 shows the three formulations designed for further testing which will include fire testing and in-situ compression testing (at UWS). No superplasticiser was used and the workability controlled by judicious addition of water. HTM 4A has a thixotropic consistency suitable for application by trowelling and will be used in the fire test evaluation. HTC 6 and 6A have a flowable concrete consistency and will be evaluated in fire testing and in-situ compressive testing. The two mixes with the concrete consistency (HTC 6 and 6A) were considered more appropriate for additional testing due to their flowable consistency and wider applicability in cast parts. All three mixes showed increased flow and compaction when subjected to mechanical vibration, (but trowel applied systems would never be vibrated).

In table 7.6 the properties of as cured samples and those fired at 1000^{o}C are listed. The measured as cured densities compare favourably with the calculated values suggesting that limited air entrainment had occurred. The calculated densities of the as cured specimens were determined from raw material weight contents and densities using the law of mixtures. No allowance was made for curing shrinkage or unfilled pores. The densities of all three systems showed no significant changes on firing possibly due to the high alumina loadings masking any phase changes in the geopolymer binder. The as cured compressive strengths ranged between 17.1 and 23.1 MPa, with increases of up to 58% recorded after firing.

Table 7.5 Final formulations.

	HTM 4A pbw	**HTC 6 pbw**	**HTC 6A pbw**
Collie fly ash	100.0	100.0	100.0
Activating solution	39.5	39.5	39.5
Wollastonite (Nyad MG)	10.0	10.0	10.0
5 mm basalt fibre	1.0	1.0	1.0
Adfil Ignis (PP fibre)	0.15	0.15	0.15
Alumina 5-3 mm	-	175.0	175.0
Alumina 2-1 mm	-	105.0	105.0
Alumina 0.5-0.2 mm	225.0	70.0	70.0
Water	4.5	5.0	7.5
Total	380.15	505.65	508.15
Vol.% alumina	41	52	51
Wt.% water	8.9	6.8	7.2
Wt.% water (on geopolymer binder)	24.3	24.7	26.5
Calculated density, g cm^{-3}	2.74	2.96	2.93

Table 7.6 Properties of High Temperature Composites.

As cured properties	**HTM 4A**	**HTC 6**	**HTC 6A**
Density, g cm^{-3}	2.50 (0.01)	2.73 (0.03)	2.74 (0.02)
Compressive strength, MPa	23.1(1.2)	17.1 (0.4)	18.6 (1.9)
Young's Modulus, GPa	1.73 (0.31)	1.6 (0.4)	1.8 (0.1)
Fired at 1000^{O}C			
Density, g cm^{-3}	2.49 (0.02)	2.75 (0)	2.73 (0.01)
Compressive strength, MPa	29.3 (4.4)	27.1 (0.5)	29.3 (4.4)
Young's Modulus, GPa	2.2 (0.2)	2.3 (0.1)	2.2 (0.2)
Weight loss,%	4.0 (0.1)	3.1 (0.1)	2.9 (0.1)
Volume shrinkage,%	2.6 (0.1)	2.5 (0.1)	1.3 (0.1)

Dilatometry.

Figures 7.5 and 7.6 show the dilatometer curves for HTM 4A and HTC 6A. The figures also show a second cycle run on the initially tested specimen. The curves again show low gradient inflexion points due to the presence of high added alumina content. The higher alumina content (HTC 6A) is showing a higher second inflexion temperature than the HTM 4A specimen. The first inflexion point is approximately the same in both cases and similar to the HTC1 value. The second cycle was substantially linear on the heating and cooling stages with less than 1% expansion evident in both specimens, as was the case with HTC1.

In these tests the alumina is resulting in marked reductions in shrinkage compared to the 10 vol. % filled composites but does not completely mask and/or eliminate the thermally induced sintering and viscous flow properties of the binder during the first heating cycle.

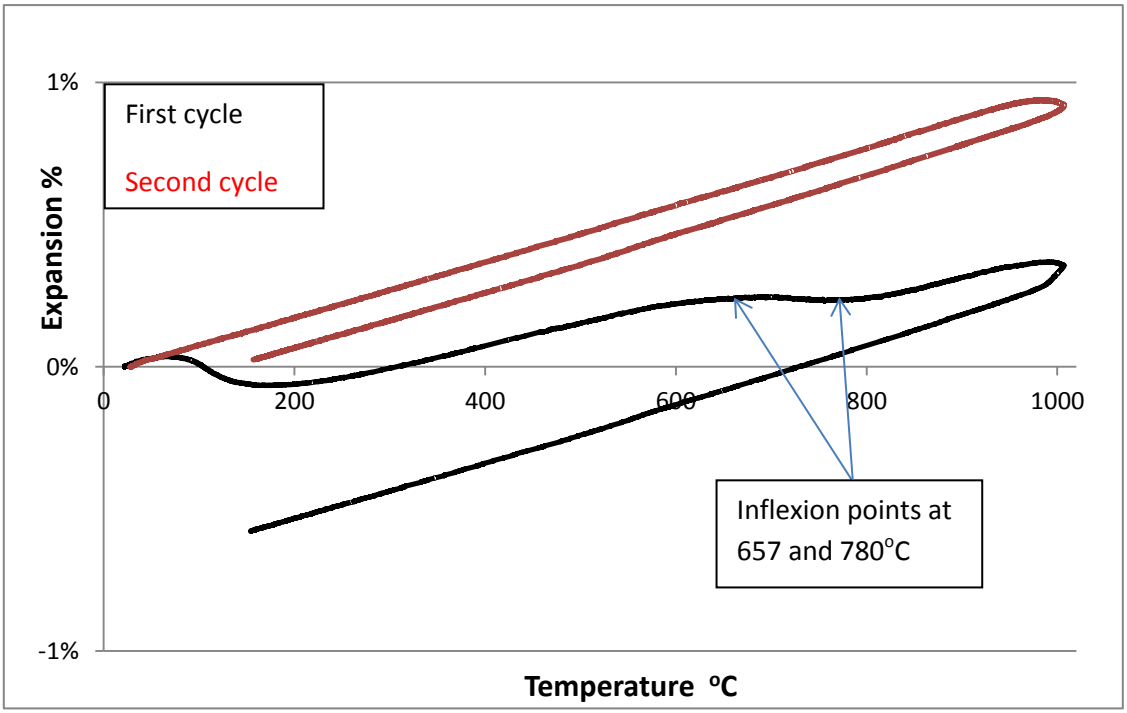

Figure 7.5 Dilatometer curves for HTM 4A.

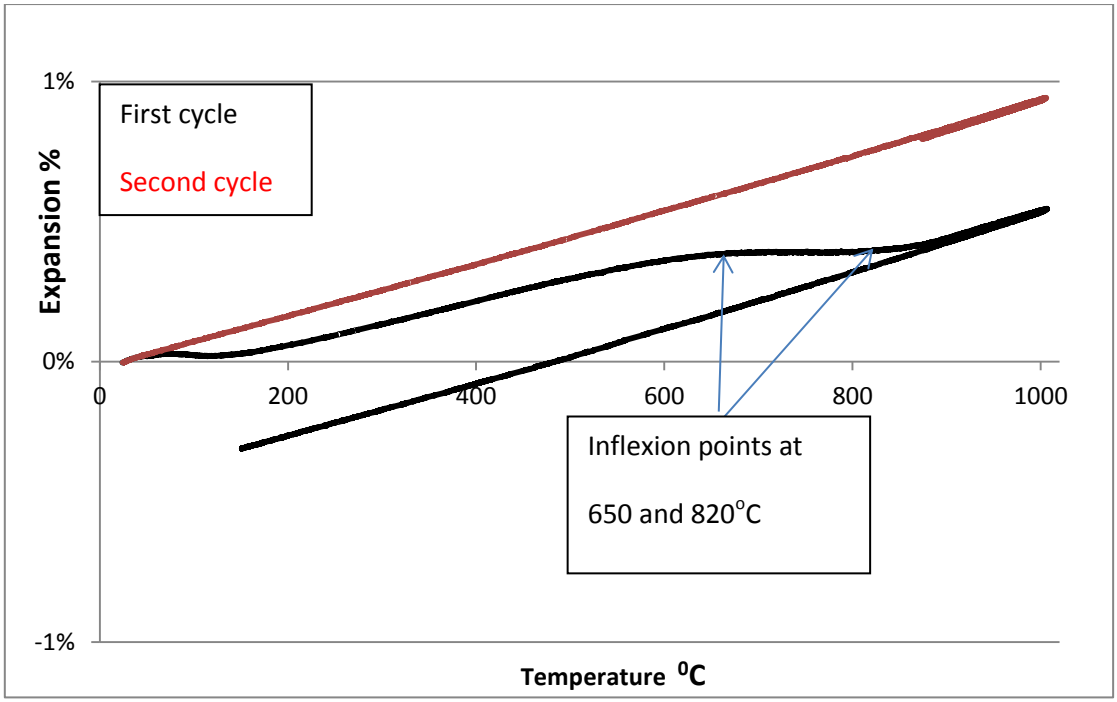

Figure 7.6 Dilatometer curves for HTC 6A.

Thermal conductivity measurements

Determination of thermal conductivity was carried out after a range of thermal treatments. The results are shown in table 7.7. The addition of significant amounts of fused alumina aggregate increased the thermal conductivity of the as cured composites by up to 40%. The thermal conductivity values obtained during thermal treatment at 1000°C were higher by up to 122% than the corresponding values of paste and lightly filled composites as shown in figures 6.31 and 6.32. This is attributed to the high value of thermal conductivity of alumina (33 W/m K at 20°C and 7.22 W/m K at 1000°C) together with the high volume percentage added. Decreases in thermal conductivity can be attributed to the loss of water at lower temperatures (<250°C) whilst increases above this temperature can be attributed in part to dehydroxylation and subsequent formation of new crystalline phases. These crystalline phases can show higher skeletal densities due to denser crystalline packing. Higher density phases are expected to show increased thermal conductivity.

Table 7.7 the influence of thermal treatment on thermal Conductivity, k, W m^{-1} K^{-1}.

	As Cured	Dried at 100°C	PC2	Fired at 600°C	Fired at 1000°C
HTC 6A	0.99 (0.02)	0.77 (0.01)	0.83 (0.01)	0.79 (0.01)	1.09 (0.01)
HTM 4A	0.91 (0.01)	0.78 (0.01)	0.70 (0.01)	0.82 (0.02)	0.92 (0.01)

7.4 Investigation into the effect of wollastonite on composites

Previous work in chapter six has shown that wollastonite can perform the dual roles of filler and fibre reinforcing agent. This produces increased flexural strength (fibre) and a reduction in thermal shrinkage (filler) together with retardation in the rate of macropore formation during exposure to elevated temperature. This retardation of macropore formation is attributed to an interaction of the wollastonite and binder phase in the region of viscous flow. This reduces the ability of the system to flow resulting in less coalescence of small pores occurring. Wollastonite's interaction with the matrix is promoted in the presence of alumina or alumina containing compounds such as mullite. It is proposed that this reaction product is an albite-anorthite compound with the higher calcium content anorthite being more abundant.

Taskiran et al. (2005) produced anorthite crystals using a feed stock of wollastonite, calcined alumina, quartz, Ukrainian ball clay and small quantities of magnesia. Wet milled samples were dried and then pressed to form pellets suitable for firing at temperatures between 1150 and 1300^{o}C with soak times of three hours at the target temperature. Optimum flexural strength (110 MPa) was found in the region of 1225 to 1250^{o}C. QXRD analysis on material fired at 1225^{o}C found that this material contained ~52 % anorthite, ~12 % corundum, and ~8 % cristobalite with the balance being glass.

Rickard et al. (2014) followed thermally induced changes in the microstructure of fly ash based geopolymers using QXRD and SEM. They found evidence of a reduction in concentration of both quartz and mullite phases at temperatures above 700^{o}C and the corresponding appearance of anorthite in the case of the fly ash with the higher CaO content. Mullite and quartz are generally stable up to 1000^{o}C and the reduction in concentration was attributed to the fluxing effect of sodium entities from the activating solution.

Hurst et al. (1996) investigated phase development on firing of three Australian Class F fly ashes using calcium oxide as the fluxing agent. In one of the ashes the fluxing agent caused a change in ash composition from the high melting mullite region to the lower melting

anorthite and gehlenite regions. Supporting evidence, using SEM, XRD and EDS, was obtained for crystallisation of anorthite and gehlenite from the melt.

These above references strongly suggest that there are reactions occurring during firing, via solid state diffusion processes, leading to the formation of members of the plagioclase series, in particular anorthite.

In this section SEM, XRD and flexural strength measurements are used to investigate the effect of wollastonite in the presence of graded alumina on composite properties. The basalt and polypropylene fibres were omitted from this work to enable a direct comparison of wollastonite only on flexural strength. The formulations are listed in table 7.8.

Table 7.8 Formulations for investigation of the effect of wollastonite in composites.

	C1.82	**C1.82 WOL**	**HT4A**	**HT 4A WOL**	**HT 6A**	**HT 6A WOL**
Collie fly ash	100.0	100.0	100.0	100.0	100.0	100.0
PQ – D	10.5	10.5	10.5	10.5	10.5	10.5
NaOH	9.0	9.0	9.0	9.0	9.0	9.0
Water	20.0	20.0	20.0	21.5	20.0	21.0
Wollastonite (Nyad MG)	-	10.0	-	10.0	-	10.0
Alumina 0.5 – 0.2 mm	-	-	225.0	225.0	70.0	70.0
Alumina 2 – 1 mm	-	-	-	-	105.0	105.0
Alumina 5 – 3 mm	-	-	-	-	175.0	175.0
Total	139.5	149.5	364.5	376.0	489.5	500.5
Wt.% alumina	-	-	61.7	59.8	71.5	69.8
Wt. % water	19.9	18.6	7.6	7.8	5.7	5.8

All quantities in table are parts by weight (pbw)

Table 7.9 summarises the flexural strength, weight loss and volume shrinkage before and after firing at 1000^{o}C. The addition of wollastonite (4.45 vol.%) to the paste (C1.82) gave increases in flexural strength before and after firing and a 22.5% reduction in volume shrinkage. Significant increases in flexural strength were measured after firing for HT 4A (127%) and HT 4A WOL (209%). For the HT6A and HT 6A WOL formulations after firing increases in flexural strength were 47.1% and 23.3%, respectively. Volume shrinkage values for the composite systems were dominated by the influence of the large amount of alumina present.

Table 7.9 Summary of as cured and fired results.

	Flexural Strength (as cured) MPa	**Flexural Strength after firing at 1000°C, MPa**	**Weight loss, % after firing at 1000°C**	**Volume shrinkage, % after firing at 1000°C**
C1.82	7.7(0.9)	7.1 (0.8)	15.3 (0.6)	15.1 (0.3)
C1.82 WOL	10.2 (1.1)	10.7 (0.3)	15.7 (0.7)	11.7 (1.2)
HT 4A	9.5 (0.6)	21.5 (1.6)	4.3 (0.2)	2.3 (0.7)
HT 4A WOL	9.9 (1.4)	30.5 (1.8)	4.7 (0.2)	2.2 0.3)
HT 6A	7.7 (0.7)	11.3 (0.9)	2.7 (0.1)	0.8 (0.2)
HT 6A WOL	9.2 (1.3)	11.4 (0.9)	3.1 (0.1)	1.5 (0.3)

An estimate of the coarse graded alumina surface area using the average particle size and density from the supplier technical data sheets together with the assumption that the particles are cubes gave the following outcomes: HT4A alumina content had a specific surface area of 5.05 m^2kg^{-1} and HT6A had 1.58 m^2kg^{-1}. The surface morphology of the three graded sizes used in this evaluation were all similar to that shown in figure 7.3. This is to be expected as they are all produced by crushing and then screening to give the required sizing range.

The large increase in flexural strength of the HTA 4A and HT4A WOL specimens are attributed to the higher alumina surface area present and the smaller alumina particle size. Even in the absence of wollastonite the higher alumina surface area may be able to nucleate / initiate some thermal diffusion reactions leading to a stronger binder composition after firing. The smaller particle size filler system (HT4A) forms a more tortuous network of the binder resulting in a longer crack path length during testing than the coarser particle size system (HT6A) leading to higher flexural strength.

The as cured flexural strength values for the alumina filled composites are lower than those from the filled paste, C1.82 WOL. This is attributed to the lower volume of wollastonite in these composites (HT4A WOL = 2.5 vol.% and HT6A WOL = 2.1%); i.e. there are less fibres

per unit fracture surface, and also the presence of a high volume loading of coarse alumina aggregate (low binder content) may be diluting the wollastonite reinforcing mechanism resulting in lower flexural strength results.

In the case of the fired composites, particularly the HT4A and HT4A WOL, the large increase in flexural strength may be attributed to a more consolidated microstructure after firing. The SEM images (figures 7.7, 7.8 and 7.9) show these changes in microstructure.

Phase Analysis

XRD diffractograms were obtained for the alumina/wollastonite containing specimens. Previous XRD results for HTC 1 (table 7.3) showed the absence of wollastonite and mullite after firing and the appearance of two new phases, albite calcian and anorthite sodian. Albite (sodium rich) and anorthite (calcium rich) are the opposite end members of the plagioclase series. Both of these materials are sodium calcium aluminosilicates of varying cation types and contents and it is proposed that they could have been formed by reaction of wollastonite with mullite (and other aluminosilicates such as nepheline) nucleated and/or catalysed by the presence of alumina. Kovalchuk and Krivenco (2009) reported that albite was evolved from the firing at 1000^{o}C of fly ash geopolymers containing ferric oxides. The formation of albite was associated with a reduction in nepheline concentration.

The ternary phase diagram for $CaO – SiO_2 – Al_2O_3$ shown in figure 7.7 shows anorthite in the centre of the triangle with wollastonite on one side and mullite and corundum on the other side. This suggests that the formation of anorthite is possible from the available composite components under the right thermal conditions.

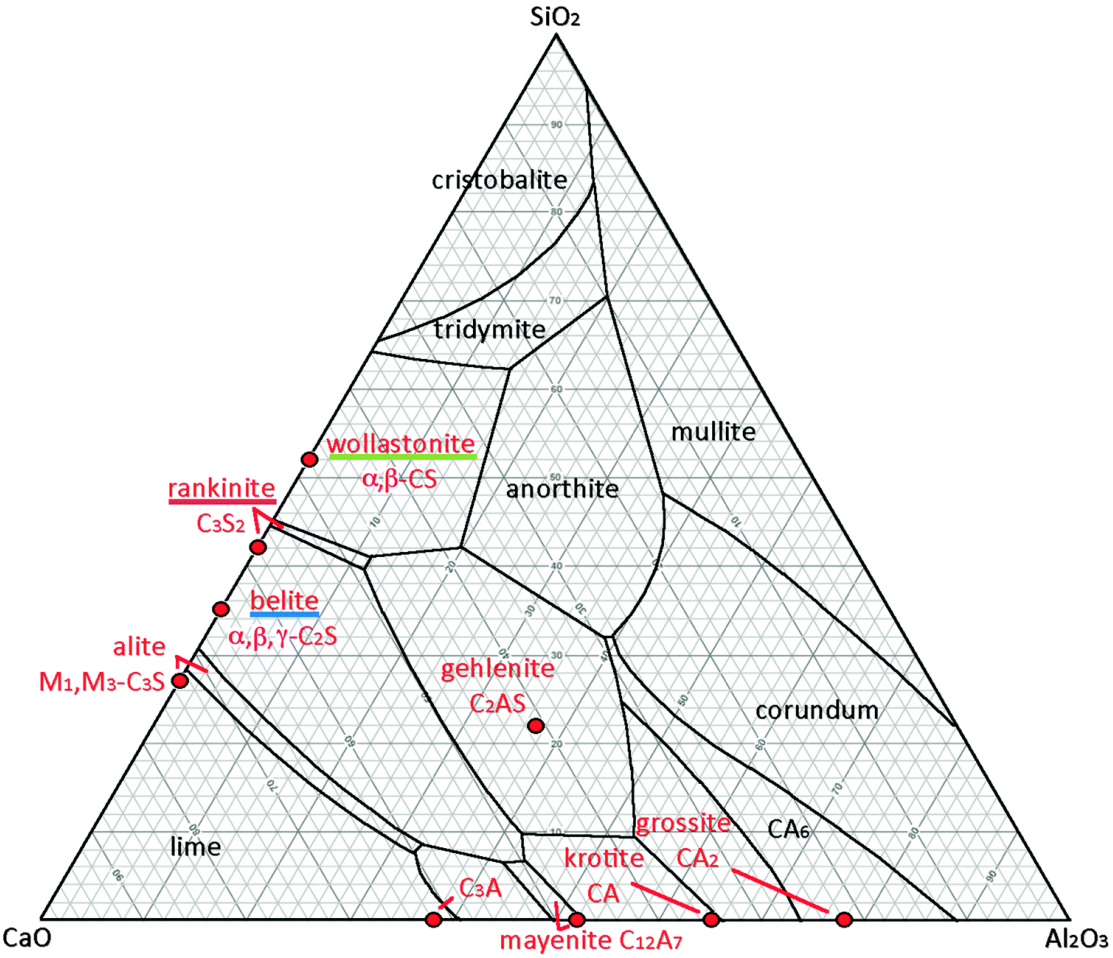

Figure 7.7 CaO – SiO_2 – Al_2O_3 ternary phase diagram (Freitas, 2015).

Table 7.10 lists the phases present during the evaluation of the formulations shown in table 7.8. In contrast to the above (section 7.2) work mullite and wollastonite were present after firing to 1000^{o}C. Nepheline and sodium aluminium oxides were present as previous. In the specimens containing wollastonite, calcium aluminium oxide hydrate was found after firing. It is postulated that this material could have formed on the alumina particle surface and could be a precursor to the albite and anorthite phases formed during the firing of HTC1. Further reaction of this precursor with mullite could have given rise to the albite and anorthite phases shown in table 7.10. At the bottom edge of figure 7.7 are several calcium-aluminium phases with little or no silicon content. These phases are similar to the calcium aluminium oxide found in the wollastonite containing composites. Additional time and/or temperature may be required for the complete evolution of these phases to the albite/anorthite phases seen previously.

If we write the component formulations in terms of oxides it appears that CaO can react with mullite to form anorthite and free silica.

$$CaO.SiO_2 + Al_2O_3 . 2SiO_2 \longrightarrow CaO .Al_2O_3 .2SiO_2 + SiO_2$$

Wollastonite + mullite anorthite + silica

Note: The HTC1 sample was fired in the original furnace which subsequently broke down. This furnace cooled down slower than the furnace used for the second series (HT 4A and HT 6A) of samples. The time difference involved between furnaces for cooling down naturally to ambient temperature is 12 to 16 hours longer for the initial furnace, which could account for the difference in XRD results.

Firing of samples was repeated in the new furnace, but with longer hold times at targeted temperature. This was to confirm if the original XRD evaluation was correct. The new firing conditions were a temperature rise of $4^oC\ min^{-1}$ and either a three hour hold at 1000^oC or a two hour hold at 1200^oC. Table 7.11 shows the XRD results of the extended elevated temperature dwell times.

Table 7.10 Phase identification for composite systems (first run).

HT4A Phases present as cured	**HT4A Phases present after firing at 1000^oC**
Corundum (04-004-5434) Al_2O_3	Corundum (04-004-5434) Al_2O_3
Hematite (01-076-4579) Fe_2O_3	Hematite (01-076-4579) Fe_2O_3
Quartz (01-087-2096) SiO_2	Quartz (01-087-2096) SiO_2
Mullite (04-016-1587) $Al_{2.26}Si_{0.74}O_{4.87}$	Mullite (04-016-1587) $Al_{2.26}Si_{0.74}O_{4.87}$
	Sodium Aluminium oxide (04-010—5172) $Na_{0.5}Al_{11.5}O_{17.5}$
	Nepheline (04-016-1738) $Na_{3.6}Al_{3.6}Si_{4.4}O_{16}$
Ancalime (01-073-6448) $NaAl(Si_2O_6)$	
Anastase (00-021-1272) TiO_2	Anastase (00-021-1272) TiO_2

HT 4A WOL Phases present as cured	HT 4A WOL Phases present after firing at 1000°C
Corundum (04-004-5434) Al_2O_3	Corundum (04-004-5434) Al_2O_3
Hematite (01-076-4579) Fe_2O_3	Hematite (01-076-4579) Fe_2O_3
Quartz (01-087-2096) SiO_2	Quartz (01-087-2096) SiO_2
Mullite (04-016-1587) $Al_{2.26}Si_{0.74}O_{4.87}$	Mullite (04-016-1587) $Al_{2.26}Si_{0.74}O_{4.87}$
Calcium aluminium oxide hydrate (00-002-0083) $Ca_3Al_2O_6\ xH_2O$	Sodium Aluminium oxide (04-010—5172) $Na_{0.5}Al_{11.5}O_{17.5}$
	Nepheline (04-016-1738) $Na_{3.6}Al_{3.6}Si_{4.4}O_{16}$
	Calcium aluminium oxide hydrate (00-002-0083) $Ca_3Al_2O_6\ xH_2O$
Wollastonite (00-043—1460) $CaSiO_3$	Wollastonite (00-043—1460) $CaSiO_3$
Ancalime (01-073-6448) $NaAl(Si_2O_6)$	
Anastase (00-021-1272) TiO_2	Anastase (00-021-1272) TiO_2

HT 6A Phases present as cured	HT 6A Phases present after firing at 1000°C
Corundum (04-004-5434) Al_2O_3	Corundum (04-004-5434) Al_2O_3
Hematite (01-076-4579) Fe_2O_3	Hematite (01-076-4579) Fe_2O_3
Quartz (01-087-2096) SiO_2	Quartz (01-087-2096) SiO_2
Mullite (04-016-1587) $Al_{2.26}Si_{0.74}O_{4.87}$	Mullite (04-016-1587) $Al_{2.26}Si_{0.74}O_{4.87}$
Sodium Aluminium oxide (04-010—5172) $Na_{0.5}Al_{11.5}O_{17.5}$	
	Nepheline (04-016-1738) $Na_{3.6}Al_{3.6}Si_{4.4}O_{16}$
Ancalime (01-073-6448) $NaAl(Si_2O_6)$	Ancalime (01-073-6448) $NaAl(Si_2O_6)$
Anatase (00-021-1272) TiO_2	Anatase (00-021-1272) TiO_2

HT 6A WOL Phases present as cured	HT 6A WOL Phases present after firing at 1000°C
Corundum (04-004-5434) Al_2O_3	Corundum (04-004-5434) Al_2O_3
Hematite (01-076-4579) Fe_2O_3	Hematite (01-076-4579) Fe_2O_3
Quartz (01-087-2096) SiO_2	Quartz (01-087-2096) SiO_2
Mullite (04-016-1587) $Al_{2.26}Si_{0.74}O_{4.87}$	Mullite (04-016-1587) $Al_{2.26}Si_{0.74}O_{4.87}$
Nepheline (04-016-1738) $Na_{3.6}Al_{3.6}Si_{4.4}O_{16}$	Nepheline (04-016-1738) $Na_{3.6}Al_{3.6}Si_{4.4}O_{16}$
Sodium Aluminium oxide (04-010—5172) $Na_{0.5}Al_{11.5}O_{17.5}$	Sodium Aluminium oxide (04-010—5172) $Na_{0.5}Al_{11.5}O_{17.5}$
Calcium aluminium oxide hydrate (00-002-0083) $Ca_3Al_2O_6\ xH_2O$	Calcium aluminium oxide hydrate (00-002-0083)$Ca_3Al_2O_6\ xH_2O$
Wollastonite (00-043—1460) $CaSiO_3$	Wollastonite (00-043—1460) $CaSiO_3$
Ancalime (01-073-6448) $NaAl(Si_2O_6)$	Ancalime (01-073-6448) $NaAl(Si_2O_6)$
Anatase (00-021-1272) TiO_2	Anatase (00-021-1272) TiO_2
	Calcium Aluminium silicide (04-012-9068) $CaAl_2\ Si_2$

The semi-quantitative results in table 7.11 show that the extended dwell times at both temperatures have again led to the appearance of anorthite with the disappearance of the added wollastonite. The mullite reduced in concentration at 1000°C and was absent at

1200^{o}C. The quartz also reduced in concentration as the temperature increased. Two other phases, nepheline and sodium aluminium oxide, tended to lower concentration at the higher temperature suggesting that they could be also involved in the formation of anorthite.

We are possibly seeing large scale micro-absorption and scattering factor differences between the corundum and fluorite standard during QXRD analysis. We have approximately seven times more corundum than fluorite but the peak intensity for the two phases is about the same. TOPAS is having difficulty trying to correct for the absorption and scattering differences of the two phases due to the large concentration of corundum. The optimum particle size after micronizing should be 1 μm with the corundum and fluorite particle sizes. Corundum is a hard material which may require extended micronizing times to achieve the required particle size.

Using the raw data fits (normalised to 100%) without performing the TOPAS analysis i.e. telling TOPAS which peaks and the amount added to use as the standard, gives a semi-quantitative estimate of the phases present. It is not possible to estimate the amorphous content using this procedure. Repacking several samples gave similar outcomes.

Table 7.11 Quantitative XRD phase abundance results (second run, extended dwell time).

	Weight %					
Phase	**HT4A WOL AC**	**2HT4A WOL_1000**	**2HT4A WOL_1200**	**HT6A WOL AC**	**2HT6A WOL_1000**	**2HT6A WOL_1200**
Anorthite, sodian	-	8.2	16.9	-	11.4	12.8
Mullite	4.3	2.9	-	3.2	4.2	-
Nepheline	-	5.6	4.1	-	7.2	2.6
Quartz	5.6	3.2	2.5	4.2	3.8	1.8
Sodium Aluminium Oxide	-	1.9	1.2	-	1.8	2.0
Wollastonite	2.7	-	-	2.0	-	-

One mole of wollastonite (132 Daltons) will theoretically give one mole of anorthite (282 Daltons). However, we have anorthite sodian consisting of mixed cations, Ca^{2+} and Na^{+}. The

amount of wollastonite present in the as cured specimens is insufficient to yield the quantities of anorthite sodian reported in the fired specimens. The short fall could be made up from the contribution of the sodium ion. Alternatively the results obtained from the QXRD were masked by the large quantities of added alumina and are high end estimates.

If we allow for the loss of water in the fired specimens the wollastonite concentrations (if not lost/modified by firing) increase slightly to 2.9% and 2.1% for HT4A WOL and HT6A WOL, respectively. The mullite disappears completely at 1200^{o}C during this testing with decreases in quartz, nepheline and sodium aluminium oxide. The trend is strongly suggesting the proposed reactions to form anorthite by reaction of wollastonite with a range of aluminosilicate phases. Additional work using less alumina, possibly a finer grade, to enable a similar surface area to be achieved may help resolve the QXRD issues experienced here.

SEM and EDS

SEM images were obtained for the composite systems and EDS evaluation carried out in selected areas. Firing produced a more compact microstructure with evidence of viscous flow and the formation of coarser pores. The unfired specimens (figures 7.8, 7.10a and 7.11) consisted of fly ash spheres coated with reaction product, partially dissolved and intact fly ash particles with little geopolymer phase evident. The wollastonite is clearly visible in as cured and fired samples (figures 7.9, 7.10b and 7.12) and appears to be bonded with the surrounding matrix and was investigated by EDS.

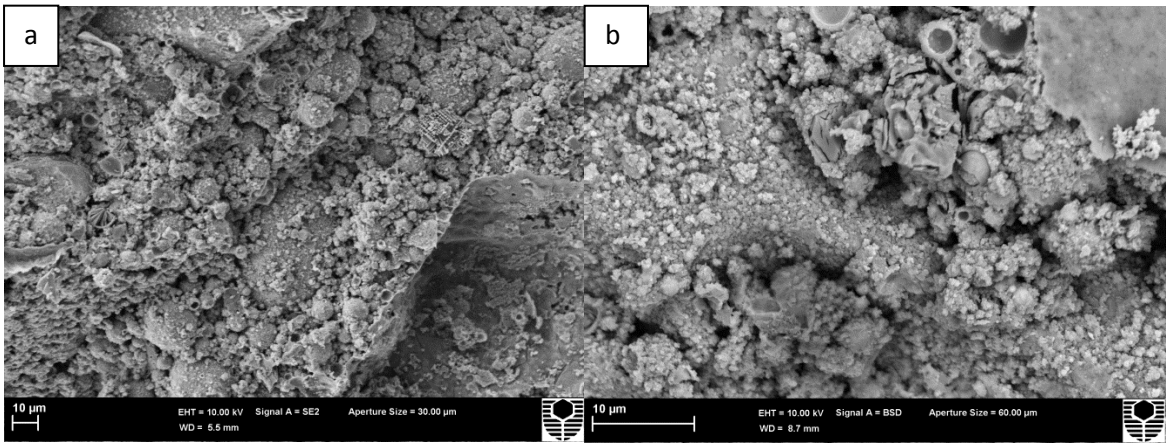

Figure 7.8 SEM images of HT 4A a and b as cured showing two views of the heterogeneous microstructure with little geopolymer phase evident.

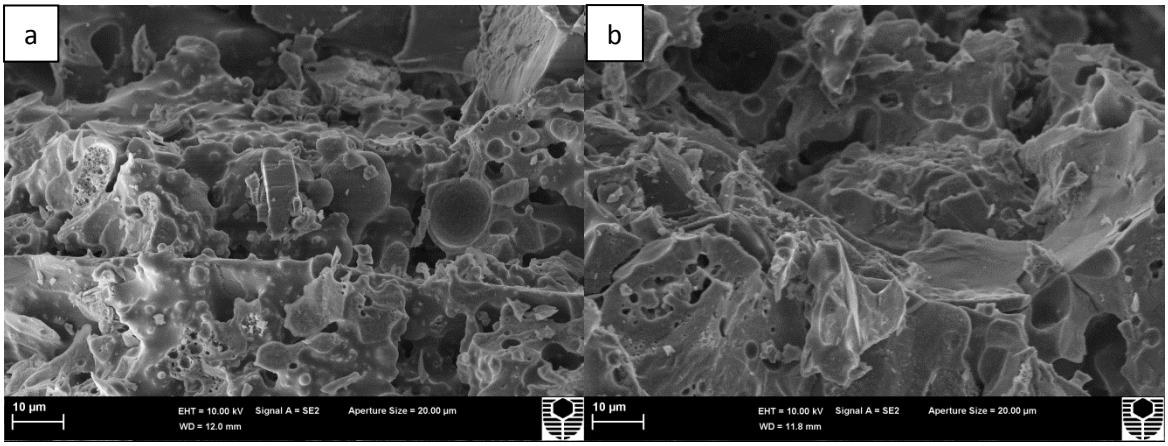

Figure 7.9 SEM images of HT 4A a and b fired at 1000^{o}C showing consolidated microstructure.

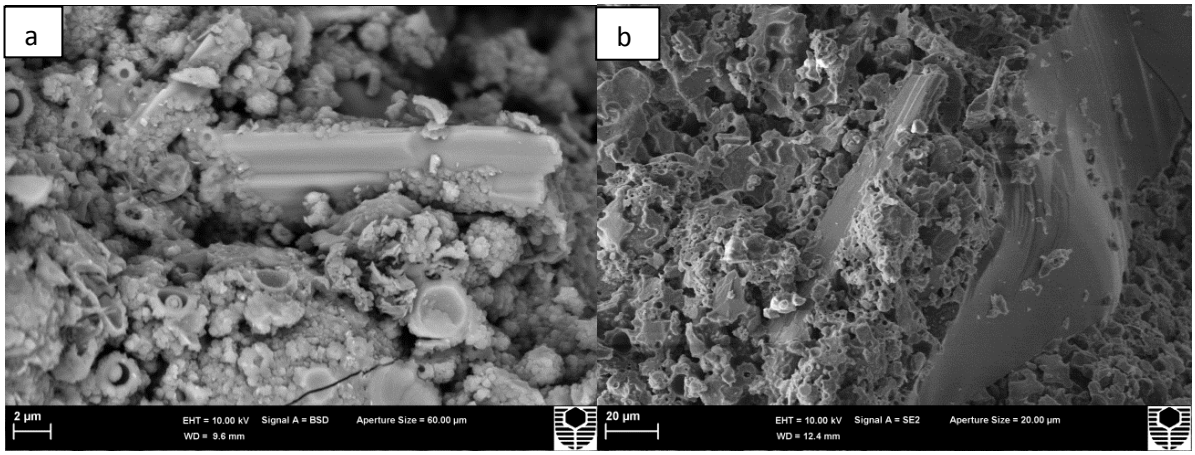

Figure 7.10 SEM images of HT 4A WOL (a) as cured and (b) fired at 1000^{o}C. A change to a more consolidated microstructure is evident after firing. In b a wollastonite particle appears to be well bonded with the matrix.

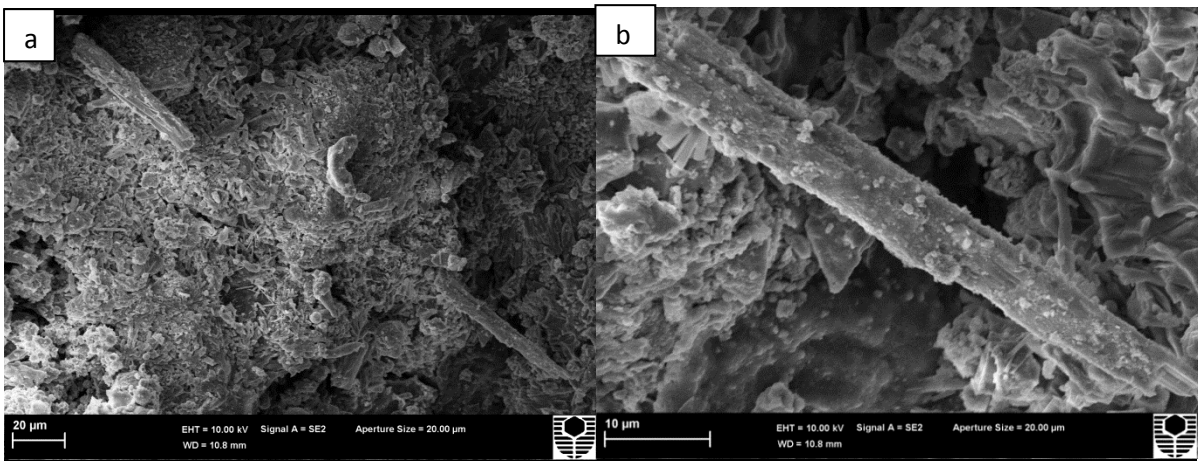

Figure 7.11 SEM images HT 6A WOL a and b as cured showing heterogeneous microstructure. In b the surface of the wollastonite particle appears to have reacted material adhered.

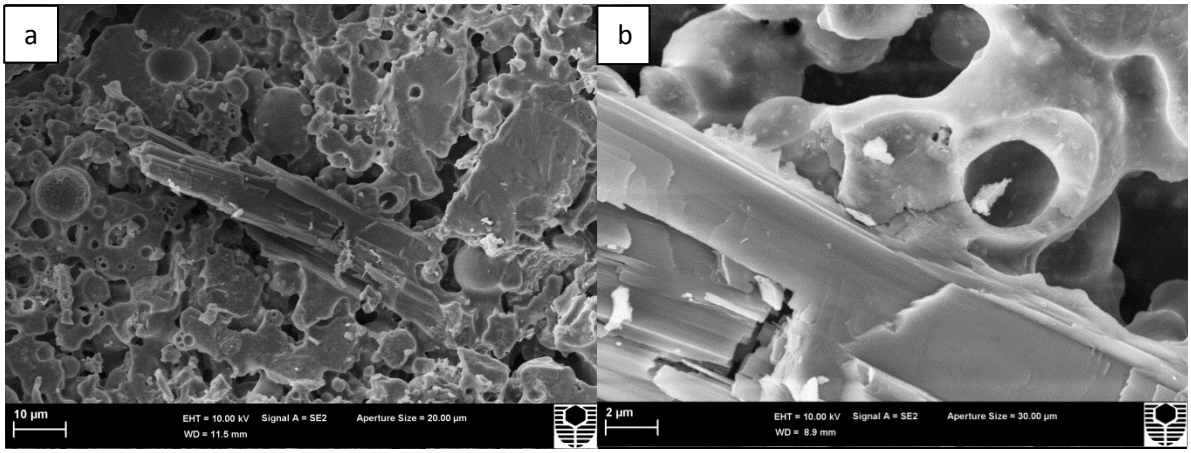

Figure 7.12 SEM images HT 6A WOL a and b fired at 1000^{o}C illustrating a compact microstructure with changes in the surface appearance of the wollastonite.

Elemental Analysis

This area spectrum of HT 4A WOL (figures 7.13 and 7.14) is taken from the fracture surface of a previously fired sample. The accelerating potential of the SEM was set to 10 kV and the beam was positioned on a wollastonite particle. The surface of the particle appears smoother than wollastonite particles in unfired samples and the spectrum is showing the presence of sodium, aluminium and silicon, indicative of a geopolymer. One explanation is that a smooth transition layer has formed on the surface of the wollastonite or has sheared in a brittle mode during testing. Additionally the surrounding material appears to be continuous with the proposed transition layer. Spectra taken at position 2 (figure 7.15) and position 8 (figure 7.17) gave very similar results to spectrum 1 (see figures 7.16 and 7.18). The material around the wollastonite particle appears to be intimately bonded (figure 7.13) and this can be contributing to the large increase in flexural strength obtained after firing.

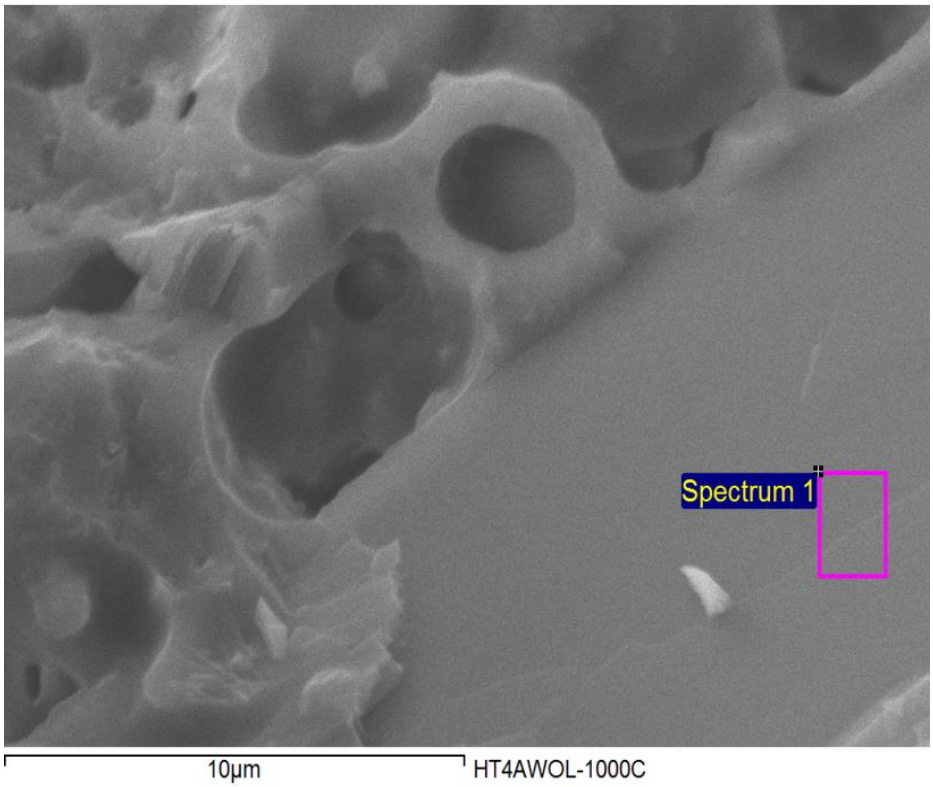

Figure 7.13 SEM image of HT 4A WOL fired showing location of collection of EDS area spectrum 1.

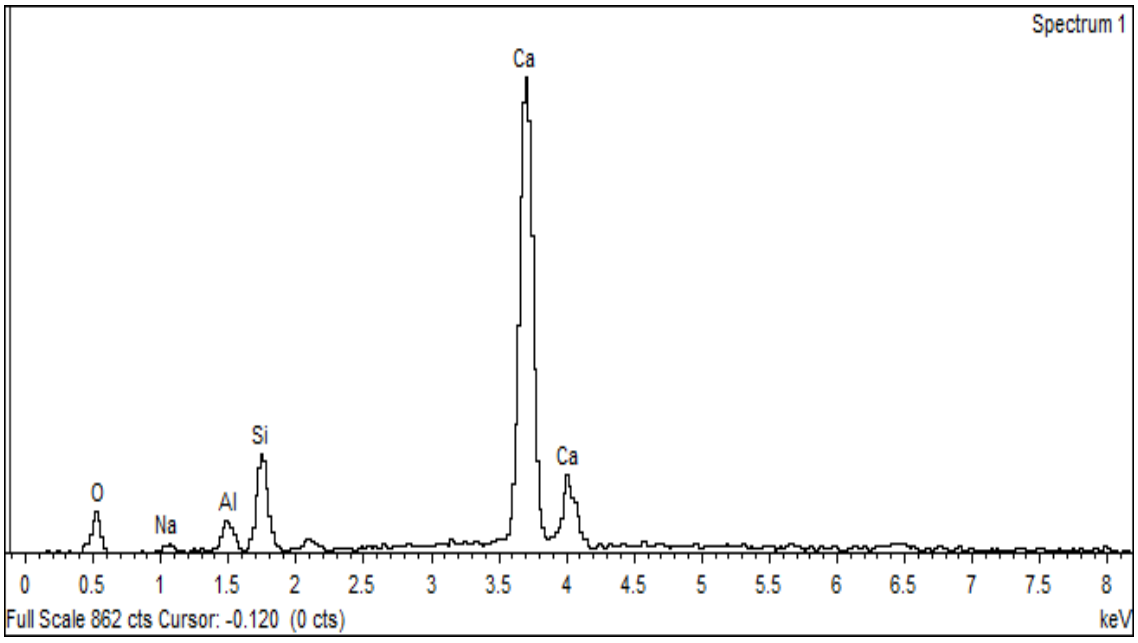

Figure 7.14 HT 4A WOL fired EDS spectrum 1 from location shown on figure 7.13.

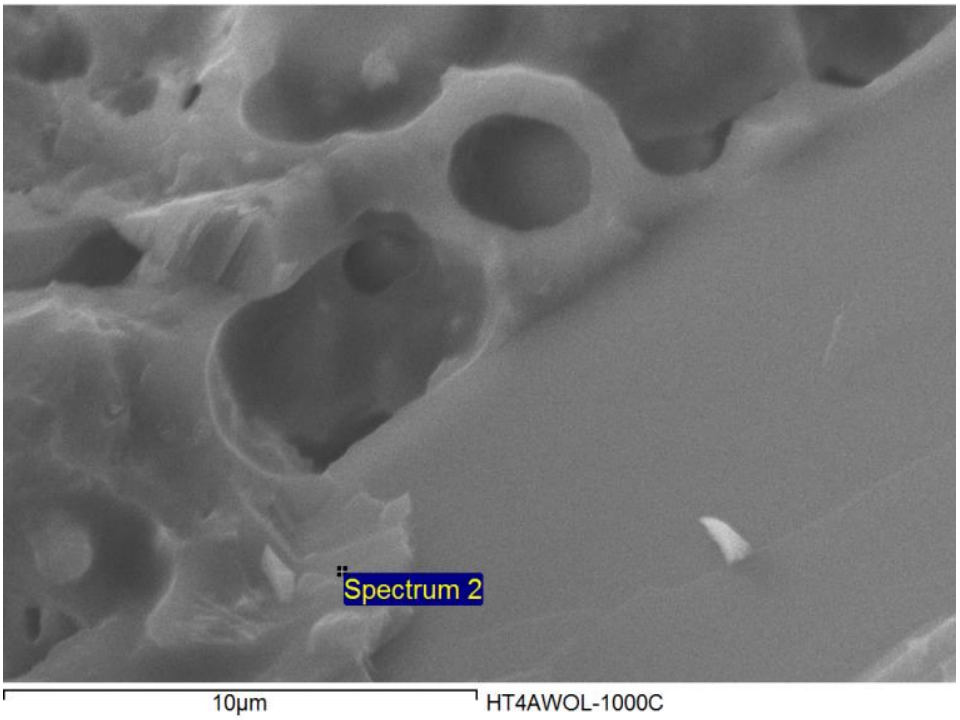

Figure 7.15 SEM image of HT 4A WOL fired showing location where EDS spectrum 2 was collected.

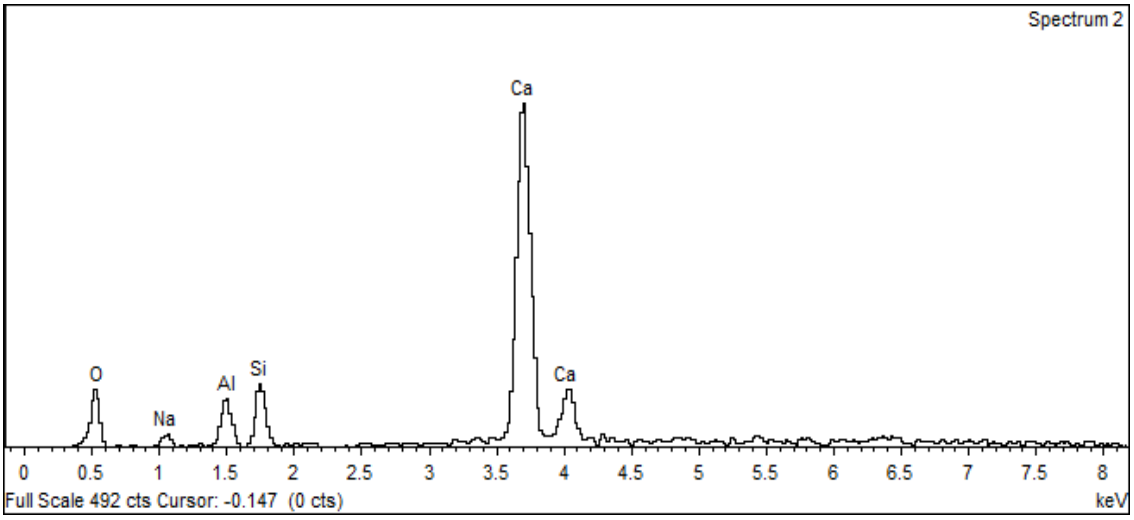

Figure 7.16 HT 4A WOL fired EDS spectrum 2 from location shown on figure 7.15.

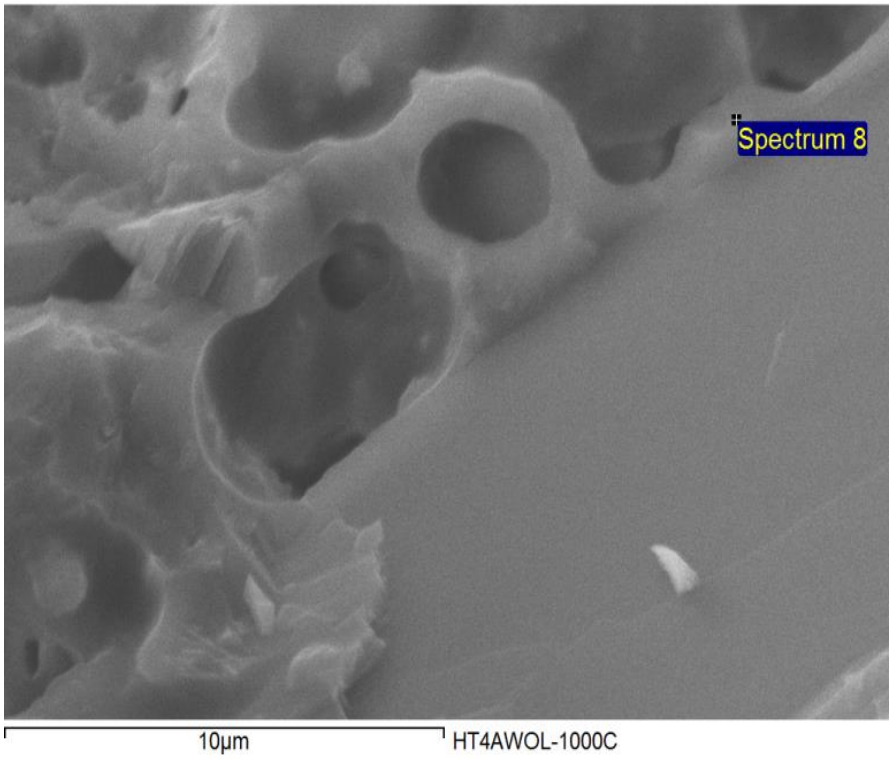

Figure 7.17 SEM image of HT 4A WOL fired where EDS spectrum 8 was collected.

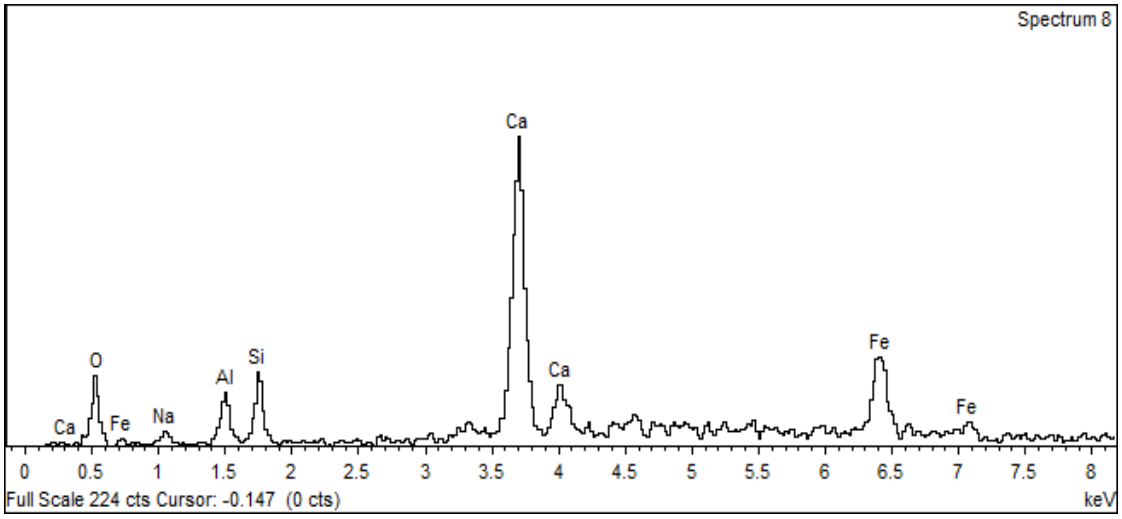

Figure 7.18 EDS spectrum from sample HT 4A WOL fired. Location of spectrum shown on figure 7.17.

Spectrum 6 (figures 7.18 and 7.19) taken further away from the wollastonite particle shows stronger elemental peaks associated with geopolymer and weaker calcium peaks. However, the calcium peaks are still present which may be further evidence for the presence of the

transition layer. I suspect that even at 10 keV the interaction volume was about 1 µm, thus the wollastonite peaks would be included.

The above results strongly suggest that wollastonite is reacting with other phases during firing to form anorthite. The presence of alumina at some minimum addition level based on surface "activity" is advantageous to the extent of this reaction.

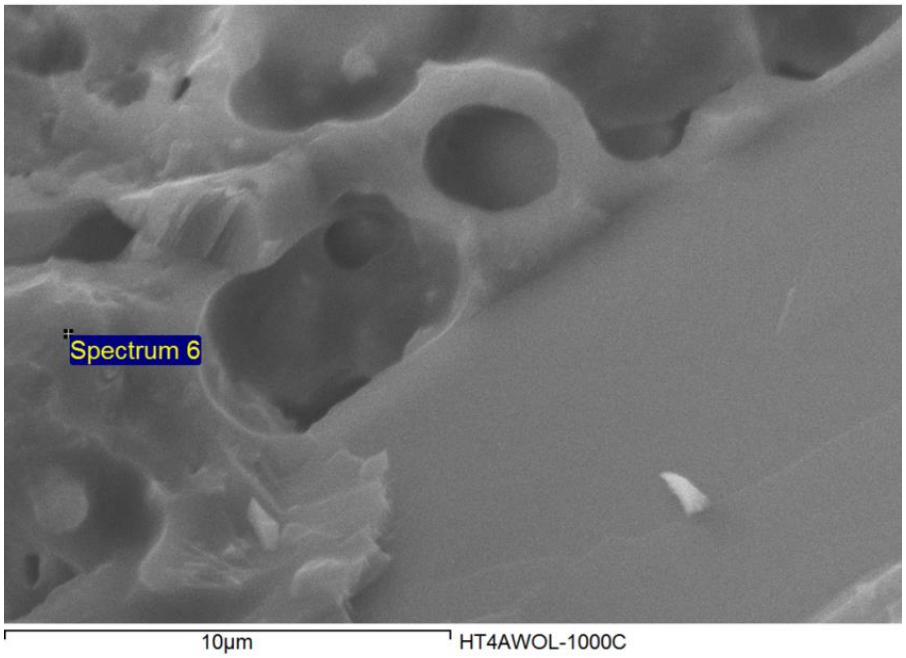

Figure 7.19 SEM image of HT 4A WOL fired where EDS spectrum 6 was collected.

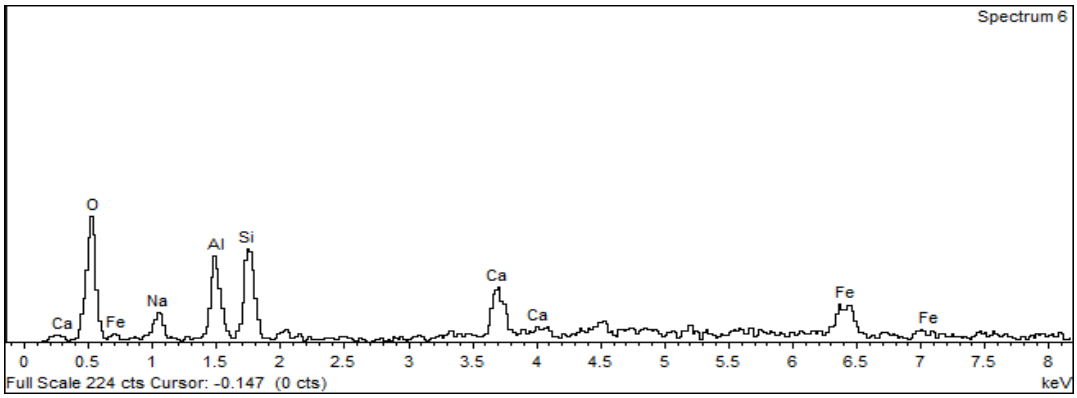

Figure 7.20 EDS spectrum 6 from sample HT 4A WOL. Location shown on figure 7.19.

7.5 In-situ elevated compressive testing of composites

Pan et al. (2010) measured compressive strength and associated strain of a fly ash based geopolymer paste at a range of temperatures. For strain measurements samples were preloaded at 0.25 or 0.5 times the ambient temperature compressive strength. The temperature was then increased at 5^{o}C min^{-1}, followed by a one hour hold at target temperature prior to testing to failure at a loading rate of 20 MPa min^{-1}.

Specimens at both preloads followed similar shaped curves with the lower preloaded set showing smaller compressive strains (i.e. less contraction). The level of preload is influencing the thermal expansion behaviour in terms of absolute strain, but did not move any deflection points with respect to temperature. Figure 7.21 shows the results obtained. Pan et al. measured a glass transition temperature of 560^{o}C for his paste system. Above this temperature significant viscous flow occurred as shown by the large strain increases (1200%) up to 680^{o}C.

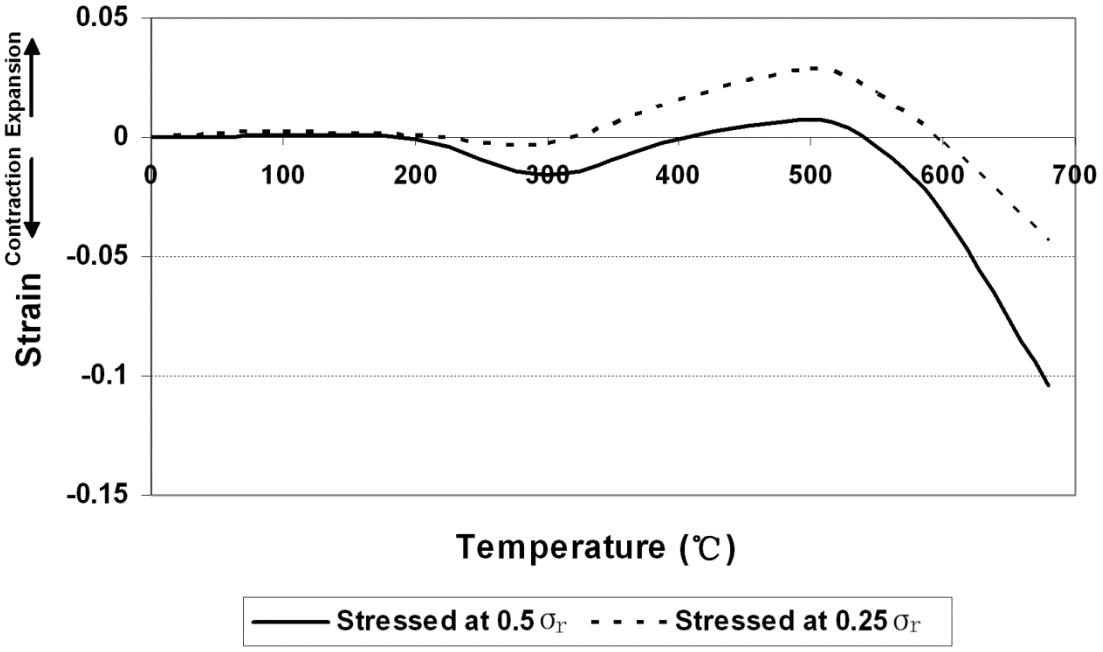

Figure 7.21 Influence of preload and temperature on strain (Pan, 2010).

Similar testing was carried out using the formulations investigated in this study in conjunction with the Institute of Infrastructure Engineering at the University of Western Sydney (UWS). Specimens (200 mm high x 100 mm diameter) were prepared using C1.82 PP and HTC 6A formulations. The as cured compressive strength and Young's modulus were initially determined to allow evaluation of a suitable preload level. A temperature rise of $3^{o}C$ min^{-1} was selected to minimise temperature gradients in the 100 mm diameter cylinders. Pan's original work had been with small (25 mm) diameter cylinders where the use of $5^{o}C$ min^{-1} would not have created large thermal gradients. The doubling of the hold time at target temperature was to ensure a uniform temperature distribution prior to testing. Figure 7.22 shows the in-situ testing equipment. The protective mesh is located around the test cylinder during testing to protect the furnace components at specimen failure.

Table 7.12 summarises the ambient and elevated temperature mechanical properties for C1.82 PP and HTC 6A. The results are based on one off tests due to the exploratory nature of this experiment, the large sample size and limited access to the testing equipment at UWS. No spalling was evident in any samples tested at elevated temperature. Only a faint tinge of red was apparent showing that oxidation of the iron components (to hematite) had not fully taken place (figure 7.23). Young's modulus determination was based on the output data from the extensometer.

Table 7.12 Summary of mechanical property results from in-situ testing.

	C1.82 PP	**HTC 6A**
Compressive strength, as cured, MPa	24.6 (2.1)	16.53 (1.2)
Young's modulus, as cured, GPa	11.43 (0.6)	10.23 (0.8)
*Hot Compressive Strength @ 500^{o}C, MPa	39.91(3.6)	-
Hot Young's Modulus @ 500^{o}C, GPa	2.08 (0.19)	-
*Hot Compressive Strength @ 700^{o}C, MPa	-	35.31 (3.4)
Hot Young's Modulus @ 700^{o}C, GPa	-	2.57 (0.20)

*Ramp to target at 3^{o}C/min; hold 2 hours at target prior to testing.

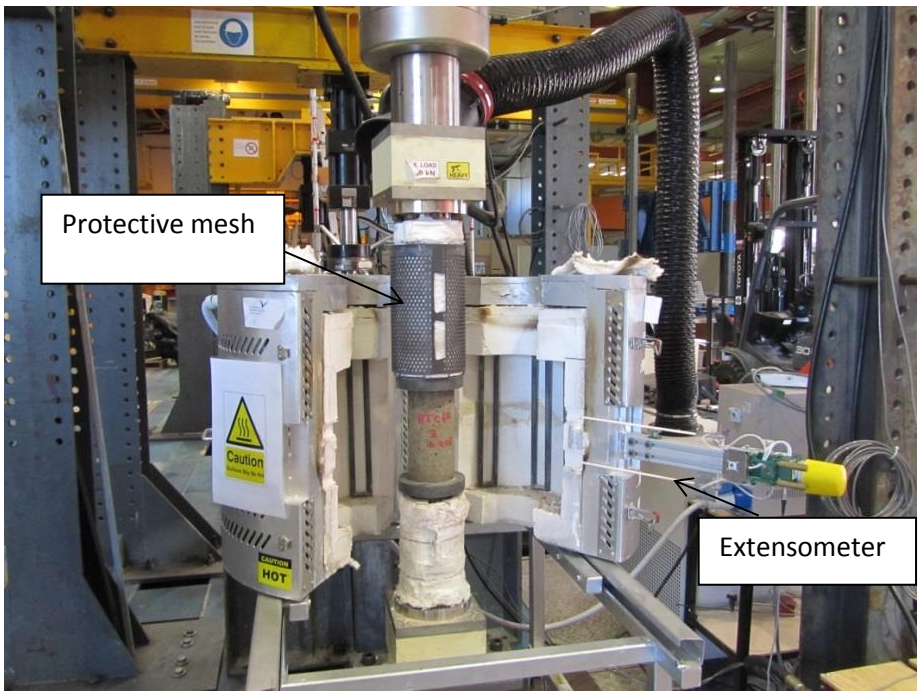

Figure 7.22 High temperature in-situ test equipment at the Institute of Infrastructure Engineering at UWS.

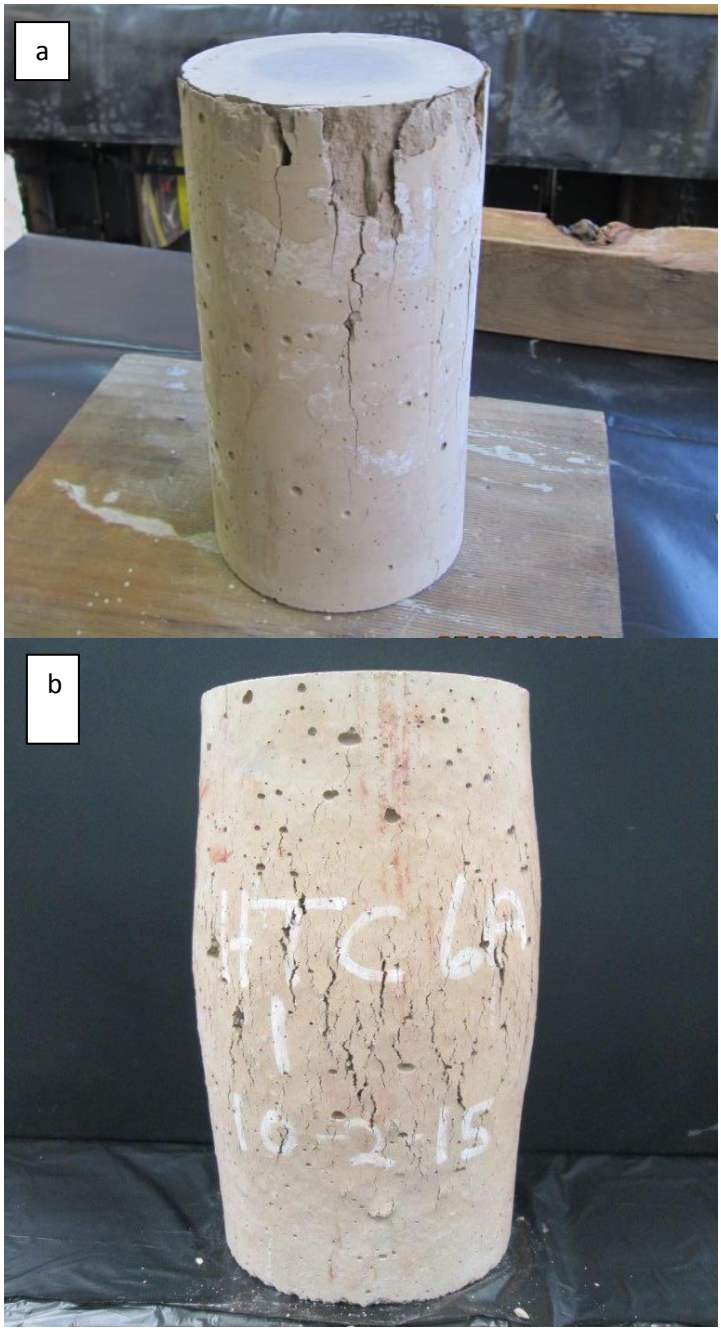

Figure 7.23 Failed cylinders; a, C1.82PP post 500^{O}C and b, HTC6A post 700^{O}C.

Figure 7.24 shows the stress strain curves for C1.82 PP tested at ambient temperature and 500^{o}C. 500^{o}C was chosen for the in-situ test temperature for C1.82 PP from the dilatometer curve which showed a temperature of 580^{o}C for the commencement of Region IV (see Chapter 6). No viscous flow would be anticipated at 500^{o}C. Similarly for HTC 6A 700^{o}C was selected based on an upward shift in the dilatometer curve at 800^{o}C. Figure 7.26 shows the stress-strain curve for HT 6A tested at ambient temperature and 700^{o}C.

Maximum component service temperatures are limited by the onset of viscous flow. Therefore the selection of a temperature for in-situ testing should be below the viscous flow temperature by some safety factor. The dilatometer is a useful instrument for determination of the onset of viscous flow particularly when backed up by SEM images of samples fired in a furnace at temperatures either side of the viscous flow onset temperature.

The effect of testing C1.82PP at 500^{o}C was to give a marked reduction in compressive stiffness shown by Young's moduli of 9.8 and 2.08 GPa, respectively and a tenfold increase in strain at maximum load (0.003 and 0.029).

The increase in compressive strength was from 24.6 to 39.3 MPa at 500^{o}C. This temperature is below the usual onset of viscous flow as seen in the dilatometer. However, the applied stress of the test may be sufficient to reduce the activation energy for the viscous flow process. The tenfold increase in strain at maximum load at 500^{o}C indicates that viscous flow is occurring leading to a more compact microstructure and crack healing with a corresponding increase in compressive strength.

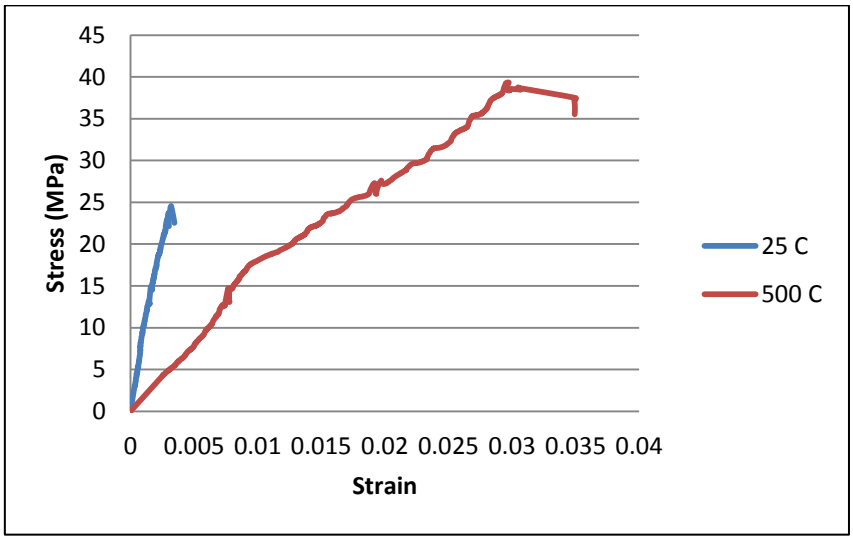

Figure 7.24 Stress-strain curves for C1.82PP at (a) ambient temperature and (b) at 500^{o}C. Note the considerable increase in strain range at 500^{o}C.

Figure 7.25 shows evidence for viscous flow during the in-situ testing. The C1.82PP compression test was performed after two hours dwell time at 500^{o}C. Viscous flow would

not have been observed in this system in low stress tests such as the dilatometer or firing unstressed specimens in the furnace. In the C1.82PP strain test the maximum temperature was 800^{o}C and extensive viscous flow is evident. We can deduce that viscous flow is promoted by the application of stress whilst temperature is being increased and for the C1.82PP system the viscous flow could be commencing as low as 250^{o}C.

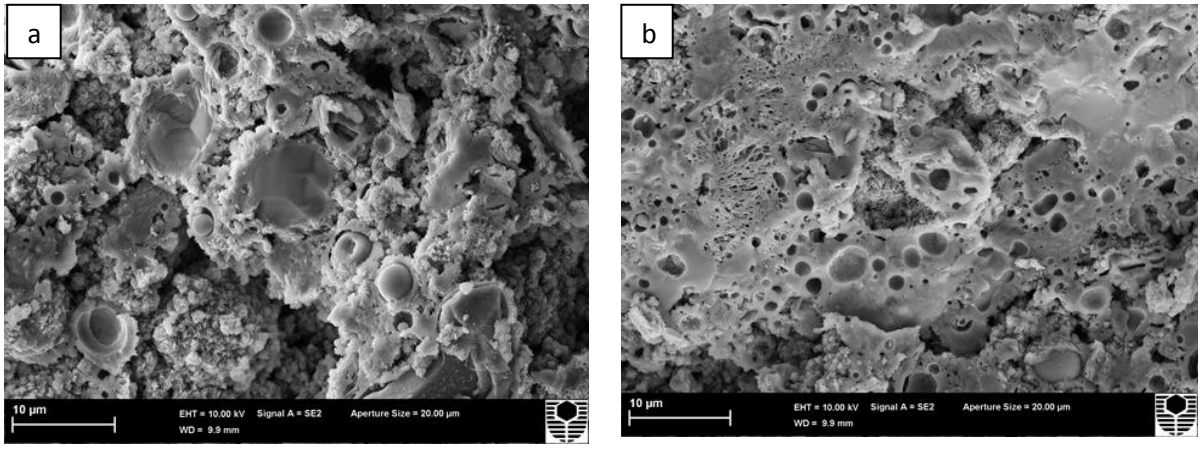

Figure 7.25 SEM images of C1.82PP (a) after compression test at 500^{o}C and (b) after strain test to a maximum of 800^{o}C.

Testing of HTC 6A at 700^{o}C (figure 7.26) gave a similar trend to the paste (C1.82PP) with a reduction in compressive stiffness shown by Young's moduli of 10.23 and 2.57 GPa, respectively and a fivefold increase in strain at maximum load (0.004 and 0.019).

The increase in compressive strength was from 16.53 to 35.31 MPa at 700^{o}C. Viscous flow would be expected to occur at 700^{o}C and that the applied stress would be reinforcing the flow characteristics. The presence of 51 vol. % alumina is expected to contribute to stress distribution during testing. A similar scenario to the paste is also happening with consolidation of microstructure leading to increased strength.

Figure 7.27 shows the presence of viscous flow after testing at 700^{0}C in the compression test and after 900^{o}C in the strain test. At 700^{o}C the viscous flow surface is less smooth than that at 900^{o}C as expected. Possibly 700^{o}C was too high for the hot in-situ testing of HTC 6A.

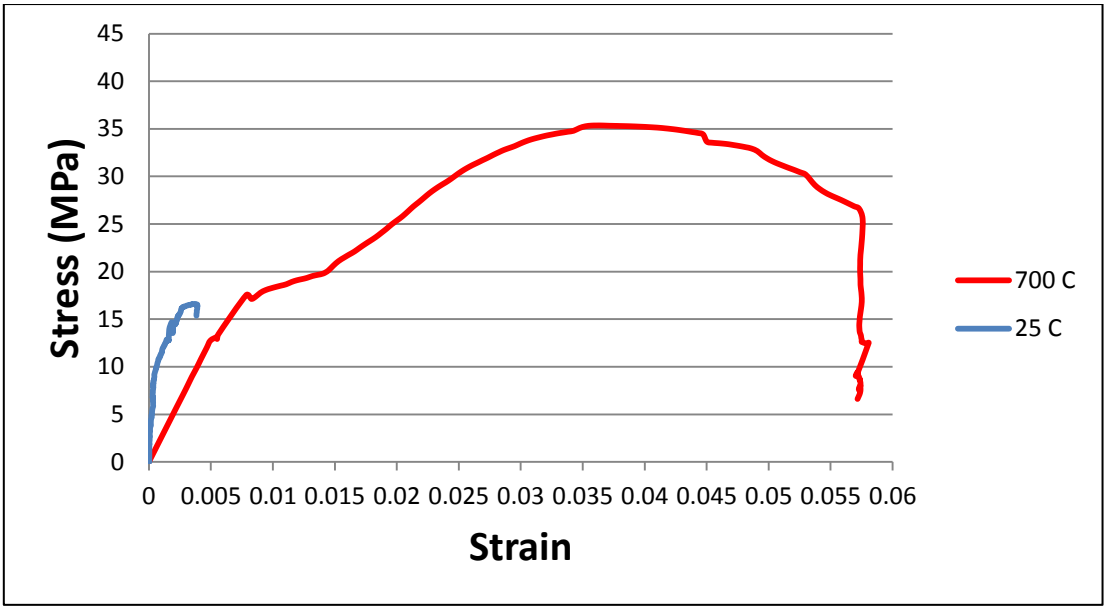

Figure 7.26 Stress-strain curves for HTC 6A at ambient temperature and at 700^{o}C.

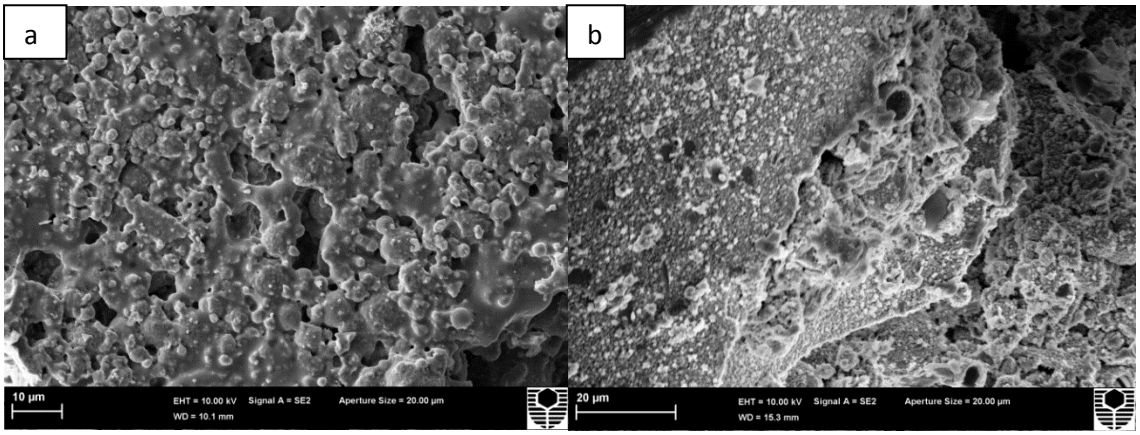

Figure 7.27 SEM images of HTC 6A (a) after compression test at 700^{o}C and (b) after strain test to a maximum of 900^{O}C.

Strain-Temperature evaluations:

To measure the onset temperature of viscous flow the following procedure was adopted; Cylinders were preloaded to 30% of their ambient temperature compressive strength. The furnace temperature is now increased at 3^{o}C min^{-1} and changes in the strain as the temperature increased was recorded. The point where the curve makes a steep, non-reversible downturn is taken at the onset temperature of viscous flow.

In figure 7.28 the C1.82 PP curve shows the graph beginning to turn down at 250^{o}C and unlike the HTC6A curve never shows any sign of recovery. It is expected that most of the

free water has been lost by this temperature and the small amount of polypropylene melted and begun to vaporise.

The commencement of shrinkage on both curves at around 250°C can be attributed to dehydroxylation of the matrix's hydroxyl groups and the commencement of viscous flow accelerated by the applied stress. In the case of C1.82 PP there is not the possibility to form a transition zone due to the absence of wollastonite and alumina hence the continuing growth of strain by ongoing viscous flow as the temperature increases. Calcium in the HTC 6A system may also be contributing to reduction in viscous flow by "crosslinking " the geopolymer network and showing lower fluxing ability compared to sodium entities.

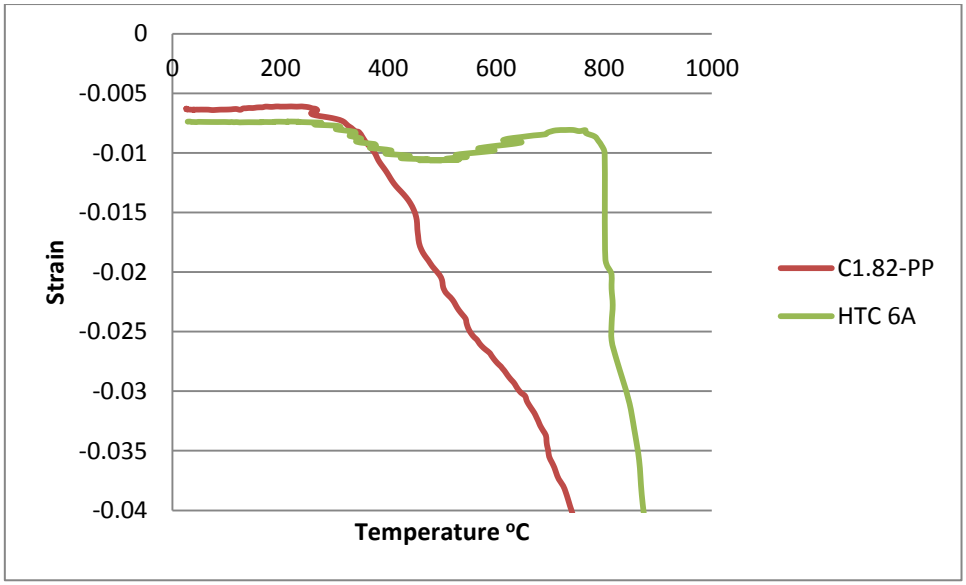

Figure 7.28 the evolution of strain with increasing temperature on preloaded specimens.

In figure 7.29, HTC 6A, region A (300 to 450°C) is attributed to dehydroxylation shrinkage. This dehydroxylation is accompanied by formation of T-O-T bonds which may inhibit viscous flow and then thermal expansion processes take over. Some viscous flow may be occurring in this region due to the applied preload. XRD results did not show that the transition zone phases mentioned above were forming. The temperature for formation of the proposed transition zone is beyond that achieved during this in-situ testing.

Region B, from 500 to 700°C, is attributed to thermal expansion of the system. At around 750°C extensive viscous flow is occurring which will be enhanced by the applied preload (30% of ambient compressive strength). Melting of crystalline phases from the fly ash

remnants and zeolites will also be contributing to viscous flow. Once again XRD did not show the transition zone phases after thermal exposure.

Estimates for glass transition temperatures at the test conditions above are:

C1.82PP = 308^{o}C HTC6A = 750^{o}C

Values obtained from dilatometry (Region IV inflexion) give the following:

C1.82PP = 698^{o}C HTC6A = 650^{o}C

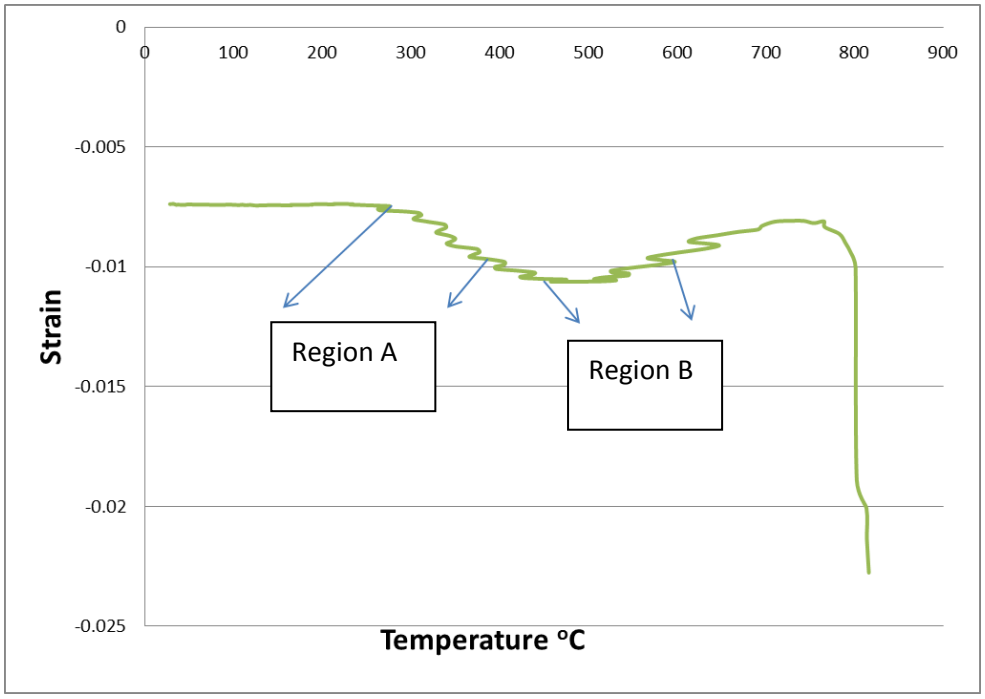

Figure 7.29 HTC6A strain temperature curve.

Menad (2010) claims that pressure assisted sintering increases the contact pressure of particles and thus the driving force for sintering, compared to pressureless solid state sintering by:

- approximately one order of magnitude in hot pressing (HP) at 20-40 MPa pressure.

- approximately two orders of magnitude in hot isostatic pressing (HIP) at 200 - 300 MPa pressure

“The excess driving force over and above that required for sintering due to externally applied pressure is frequently used to decrease the processing temperature (usually by 100 to 500°C) rather than to achieve rapid densification rates”. This would indicate that the applied preloaded stress could be reducing the onset temperature of viscous flow events shown in figures 7.24 and 7.26 compared to values obtained in low stress dilatometry.

7.6 Summary

The low levels of thermal shrinkage (<1%) obtained by the addition of alumina aggregate will be beneficial to the structural stability of samples during thermal cycling and fire testing. On the negative side the higher values of thermal conductivity obtained can lead to lower fire ratings due to faster heat conduction. The higher thermal conductivity values for these composites may be beneficial in novel applications where heat dissipation is important. These could include heat exchange equipment and heat generating electrical equipment which must maintain controlled temperatures without being electrically conductive.

SEM/EDS results indicated that the interaction of the wollastonite with the geopolymer matrix is occurring particularly after firing with the as expected formation of a more compact microstructure.

This compact microstructure and generation of crystalline phases after firing is contributing to increases in flexural strength which will translate into increases in other strength properties. The presence of anorthite, confirmed by XRD, after extended thermal exposure reinforces the occurrence of a reaction involving the added wollastonite and mullite in the presence of alumina.

Whilst the mechanical properties are only moderate, they will be adequate for thermal insulation components, and firing produces strength increases. In-situ compressive testing led to increases in compressive strength, but stiffness properties as indicated by strain at failure and Young’s modulus decreased. The evolution of strain as temperature increased enabled the glass transition temperature (Tg) to be determined. The addition of graded

alumina showed an increase of approximately 500^{o}C in Tg compared to the paste. Further investigations are required to explain this phenomenon.

CHAPTER 8

FIRE TESTING OF GEOPOLYMERS

8.1 Introduction

In this chapter the effect of simulated fire testing based on using a cellulosic test curve is evaluated. Cellulosic fire curves are designed to replicate a fire in situations such as offices, hospitals and domestic dwellings. Australian Standard AS1530.4 was the applicable standard used in this test programme. The standard time-temperature curve for the fire test is shown in figure 2.30 and the time-temperature relationship is shown in equation 3.11. The specified temperature profile is shown in table 8.1.

Table 8.1 AS1530.4 time-temperature requirements for fire testing

Time (t), minutes	Prescribed furnace temperature, ^{o}C
0	20
5	576
10	679
15	738
30	841
60	945
90	1006
120	1049
180	1110
240	1153
360	1213

The Cement, Concrete and Aggregates Association of Australia issued report TC 61 (2010) and listed three relevant concrete failure criteria related to fire exposure:

4. Structural adequacy (ability to resist load);
5. Integrity (ability to resist the passage of flames);
6. Insulation (the ability to prevent fire spread due to unacceptable temperature rise of the unheated face).

The thermal insulation requirements of the AS1530.4-2005 fire test can be summarised as follows:

Failure in relation to thermal insulation is determined when measurement of temperature is made by thermocouples on the unexposed face, and the initial temperature is the average temperature on the unexposed face measured less than 5 min before commencement of the test. The specimen is deemed to have failed when:

(a) Failure criteria 1 (FC1): The average temperature of the unexposed face of the test specimen exceeds the initial temperature by more than 140 K; or

(b) Failure criteria 2 (FC2): The temperature at any location on the unexposed face of the test specimen exceeds the initial temperature by more than 180 K.

Structural adequacy is defined as when a sample either collapses or when the deflection under a given load exceeds that specified in AS1530.4.

Integrity failure can show three failure criteria:

- Continuous flaming on the cold side surface;
- Through gaps into the furnace, as determined by standard gauges, exceeding the sizes specified in AS1530.4;
- Ignition during the cotton wool pad test.

The gap gauges are 6 and 25 mm in diameter. The dimensions of any cracks are quantified as follows and the timing of crack formation recorded:

- The 6 mm gauge can pass into the furnace and also move 150 mm along the gap.
- The 25 mm gauge can enter into the furnace.

Several authors (Rickard et al., 2013, Rickard, 2012, Rickard, 2014, Masi, 2014) have investigated fire resistant geopolymers using the small scale methodology described here. The systems investigated were geopolymers, either as solids or foams, but with no aggregate present. This work introduces thermally stable fillers at loadings up to 51 vol. % to produce specimens with minimal cracking and integrity. The fire rating (FC1) expectation for these high temperature composites was in the order of 60 minutes based on the high density and high thermal conductivity measurements (chapter 7).

The above authors obtained fire ratings for 50mm thick panels in the range of 70 to 100 minutes for fly ash based solid geopolymer pastes and ratings in the order of 60 to 80 minutes for foamed geopolymers, the fire rating decreasing as the fly ash based geopolymer foam density decreased.

8.2 Testing of specimens

The C1.82 paste was used as the original reference specimen. All other specimens contained 0.15 pbw of Adfil Ignis polypropylene fibre. This is based on 100 pbw of fly ash and will reduce in volume terms as the amount of filler increases. This addition was to ensure that any potential for spalling was eliminated during testing and to allow the insulation test to proceed without unwanted side effects from any spalling.

Specimens containing 5 vol. % of either Nyad MG (wollastonite), WOL 5PP, or -45 µm alumina, ALOX 5PP, were included in the test programme.

The high temperature composites described in chapter 7, HTM 4A and HTC 6A were also included. These contain 41.0 and 51.8 vol. % of graded alumina, respectively and are additionally modified with a fibre tri-blend. This tri-blend is based on basalt fibres, monofilament polypropylene fibres and wollastonite.

The moulding of the C1.82 and ALOX 5PP specimens resulted in very few air bubbles being present. This was not the case with WOL 5PP, HTM 4A and HTC 6A, where the highly viscous nature of the mixes allowed air entrainment cavities (bug holes) to occur even with vibration and rodding. The high weight of filled moulds from these two mixes was too great for the vibrating table to facilitate air removal. Photographs of as cured samples shown later in this chapter show the presence of air pockets on the surface prior to fire testing.

Testing was limited to the thermal insulation determination method of AS1530.4. However, where relevant, comments on crack formation, colour changes and other events during testing are made. Testing was carried out on specimens conditioned at 50% relative humidity and 23^{o}C for at least 28 days prior to testing. Weight changes over this period were monitored to ensure a consistent weight was achieved (+/-20 g) prior to testing. Specimens were a nominal 50 mm thick and 290 x 290 mm wide to allow adequate support and exposure to the 200 x 200 mm furnace test window.

8.3 Results

Photographs of specimens before and after fire testing are shown in the figures 8.1 to 8.13. The unfilled specimens (C1.82 and C1.82PP) showed extensive hot side cracking which appeared to have under gone crack healing in some areas on cooling (figures 8.1D and 8.2D).This may be attributed to the ability of these unfilled systems to exhibit extensive viscous flow and sintering. The cold side formed wide cracks (2 mm) which remained after cooling but did not penetrate the specimen thickness and therefore did not compromise the integrity of the specimen. In figure 8.3 showing C1.82PP hot side post fire testing delamination of areas is evident and attributed to differential thermal expansion events.

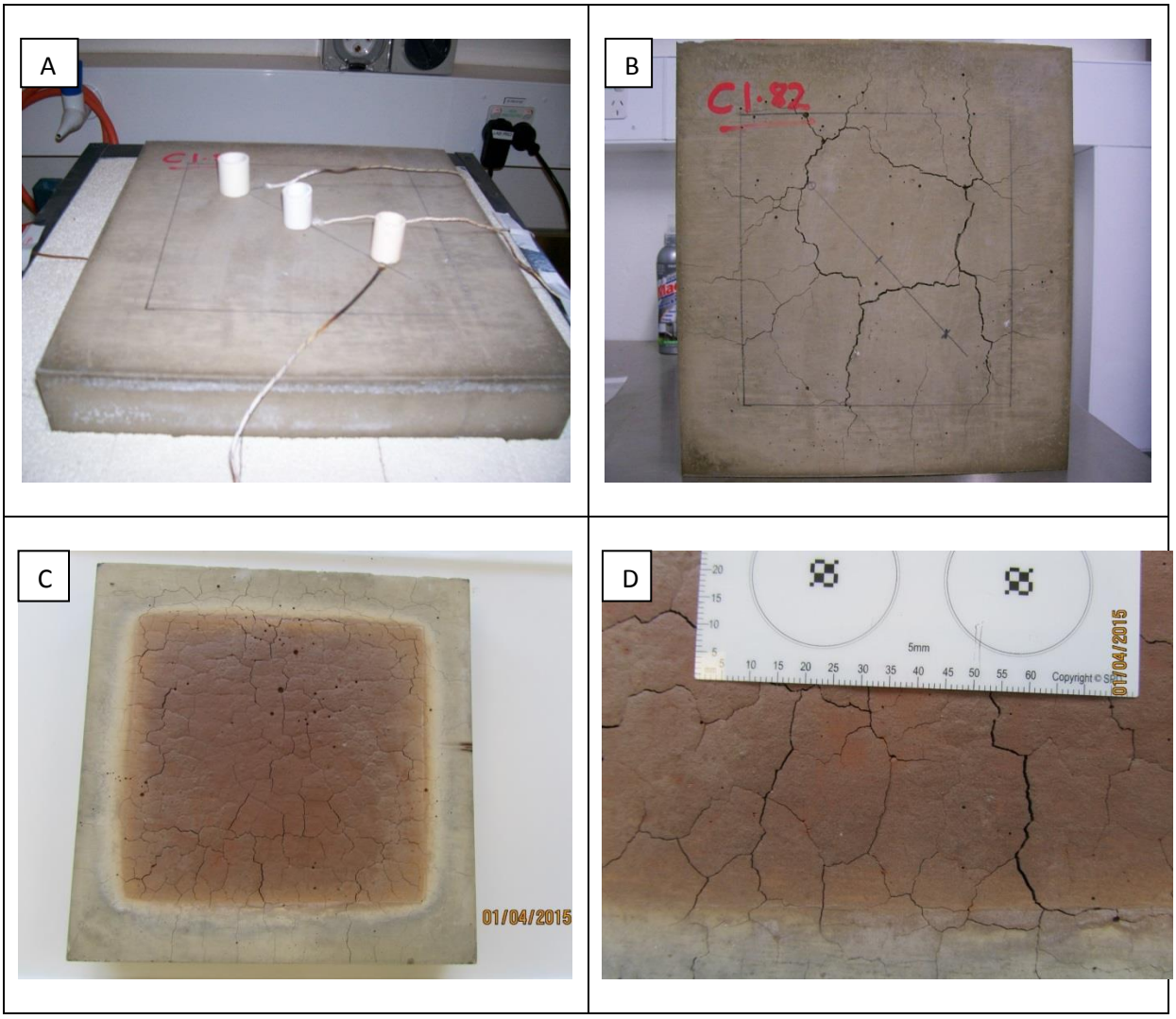

Figure 8.1 C1.82 fire test images

A: C1.82 prior to fire test. The white alumina tubes are used to hold the thermocouples in place.

B: C1.82 cold side after fire test. The square marked in black indicates the area below exposed to the fire.

C: C1.82 hot side after fire test

D: Close up view of C1.82 hot side after fire test.

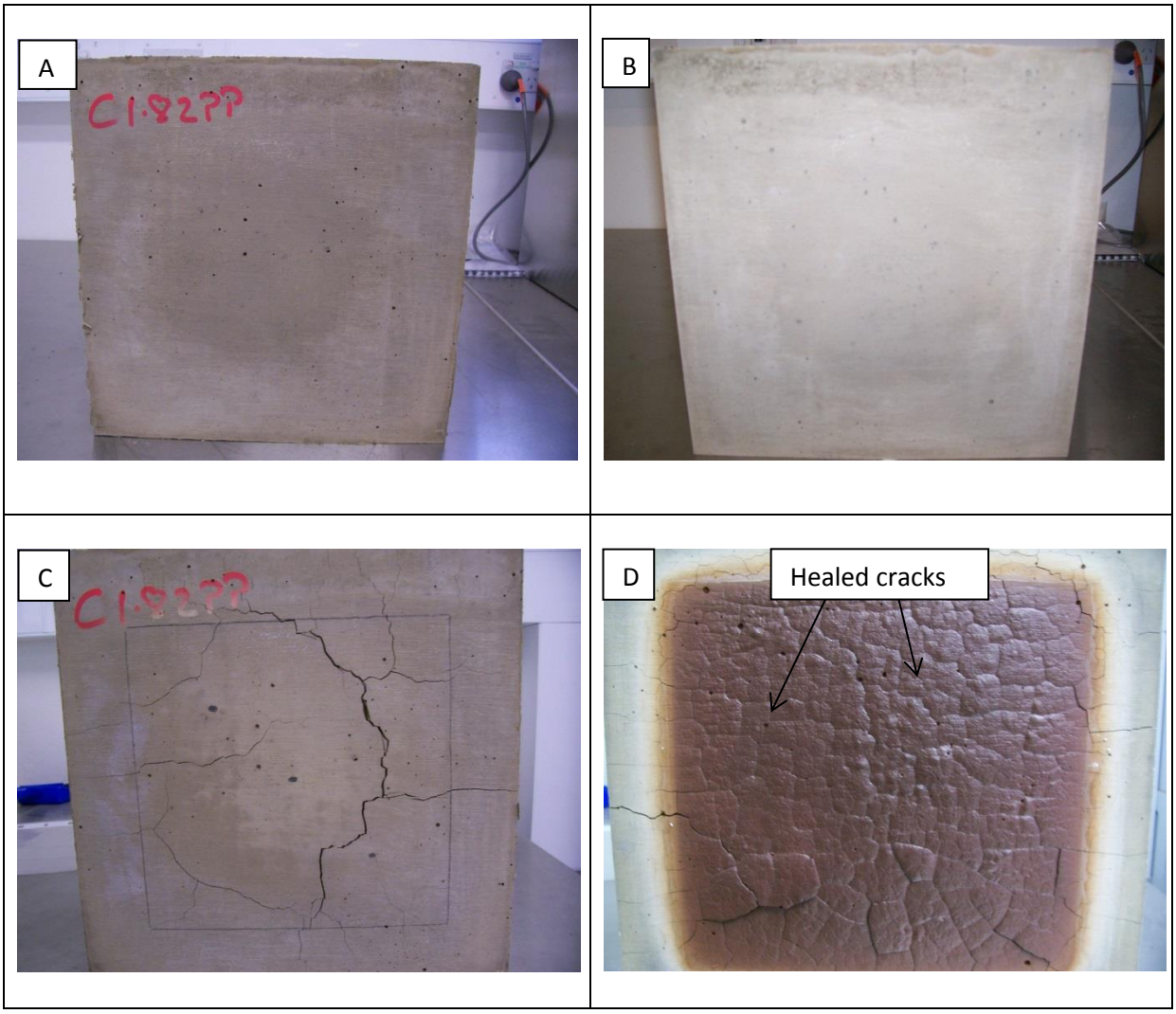

Figure 8.2 C1.82PP fire test images

A: C1.82PP cold side prior to fire test showing few small air cavities

B: C1.82PP hot side prior to fire test showing few small air cavities

C: C1.82PP cold side after fire test

D: C1.82PP hot side after fire test. Some evidence of crack healing is evident.

Figure 8.3 C1.82PP hot side close up showing lifting section attributed to differential thermal expansion / delamination.

Figures 8.4A and 8.4B show the prescence of larger air cavities than seen in the paste samples prior to fire testing. These cavities appear unchanged after firing (figures 8.4C and 8.4D).The addition of 5 vol. % of wollastonite, WOL 5PP, showed reduced cracking on the hot side (figure 8.5) and this is attributed to reduced thermal shrinkage of this material contributing to improved crack resistance as shown in chapter 6. The improved flexural strength shown by this material will also contribute to improved crack resistance. Cold side cracking was similar to the unfilled specimens.

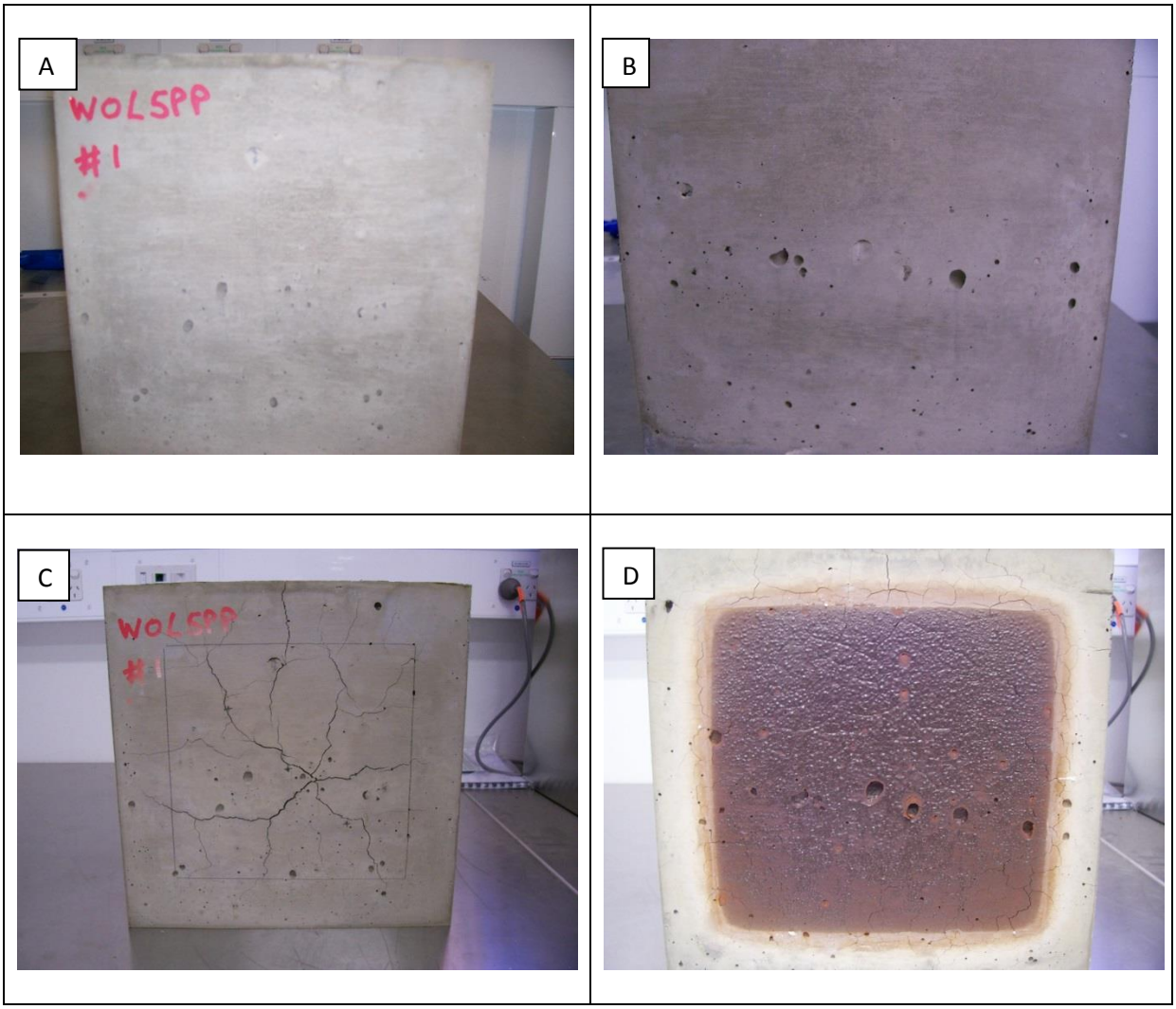

Figure 8.4 WOL 5PP fire test images

A: WOL 5PP cold side after fire test

B: WOL 5PP hot side prior to fire test (note: air cavities/ (bug holes)

C: WOL 5PP cold side after fire test

D: WOL 5PP hot side after fire test showing only minor crack formation.

Figure 8.5 WOL 5PP hot side close up showing crack healing.

Figures 8.6A and 8.6B show very few small air cavities prior to fire testing. After testing the cold side cavities were still visible (figure 8.6C) whilst those on the hot side (figure 8.D) in the area exposed to the furnace were no longer evident. The small size of these cavities has possibly allowed viscous flow to fill them. The specimen with 5 vol. % alumina, ALOX 5PP, showed hot side crack sizes between those of the paste and WOL 5PP specimens (figures 8.6C and 8.7D). The cold side exhibited several cracks (< 1 mm) which ran to the edges of the specimen and in one case the furnace glow was visible (figure 8.7C). No flaming through this gap was evident. The equipment was not available to conduct the ignition during the cotton wool pad test. Several through cracks were evident on the edges of specimens (figures 8.6D and 8.7A and B). The greater amount and severity of cold side cracking of ALOX 5PP compared to the WOL 5PP specimens can be attributed to the acicular shape of the wollastonite mitigating crack propagation more efficiently than the irregular “blocky” alumina particles.

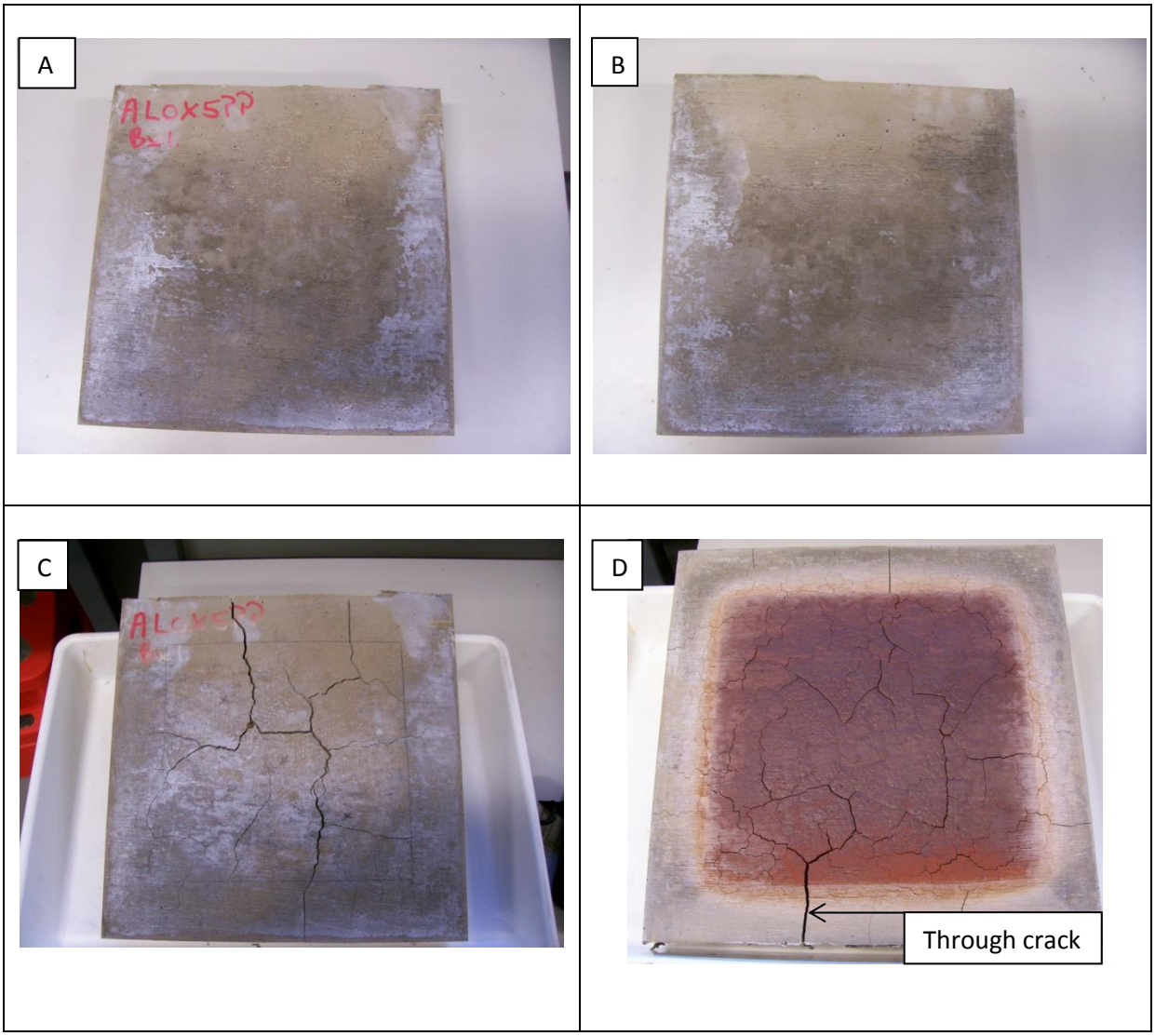

Figure 8.6 ALOX 5PP fire test images

A: ALOX 5PP cold side prior to fire test

B: ALOX 5PP hot side prior to fire test

C: ALOX 5PP cold side after fire test

D: ALOX 5PP hot side after fire test showing a through crack.

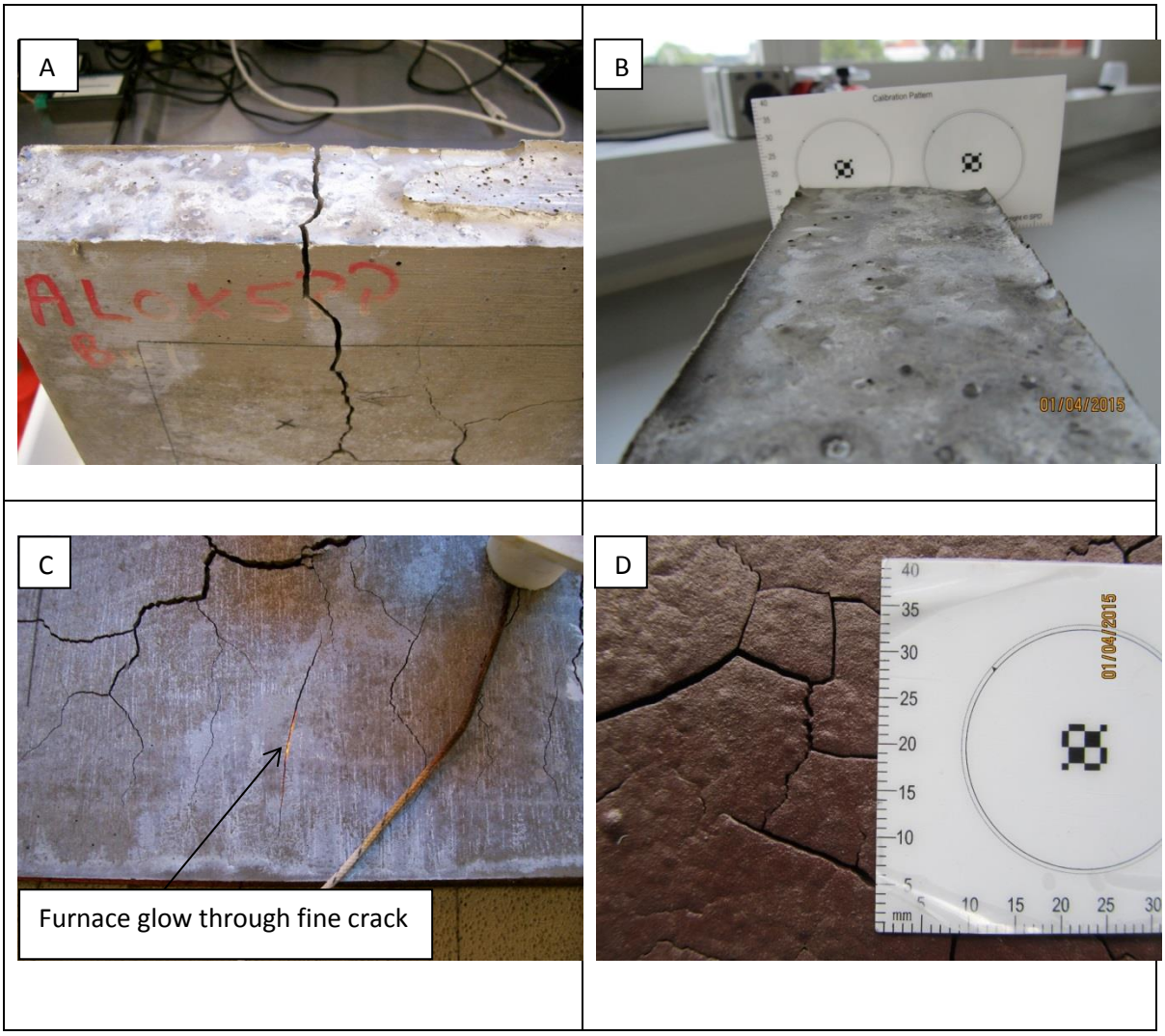

Figure 8.7 ALOX 5PP fire test images #2

A: ALOX 5PP through crack after fire test

B: ALOX 5PP after fire test, crack depth for crack shown in figure 8.6A

C: ALOX 5PP furnace glow visible through edge crack

D: ALOX 5PP hot side after fire test.

In the case of the specimens with increased loadings of graded alumina, HTM 4A and HTC 6A, many large air cavities were evident prior to fire testing (figures 8.8A, 8.8B, 8.11A, 8.11B). These cavities were evident after fire testing (figures 8.8C, 8.8B, 8.11C and 8.11D). Very few, fine cold side cracks formed during the fire test (figures 8.9, and 8.12,). The hot side showed similar fine crack formation (figures 8.10 and 8.13). This may be attributed to the low thermal shrinkage values demonstrated by these filled composites. The higher thermal conductivity values for these systems led to reduced thermal gradients across the thickness of the test specimens and this is clearly shown by the higher cold side temperatures attained during testing. These lower thermal gradients are expected to contribute to a reduced number and smaller crack formation.

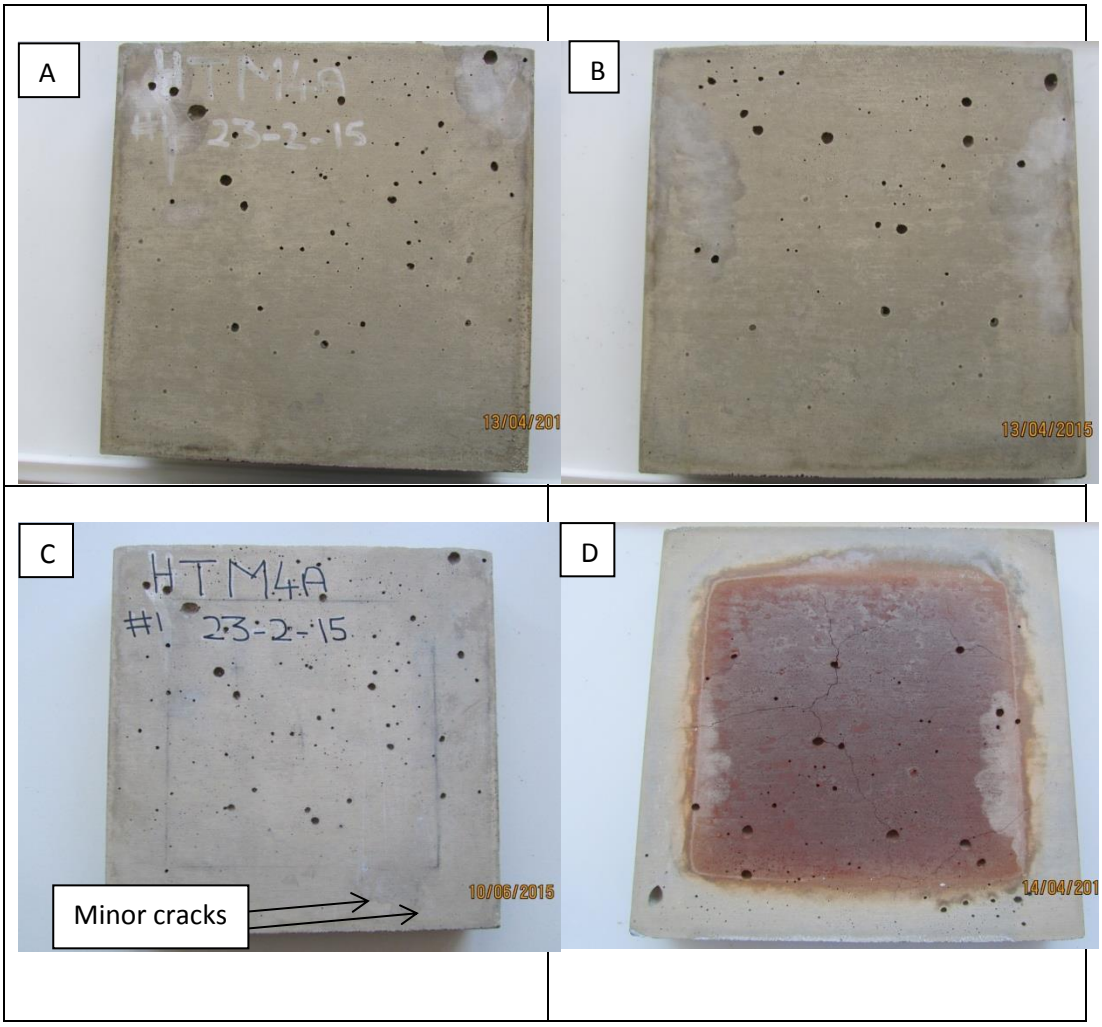

Figure 8.8 HTM 4A fire test images

A: HTM 4A cold side prior to fire test (note air cavities)

B: HTM 4A hot side prior to fire test (note air cavities)

C: HTM 4A cold side after fire test showing minor cracks

D: HTM 4A hot side after fire test.

Figure 8.9 HTM 4A Edge and cold side crack after fire test.

Figure 8.10 HTM 4A hot side cracks.

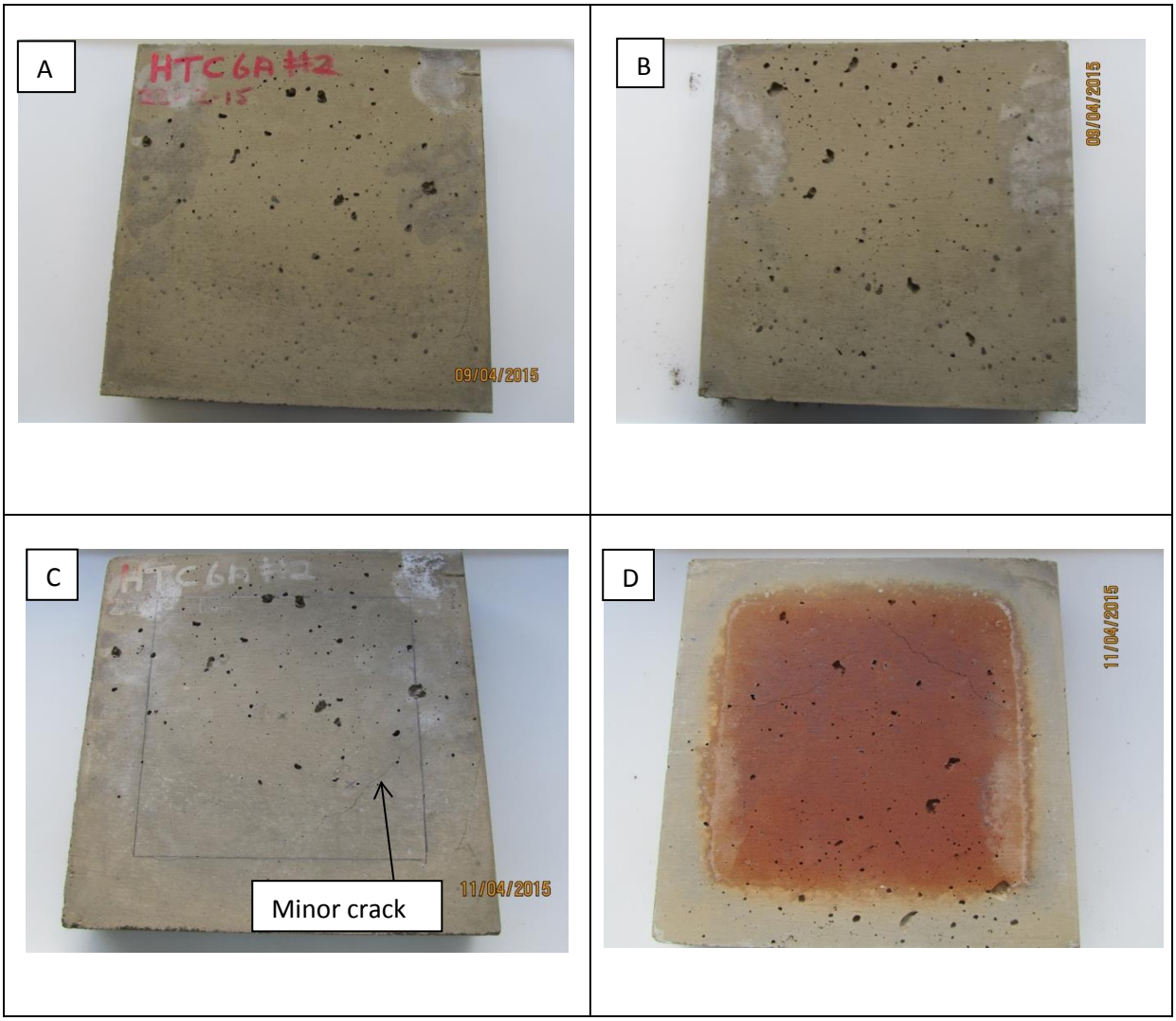

Figure 8.11 HTC 6A fire test images

A: HTC 6A cold side prior to fire test (note air cavities)

B: HTC 6A hot side prior to fire test (note air cavities)

C: HTC 6A cold side after fire test

D: HTC 6A hot side after fire test showing few minor cracks.

Figure 8.12 HTC 6A cold side after fire test.

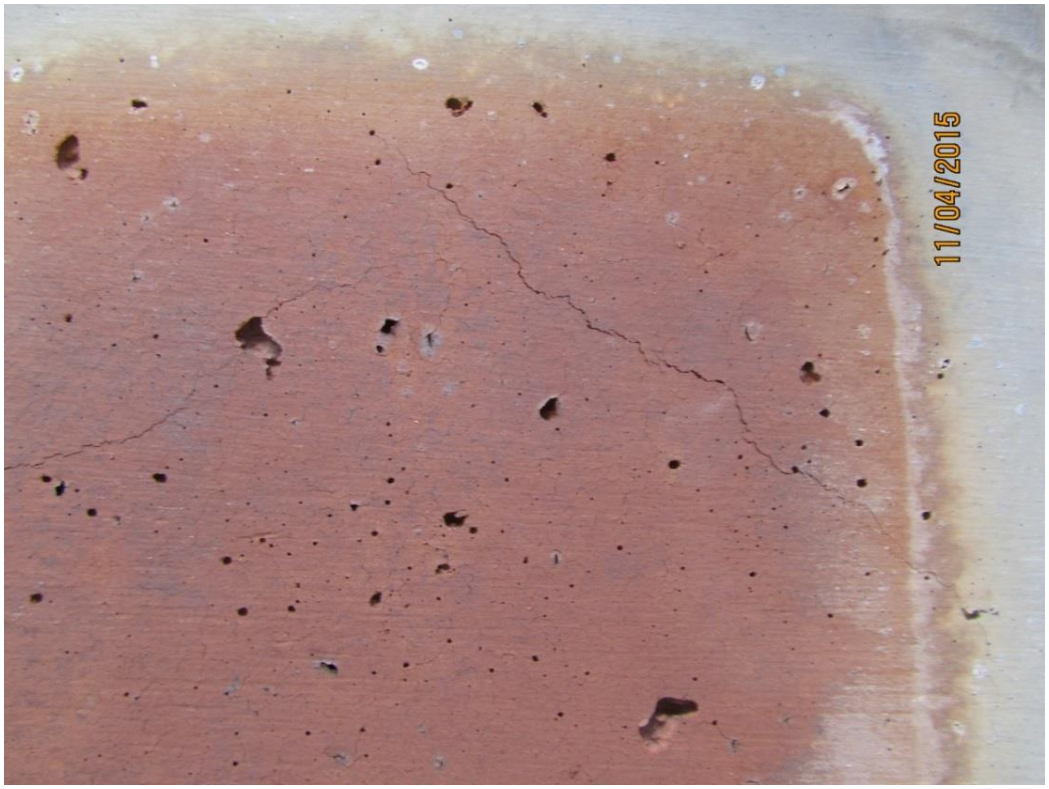

Figure 8.13 HTC 6A hot side after fire test showing fine cracks.

In table 8.2 the fire test results are summarised. The key features are the dehydration plateau duration (indicative of water content) and the FC1 times. A single initial test, C1.82 was run for 100 minutes. Evaluating this data suggested an extended test period and 180 minutes was selected for all subsequent testing to allow the cold side temperature to approach a quasi-equilibrium temperature.

Table 8.2 Summary of fire test results.

	C1.82	**C1.82 PP**	**WOL 5PP**	**ALOX 5PP**	**HTM 4A**	**HTC 6A**
Vol. % alumina	0	0	5 vol. % wollastonite*	5	41	51
Calculated wt. % water	20	20	18.2	18.2	8.9	7.2
Weight loss, %	11.9	12.0	11.3	10.6	4.2	3.2
Start of plateau, min	39.4	37.4	40	38.4	19.1	15.9
Plateau duration, min	37.1	32.5	26.7	26.7	10.8	7.5
Plateau gradient, $^{o}C\ min^{-1}$	0.63	0.65	0.75	0.71	2.39	1.56
Cold side temp at 120 min, ^{o}C	185 @100 min	247	247	264	429	444
Cold side temp at 180 min, ^{o}C	-	279	272	301	457	476
FC 1, min	97	87	82	82.25	34.75	32.3
k, as cured $W\ m^{-1}K^{-1}$	0.70	-	-	-	0.91	0.99
k, after PC2 $W\ m^{-1}K^{-1}$	0.43	-	-	-	0.70	0.83
k, after firing at $1000^{o}C$ $W\ m^{-1}K^{-1}$	0.49	-	-	-	0.92	1.09

*WOL 5PP contains no alumina only wollastonite

k is the thermal conductivity measured at ambient temperature after the indicated thermal exposure

The plateau referred to is the “boiling front” which is attributed to the latent heat of evaporation of water. This is illustrated in figure 8.14 together with the FC1 and FC2 temperature failure criteria.

The measured weight loss values are lower than the total calculated values as the specimens were allowed to equilibrate at 23^{o}C and 50 +/- 5 % relative humidity for at least 28 days prior to fire testing. The decreasing water content (indicated by weight loss in table 8.2) as the alumina content increases will lead to shorter plateau durations. Thermal conductivity also increases with decreasing water content. The water content will only play a role up to the end of the dehydration plateau.

The C1.82 plateau commenced two minutes after the C1.82 PP plateau. This is likely due to the polypropylene fibres used allowing easier transport of water. The addition of either polyethylene or polypropylene fibres showed higher water loss during the PC2 cycle compared with the reference paste (C1.82) (tables 6.3 and 6.4 show this data). This can explain the earlier commencement and shorter duration of the dehydration plateau for C1.82PP.

The temperature gradient, across the 50 mm thick test slab, for paste and lightly filled composites (WOL 5 and ALOX 5) is 16^{o}C mm^{-1} and 12^{o}C mm^{-1} for the aggregate filled test slabs at 120 minutes into the test. At 180 minutes the temperature gradients are 16.6^{o}C mm^{-1} and 12.8^{o}C mm^{-1}, respectively. The lower thermal gradients for the aggregate filled composites would suggest lower thermal stresses are present during the test and together with the lower COTE would produce fewer, smaller cracks. The actual differences between the cold face temperature of paste/lightly filled specimens and aggregate filled composites is in the order of 180 to 200^{o}C at 120 minutes into the test and 175 and 205^{o}C after 180 minutes. The furnace temperatures for 120 and 180 minutes from table 8.1 were used as reference points for calculating the thermal gradient across the slab.

The temperature increases between 120 and 180 minutes is in the region of 30^{o}C for all the tests. After the dehydration plateau has passed the specimens begin to heat up more rapidly depending on the temperature difference between the furnace and the cold side and the thermal conductivity of the slab. The rate of furnace temperature increase is reduced from 104^{o}C in 30 minutes (208^{o}C hr^{-1}) between the 30 and 60 minute test period to

61°C in 60 minutes for the 120 to 180 minutes test period. This explains the consistent temperature increase in this area of the test. The thermal conductivity of the systems will also be changing as the temperature increases and the plateau gradient is an indication of the specimen thermal conductivity (higher plateau gradient is equivalent to higher thermal conductivity). The rate of furnace temperature increase appears to have more influence on cold face temperature than thermal conductivity as shown by the narrow temperature increase range of around 30°C, across all the samples (which will have differing thermal conductivities).

The trend in thermal conductivity shown in table 8.2 shows an initial decrease in value due to water loss in the PC2 cycle (250°C maximum exposure). An increase in thermal conductivity then occurs due to firing at 1000°C attributed to densification and new crystalline phase formation. In the case of the highly filled alumina composites the fired value exceeds the as cured value. The high thermal conductivity of alumina is dominating the thermal conductivity of the composite. In the case of the C1.82 paste the fired thermal conductivity only reaches 70% of the as cured value, accounting for the lower cold side temperature achieved for pastes and lightly filled composites.

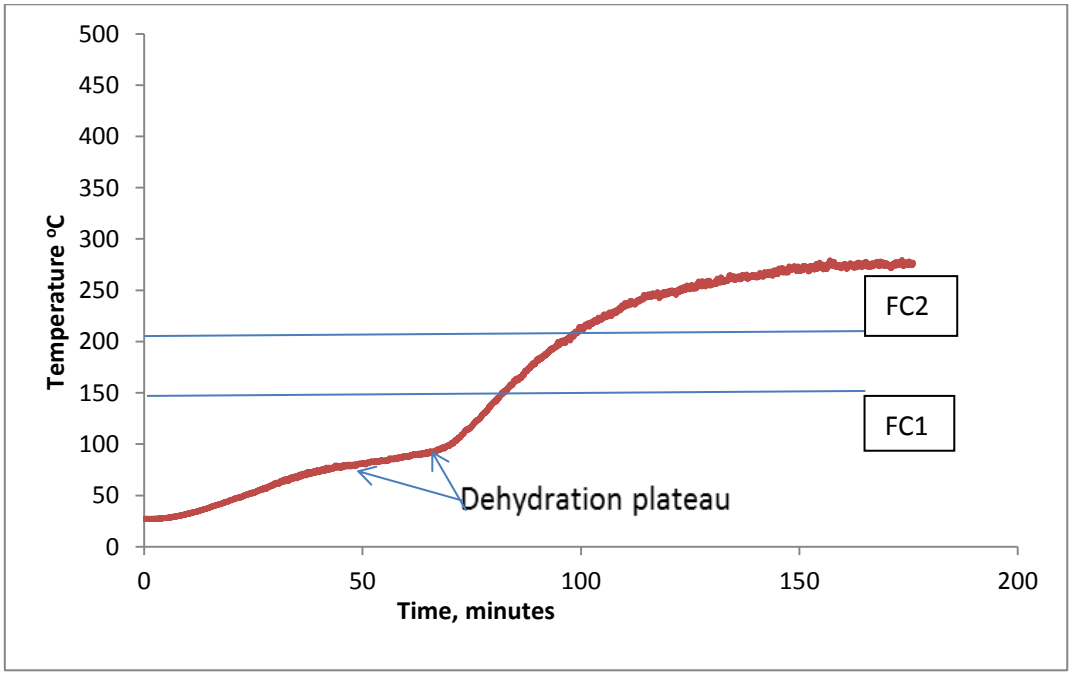

Figure 8.14 C1.82PP fire curve showing dehydration plateau and temperature failure criteria.

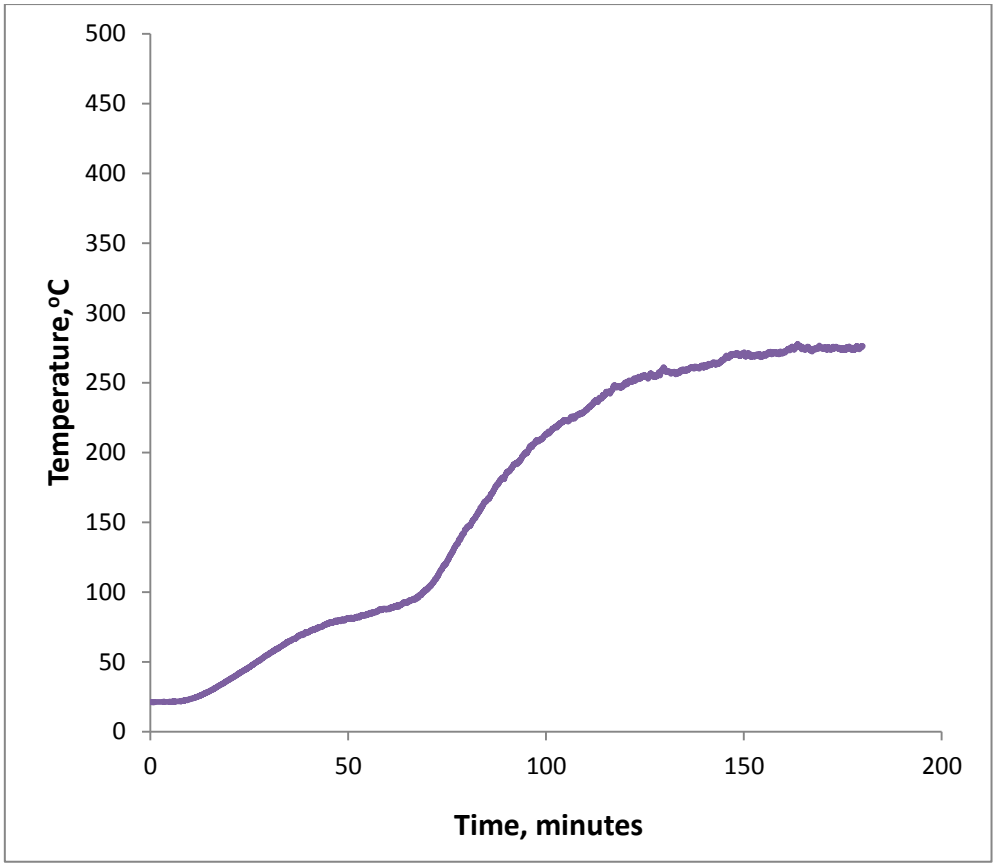

Figure 8.15 WOL 5PP fire test curve.

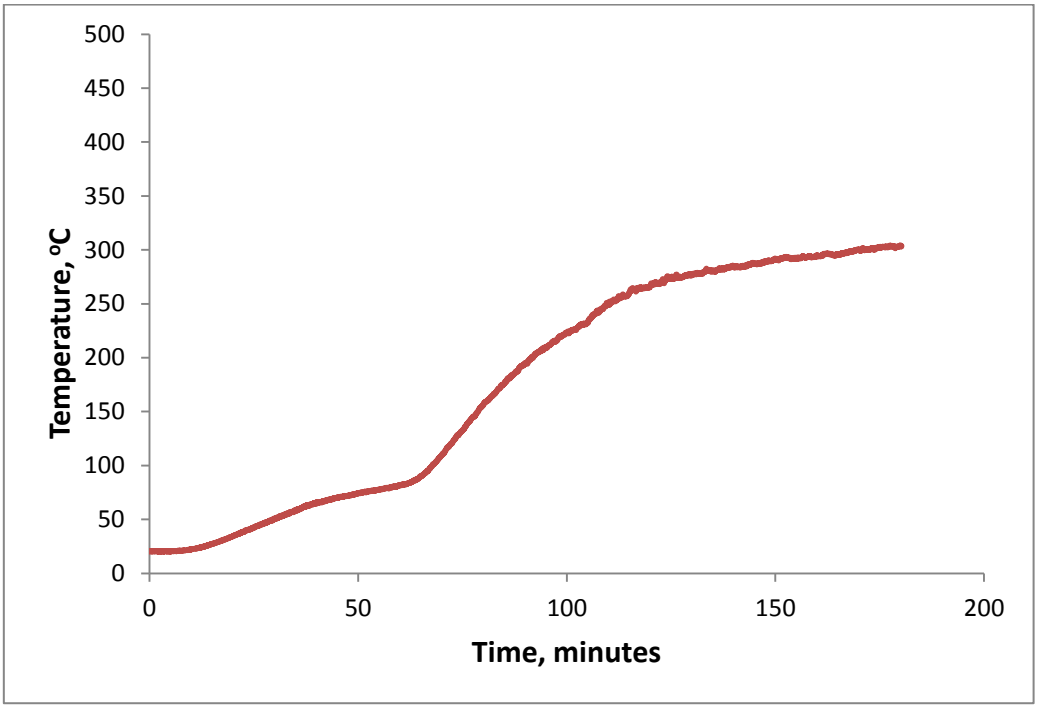

Figure 8.16 ALOX 5PP fire test curve.

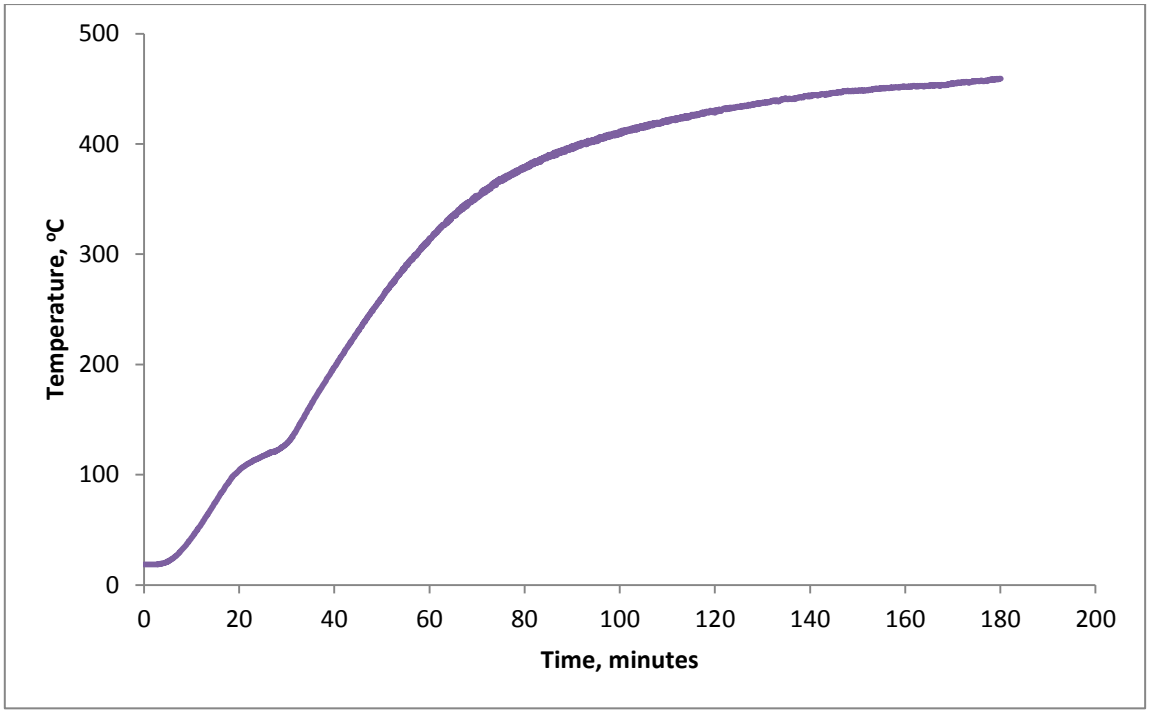

Figure 8.17 HTM 4A fire test curve.

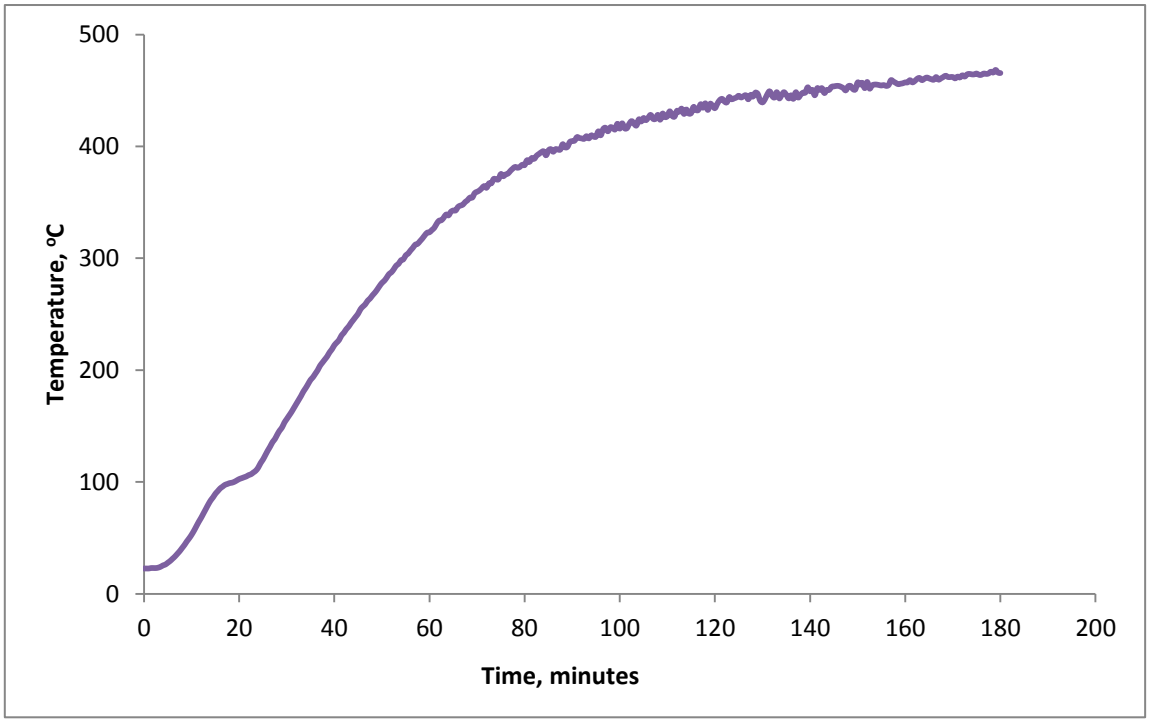

Figure 8.18 HTC 6A fire test curve.

Plotting of the fire test data gave rise to the graphs illustrated in figures 8.19 to 8.22.The influence of increasing water content (weight loss) on longer fire ratings is clearly shown in figure 8.22.

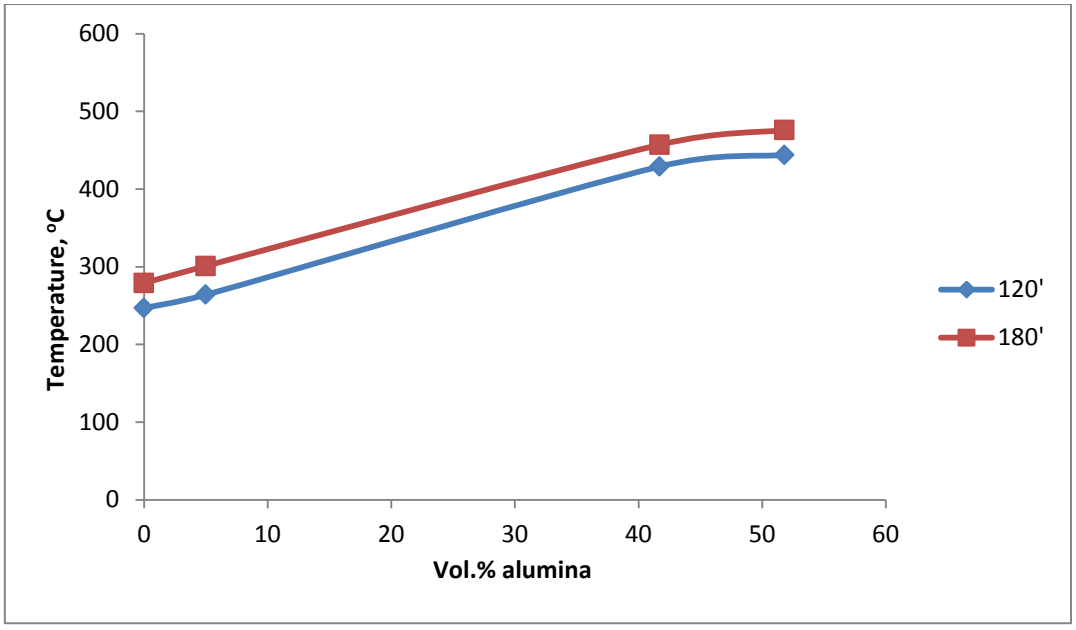

Figure 8.19 the effect of alumina content on cold side temperature at 120 and 180 minutes.

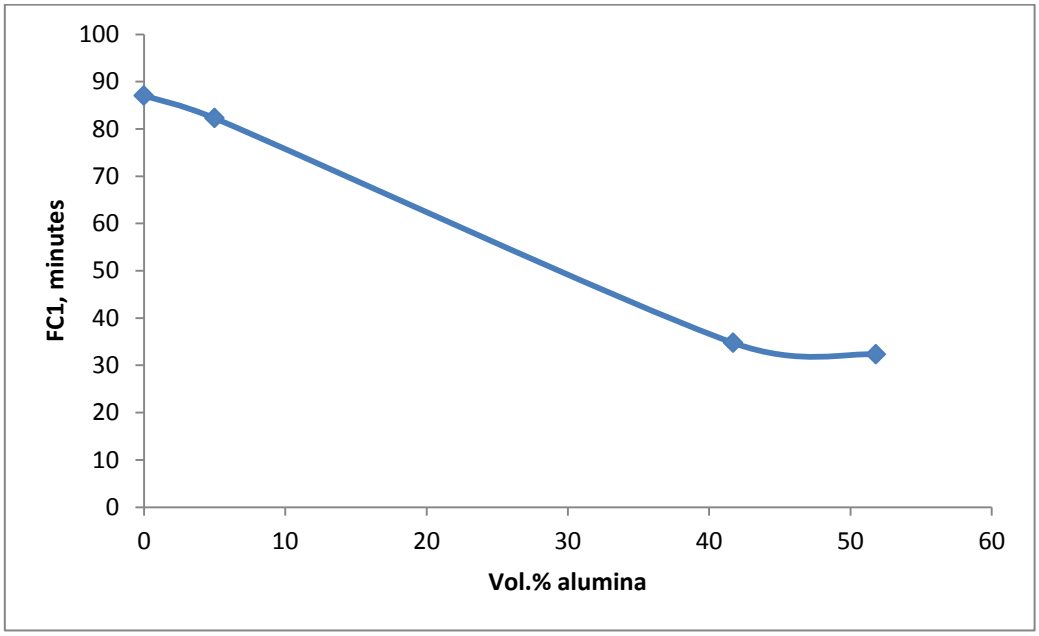

Figure 8.20 the effect of alumina content on FC1.

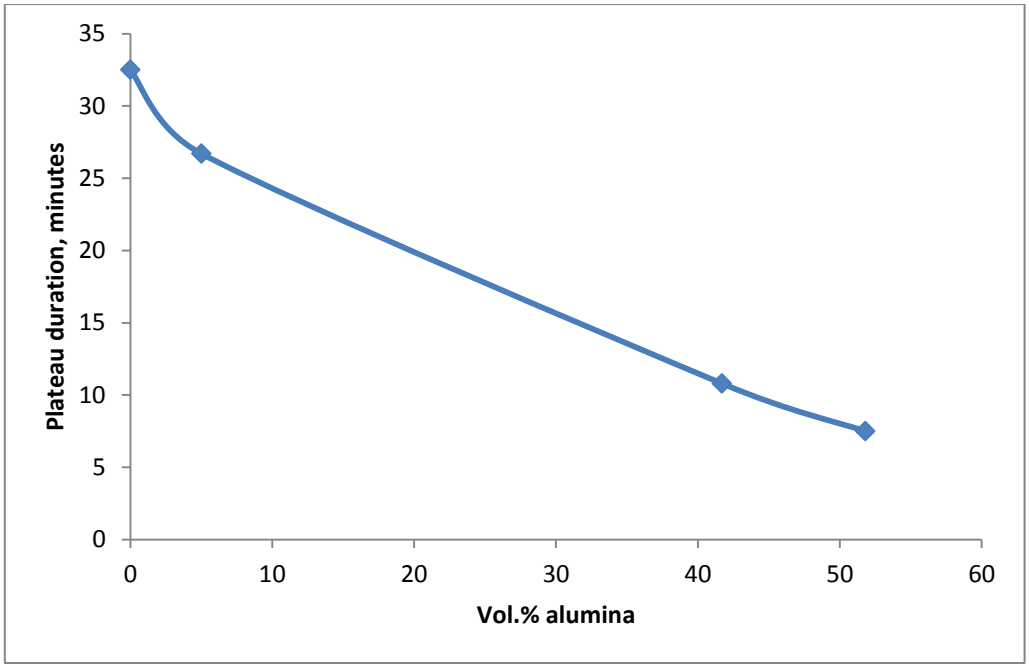

Figure 8.21 the impact of alumina content and thus water content on dehydration plateau duration time.

Figure 8.22 the relationship between weight loss and dehydration plateau duration time.

Increasing the volume of alumina in the composites has a marked effect on their response to the fire test. The rapid increase in cold side temperature following the early

commencement of the dehydration plateau gives relatively short fire ratings (FC1) compared to paste and lightly filled composites. The addition of alumina increases the thermal conductivity of the composite (see table 7.7) and the water content is reduced as the alumina content increased (due to a lower paste content). Drying of the composites at 100 and 250^{o}C also reduced the thermal conductivity which supported the effect of reduced water content. This reduction in water content means that less energy is required to supply the latent heat of evaporation of the water corresponding to a shorter duration of the dehydration plateau.

Whilst the more filled composites (HTM 4A and HTC 6A) gave a reduced fire rating their integrity as shown by the formation of only small cracks, even after a 3 hour fire exposure time, is maintained. This is despite these systems reaching cold side temperatures of 457 and 476^{o}C, respectively. Examination of the hot side of these specimens also showed minimal cracking. The brown colouration after firing was lighter than the paste due to the lower percentage of binder, and hence less oxidisable iron, in the composites.

8.4 Summary

The use of alumina filler in conjunction with a fibre tri-blend has enabled the production of composites showing good integrity after fire testing for 3 hours. This has been at the expense of the fire rating defined in AS1530.4 due to the increased thermal conductivity imparted by the added alumina. However, observed cracking on hot and cold faces was minimal.

Increasing the additional water content may extend this fire rating, but care must be taken that as cured physical properties are not overly reduced.

The high thermal conductivity shown by these composites may be beneficial when rapid heat dissipation from components is required. It may also be beneficial in the response to thermal shock loading where reductions in thermal gradients are beneficial.

The selection of alternative fillers to alumina, added as a total replacement or as part of a blend with alumina, may be beneficial in increasing the fire rating without impacting on the integrity of the composite.

The above testing was carried out using 50 mm thick samples. Thicker samples would be expected to increase the fire rating, whilst thinner samples would achieve the reverse. These changes to fire ratings for a given composite (as thickness changes) will be dictated by the passage of the water boiling front through to the cold face. After the boiling front has reached the cold face with accompanying loss of water we then begin to measure transient heat flow which is a function of power input from the furnace (varies with time) and the inverse of the temperature difference with thickness and exposed area constant.

The FC1 values obtained in this work can be separated into two groups, that for paste and lightly filled composites and that for the highly filled alumina composites. The values obtained in the first group ranged from 97 minutes for paste to 82 minutes for lightly filled composites. This is in line with other results for fly ash based geopolymer pastes using 50 mm thick samples (Rickard, 2012, Rickard, 2014, Rickard et al., 2013). The results for the highly filled alumina (~ 35 minutes) are believed to be unique.

Table 8.3 Summary of the factors for obtaining required fire ratings.

	Low fire rating	**High fire rating**
Thermal conductivity	High value	Low value
Water content	Low value	High value
Integrity (minimal cracking)	Few small cracks	More cracks > 5mm

Fire rating based on the FC1 criterion of Australian Standard AS 1530.4

One possibility to improve and maintain a system's fire rating over time would be to increase the available water content of the system. The real challenge lies in maintaining a sufficiently high water level throughout the life of the component which could be many years. This would involve manufacturing a composite with a controlled interconnecting pore network e.g. by foaming and/or the use of sacrificial fibres followed by a post cure cycle to remove the fibres. The addition of water to the post cured component is now required. Immediately prior to installation components could be saturated by controlled immersion in water and allowed to come to equilibrium with its environment. One other possible scenario is based on the drip irrigation systems, based on semi permeable plastic piping, used in agriculture in arid areas. A controlled flow of water is made to the component to maintain a pre-determined level of saturation.

Okada (2011) investigated this saturation technique using oriented sacrificial fibres to produce building panels which demonstrated capillary rise of water as ambient temperature changed throughout the day. Up to 28 vol. % of these fibres were used to obtain sufficient porosity for adequate water flow to occur.

Whilst we can formulate composite systems to give improved fire ratings this should only be part of the overall picture which can involve additional component processing and/or combination with engineered systems to give further improvements.

CHAPTER 9

CONCLUSIONS

9.1 Conclusions

The objective of this thesis was to develop suitable geopolymer based systems for high temperature applications. The initial step involved a review of existing fly ash based geopolymer research related to thermal/fire resistance. The previously investigated systems used with the locally available Collie fly ash required modification particularly in the reduction of the Si: Al ratio to give reductions in the system thermal shrinkage. The addition of thermally stable fillers and fibres to this improved binder led to further reductions in thermal shrinkage coupled with increases in residual strength after firing. The influence of water content on thermal shrinkage was significant up to 300^{o}C and a post curing strategy to remove this water prior to firing was investigated. Finally composites, using graded alumina and a fibre tri-blend, were produced and subjected to elevated temperature testing. In situ elevated temperature testing was carried out using two scenarios, in-situ compressive testing resulting in strength and viscous flow information and simulated fire testing using a custom designed furnace allowing the requirements of Australian Standard AS 1530.4 to be investigated.

Fire testing of geopolymer paste as a control and three addition levels of graded alumina blends was undertaken. The outcome of the fire testing clearly showed that the graded alumina filled geopolymer system was able to withstand the fire test exposure and maintain the integrity of the panel specimens despite reductions in the expected fire rating of around 60 minutes to achieved values of 30 to 35 minutes. The reduced fire ratings resulted from the higher thermal conductivity of the composites compared to paste and the associated lower water content. These composites contained a tri-blend of fibres which contributed to the thermal resistance by eliminating spalling and minimising the formation of cracks. This objective was achieved, and several new possibilities such as thermally insulating and conductive components, and foamed systems also arose from this work. Thicker panels could have produced longer fire ratings and could be suitable in some applications.

One of the targets of this research was to develop systems with the maximum local content. In this case we were able to use fly ash from the Collie power station (250 km south of Perth) and graded alumina produced by Doral Fused Materials (30 km south of Perth). These two materials accounted for approximately 94 vol. % of the high temperature composite

system. Additionally the use of fly ash has sustainability benefits compared to some other geopolymer precursors such as metakaolin.

The utilisation of Collie fly ash at the targeted Si: Al of 1.82 enabled geopolymer specimens with much reduced thermal shrinkage characteristics to be produced while at the same time benefiting from strength increases after firing. This was further improved by the addition of thermally stable fillers such as alumina and synthetic mullite. Analysis of the microstructure of these systems was complicated by the wide variations in starting fly ash microstructure. The Si: Al ratio selected did not result in the formation of large amounts of geopolymer reaction product due to the low level of soluble silicate additions to attain this ratio. This also made determination of compositional information difficult by QEDS. Regions of Si: Al < 1 were found during EDS evaluations. This was attributed to early release of aluminium from the fly ash which reacted with silicate either from the activating solution or the fly ash. This gave reaction product which coated the fly ash spheres with a resultant decrease in dissolution rate.

The characterisation of the amorphous components and their relative quantities is essential to ensure successful production of thermally resistant composites. The achieved Si: Al of the geopolymer is probably the most important single criteria governing thermal resistance. The level of water used in geopolymer synthesis also played a crucial role in the amount of reaction product initially formed and the level of mechanical properties developed.

No excessive thermal expansion events were observed with the C1.82-based system. The addition of filler further reduced the range of thermal expansion seen on the dilatometer and confirmed by firing in the furnace. The use of a thermal post cure enhanced the reduction in thermal expansion up to the onset of viscous flow. Beyond this point the filler containing composites showed reduced shrinkage up to 1000^{o}C.

The use of the thermal post cure also removed added polyolefin fibres leaving a pore system which enhances the transport of water which can be beneficial in the case of fire but potentially detrimental for chemical resistance and durability. Increases in compressive strength were obtained after post cure and this is attributed to further binder formation activated by the alkali deposited on the pore walls and increased temperature.

The addition of wollastonite gave an interesting blend of properties, showing low thermal shrinkage and increased flexural strength which was improved after firing. The wollastonite filled system also showed delayed conversion from meso to macro pores during firing. The maximum level of wollastonite that could be added during synthesis is limited. At 10 vol. % addition there was no workability at the 20 wt. % water utilised setting this as the practical maximum loading for wollastonite. The acicular nature of the wollastonite contributed to the lack of workability. Smaller size alumina particles added at the same volume loading showed better workability. When wollastonite is used in conjunction with alumina a more compact microstructure is obtained after firing which showed significant increases in fired flexural strength. There is evidence from XRD data that in the presence of large volumes of alumina both mullite and wollastonite disappear from the system and are replaced by albite and anorthite phases. A study of the relative ternary phase diagrams confirms that this is feasible. It is proposed that the alumina has a nucleating effect in this process. The ability to readily form these new phases creates a new area of applicability for fly ash as a raw material for industrial ceramic production.

The use of alumina also gave thermal shrinkage and property development similar to wollastonite and also exhibited better workability under equivalent conditions. The addition of large quantities of graded alumina (>40 vol. %) led to increases in thermal conductivity which gave rise to reduced fire ratings. The utilisation of mullite gave similar results to alumina at the 10 vol. % level and its lower thermal conductivity could give rise to composites with low thermal shrinkage and thermal conductivity.

The elevated in-situ evaluation of stress-strain properties at UWS indicated that the high temperature composites exhibited superior thermal resistance to the reference paste system (Tg = ~250^{o}C) with an increase in Tg to approximately 750^{o}C for HTC 6A. Increasing temperature brought about a decrease in stiffness as measured by increases in compressive strain by a factor of ten for C1.82PP at 500^{o}C and at 700^{o}C for HTC 6A. The fire testing confirmed that the addition of thermally resistant aggregate to the low Si:Al geopolymer binder produced composites with better post firing integrity if somewhat lower than expected fire ratings.

9.2 Future Work

Several areas of interest are possibilities for further research. Limits on resources (time, equipment and funding) put constraints on the amount research that could be performed.

- Thermally resistant fillers with low thermal conductivity:

The alumina filled systems developed in this thesis are characterised by high thermal conductivity with resulting fire ratings of around 30 minutes for 50 mm thick panels. Selection of fillers which impart lower thermal conductivity without sacrificing the thermal shrinkage levels obtained above could show benefits. Mullite would appear to be a suitable candidate for additional work.

- In-situ testing at elevated temperatures:

This type of testing can give information on strength development and softening behaviour at elevated temperature. Preloading of specimens can confirm the maximum allowable operating temperatures and hence the suitability of systems in specific applications. Some exploratory work carried out at UWS suggests that this area can lead to critical service data acquisition for thermally resistant components. This technique could be extended to include in-situ flexural testing.

- Wollastonite – Alumina reactions:

The evidence presented in this thesis suggests that these two materials (or alumina from mullite) react forming new crystalline phases, in particular anorthite. Additional work to confirm the initiation temperatures and the stoichiometry of these reactions together with SEM and/or TEM imaging to clarify the situation and determine if useful products can be synthesised.

- Ambient temperature curing without added calcium:

Generally fly ash based geopolymers require heat curing to achieve acceptable physical properties. The addition of lime from slag can bring about realistic cure cycles at ambient temperature. However, the prescence of calcium silicate hydrates has an adverse effect on thermal and chemical resistance.

Possible alternative routes are the use of polyhydroxyl compounds, use of amines, and the addition of metakaolin to accelerate the setting reaction.

- Process Aids

The workability of filled composites was marginal at best and the need for suitable additives, to improve flow without detracting significantly from mechanical properties, must be high on any future development list. The limited attempts reported on in this thesis generally gave limited flow improvements with marked reductions in as cured mechanical properties. This is indicative of these added compounds “competing with the activating solution for available fly ash surface”.

Improvements in the rheology of FAGP pastes are required to meet the wide range of processes which may be utilised with FAGP. Conventional materials suitable for OPC processing do not appear to perform consistently or beneficially in geopolymers, hence the use of the term process aids rather than (super) plasticisers.

Measurement of surface tension and zeta potential would be required to characterise the additives and the modified systems. Standard OPC test methods such as flow and slump would also be utilised. The point of addition to the FAGP paste needs study to check for interference with the geopolymerisation mechanism steps. Scale up to at least 100 litre batches is essential.

- Ammonia based alkali activating solutions:

The property of interest for thermal resistance is the ammonium ion’s fluxing ability compared to sodium and potassium ions (Note: ammonium and potassium ions have approximately the same hydration sphere diameter, about 30% larger than that of sodium). This fluxing ability can be evaluated using the dilatometer and changes in fired properties and pore structure over a range of temperatures. Pre-leaching of samples in water prior to testing may also be of interest (leaching out the majority of fluxing agents leaving H_3O^+ for charge balancing). What is the effect of ammonium ions on efflorescence?

Ammonium hydroxide is commercially available up to 35% w/w (880 ammonia). This is 308 g/l (18 M). In 1 M ammonia solution 0.42% ammonia converts to NH^+_4 with a pH of 11.63. If the ammonium ion is “consumed” during geopolymerisation more ammonia will convert to balance the equation. This may be a slow reaction requiring long times and/or heat.

Ammonium silicate is not readily available, but could be produced by dissolving silica fume in 880 ammonia.

- Evaluation of other fly ashes at Si: Al <2 for thermal resistance

The calculation of amorphous composition of the fly ash is critical to the design of a geopolymer composition suitable for thermal applications. Whilst fly ash with a low amorphous Si: Al such as Collie have given suitable compositions, the techniques to use high amorphous Si: Al fly ash for thermal resistance need refining.

- Fire resistant components

Water content plays a significant role in determining fire ratings, but too much reduces the achieved as cured properties. Post treatment of components should be investigated to main a level of water in the component which will extend fire ratings.

Alternating layers of geopolymer could be moulded together. For example a foamed geopolymer (low thermal conductivity) could be faced with a composite with a high temperature integrity

9.3 Summary

Fly ash based geopolymers, filled with graded alumina have been shown to possess good thermal resistance with increases in mechanical properties after firing. These composites exhibit low thermal shrinkage values with the formation of few fine cracks after firing. The addition of the fibre tri-blend helps mitigate crack initiation and propagation. There was no evidence of spalling in any of the performed fire tests. The high thermal conductivity of these systems contributes to improved thermal shock resistance.

The wide spread of available fly ash compositions and the equally wide response to alkali activation is a major area of concern for the manufacture of consistent geopolymer based components. A widely recognised methodology and nomenclature for testing of fly ashes and their suitability for geopolymer manufacture must be a priority for all organisations involved.

The value added products focused on in this thesis, together with products for chemical resistance and engineered components such as railway sleepers, will not be primarily driven by costs, but by technical advantages accruing from the use of geopolymers. The same cannot be said for general purpose applications competing directly with OPC. Here environmental issues need to be taken into account. The geographic location of raw material feed stocks relative to geopolymer manufacturing facilities will play a critical pole here as any carbon benefits can be lost to increased transport carbon inputs. The application focused on in this thesis, thermal resistant systems, will be able to remain competitive using imported raw materials. This is supported by three Perth based manufacturing companies, one refractory and two wear composite based, replacing no longer available local alumina with imported alumina. All three companies also export finished product.

Appendix A

Preparation of geopolymer samples

This appendix describes the mixing, flowability and moulding issues of fly ash based geopolymers studied in this research. It is included as an appendix as the subject matter is not directly related to thermal properties.

In the mixing of OPC the cement and water are added to the mixer together with the aggregate at the beginning of the cycle and then mixed for about six minutes. Minor admixtures (fibres and plasticisers) may be added now but generally the mix is ready for transportation and placing.

In the case of geopolymers we need the alkaline activating solution to dissolve the aluminosilicate precursor and initiate the geopolymerisation mechanism. Additions of other components at this stage may well interfere with this mechanism by:

- diluting the activating solution
- preferentially reacting with the activating solution
- preferentially interacting with the precursers.

The addition of other components may also act a heat sink for any exothermic heat generated in the early stages of geopolymerisation.

Mixing Procedures

In order to minimise these effects the Hobart mixing cycle used in this work allowed only the precursor and activating solution to be blended together for five minutes prior to the addition of other components. The first minute of the cycle was run at low speed (speed 1) to allow wetting of the fine material; the final four minutes was run at high speed (speed 3). Additions of other components were now made initially at low speed for one minute with the final four minutes at high speed.

The recommended mixing procedure for the Thinky mixer was to add the liquid components to the mixing container followed by the solids. The mixer was then run for the nominated time at the nominated speed as set out in table A.1. One exception to this was when superplasticisers were evaluated. The superplasticiser (Tamol NH3703 or Sikament NN) was withheld until the final minute of the mix cycle. This was to reduce the influence of these materials on the dissolution and geopolymerisation process.

Table A.1 shows the temperature increases (compared to initial activating solution temperature, T_{AS}) for mixes carried out in the Hobart and Thinky mixers.

Table A.1 Thinky and Hobart mixer temperature evolution.

Mix sequence	Mix	T_{AS}, ^{o}C	Mixer	Temperature increase., ^{o}C
SERIES 1				
1	C1.82	20	Thinky 5 min/1500 rpm	12
2	C1.82 + 2.5 wt.% water	20	Thinky 5 min/1500 rpm	12
3	C1.82 + 5 wt.% water	20	Thinky 5 min/1500 rpm	12
SERIES 2				
1	C1.82 + 5 wt.% water	19	Thinky 5 min/1300 rpm	7
2	C1.82	19	Thinky 5 min/1300 rpm	13
3	C1.82 + 2.5 wt.% water	19	Thinky 5 min/1300 rpm	13

Mix sequence	Mix	T_{AS}, ^{o}C	Mixer	Temperature increase., ^{o}C
SERIES 3				
1	C1.82 +1 wt.% ethanol	20	Thinky 4+1 min/1300 rpm	10
2	C1.82 +1 wt.% ethylene glycol	20	Thinky 4+1 min/1300 rpm	12
3	C1.82 +1 wt.% glycerol	20	Thinky 4+1 min/1300 rpm	14
4	C1.82 +2.5 wt.% Tamol	20	Thinky 4+1 min/1300 rpm	15
5	C1.82 +2.5 wt.% Sikament NN	20	Thinky 4+1 min/1300 rpm	16
SERIES 4				
1	C1.82 WOL 10 Tamol	20	Hobart	5min = 2
2	C1.82 ALOX 10 Tamol	20	Hobart	5min = 2 10 min = 2

2.5 wt. % Tamol NH3703 or Sikament NN is equivalent to 1 wt. % of active ingredient. These materials are described in Chapter 3.

As expected the higher rpm of the Thinky mixer generated higher mix temperatures than the Hobart mixer (series 4). In series 3 in the Thinky mixer the final mix temperature increased down the mix series. In the series 2 mixes a reduced final mix temperature effect was seen with the first mix running 6^{o}C cooler than the next two mixes. This effect can be attributed to the frictional and/or chemical exotherm heating from the first mix increasing the temperature of the mixer. If the subsequent mixes occur before significant cooling of the mixer occurs they will acquire a higher level of temperature at the end of the mixing cycle. The activating solution temperature is used as a datum point.

In the Hobart mixer the temperature increase is limited to 2^{o}C after 10 minutes mixing time. These differences are explained by the mixer configuration and materials of construction. The Thinky mixer uses a polypropylene (k = 0.12-0.17 W m^{-1} K^{-1}) screw cap vessel to contain the mix. The plastic mixing vessel, which was at ambient temperature in each case, sits snuggly in a rotating steel carrier and this assembly is located in a plastic composite casing.

In the case of the initial mix some of the heat generated in the mix will flow into the metal cup where it is retained by the plastic composite casing. In subsequent mixes less heat can flow to the warmer steel carrier and mix temperatures are correspondingly higher.

In the Hobart mixer the mixing vessel is made from 2 mm stainless steel (k = 16-24 W $m^{-1}K^{-1}$) with both inner and outer surfaces exposed to atmosphere. The mixing action of the beater blade transfers material to and from the mixing vessel walls and also exposes new material to the atmosphere at the material surface. This allows the possibility of heat transfer from the mix (and mixing bowl) to atmosphere with a lower resulting mix temperature. The Hobart more closely resembles the type of mixer used on an industrial basis.

The mix volumes were limited to 150 cm^{-3} in the case of the Thinky mixer and between 500 and 1000 cm^{-3} in the case of the Hobart mixer. Whilst it would be expected that larger volumes of material (in bigger mixers) would generate more heat due to larger chemical exothermic heat generation, the generation of lower frictional heat is possible due to lower applied shear rates. The thermal insulating effects of the mixers appear to be the dominant factors with the equipment used here.

Processibility

A wide range of national standards (Koehler and Fowler, 2003) are available to measure the processibility of mortars, pastes and concretes based on Portland cement. The majority of these tests are simple one point measurements to enable evaluation at the construction site. Some of these tests have been scaled down to allow evaluation of small quantities of material produced in the laboratory. The mini-cone is a typical example and is used in this evaluation (Kantro, 1980).

OPC rheology (Wallevik, 2011) generally conforms to a Bingham model (equation A.1).

$$\tau = \tau_{o} + \mu\dot{\varepsilon} \qquad \text{Equation A.1}$$

where: τ = Shear stress; τ_o = Yield stress

μ = Plastic viscosity $\dot{\varepsilon}$ = Shear rate

When the ratio of plastic viscosity to yield stress is greater than 10 empirical methods such as slump testing cannot adequately describe workability.

Bhattacharjee et al. (2010) showed that geopolymer concrete also exhibited Bingham behaviour. Bouvet et al. (2010) used a mini cone slump test to calculate the yield stress from the final flow diameters for an OPC paste derived from a SCC mix. Roussel et al. (2005) linked the spread of paste in the flow test to the plastic yield value, and demonstrated that for low yield stress systems it is necessary to take into account surface tension effects. Adding polycarboxylate super plasticisers decreased the plastic yield stress and lowered surface tension.

Nematollahi et al. (2014) used a relative slump term derived from ASTM C1437 (2013) to characterise the effects of superplasticisers in geopolymer systems. In this research a relative flow, F_r, term based on ASTM 1437 is used as shown in equation A.2.

$$F_r = \frac{\emptyset_f - \emptyset_o}{\emptyset_o} \qquad \text{Equation A.2}$$

Where $\emptyset_f$ = flow diameter after 1 minute

$\emptyset_o$ = bottom diameter of cone. 38 mm for the mini-cone used in this work.

Mini-cone test results:

Influence of water content

Figure A.1 shows how the mini-cone relative flow is influenced by the total water content of the geopolymer mix, C1.82. Series 1, 2 and 3 are three separate determinations. The point at 17.0 wt. % water is based on one test. The other points (20.0, 22.5 and 25.0 wt. % water) are the average of three separate tests. Test series 1 (in blue) shows a wide fluctuation in values compared to the other two test series, but a dip in value at 22.5 wt. % water is common to all three test series. If we put test series 1 to one side there is only a small difference in flow until 25 wt. % total water is reached. The high surface tension of the system could be more significant than the dilution effect of water thus preventing the fluid mix from spreading on the metal plate.

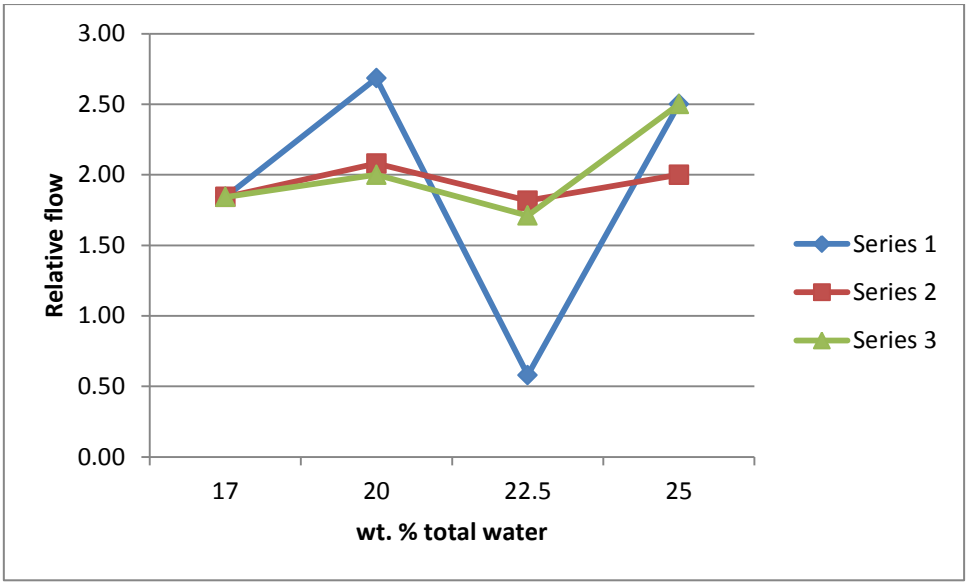

Figure A.1 Influence of total water content on relative flow.

A simple test was carried out using Collie fly ash/water slurry only in the mini-cone and the results are shown in table A.2. The slurries were mixed in the Thinky mixer (5 minutes at 1300 rpm) as per the geopolymer mix conditions. An initial mix cycle was run with the same weight of water as slurry mix to try to eliminate "the cold mixer" effect. Demineralised water temperature was 21.3^{o}C and "mixed" water temperature was 22.6^{o}C. The temperature of the two slurry mixes was within 1.3^{o}C suggesting that the initial water mix had helped to decrease any cold mixer effect.

The flow values for the fly ash slurry are lower than the relative geopolymer values, which suggest that water is absorbed onto the fly ash surface via hydrogen bonding and that surface tension effects are also reducing wetting out of the stainless steel plate by the slurry.

Table A.2 Flow of Collie fly ash slurries.

	20 wt. % total water	25 wt. % total water
Collie fly ash BB09,wt.%	80.0	75.0
Demineralised water, wt.%	20.0	25.0
Slurry temperature, ^{o}C	28.9	29.9
Flow diameter, mm	91x89	128x128.5
Relative flow	1.37	2.38

Comparison of processing aids (PAIDs)

Two commercially available superplasticisers, Tamol NH3703, ex BASF and Sikament NN, ex Sika were evaluated at 1 vol. % active component. Both are sodium salts of naphthalene formaldehyde sulphonate polymers with an active solids content of 40 wt. %. The molecular weight of this type of polymer is in the 100,000 to 200,000 range allowing for the possibility of large steric effects. Three hydroxyl containing compounds were also evaluated at 1 vol. % active content. They are shown in table A.3. They all show a lower surface tension than water (73 mN m^{-1}) and could reduce the surface tension effects seen in geopolymer flow experiments. Other alcohols with longer alkyl groups could also be evaluated in future, e.g. n-decanol exhibits a surface tension of 28.9 mN m^{-1}. The larger alkyl groups, C_8+, have the possibility to show surfactant effects due to the hydrophobicity of the alkyl groups compared to the hydroxyl group.

Table A.3 Hydroxyl compounds evaluated as PAIDs (Green and Perry, 2007).

	Ethanol	Ethylene glycol	glycerol
Hydroxyl groups	1 x 1^{o}	2 x 1^{o}	2 x 1^{o}, 1 x 2^{o}
Density (20^{o}C) g cm^{-3}	0.789	1.113	1.264
Surface tension (20^{o}C) mN m^{-1}	22.3	48.43	63.1
Molecular weight	46	62	92

Figure A.2 and A.3 Show the results obtained with the evaluated PAIDS.

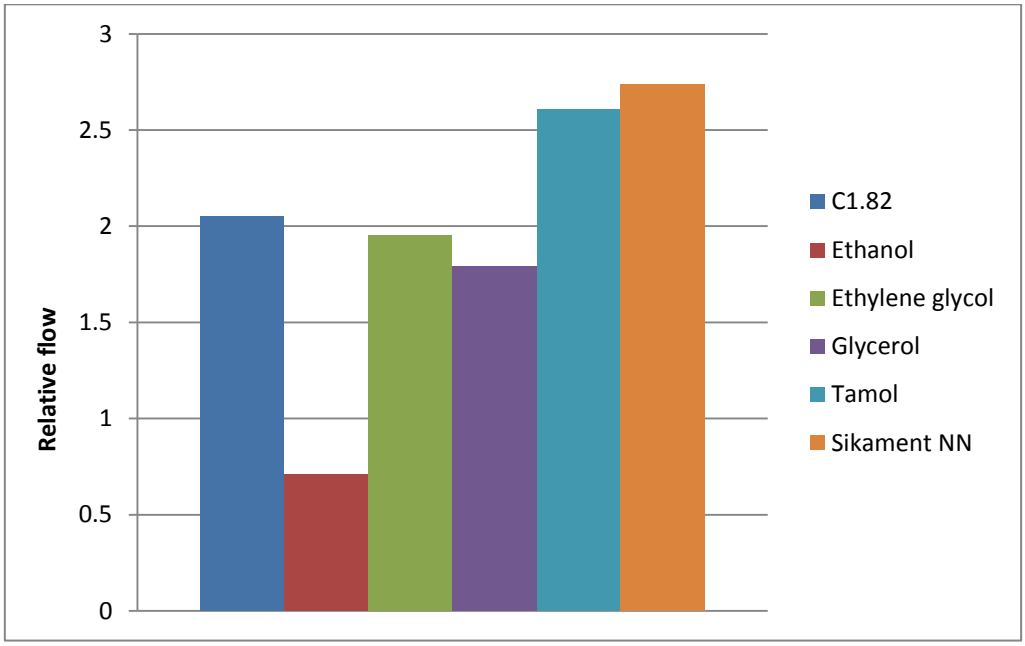

Figure A.2 Relative flow of PAID mixes.

The mix containing ethanol showed a paste like consistency hence the low relative flow. This is attributed to reaction of the ethanol with sodium silicate to form crosslinks between the silicate species. The ethylene glycol and glycerol showed slightly reduced flow compared to C1.82. This is attributed to hydrogen bonds forming between the added hydroxyl compounds and the surface of the fly ash.

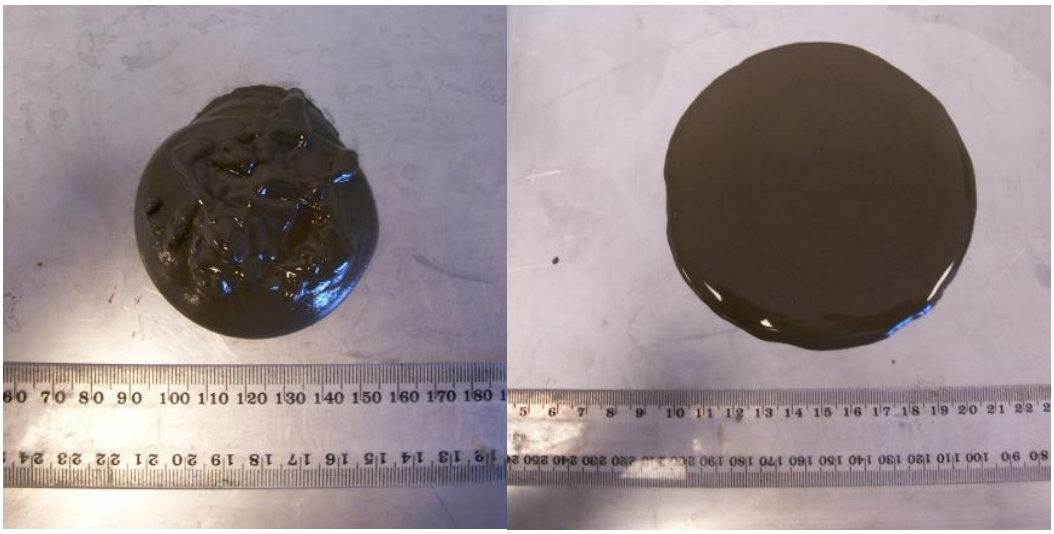

Figure A.3 Ethanol (LHS) and C1.82 (RHS) mini-cone flow discs.

In the cases of the two commercial products higher relative flow was achieved and both mixes showed good release from the mini-cone. This is a good indication that the surface tension of the mixes is reduced compared to the control (C1.82).

In table A.4 the physical properties obtained with the PAID mixes are detailed. All the materials evaluated showed marked reductions in physical properties compared to the control (C1.82). All the evaluated materials have the ability to hydrogen bond to the fly ash surface where they can show steric interference effects which interfere with the geopolymerisation mechanism.

Table A.4 PAID mix physical properties.

	Density, g cm^{-3}	Compressive Strength, MPa	Young's Modulus, GPa
C1.82	1.91 (0.01)	27.88 (3.26)	1.67 (0.07)
Ethanol	1.97 (0.01)	6.89 (0.95)	0.88 (0.11)
Ethylene glycol	1.98 (0.01)	11.98 (1.83)	1.17 (0.12)
Glycerol	1.99 (0.03)	6.10 (0.19)	0.86 (0.05)
Tamol	1.96 (0.01)	11.51 (1.34)	1.25 (0.11)
Sikament NN	1.96 (0.01)	12.06 (0.98)	1.33 (0.01)

Additional PAID evaluations were undertaken with filled systems. The major outcome of this work was the ability of Tamol and Sikament NN to act as air entrainment admixtures at the levels used in the filled mixes as shown by marked decreases in density. This decrease in density coupled with the negative effect on compressive strength development (see table A.4) lead to the lower values shown in table A.5. The consistency of these mixes did not allow mini-cone flow tests to be carried out.

Table A.5 PAID in filled C1.82.

	Density, g cm^{-3}	Compressive strength, MPa	Young's modulus GPa
ALOX 10 (no Tamol)	2.10 (0.01)	23.5 (4.24)	1.96 (0.11)
ALOX 10 (2.5% Tamol)	1.47 (0.03)	4.73 (0.64)	0.78 (0.21)
WOL 10 (no Tamol)	2.01 (0.04)	29.37 (3.0)	1.88 (0.1)
WOL 10 (2.5% Tamol)	1.23 (0.01)	4.6 (0.23)	0.87 (0.07)

The reduction in strength of geopolymer systems containing superplasticisers is a major concern in the development of systems with acceptable workability. Work is required in this field.

Moulding of geopolymer composite samples

Conversion of the fluid mixed material to the required shape needs moulds which will retain the fluid mixture whilst it cures and then enable easy release of the cured geopolymer. The mould materials must be able to withstand repeated cycles of mechanical handling, including vibration and thermal curing.

Adequate sealing of all the mould assemblies is essential to control the water content in the elevated temperature curing step. Water content plays a critical pole in the initial precursor dissolution step. Open moulds were sealed with plastic film and/or self-adhesive duct tape. Vibration was applied during mould filling and continued after completion of filling. This enables consolidation of the geopolymer mix and aids in air bubble removal. The consolidation effect is determined by the acceleration of the vibrating table. Accelerations of between 5 and 10 g (for the unloaded table) prior to the moulds being placed on the table and 2 to 4 g are required during vibration (CCANZ, 2005).

When filling moulds with compositions of pasty consistency the use of vibration facilitated flow of this material. Without vibration, i.e. using hand compaction many air bubbles of varying sizes are trapped in the specimens. The vibrating table is supplying sufficient energy to the composition to overcome the yield stress barrier.

Mould materials must be resistant to the alkaline (pH > 12) nature of the geopolymer mixes. This excludes the use of untreated timber moulds and galvanised steel. In this research work several materials were evaluated. Steel moulds with release agents suitable for geopolymers were found to be suitable. However moulds based on materials such as plastics and concrete form board, which could be produced with standard hand tools, were preferred for production simplicity, cost and safe handling techniques.

Concrete formwork board is widely used in the construction industry and consists of several layers of laminated bonded board with a radiate core and hardwood veneer faces with a high density resin overlay which enhances release properties. However cut edges expose the ply layers which must be protected against alkaline attack. Several coats of a hard carnuba wax polish was applied to these cut edges to seal the grain. The interior surfaces of the mould are treated with two coats of water based release agent. The joints on the exterior of the mould are sealed with silicone sealant to ensure no leaking takes place. Figure A.4 shows the attack on the resin overlay with the formation of wrinkles on the surface. These moulds, which are economical and simple to construct, are only suitable for a few castings.

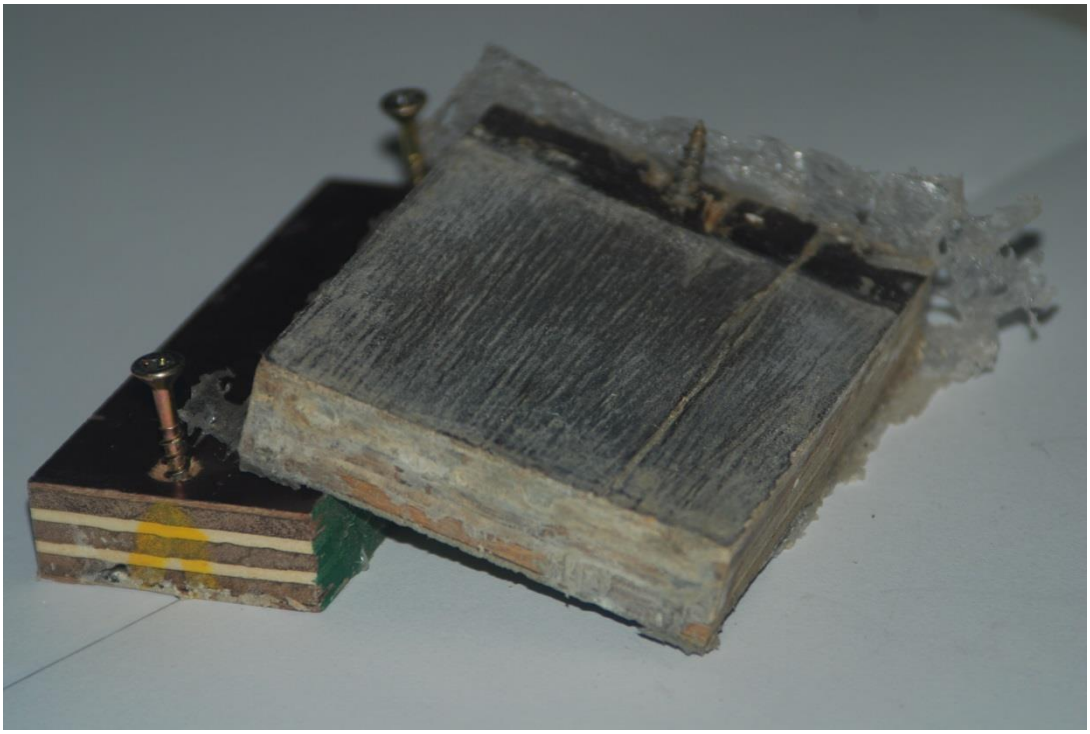

Figure A.4 Formwork board mould after multiple uses.

Geopolymers do not generally show adhesion to organic polymers (Glad et al., 2012). Therefore the use of plastic materials as moulds for geopolymer compositions can be considered.

An internal study carried out by the geopolymer group (2012) at Curtin University demonstrated the unsuitability of PTFE (Teflon) moulds due to a high percentage of air bubbles trapped at the mould surface (figure A.5). This is attributed to the high contact angle exhibited by this low energy surface.

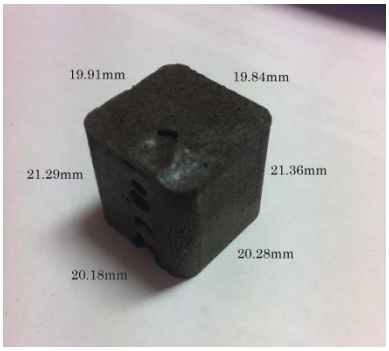

Figure A.5 Geopolymer sample prepared in PTFE mould showing surface air bubbles.

Other plastic materials evaluated included polypropylene, uPVC, UHMWPE and acrylic. Both polyolefines (polypropylene and UHMWPE) had a tendency to allow air bubbles to form at the mould surface. These bubbles were in the main removed by rodding during the mould filling process whilst using applied vibration. The use of clear acrylic moulds allowed any entrained air to be removed more efficiently. The geopolymer composition could also be seen to wet out the acrylic surface readily. Release from this surface (without release agent) was good. uPVC pipes were used to mould cylinders for compressive strength and thermal conductivity testing and again the release characteristics were good in the absence of release agent. These moulds were sacrificial in nature.

In the case of UHMWPE moulds initial release was good, but repeated usage resulted in deposits of geopolymer being left on the mould after demoulding (figure A.6). This is attributed to oxidation of the mould surface and surface roughening caused by cleaning. Both factors will increase the material surface energy leading to higher adhesion tendencies. Mould release agents are considered necessary with all re-useable moulds to facilitate multiple releases and aid in mould cleaning operations.

Figure A.6 Cured geopolymer deposits on UHMWPE mould.

Mould Release Agents

A mould release coating (or untreated mould surface) has to carry out two conflicting primary functions:

- Exhibit low surface energy to inhibit adhesion of the moulding compound to the mould surface.
- Exhibit a sufficiently high surface energy to allow adequate wetting out of the mould surface by the moulding composition.

For complete wetting i.e. spreading, the contact angle between solid surface and liquid is 0^o. Between 0 and 90^0 the solid is wettable and above 90^o it is not wettable. This is illustrated in figure A.7.

Figure A.7 Surface wetting related to contact angle (Kruss, 2014).

Young's equation (equation A.3)(Kruss, 2014) describes the relationship between contact angle and surface tension of the liquid and this is illustrated in figure A.8.

$$\sigma_S = \gamma_{sl} + \sigma_l \,.\, cos\theta \qquad \text{Equation A.3}$$

Where σ_s = surface free energy of the solid. Υ_{sl} = interfacial tension.

σ_l= surface tension of the liquid. Cos θ = contact angle.

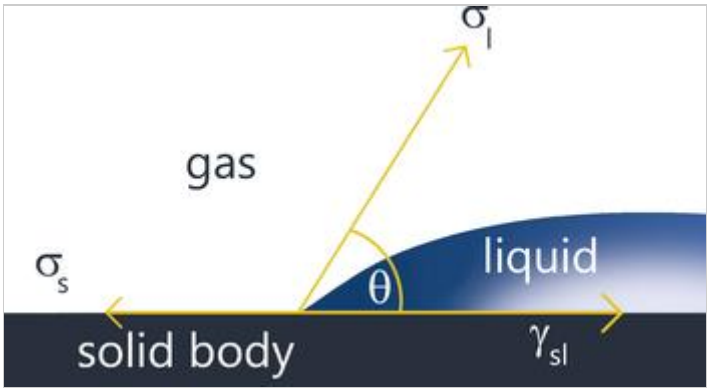

Figure A.8 Schematic illustration of surface tension parameters (Kruss, 2014).

Table A.6 shows the surface energy and contact angle of water with a range of materials.

Table A.6 Surface tension and contact angles (Diversified Enterprises, 2009).

Material	Surface Tension, mN m^{-1}	Water contact angle, θ^{o}
PTFE (Teflon)	19.4	109.2
Polyethylene	31.6	96
Polypropylene	30.5	102.1
Acrylic	37.5	70.9
uPVC	37.9	85.6
Stainless Steel	700-1100	72
Aluminium	840	61
Water	73	
Silicone Oil	19	

The surface tension values for metals are dependent on surface roughness (increasing as the roughness increases) and the presence of oxide film or other surface constituents. Aluminium is not a suitable mould making material for geopolymer systems due to its high alkaline reactivity.

Silicone oils, traditionally used as release agents for organic polymers, are attacked by highly alkaline solutions rendering them unsuitable for use with geopolymers.

With OPC systems mineral oil based release agents are the most commonly utilised systems. They possess several environmental and health and safety issues which has led to developments with vegetable oils as replacement release agents (de Brito et al., 2000). Djelal et al. (2004) compared two vegetable oil release agents and showed that viscosity and surface active properties, in this case wetting contact angle, play an important role in the

efficiency of release agents. Application of excessive oil can produce defects such as air holes (bug holes) stains and tears in the concrete surface.

The Cresset Chemical Company (2012a) manufactures concrete release agents and has published a set of standard photographs showing the influence of release agent film thickness on the formation of bugholes. Bugholes are surface voids that result from the migration of entrapped air (and to a lesser extent water) to the fresh concrete-form interface. Film thicknesses as thin as 12.7 μm promote virtually defect free release surfaces whilst at 50 μm bugholes are very evident.

Cresset (2012b) propose that there two classes of release agents, barrier and chemically reactive. The barrier type form a barrier between the mould/form work and the concrete and are based on oils such as diesel oil and paraffin wax. However, thick films are required to obtain the release effects, resulting in surface defects. Diesel oil is volatile and frequent reapplication is required.
The chemically active release agents have an active ingredient (fatty acid) which reacts with the calcium hydroxide in concrete to form the calcium soap of the fatty acid. This calcium soap is the release agent for the concrete. These systems are claimed to give multiple releases even after long lay over times.

This type of chemistry may not be compatible with geopolymer chemistry. It may be possible to coat moulds with pre-dispersed calcium soaps, typically the stearate, and a film former to act as a release agent for geopolymers. The calcium soap and film former must have a melting/softening point greater than the cure temperature to remain effective.

Summary

The use of SNF type superplasticisers is not beneficial to the geopolymerisation process in the systems studied here as they markedly reduce the extent of geopolymerisation as indicated by compressive strength and Young's modulus values. Both materials are behaving as air entraining admixtures as indicated by the decrease in density particularly when fillers are included in the mix. Improvements in relative flow were only obtained with paste. The addition of filler gave a non-flowing paste which did not improve with the addition of

superplasticiser. One noticeable advantage with the addition of superplasticiser was the clean release from the cone which is attributed to a reduction in surface tension. Investigation of the use of materials which reduce the surface tension of water may be a useful starting point in the development of process aids for geopolymers.

The mould making material of choice for long term service is steel, although other materials may be suitable for prototyping and short run batches. The use of mould release agents is mandatory for easy product release and improved mould cleaning and maintenance.

APPENDIX B

Thermal evolution of Collie Fly Ash Composites

The following SEM images show the evolution of the composite microstructure as the samples are fired in 200^{o}C steps up to 1000^{o}C. This work complements Chapter 6.

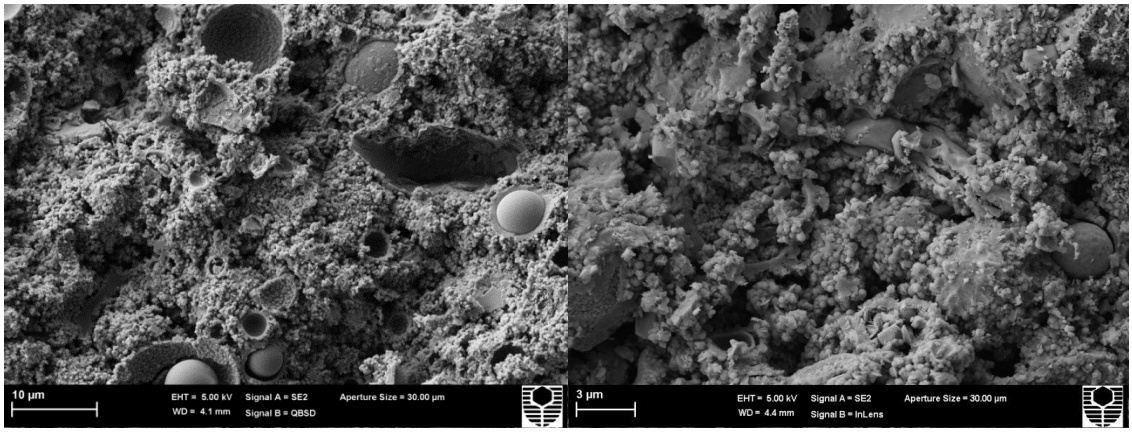

C1.82 unfired 7 day cure C1.82 fired at 200°C

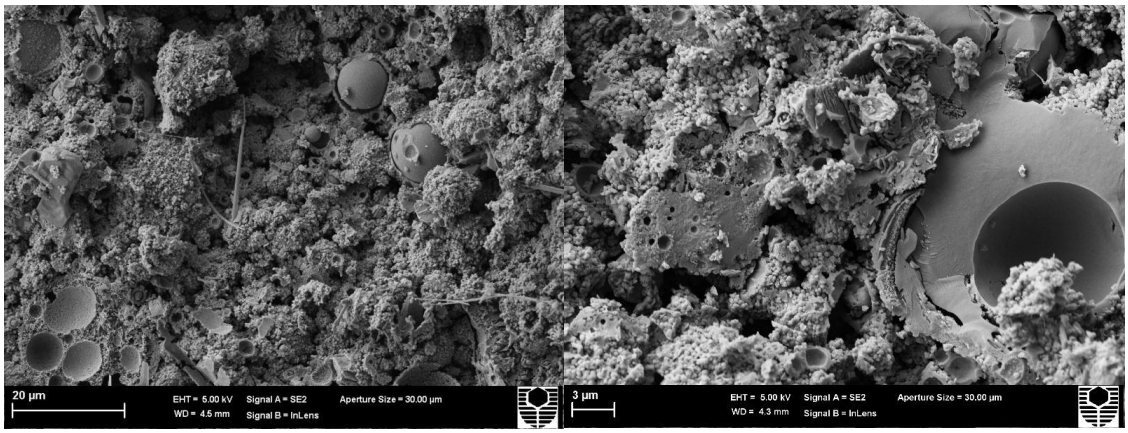

C1.82 fired at 400°C C1.82 fired at 600°C

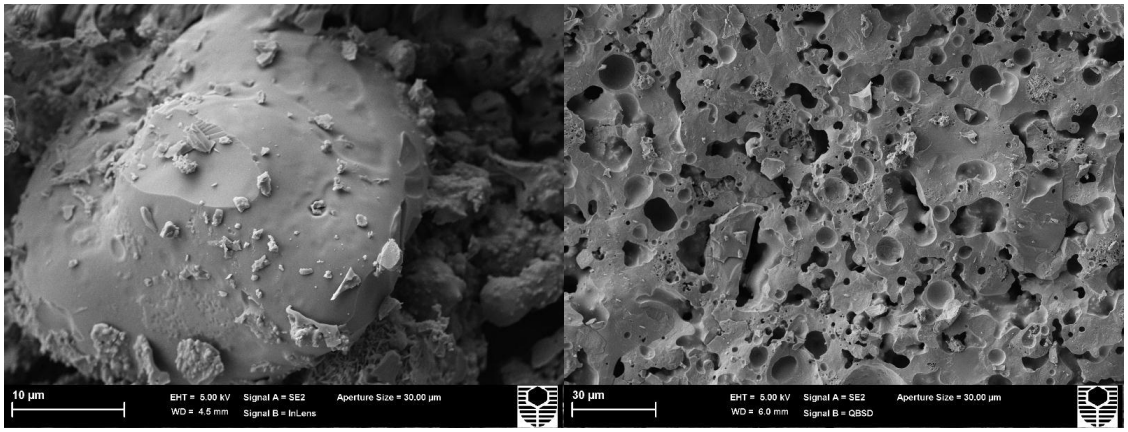

C1.82 fired at 800°C C1.82 fired at 1000°C

Figure B.1 Thermal evolution of C1.82 paste

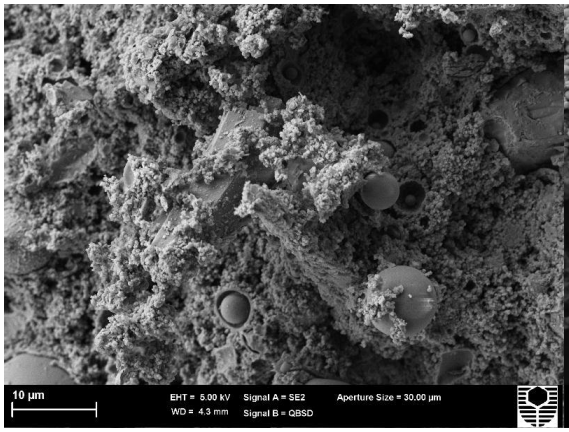

WOL 5 unfired 7 day cure

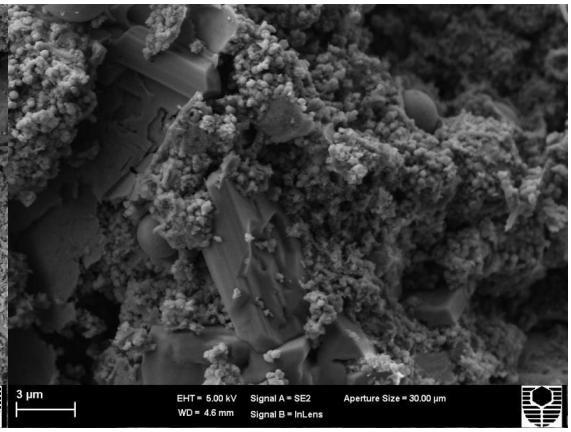

WOL 5 fired at 400^{o}C

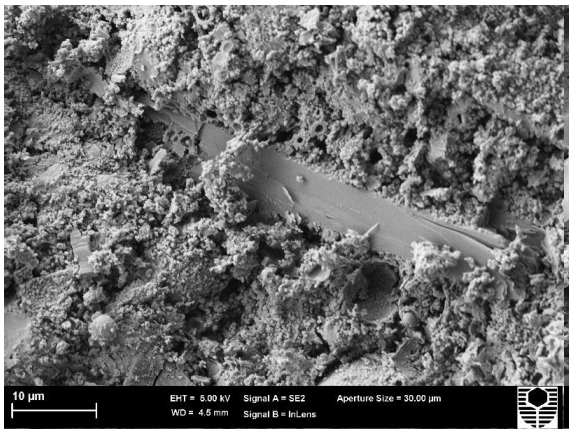

WOL 5 fired at 600^{o}C

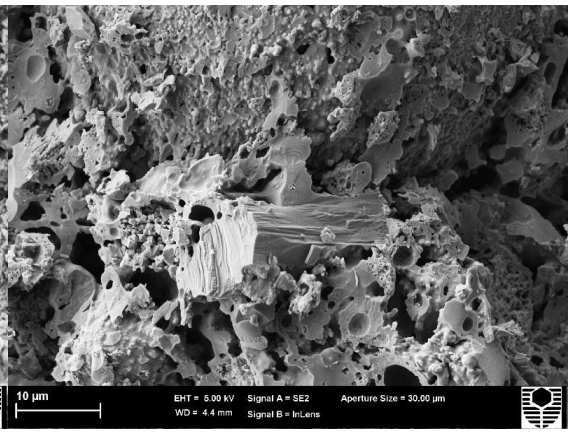

WOL 5 fired at 800^{o}C

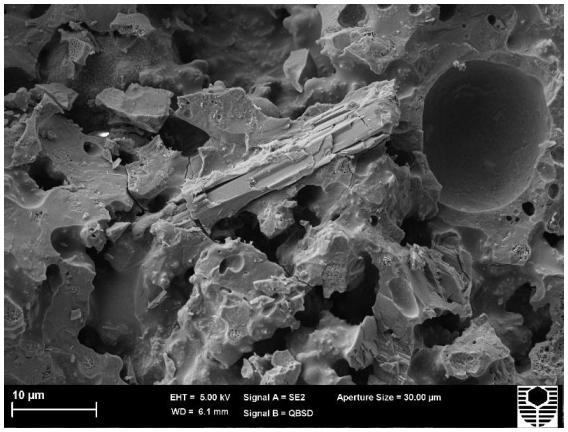

WOL 5 fired at 1000^{o}C

Figure B.2 Thermal evolution of WOL 5

WOL 10 unfired 7 day cure

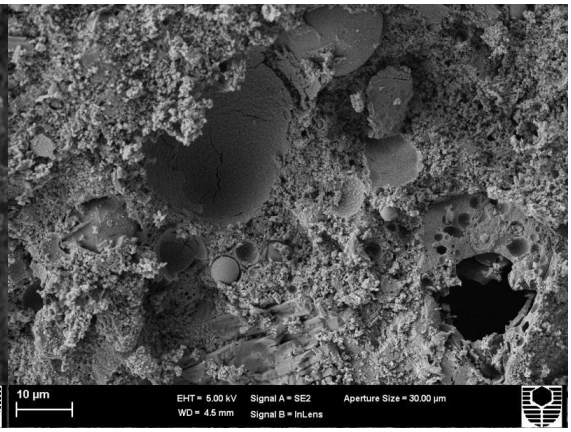

WOL 10 fired at 200^{o}C

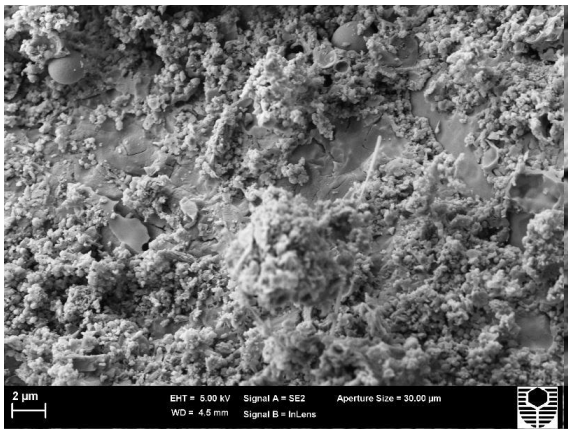

WOL 10 fired at 600^{o}C

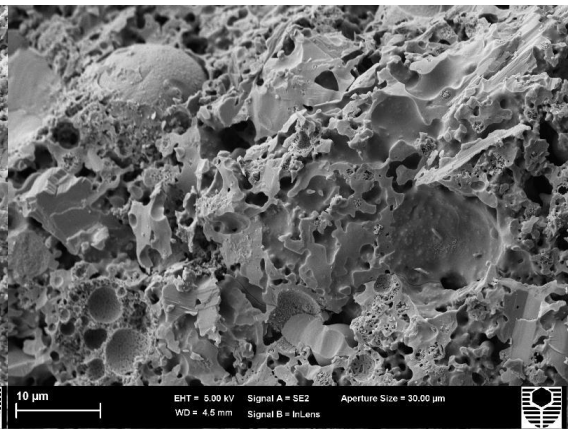

WOL 10 fired at 800^{o}C

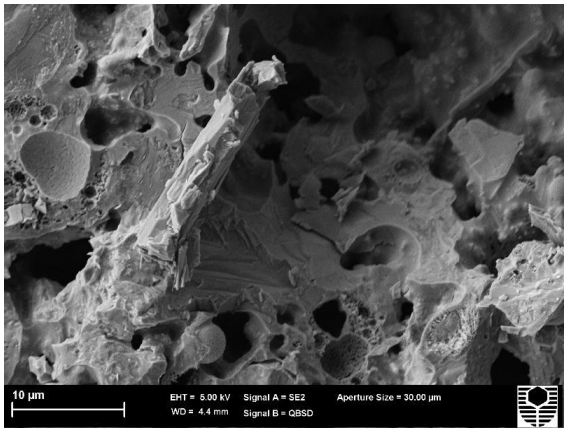

WOL 10 fired at 1000^{o}C

Figure B.3 Thermal evolution of WOL 10

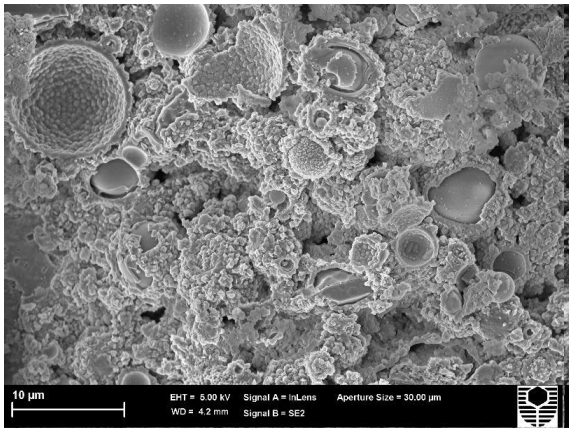

ALOX 5 unfired 7 day cure

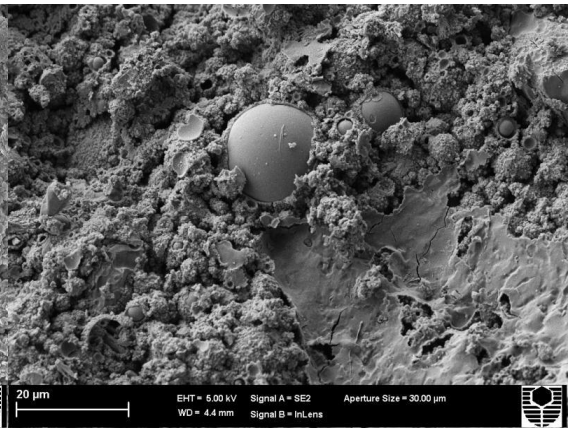

ALOX 5 fired at 200^{o}C

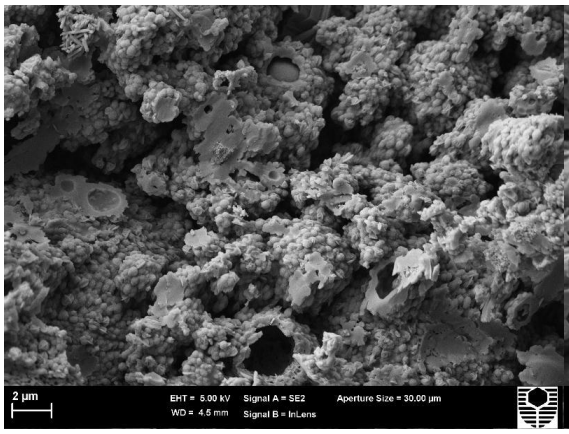

ALOX 5 fired at 600^{o}C

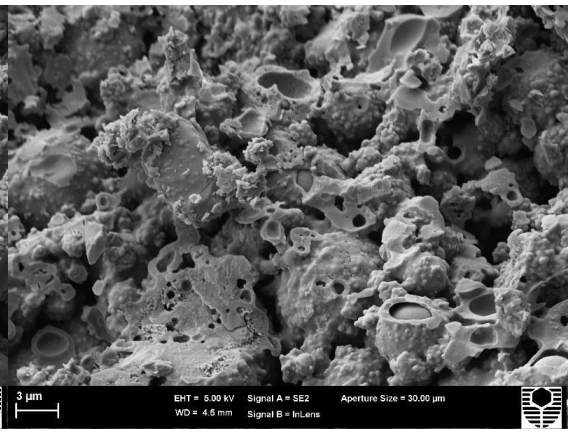

ALOX 5 fired at 800^{o}C

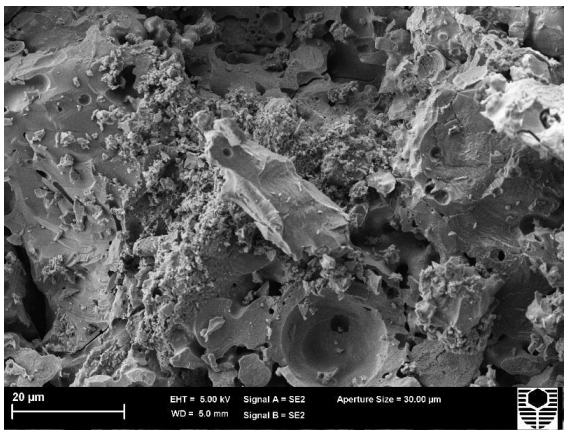

ALOX 5 fired at 1000^{o}C

Figure B.4 Thermal evolution of ALOX 5

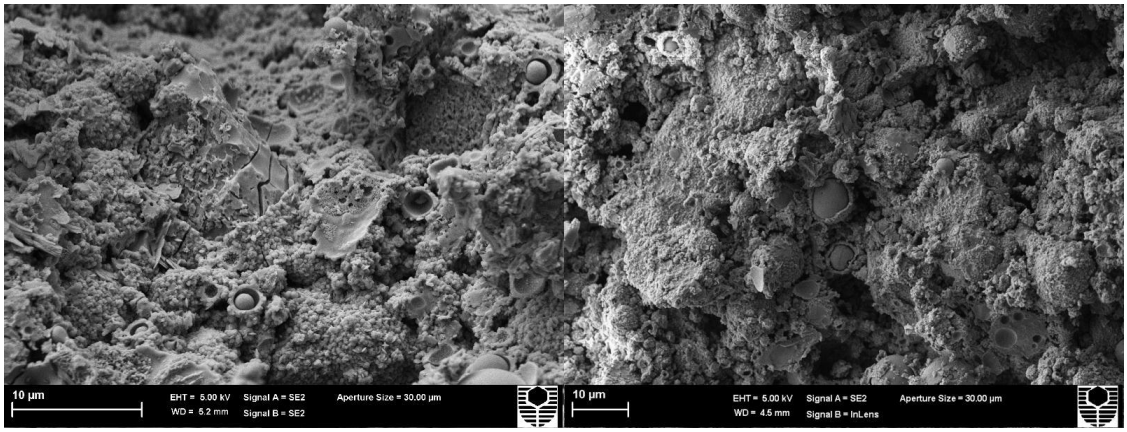

ALOX 10 unfired 7 day cure

ALOX 10 fired at 400^{o}C

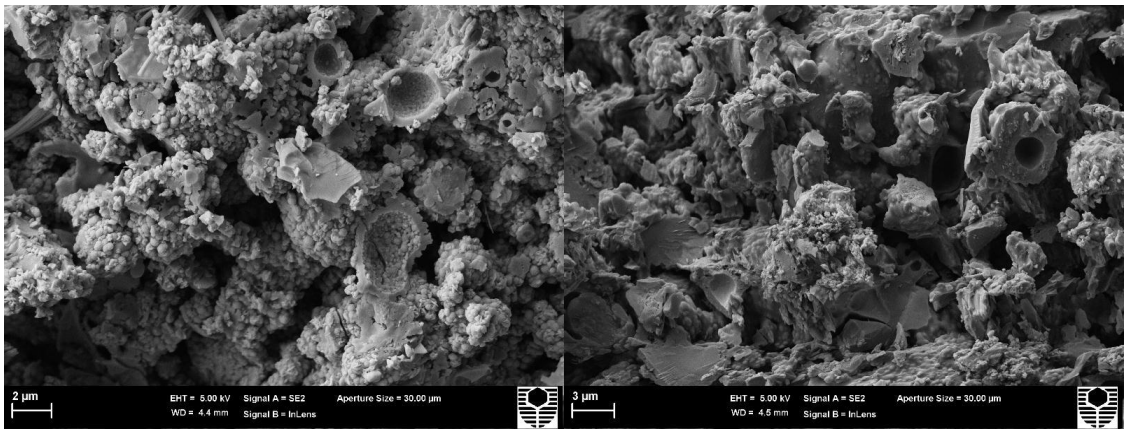

ALOX 10 fired at 600^{o}C

ALOX 10 fired at 800^{o}C

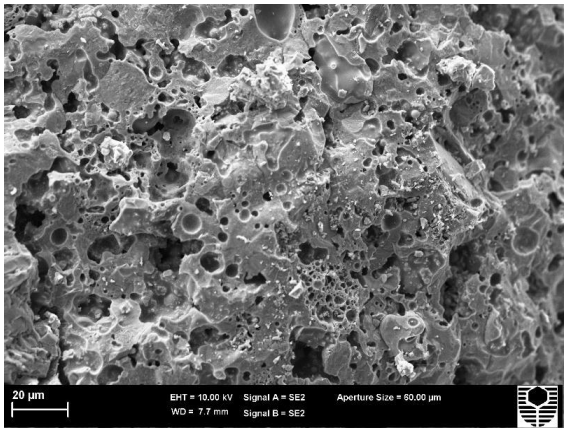

ALOX 10 fired at 1000^{o}C

Figure B.5 Thermal evolution ALOX 10

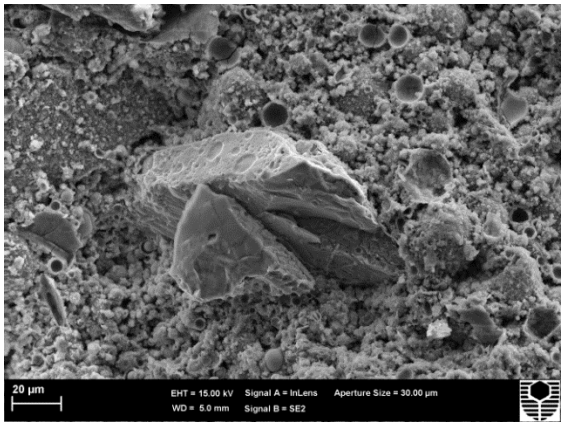

CH 10 as cured

CH 10 fired at 200^{o}C

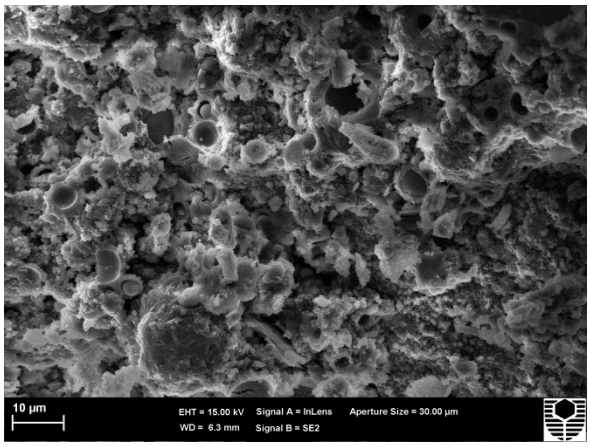

CH 10 fired at 400^{o}C

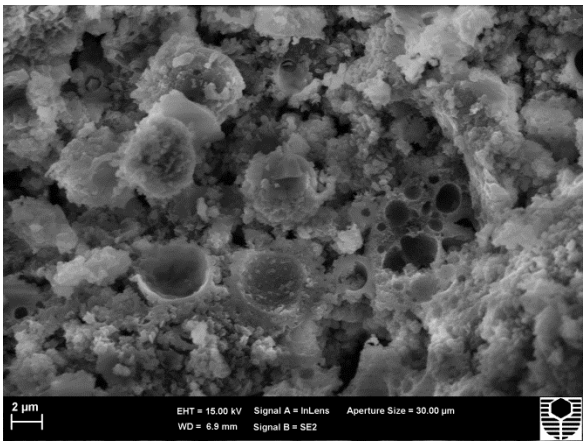

CH 10 fired at 600^{o}C

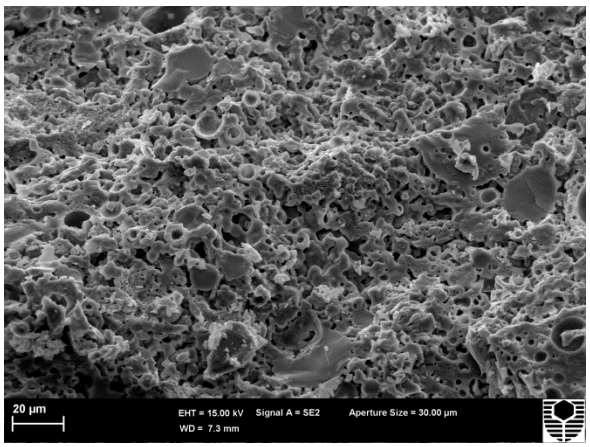

CH 10 fired at 800^{o}C

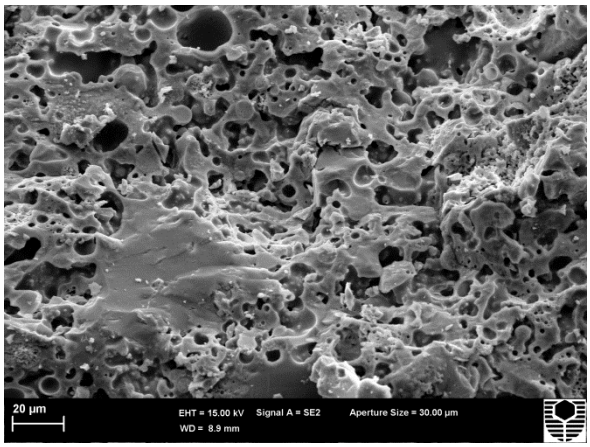

CH 10 fired at 1000^{o}C

Figure B.6 Thermal evolution of CH 10

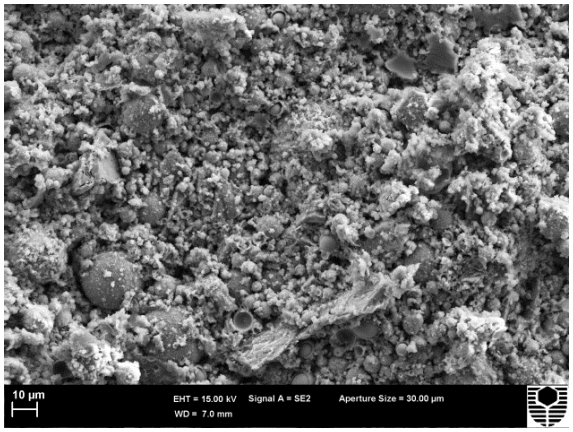

MUL 10 as cured

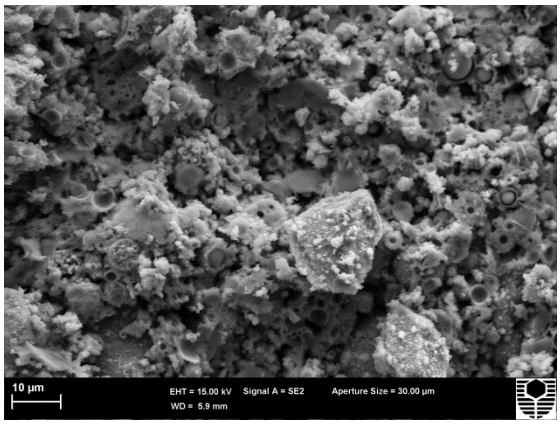

MUL 10 fired at 200^{o}C

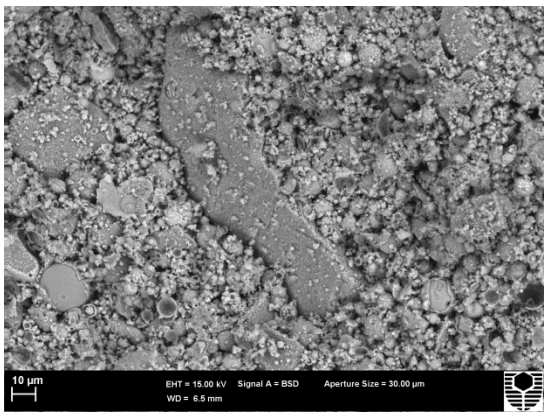

MUL 10 fired at 400^{o}C

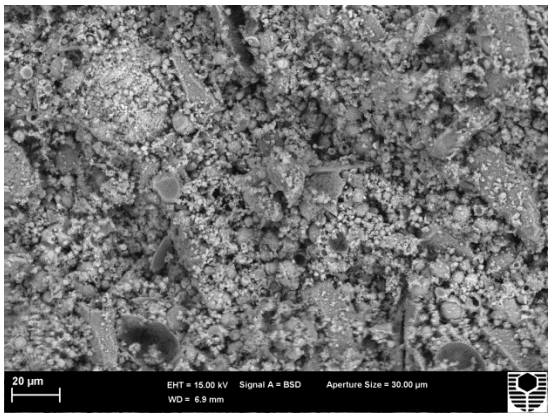

MUL 10 fired at 600^{o}C

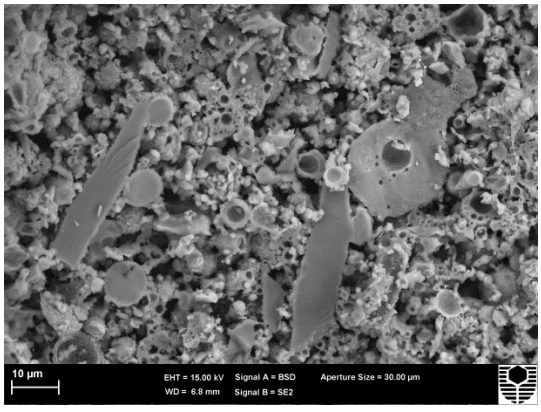

MUL 10 fired at 800^{o}C

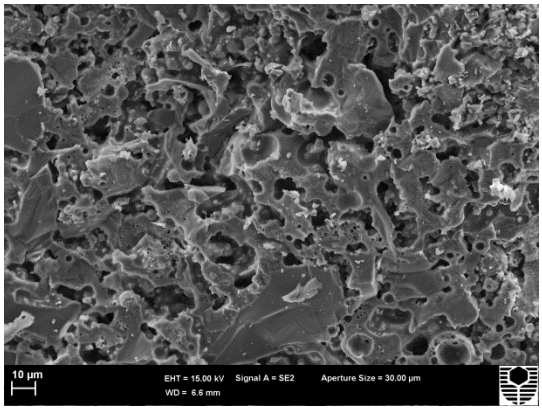

MUL 10 fired at 1000^{o}C

Figure B.7 Thermal evolution of MUL 10

Appendix C

Quantitative Energy Dispersive X-ray Spectrometry (QEDS) investigation of wollastonite containing composite

This evaluation was undertaken to investigate the possible presence of a transition zone between the wollastonite surface and the geopolymer matrix. The level of compressive and flexural strengths of these composites suggests that some interaction between wollastonite and geopolymer matrix is occurring in the as cured state.

The microstructure of the samples was not conducive to the polishing procedure required for QEDS due to small amounts of geopolymer binder, which influenced the accuracy of the acquisition of spectra. This is due to the interaction volume of the specimen-electron beam either penetrating to different microstructure areas below the surface or covering an area larger than the site of interest. However, analysis of the spectra data suggested that a transition zone adjacent to the wollastonite particles had formed. This zone had reduced calcium levels compared to wollastonite, but higher than the base fly ash, together with the appearance of sodium and aluminium indicative of geopolymer formation.

This suggests that calcium is taking part in the geopolymerisation reactions and is contributing to the higher mechanical properties of wollastonite containing composites reported earlier. These reactions may also be contributing to the lower concentration of macropores in the as cured samples, due to reduced viscous flow effects. The calcium containing reaction product may have an higher activation energy for viscous flow compared to sodium activated fly ash geopolymers (see figure 5.10)

In figure C.1 the location of spectra detailed in table C.1 is shown. Spectrum 14 is taken on the wollastonite particle and is basically $CaSiO_3$ as expected. Spectra 15, 16 and 17 taken at the edges of the particle have a convoluted elemental analysis containing calcium and together with sodium and aluminium which is indicative of geopolymer formation. Spectrum 18 is possibly not associated with the proposed transition zone and may not be geopolymer.

Table C.1 QEDS results for WOL 5PP.

Element	Spectrum 14, wt.%	mole	Spectrum 15, wt.%	mole	Spectrum 16, wt.%	mole	Spectrum 17, wt.%	mole	Spectrum 18, wt.%	mole
Oxygen	41.2 (0.3)	2.58	37.0 0.3)	2.31	42.9 (0.2)	2.68	49.8 (0.2)	3.11	50.6 (0.1)	3.16
Silicon	24.3 (0.2)	0.87	24.9 (0.2)	0.89	27.6 (0.1)	0.99	22.3 (0.1)	0.80	21.5 (0.1)	0.77
Calcium	34.2 (0.2)	0.86	16.0 (0.1)	0.4	16.4 (0.1)	0.41	6.2 (0.1)	0.16	21.8 (0.1)	0.55
Iron	0.3(0.1)	0.01	5.8 (0.1)	0.10	3.3 (0.1)	0.06	3.3 (0.1)	0.06	1.2 (0.1)	0.02
Aluminium			8.4 (0.1)	0.31	6.1 (0.1)	0.23	10.4 (0.1)	0.39	2.0 (0)	0.07
Sodium			6.1 (0.1)	0.27	3.2 (0.1)	0.14	6.5 (0.1)	0.28	3.0 (0.1)	0.13
Potassium			0.7 (0.1)	0.02	0.5 (0)	0.01	0.5 (0)	0.01		
Sulphur			0.6	0.02			0.4 (0)	0.01		
Total	100		99.5		100		99.4		100.1	

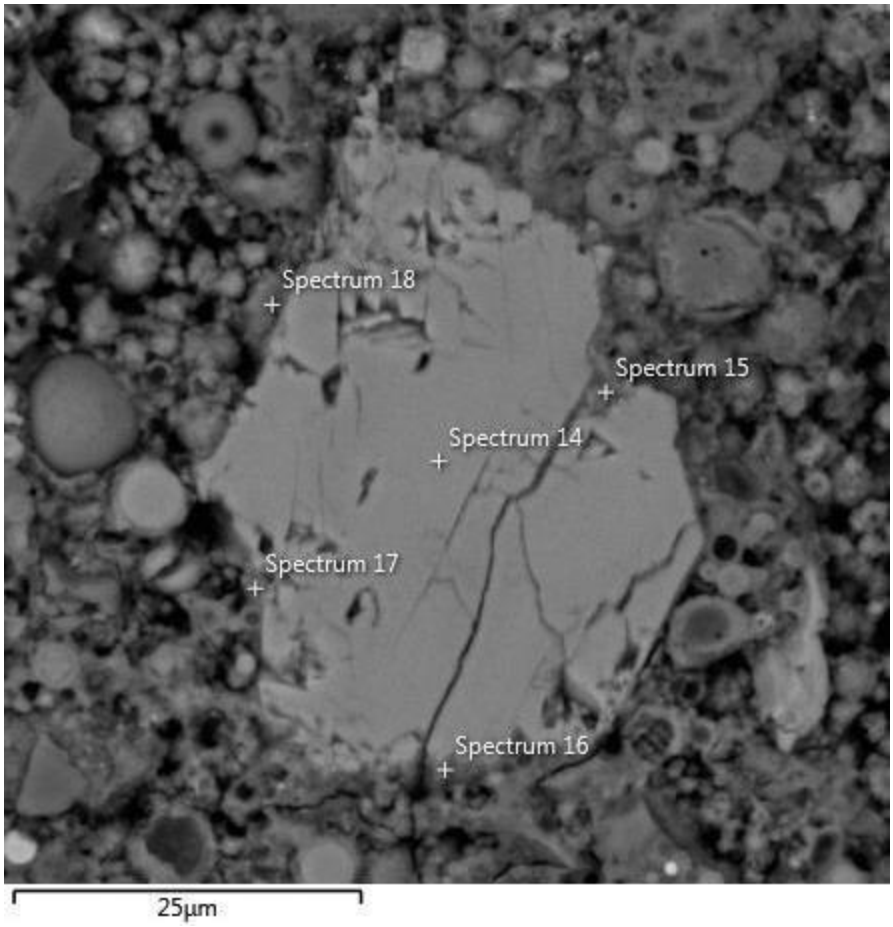

Figure C.1 Location of collected QEDS BSE spectra, WOL 5PP sample.

Figure C.2 shows the location of spectra detailed in table C.2. Similar trends to the above spectra are seen. Spectra 22, 23 and 24 were taken close to the edge of the wollastonite particle. Spectrum 25 was taken on a shaded area of the wollastonite particle.

Table C.2 QEDS results for WOL 5.

Element	Spectrum 21, wt.%	mole	Spectrum 22, wt.%	mole	Spectrum 23, wt.%	mole	Spectrum 24, wt.%	mole	Spectrum 25, wt.%	mole
Oxygen	40.7 (0.2)	2.54	32.3 (0.3)	2.02	43.8 (0.2)	2.68	43.5 (0.2)	2.72	32.6 (0.2)	2.04
Silicon	24.9 (0.1)	0.89	33.2 (0.2)	1.19	23.9 (0.1)	0.99	23.3 (0.1)	0.83	25.2 (0.1)	0.9
Calcium	33.9 (0.1)	0.85	13.4 (0.1)	0.34	17.2 (0.1)	0.41	18.0 (0.1)	0.45	33.4 (0.1)	0.84
Iron	0.3(0.1)	0.01	6.8 (0.2)	0.12	3.9 (0.3)	0.06	4.2 (0.1)	0.08	1.1 (0.1)	0.02
Aluminium			8.1 (0.1)	0.3	5.3 (0.1)	0.23	5.6 (0.1)	0.21	1.2 (0)	0.04
Sodium			3.9 (0.1)	0.17	5.0 (0.1)	0.14	3.9 (0.1)	0.17	6.6 (0.1)	0.29
Potassium			0.9 (0.1)	0.02	0.5 (0)	0.01	0.6 (0)	0.02		
Magnesium			0.7(0.1)	0.03	0.5 (0)	0.02	0.5 (0)	0.02		
Total	100		99.3		100.1		99.6		100.1	

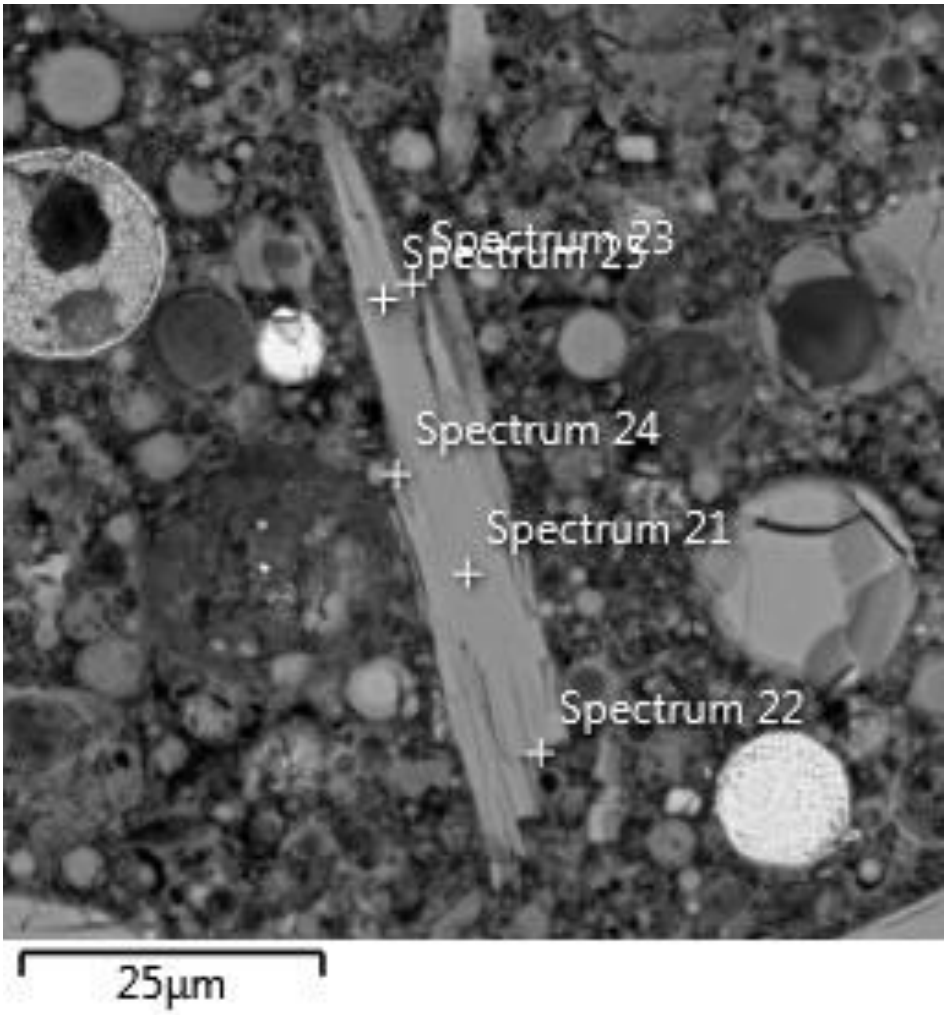

Figure C.2 BSE image of WOL 5 sample showing position of collected spectra for QEDS.

The formation of a transition zone during the geopolymerisation process is associated with the relatively high calcium content and/or surface morphology of the wollastonite.

The wollastonite has reacted with the geopolymer during synthesis leading to a structure which has reduced viscous flow (compared to C1.82 and ALOX 10) as shown by low shrinkage values and macropore content of the specimens. This structure may be exhibiting a higher degree of crosslinking due to the presence of calcium, reducing the viscous flow with corresponding shrinkage reductions. This reduced flow may be hindering the formation of macropores (from coalescence of micropores), which are the energetically preferred structure. Calcium ions do not have a fluxing effect similar to sodium ions (see figure 5.10) which again would have contributed to reduced flow.

More clarification of the phenomena occurring here is required. The use of transmission electron microscopy (TEM) may facilitate imaging of the proposed transition zone by reducing the size of the interaction volume.

Appendix D

Measurement of Young's Modulus

Measurement of compressive strength when using a digital stress-strain facility also enables Young's modulus to be determined based on the gradient of the linear elastic portion of the graph. Although this is a common technique for determining Young's modulus accuracy of this method has frequently been questioned (Lord and Morrell, 2006). This does not prevent this method being used in a comparative way between a series of measurements within a laboratory but it does prevent comparisons across different laboratories.

The measurement of Young's modulus for geopolymers on the Lloyds EZ50 in the Physics department has raised comments over the years regarding the low levels obtained and whether this is truly representative of material properties being measured. We were able to determine Young's modulus on the C1.82 paste system using two different methods at two different facilities and compare them with values obtained at Curtin.

At Curtin the strain is determined by measurement of the displacement of the top (moving) platen compared to the static bottom plate. The strain determined by this method appears to be overstated by a factor of around 10 leading to correspondingly low values for Young's modulus. This can be attributed to the low resolution and poor sensitivity of the measuring arrangement.

We were able to use an extensometer fitted to a compression testing machine at UWS (Figure D1). This extensometer is able to measure dimensional changes of +/-3 μm.

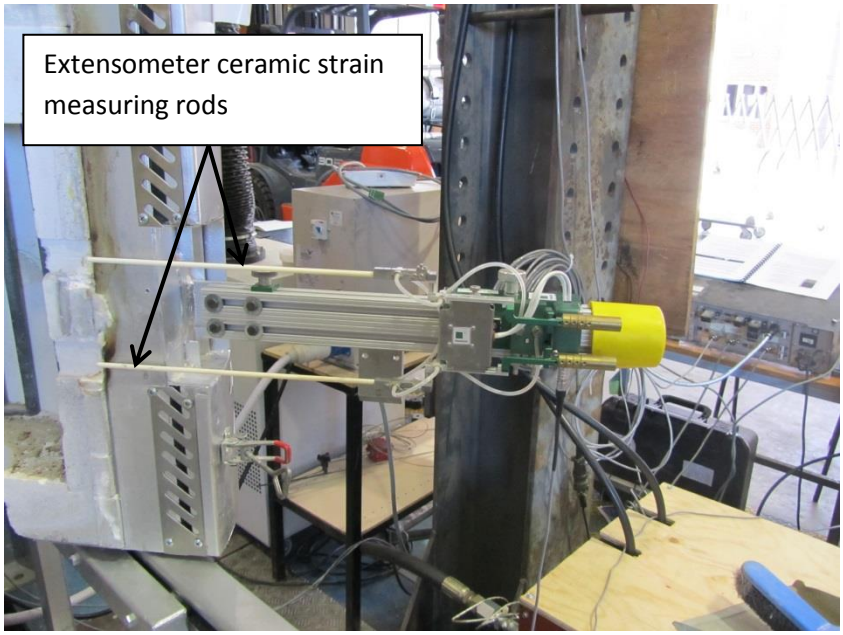

Figure D.1 Extensometer fitted to in-situ furnace set up

IMCE of Belgium have developed test equipment using a pulse excitation technique which measures the resonant frequency and damping (RFDA) which is then used to calculate Young's modulus. The equipment has the capability to run tests at a wide range of temperatures.

To determine the Young's modulus, the RFDA equipment measures the flexural vibration frequency and calculates the Young's modulus using the mass and dimensions of the sample. In the following example (figure D.2) the Young's modulus of a rectangular bar is determined. The same principle, with other formulas, can be used to determine the Young's modulus of discs, rods and grinding wheels.

Figure D.3 shows the RFDA results for C1.82 geopolymer over the temperature range 20 to 1000^{o}C. The heating curve shows a decrease in modulus as water is lost up to 170^{o}C, which then begins to increase again up to 400^{o}C. The modulus drops until 540^{o}C when it again increases before levelling off at 800^{o}C. After a 30 minute hold at around 1000^{o}C, cooling begins and a significant increase in modulus is seen. The cooling curve is smoother than the heating curve suggesting a more uniform, stable microstructure has developed during firing.

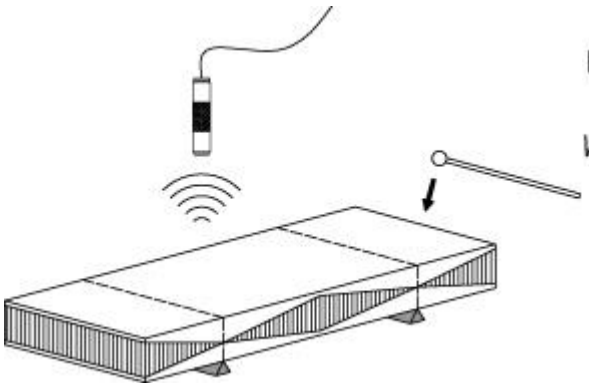

$$E = 0.9465\left(\frac{mf_f^2}{w}\right)\left(\frac{l^3}{t^3}\right)T$$

Width : E = Young's modulus

f_f = Flexural frequency

m = mass

l = Length

w = Width

t = Thickness

T = Correction coefficient

Figure D.2 Test set up for Young's modulus determination

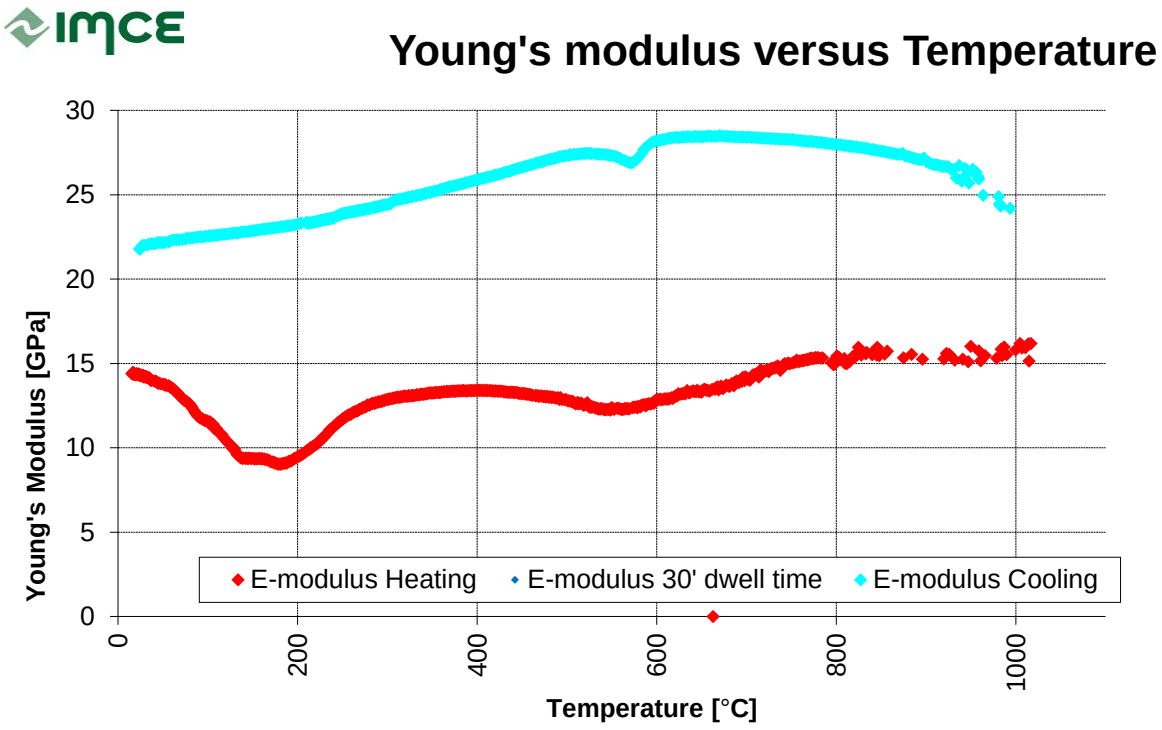

Figure D.3 Variation in Young's Modulus of C1.82 geopolymer with increasing and decreasing thermal cycles.

Table D.1 shows the compilation of Young's modulus results from three different sources.

Table D.1 Young's modulus (GPa) results for C1.82.

	Young's Modulus @ 25^{o}C GPa	**Young's Modulus @ Elevated temperature, GPa**
Curtin	1.67	2.24^{+} (fired at 1000^{o}C, tested at ambient temperature)
UWS (in-situ)	9.8*	2.08^{+} (500^{o}C)
IMCE, heating cycle	13.73	15.81 (1000^{o}C)
IMCE. Cooling cycle	21.79	24.18 (994^{o}C)

*Tested with extensometer; $^{+}$Tested using platen displacement

The results show that use of the displacement of the test machine platens to measure strain values for Young's modulus determination does not have sufficient resolution. The use of extensometers and dynamic methods are more accurate. In table D.2 tensile and dynamic test methods are compared. The requirement for high accuracy strain measurement is listed for tensile testing.

Table D.2 Comparison of tensile test and dynamic methods for Young's Modulus determination (Lord and Morrell, 2006)

Tensile Test	Dynamic Method
Advantages: • "Engineering value" for modulus • Generation of stress-strain curve • Widely available test equipment	Advantages: • Quick, simple, non-destructive • Good inherent accuracy • Uses small specimens • High Temperature measurement • Can readily measure shear modulus and Poisson's ratio
Disadvantages: • High accuracy strain measurement required • Need averaging extensometry • Specialised test • Larger specimens required • Large inter laboratory scatter • Accurate high temperature measurements are difficult	Disadvantages: • Relevance of dynamic modulus to engineering applications and design • Sensitive to dimensional tolerances • Methods do not always work well for some materials and composites • Calculations require some knowledge of other material parameters • Equipment not widely available

There is a paucity of information reported on the Young's Modulus of geopolymer pastes and concretes. This may be related to difficulties in determining Young's modulus on commonly available test equipment. The two geopolymer paste references below both use the gradient of the initial linear section of the stress-strain curve for the determination.

Duxon et al (2005) measured the elastic modulus of a sodium silicate activated metakaolin geopolymer paste with Si: Al between 1.15 and 2.15. They calculated the elastic modulus from the gradient of the initial linear section of the stress strain curve. Values between 2.4 and 5.1 GPa were reported. They used a constant displacement of 0.6mm min^{-1} rather than a constant rate of stress application.

Alzeer et al. (2012) used a similar methodology to Duxon and reported an elastic modulus of 9.6Gpa for a geopolymer paste.

Hardjito et al. (2005) tested 90 day fly ash geopolymer concrete using granite as the coarse aggregate. He determined the 40% secant modulus according to AS 1012.17 and obtained values in the range of 23.0 to 30.8 GPa for four different mixes.

Pan et al. (2011) measured the elastic modulus, using AS 1012.17, of a fly ash based geopolymer paste at 11.2 GPa and used the same paste to produce a concrete using 14mm basalt aggregate and fine sand obtaining an elastic modulus value of 35.5 GPa.

The values for Young's modulus for the above geopolymer pastes are in line with the value (9.8 GPa) obtained at UWS on as cured C1.82PP.

References

3M. 2003. Nexel Selector guide and specification sheet, www.3m.com/ceramics. *Technical Data Sheet*.

ABU-HAMATTEH, Z. S. H. & AL-TAIE, M. 2003. Improvements of Thermal and Chemical Properties of Fire Clay Refractory Bricks. *Pakistan Journal of Applied Sciences,* 3**,** 103-109.

ACHILLE, F. 2010. Geo-green Crete. *National Ready Mixed Concrete Association, 2010 Concrete Sustainability Conference Dec 13-14 Dubai, UAE.***,** 16.

ACI E2-00, C. 2006. Reinforcement for concrete- Materials and applications. *ACI Education Bulletin E2-00. www.concrete.org***,** 16.

ACI E-107, C. 2007. Aggregates for Concrete. *ACI Education Bulletin E-107. www.concrete.org***,** 29.

ADFIL 2010. Adfil Ignis. *Technical Data Sheet www.adfil.co.uk***,** 1.

AGULLO, L., TORALLES-CARBONARI, B., GETTU, R. & AGUADO, A. 1999. Fluidity of cement pastes with mineral admixtures and superplasticizer- A study based on the Marsh cone test. *Materials and Structures, ,* 32**,** 479-485.

AKERS, S., KAUFMANN, J., LÜBBEN, J. & SCHWITTER, E. 2009. Reinforcement of Concrete and Shotcrete using Bi-Component Polyolefin Fibres. *Conference Paper, Concrete Solutions 09, Australia***,** 9.

ALARCON-RUIZA, L., PLATRET, G., MASSIEU, E. & EHRLACHER, A. 2005. The use of thermal analysis in assessing the effect of temperature on a cement paste. *Cement and Concrete Research* 35**,** 609-613.

ALONSO, S. & PALOMO, A. 2001. Alkaline activation of metakaolin and calcium hydroxide mixtures: influence of temperature, activator concentration and solids ratio. *Materials Letters* 47**,** 55-62.

ALZEER, M. & MACKENZIE, K. J. D. 2012. Synthesis and mechanical properties of new fibre-reinforced composites of inorganic polymers with natural wool fibr. *J Mater Sci,* 47**,** 6958-6965.

ANASYS THERMAL METHODS CONSULTANCY 2012. Introduction to Thermomechanical Analysis. *Web page www.anasys.co.uk*.

APPLIED SCIENCES INC 2001. Research and Development Company. *Web page, www.apsct.com*.

APPLIN, K. R. 1987. The diffusion of dissolved silica in dilute aqueous solution. *Geochima and Cosmochimica Acta,* 51**,** 2147-2151.

ARIOZ, O. 2007. Effects of elevated temperatures on properties of concrete. *Fire Safety Journal,* 42**,** 516-522.

ASTM COMMITTEE A01-05 2011. A820/A820M − 11 Standard Specification for Steel Fibers for Fiber-Reinforced Concrete. *ASTM Standard*.

ASTM COMMITTEE C01.22 2013. C1437-13 Standard Test Method for Flow of Hydraulic Cement Mortar. *ASTM Standard***,** 2.

ASTM COMMITTEE C08.03 2000. C20-00 Standard Test Methods for Apparent Porosity, Water Absorption, Apparent Specific Gravity, and Bulk Density of Burned Refractory Brick and Shapes by Boiling Water. *ASTM Standard***,** 3.

ASTM COMMITTEE C09 2012. C39/C39M − 12a Standard Test Method for Compressive Strength of Cylindrical Concrete Specimens. *ASTM Standard***,** 7.

ASTM COMMITTEE C09.60 2012. C143/C143M − 12 Standard Test Method for Slump of Hydraulic-Cement Concrete. *ASTM Standard***,** 4.

ASTM COMMITTEE D20 2010. D790 − 10 Standard Test Methods for Flexural Properties of Unreinforced and Reinforced Plastics and Electrical Insulating Materials. *ASTM Standard*.

ASTM COMMITTEE C01 2008. C191 − 08 Standard Test Methods for Time of Setting of Hydraulic Cement by Vicat Needle. *ASTM Standard***,** 8.

ASTM COMMITTEE C09 2010. C1609M - 10 Standard Test Method for Flexural Performance of Fiber-Reinforced Concrete (Using Beam With Third-Point Loading). *ASTM Standard***,** 9.

ASTM COMMITTEE C09 2012a. C618-12 Coal Fly Ash and Raw or Calcined Natural Pozzolan for use in Concrete. *ASTM Standard*, 3.

ASTM COMMITTEE C09 2012b. C 494M-12 Standard Specification for Chemical Admixtures for Concrete. *ASTM Standard*, 10.

ASTM COMMITTEE C16.30 2010a. C177 − 10 Standard Test Method for Steady-State Heat Flux Measurements and Thermal Transmission Properties by Means of the Guarded-Hot-Plate Apparatus. *ASTM Standard*, 23.

ASTM COMMITTEE C16.30 2010b. C518 − 10 Standard Test Method for Steady-State Thermal Transmission Properties by Means of the Heat Flow Meter Apparatus. *ASTM Standard*, 16.

ASTM COMMITTEE C27-40 2008. ASTM C1666/C1666M-08 Standard Specification for Alkali Resistant (AR) Glass Fiber for GFRC and Fiber- Reinforced Concrete and Cement. *ASTM Standard*, 4.

ASTM COMMITTEE D01-36 2012. D7357 − 07 (Reapproved 2012) Standard Specification for Cellulose Fibers for Fiber-Reinforced Concrete1. *ASTM Standard*, 3.

ASTM COMMITTEE D13-58 2010. D7508/D7508M – 10 Standard Specification for Polyolefin Chopped Strands for Use in Concrete1. *ASTM Standard*, 4.

ASTM COMMITTEE D20.30 2009. D5930 − 09 Standard Test Method for Thermal Conductivity of Plastics by Means of a Transient Line-Source Technique. *ASTM Standard*.

ASTM COMMITTEE E37 2010. E289 -04 (reapproved 2010) Standard Test Method for Linear Thermal Expansion of Rigid Solids with Interferometry. *ASTM Standard*, 9.

ASTM COMMITTEE E37 2011. E228-11 Standard Test Method for Linear Thermal Expansion of Solid Materials With a Push-Rod Dilatometer. *ASTM Standard*, 10.

ASTM COMMITTEE E37 2012. E831-12 Standard Test Method for Linear Thermal Expansion of Solid Materials by Thermomechanical Analysis. *ASTM Standard*, 4.

ASTMCOMMITTEEC09-42 2010. C1116/C1116M – 10a Standard Specification for Fiber-Reinforced Concrete1. *Astm Standard*, 7.

ATKINS, P., OVERTON, T., ROURKE, J., WELLER, M. & ARMSTRONG, F. 2006. Inorganic Chemistry. *Book. Publisher: Oxford University Press*, 594-597.

AUSTRALIAN MUSEUM 2007. Classification of igneous rocks *web site. www. australianmuseum.net.au*, 2.

BABATUNDE, A. O. Z., Y.Q. 2007. Constructive Approach towards water treatment works sludge management: An international review of beneficial reuses. *Critical reviews in Environmental Science and Technology,* 37, 129-164.

BAKHAREV, T. 2005a. Resistance of Geopolymer materials to acid attack. *Cement and Concrete Research,* 35, 1233-1246.

BAKHAREV, T. 2005b. Resistance of geopolymer materials to acid attack. *Cement and Concrete Research,* 35, 658-670.

BAKHAREV, T. 2006. Thermal behaviour of Geopolymers prepared using class F fly ash and elevated temperature curing. *Cement and Concrete Research,* 36, 1134-1147.

BAKHAREVA, T., SANJAYAN, J. G. & CHENG, Y. B. 2000. Effect of admixtures on properties of alkali-activated slag concrete. *Cement and Concrete Research* 30, 1367-1374.

BANH UK LTD 2010. banahCEM Geopolymer cement system. *Techncal Data Sheet. www.banahuk.co.uk*, 2.

BANTHIA, N. 1994. Carbon Fibre Cements: Structure, Performance, Applications and reseach Needs. *Fiber Reinforced Concrete, Developments and Innovations. American Concrete Institute. Ed. JI Daniel and SP Shah,* SP-142, 91-120.

BANTHIA, N. & GUPTA, R. 2006. Influence of polypropylene fiber geometry on plastic shrinkage cracking in concrete. *Cement and Concrete Research,* 36, 1263-1267.

BARBOSA, V. & MACKENZIE, K. 2003a. Synthesis and thermal behaviour of potassium sialate geopolymers. *Materials Letters* 57, 1477-1482.

BARBOSA, V., MACKENZIE, K. & THAUMATURGO, C. 2000a. Synthesis and Characterisation of materials based on inorganic polymers of alumina and silica: sodium polysialate polymers. *International Journal of Inorganic Materials 2* **2,** 309-317.

BARBOSA, V. F. F. & MACKENZIE, K. 2003b. Thermal behaviour of inorganic geopolymers and composites derived from sodium polysialate. *Materials Research Bulletin,* 38**,** 319-331.

BARBOSA, V. F. F., MACKENZIE, K. J. D. & THAUMATURGOA, C. 2000b. Synthesis and characterisation of materials based on inorganic polymers of alumina and silica: sodium polysialate polymers. *International Journal of Inorganic Materials 2 (2000) 309–317*.

BARLET-GAUDEDARD, V., ZUSATZ-AYACHE, B. & PORCHERIE, O. 2010. Geopolymer Composition and Application in Oilfield Industry. *US Patent 7,794,537***,** 18.

BASF 2008. Mode of Action for superplasticisers for cement based construction Chemicals. *Technical leaflet. www.construction-polymers.com*.

BASSIONI, G. 2010. The influence of cement composition on superplasticizers' efficiency. *International Journal of Engineering (IJE),* 3**,** 577-587.

BAUER, S. W. 2007. The History of the Ancient World. *Book. published by W.W. Norton and Company Inc. New York***,** 4-5.

BAYER MATERIALS SCIENCE 2007. BMS wins new partner for it's attractive market sector. *nanotechnology-now.com,* 21-8-2007**,** 1.

BAYER MATERIALS SCIENCE 2008. Dispersion-Low Viscosity Material. *Web page. www.baytubes.com/technology_and_applications/low_viscosity***,** 1.

BELL, J. L. & KRIVEN, W. M. 2009. Preparation of ceramic foam from metakaolin based geopolymer gels. *Developments in strategic materials, Edited by Hua-Tay Lin, Kunihito Koumoto, Waltraud M. Kriven, Edwin Garcia, Ivar E. Reimanis and David P. Norton. Copyright 0 2009 The American Ceramic Society.***,** 97-111.

BENTUR, A., DIAMOND, S. & MINDESS, S. 1985. The microstructure of the steel fibre-cement interface. *Journal of Materials Science,* 20**,** 3610-3620.

BERNAL, S., DE GUTIERREZ, R., DELVASTO, S. & RODRIGUEZ, E. 2006. Performance of geopolymeric concrete reinforced with steel fibres. *Conference Paper. IIBCC 10th International Inorganic Bonded Fibre Composites Conference, Nov. 15-18, Sao Paulo, Brazil.***,** 156-167.

BERNAL, S. A., BEJARANO, J., GARZÓN, C., MEJÍA DE GUTIÉRREZ, R., DELVASTO, S. & RODRÍGUEZ, E. D. 2012a. Performance of refractory aluminosilicate particle/fiber-reinforced geopolymer composites. *Composites Part B: Engineering,* 43**,** 1919-1928.

BERNAL, S. A., RODRIQUEZ, E. D., MEGIA DE GUITERREZ, R., PROVIS, J. L. & DELVASTO, S. 2012b. Activation of Metakaolin/slag blends using alkaline solutions based on chemically modified silica fume and rice husk ash. *Waste Biomass Valor,* 3**,** 99-108.

BHATTACHARJEE, R. & LASKAR, A. I. 2010. RHEOLOGICAL BEHAVIOR OF FLY ASH BASED GEOPOLYMER CONCRETE. *35th Conference on OUR WORLD IN CONCRETE & STRUCTURES: 25 – 27 August 2010, Singapore***,** 7.

BILODEAU, A., KODUR, V. K. R. & HOFF, G. C. 2004. Optimization of the type and amount of polypropylene fibres for preventing the spalling of lightweight concrete subjected to hydrocarbon fire. *Cement & Concrete Composites,* 26**,** 163-174.

BLISSETT, R. S. & ROWSON, N. A. 2012. A review of multi component utilisation of Coal Fly Ash. *Fuel,* 97**,** 1-23.

BONDAR, D., LYNSDALE, C. J., MILESTONE, N. B., HASSANI, N. & RAMEZANIANPOUR, A. A. 2010. Geopolymer Cement from Alkali-Activated Natural Pozzolans: Effect of Addition of Minerals. *Conference paper, Second International Conference on Sustainable Construction Materials And Technologies,June 28-30,Universita Politechnica delle Marce, Anacona, Italy***,** 9.

BORINAGO-TREVINO, R., PASCUAL-MUNOZ, P., CASTRO-FRESNO, D. & DEL COZ-DIAZ, J. J. 2012. Study of different grouting materials used invertical geothermal closed loop heat exchangers. *Applied Thermal Energy*.

BOTH, C. 2003. Tunnel Fire safety. *Heron,* 48**,** 3-16.

BOUVET, A., GHORBEL, E. & BENNACER, R. 2010. The mini-conical slump flow test: Analysis and numerical study. *Cement and Concrete Research* 40**,** 1517-1523.

BREW, D. R. M. & MACKENZIE, K. J. D. 2007. Geopolymer synthesis using silica fume and sodium aluminate. *J Mater Sci*

BRUGGE, C. 2011. Concrix, Macrofiber bi-component and high performance. *Technical Data Sheet.* **,** 4.

BUCHWALD, A., VICENT, M., KRIEGEL, R., KAPS, C., MONZÓ, M. & BARBA, A. 2009. Geopolymeric binders with different fine fillers — Phase transformations at high temperatures. *Applied Clay Science,* 46**,** 190-195.

BUCHWALD, A. W., J. 2009. ASCEM Cement Technology: Alkali Activated Cement based on synthetic slag made from fly Ash *Conference Paper. 1st Int. Conf. on Advances in Chemically-activated Materials (CAM´2010, China). ,* Shi, C. and Shen, X. eds., RILEM Publications S.A.R.L., ISBN 978-2-35158-101-8, pp. 15-21.**,** 8.

BUCKEYE BUILDING FIBRES 2009. Ultrafibre 500, Secondary Reinforcement for Concrete. *Technical Data Sheet. www.ultrafiber.com***,** 2.

BUDINSKI, K. G. & BUDINSKI, M. K. 2005. Engineering Materials: Properties and Selection. . *Book. published by Pearson Education Inc., New Jersey,* 8th Edition**,** 195.

C-THERM 2010. C-therm TCI Thermal Conductivity Analyser. *Product Bulletin. www.ctherm.com***,** 6.

CATLOW, C. R. A., GEORGE, A. R. & FREEMAN, C. M. 1996. Ab initio and molecular-mechanics studies of aluminosilicate fragments, and the origin of Lowenstein's rule. *Chem. Commun.***,** 1331-1332.

CCANZ, C. C. A. O. N. Z. 2005. Vibration of Concrete. *Information Bulletin. www.cca.org.nz*.

CCANZ, C. C. A. O. N. Z. 2009. Fibre reinforced Concrete. *Information Bulletin. www.cca.org.nz,* IB39**,** 19.

CEMENT & CONCRETE INSTITUTE, S. A. 2010. Fibre reinforced Concrete. *Information Bulletin. www.cnci.org.za***,** 6.

CEMENT CONCRETE & AGGREGATES AUSTRALIA 2008. Use of Recycled aggregates in construction. *Executive Report. www.ccaa.com.au***,** 25.

CEMENT CONCRETE & AGGREGATES AUSTRALIA 2010. Fire Safety of Concrete Buildings. *Technical report CCAA T61***,** 37.

CEMENT CONCRETE AND AGGREGATES, A. 2005. Plastic Shrinkage Cracking. *Technical Data Sheet*.

CENTRAL FEDERAL LANDS HIGHWAY DIVISION 2008. Concrete defects and curing Chemistry. *Technical Report. www.cflhd.org***,** 16.

CERATECH 2011. Firerok High Temperature Concrete. *Technical Data Sheet. www.ceratechinc.com***,** 3.

CHANH, N. V. 2004. Steel fibre reinforced concrete. *Faculty of Civil Engineering, Ho Chi Minh City University***,** 108-116.

CHEN-TAN, N. W., VAN RIESSEN, A., LY, C. V. & SOUTHAM, D. C. 2009. Determining the reactivity of a fly Ash for the production of a geopolymer. *Journal of the American Ceramic Society,* 92**,** 881-887.

CHEN, L., HAN, W., ZHEN, L., WEI, T. & XIAO, C. 2011a. Preparation and Properties of Alkali Stimulated Geopolymer and its Application in Thermal Insulating Coatings. *Advanced Materials Research* 233-235**,** 2443-2446.

CHEN, N., LIU, M. & YANG, J. 1992. Influence of Preparative History on Physio- Chemical Properties of Sodium Aluminate Solutions. *Chin.J.Met.Sci.Tech.,* 8**,** 135-137.

CHEN, P.-W. & CHUNG, D. D. L. 1993. Carbon fiber reinforced concrete as an electrical contact material for smart structures. *Smart Mater. Struct. ,* 2**,** 181-188.

CHEN, S. J., COLLINS, F. G., MACLEOD, A. J. N., PAN, Z., DUAN, W. H. & WANG, C. M. 2011b. Review paper Carbon nanotube–cement composites: A retrospect. *The IES Journal Part A: Civil & Structural Engineering,* 4**,** 254-265.

CHENG, T.-W. 2003. Fire resistant geopolymer produced by waste serpentine cutting. *Proceedings of the 7th International Symposium on East Asian Resources Recycling Technology*, 4.

CHENG, T. W. & CHIU, J. P. 2003. Fire-resistant geopolymer produced by granulated blast furnace slag. *Minerals Engineering,* 16, 205-210.

CHINDAPRASIRT, P. & RATTANASAK, U. 2010. Utilization of blended fluidized bed combustion (FBC) ash and pulverized coal combustion (PCC) fly ash in geopolymer. *Waste Management,* 30, 667-672.

CHOMARAT 2009. C-GRID. *web site www.chomarat.com*.

CHUNG, D. D. L. 1992. Carbon Fibre Reinforced Concrete. *Strategic Highway Research Program,* Report SHRP.ID/UFR-92-605, 92.

CHUNG, D. D. L. 2005. Dispersion of Short Fibers in Cement. *Journal of Materials in Civil Engineering,* 17, 379-383.

CLARKE, D. R. 2002. Materials Selection Guidelines for Low Thermal Conductivity Thermal Barrier Coatings. *Surface and coatings Technology,* 163-164, 67-74.

COI CERAMICS 2006. Sylramic SiC Fiber. *Technical Data Sheet. www.coiceramics.com*, 2.

COLLEPARDI, M. 2000. Ettringite formation and sulphate attack on concrete. *Conference Paper., 5th CANMET/ACI international conference on durability of concrete, Spain 2000.*, 25-41.

CONCRETE INSTITUTE OF QUEENSLAND 2010. Geopolymer concrete. *Concrete IQ. www.ciaq.com.au*, 3.

CONCRETE SOCIETY 2010. Specification for the manufacture curing and testing of GRC products. *Specification. www.grca.co.uk*, 13.

COOGEE CHEMICALS 2012. Sodium Aluminate. *Specification. www.coogee.com.au*, 1.

COOK R.A., H., K.C. 1999. Mercury porisimetry of hardened cement paste. *Cement & Concrete Research,* 29, 933-943.

CRESSET CHEMICAL CO. 2012a. CCS GUIDE – (CRESSET CONCRETE STANDARDS. *web site. www.cresset.com/images*.

CRESSET CHEMICAL CO. 2012b. Release Agents – What are they? How do they work? *web site. www.cresset.com*, 3.

CRIADO, M., FERNÁNDEZ-JIMÉNEZ, A., DE LA TORRE, A. G., ARANDA, M. A. G. & PALOMO, A. 2007. An XRD study of the effect of the SiO2/Na2O ratio on the alkali activation of fly ash. *Cement & Concrete Research,* 37, 671-679.

CWIRZEN, A., HABERMEHL-CWIRZEN, K. & MÄKINEN, K. 2009. The effect of carbon nano- and microfibers on microcrack formation. *Conference Paper, Concrete Solutions 09, Australia*, 8.

DAVIDOVITS, D. 2011. Geopolymer Chemistry & Applications. *Book. Publisher: Institut Geopolymere*, 433-443.

DAVIDOVITS, F. & DAVIDOVITS, J. 1999. Long lasting Roman cements and concretes. *Géopolymère '99 Proceedings*.

DAVIDOVITS, J. 1989. Geopolymers and Geopolymeric Materials. *Journal of Thermal Analysis,* 35, 429-441.

DAVIDOVITS, J. 1991. Geopolymers: Inorganic geopolymeric new materials. *Journal of thermal analysis,* 37, 1633-1656.

DAVIDOVITS, J. 2008a. Geopolymer Chemistry & Applications 3rd edition. *Book. published by Institut Geopolymere, St. Quinten*, 149-200.

DAVIDOVITS, J. 2008b. Geopolymer Chemistry & Applications 3rd edition. *Book. published by Institut Geopolymere, St. Quinten*, 398-406.

DAVIDOVITS, J. 2008c. Geopolymers Chemistry & Applications 3rd edition. *Book. published by Institut Geopolymere, St. Quinten*, 392-398.

DAVIDOVITS, J. 2008d. Geopolymers Chemistry and Applications 3rd edition. *Book. published by Institut Geopolymere, St. Quinten*, 488-490.

DAVIDOVITS, J. 2008e. Geopolymers Chemistry and Applications 3rd edition. . *Book. published by Institut Geopolymere, St. Quinten,* , 315-336.

DAVIS, B. 2007. Natural Fiber Reinforced Concrete. *Presentation, people.ce.gatech.edu/~kk92/natfiber.pdf***,** 21.

DE BRITO, J., DOS SANTOS , R. & BRANCO, F. A. 2000. Evaluation of the technical performance of concrete vegetable oil based release agents. *Materials and Structures/Materiaux et Constructions. ,* 33**,** 262-269.

DE FAZIO, P. 2011. Basalt fibre: From earth an ancient material for innovative and modern application. *ENEA report.* **,** 8.

DE LACAILLARIE, J. B. D. E., BOURLON, A., FAVIER, A., HABERT, G. & ROUSSEL, N. 2012. What is geopolymerization? A combined chemical (NMR), structural (SAXS) and rheology study. *Conference Paper, Monteverita Sunday 12 to 15.***,** 16.

DE SILVA, P. & SAGOE-CRENSTIL, K. 2008. The Effect of Al2O3 and SiO2 On Setting and Hardening of Na2O-Al2O3-SiO2- H2O Geopolymer Systems. *J. Aust. Ceram. Soc. ,* 41**,** 39-46.

DEBELIE, N., BEBRUYCKERE, M., VAN NIEUWENBURG, D. & DEBLAERE, B. 1997. Attack of concrete floors in pig houses by feed acids: Influence of Fly ash addition and cement bound surface layers. *Journal of Agriculutural Engineering Research,* 68**,** 101-108.

DEFAZIO, C., ARAFA, M. D. & BALAGURU, P. N. 2006. Functional Geopolymer Composites f. *Technical Report, Center for Advanced Infrastructure & Transportation (CAIT) Civil & Environmental Engineering Rutgers, The State University,* Ceram-RU9163**,** 18.

DEMORTIER, G. 2004. PIXIE,PIGE and NMR study of the masonry of the pyramid of Cheops at Gaza. *Nuclear Instruments and Methods in Physics Research,* B226**,** 98-109.

DENOËL, J. F. 2007. Fire Safety and Concrete Structures. *Technical Review Federation of Belgian Cement Industry. www.febelcem.be***,** 90.

DIAS, D. P. & THAUMATURGO, C. 2005. Fracture toughness of geopolymeric concretes reinforced with basalt fibers. *Cement and Concrete Composites,* 27**,** 49-54.

DIAZ, E. I., ALLOUCHE, E. N. & EKLUND, S. 2010. Factors affecting the suitability of fly ash as source material for geopolymers. *Fuel,* 89**,** 992-996.

DIVERSIFIED ENTERPRISES 2009. Accudyne test. *web page. www.accudynetest.com*.

DJELALA, C., VANHOVEA, Y. & MAGNINB, A. 2004. Tribological behaviour of self compacting concrete. *Cement and Concrete Research* 34**,** 821-828.

DOMBROWSKI, K., BUCHWALD, A. & WEIL, M. 2007. The influence of calcium content on the structure and thermal performance of fly ash based geopolymers. *J Mater Sci* 42**,** 3033-3043.

DORAL 2011. White fused alumina. *Technical Data Sheet*.

DUXON, P., LUKEY, G. C., SEPAROVIC, F. & VAN DEVENTER, J. S. J. 2005. Effect of Alkali Cations on Aluminium Incorporation in Geopolymeric gels. *Industrial Engineering and Chemical Research,* 44**,** 832-839.

DUXON, P., LUKEY, G. C. & VAN DEVENTER, J. S. J. 2006. Thermal Conductivity of Metakaolin Geopolymers Used as a First Approximation for Determining Gel Interconnectivity. *Ind. Eng. Chem. Res.,* 45**,** 7781-7788.

DUXON, P., LUKEY, G. C. & VAN DEVENTER, J. S. J. 2007a. Physical evolution of Na-geopolymer derived from metakaolin up to 1000 C. *J Mater Sci,* 42**,** 3044-3054.

DUXON, P., LUKEY, G. C. & VAN DEVENTER, J. S. J. 2007b. The thermal evolution of metakaolin geopolymers: Part 2 – Phase stability and structural development. *Journal of Non-Crystalline Solids* 353**,** 2186-2200.

DUXSON, P., FERNANDEZ-JIMENEZ, A., PROVIS, J. L., LUKEY, G. C., PALOMO, A. & VAN DEVENTER, J. S. J. 2007. Geopolymer technology: the current state of the art. *J Mater Science,* 42**,** 2917-2933.

DUXSON, P., LUKEY, G. C. & VAN DEVENTER, J. S. J. 2006a. Nanostructural design of multifunctional geopolymeric materials. *Ceramic Transactions,* 175**,** 203-214.

DUXSON, P., LUKEY, G. C. & VAN DEVENTER, J. S. J. 2006b. Thermal Evolution of metakaolin geopolymers. Part 1 Physical Evolution. *Journal of Non-Crystalline Solids,* 352**,** 5541-5555.

DUXSON, P., PROVIS, J. L., LUKEY, G. C., MALLICOAT, S. W., KRIVEN, W. M. & VAN DEVENTER, J. S. J. 2005. Understanding the relationship between geopolymer composition, microstructure and mechanical properties. *Colloids and Surfaces A: Physicochemical and Engineering Aspects,* 269**,** 47-58.

DUXSON, P., PROVIS, J. L., LUKEY, G. C., VAN DEVENTER, J. S. J., SEPAROVIC, F. & GAN, Z. H. 2006c. 39 K NMR of free potassium in geopolymers. *Industrial Engineering and Chemical Research,* 45**,** 9208-9210.

EDEN ENERGY 2011. Encouraging results on Eden's Nano-Carbon in Concrete. *Press Release. www.edenenergy.com.au*.

ESWARI, S., RAGUNATH, P. N. & SUGUNA, K. 2008. Ductility Performance of Hybrid Fibre Reinforced Concrete. *American Journal of Applied Sciences* 5**,** 1257-1262.

FARADAY, M. 1861. The Chemical History of a Candle. *Book, Published by Oxford University Press. Sesquicentenary Edition edited by F.A.J.L. James***,** 152.

FELLICETTI, R., MEYER, C. & SHIMANOVICH, S. 2001. Basalt Fibre Reinforced Oil well cement Slurries. *Conference paper, Proceedings of the 3rd Int. Conf. on Concrete under severe conditions, Vancouver.***,** 8.

FERDOUS, W., MANALO, A., 2014. Failures of Mainline Railway Sleepers and Suggested Remedies - Review of Current Practice. *Engineering Failure Analysis*.

FERNÀNDEZ-ALTABLE, V. & CASANOVA, I. 2006a. Influence of mixing sequence and superplasticiser dosage on the rheological response of cement pastes at different temperatures. *Cement and Concrete Research* 36**,** 1222-1230.

FERNÀNDEZ-ALTABLE, V. & CASANOVA, I. 2006b. Influence of mixing sequence and superplasticiser dosage on the rheological response of cement pastes at different temperatures. *Cement and Concrete Research,* 36**,** 1222-1230.

FERNÁNDEZ-JIMÉNEZ, A. & PALOMO, A. 2003. Characterisation of fly ashes. Potential reactivity as alkaline cements. *Fuel,* 82**,** 2259-2265.

FERNÁNDEZ-JIMÉNEZ, A. & PALOMO, A. 2005. Composition and microstructure of alkali activated fly ash binder: Effect of the activator. *Cement and Concrete Research* 35**,** 1984-1992.

FERNÁNDEZ-JIMÉNEZ, A., PALOMO, A. & CRIADO, M. 2005. Microstructure development of alkali-activated fly ash cement: a descriptive model. *Cement and Concrete Research,* 35**,** 1204-1209.

FERNÁNDEZ-JIMÉNEZ, A., PALOMO, A., SOBRADOS, I. & SANZ, J. 2006. The role played by the reactive alumina content in the alkaline activation of fly ashes. *Microporous and Mesoporous Materials,* 91**,** 111-119.

FERNÁNDEZ-JIMÉNEZ, A., PALOMO, J. G. & PUERTAS, F. 1999. Alkali-activated slag mortars: Mechanical strength behaviour. *Cement and Concrete Research,* 29**,** 1313-1321.

FERNÁNDEZ-JIMÉNEZ, A., PASTOR, J. Y., MARTı´N, A. & PALOMO, A. 2010. High-Temperature Resistance in Alkali-Activated Cement. *J. Am. Ceram. Soc.,,* 93**,** 3411-3417.

FERRARIS, C. F. 1995. Alkali-Silica Reaction and High Performance Concrete. *Report, Building and Fire Research Laboratory National Institute of Standards and Technology, Gaithersburg, MD 20899,* NISTIR5742**,** 24.

FIBRES UNLIMITED 2007. Test Report of Basalt fibre reinforced concrete, polypropylene reinforced concrete, polyacrylonitrile reinforced concrete. *Test Report. www.basalt-fibers.com/sites/default/files/FUBV_Test_Report.pdf***,** 11.

FIBRETECH 2001. METALX Stainless Steel Fibres offer new improvements in refractory performance, and new opportunities to reduce costs. *Technical Data Sheet. www.fibretech.com***,** 2.

FLETCHER, R. A., MCKENZIE, K. J. D., NICHOLSON, C. L. & SHIMADA, S. 2005. The composition range of aluminosilicate geopolymers. *Journal of European Ceramic Society,* 25**,** 1471-1477.

FOERSTER, S. C., GRAULE, T. & GAUCKLER, L. J. 1994. Strength and Toughness of Reinforced Chemically bonded ceramics. *Cement Technology, Ceramic Transactions, American ceramic Society,* 40**,** 247-256.

FONT, O. M., N.QUEROL, X., IZQUIERDO, M. A., E., DIEZ, S. E., J., ANTENUCCI, D. N., H., PLANA, F. L., A. & COCA, P. P., F. G. 2010. X-ray powder diffraction-based method for the determination of the glass content and mineralogy of coal (co)-combustion fly ashes. *Fuel,* 89**,** 2971-2976.

FORTA CORPORATION 1999. Fiber-Reinforced Shotcrete. *Technical Report FORTA Corporation and Technical Data Sheet. www.forta-ferro.com***,** 15.

FREITAS, A. A., SANTOS, R.L., COLACO, R., BAYAO HORTA, R., CANONGIA LOPES, J.N. 2015. From lime to silica and alumina: systematic modeling of cement clinkers using a general force field. *Phys.Chem.Chem.Phys.,* 17**,** 18477-18494.

FRENCH, D. & SMITHAM, J. 2007. Fly ash characteristics and feed coal properties. *CSIRO Energy Technology Research Report 73***,** 55.

GANI, M. S. J. 1997. Concrete. *Materials Forum,* 21**,** 171-185.

GASTUCHE, M. C., TOUSSAINT, F., FRIPIAT, J. J., TOUILLEAUX, R. & VAN MEERSCHE, M. 1962. Study of intermediate stages in the kaolin-metakaolin transformation. *Clay Minerals,* 5**,** 227-236.

GAY, C. & SANCHEZ, F. 2010. Performance of Carbon Nanofiber–Cement Composites with a High-Range Water Reducer. *Transportation Research Record: Journal of the Transportation Research Board, No. 2142, Transportation Research Board of the NationalAcademies, Washington, D.C.,* 2142**,** 109-113.

GEOPOLYMER GROUP CURTIN UNIVERSITY 2012. Cube Mould materials.

GHOSH, K. & GHOSH, P. 2012. Effect Of Na2o/Al2o3, Sio2/Al2o3 And W/B Ratio On Setting Time And Workability Of Flyash Based Geopolymer. *International Journal of Engineering Research and Applications (IJERA),* 2**,** 2142-2147.

GIANCASPRO, J., BALAGURU, P. N. & LYON, R. E. 2006. Use of Inorganic Polymer to Improve the Fire Response of Balsa Sandwich Structures. *J. Mater. Civ. Eng. ,* 18**,** 390-397.

GIESCHE, H. 2006. Mercury Porosimetry: A General (Practical) Overview. *Part.Part.Syst.Character,* 23**,** 11.

GLAD, B. E., HAN, C. & KRIVEN, W. M. 2012. Polymer Adhesion to Geopolymer via Silane Coupling Agent Additives. *J. Am. Ceram. Soc., ,* 95 3758-3762.

GLATZMAIER, G. C. & RAMIREZ, W. F. 1988. Use of volume averaging for the modeling of thermal properties of porous materials. *Chemical Engineering Science,* 43**,** 3157-3169.

GOŁASZEWSKI, J. & SZWABOWSKI, J. 2004. Influence of superplasticizers on rheological behaviour of fresh cement mortars. *Cement and Concrete Research,* 34**,** 235-248.

GOURLEY, J. T. 2014. Geopolymers in Australia. *Journal of the Australian Ceramics Society,* 50**,** 102-110.

GRANIZO, M. L., BLANCO VARELA, M. T. & MARTINEZ-RAMIREZ, S. 2007. Alkali Activation of metakaolins: Parameters affecting mechanical, structural and microstructural properties. *Journal of Materials Science,* 42**,** 2934-2943.

GREEN, D. W. & PERRY, R. H. 2007. Perry's Chemical Engineers' Handbook. *Book,* 8th Edition**,** 2-413, Table 2-305.

GREENHALGH, J. 2003. Segmental linings- the future is steel fibre reinforcement. *Concrete Magazine,* October**,** 19-20.

GUAN, S. W. 2003. 100% solids polyurethane and polyurea coatings Technology. *Coatings World***,** 49-58.

GUERRIERI, M. & SANJAYAN, J. G. 2010. Behavior of combined fly ash/slag-based geopolymers when exposed to high temperatures. *Fire and Materials,* 34**,** 163-175.

GURBA, L., HEIDRICH, C. & WARD, C. 2007. Coal Combustion Products Handbook. *Book, Publisher: Cooperative Research Centre for Coal in Sustainable Development*.

HAJIMOHAMMADI, A., PROVIS, J. L. & VAN DEVENTER, J. S. J. 2008. One-Part Geopolymer Mixes from Geothermal Silica and Sodium Aluminate. *Ind. Eng. Chem. Res. ,* 47**,** 9396-9405.

HAMEED, R., TURATSINZE, A., DUPRAT, F. & SELLIER, A. 2009. Metallic fibre reinforcedconcrete:Effect of fiber aspect ratio on the flexural properties. *ARPN Journal of Engineering and Applied Sciences,* 4**,** 67-72.

HANSEN, A. S. 1994. US Patent 5330827, 17-7-1994, Reinforcing Fibres and a method of producing the same. *US Patent 5330827***,** 11.

HARDJITO, D. & RANGAN, B. V. 2005. Development and Properties of low calcium fly ash based Geopolymer concrete. *Curtin University Research report GC-1*.

HE, X. Y., SUN, W., GAN, X. C., SU, Y. & YU, M. 2005. Influence of Wet-milling on Physico-chemical Properties and Strength of Fly Ash. *Journal of Wuhan University of Technology,* 12**,** 6.

HEIDRICH, C., FEUERBORN, H.-J. & WEIR, A. 2013. Coal Combustion Products: a Global Perspective. *Conference Paper. World of Coal Ash Conference, April 22-25 Lexington, KY.***,** 17.

HENRY, M., JOLIVET, J. & LIVAGE, J. 1992. Aqueous chemistry of metal cations: Hydrolysis, condensation and complexation. *In:* REISFELD, R. & JJØRGENSEN, C. K. (eds.) *Chemistry, Spectroscopy and Applications of Sol-Gel Glasses.* Springer Berlin Heidelberg.

HEO, Y. S., SANJAYAN, J. G., HAN, C. G. & HAN, M. C. 2012. Relationship between interaggregate spacing and optimum fibre length for spalling protection of concrete in fire. *Cement and Concrete Research,* 42**,** 549-557.

HERCULES FIBRES 2011a. D5 Product Overview. *Technical Data Sheet. www.herculesfibers.com***,** 2.

HERCULES FIBRES 2011b. D5 Product overview. *Technical Data Sheet*.

HERTZ, K. D. 2003. Limits of spalling of fire-exposed concrete. *Fire Safety Journal* 38**,** 103-116.

HIGGINS, L. 2008. HAZMAT Articles Chemistry of Fire. *Information sheet, Fire & Emergency Services Authority of Western Australia (FESA)***,** 2.

HOBART CORPORATION 2011. Hobart N50 mixer specification F-7533. *Specification***,** 4.

HONEYWELL 2010. SPECTRA® fiber 900 high-strength, light-weight polyethylene fiber. *Technical Data Sheet. www.honeywell.com/spectra***,** 2.

HU, S. G., WU, J. & WANG, F. Z. 2010. Preparation technology of high-strength and high-toughness lightweight aggregate concrete 7.

HUKSEFLUX THERMAL SENSORS, B. V. 2012. HFP 01. *Techncal Data Sheet***,** 6.

HURST, H. J., NOVAK, F., PATTERSON, J.H. 1996. Phase Diagram approach to the fluxing effect of additions of CaCO3 on Australian Coal Ash. *Energy and Fuel,* 10**,** 1215-1219.

IKAI, S., REICHERT, J. R., VASCONCELLOS, A. R. & ZAMPIERI, V. A. 2006. Asbestos free technology with new high tenacity PP-Polypropylene fibres in air cured Hatschek process. *Conference Paper, 10th International Inorganic bonded fibre composites conference, Sao Paolo, Brazil***,** 16.

IMERYS PERFORMANCE MINERALS 2010. MICA for polypropylene reinforcement. *Techncal Data Sheet***,** 2.

INSTITUTION OF ENGINEERS AUSTRALIA, W. P. O. F. E. T. N. C. O. S. E. 1989. Fire Engineering for Building Structures and Safety. *Report www.engineersaustralia.org.au*.

INTERNATIONAL ORGANISATION FOR STANDARDISATION 2010. ISO 11925-2:2010 Reaction to fire tests - Ignitability of products subjected to direct impingement of flame. Part 2: Single source flame.

JAMIESON, E. J., VAN RIESSEN, A., KEALLY, C. & HART, R. D. 2012. Development of bayer Geopolymer paste and use as Concrete. *Proceedings of the ninth International Alumina quality Workshop*.

JANSSON, A. 2008. Fibres in reinforced concrete structures - analysis, experiments and design. *Thesis, Department of Civil and Environmental Engineering Division of Structural Engineering CHALMERS UNIVERSITY OF TECHNOLOGY Göteborg, Sweden.***,** 66.

JEWELL, J. M., SHAW , C. M. & SHELBY, J. E. 1993. Effects of water content on aluminosilicate glasses and the relation to strong/fragile liquid theory. *Journal of Non-Crystalline Solids,* 152**,** 32-41.

JIANG, S., KIM, B.-G. & AïTCIN, P.-C. 1999. Importance of adequate soluble alkali content to ensure cement/superplasticizer compatibility. *Cement and Concrete Research,* 29**,** 71-78.

JONKER, A., MCCRINDLE, R. I. & VAN DER MERWE, M. J. 2009. Insulating Refractory Materials From Inorganic Waste Resources. *The Refractories Engineer***,** 14-18.

JUNG, T. H. & SUBRAMANIAN, R. V. 1994. Alkali Resistance enhancement of basalt fibres by hydrated zirconia films formed by the sol-gel process. *Journal of Material Research,* 9**,** 1006-1013.

KALIFA, P., CHÉNÉ, G. & GALLÉ, C. 2001. High-temperature behaviour of HPC with polypropylene fibres: From spalling to microstructure. *Cement and Concrete Research,* 31**,** 1487-1499.

KAMENNY VEK 2012. Basfiber for construction. *Technical Data Sheet. www.basfiber.com***,** 4.

KAMSEU, E., CERON, B., TOBIAS, H., E., L., BIGNOZZI, M. C., MUSCIO, A. & LIBBRA, A. 2012a. Insulating behavior of metakaolin-based geopolymer materials assess with heat flux meter and laser flash techniques. *J Therm Anal Calorim,* 108**,** 1189-1199.

KAMSEU, E., NAIT-ALI, B., BIGNOZZI, M. C., LEONELLI, C., ROSSIGNOL, S. & SMITH, D. S. 2012b. Bulk composition and microstructure dependence of effective thermal conductivity of porous inorganic polymer cements. *Journal of the European Ceramic Society* 32**,** 1593-1603.

KAMSEU, E., RIZZUTI, A., LEONELLI, C. & PERERA, D. 2010. Enhanced thermal stability in K_2O-metakaolin-based geopolymer concretes by Al_2O_3 and SiO_2 fillers addition. *J Mater Sci,* 45**,** 1715-1724.

KANI, N. E., ALLAHVERDI, A., PROVIS J.L. 2012. Efflorescence control based on geopolymer binders based on natural pozzolan. *Cement & Concrete Composites,* 34**,** 25-33.

KANTRO, D. L. 1980. Influence of Water-Reducing Admixtures on Properties of Cement Paste ,, A Miniature Slump Test. *Cement,Concrete. and Aggregates,* 2**,** 95-102.

KARBHARI, V. M. 1998. Short Carbon Fiber reinforced Concrete. *WTEC Monograph, Use of Composite Materials in Civil Infrastructure in Japan,* Chapter 2**,** 211.

KATZER, J. 2006. Steel Fibers and Steel Fiber Reinforced Concrete in Civil Engineering. *The Pacific Journal of Science and Technology,* 7**,** 53-58.

KENDALL, A., KEOLEIAN, G. A. & LEPECH, M. D. 2008. Materials design for sustainability through life cycle modeling of engineered cementitious composites. *Materials and Structures* 41**,** 1117-1131.

KHALE, D. C., R. 2007. Mechanism of geopolymerization and factors influencing its development: a review. *J Mater Science,* 42**,** 729-746.

KHAN, M. I. 2002. Factors affecting the thermal properties of concrete and applicability of its prediction models. *Building and Environment,* 37**,** 607-614.

KHOURY, G. A. 2000. Effect of fire on concrete and concrete structures. *Progress in Structural Engineering and Materials,* 2**,** 429-447.

KIM, J.-H. J., MOOK LIM, Y., WON, J. P. & PARK, H. G. 2010. Fire resistant behavior of newly developed bottom-ash-based cementitious coating applied concrete tunnel lining under RABT fire loading. *Construction and Building Materials,* 24**,** 1984-1994.

KINRADE, S. D. & POLE, D. L. 1992. Effect of Alkali-Metal Cations on the Chemistry of Aqueous Silicate Solutions. *Inorg. Chem. ,* 31**,** 4558-4563.

KIRK-OTHMER 1991. Sodium Aluminate production. *Encyclopedia of Chemical Technology,* volume 2 4th edition publisher John Wiley.

KLEMENS, P. G. & GELL, M. 1998. Thermal conductivity of thermal barrier coatings. *Materials Science and Engineering* A245**,** 143-149.

KLOBES, P., MEYER, K. & MUNRO, R. G. 2006. Porosity and Specific Surface Area Measurements for Solid Materials. *NIST Special Publication 960 -17***,** 91.

KOEHLER, E. P. 2009. Test Methods for Workability and Rheology of Fresh Concrete. *ACI Fall Convention Nov. 2009***,** 35.

KOEHLER, E. P. & FOWLER, D. W. 2003. Summary of Concrete Workability Test Methods. *ICAR 105-1 International Center for Aggregates Research The University of Texas at Austin***,** 93.

KONG, D., SANJAYAN, J. G. & SAGOE-CRENTSIL, K. 2007. Comparative performance of geopolymers made with metakaolin and fly ash after exposure to elevated temperatures. *Cement and Concrete Research,* 37**,** 1583-1589.

KONG, D., SANJAYAN, J. G. & SAGOE CRETSIL, K. 2005. Damage due to elevated temperatures in metakaolinite based geopolymer pastes. *Geopolymer Cements and Concrete conference 2005 Perth***,** 11.

KONG, D. L. Y. & SANJAYAN, J. G. 2008. Damage behavior of geopolymer composites exposed to elevated temperatures. *Cement and Concrete Composites,* 30**,** 986-991.

KONG, D. L. Y. & SANJAYAN, J. G. 2010. Effect of elevated temperatures on geopolymer paste, mortar and concrete. *Cement and Concrete Research,* 40**,** 334-339.

KONSTA-GDOUTOS, M. S., METAXA, Z. S. & SHAH, S. P. 2010. Highly dispersed carbon nanotube reinforced cement based materials. *Cement and Concrete Research,* 40**,** 1052-1059.

KOVALCHUK, G. & KRIVENCO, P. V. 2009. Producing fire and heat resistant geopolymers. Chapter 12. *Geopolymers; Structure,processing,properties and structural applications. Ed. Provis, J. L. and van Deventer, J.S.J.***,** 227- 266.

KRIVEN, W. M., BELL, J. & GORDON, M. 2008. Geopolymer Refractories for the Glass Manufacturing Industry. *Conference Paper, 64th Conference on Problems with glass***,** 8.

KRIVENKO, P. 2005. Development of alkaline cements supported by theory and Practice. *Conference Paper*.

KRUSS 2014. Contact angle theory. *web page. www.kruss.de/services/education-theoty/glossary/contact-angle*.

KUDER, K. G. & SHAH, S. P. 2010. Processing of high-performance fiber-reinforced cement-based composites. *Construction and Building Materials,* 24**,** 181-186.

KUMAR, R., KUMAR, S. & MEHROTRA, S. P. 2007. Towards sustainable solutions for fly ash through mechanical activation. *Resources, Conservation and Recycling,* 52**,** 157-179.

KUMAR, S., KOLAY, P., MALLA, S. & MISHRA, S. 2012. Effect of Multiwalled Carbon Nanotubes on Mechanical Strength of Cement Paste. *Journal of Materials in Civil Engineering***,** 84-91.

KUMAR, S. & KUMAR, R. 2010. Tailoring Geopolymer Properties Through Mechanical Activation of Fly Ash. *Conference paper. Second International Conference on Sustainable Construction Materials and Technologies***,** 8.

KURARAY 2007. Kuraray, Structural fibres for concrete reinforcement. *Company web site www.kuraray-am.com*.

KUTCHKO, B. K., AG. 2006. Fly ash characterisation by SEM_EDS. *Fuel,* 85**,** 2537-2544.

LAWSON, J. R. 2009. A History of Fire Testing: Past, Present, and Future. *Journal of ASTM International,* 6**,** 39.

LEE, G. W., PARK, M., KIMA, J., LEEB, J. I. & YOON, H. G. 2006. Enhanced thermal conductivity of polymer composites filled with hybrid filler. *Composites: Part A* 37**,** 727-734.

LEMOUGNA, P. N., MACKENZIE, K. J. D. & CHINJE MELO, U. F. 2011. Synthesis and Thermal Properties of inorganic polymers(Geopolymers for structural and refractory applications from volcanic ash. *Ceramics International,* 37**,** 3011-3018.

LEPECH, M. D., LI, V. C., ROBERTSON, R. E. & KEOLEIAN, G. A. 2008. Design of Green Engineered Cementitious Composites for Improved Sustainability. *ACI Materials Journal,* 105**,** 567-575.

LI, V. C. 1998. Engineered Cementitious Composites for Structural Applications*. *ASCE J. Materials in Civil Engineering,* 10**,** 66-69.

LI, V. C. & MAALEJ, M. 1996. Toughening in Cement Based Composites. Part II: Fiber Reinforced Cementitious Composites. *Cement & Concrete Composites* 18**,** 239-249.

LI, Z. 2011. Advanced Concrete Technology. *Book, published by John Wiley & Sons New Jersey*.

LIEFKE, E. 1999. Industrial Applications of foamed Inorganic polymers. *Conference Paper Geopolymere 99 proceedings***,** 189-199.

LIN, T., JIA, D., WANG, M., HE, P. & LIANG, D. 2009a. Effects of fibre content on mechanical properties and fracture behaviour of short carbon fibre reinforced geopolymer matrix composites. *Bulletin of materials science,* 32**,** 77-81.

LIN, T. S., JIA, D. C., HE, P. G. & WANG, M. R. 2009b. Thermomechanical and microstructural Characterisation of Geopolymers with alpha alumina particulate filler. *Int J Thermophys,* 30**,** 1568-1577.

LIPATOV, Y. A., GUTNIKOV, S. I., MANYLOV, M. S. & LAZORYAK, B. I. 2012. Effect of ZrO2 on the Alkali Resistance and Mechanical Properties of Basalt Fibers. *Inorganic Materials, © Pleiades*

Publishing, Ltd., 2012. Original Russian Text © Ya.V. Lipatov, S.I. Gutnikov, M.S. Manylov, B.I. Lazoryak, 2012, published in Neorganicheskie Materialy, 2012, Vol. 48, No. 7, pp. 858–864., 48**,** 751-756.

LIU, J., SUN, W., MIAO, C., ZHANG, Q. & LIU, J. 2012. Influence of Superplasticisers and Mineral Admixtures on the workability of Mortar at low water-binder ratio. *Proceedings Second international Conference on microstructural related Durability of Cementitious Composites.,* 11-13 April 2012, Amsterdam, The Netherlands**,** 8.

LORD, J. D. & MORRELL, R. 2006. Elastic Modulus Measurement. *Measurement Good Practice Guide No. 98. Published by the National Physical Laboratory, UK.***,** 100.

LOUISIANA TECHNICAL UNIVERSITY 2012. trenchless Technical centre. *Web page www.ttc.latech.edu*.

LYON, R. E. 1996. Fire response of geopolymer structural Composites. *Technical Note DOT/FAA/AR-TN95/22***,** 15.

LYON, R. E., BALAGURU, P. N., FODEN, M., SORATHIA, U., DAVIDOVITS, J. & DAVIDOVITS, D. 1997. Fire Resistant Aluminosilicate composites. *Fire and Materials,* 21**,** 67-73.

LYON, R. E. F., A.J. BALAGURU, P. DAVIDOVITS, J. DAVIDOVITS, M. 1999. Properties of Geopolymer matrix in Carbon Fibre Composites. *Geopolymer 99 Proceedings*.

MA, S., ZHENG, S., XU, H. & ZHANG, Y. 2007. Spectra of sodium Aluminate Solutions. *Trans.Nonferrous Met.Soc.China,* 17**,** 853-857.

MA, Y., HU, J. & YE, G. 2013. The pore structure and permeability of alkali activated fly ash. *Fuel,* 104**,** 771-780.

MACKENZIE, K. J. D. 2011. Inorganic polymers for environmental protection applications. *IOP Conference series: Materials Science and Engineering,* 18**,** 7.

MACLAREN, D. C. & WHITE, M. A. 2003. Cement: Its Chemistry and Properties. *Journal of Chemical Education,* 80**,** 623-635.

MAITLAND, C. F., BUCKLEY, C. E., O'CONNOR, B. H. & HART, R. D. 2011. Characterisation of porestructure of metakaolin derived geopolymers by neutron scattering and electron microscopy. *Journal of Applied Crystallography,* 44**,** 697-707.

MALVERN INSTRUMENTS 2012. A basic guide to particle characterisation. *Technical Bulletin* 26.

MALVERN INSTRUMENTS LTD 2005. Mastersizer 2000. *Product Bulletin***,** 12.

MANZUR, T. & YAZDANI, N. 2010. Strength Enhancement of Cement Mortar with Carbon Nanotubes Early Results and Potential. *Transportation Research Record: Journal of the Transportation Research Board, No. 2142, Transportation Research Board of the National Academies, Washington,D.C.,* 2142**,** 102–108.

MARCIANO, S., MUGNIER, N., CLERIN, P., CRISTOL, B. & MOULIN, P. 2006. Nanofiltration of Bayer process solutions. *Journal of Membrane Science,* 281**,** 260-267.

MASI, G. R., W.D.A., BIGNOZZI, M.C., VAN RIESSEN, A. 2014. The influence of short fibres and foaming agents on the physical and thermal behaviour of geopolymer composites. *CIMTEC conference presentation*.

MAZAHERIPOUR, H., GHANBARPOUR, S., MIRMORADI, S. H. & HOSSEINPOUR, I. 2011. The effect of polypropylene fibers on the properties of fresh and hardened lightweight self-compacting concrete. *Construction and Building Materials* 25**,** 351-358.

MCCORMICK, L. 2007. Metakaolin. *Materials Science of Concrete. www.people.ce.gatech.edu/~kk92/mkgrad.pdf*.

MEDRI, V., FABBRI, S., RUFFINI, A., DEDECEK, J. & VACCARI, A. 2011. SiC-based refractory paints prepared with alkali aluminosilicate binders. *Journal of the European Ceramic Society* 31**,** 2155-2165.

MEHTA, P. K. & MERYMAN, H. 2009. Tools for reducing carbon emissions due to Cement Consumption. *Structure Magazine,* January**,** 11-15.

MEMON, F. A., NURUDDIN, M. F., DEMIE, S. & SHAFIQ, N. 2012. Development of Fly ash-based Self-compacting Geopolymer Concrete. *eprints.utp.edu.my*.

MENAD, N. 2010. Sintering and Consolidation of Ceramics. *Lulea University Course KGP 003***,** 34.

METAXA, Z. S., KONSTA-GDOUTS, M. S. & SHAH, S. P. 2010. Carbon Nanofibre Reinforced Cement Based Materials. *Journal of the Transportation Research Board,***,** 114-118.

MINIFIBERS 2006. The Technology of Fybrel™ Synthetic Pulp in Fiber Cement. *Technical Data Sheet. www.minifibers.com***,** 5.

MINIFIBERS 2010. Polyethylene fibers Low-Melt LLDPE. *Technical Data Sheet. www.minifibers.com***,** 1.

MONTES, C. & ALLOUCHE, E. 2008. Applications of geopolymer concrete in the rehabilitation of waste water conveyance systems in extreme environments. *Conference Paper, 32nd international Conference and Exposition on Advanced Ceramic and Composites Daytona***,** 24.

MOOLENAAR, R. J., EVANS, J. C. & MCKEEVER, L. D. 1970. The Structure of the Aluminate Ion in Solutions at High pH. *Journal of Physical Chemistry, ,* 74**,** 3629-3636.

MORRISON, I. J. 2008. GRC Standards and testing. *Concrete* June**,** 12-13.

MOURA, D., VASCONCELOS, E., PACHECO-TORGAL, F. & DING, Y. 2011. Concrete Repair With Geopolymeric Mortars. Influence of Mortars Composition on their workability and mechanical strength. *repositorium.sdum.uminho.pt***,** 6.

MUNRO, R. G. 1997. Evaluated Material Properties for a Sintered alpha-Alumina. *J. Am. Ceram. Soc.,* 80**,** 1919-1928.

NAAMAN, N. A. 2003. Engineered Steel Fibres with optimal properties for reinforcement of cement composites. *Journal of Advanced Concrete Technology,* 1**,** 241-252.

NAAMAN, N. A. 2008. High Performance Fiber Reinforced Cement Composites. *Book, High Performance Construction Materials Science and Applications. World Scientific Publishing, Singapore,* Chapter 3**,** 91-153.

NAIK, T. R. 2002. Greener Concrete using Recycled Materials. *Concrete International,* July.

NASVI, M. C. M., RANJITH, P. G. & SANJAYAN, J. 2012. The permeability of geopolymer at down-hole stress conditions: Application for carbon dioxide sequestration wells. *Applied Energy* 7**,** 62-70.

NAZARI, A., RIAHI, S., RIAHI, S., SHAMEKHI, S. F. & KHADEMNO, A. 2010. Mechanical properties of cement mortar with Al2O3 nanoparticles. *Journal of American Science* 6**,** 94-97.

NEMATOLLAHI, B. & SANJAYAN, J. 2014. Effect of different superplasticizers and activator combinations on workability and strength of fly ash based geopolymer. *Materials and Design* 57**,** 667-672.

NEVILLE, A. M. 1995. Properties of Concrete. *Book, publisher: Longman group, Harlow***,** 148-149, 394-396, 513, 537-538.

NGUYEN THANG, X., KROISOVA, D., LOUDA, P. & BORTNOVSKY, O. 2010. Microstructure and flexural properties of geopolymer matrix-fibre reinforced composite with additives of alumina (Al2O3) nanofibres. *Texsci 2010, 7th international conference Czech republic***,** 8.

NIANYI , C. & HONGLIN, L. 1994. Structure and relative stability of the aluminate anion studied by quantum chemical methods. *Journal of Molecular Structure (Theochem), ,* 305**,** 283-286.

NICHOLSON, C., FLETCHER, R., MILLER, N., STIRLING, C., MORRIS, J., HODGES, S., MACKENZIE, K. & SCHUMUCKER, M. 2005. Building Innovation through Geopolymer Technology. *Chemistry in New Zealand*.

NILI, M. & AFROUGHSABET, V. 2010. The effects of silica fume and polypropylene fibers on the impact resistance and mechanical properties of concrete. *Construction and Building Materials* 24**,** 927-933.

NIPPONELECTRICGLASS. 2000. Control of plastic shrinkage cracking of concrete with ARG chopped strands. *Technical Data Sheet. www.negamerica.com***,** 7.

NIPPONELECTRICGLASS. 2007. High Zirconia Alkali resistant glass fibre. *Technical Data Sheet. www.negamerica.com***,** 12.

NIST 2001. Sintered Alumina Property Data Summary. *: NIST Structural Ceramics Database, SRD Database Number 30.***,** 3.

NUGTEREN, H. W., BUTSELAAR-ORTHLIEB, V. C. L. & IZQUIERDO, M. 2009. High Strength geopolymers from coal combustion fly ash. *Global Nest Journal,* 11**,** 155-161.

NUGTEREN, H. W., OGUNDIRAN, M. B., WITKAMP, G.-J. & KREUTZER, M. T. 2011. Coal Fly Ash Activated by waste sodium aluminate solutions as an immobiliser for toxic waste. *World of Coal Ash Conference Denver USA***,** 1-10.

NYCO MINERALS 2013. NYAD MG. *Technical Data Sheet***,** 2.

NYCON Nycon AR-DM. *Technical Data Sheet. www.nycon.com***,** 2.

NYCON 2009. Nycon G. *Technical Data Sheet. www.nycon.com***,** 2.

NYCON 2011a. NYCON-AR-HD (HIGH DISPERSION FIBERGLASS). *Technical Data Sheet. www.nycon.com*.

NYCON 2011b. Nycon-PVA RF4000 PVA (Polyvinyl Alcohol), Large Denier Macro, Superior Bond. *Technical Data Sheet. www.nycon.com***,** 2.

NYCON 2012. Nycon-PVA Macro, Micro fiber blend toughens slabs. *Web site www.concreteproducts.com*.

O'CONNOR, S. J., MACKENZIE, K. J. D., SMITH, M. E. & HANNA, J. E. 2010. Ion Exchange in charge balancing sites of Aluminosilicate Inorganic Polymers. *Journal of Materials Chemistry,* 20**,** 10234-10240.

OHIO COAL DEVELOPMENT OFFICE 2004. Fly Ash Enhanced Carbon Nanofiber-Reinforced High Strength Concrete. *Project CDO/D-99-14 Report***,** 7.

OKADA, K., IMASE, A., ISOBE, T. & NAKAJIMA, A. 2011. Capillary rise properties of porous geopolymers prepared by an extrusion method using polylactic acid (PLA) fibers as the pore formers. *Journal of the European Ceramic Society,* 31**,** 461-467.

ORICA CHEMICALS 2011. Sodium Aluminate S grade. *Product data sheet. www.orica.com*.

OUALIT, M., JAUBERTHIE, R., RENDELL, F., MELINGE, Y. & ABADLIA, M. T. 2012. External Corrosion to concrete sewers: a case study. *Urban Water Journal***,** 1-6.

PACHECO-TORGAL, F., CASTRO-GOMES, J. & JALALI, S. 2008a. Alkali-activated binders: A review. Part 2. About materials and binders manufacture. *Construction and Building Materials,* 22**,** 1315-1322.

PACHECO-TORGAL, F., CASTRO-GOMES, J. & JALALI, S. 2008b. Alkali-activated binders: A review: Part 1. Historical background, terminology, reaction mechanisms and hydration products. *Construction and Building Materials,* 22**,** 1305-1314.

PACHECO-TORGAL, F., CASTRO GOMES, J. P. & JALALI, S. 2008c. Durability of historic Mortars. *Historic mortars conference***,** 1-7.

PALACIOS, M. & PUERTAS, F. 2005. Effect of superplasticizer and shrinkage-reducing admixtures on alkali-activated slag pastes and mortars. *Cement and Concrete Research* 35**,** 1358-1367.

PALOMO, A. & FERNÁNDEZ-JIMÉNEZ, A. 2011. Alkali Activation Procedure for Transforming Fly Ash into New Materials Part 1: Applications. *World of Coal Ash(WOCA) conference***,** 14.

PALOMO, A., GRUTZECK, M. W. & BLANCO, M. T. 1999. Alkali Activated Fly Ashes: A cement for the future. *Cement and Concrete Research,* 29**,** 1323-1329.

PAN, Z., SANJAYAN, J. & RANGAN, B. V. 2011. Fracture Properties of Geopolymer Paste and Concrete. *Magazine of Concrete Research,* 63**,** 763-771.

PAN, Z. & SANJAYAN, J. G. 2012. Factors influencing softening temperature and hot-strength of geopolymers. *Cement & Concrete Composites* 34**,** 261-264.

PAN, Z., SANJAYAN, J. G. & RANGAN, B. V. 2009. An investigation of the mechanisms for strength gain or loss of geopolymer mortar after exposure to elevated temperature. *J Mater Sci* 44**,** 1873-1880.

PAN, Z., SANJAYAN, J.G. 2010. Stress-strain behaviour and abrupt loss of stiffness of geopolymer at elevated temperatures. *Cement & Concrete Composites,* 32**,** 657-664.

PANNEER SELVAM, R. & HALE, M. 2011. Evaluation of high temperature concrete for thermal Energy storage for solar power generation. *US DOE CSP programme***,** 29.

PAPWORTH, F. 2000. Affect of synthetic fibres and silica fume on explosive spalling of HPC exposed to fire. *South East Asia Construction, Singapore*, 6.

PENG, G. F., YANG, W.-W., ZHAO, J., LIU, Y.-F., BIAN, S.-H. & ZHAO, L.-H. 2006. Explosive spalling and residual mechanical properties of fiber-toughened high-performance concrete subjected to high temperatures. *Cement and Concrete Research* 36, 723-727.

PERRY, B. 2006. Synthetic macrofibres storm to the front of coastal defence innovation. *Concrete magazine,* November, 72-73.

PETERS, S. J., RUSHING, T. S., LANDIS, E. N. & CUMMINS, T. K. 2010. Nanocellulose and Microcellulose Fibers for Concrete. *Journal of the Transportation Research Board,Transportation Research Board of the National Academies, Washington,,* 2142, 25-28.

PHAIR, J. W. & VAN DEVENTER, J. S. J. 2001. Effect of silicate activator pH on the leaching and material characteristics of waste-based inorganic polymers. *Minerals Engineering,* 14, 289-304.

PHAIR, J. W. & VAN DEVENTER, J. S. J. 2002. Characterisation of Fly Ash based Geopolymeric Binders Activated with Sodium Aluminate. *Ind.Eng.Chem.Res.,* 41.

PHAIR, J. W., VAN DEVENTER, J. S. J. & SMITH, J. D. 2004. Effect of Al source and alkali activation on Pb and Cu immobilisation in fly-ash based ‘‘geopolymers". *Applied Geochemistry* 19, 423-434.

PORTLAND CEMENT ASSOCIATION 2012. What is ettringite and does it or the sulphate in cement contribute to expansion and disintegration of portland cement concrete? *Web page www.cement.org/tech/faq_DEF.asp*, 1.

PQ CORPORATION 2005. Fundamentals of Silicate Chemistry. *Brochure. www.pqcorp.com*.

PQ CORPORATION 2013. Typical Property Data for PQ® Liquid Sodium Silicates. *Technical Bulletin 17-2A. www.pqcorp.com*, 1.

PQ EUROPE 2004. Sodium and potassium silicates, versatile compounds for your applications. *brochure www.pqcorp.com*.

PROVIS, J. L. 2009. Activating solution chemistry for geopolymers Chapter 4. *Book Geopolymers Structure,processing and industrial applications. Ed. JL Provis and JSJ van Deventer Woodhead Publishing Ltd*, 50-71.

PROVIS, J. L. 2010. Fire Resistance of Geopolymer Concretes. *Project Report AOARD-084096, University of Melbourne.*, 8.

PROVIS, J. L. 2014. Geopolymer Schematic *Alkali Activated Materials: State of the art report, Rilem TC224-AAM pp1-9 Springer/RILEM, Dordrecht.*, 1.

PROVIS, J. L., HARREX, R. M., BERNAL, S. A., DUXSON, P. & VAN DEVENTER, J. S. J. 2012. Dilatometry of geopolymers as a means of selecting desirable fly ash sources. *Journal of Non-Crystalline Solids,* 358, 1930-1937.

PUERTAS, F., AMAT, T., FERNA´NDEZ-JIME´NEZ, A. & VA´ZQUEZ, T. 2003. Mechanical and durable behaviour of alkaline cement mortars reinforced with polypropylene fibres. *Cement and Concrete Research* 33, 2031-2036.

PUERTAS, F., MARTINEZ-RAMIREZ, S., ALONSO, S. & VASQUEZ, T. 2000. Alkali Activared Fly Ash/Slag Cement Strength behavior and hydration products. *Cement and Concrete Research,* 30, 1625-1632.

PURDON, A. O. 1940. The action of Alkalis on Blast Furnace Slag. *Journal of the Society of the Chemical Industrey,* 59, 191-202.

QUANTACHROME INSTRUMENTS 2013. Automatic pycnometers. *Brochure*, 4.

RAHIER, H., SIMONS, W., VAN MELE, B. & BIESEMENS, M. 1997. Low Temperature synthesized Aluminosilicate Glasses Part 3 Influence of thecomposition of the silicate solution on production,structure and properties. *Journal of Material Science,* 32, 2237-2247.

RAHIER, H., VAN MELE, B., BIESEMANS, M., WASTIELS, J. & WU, X. 1996. Low-temperature synthesized aluminosilicate glasses Part I Low-temperature reaction stoichiometry and structure of a model compound. *J Mater Sci,* 31, 71-79.

RAHIER, H., WASTIELS, J., BIESEMANS, M., WILLLEM, R., VAN ASSCHE, G. & VAN MELE, B. 2007. Reaction mechanism, kinetics and high temperature transformations of geopolymers. *J. Mater. Science,* 42**,** 2982-2996.

RAYZMAN, V., FILIPOVICH, I., NISSE, L. & VLASENKO, Y. 1998. Sodium Aluminate from Alumina-Bearing Intermediates and Wastes. *JOM*.

REES, C. A. 2007. Mechanism and kinetics of gel formation in geopolymers. *PhD thesis, University of Melbourne*.

REID, M. 2011. Window or door frame. *UK Patent Application GB 2478535 A CSENG Ventures***,** 13.

REOCO PERFORMANCE FIBRES 2011. Adfil Ignis. *Technical Data Sheet***,** 1.

REOFORCETECH 2012a. Basalt Fibre Reinforcement Technology. *Technical Data Sheet. www.reforcetech.com***,** 2.

REOFORCETECH 2012b. BFRP Minibars. *Technical Data Sheet. www.reforcetech.com***,** 2.

RICKARD, W. D. A. 2012. Assessing the suitability of fly ash geopolymers for high temperature applications. *PhD thesis, Curtin University*.

RICKARD, W. D. A., KEALLEY, C. S. & VAN RIESSEN, A. 2014. Thermally induced microstructural changes in fly ash geopolymers: experimental results and proposed model. *Journal of the American Ceramic Society***,** 1-11.

RICKARD, W. D. A., TEMUUJIN, J. & VAN RIESSEN, A. 2012. Thermal Analysis of geopolymer pastes synthesised from five fly Ashes of variable composition. *Journal of Non-Crystalline Solids***,** 10.

RICKARD, W. D. A., VAN RIESSEN, A. & WALLS, P. 2010. Thermal Character of Geopolymers Synthesized from Class F Fly Ash Containing High Concentrations of Iron and alpha-Quartz. *Int. J. Appl. Ceram. Techn. ,* 7**,** 81-88.

RICKARD, W. D. A., VAN RIESSEN, A. 2014. Performance of solid and cellular structured fly ash geopolymers exposed to a simulated fire. *Cement and concrete composites,* 48**,** 75-82.

RICKARD, W. D. A., VICKERS, L. & VAN RIESSEN, A. 2013. Performance of fibre reinforced, low density metakaolin geopolymers under simulated fire conditions. *Applied Clay Science,* 73**,** 71-77.

RICKARD, W. D. A., WILLIAMS, R., TEMUUJIN, J. & VAN RIESSEN, A. 2011. Assessing thesuitability of three Australian fly Ashes as an aluminosilicate source for geopolymers in high temperature applications. *Materials Science and Engineering: A 528***,** 3390-3397.

RILEM TC129MHT COMMITTEE 1995. 129-MHT Test Methods for mechanical properties of concrete at high temperature. *Materials and structures,* 28**,** 410-414.

RILL, E., LOWRY, D. R. & KRIVEN, W. M. 2010. Properties of Basalt Fiber Reinforced Geopolymer Composites. *Strategic Materials and Computational Design.* John Wiley & Sons, Inc.

ROBINSON, S. 2006. Wollastonite strength in legacy. . *Conference paper, Fillers 2006***,** 47.

RODRIQUEZ, R., HOWSER, R. & MO, Y. L. 2010. Structural Behavior of Self-Consolidating Carbon Nanofiber Concrete. *University of Houston report***,** 32.

ROLLETT, A. D. 2007. L8: Thermal Properties.

ROMUALDI, J. P. & BATSON, G. B. 1963. Behaviour of reinforced Concrete Beams with closely spaced Reinforcement. *Journal of the American Concrete Institute,* 60**,** 775-790.

ROMUALDI, J. P. & MANDEL, J. A. 1964. Tensile strength of concrete affected by uniformly distributed and closely spaced short lengths of wire reinforcement. *Journal of the American Concrete Institute,* 61**,** 657-672.

ROSS, A. 2009. Steel fibre reinforced concrete (SFRC) – Quality, performance and specification. *Conference paper New Zealand concrete conference 09***,** 7.

ROSS, A. 2012. Steel Fibre reinforced Concrete(SFRC) combined with conventional reinforcing. *Concrete in Australia***,** 1.

ROSTAMI, H. & BRENDLEY, W. 2003. Alkali Ash Material: A novel Fly Ash Cement. *Environmental Science and Technology,* 37**,** 3454-3457.

ROTSTEIN, C. 2011. New Developments in the research of strain herdening concrete. *Conference Paper, 2011 Concrete Institute Conference, Perth 2011*.

ROUSSEL, N., STEFANI, C. & LEROY, R. 2005. From mini-cone test to Abrams cone test: measurement of cement-based materials yield stress using slump tests. *Cement and Concrete Research* 35**,** 817-822.

ROWLES, M. & O'CONNOR, B. H. 2003. Chemical optimisation of the compressive strength of aluminosilicate geopolymers synthesised by sodium silicate activation of metakaolinite. *J. Mater. Chem.,* 13**,** 1161-1165.

ROY, D. M. 1999. Alkali Activated Cements, Opportunities and Challenges. *Cement and Concrete Research,* 29**,** 249-254.

SAMPLING TECHNOLOGIES 2012. What is XRF technology. *Web page www.sampletech.com.au***,** 2.

SCHEFFLER, C., FÖRSTER, T., MÄDER, E., HEINRICH, G., HEMPEL, S. & MECHTCHERINE, V. 2009. Aging of alkali-resistant glass and basalt fibers in alkaline solutions: Evaluation of the failure stress by Weibull distribution function. *Journal of Non-Crystalline Solids,* 355**,** 2588-2595.

SCRIVENER, K. 2011. Straight talk with Karen Scrivener on cements, CO2 and sustainable development. *American Ceramic Society Bulletin,* 91**,** 47-50.

SCRIVENER, K. L., CRUMBIE, A. K. & LAUGESEN, P. 2004. The Interfacial Transition Zone (ITZ) Between Cement Paste and Aggregate in Concrete. *Interface Science Kluwer Academic Publishers.,* 12**,** 411-421.

SERWAY, A. S. 1992. Physics for Scientists and Engineers with modern physics, 3rd edition. *Book, Chapter 20, published by Saunders HBJ Florida***,** 526-559.

SHACKLETON, J. F. 2005. Introduction to Materials Science for engineers. *Book,* 6th edition**,** 257-260.

SHI, C., KRIVENKO, P. & ROY, D. M. 2006. Alkali Activated Cements and Concretes. *Book, publisher Taylor & Francis, Abingdon UK,* Capter 11**,** 277- 297.

SHI, C. & MO, Y. L. 2008. High Performance Construction Materials Science and Applications. *Book, High Performance Construction Materials Science and Applications. World Scientific Publishing, Singapore*.

SILVA, F. J., MATHIAS, A. F. & THAUMATURGO, C. 1999. Evaluation of the fracture Toughness in poly(sialate-siloxo) Composite matrix. *Conference Paper, Geopolymere 99***,** 97-106.

SILVA, F. J. & THAUMATURGO, C. 2003. Fibre reinforcement and fracture response in geopolymeric materials. *Fatigue Fract. Engng. Mater. Struct.,* 26.

SILVERSTRIM, T., ROSTAMI, H., LARRALDE, J. & SAMADI, A. 1997. Fly Ash Cementitious Material and a Method of making aproduct. *US Patent 5601643***,** 10.

SING, K. S. W. 1985. Reporting Physisorption Data for Gas/Solid Systems with Special Reference to the Determination of Surface Area and Porosity. *Pure & Appl. Chem.,* 57**,** 603-619.

SIPOS, P. 2009. The structure of Al(III) in strongly alkaline aluminate solutions — A review. *Journal of Molecular Liquids* 146**,** 1-14.

SKVARA, F., SVOBODA, P., DOLEZAL, J., KOPECKY, L., PAWLASOVA, S., MYSKOVA, L., LUCUK, M., DVORACEK, K., BEKSA, M. & SULC, R. 2006. Concrete based on Fly Ash Geopolymer. *10th east Asia-Pacific Conference on Structural Engineering and Construction***,** 407-412.

SOFI, M., VAN DEVENTER, J. S. J., MENDIS, P. A. & LUKEY, G. C. 2007. Engineering Properties of Inorganic polymer Concretes(IPCs). *Cement&Concrete Research* 37**,** 251-257.

SOUTHERN IONICS 2006. Sodium Aluminate, 38%. *Product Bulletin. www.southernionics.com*.

STANDARDS AUSTRALIA 2005. AS1530.4 - 2005 Methods for fire tests on building materials, components and structures - Fire resistance test of elements of construction.

STAVINOHA, R. 1991. Protecting Concrete from exposure to aggressive chemicals. *Concrete Construction,* July**,** 3.

STEINS, P., POULESQUEN, A., DIAT, O. & F, F. 2012. Structural Evolution during Geopolymerization from an Early Age to Consolidated Material. *Langmuir* 28**,** 8502-8510.

STEPHENS, R. 2009. Coal sludge Flood and Public Response, Roane County Tennessee. *Disaster response, Environmental Health, Environmental Health Professionals***,** 7.

SUBAER & VAN RIESSEN, A. 2007. Thermo-mechanical and microstructural characterisation of sodium-poly(sialate-siloxo) (Na-PSS) geopolymers. *J Mater Sci* 42**,** 3117-3123.

SWAMY, R. N. & MANGAT, P. S. 1974. Influence of fiber geometry on the properties of steel fiber reinforced concrete. *Cement and Concrete Research,* 4**,** 451-465.

SWEETMAN, B. 2011. F35B concrete Buster. *Defense Technology International,* October 2011**,** 36.

TARADA, F. & KING, M. 2009. Structural fire protection of railway tunnels. *Conference Paper. Railway Engineering Conference, University of Westminster, UK, 24-25 June 2009***,** 10.

TASKIRAN, M. U., DEMIRKOL, N., CAPOGLU, A. 2005. A new porcelinised stoneware material based on Anorthite. *Journal of the European Ceramic Society,* 25**,** 293-300.

TCHAKOUTE KOUAMOA, H., MBEYA, J. A., ELIMBIA, A., KENNE DIFFOA, B. B. & NJOPWOUO, D. 2012. Synthesis of volcanic ash-based geopolymer mortars by fusion method: Effects of adding metakaolin to fused volcanic ash. *Ceramics International,* 39**,** 1613-1621.

TECHNOBASALT 2012. Chopped basalt fibres. *web page www.technobasalt.com*.

TEMUUJIN, J., MINJIGMA, A., RICKARD, W. & VAN RIESSEN, A. 2012. Thermal properties of spray-coated geopolymer-type compositions. *J Therm Anal Calorim* 107**,** 287-292.

TEMUUJIN, J., MINJIGMAA, A., RICKARD, W., LEE, M., WILLIAMS, I. & VAN RIESSEN, A. 2009a. Preparation of metakaolin based geopolymer coatings on metal substrates as thermal barriers. *Applied Clay Science,* 46**,** 265-270.

TEMUUJIN, J., MINJIGMAAB, A., RICKARD, W., LEE, M., WILLIAMS, I. & VAN RIESSEN, A. 2010. Fly ash based geopolymer thin coatings on metal substrates and its thermal evaluation. *Journal of Hazardous Materials* 180**,** 748-752.

TEMUUJIN, J. & VAN RIESSEN, A. 2009. Effect of fly ash preliminary calcination on the properties of geopolymer. *Journal of Hazardous materials,* 164**,** 634-639.

TEMUUJIN, J., VAN RIESSEN, A. & WIILLIAMS, R. 2009b. Influence of Calcium compounds on the mechanical properties of fly ash geopolymer pastes. *Journal of Hazardous materials,* 167**,** 82-88.

TEMUUJIN, J., WILLIAMS, R. P. & VAN RIESSEN, A. 2009c. Effect of mechanical activation of fly ash on the properties of geopolymer cured at ambient temperature. *Journal of Materials Processing Technology,* 209**,** 5276-5280.

TEMUUJIN, T., RICKARD, W. D. A., LEE, M. & VAN RIESSEN, A. 2011. Preparation and thermal Properties of Fire Resistant Metakaolin based geopolymer type coatings. *Journal of Non-Crystalline solids,* 357**,** 1399-1404.

THANG, X. N., KROISOVA, D., LOUDA, P. & O., B. 2010. Microstructure and flexural strength properties of geopolymer matrix-fibre reinforced composite with additives of alumina (Al2O3) nanofibres. *Conference Paper 7th International Conference - TEXSCI 2010 September 6-8, Liberec, Czech Republic***,** 8.

THE QUARTZ PAGE 2012. Quartz, Dependence of structure on temperature. *web page www.quartzpage.de*.

TONOLI, G. H. D., RODRIGUES FILHO, U. P., SAVASTANO JR, H., BRAS, J., BELGACEM, M. N. & ROCCO LAHR, F. A. 2009. Cellulose modified fibres in cement based composites. *Composites: Part A* 40**,** 2046-2053.

TOUTANJI, H., MCNEIL, S. & BAY, Z. 1998. Chloride permeability and impact resistance of polypropylene fiber reinforced silica fume concrete. *Cement and Concrete Research,* 28**,** 961-968.

TRAN, D. H., KROISOVÁ, D., LOUDA, P., BORTNOVSKY, O. & BEZUCHA, P. 2009. Effect of curing temperature on flexural properties of silica-based geopolymer-carbon reinforced composite. *Journal of Achievements in Materials and Manufacturing Engineering* 37**,** 492-497.

TRANSPORTATION RESEARCH BOARD 2006. Control of Cracking in Concrete, State of the Art. *Transportation Research Circular,* E-C107**,** 56.

VAN ALKEN, S. 2012. Cracking at the unheated side of a tunnel during the heating and cooling phase of a fire. *MSc Thesis, Delft University of Technology*.

VAN DEVENTER, J. S. J. & PROVIS, J. L. 2014. Alkali Activated Materials State of the Art report, RILEM TC 224-AAM. publisher: Springer Dordrecht. *Book*.

VAN DEVENTER, J. S. J., PROVIS, J. L., DUXSON, P. & LUKEY, G. C. 2007. Reaction mechanisms in the geopolymeric conversion of inorganic waste to useful products. *Journal of Hazardous materials,* 139**,** 506-513.

VAN JAARSVELD, J. G. S. & VAN DEVENTER, J. S. J. 1999. Effect of the Alkali Metal Activator on the Properties of Fly Ash-Based Geopolymers. *Ind. Eng. Chem. Res. ,* 38**,** 3932-3941.

VAN JAARSVELD, J. G. S., VAN DEVENTER, J. S. J. & LORENZEN, L. 1997a. The potential use of geopolymeric materials to immobilise toxic metals: Part I. Theory and applications. *Minerals Engineering,* 10**,** 659-669.

VAN JAARSVELD, J. G. S., VAN DEVENTER, J. S. J. & LUKEY, G. C. 2003. The characterisation of source materials in fly ash based geopolymers. *Material Letters,* 57.

VAN JAARSVELD, J. S. G., VAN DEVENTER, J. S. J. & LORENZEN, L. 1997b. The potential use of Geopolymeric materials to immobilise toxic metals. Part 1 Theory & Application. *Minerals Engineering,* 10**,** 659-669.

VAN OSS, H. G. 2012. Cement. *US Geological Survey,Mineral Commodity Summaries***,** 1-2.

VAN OSS, H. G. 2014a. Cement. *USGS report. Mineral Commodities Summaries***,** 2.

VAN OSS, H. G. 2014b. Iron and steel slag. *USGS report. Mineral Commodities Summaries***,** 2.

VAN RIESSEN, A. 2010. Geopolymer Highlights. *CSRP 2010 Geopolymer Conference***,** 22.

VAN RIESSEN, A. & CHEN TAN, N. 2013. Beneficiation of Collie fly ash for synthesis of geopolymer: Part 1 – Beneficiation. *Fuel* 106**,** 569-575.

VAN RIESSEN, A., RICKARD, W. & SANJAYAN, J. 2009. Thermal properties of Geopolymers. *Book. Geopolymers: Structure, Processing, Properties and Industrial Applications. Edited by JL Provis and JAS van Derventer. Woodhead Publishing Ltd***,** 315-342.

VAN ZIJL, G. P. A. G. & WITTMANN, F. H. 2010. On Durability of SHCC. *Journal of Advanced Concrete Technology,* 8**,** 261-271.

VAOU, V., PANIAS, D. & LABORATORY OF METALLURGY, S. O. M. 2010. Thermal insulating foamy geopolymers from perlite. *Minerals Engineering 23 (2010) 1146–1151,* 23**,** 1146-1151.

VERA-AGULLO, J., CHOZAS-LIGERO, V., PORTILLO-RICO, D. & GARCIA-CASAS, M. J. 2009. Mortar and concrete reinforced with nanomaterials. *Nanotechnology in Construction,* 3**,** 383-388.

VERDOLOTTI, L., IANNACE, S., LAVORGNA, M. & LAMANNA, R. 2008. Geopolymerization reaction to consolidate incoherent pozzolanic soil. *J Mater Sci,* 43**,** 865-873.

VICKERS, L., VAN RIESSEN, A. & RICKARD, W. D. A. 2014. Strategies to control the high temperature shrinkage of fly ash based geopolymers. *Thermochimica Acta,* 580**,** 20-27.

VIJAI, K., KUMUTHAA, R. & VISHNURAMB, B. G. 2012. Properties of glass fibre reinforced geopolymer concrete composites. *Asian Journal of civil engineering (building and Housing),* 13**,** 511-520.

VITRO MINERALS 2010. Portland Cement and Pozzolans Technical Background for the Effective Use of VCAS Pozzolans in Portland Cement Concrete. *Technical Data Sheet. www.VitroMinerals.com*.

WALLEVIK, O. H. 2011. Rheology my way of life. *36th Conference on Our World in Concrete & Structures, Singapore, August 14-16, 2011*.

WAN, H., SHUI, Z. & LIN, Z. 2004. Analysis of geometric characteristics of GGBS particles and their influences on cement properties. *Cement & Concrete Research,* 34**,** 133-137.

WANG, C. & NIU, D. 2012. Research on the durability of polypropylene fiber concrete under freeze-thaw damage. *Conference Paper, Second International Conference on Microstructural-related Durability of Cementitious Composites, 11-13 April 2012, Amsterdam, The Netherlands***,** 6.

WANG, M.-R., JIA, D.-C., HE, P.-G. & ZHOU, Y. 2011. Microstructural and mechanical characterization of fly ash cenosphere/metakaolin-based geopolymeric composites. *Ceramics International,* 37**,** 1661-1666.

WANG, S. D. & SCRIVENER, K. L. 1995. Hydration products of alkali activated slag cement. *Cement and Concrete Research,* 25**,** 561-571.

WANG, X. H., JACOBSEN, S., LEE, S. F., HE, J. Y. & LIANG ZHANG, Z. L. 2010. Effect of silica fume, steel fiber and ITZ on the strength and fracture behavior of mortar. *Materials and Structures* 43**,** 125-139.

WANG, Y., LI, V. C. & BACKER, S. 1991. Tensile failure mechanisms in synthetic fibre-reinforced mortar. *J Mater Sci,* 26**,** 6565-6575.

WASHINGTON MILLS 2008. Duramul. *Technical data sheet. www.washingtonmills.com*.

WEEKMANN, S. 1997. Chapter 2 The Thermopile. *MSc Thesis Virginia tech.*

WENG, L. & SAGOE-CRETSIL, K. 2007. Dissolution processes, hydrolysis and condensation reactions during geopolymer synthesis: Part I—Low Si /Al ratio systems. *J Mater Science,* 42**,** 2997-3006.

WILD, S., KHATIB, J. M. & JONES, A. 1996a. Relative strength, pozzolanic activity and cement hydration in superplasticised metakaolin concrete. *Cement and Concrete Research,* 26**,** 1537-1544.

WILD, S., KHATIB, J. M. & JONES, A. 1996b. Relative strength,pozzolanic activity and cement hydration in superplasticised metakaolin concrete. *Cement and Concrete Research, ,* 26**,** 1537-1544.

WILLIAMS, R. P., HART, R. D. & VAN RIESSEN, A. 2011. Quantification of the Extent of Reaction of Metakaolin-Based Geopolymers using X-Ray Diffraction, Scanning Electron Microscopy, and Energy-Dispersive Spectroscopy. *J. Am. Ceram. Soc.,* 94**,** 2663-2670.

WILLIAMS, R. P. & VAN RIESSEN, A. 2010. Determination of the reactive component of fly ashes for geopolymer production using XRF and XRD. *Fuel,* 89**,** 3683-3692.

WIMPENNY, D., ANGERER, W., COOPER, T. & BERNARD, S. 2009. The use of steel and synthetic fibres in concrete under extreme conditions. *Conference Paper concrete solutions 09,* paper 4b-5**,** 10.

WON, J. P., KANG, H. B., LEE, S. J. & KANG, J. W. 2012. Eco-friendly fireproof high-strength polymer cementitious composites. *Construction and Building Materials,* 30**,** 406-412.

XIAO, L. Z., WEI, X. S. & LI, Z. J. 2011. Retarding effect of superplasticizer on the hydration of Portland cement. 8.

XU, H. & VAN DEVENTER, J. S. J. 2000. The geopolymerisation of alumino silicate materials. *International Journal of Mineral Processing,* 59**,** 247-266.

YATSENKO, N. D. & RAT'KOVA, E. O. 2003. Refactory ceramics based on local materials. *Glass and Ceramics,* 62**,** 15-16.

YAZDANBAKHSH, A., GRASLEY, Z., TYSON, B. & ABU AL-RUB, R. K. 2010. Distribution of Carbon Nanofibers and Nanotubes in Cementitious Composites. *Journal of the Transportation Research Board,No. 2142, Transportation Research Board of the National Academies, Washington,D.C., 2010.,* 2142**,** 89-95.

YILMAZ, V. T., ODABA¢OĞLU, M., İÇBUDAK, H. & ÖLMEZ, H. 1993. The degradation of cement superplasticizers in a high alkaline solution. *Cement and Concrete Research,* 23**,** 152-156.

YIP, C. K., LUKEY, G. C., PROVIS, J. L. & VAN DEVENTER, J. S. J. 2008. Effect of calcium silicate sources on geopolymerisation. *Cement and Concrete Research* 38**,** 554-564.

YLLMAZ, V. T., ODABASOGLU, M., ICBUDAK, H. & OLMEZ, H. 1993. The degradation of cement superplasticizers in a high alkaline solution. *Cement and concrete research,* 23**,** 152-156.

YUNSHENG, Z., WEI, S. & ZONGJIN, L. 2006. Impact behavior and microstructural characteristics of PVA fiber reinforced fly ash-geopolymer boards prepared by extrusion technique. *J Mater Sci,* 41**,** 2787-2794.

YUNSHENG, Z., WEI, S., ZONGJIN, L., XIANGMING, Z. & CHAU CHUNGKONG, E. 2008. Impact properties of geopolymer based extrudates incorporated with fly ash and PVA short fiber. *Construction and Building Materials* 22**,** 370-383.

ZHANG, S., LI, G. Z. & YUAN, H. Y. 2011. Effect of the chemical Treated Kevlar fibre on the behaviours of cement. *Advanced Materials Research,* 306-307**,** 758-761.

ZHANG , Z., YAO, X. & WANG, H. 2010. Thermochemistry study of the effect of alkali content on the early geopolymerisation at room temperature. *Conference, CAMS 2010***,** 8.

ZHANG, Z., YAO, X., ZHU, H., HUA, S. & CHEN, Y. 2009. Preparation and mechanical properties of polypropylene fiber reinforced calcined kaolin-fly ash based geopolymer. *J. Cent. South Univ. Technol. ,* 16**,** 0049-0052.

ZHANG, Z. Y., X. WANG, H., YAO, X. & ZHU, H. 2010. Potential application of geopolymers as protection coatings for marine concrete: II. Microstructure and anticorrosion mechanism. *Applied Clay Science,* 49**,** 7-12.

ZHAO, R. & SANJAYAN, J. 2012. Geopolymer and Portland cement concretes in simulated fire. *Magazine of Concrete Research,* 63**,** 163-173.

ZHU, H. J., YAO, X. & ZHANG, Z. H. 2010. Study on non-cement based Alkali Activated material for Oil and Gas well cementing at low to moderate temperatures. *Conference paper*.

ZIVICA, V. & BAJZA, A. 2001. Acidic attack of cement based materials — a review.: Part 1. Principle of acidic attack. *Construction and Building Materials,* 15**,** 331-340.

ZUHUA, Z., XIAO, Y., HUAJUN, Z. & YUE, C. 2009a. Role of water in the synthesis of calcined kaolin-based geopolymer. *Applied Clay Science* 43**,** 218-223.

ZUHUA, Z., XIAO, Y., HUAJUN, Z. & YUE, C. 2009b. Role of water in the synthesis of calcined kaolin-based geopolymer. *Applied Clay Science,* 43**,** 218-223.